ASME
SETTING THE STANDARD

# Journal of Fluids Engineering

Published Monthly by ASME

VOLUME 130 • NUMBER 8 • AUGUST 2008



**Transactions of the ASME, Journal of Fluids Engineering** (ISSN 0098-2202) is published monthly by The American Society of Mechanical Engineers, Three Park Avenue, New York, NY 10016. Periodicals postage paid at New York, NY and additional mailing offices.
POSTMASTER: Send address changes to Transactions of the ASME, Journal of Fluids Engineering, c/o THE AMERICAN SOCIETY OF MECHANICAL ENGINEERS, 22 Law Drive, Box 2300, Fairfield, NJ 07007-2300.
**CHANGES OF ADDRESS** must be received at Society headquarters seven weeks before they are to be effective. Please send old label and new address.
**STATEMENT from By-Laws.** The Society shall not be responsible for statements or opinions advanced in papers or ... printed in its publications (B7.1, Par. 3).


## SPECIAL ISSUE ON FLUID MECHANICS AND RHEOLOGY OF COMPLEX FLUIDS AND ELECTRICAL EFFECTS AT THE MICRO AND NANO SCALE

## EDITORIAL



## RESEARCH PAPERS

### Non-Newtonian Behavior and Rheology



### Electrical Effects at the Macro and Micro Scale



(Contents continued on inside back cover)

This journal is printed on acid-free paper, which exceeds the ANSI Z39.48-1992 specification for permanence of paper and library materials. ♾™
♻ 85% recycled content, including 10% post-consumer fibers.

Journal of Fluids Engineering Volume 130, Number 8 AUGUST 2008



## Suspensions and Soret Effect



The ASME Journal of Fluids Engineering is abstracted and indexed in the following:

*Applied Science & Technology Index, Chemical Abstracts, Chemical Engineering and Biotechnology Abstracts (Electronic equivalent of Process and Chemical Engineering), Civil Engineering Abstracts, Computer & Information Systems Abstracts, Corrosion Abstracts, Current Contents, Ei EncompassLit, Electronics & Communications Abstracts, Engineered Materials Abstracts, Engineering Index, Environmental Engineering Abstracts, Environmental Science and Pollution Management, Excerpta Medica, Fluidex, Index to Scientific Reviews, INSPEC, International Building Services Abstracts, Mechanical & Transportation Engineering Abstracts, Mechanical Engineering Abstracts, METADEX (The electronic equivalent of Metals Abstracts and Alloys Index), Petroleum Abstracts, Process and Chemical Engineering, Referativnyi Zhurnal, Science Citation Index, SciSearch (The electronic equivalent of Science Citation Index), Shock and Vibration Digest, Solid State and Superconductivity Abstracts, Theoretical Chemical Engineering*

Journal of Fluids Engineering

# Editorial

The theme of this special issue of JFE is the flow behavior and Rheology of complex fluids and electric phenomena at the micro and nano scale. The papers are drawn from those presented at the IMECE2006 and FEDSM 2007 in related Symposia sponsored by the Fluids Engineering Division and the Materials Division organized by Dennis Siginer.

It is well known that many fluids in engineering applications, such as polymer melts and solutions, muds and drilling fluids in petroleum industry, food products, cosmetics, paints and others, present non-Newtonian behavior. They exhibit features such as shear-thinning or shear-thickening, normal stress differences in shearing flows, viscoplasticity, extension-hardening and memory effects due to elasticity. The first seven papers in this collection address issues at the forefront of this area. The next set of five papers explores aspects of the increasingly important applications of electrical effects both at the macro and micro level such as electro-chemical machining, electrowetting and dielectrophoresis, and the last set of three papers look at cold spray, a very promising new coating technique, and the Ludwig-Soret effect which plays an important role in reservoir engineering.

The rate of material processing in film casting and fiber spinning, widely used multi-purpose industrial manufacturing processes, is limited by the draw resonance instability. Beyond a critical draw ratio, the ratio of the take-up velocity to the velocity at the die exit, stable operation is impossible as the instability results in a spatio-temporal periodic variation in film thickness. Since take-up velocity is much greater than the velocity at the die exit, the conservation of mass requires change in the cross-sectional area. Thus, the film thickness is reduced to a desired value at the take-up point by choosing the appropriate draw ratio. Inertial effects on film casting have been widely ignored in the literature. Inertia can, however, have a significant effect on the stability. Radoslav German and Roger E. Khayat examine the effects of inertia, elasticity and boundary conditions on the film casting of a PTT fluid and show that inertia plays an important role in the process and has a stabilizing effect on the film-casting flow. They also demonstrate that the choice of stress boundary conditions becomes important with increasing fluid elasticity.

The study of confined and/or free surface swirling flows due to rotating top and bottom covers of cylindrical containers yields a wealth of information about the fundamental behavior of viscoelastic fluids and instabilities in strong flows. This geometry is also used in testing the validity of the predictions of constitutive equations. Shinji Tamano et al. report an experimental study of strong flows of surfactant solutions much less prone to degradation than polymeric fluids in cylindrical casings of aspect ratio one and two using a sectional flow visualization technique and a two-component laser Doppler velocimetry (LDV) system and compare their results to the behavior of polymer solutions. Perhaps more importantly they find that the popular Giesekus model cannot predict the flow structure.

Products made from liquid crystalline polymers (LCP) have many advantages over conventional polymers, higher modulus and higher heat resistance among others. It is generally thought that the alignment structure of the LCP molecules is the cause of these useful properties. However, it is difficult to control the LCP structure in a molding process, because the flow behavior of LCP strongly depends on its deformation history and there is a variety of complicated geometries used in the molding flows. Takatsune Narumi et al. report an experimental study of the unstable behavior which is manifested as wavy textures in elongational flows in a curved slit geometry with a right-angle corner in an L-shaped channel of a solution of LCP, hydroxyl-propylcellulose (HPC).

Applications of liquid thread breakup are widespread in industry such as encapsulation processes for controlled drug delivery, inkjet printing, spray drying of starches, spray painting, and emulsification. The physics of Newtonian liquid thread breakup is understood well enough. In contrast, the analysis of viscoelastic liquid threads and the breakup of purely viscous, shear-thinning non-Newtonian liquid threads are still in their infancy. While similarity solutions explain the singularity of the jet at breakup, they are unable to predict drop sizes or drop shapes in shear-thinning jets. To address this limitation V. Dravid et al. report the effect of power-law shear-thinning behavior when the filament is two-dimensional and axisymmetric by solving the entire Navier–Stokes equations at $Re=5$ and compare model predictions against experimental data obtained using jets of power-law non-Newtonian fluids exiting from capillary tubes. Drop formation from these capillary jets is captured using a high speed digital camera. They report good agreement.

Surfactant solutions are extensively used in many industrial processes, examples of which are foaming, jet printing, emulsification and coating. The practical importance of surfactants is based on the ability of these molecules to quickly reach an equilibrium state at the freshly created solution/air interface, thus decreasing the surface tension from the value of bulk solution to the equilibrium value at the surface (DST). Hasegawa et al. propose a new model based on the concept that surfactant molecules rotate during the process of reaching the equilibrium surface state. This is different from the conventional adsorption theory. They obtain a simple expression of DST as a function of the surface age. In addition, an experiment is carried out to determine DST by measuring the period and weight of droplets falling from a capillary. The predictions of the proposed model are compared to their own experimental data and to those reported previously by several other authors, and good agreement is shown. Furthermore, the characteristic time in the model is shown to be correlated with the concentrations of solutions regardless of the type of solution examined.

Welan gum, a commercially available highly stable biopolymer, is extensively pumped through straight and coiled tubing in various petroleum installations. It is suitable for drag reduction and viscosity enhancement in many oil and gas production operations including hydraulic fracturing, acidizing, wellbore cleanup, cementing and drilling. Fluid flow behavior in coiled tubing differs significantly from that in straight tubing. Asubiaro and Shah report an extensive experimental investigation of the behavior of Welan gum suspensions of different concentrations in straight and coiled tubing and develop correlations for the friction factor.

Computational methods to solve non-Newtonian flow problems

  

are afflicted by numerical instabilities and spurious oscillations. In the case of purely viscous inelastic fluids highly steep and non-smooth viscosity models are the cause of locally advection dominated regions and severe gradients. Zinani and Frey present a Galerkin least-squares (GLS) multi-field finite element formulation for extra-stress, velocity and pressure as primal variables for the approximation of inelastic non-Newtonian fluid flows. GLS enhances the stability of the classical Galerkin approximation for incompressible flows and also circumvents compatibility between the approximation functions of stress, velocity and pressure.

Electro-Chemical Machining (ECM) is an advanced machining technology widely used in aerospace, defense and medical industries among others. The applications of ECM in the automobile and turbo-machinery manufacturing also have been on the rise because ECM has no tool wear and difficult-to-cut metal parts and complex geometries can be machined with relatively high accuracy and extremely smooth surfaces. Fujisawa et al. develop a multi-physics model and the associated numerical procedure to predict the ECM process. The model and the numerical procedure satisfactorily simulated a typical ECM process for a two-dimensional flat plate and for a three-dimensional compressor blade.

Light-emitting diodes (LED) are an attractive alternative to incandescent bulbs and fluorescent lamps. The typical life span of LEDs is about ten years, twice as long as fluorescent lamps and approximately twenty times longer than the incandescent bulbs. They generate much less thermal energy than incandescent bulbs with the same light output and are free of environmental pollutants such as neon, helium, and argon discharged from fluorescent lamps. Lighting modules with combination of red, green, and blue LEDs can emit light of an intended color without additional color filters that traditional lighting methods adopt. Kim et al. investigate a combination of discrete red, green, and blue LEDs to realize a high efficacy white LED. Compared to red and blue LEDs, green LED leaves much more room for improvement in luminescent efficacy. The production of green LEDs by metal organic vapor phase epitaxy (MOVPE) is closely related to the ability to grow InGaN/GaN multi-quantum-wells (MQWs) with high indium compositions. Kim et al. report their study of the characterization of three different commercial MOVPE reactors for performance enhancement.

The manipulation of discrete droplets has seen rapid development from engineering to life sciences including variable focus lenses, display technology, fiber-optics, and lab-on-a-chip devices. Accurate description of actuation forces and resultant droplet velocities must be available when designing an integrated device making use of discrete flows. Currently the leading methods for electrostatically actuating microdroplets in microfluidic devices are electrowetting on dielectric (EWOD) for conductive droplets and dielectrophoresis (DEP) for electrically insulating droplets. In each case, a transverse electric field is used to create an electrostatic pressure giving rise to the transport of individual liquid slugs. Young and Mohseni examine the nature of the force distribution for both EWOD and DEP actuated droplets and the effect of system parameters such as contact angle and electrode length on the shape of the force density.

Micro-pumps have many applications in medical devices, portable fuel cells and electronic cooling among others. Mechanical micro-pumps with moving parts are subject to high friction wear, generate noise and are not appropriate for applications with high pressure requirements such as chromatography and micro-cooling of power electronics. In contrast electro-kinetic (EK) pumps, which convert electrical energy into kinetic energy in the fluid do not suffer from these disadvantages. One of the most popular EK pumps is the electro-osmotic (EO) pump. It is very cheap to fabricate in comparison to other EK pumps and can generate high pressure with a small volume substrate. Nevertheless, because the shear stress is confined to a thin Debye layer, EO pumps suffer from high viscous dissipation and exhibit a very low thermodynamic efficiency like all other EK pumps. In addition, Faradaic reactions at the electrodes generate bubbles by electrolysis and change the pH of the working fluid limiting the continuous operation of EO pumps to a few hours. Berrouche et al. present a new theory for optimizing the thermodynamic efficiency of an EO pump with a large surface area and highly charged nano-porous silica disk substrate.

Dielectrophoresis (DEP) and traveling wave dielectrophoresis (twDEP) are very effective AC electrokinetic techniques for the manipulation and separation of particles in micro- and nano-fluidics for instance biological particles such as DNA, cells, and bacteria. AC field suppresses undesirable electrolytic effects such as Faradaic reactions and electro-convection in the liquid, and employs polarization forces that are insensitive to the particle charge making dielectrophoresis a vastly superior method. Song and Bennett solve the electric potential equation with mixed type of boundary conditions for dielectrophoresis and traveling wave dielectrophoresis generated by an interdigitated parallel electrode array.

The cold spray is a novel and promising coating technology and was originally developed in the mid-1980s at the Institute of Theoretical and Applied Mechanics of the Russian Academy of Sciences in Novosibirsk. In the conventional cold spray process, powder particles are accelerated through the momentum transfer from the supersonic gas jet. The temperature of supersonic gas jet is always lower than the melting point of the powder material. Thus the coating is formed from the particles in solid state and the problems associated with traditional thermal spray methods are eliminated. The adhesion of the particles in a cold spray process occurs only when the kinetic energy is large enough to cause their extensive plastic deformation at the contact surface. Takana et al. explore the use of electrostatic force to assist the acceleration of the particles in addition to the acceleration imparted by supersonic flow, and Samareh and Dolatabadi examine the effect of the presence of a dense particulate flow on the supersonic gas.

Ludwig-Soret effect refers to the phenomenon of component separation in a convection free liquid or gaseous mixture under a temperature gradient. This separation mechanism is of importance in petroleum engineering applications as it can in tandem with natural convection greatly influence the composition distribution in hydrocarbon reservoirs. Jaber et al. report a numerical study based on a non-equilibrium irreversible thermodynamic model of the Soret effect for a ternary mixture in a porous cavity.

In closing I would like to convey my thanks and appreciation to the authors and the anonymous reviewers for their contributions to this special issue.

**Dennis A. Siginer**
**Associate Editor**

# Interplay Between Inertia and Elasticity in Film Casting

**Radoslav German**

**Roger E. Khayat**[1]
e-mail: rkhayat@eng.uwo.ca

Department of Mechanical and Materials Engineering,
The University of Western Ontario,
London, ON, N6A 5B9, Canada

*The influence of inertia and boundary conditions on the steady state and stability of isothermal film casting of viscoelastic fluids is examined using a Phan-Thien–Tanner rheological model. The elongational flow between the die exit and the take-up point is investigated. In general, the steady-state film tends to contract for low-inertia flow; this contraction, however, is significantly diminished by inertia. The polymeric normal stresses and primary normal stress difference decrease in the most of the air gap as inertia increases. In contrast, the stress and stress difference increase considerably near the take-up point due to a dramatic increase in the elongation rate. The linear stability analysis for two-dimensional disturbances is carried out. For a polymer with no degradation, and in the absence of inertia ($Re=0$), the analysis predicts critical draw ratios that form an envelope to an unstable region. This region of unstable conditions reduces as inertia increases. Two branches of neutral stability curve are observed for higher-inertia flow as opposed to a single curve for $Re=0$. The unstable region expands as $\alpha$ increases, where $\alpha$ is a measure of polymer degradation. When $\alpha$ becomes sufficiently large, the elasticity tends to destabilize the flow. It is also found that boundary conditions have an important influence on the steady-state profiles and stability region, particularly for high-elasticity fluids.* [DOI: 10.1115/1.2956592]

## 1 Introduction

Draw resonance is an important phenomenon occurring in processes, such as film casting and fiber spinning. In film casting, a molten polymer is extruded through a slit die, stretched in the ambient air, and then cooled on the chill roll. The process is schematically illustrated in Fig. 1. Since the take-up velocity is much greater than the velocity at the die exit, the conservation of mass requires change in the cross-sectional area. Thus, the film thickness is reduced to a desired value at the take-up point by choosing the appropriate draw ratio (ratio of the take-up velocity to the velocity at the die exit). Film casting is frequently limited at high take-up rates by an oscillatory variation in film thickness. There exists a critical draw ratio, beyond which stable operation is impossible. When this draw ratio is exceeded, draw resonance occurs and spatiotemporal periodic variation in film thickness is observed.

Due to the importance of the problem in industrial applications, a number of studies have been carried out dealing with theoretical as well as experimental aspects of the subject. Experimental studies typically focused on the temperature and velocity variation in the cast film as a function of a position within the air gap [1–3]. Yeow [4] was the first to investigate the problem numerically. He carried out the stability analysis of film-casting flow. Surface tension, aerodynamic drag, inertia, and gravity were neglected in his study, and small curvature and uniform streamwise velocity across the film were assumed. The analysis confirmed the importance of the draw ratio in controlling the onset of draw resonance. The theoretical results for casting a Newtonian fluid under isothermal, constant force conditions show that the process is unstable for a draw ratio greater than a value of 20.21, which is identical to the critical value for fiber spinning [5].

However, it is well known that commercial film casting can be operated at a draw ratio higher than 20.21 without encountering instability. Several factors can contribute to this enhanced stability. Chief among these is the non-Newtonian behavior of the material being cast. Extensive work has been done to investigate non-Newtonian effects stemming from shear-thinning or viscoelastic effects. Another important factor is inertia. Considering inertia, gravity, and surface tension forces respectively, Shah and Pearson [6] assessed their effects on stability of fiber spinning. Their work showed that, in addition to the draw ratio, these three terms also play very important roles in fiber spinning stability. While inertial and gravity forces enhance flow stability, surface tension destabilizes the flow. Inertia becomes particularly important in modern high-speed film casting, and its coupled effect with elasticity is the main object of the present study. Aird and Yeow [7] examined the film casting of inelastic power-law fluid. They derived an analytical steady-state solution and carried out a linear stability analysis. It was found that the critical draw ratio increases with power-law index. Anturkar and Co [8] examined the influence of elasticity on draw resonance. They carried out a linear stability analysis for isothermal film casting of a modified convected-Maxwell fluid. Their results indicate that film casting is stable below a lower critical draw ratio and above an upper critical draw ratio. They also showed that shear-thinning fluids are less stable and fluids with higher relaxation time are more stable when used in film casting. An isothermal and a nonisothermal steady-state analysis of the film casting of a BKZ-type fluid was carried out by Alaie and Papanastasiou [9]. It was concluded that thinning of the extruded film is enhanced by shear thinning and by air-cooling often down to solidification at about the glass transition temperature upstream the chill roll. The required tension decreases with shear thinning and increases with relaxation time. The temperature profile along the film departs from linear, as the temperature of the cooling air decreases to about ambient level. Steady-state and stability analyses of film casting of a modified Giesekus fluid were carried out by Iyengar and Co [10,11]. Both linear and nonlinear stability analyses were conducted. In the linear analysis, the eigenvalue problem was treated as an initial-value problem (the standard approach used by the former researchers and scientists) [4,7,8]. They found that the behavior of the elongational viscosity (extensional thinning or thickening) affects the critical draw ratio and the film stability. Recently, Doufas and McHugh [12] carried out numerical analysis of melt spinning using a model coupling the polymer microstructure with the macroscopic velocity/stress and temperature fields. They included the effect of

[1]Corresponding author.

Contributed by the Fluids Engineering Division of ASME for publication in the JOURNAL OF FLUIDS ENGINEERING. Manuscript received February 19, 2007; final manuscript received August 24, 2007; published online July 23, 2008. Assoc. Editor: Dennis Siginer.

  

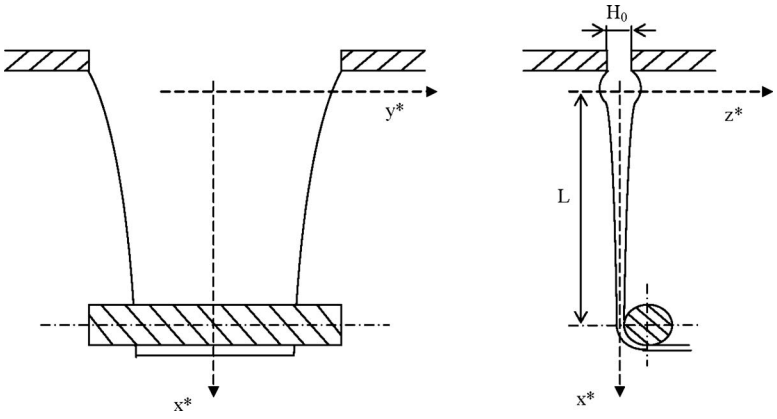


**Fig. 1 Schematic of film-casting flow and coordinates used**

flow-induced crystallization, viscoelasticity, filament cooling, air drag, inertia, surface tension, and gravity. They report a good quantitative agreement with experimental data of nylon 6,6 for fiber velocity, diameter, and temperature fields.

The choice of boundary conditions in film casting and fiber spinning analyses becomes complicated when a viscoelastic fluid is considered. In addition to the velocities at the die exit and take-up point, conditions on stress are also needed. In some previous works, the stress at the die exit is assumed to be purely Newtonian, based on the assumption that in this region polymer molecules have not been significantly stretched yet [13]. Denn et al. [14] carried out an asymptotic analysis of fiber spinning for limit case of a highly viscoelastic fluid and found that initial stresses have minor effect on the flow. Anturkar and Co [8] and Silagy et al. [15] calculated the axial stress at the die exit from a fully developed flow inside the die. Their analysis indicates that the velocity profiles and tensile force are influenced by exit stress conditions except for nearly inelastic fluids and for very large tensile force [8]. In an analysis of fiber spinning, Beris and Liu [16] derived an estimate of the ratio between the radial and axial stress components assuming a homogeneous steady elongational flow at the maximum die swell and the limiting value of the Deborah number derived by Denn et al. [14]. They used this estimate as a boundary condition. A combination of stress conditions proposed by Anturkar and Co [8] and Beris and Liu [16] was used in the work of Iyengar and Co [10]. Upon comparison of results obtained based on slit flow and planar elongation flow at the die swell, they concluded that corresponding stress profiles differ only near the die exit and quickly converge to the same solution. The importance of stress boundary conditions has also been recognized in the case of multimode models. Christodoulou et al. [17] examined the stability of multimode Phan-Thien–Tanner (PTT) fluids and showed that the stability region at relatively high De is sensitive to the choice of stress conditions. The stable region was found to be larger (smaller) when the longest (shortest) mode of the streamwise elastic stress is left unspecified and all other elastic stress components are set to zero at the inflow boundary. Tsou and Bogue [18] examined theoretically and experimentally the effect of die flow variables on the stability of isothermal fiber spinning. In general, they observed that increasing the shear rates, which subsequently increases die swells, is destabilizing.

In this work, the PTT constitutive equation is used to examine the film-casting process. This constitutive model was introduced by PTT [19,20] to analyze strong flows (such as fiber spinning or film casting). Results of the steady-state analysis showed a good agreement with experimental data when inertia is negligible. Using the same model, Lee et al. [21] investigated the dynamic behavior of the nonisothermal melt spinning. The spinline cooling was found to have a stabilizing effect on the process. Silagy et al. [15] used an isothermal, time dependent two-dimensional membrane model in combination with the PTT constitutive equation to analyze the film-casting process. The onset of draw resonance was studied by the linear stability analysis and through the dynamic response to small perturbations. They showed that the onset of draw resonance depends on the aspect ratio (ratio of length to width of the film in the air gap) of the process. Christodoulou et al. [17] conducted a linear stability analysis of film casting using the multimode PTT constitutive equation. They used the fitted PTT relation in a finite-element model of the stability of film-casting flow based on the thin-membrane approximation.

Inertial effects on film casting have been widely ignored in the literature. Inertia can, however, have a significant effect on the stability region and its value may still be small but not negligible, as experiments [3,12] on film casting and fiber spinning suggest. In the present study, the effects of inertia, elasticity, and boundary conditions are examined for the film casting of a PTT fluid. Linear stability analysis is carried out. It is shown that inertia plays an important role in the process and has a stabilizing effect on the film-casting flow. It is also shown that the choice of stress boundary conditions becomes important with increasing elasticity in the fluid.

## 2 Problem Formulation and Solution Procedure

In this section, the flow configuration is introduced and the general conservation and constitutive equations as well as the boundary conditions are briefly reviewed. The disturbance equations for film casting are then derived and the resulting eigenvalue problem is discussed.

**2.1 General Equations.** Consider the film-casting process as illustrated schematically in Fig. 1. Here $L$ is the film length (air gap) between the channel exit and the take-up point, and $H_0$ is the die gap at the die or channel exit. The mean velocity at the die exit is $U_0$. The coordinates $x^*$, $y^*$, and $z^*$ coincide with the streamwise, spanwise, and depthwise directions of the flow, respectively. The film is taken to be symmetric with respect to the $z^*$ axis. In this case, $z^*=h^*(x^*,y^*,t^*)$ denotes the free surface height of half width of the film. The thin-film flow is assumed to be isothermal and incompressible. The fluid is taken as a viscoelastic polymeric solution of density $\rho$, relaxation time $\theta$, and viscosity $\mu$. In this study, inertia is assumed to be important, while gravity and surface tension effects are neglected. The polymeric solution is assumed to be composed of a Newtonian solvent of viscosity $\mu_S$, and a polymeric solute of viscosity $\mu_P$, such that the solution viscosity is given by $\mu=\mu_S+\mu_P$.

Regardless of the nature of the fluid, the continuity and momentum conservation equations must hold. The conservation of mass and linear momentum equations for an incompressible fluid can be written, respectively, as

$$u^*_{i,i} = 0 \tag{1}$$

$$\rho(u^*_{i,t*} + u^*_j u^*_{i,j}) = \sigma^*_{ji,j} \tag{2}$$

where $i$, $j = x^*$, $y^*$, $z^*$. Here $t^*$ is time, $u^*_x$, $u^*_y$, and $u^*_z$ are the velocity components in the streamwise, spanwise, and depthwise directions, respectively, and $\sigma^*_{ij}$ are the components of the total stress tensor. The summation convention is assumed, and a subscript after a comma denotes partial differentiation. The deviatoric part of the stress tensor is composed of a Newtonian component, corresponding to the solvent, and a polymeric component $\tau^*_{ij}$, corresponding to the solute. Thus, $\sigma^*_{ij} = -p^*\delta_{ij} + \mu_S(u^*_{i,j} + u^*_{j,i}) + \tau^*_{ij}$, where $p^*$ is the hydrostatic pressure and $\delta_{ij}$ is the Kronecker delta. The constitutive equation for $\tau^*_{ij}$ is taken to correspond to PTT fluid, which can be written as [19,20]

$$\exp\left(\frac{\alpha\theta}{\mu_p}\mathrm{tr}(\boldsymbol{\tau}^*)\right)\tau^*_{ij} + \theta\left(\frac{d\tau^*_{ij}}{dt^*} - \tau^*_{ik}L^*_{jk} - \tau^*_{jk}L^*_{ik}\right) = \mu_p(u^*_{i,j} + u^*_{j,i}) \tag{3}$$

where $d/dt^*$ is the convective derivative, and

$$L^*_{ij} = u^*_{i,j} - \frac{1}{2}\xi(u^*_{i,j} + u^*_{j,i}) \tag{4}$$

is the effective gradient and $\alpha$ and $\xi$ are the material parameters. The term containing $\alpha$ is related to the rate of destruction of junctions in polymeric network and $\xi$ depends on the shear rate [20]. All calculations reported here were carried out with $\xi = 0$, since the flow is predominantly elongational [13]. In this case, the shear viscosity is constant except for negligible contribution due to nonzero $\alpha$ [22].

The boundary conditions for the problem consist of free surface and edge conditions. At the free surface, $z^* = h^*(x^*, y^*, t^*)$, the kinematic condition reads

$$u^*_z = h^*_{,t^*} + u^*_x h^*_{,x} + u^*_y h^*_{,y} \tag{5}$$

In the absence of surface tension (which is typically negligible for polymeric flow), the dynamic condition reflects the vanishing of the traction at the free surface, namely,

$$\sigma^*_{ij}\mathbf{n}_j = 0 \tag{6}$$

where $\mathbf{n}$ is the normal vector at the free surface. At the die of channel exit, both the velocity and the film thickness are assumed to be specified. The thickness is also specified at the take-up point (see below). The imposition of adequate stress conditions is an important issue, since the flow and the stability diagram are strongly influenced by these conditions. This issue will be examined in detail in Sec. 3.

**2.2 Reduced Equations and Boundary Conditions.** In the film-casting process, the span of the film is very large compared with its thickness and is often much larger than the distance between the die and the take-up point. The film contraction in the spanwise direction ($y^*$) can thus be neglected, and the flow can be considered as two dimensional. Note in this case that the edge bead phenomenon will not be accounted for. Given the small thickness of the film, the equations above are reformulated in the thin-film limit. In this case the velocity $u^*_x$, stress $\tau^*_{xx}$, and pressure $p^*$ are only functions of $x^*$ and $t^*$. This approximation ignores any die swell near the die exit. Based on the calculations of the velocity profile development in fiber spinning, Keunings et al. [22] suggested that, within a small region from the die exit, the axial velocity becomes uniform across the film. It is convenient to cast the governing equations and boundary conditions in dimensionless form. The dimensionless variables may be introduced as follows:

$$(x,z) = \frac{1}{L}(x^*, z^*), \quad t = \frac{U_0}{L}t^*, \quad u_i = \frac{u^*_i}{U_0}, \quad h = \frac{h^*}{L}$$

$$(\sigma_{ij}, \tau_{ij}, p) = \frac{L}{\mu U_0}(\sigma^*_{ij}, \tau^*_{ij}, p^*) \tag{7}$$

In addition to the fluid parameters $\alpha$ and $\xi$, there are five similarity groups that emerge in the problem, namely, the Reynolds number, Re, the Deborah number De, the solvent-to-solute viscosity ratio $R_v$, the draw ratio $D_r$, and the aspect ratio $\varepsilon$, which are explicitly written as

$$\mathrm{Re} = \frac{\rho U_0 L}{\mu}, \quad \mathrm{De} = \frac{\theta U_0}{L}, \quad R_v = \frac{\mu_s}{\mu_p}, \quad D_r = \frac{U_L}{U_0}, \quad \varepsilon = \frac{H_0}{L} \tag{8}$$

Another related parameter is the solute-to-solution viscosity ratio, or $a = 1/R_v + 1$. The scaling above is adopted for convenience and is not meant to help reduce Eqs. (1)–(3) to those corresponding to thin-film casting. This was already done by Schultz and Davis [23] for fiber spinning and is being implemented here for film casting. The reduced one-dimensional transient equations below are obtained as the leading order terms in the thin-film double expansion in the thinness variable $z$ and the thinness parameter $\varepsilon$. This double expansion, based on the separation-of-variable property of the Navier–Stokes equations noted in 1921 by von Karman, is necessary and sufficient for mathematical closure at each order. The reader is referred to the works of Bechtel et al. for the analogous perturbation theory for slender jets, with pointwise expansion of the stresses [24], and with stresses integrated over the cross section [25]. In this case, the governing equations relevant to the problem reduce to the following dimensionless form of the continuity equation (1):

$$u_{x,x} + u_{z,z} = 0 \tag{9}$$

and the momentum conservation equation (2) in the $x$ direction:

$$\mathrm{Re}(u_{x,t} + u_x u_{x,x}) = \sigma_{xx,x} + \sigma_{xz,z} \tag{10}$$

Since $\sigma_{xx}$ is only function of $x$ and $t$, an integration of Eq. (10) between 0 and $h$ gives

$$\mathrm{Re}h(u_{x,t} + u_x u_{x,x}) = h\sigma_{xx,x} + \sigma_{xz}\big|^h_0 \tag{11}$$

In the absence of surface tension, the dynamic condition, which consists of the vanishing of the traction at the free surface, reduces to

$$\sigma_{xx}n_x + \sigma_{xz}n_z = 0, \quad \sigma_{zx}n_x + \sigma_{zz}n_z = 0 \tag{12}$$

where $n_x$ and $n_z$ are the components of the unit outward normal to the free surface in the $x$ and $z$ directions, respectively. Noting that $n_x/n_z = -h_{,x}$, the depthwise shear and normal stress components become

$$\sigma_{zx} = h_{,x}\sigma_{xx}, \quad \sigma_{zz} = (h_{,x})^2\sigma_{xx} \tag{13}$$

Noting that the dimensionless height $h$ is scaled with respect to $L$, $\sigma_{zz}$ becomes of second order in the slope of the film height, which is typically small for drawn film. Hence, the depthwise stress component becomes negligible everywhere $\sigma_{zz} \approx 0$. Substituting the first expression of Eq. (11) into Eq. (9) gives

$$\mathrm{Re}h(u_{x,t} + u_x u_{x,x}) = (h\sigma_{xx})_{,x} \tag{14}$$

The dimensionless components $\sigma_{xx}$ and $\sigma_{zz}$ of the total stress tensor can be expressed as follows:

$$\sigma_{xx} = -p + 2aR_v u_{x,x} + \tau_{xx}, \quad \sigma_{zz} = -p + 2aR_v u_{z,z} + \tau_{zz} \tag{15}$$

Since $\sigma_{zz}(x,h,t) \approx 0$ and $u_{z,z} = -u_{x,x}$, combination of expressions (15) leads to

$$\sigma_{xx} = 4aR_v u_{x,x} + \tau_{xx} - \tau_{zz} \tag{16}$$

Upon substitution of expression (16) into Eq. (14) the momentum conservation equation in the $x$ direction becomes

$$\mathrm{Re}h(u_{x,t} + u_x u_{x,x}) = \lfloor h(4aR_v u_{x,x} + \tau_{xx} - \tau_{zz})\rfloor_{,x} \tag{17}$$

Since $u_z = dh/dt$ at the free surface, the continuity equation and the kinematic condition can be combined to give

$$h_{,t} + (hu_x)_{,x} = 0 \tag{18}$$

As the flow is predominantly elongational, the quadratic shear terms in the stress equations can be neglected. In this case, the relevant dimensionless constitutive equations for PTT fluid reduce to

$$\exp\left[\frac{\alpha \mathrm{De}}{a}\mathrm{tr}(\boldsymbol{\tau})\right]\tau_{xx} + \mathrm{De}[\tau_{xx,t} + u_x\tau_{xx,x} - 2(1-\xi)\tau_{xx}u_{x,x}] = 2au_{x,x} \tag{19}$$

$$\exp\left[\frac{\alpha \mathrm{De}}{a}\mathrm{tr}(\boldsymbol{\tau})\right]\tau_{zz} + \mathrm{De}[\tau_{zz,t} + u_x\tau_{zz,x} + 2(1-\xi)\tau_{zz}u_{x,x}] = -2au_{x,x} \tag{20}$$

The boundary conditions are prescribed as follows. The velocity is given at the die exit and at the take-up point. The film thickness and stress components are given at the die exit only, so that

$$u_x(t,x=0) = h(t,x=0) = 1, \quad u_x(t,x=1) = D_r$$

$$\tau_{xx}(t,x=0) = \tau_{xx}^0, \quad \tau_{zz}(t,x=0) = \tau_{zz}^0 \tag{21}$$

where $\tau_{xx}^0$ and $\tau_{zz}^0$ will be specified below. The solution procedure of the above stated problem is described in the next section. As mentioned earlier, Eqs. (18)–(20) correspond to equations to leading order in $\varepsilon$ and is therefore ceases to be valid under some flow conditions [24,25]. A related issue is the transition of the quasilinear hyperbolic type of the equations to mixed elliptic/hyperbolic type, depending on the relative magnitudes of the dimensional groups. A simulation, which begins hyperbolic and evolves into the ill-posed mixed at a particular time and place, corresponds to a departure from slender behavior and breakdown of the one-dimensional theory, which is indicative of the onset of failure [26].

**2.3 Linear Stability Analysis.** In this section, the formulation for linear stability analysis is presented. Given the unavailability of the steady-state solution in analytical form, the steady state is obtained as part of the eigenvalue problem. In this case the film thickness, velocity, and stress components are written as

$$h(x,t) = h^s(x) + h'(x)e^{\lambda t}$$

$$u_x(x,t) = u_x^s(x) + u_x'(x)e^{\lambda t}$$

$$\tau_{xx}(x,t) = \tau_{xx}^s(x) + \tau_{xx}'(x)e^{\lambda t}$$

$$\tau_{zz}(x,t) = \tau_{zz}^s(x) + \tau_{zz}'(x)e^{\lambda t} \tag{22}$$

where $h^s$, $u_x^s$, $\tau_{xx}^s$, and $\tau_{zz}^s$ are the steady-state variables, $h'$, $u_x'$, $\tau_{xx}'$, and $\tau_{zz}'$ are the complex perturbations, and $\lambda$ is the complex eigenvalue in the problem ($\lambda_r$ being the growth or decay rate, and $\lambda_i$ the disturbance frequency). It is useful to introduce the following expressions for the steady and perturbation rates of elongation, namely, $\gamma^s = du_x^s/dx$ and $\gamma' = du_x'/dx$, respectively. The steady state is determined from the following equations:

$$\frac{d(h^s u_x^s)}{dx} = 0 \tag{23}$$

$$\mathrm{Re}h_s u_x^s \frac{du_x^s}{dx} = \frac{d}{dx}\left[h_s\left(4aR_v\frac{du_x^s}{dx} + \tau_{xx}^s - \tau_{zz}^s\right)\right] \tag{24}$$

$$\tau_{xx}^s \exp\left(\frac{\alpha \mathrm{De}}{a}(\tau_{xx}^s + \tau_{zz}^s)\right) + \mathrm{De}\left(u_x^s\frac{d\tau_{xx}^s}{dx} - 2(1-\xi)\frac{du_x^s}{dx}\tau_{xx}^s\right) = 2a\frac{du_x^s}{dx} \tag{25}$$

$$\tau_{zz}^s \exp\left(\frac{\alpha \mathrm{De}}{a}(\tau_{xx}^s + \tau_{zz}^s)\right) + \mathrm{De}\left(u_x^s\frac{d\tau_{zz}^s}{dx} + 2(1-\xi)\frac{du_x^s}{dx}\tau_{zz}^s\right) = -2a\frac{du_x^s}{dx} \tag{26}$$

The corresponding boundary conditions are readily obtained from Eq. (21), which are given by

$$u_x^s(x=0) = 1, \quad u_x^s(x=1) = D_r, \quad h^s(x=0) = 1$$

$$\tau_{xx}^s(x=0) = \tau_{xx}^0, \quad \tau_{zz}^s(x=0) = \tau_{zz}^0 \tag{27}$$

Equation (23) is readily integrated to give a relation between the velocity and the thickness, namely, $h^s = 1/u_x^s$. Upon substitution of expressions (22) into Eqs. (17)–(20), the eigenvalue problem is obtained. A variety of solution methods can be applied to solve the problem, most of which treat it as an initial-value problem. See, for instance, Refs. [16,27] for fiber spinning, and Refs. [4,7,8] for film casting. In this study, the problem is solved as a nonlinear two-point boundary-value problem. Since only the critical conditions for the onset of instability are sought, one sets $\lambda_r = 0$ and $D_r = D_r^c$ in the analysis. The resulting augmented eigenvalue problem is cast in the following form:

$$\frac{dh'}{dx} = \frac{1}{u_x^s}\left(\frac{u'\gamma^s}{u_x^{s2}} - h'\lambda - \frac{\gamma'}{u_x^s} - h'\gamma^s\right) \tag{28}$$

$$\frac{du_x^s}{dx} = \gamma^s \tag{29}$$

$$\frac{d\gamma^s}{dx} = \frac{\gamma^s}{4aR_v u_x^s}\left\{\mathrm{Re}u_x^{s2} - 2(1-\xi)(\tau_{xx}^s + \tau_{zz}^s) + 4aR_v\gamma^s + \tau_{xx}^s - \tau_{zz}^s - \frac{4a}{\mathrm{De}} + \frac{\tau_{xx}^s - \tau_{zz}^s}{\mathrm{De}\gamma^s}\exp\left(\frac{\alpha \mathrm{De}}{a}(\tau_{xx}^s + \tau_{zz}^s)\right)\right\} \tag{30}$$

$$\frac{d\tau_{xx}^s}{dx} = 2\frac{\gamma^s}{u_x^s}\left[\frac{a}{\mathrm{De}} + (1-\xi)\tau_{xx}^s\right] - \frac{\tau_{xx}^s}{\mathrm{De}u_x^s}\exp\left(\frac{\alpha \mathrm{De}}{a}(\tau_{xx}^s + \tau_{zz}^s)\right) \tag{31}$$

$$\frac{d\tau_{zz}^s}{dx} = -2\frac{\gamma^s}{u_x^s}\left[\frac{a}{\mathrm{De}} + (1-\xi)\tau_{zz}^s\right] - \frac{\tau_{zz}^s}{\mathrm{De}u_x^s}\exp\left(\frac{\alpha \mathrm{De}}{a}(\tau_{xx}^s + \tau_{zz}^s)\right) \tag{32}$$

$$\frac{du_x'}{dx} = \gamma' \tag{33}$$

$$\frac{d\gamma'}{dx} = \frac{1}{u_x^s}\left[u_x'\gamma^s - u_x^{s2}\frac{d}{dx}(h'\gamma^s)\right] + \frac{1}{4aR_v u_x^s}\left\{\mathrm{Re}u_x^s(u_x'\lambda + u_x^s\psi + u_x^{s2}h'\gamma^s) - u_x^s\frac{d}{dx}(\tau_{xx}' - \tau_{zz}') + \gamma^s(\tau_{xx}' - \tau_{zz}') - u_x^{s2}\frac{dh'}{dx}(\tau_{xx}^s - \tau_{zz}^s) - u_x^{s2}h'\frac{d}{dx}(\tau_{xx}^s - \tau_{zz}^s)\right\} \tag{34}$$

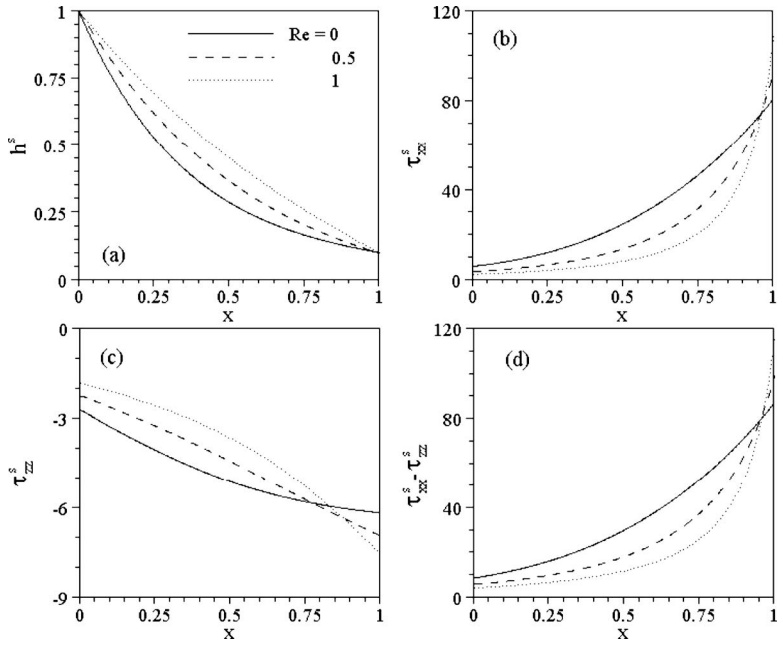


**Fig. 2 Influence of inertia on (*a*) the film thickness $h^s$, (*b*) the polymeric stress in the streamwise direction $\tau_{xx}^s$, (*c*) the polymeric stress in the depthwise direction $\tau_{zz}^s$, and (*d*) the primary normal stress difference $\tau_{xx}^s - \tau_{zz}^s$, for the range $\mathrm{Re} \in [0,1]$ at $D_r=10$, $\mathrm{De}=0.05$, $R_v=0.1$, and $\alpha=0.1$**

$$\frac{d\tau_{xx}'}{dx} = \frac{1}{u_x^s}\left\{ 2\frac{a}{\mathrm{De}}\gamma' - \tau_{xx}'\lambda - u_x'\left[ 2\frac{\gamma^s}{u_x^s}\left(\frac{a}{\mathrm{De}} + (1-\xi)\tau_{xx}^s\right) - \frac{\tau_{xx}^s}{\mathrm{De}u_x^s}\exp\left(\frac{\alpha\mathrm{De}}{a}(\tau_{xx}^s + \tau_{zz}^s)\right)\right] + 2(1-\xi)(\gamma^s\tau_{xx}' + \tau_{xx}^s\gamma') - \left[\left(\frac{1}{\mathrm{De}} + \frac{\alpha}{a}\tau_{xx}^s\right)\tau_{xx}' - \frac{\alpha}{a}\tau_{xx}^s\tau_{zz}'\right]\exp\left(\frac{\alpha\mathrm{De}}{a}(\tau_{xx}^s + \tau_{zz}^s)\right)\right\} \tag{35}$$

$$\frac{d\tau_{zz}'}{dx} = -\frac{1}{u_x^s}\left\{ 2\frac{a}{\mathrm{De}}\psi + \tau_{zz}'\lambda - u_x'\left[ 2\frac{\gamma^s}{u_x^s}\left(\frac{a}{\mathrm{De}} + (1-\xi)\tau_{zz}^s\right) + \frac{\tau_{zz}^s}{\mathrm{De}u_x^s}\exp\left(\frac{\alpha\mathrm{De}}{a}(\tau_{xx}^s + \tau_{zz}^s)\right)\right] + 2(1-\xi)(\gamma^s\tau_{zz}' + \tau_{zz}^s\gamma') + \left[\left(\frac{1}{\mathrm{De}} + \frac{\alpha}{a}\tau_{zz}^s\right)\tau_{zz}' + \frac{\alpha}{a}\tau_{zz}^s\tau_{xx}'\right]\exp\left(\frac{\alpha\mathrm{De}}{a}(\tau_{xx}^s + \tau_{zz}^s)\right)\right\} \tag{36}$$

$$\frac{dD_r^c}{dx} = 0 \tag{37}$$

$$\frac{d\lambda_i}{dx} = 0 \tag{38}$$

For given Re, there are 11 real variable unknowns to be determined, including the critical draw ratio, frequency, and the steady-state velocity and stress components. System (28)–(38) is solved subject to conditions (27) and the following homogeneous boundary conditions:

$$h'(0) = u_x'(0) = \tau_{xx}'(0) = \tau_{zz}'(0) = u_x'(1) = 0 \tag{39}$$

In addition, two boundary conditions are needed. Without loss of generality, and since the equations are homogeneous, one sets $\psi(0)=1$. Finally, it is noted that $D_r^c(0)=D_r^c(1)$. The resulting problem is of the two-point boundary-value type and is now nonlinear since both the frequency and critical draw ratio are part of the unknown variables. The problem is solved using the DBVPFD subroutine from the IMSL library.

## 3 Discussion and Results

Results for steady film-casting flow and its linear stability are reported in this section. The influence of fluid and flow parameters on the stability diagram is examined first with focus on the interplay between inertia and elasticity. The effect of boundary conditions is then examined in detail.

**3.1 Steady-State Flow.** The interplay between inertia and elasticity is first examined in this section for steady-state flow. Following Iyengar and Co [11], the flow at the location of maximum thickness (due to die swell) is approximated by a homogeneous elongational flow. In this case, the variation of normal stress is assumed to be negligible and the stress conditions are determined from Eqs. (25) and (26), which reduce to a nonlinear algebraic system. However, the elongational rate $du_x^s/dx$ is not known at $x=0$ and is therefore determined iteratively. The influence of inertia on steady film-casting flow is investigated by varying the Reynolds number over the range $\mathrm{Re} \in [0,1]$, with the draw ratio fixed at $D_r=10$, Deborah number at $\mathrm{De}=0.09$, the solvent-to-solute viscosity ratio at $R_v=0.1$, and the model parameter at $\alpha=0.1$. De and $\alpha$ are chosen within the range of fitted parameter values of PTT model for PET [17,28]. An experimental value of $R_v \approx 0.1$ was reported by Joo et al. [27] for nylon 6,6. Since the viscosity of polymeric fluids varies from $10^2$ to $10^5$ Pa s in the commercial fiber-spinning and film-casting processes (depending on the type of polymer), the Reynolds number may have a wide range of values. Typical Reynolds numbers reported in experimental studies range from $O(10^{-3})$ to $O(10^{-1})$ [2,3,12,29]. The flow response is depicted in Fig. 2, where the distributions of $h^s$, $\tau_{xx}^s$, $\tau_{zz}^s$, and $\tau_{xx}^s - \tau_{zz}^s$ are plotted against $x$. Figure 2(*a*) shows that the film thickness decreases monotonically with $x$ for any Reynolds number and increases with Re at any $x$ position. For $\mathrm{Re}=0$, the decrease in $h^s$ is expected to be near exponential. The film tends therefore to contract more near the die exit at lower Re (as

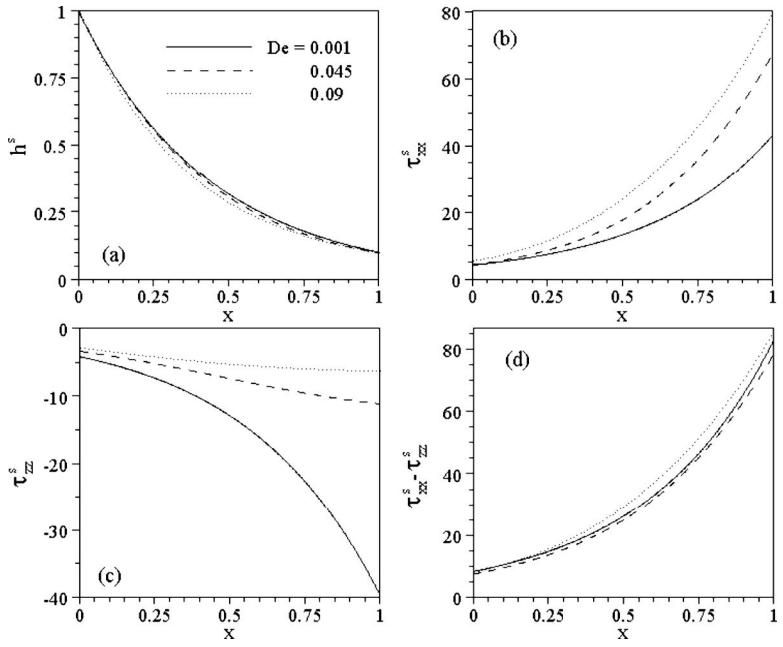


**Fig. 3 Influence of elasticity on (*a*) the film thickness $h^s$, (*b*) the polymeric stress in the streamwise direction $\tau^s_{xx}$, (*c*) the polymeric stress in the depthwise direction $\tau^s_{zz}$, and (*d*) the primary normal stress difference $\tau^s_{xx}-\tau^s_{zz}$, for the range De $\in[0,0.1]$ at $D_r=10$, Re=0, $R_v=0.1$, and $\alpha=0.1$**

a result, for instance, of smaller air gap). Noting that $u^s_x=1/h^s$, elongational effects are expected to be higher for flow with lower inertia as depicted from the distributions of normal stresses (Figs. 2(*b*) and 2(*c*)) and normal stress difference (Fig. 2(*d*)). However, there is a significant increase in normal stress near the take-up point (relative to the level at the die exit) resulting from inertia. The origin of this localized normal stress buildup lies in the increase of elongational rate, $du^s_x/dx$ with inertia (see Fig. 2(*a*)). In this case, $\tau^s_{xx}$ becomes clearly the dominant normal stress component, reaching approximately ten times the level of $\tau^s_{zz}$ at the take-up point. Note that the overall normal stress ratio can be estimated to be roughly equal to $\tau^s_{xx}/\tau^s_{zz}\approx 2\mathrm{De}u^s_{x,x}+1/2\mathrm{De}u^s_{x,x}-1$. Seyfzadeh et al. [3] recently published quantitative experimental results for the characterization of film-casting process of PET. They measured the temperature and the local velocity over the region between the die exit and the take-up point. Their data indicate that the film velocity within the air gap decreases with increasing velocity at the die exit. This trend corresponds to the film thickness increasing with Reynolds number, a trend confirmed in Fig. 2(*a*) of the current work. A similar effect of inertia was also predicted by Beris and Liu [16], who theoretically examined fiber spinning, but limited their analysis to upper-convected-Maxwell fluids.

The effect of elasticity is examined by varying the Deborah number over the range De $\in[0,0.09]$, at $D_r=10$, in the absence of inertia. The remaining parameters are the same as in Fig 2. The resulting steady-state profiles are depicted in Fig. 3. The film thickness is essentially unaffected by elasticity over the range of De considered but decreases overall as De increases. In addition, and in contrast to the normal stress profiles, the effect of elasticity on $h^s$ is opposite to that of inertia. This is consistent with the numerical results on film casting of viscoelastic fluids (modified convected-Maxwell model) by Anturkar and Co [8], who observed the velocity to increase with Deborah number. More importantly, Figs. 3(*b*) and 3(*c*) indicate that elasticity has a drastic influence on the normal stress components. Interestingly, however, elasticity does not seem to affect the normal stress difference (see Fig. 3(*d*)). This can be seen by recalling normal stress estimates as $\tau^s_{xx}\approx 2au^s_{x,x}/1-2\mathrm{De}u^s_{x,x}$ and $\tau^s_{zz}\approx 2au^s_{x,x}/1+2\mathrm{De}u^s_{x,x}$ Clearly, in this case, since $u^s_{x,x}>0$, the streamwise component increases as De increases, while the transverse component decreases in magnitude with De. This trend is in agreement with Olagunju's numerical analysis results of the extensional deformation of a viscoelastic filament under exponential stretching [30]. The resulting normal stress difference, which is estimated by $\tau^s_{xx}-\tau^s_{zz}\approx 4au^s_{x,x}/1-4\mathrm{De}^2u^{s2}_{x,x}$, remains unaffected in the relatively small elasticity range.

It is surprising, nevertheless, to find that the normal stress difference is insensitive to changes in De given its relation to the axial force, $F^S$, in the film. This relation is recalled here for convenience:

$$F^s=h^s\sigma^s_{xx}=h^s(4aR_vu^s_{x,x}+\tau^s_{xx}-\tau^s_{zz}) \tag{40}$$

Indeed, Chang and Denn measured this force for fiber spinning for Newtonian corn syrup and viscoelastic dilute solution of polyacrilamide in corn syrup [31]. They found that the force increases with elasticity, which contradicts the present theoretical predictions. Since the film thickness and the normal stress difference change very little with De, so does the force, according to Eq. (40). This contradiction can be explained as follows. First, consider the case De=0.001, which should essentially correspond to Newtonian film. Indeed, with inertia and gravity effects neglected, the velocity and total stress component in the streamwise direction reduce, respectively, to

$$u^s_x=e^{x\ln(D_r)},\quad \sigma^s_{xx}=4u^s_{x,x}=\ln(D_r)e^{x\ln(D_r)} \tag{41}$$

At the take-up point and for $D_r=10$, $\sigma^s_{xx}=92$. The total stress for the PTT film considered here with De=0.001 and $\alpha=0.1$ is $\sigma^s_{xx}=93.2$, a value that is very close to that for Newtonian fluid. In the experiment [32], the two fibers were of equal constant viscosity and were drawn isothermally at the same extrusion rate and spinline length. The force required to draw the viscoelastic fiber was observed to be considerably greater than the force for Newtonian fiber. The discrepancy between experiment and current theory can be attributed to the relatively large value of the parameter $\alpha$

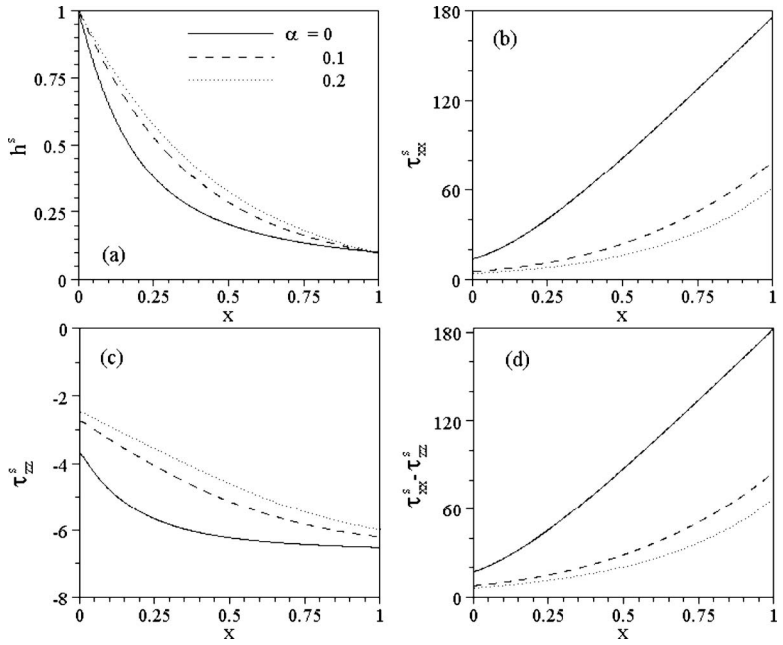


**Fig. 4 Influence of parameter $\alpha$ on (*a*) the film thickness $h^s$, (*b*) the polymeric stress in the streamwise direction $\tau^s_{xx}$, (*c*) the polymeric stress in the depthwise direction $\tau^s_{zz}$, and (*d*) the primary normal stress difference $\tau^s_{xx} - \tau^s_{zz}$, for the range $\alpha \in [0, 0.2]$ at $D_t = 10$, Re = 0, $R_v = 0.1$, and De = 0.05**

(=0.1), which is not unrealistic [28], and which tends to oppose the effect of elasticity on the flow. As a result, significant rise of the stress difference is not observed. The effect of $\alpha$ is therefore important and will be examined next.

The role of the parameter $\alpha$, which is related to the rate of destruction of polymeric network junctions, is now examined over the range $\alpha \in [0, 0.2]$, De = 0.09, and $R_v = 0.1$. In order to emphasize elastic effects, inertia is neglected in this case (Re = 0). Figure 4 shows the resulting steady-state profiles. In general, the film thickness (Fig. 4(*a*)) increases and stress (Figs. 4(*b*) and 4(*c*)) decreases with increasing $\alpha$. The effect of $\alpha$ on $h^s$ is similar to the effect of inertia observed in Fig. 2. This is understandable since increasing the rate of destruction of polymer junctions is expected to make the fluid behave more like Newtonian. This is reflected by Eqs. (25) and (26), which, in the limit of large $\alpha$, lead to vanishing (polymeric) normal stress components. This is also confirmed from Figs. 4(*b*)–4(*d*), which show the overall decrease in normal stress effect with $\alpha$. Figure 4(*b*) indicates that $\tau^s_{xx}$ increases linearly near the take-up point. In particular, the stress value is significantly large for $\alpha = 0$ (Oldroyd-B film). This latter case represents nearly critical conditions (for De = 0.09). Indeed, for an Oldroyd-B fluid, $\tau^s_{xx}$ becomes singular at the take-up point as De approaches 0.1. The stress decreases considerably as $\alpha$ increases, thus eliminating the singularity (for $\alpha > 0$). It is interesting to observe that, as $\alpha$ increases, the maximum drop in $\tau^s_{zz}$ occurs at $x \approx 0.25$, whereas the maximum jump in $\tau^s_{xx}$ occurs at the take-up point. Comparison between Figs. 3(*d*) and 4(*d*) clearly reflects a dramatic increase as $\alpha$ decreases. In fact, the force has more than doubled between $\alpha = 0.1$ and 0 for De = 0.09. In this case, since a decrease in the level of fluid degradation is commensurate with an increase in elasticity level, the current theory agrees with the findings of Chang and Denn [32], suggesting that the viscoelastic liquid used in the experiment is close to an Oldroyd-B fluid. This is further demonstrated next.

The force in the film does not always increase with Deborah number; however, as it depends on the level of inertia and $\alpha$. The interplay between inertia and elasticity is depicted in Fig. 5. The primary normal stress difference at the take-up point is plotted in

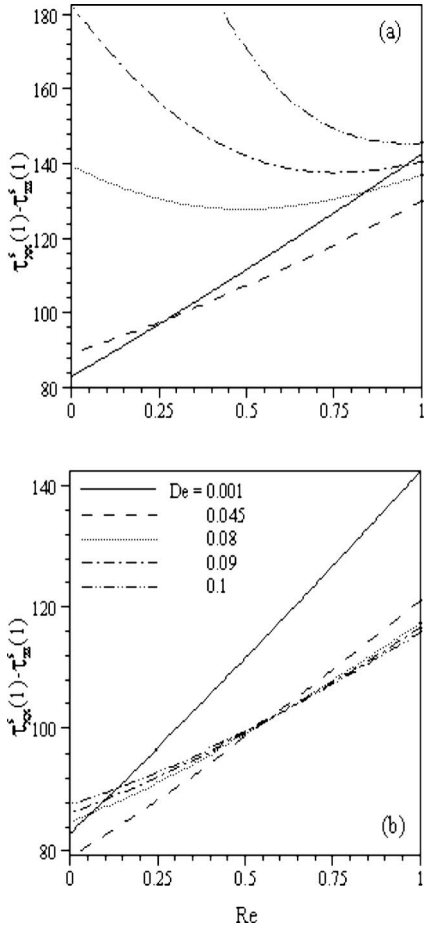


**Fig. 5 Dependence of the primary normal stress difference at $x = 1$ on Reynolds number for the range $\mathrm{De} \in [0.001, 0.1]$ at $R_v = 0.1$, (*a*) $\alpha = 0$, and (*b*) $\alpha = 0.1$**

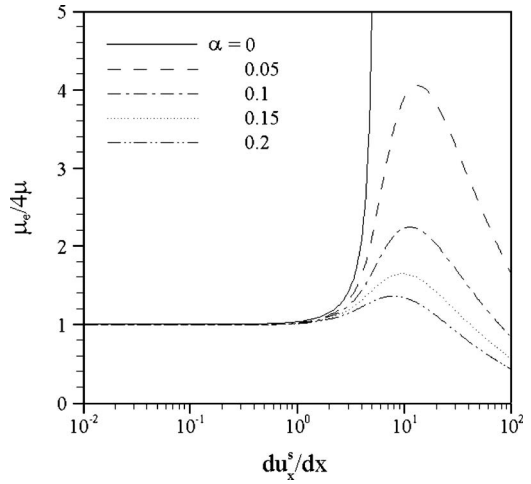


**Fig. 6 Dependence of the elongational viscosity on the rate of elongation for the range $\alpha \in [0, 0.2]$ at De=0.09 and $R_v$=0.1. Homogeneous elongational flow is considered.**

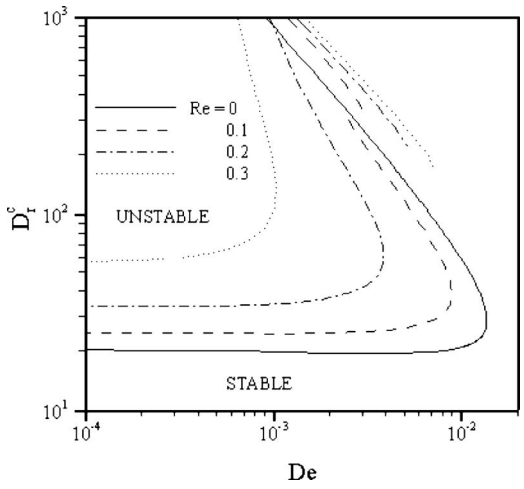


**Fig. 7 Effect of inertia on the critical draw ratio $D_r^c$, for the range Re $\in [0, 0.2]$ at $\alpha$=0 and $R_v$=0.1**

the figure against Re over the range De $\in [0.001, 0.1]$ at $D_r$=10 for $\alpha$=0 (Fig. 5(*a*)) and 0.1 (Fig. 5(*b*)). The dependence of the normal stress difference on Re at $\alpha$=0 is linear for small De (Fig. 5(*a*)). However, as De increases, this dependence becomes nonmonotonic, exhibiting a minimum. This minimum occurs at Re $\approx$0.5 when De=0.08. It is approximately at this level of elasticity that the normal stress difference is least sensitive to change in inertia. The value of Re at the minimum of the normal stress difference increases with De. There is a strong increase of normal stress effect with De for small Re. Eventually, a singularity emerges at De=0.1 (infinite normal stress in the limit Re $\to$ 0). This reflects an anomalous or unrealistic response when inertia is neglected for fluids of the Boger type. For higher-inertia flow (Re $>$ 0.25), the response of normal stress with elasticity is nonmonotonic.

This nonmonotonicity is further accentuated when $\alpha > 0$. The situation is typically illustrated in Fig. 5(*b*) for $\alpha$=0.1. In contrast to Oldroyd-B fluids (Fig. 5(*a*)), normal stress difference increases monotonically (almost linearly) with inertia as Fig. 5(*b*) indicates. However, the dependence of normal stress on De is less obvious. For small inertia (Re $<$ 0.5), the normal stress difference decreases as De increases, reaching a minimum (in the vicinity of De =0.045) and increases thereafter with De. For higher-inertia flow (Re $>$ 0.5), normal stress decreases monotonically with De. In the experiment of Chang and Denn [32], Re was in the order of $10^{-3}$, and the force was found to increase with elasticity. Since the experiment was performed for the range De $<$ 0.1, the current theory agrees with experiment (based on the low-Re values in Fig. 5(*a*)), suggesting that the experimental fluid used has a very small $\alpha$ value.

The effect of $\alpha$ is further assessed by examining the elongational viscosity, $\mu_e$, which is defined as the ratio of the normal stress difference and the elongation rate. Figure 6 shows the dependence of $\mu_e/\mu$ on the rate of elongation over the range $\alpha \in [0, 0.2]$ at De=0.09. Homogeneous elongational flow conditions are assumed. When $\alpha$=0, the Oldroyd-B model is recovered and the viscosity increases indefinitely with $du_x^s/dx$ as it approaches asymptotically some critical value of the elongation rate. This value changes with the Deborah number as $1/(2\text{De})$. When $\alpha > 0$, the viscosity profile exhibits a maximum instead of a singularity. The maximum weakens and occurs at lower elongation rate as $\alpha$ increases. Monotonic increase of elongational viscosity with elongation rate, as predicted with the Oldroyd-B model, is not characteristic of most experimental data. Experiments usually show a maximum in the elongational viscosity [33]. A good fit of experimental data with the PTT model for elongational flow has been reported in the literature [17,20,28]. There is a strong connection between the dependence of elongational viscosity on the rate of elongation and the marginal stability picture. This will be discussed next.

**3.2 Linear Stability.** The interplay between elasticity and inertia and the onset of draw resonance are now examined through linear stability analysis. The eigenvalue problem is treated as two-point boundary-value problem as discussed above. This approach is convenient, and its validity has been established for a Newtonian fluid by Cao et al. [34]. The influence of inertia and elasticity on the stability of the film is assessed first by examining the dependence of the critical draw ratio on Re and De. The neutral stability curves, which separate the stable and unstable domains, are obtained for the range Re $\in [0, 0.3]$ at $R_v$=0.1 and $\alpha$=0, which corresponds to the Oldroyd-B fluid. The critical draw ratio is plotted against De in Fig. 7. The neutral stability curves in the figure show that two or three critical draw ratios may exist for a given De. In the absence of inertia (Re=0), only one marginal stability branch exists. A similar branch exists for Re $>$ 0, which will be referred to as the primary branch. The region of instability is engulfed by the branch. Anturkar and Co [8] used a shooting method in their linear stability analysis of film casting of the modified convected-Maxwell model. They neglected inertia in their analysis. In the limit of zero Reynolds number, the current results agree with those of Anturkar and Co [8]. As the Reynolds number increases, secondary branches appear. The primary branch indicates a reduction in the unstable region resulting from inertia. As Re increases from zero, the primary branch breaks, leading to a secondary branch, as illustrated by the stability curves for Re =0.1. Similar abrupt ending of the stability curves was reported by Beris and Liu [16] for fiber spinning of upper-convected-Maxwell fluids. However, no secondary branches were reported. As Re increases further (refer to the flow with Re=0.2 and 0.3), the gap between the two branches widens.

Further insight into solution multiplicity and branching is gained by varying $\alpha$. Recall that an increase in polymer degradation should lead to somewhat similar qualitative flow response as an increase in inertia since in both cases the flow behaves closer to that of a Newtonian fluid. The influence of $\alpha$ on the marginal stability is examined in Fig. 8 for the range $\alpha \in [0, 0.2]$ in the absence of inertia. It is interesting to note at the outset the close correlation between the marginal stability curves in Fig. 8 and the curves for elongational viscosity in Fig. 6. Figure 8 shows that the lower critical draw ratio is insensitive to changes in $\alpha$ for small Deborah number (up to De $\approx$ 0.002). As De further increases, the

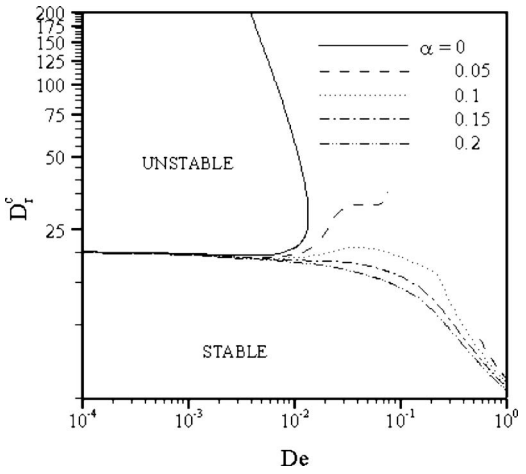


**Fig. 8 Effect of parameter $\alpha$ on the critical draw ratio $D_r^c$, for the range $\alpha \in [0, 0.2]$ at $R_v$=0.1. Inertia is neglected.**

curves for zero and nonzero $\alpha$ exhibit different behaviors. For large $\alpha$ ($\alpha > 0.15$), the critical draw ratio decreases monotonically with De, indicating that elasticity has a consistent destabilizing effect. For moderately large $\alpha$ ($0.05 < \alpha < 0.15$), $D_r^c$ increases with De, reaches a maximum, and then decreases. This maximum in critical draw ratio corresponds to the maximum in the elongational viscosity. In this case, elasticity tends to have a stabilizing effect for a small range of De values (in the vicinity of the maximum). For small $\alpha$ ($0 < \alpha < 0.1$), the maximum becomes more localized, and eventually the marginal curve displays a discontinuity. Correspondingly, the elongational viscosity experiences a sharp increase (see Fig. 6). For an Oldroyd-B fluid, only one branch exists with a turning point, and elasticity is entirely stabilizing in the range $De > 0.013$. It is somewhat surprising to find that elasticity can be stabilized for moderately small $\alpha$ (near the maximum in critical draw ratio), given the relatively significant normal stress effect. However, one should expect that for real fluids, $\alpha$ would be large enough for the stability curve to remain continuous.

It is expected that real fluids exhibit some degree of polymer degradation and a certain level of inertia upon flow. Figure 9 illustrates the interplay between inertia and elasticity over the ranges $Re \in [0, 0.15]$ and $De \in [0, 1]$ at $\alpha = 0.1$. In general, inertia tends to have a stabilizing effect at any elasticity level. Moreover, there exists a range of De values for which this stabilization is enhanced. This is reflected here by the strengthening of the maximum and the emergence of a second maximum as Re increases. The degree of stabilization due to inertia is further depicted from Fig. 9(*b*), where $D_r^c$ is plotted against Re over four decades of the Deborah number. $D_r^c$ increases monotonically with Re, essentially exponentially in the higher Re range. The strongest stabilizing effect of inertia is observed for intermediate elasticity level ($De = 0.1$). The overall influence of inertia and elasticity on the stability is inferred from the three-dimensional perspective in Fig. 9(*c*).

Further increase of Re leads to the breakup of the neutral stability curves. This situation is depicted in Fig. 10, where the dependence of $D_r^c$ on De is plotted over the range $Re \in [0.1, 0.3]$ at $\alpha = 0.1$. It is observed from the figure that the first maximum weakens and eventually disappears, while the second maximum shifts to infinity as Re increases.

In the absence of inertia, $\alpha$ was shown above to have a strong effect on the stability picture. In particular, it was found that the marginal stability curves tend to exhibit a discontinuity for small $\alpha$ (refer to Fig. 8). The emergence of this discontinuity can be further understood in the presence of small inertia. Figure 11 displays the marginal stability curves when $Re = 0.1$, over the ranges

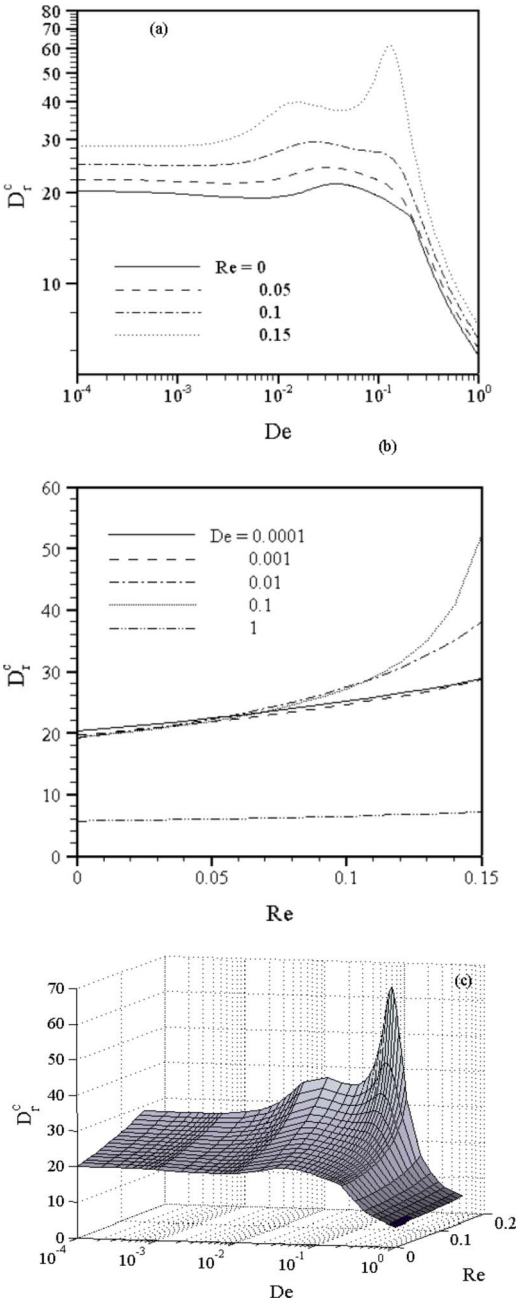


**Fig. 9 Influence of inertia and elasticity on the critical draw ratio $D_r^c$, over the range $Re \in [0, 0.15]$ and $De \in [0.0001, 1]$, at $\alpha$ = 0.1 and $R_v$=0.1**

$\alpha \in [0, 0.1]$ and $De \in [0.0001, 1]$. The neutral stability curve is continuous for large $\alpha$ ($>0.075$). As $\alpha$ decreases, a maximum develops, at which the curve eventually splits into two branches, the primary branch (on the left) and the secondary branch (on the right). For yet smaller $\alpha$, only the primary branch seems to persist, exhibiting a change in concavity, leading eventually to the emergence of a minimax. The maximum becomes particularly stronger as $\alpha$ decreases, leading eventually to a new split in the (primary) branch at the maximum location. This phenomenon is typically illustrated by the curves $\alpha = 0.01$ and 0.005.

**3.3 Effect of Stress Boundary Conditions.** The effect of stress boundary conditions on the steady-state flow and its stability is examined in this section. The boundary conditions for stress are not obvious, as they depend on the prehistory of the fluid

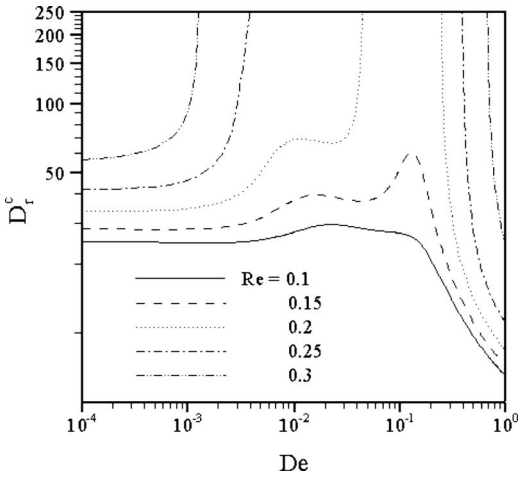


**Fig. 10 Influence of inertia and elasticity on the critical draw ratio $D_r^c$, over the range $\mathrm{Re} \in 0.1, 0.3$ and $\mathrm{De} \in [0.0001, 1]$ at $\alpha = 0.1$ and $R_v = 0.1$**

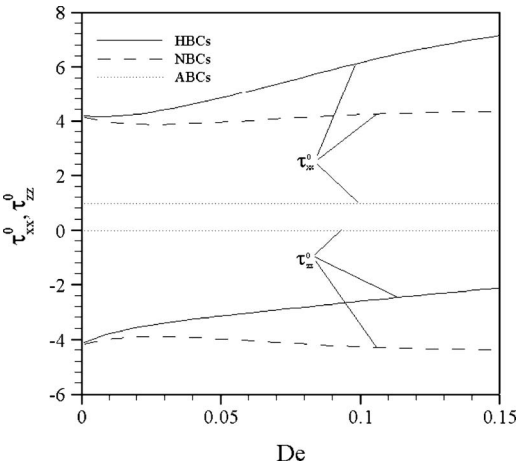


**Fig. 12 Effect of elasticity on normal stresses at $x=0$ for HBCs, NBCs, and ABCs**

inside the die and in the die swell region. Different boundary conditions have been adopted in the literature, such as a homogeneous elongational flow (maximum die swell) [11,16], Newtonian exit conditions [13], and stress values determined from an asymptotic analysis [14]. In what follows, the homogeneous, Newtonian, and asymptotic boundary conditions will be referred to as HBCs, NBCs and ABCs, respectively. The implementation of HBCs has already been outlined in Sec. 3.1. The NBCs are obtained by setting $\mathrm{De}=0$ in Eqs. (25) and (26), leading to

$$\tau_{xx}^0 = 2a\frac{du_x^s}{dx}, \quad \tau_{zz}^0 = -2a\frac{du_x^s}{dx} \tag{42}$$

Purely Newtonian conditions are justified by the assumption that existing extra stresses are relaxed during the die swell and polymer molecules have not been significantly stretched yet in this region [13]. The third type of boundary conditions, ABCs, was obtained Denn et al. [14] who carried out an asymptotic analysis of the drawn viscoelastic fiber at very large tensile stress, $1/\mathrm{De}F^s \to 0$, where $F^S$ is a dimensionless tensile force. In this limit, an asymptotic series in $1/\mathrm{De}F^s$ can be obtained as regular perturbation expansion. They conclude that the influence of $\tau_{xx}^0$ is important only close to $x=0$, and $\tau_{xx}^0$ can be set equal to 1 without seriously affecting the flow further downstream. The analysis also indicates that in this limit case, the ratio of radial-to-axial stress becomes small, thus $\tau_{zz}^0 \cong 0$ [28]. Similar analysis for film casting was carried out by Anturkar and Co [8]. Their results lead to the same conclusions as those of Denn et al. [14].

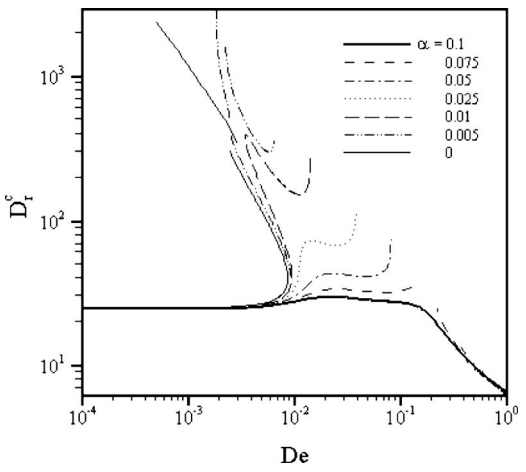


**Fig. 11 Effect of parameter $\alpha$ on the critical draw ratio $D_r^c$, over the range $\alpha \in [0, 0.1]$ at $\mathrm{Re}=0.1$ and $R_v=0.1$**

The effect of elasticity on the boundary condition (HBCs, NBCs, and ABCs) for normal stress at $x=0$ is illustrated in Fig. 12. The range of Deborah numbers is $\mathrm{De} \in [0, 0.15]$, with $\alpha = 0.1$, $R_v = 0.1$, $\mathrm{Re}=0$, and $D_r = 10$. The stress magnitudes using ABCs are consistently lower than those using HBCs and NBCs. Expectedly, the curves corresponding to HBCs and NBCs emanate from the same values for very small De. However, the curves deviate one from another as De increases. The increase (decrease) in the magnitude of $\tau_{xx}^0$ ($\tau_{zz}^0$) with the level of elasticity is of course expected. Hence, the HBCs lead to a more realistic prediction for stress boundary conditions than both the NBCs and ABCs.

Regardless of the type of stress conditions imposed at $x=0$, the crucial issue remains as to the way these boundary conditions influence the flow further downstream. This issue is now addressed by examining the steady-state profiles for the three types of stress conditions. Figure 13 shows the film thickness, the streamwise stress, the depthwise stress, and the primary normal stress difference distributions along $x$ for $D_r = 10$, $\mathrm{De}=0.09$, $\mathrm{Re}=0$, $R_v=0.1$, and $\alpha=0.1$. The film thickness profiles (Fig. 13(*a*)) do not seem to differ significantly when the HBCs and NBCs are used. However, the thickness predicted with ABCs experiences a sudden drop near $x=0$ and then slowly approaches the curves based on HBCs and NBCs. Overall, the type of exit stress conditions used does not have a significant effect on film thickness far downstream. However, the streamwise stress profiles in Fig. 13(*b*) and the normal stress difference profiles in Fig. 13(*d*) clearly show that different stress conditions affect the stress distribution up to the take-up point. The streamwise stress profiles with NBCs and ABCs lie consistently below the HBC curve. Agreement in all three cases appears to be limited to the middle air-gap region. In contrast, significant discrepancy is predicted for the depthwise stress near the exit (Fig. 13(*c*)). The depthwise stress based on NBCs exhibits a rather strong maximum near $x=0$. Note also that the profile for HBCs predicts in the most of the domain smallest stress.

Since the stress boundary conditions are found to influence the steady-state flow, it is useful to assess their effect on the stability region. Figure 14 shows the $D_r^c$ curves against De at $\mathrm{Re}=0$, $R_v = 0.1$, and $\alpha=0.1$, for the three stress boundary conditions. The critical draw ratio is insensitive to changes in imposed stress conditions for small Deborah number ($\mathrm{De} < 0.003$). For larger De, the critical draw ratios predicted for the three boundary conditions remain only qualitatively the same. If the homogeneous elonga-

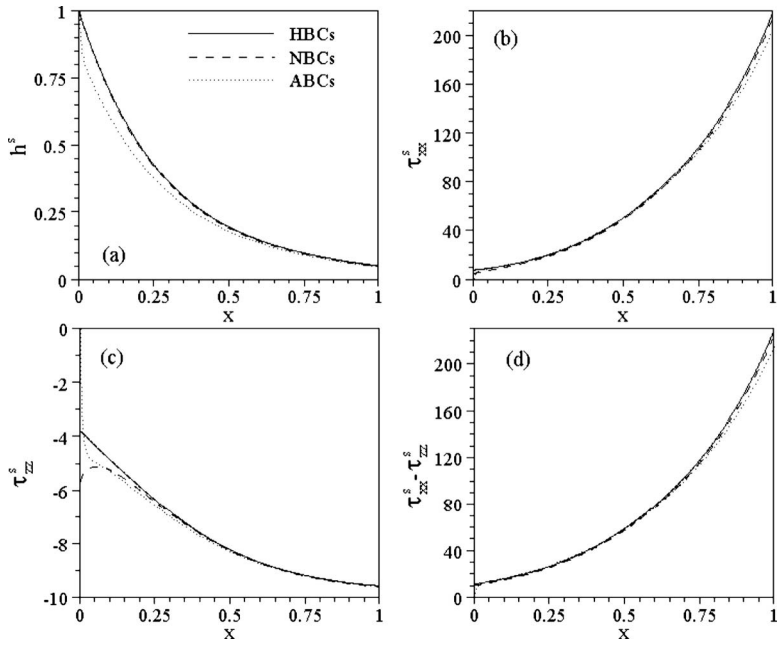


**Fig. 13 Effect of the stress boundary conditions on (*a*) the film thickness $h^s$, (*b*) the polymeric stress in the streamwise direction $\tau^s_{xx}$, (*c*) the polymeric stress in the depthwise direction $\tau^s_{zz}$, and (*d*) the primary normal stress difference $\tau^s_{xx}-\tau^s_{zz}$, at $\alpha=0.1$, $D_r=10$, De=0.09, $R_v=0.1$, and Re=0**

tional flow is considered to be closest to the exact conditions at $x=0$, then the NBCs (ABCs) cause $D_r^c$ to notably underestimate (overestimate) the critical draw ratio.

## 4 Concluding Remarks

The interplay between inertia and elasticity is examined for the film casting of PTT fluids. This constitutive model is used for its accurate prediction of elongational flow [20]. Linear stability analysis is carried out to predict the critical draw ratio for instability. The resulting eigenvalue problem is treated as a two-point boundary-value problem. The steady state is determined simultaneously as part of the eigenvalue problem. It is found that seemingly negligible inertia can have a drastic influence on the steady state and stability picture. This is the case of flow at Re $\sim$O(0.1), which can correspond to practical processing conditions. The steady-state film tends to contract at low Reynolds number; this contraction, however, is significantly diminished by inertia. The polymeric normal stresses and the primary normal stress difference decrease in the most of the air gap as inertia increases. In contrast, the stress and stress difference increase considerably near the take-up point due to a dramatic increase in the elongation rate. Elasticity is found to oppose inertia effect as it enhances film contraction and increases the stremwise stress. The depthwise stress decreases as elasticity increases. The resulting normal stress difference remains relatively unaffected by elasticity. However, experimental results suggest that the drawing force increases with elasticity [32]. This discrepancy is attributed to a relatively large value of the polymer destruction parameter $\alpha$, which opposes the effect of elasticity. This is also supported by the results on the effect of $\alpha$, where the film thickness and normal stress profiles approach Newtonian levels as $\alpha$ increases.

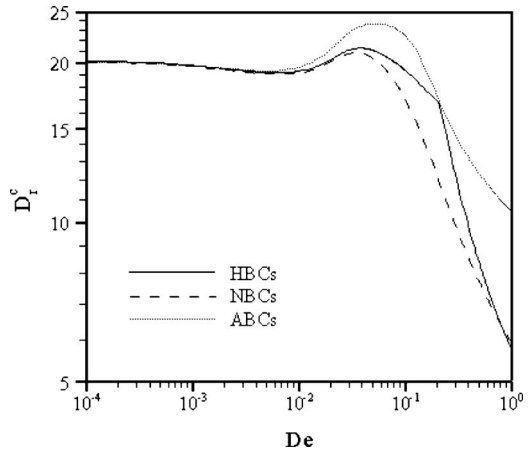


**Fig. 14 Effect of the stress boundary conditions on the critical draw ratio $D_r^c$, at Re=0, $R_v=0.1$, and $\alpha=0.1$**

Inertia is generally found to enhance flow stability. In the absence of inertia and at $\alpha=0$, the analysis predicts critical draw ratios that form an envelope to an unstable region. The flow is stable to the infinitesimal disturbances outside the envelope. The unstable region reduces as inertia increases. For Re$>$0.05, there are two branches of the neutral stability curve as opposed to only one branch in the absence of inertia. The situation changes significantly when $\alpha>0$. In this case, the unstable region expands with $\alpha$. Moreover, the elasticity destabilizes the flow at large values of $\alpha$. The inertia is in this case most effective in stabilizing the flow of a fluid with viscosity increasing with elongation. Finally, the influence of stress boundary conditions on the steady-state flow and its stability is also examined. In this case, HBCs, NBCs, and ABCs are considered. Low-elasticity fluids are found to be insensitive to the different stress boundary conditions imposed. However, appreciable differences in the predicted onset of draw resonance are observed for higher-elasticity fluids. Critical draw ratios based on Newtonian (asymptotic) conditions are found to overestimate (underestimate) the critical draw ratios based on homogeneous stress boundary conditions.

## Acknowledgment

This work was supported in part by Material and Manufacturing Ontario, and the Natural Science and Engineering Research Council of Canada.

## References


[1] Lamberti, G., Titomanlio, G., and Brucato, V., 2001, "Measurement and Modeling of the Film Casting Process 1. Width Distribution Along Draw Direction," Chem. Eng. Sci., **56**, p. 5749.

[2] Acierno, D., Di Maio, L., and Ammirati, C. C., 2000, "Film Casting of Polyethylene Terephthalate: Experiments and Model Comparisons," Polym. Eng. Sci., **40**, p. 101.

[3] Seyfzadeh, B., Harrison, G. M., and Carlson, C. D., 2005, "Experimental Studies on the Development of a Cast Film," Polym. Eng. Sci., **45**, p. 443.

[4] Yeow, Y. L., 1974, "On the Stability of Extending Films: A Model for the Film Casting Process," J. Fluid Mech., **66**, p. 613.

[5] Pearson, J. R. A., and Matovich, M. A., 1969, "Spinning a Molten Thread Line: Stability," Ind. Eng. Chem. Fundam., **8**, p. 605.

[6] Shah, Y. T., and Pearson, J. R. A., 1972, "On the Stability of Nonisothermal Fiber Spinning-General Case," Ind. Eng. Chem. Fundam., **11**, p. 150.

[7] Aird, G. R., and Yeow, Y. L., 1983, "Stability of Film Casting of Power-Law Liquids," Ind. Eng. Chem. Fundam., **22**, p. 7.

[8] Anturkar, N. R., and Co, A., 1988, "Draw Resonance in Film Casting of Viscoelastic Fluids: A Linear Stability Analysis," J. Non-Newtonian Fluid Mech., **28**, p. 287.

[9] Alaie, S. M., and Papanastasiou, T. C., 1991, "Film Casting of Viscoelastic Liquid," Polym. Eng. Sci., **31**, p. 67.

[10] Iyengar, V. R., and Co, A., 1993, "Film Casting of a Modified Giesekus Fluid: A Steady-State Analysis," J. Non-Newtonian Fluid Mech., **48**, p. 1.

[11] Iyengar, V. R., and Co, A., 1996, "Film Casting of a Modified Giesekus Fluid: Stability Analysis," Chem. Eng. Sci., **51**, p. 1417.

[12] Doufas, A. K., and McHugh, A. J., 2001, "Simulation of Melt Spinning Including Flow-Induced Crystallization. Part III. Quantitative Comparison With PET Spinline Data." J. Rheol., **45**, p. 403.

[13] Kim, J. M., Lee, J. S., Shin, D. M., Jung, H. W., and Hyun, J. C., 2005, "Transient Solutions of the Dynamics of Film Casting Process Using a 2-D Viscoelastic Model," J. Non-Newtonian Fluid Mech., **132**, p. 53.

[14] Denn, M. M., Petrie, C. J. S., and Avenas, P., 1975, "Mechanics of Steady Spinning of a Viscoelastic Liquid," AIChE J., **21**, p. 791.

[15] Silagy, D., Demay, Y., and Agassant, J. F., 1998, "Stationary and Stability Analysis of the Film Casting Process," J. Non-Newtonian Fluid Mech., **79**, p. 563.

[16] Beris, A. N., and Liu, B., 1988, "Time-Dependent Fiber Spinning Equations. 1. Analysis of the Mathematical Behavior," J. Non-Newtonian Fluid Mech., **26**, p. 341.

[17] Chrisodoulou, K., Hatzikiriakos, S. G., and Vlassopoulos, D., 2000, "Sability Analysis of Film Casting for PET Resin Using a Multimode Phan-Thien-Tanner Constitutive Equation," J. Plast. Film Sheeting, **16**, p. 312.

[18] Tsou, J. D., and Bogue, D. C., 1985, "The Effect of Die Flow on the Dynamics of Isothermal Melt Spinning," J. Non-Newtonian Fluid Mech., **17**, p. 331.

[19] Phan-Thien, N., and Tanner, R. I., 1977, "A New Constitutive Equation Derived From Network Theory," J. Non-Newtonian Fluid Mech., **2**, p. 353.

[20] Phan-Thien, N., 1978, "A Nonlinear Network Viscoelastic Model," J. Rheol., **22**, p. 259.

[21] Lee, J. S., Jung, H. W., and Hyun, J. C., 2000, "Melt Spinning Dynamics of Phan-Thien–Tanner Fluids," Korea-Aust. Rheol. J., **12**, p. 119.

[22] Keunings, R., Crochet, M. J., and Denn, M. M., 1983, "Profile Development in Continuous Drawing of Viscoelastic Liquids," Ind. Eng. Chem. Fundam., **22**, p. 347.

[23] Schultz, W. W., and Davis, S. H., 1982, "One-Dimensional Liquid Fibers," J. Rheol., **26**, p. 31.

[24] Bechtel, S. E., Cao, J. Z., and Forest, M. G., 1992, "Practical Application of a Higher OrderPerturbation Theory for Slender Viscoelastic Jets and Fibers," J. Non-Newtonian Fluid Mech., **41**, p. 201.

[25] Bechtel, S. E., Forest, M. G., and Lin, K. J., 1992, "Closure to All Orders in 1-D Models for Slender Viscoelastic Free Jets I. An Integrated Theory for Axisymmetric, Torsionless Flows, Stability and Applied Analysis of Continuous Media," Journal of Stability and Applied Analysis of Continuous Media, **2**, p. 59.

[26] Wang, Q., Forest, M. G., and Bechtel, S. E., 1995, "Modeling and Computation of the Onset of Failure in Polymeric Liquid Filaments," J. Non-Newtonian Fluid Mech., **58**, p. 97.

[27] Fisher, R. J., and Denn, M. M., 1976, "A Theory of Isothermal Melt Spinning and Draw Resonance," AIChE J., **22**, p. 236.

[28] Devereux, B. M., and Denn, M. M., 1994, "Frequency Response Analysis of Polymer Melt Spinning," Ind. Eng. Chem. Res., **33**, p. 2384.

[29] Joo, Y. L., Sun, J., Smith, M. D., Armstrong, R. C., Brown, R. A., and Ross, R. A., 2002, "Two-Dimensional Numerical Analysis of Non-Isothermal Melt Spinning With and Without Phase Transition," J. Non-Newtonian Fluid Mech., **102**, p. 37.

[30] Olagunju, D. O., 1999, "A 1-D Theory for Extensional Deformation of a Viscoelastic Filament Under Exponential Stretching," J. Non-Newtonian Fluid Mech., **87**, p. 27.

[31] Shimizu, J., Okui, N., Kaneko, A., and Toriumi, K., 1978, "High Speed Melt Spinning of Polyethylene Terephthalate (PET); Effects of Melt-Draw Ratio and Flow Rate," Sen'i Gakkaishi, **34**, p. T-64.

[32] Chang, J. C., and Denn, M. M., 1979, "An Experimental Study of Isothermal Spinning of a Newtonian and a Viscoelastic Liquid," J. Non-Newtonian Fluid Mech., **5**, p. 369.

[33] Laun, H. M., and Schuch, H., 1989, "Transient Elongational Viscosities and Drawability of Polymer Melts," J. Rheol., **33**, p. 119.

[34] Cao, F., Khayat, R. E., and Puskas, J. E., 2005, "Effect of Inertia and Gravity on Draw Resonance in High-Speed Film Casting of Newtonian Fluids," Int. J. Solids Struct., **42**, p. 5734.

# Confined Swirling Flows of Aqueous Surfactant Solutions Due to a Rotating Disk in a Cylindrical Casing

**Shinji Tamano**
e-mail: tamano.shinji@nitech.ac.jp

**Motoyuki Itoh**

Graduate School of Engineering,
Nagoya Institute of Technology,
Gokiso-cho, Showa-ku,
Nagoya,
Aichi 466-8555, Japan

**Mitsunori Yoshida**
Toyota Industries Corporation,
2-1 Toyoda-cho,
Kariya,
Aichi 448-8671, Japan

**Kazuhiko Yokota**
Graduate School of Engineering,
Nagoya Institute of Technology,
Gokiso-cho, Showa-ku,
Nagoya,
Aichi 466-8555, Japan

*In this study, confined swirling flows of an aqueous surfactant solution due to a rotating disk in a cylindrical casing were investigated using a sectional flow visualization technique and a two-component laser Doppler velocimetry system. The concentrations of aqueous surfactant solutions ($C_{14}$TASal) are 0.4 wt %, 0.8 wt %, and 1.2 wt %. Rheological properties such as shear viscosity and first normal stress difference of the surfactant solution were measured with a rheometer. The patterns of secondary flow were classified using the Reynolds and elasticity numbers. We revealed that the projection formed near the center of the rotating disk moved up and down at a constant frequency for $C_{14}$TASal 0.8 wt % and 1.2 wt %, which has not been reported as far as we know. The effects of the Reynolds number, elasticity number, and aspect ratio on the velocity profiles were clarified. It was also found that the region of rigid body rotation existed at the higher Reynolds number tested for $C_{14}$TASal 0.4 wt %.* [DOI: 10.1115/1.2956593]

*Keywords: confined swirling flow, surfactant solution, secondary flow, flow visualization, LDV measurement*

## 1 Introduction

The study of confined swirling flows of viscoelastic fluids is attractive from a scientific point of view for constructing rheological models owing to the well-defined boundary condition, and its understanding is of great importance in many process engineering applications, fluid machinery such as viscous coupling and viscous heater that uses fluid friction, and rotary agitators of viscoelastic fluids. Therefore, many experimental studies have been conducted to examine the fundamental flow behavior in the confined swirling flow of a polymer solution, which is a typical viscoelastic fluid.

A pioneering study on the viscoelastic swirling flow due to a rotating disk in a cylindrical casing was conducted by Hill [1], who observed that the secondary flow direction of polymer solutions was opposite to that of Newtonian fluids due to the elastic force. Day et al. [2] observed the ring vortex near the center of the rotating disk, and Escudier and Cullen [3] found the double-cell structure of the secondary flow using the flow visualization technique. Recently, Moroi et al. [4] and Itoh et al. [5] investigated the velocity fields of the confined swirling flow using particle tracking velocimetry (PTV) and laser Doppler velocimetry (LDV) measurements, respectively. Moreover, Stokes et al. [6,7] performed particle image velocimetry (PIV) measurements of confined swirling flows of a range of low-to high-viscosity flexible polyacrylamide solutions with a constant viscosity (Boger fluids) and a semirigid xanthan gum Boger fluid and clarified the inertia and elasticity effects on velocity fields. Stokes and Boger [8] investigated unsteady (chaotic) secondary flow using flow visualization and presented a stability boundary diagram for the confined swirling flow of polyacrylamide Boger fluids. Quite recently, Tamano et al. [9] investigated the unsteady confined swirling flow of polymer solutions with the shear-thinning property using the flow visualization technique and found a new phenomenon of vortex shedding. The ring vortex is formed near the center of the rotating disk and grows larger, and it is finally shed in the axial direction. This process is repeated periodically and is totally different from the spiral instability (continuous vortex shedding) described in Day et al. [2], Stokes et al. [7], and Stokes and Boger [8].

In addition to the experimental study, there are some analytical and numerical studies on the confined swirling flow of viscoelastic fluids. A pioneering analytical study on the confined swirling flow of viscoelastic fluids due to a rotating disk in a cylindrical casing was performed by Kramer and Johnson [10], who showed the reversed secondary flow and double-cell structure. Xue et al. [11] performed a fully three-dimensional numerical simulation of viscoelastic swirling flows in a confined cylinder using the upper convected Maxwell (UCM) and Phan-Thien–Tanner (PTT) models and compared the results with the available experimental results in terms of the vortex breakdown and double-cell structure. Moroi et al. [4] and Itoh et al. [5] performed the axisymmetric numerical simulation of confined swirling flows of viscoelastic fluids due to a rotating disk using the constitutive models, such as the power law, PTT, and Giesekus models, and compared the results with the experimental data on the velocity profiles. Siginer [12] analytically investigated the instability and bifurcations of the secondary flow pattern of viscoelastic fluids in the meridional plane in the confined rotating disk geometry.

The rheological properties of surfactant and polymer solutions are generally similar since the behavior of wormlike micelle solutions is similar to that of polymer solutions. However, the micelles, which are in a state of thermodynamic equilibrium within the solvent, can be continuously broken and reformed, unlike a covalently bonded polymer backbone [13]. Therefore, a surfactant solution can be a promising fluid for engineering applications. However, there have been no studies on the confined swirling flow of a surfactant solution, which is less affected by the mechanical degradation, unlike the polymer solution, while there are experimental studies on a swirling flow of dilute surfactant solutions with a free surface due to a rotating disk [14–16] and correspond-

Contributed by the Fluids Engineering Division of ASME for publication in the JOURNAL OF FLUIDS ENGINEERING. Manuscript received February 27, 2007; final manuscript received August 23, 2007; published online July 23, 2008. Assoc. Editor: Dennis Siginer.

  

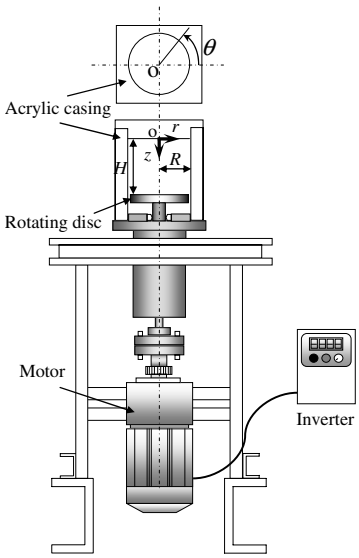


**Fig. 1 Experimental apparatus**

ing analytical and numerical studies [17–19]. There are also experimental studies of a turbulent swirling pipe flow of dilute surfactant solutions [20,21].

In this study, first, the flow patterns of confined swirling flows for the concentrated surfactant solutions (0.4 wt %, 0.8 wt %, and 1.2 wt %) due to a rotating disk were clarified by the sectional flow visualization. Then, LDV measurements were conducted to clarify the radial and axial distributions of azimuthal and axial velocity components in order to clarify the effects of the Reynolds number, elasticity number, and aspect ratio. In addition, we investigated the period and region of the projection oscillation observed for $C_{14}$TASal 0.8 wt % and 1.2 wt %.

## 2 Experimental Apparatus and Procedure

The experimental apparatus used in the present study is shown in Fig. 1. The main body consists of a rotating disk enclosed in a casing. The surface of the rotating disk is smooth, and the outside diameter is 180 mm ($R$=90 mm). The disk is painted black to reduce the effect of reflected light. The aspect ratios of the distance $H$ between the casing end wall and the rotating disk to the radius of the rotating disk $R$ were $H/R$=2.0 and 1.0. The disk is driven by a motor and decelerator with an inverter control. The clear acrylic casing is cylindrical with an inner diameter of 181 mm. The exterior is rectangular, with a length on one side of 215 mm, to minimize the effect of light refraction while observing cross sections. In this study, $r$, $\theta$, and $z$ represent the radial, azimuthal, and axial directions, respectively, and their origin is at the center of the upper stationary disk (see Fig. 1).

The working fluids were aqueous surfactant solutions ($C_{14}$TASal), whose concentrations were 0.4 wt %, 0.8 wt %, and 1.2 wt %, and consisted of *n*-tetra decyltrimethyl ammonium bromide ($C_{14}$TABr) and sodium salicylate (NaSal). The molar ratio of NaSal to $C_{14}$TABr was 1. Working fluids were mixed by the stirrer for more than 5 h, then allowed to rest for more than 2 day to allow air bubbles to escape.

The shear viscosity $\eta$ and the first normal stress difference $N_1$ of the working fluid were measured using a cone-and-plate-type rheometer (rheology, SR-5, cone angle $\theta$=2.3 deg, diameter $d$ =40 mm). The uncertainty intervals of the data for $\eta$ and $N_1$ are 5% and 10%, respectively, of their absolute values. Measurements of $\eta$ and $N_1$ were conducted at the solution temperature $T$ =22°C.

As a visualization dye, the mixture of rhodamine B and the working fluid ($C_{14}$TASal) was used. Note that the chemical reaction between the rhodamine B and $C_{14}$TASal solutions was not observed in the present study. For the sectional visualization, the visualization dye was quasisteadily injected in the meridian section ($r$-$z$ section) using a homemade injector, and the meridian section was illuminated by the slit light source (halogen, output: 1500 W, slit width: 3 mm). After increasing the rotation speed of the disk quasisteadily, the streak line was observed and maintained for more than 2 h. The images obtained for sectional flow visualization were captured by a digital video camera (DCR-VX200, Sony, Ltd.).

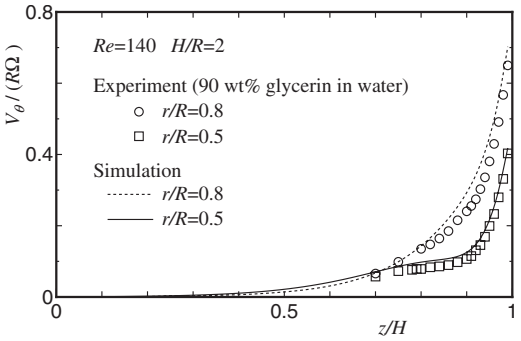


**Fig. 2 Axial distribution of azimuthal velocity component for Newtonian fluid at Re=140 and H/R=2**

The two-component LDV system (300 mW argon-ion laser, Kanomax, Ltd.) was used in the backscatter mode. The laser light was separated into blue and green beams with wavelengths of 514.5 nm and 488.0 nm, respectively. The measuring volumes are $0.072\times0.864$ mm$^2$ for the green beams and $0.068\times0.824$ mm$^2$ for the blue beams. The flow was seeded with nylon powder particles (mean diameter: 4.1 $\mu$m and specific gravity: 1.02, Kanomax, Ltd.). LDV measurements under fluid temperature $T$ =22°C were made. The pedestal component was reduced by the high-pass filter of the commercial signal processing system (Model 8007, Kanomax, Ltd.), and the high-frequency noise and Nyquist frequency were reduced by the low-pass filter. In order to validate the present LDV measurements, we performed the LDV measurements at the aspect ratio $H/R$=2 and at the Reynolds number Re=140 for the confined swirling flow of a Newtonian fluid (90 wt % glycerin in water), and we compared the experimental data on the axial distribution of the azimuthal velocity component $V_\theta/(R\Omega)$ at radial locations $r/R$=0.5 and 0.8 with the corresponding numerical data obtained by the axisymmetric numerical simulation for Newtonian fluids (see Fig. 2). Figure 2 shows that the accuracy of present LDV measurements is almost satisfactory.

## 3 Rheological Properties

Figures 3($a$) and 3($b$) show measurements of the shear viscosity $\eta$ and the first normal stress difference $N_1$ at the solution temperature of 22°C, respectively. The solid lines represent the fitting curves of the Giesekus model [22]. The shear viscosity $\eta$ increases with the increase in the concentration $C$ of $C_{14}$TASal solutions. Shear thinning can also be observed where the shear viscosity decreases gradually with the increase in shear rate $\dot{\gamma}$. The first normal stress difference $N_1$ increases by increasing both $C$ and $\dot{\gamma}$. It was confirmed that the shear viscosity and the first normal stress difference hardly changed before and after a test run, which indicates no appreciable degradation of working fluids during a test run. The density $\rho$ of water was used for $C_{14}$TASal solutions.

Table 1 shows Giesekus model parameters $\eta_0$, $\alpha$, and $\lambda$, which were obtained by fitting the Giesekus model curve with measurements of $\eta$ and $N_1$ best. $\eta_0$ and $\lambda$ are the zero shear viscosity and relaxation time, respectively. $\alpha$ is the mobility factor, which is

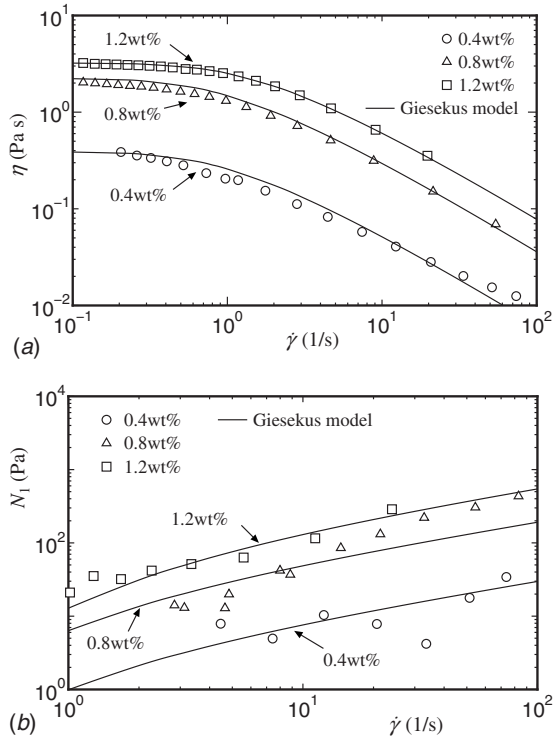


**Fig. 3 Rheological properties for steady shear flow of surfactant solutions at $T=22°C$: (*a*) shear viscosity and (*b*) first normal stress difference**

between 0 and 1 [22]. Note that the Giesekus model curve coincides better with the measurement of $\eta$, rather than the measurement of $N_1$.

In the present study, the Reynolds number $\mathrm{Re}_0$ and elasticity number $E_0$ are defined as follows:

$$\mathrm{Re}_0 = \frac{\rho R^2 \Omega}{\eta_0} \tag{1}$$

$$E_0 = \frac{\lambda \eta_0}{\rho R^2} \tag{2}$$

Here, $\Omega$ is the angular velocity of the rotating disk and was varied from 1 to 37 rad/s in the present study. $\mathrm{Re}_0$ and $E_0$ are evaluated by the Giesekus model parameters shown in Table 1. The elasticity number $E_0$ increases with the increase in the concentration $C$, and it is constant for a value of $C$.

## 4 Flow Visualization

**4.1 Secondary Flow Patterns.** Figure 4 shows the three kinds of typical secondary flow patterns observed for $C_{14}$TASal 0.8 wt % at $H/R=2$. The secondary flow, whose direction is opposite to that of the Newtonian fluid, i.e., inward near the rotating disk in the radial direction, is formed. This reverse flow pattern is generated due to the elastic stress [1,5,7,8], and it is termed "type R" in the present study. Figure 4(*a*) shows the secondary flow pattern, in which an unsteady spiral vortex appears in the vicinity of the central axis in addition to type *R*, that is termed "type Rs" (reverse spiral). Type Rs is different from the secondary flow pattern for polymer solutions, in which an unsteady spiral vortex appears in the vicinity of the central axis in addition to type R, as reported in the previous studies [2,4,5,7,8], which is termed "type Rt" (reverse transition). Thus, the pitch of the spiral vortex near the central axis for surfactant solutions (type Rs) is much smaller than that for polymer solutions (type Rt).

**Table 1 Giesekus model parameters and elasticity number for surfactant solutions**

| | $\eta_0$ (Pa s) | $\alpha$ | $\lambda$ (s) | $E_0$ |
|---|---|---|---|---|
| $C_{14}$ TASal 0.4 wt % | 0.39 | 0.050 | 2.5 | 0.145 |
| $C_{14}$ TASal 0.8 wt % | 2.24 | 0.040 | 2.8 | 0.774 |
| $C_{14}$ TASal 1.2 wt % | 3.23 | 0.015 | 3.0 | 1.20 |

Figure 4(*b*) shows the flow pattern, in which a projection is formed near the rotating disk and then periodically moves up and down. This flow pattern is termed "type PO" (projection oscillation). In the case of type PO, the fluid transport can be observed between the region within the projection and the region represented by the symbol A in the illustration of Fig. 4(*b*).

The flow pattern, in which the secondary flow direction is the same as that of Newtonian fluids, is termed "type N." The flow pattern, in which the steady projection is formed near the rotating disk in addition to type N, is termed "Type Np" (Newtonian projection). The typical secondary flow pattern for type Np is shown in Fig. 4(*c*).

In addition to the above flow patterns, we observed a flow pattern, in which a double-cell structure with two cells aligned laterally in the radial direction is formed. It is termed "type DC," and has been reported in the previous study [3,5,7] (not shown here).

Figure 5 shows the flow pattern for $C_{14}$TASal 0.4 wt % at $H/R=2$ and $\mathrm{Re}_0=609$, in which the flow around the rotating axis is unstable and the axial flow along the rotating axis cannot be observed. This flow pattern is termed "type VB" since the flow pattern is somewhat similar to the vortex breakdown observed by Stokes et al. [6]. Note that type VB is not quite the same as the classic vortex breakdown bubble, but it is a typical flow pattern observed for polymer solutions and Boger fluids when the elastic flow competas with the Newtonian flow.

**4.2 Summary of Flow Patterns.** Using the Reynolds number $\mathrm{Re}_0$ and the elasticity number $E_0$, the secondary flow patterns observed at $H/R=1$ and 2 in the present study are classified, as shown in Fig. 6(*a*) and 6(*b*), respectively. It is found that the secondary flow pattern of surfactant solutions is basically the same as those of polymer solutions and Boger fluids except for type PO. For $C_{14}$TASal 0.4 wt % in which the elasticity number is smallest, the flow pattern changes with increasing $\mathrm{Re}_0$ to types R, DC, N, and VB. For both $C_{14}$TASal 0.8 wt % and 1.2 wt %, the structure of the secondary flow changes to types Rs, DC, PO, Np, and N, as the Reynolds number increases. Such variation in flow pattern is the same at $H/R=1$ and 2. Note that type PO was not observed for $C_{14}$TASal 0.4 wt %, while type VB was not observed for $C_{14}$TASal 0.8 wt % and 1.2 wt %.

## 5 LDV Measurement

**5.1 Effect of the Reynolds Number.** Figures 7(*a*) and 7(*b*) show the velocity vectors obtained by the LDV measurement which is superimposed on the sectional flow visualization at $H/R=2$ for $C_{14}$TASal 0.4 wt % at $\mathrm{Re}_0=87.0$ and 261, respectively. Velocity vectors at both Reynolds numbers show that the secondary flow direction is the same as that of Newtonian fluids and is consistent with the flow visualization (type N). With increasing Reynolds number, the circulation region of secondary flow becomes larger and the center of circulation moves away from the rotating disk.

In order to investigate the effect of Reynolds number on the velocity profile quantitatively, radial distributions of azimuthal and axial velocity components for $C_{14}$TASal 0.4 wt % at $z/H=0.9$ and $H/R=2$ are shown in Figs. 8(*a*) and 8(*b*), respectively. In these figures, numerical simulation results for the Newtonian fluid are also presented for comparison. Figure 8(*a*) shows that with increasing Reynolds number, the radial location of the maxi-

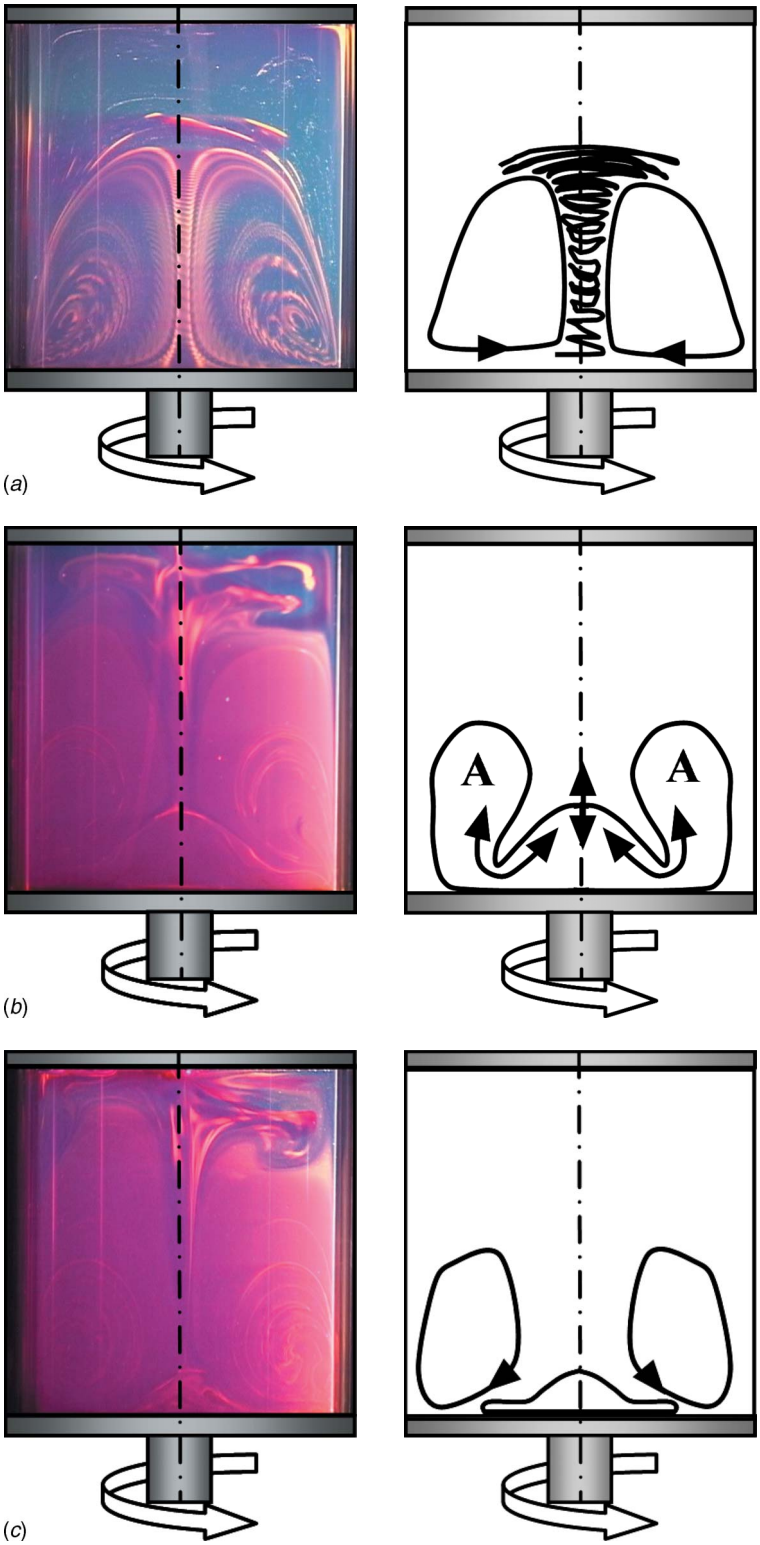


**Fig. 4 Typical secondary flow patterns for $C_{14}$TASal 0.8 wt % at H/R=2: (*a*) type Rs at $Re_0$=1.51, (*b*) type PO at $Re_0$=22.7, and (*c*) type Np at $Re_0$=49.2**

mum of the azimuthal velocity $V_\theta/(R\Omega)$ becomes closer to the sidewall of the cylindrical casing, which indicates that the boundary layer on the sidewall becomes thinner. The location of the maximum of $V_\theta/(R\Omega)$ for $C_{14}$TASal 0.4 wt % is closer to the sidewall compared to the Newtonian fluid at the corresponding Reynolds number $Re_0$. Considering that for a Newtonian fluid the maximum of the azimuthal velocity shifts toward the sidewall with an increase in the Reynolds number, this may be due to the Reynolds number effect caused by the shear-thinning property, which yields a decrease in the shear viscosity near the sidewall of the cylindrical casing. The same tendency has also been observed in a previous study (Moroi et al. [4]) at a lower Reynolds number.

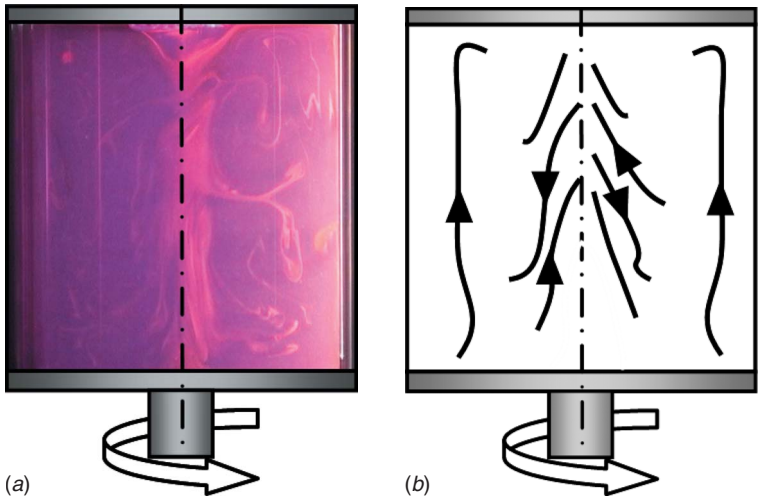


**Fig. 5 Secondary flow pattern for $C_{14}$TASal 0.4 wt % at H/R=2 and $Re_0$=609 (type VB)**

Note that the maximum of the azimuthal velocity shifts toward the rotating axis due to the effect of the first normal stress difference (see Fig. 9(*b*)). Positive and negative values of the axial velocity component $V_z/(R\Omega)$ indicate that the secondary flow is directed toward and away from the rotating disk, respectively. Therefore, Fig. 8(*b*) indicates that the secondary flow direction for $C_{14}$TASal 0.4 wt % at $Re_0$=10.4 is opposite to those for $C_{14}$TASal 0.4 wt % at higher Reynolds numbers and that for the Newtonian fluid (type R).

**5.2 Effect of the Elasticity Number.** In order to investigate the effect of an elasticity number on the velocity profile, radial

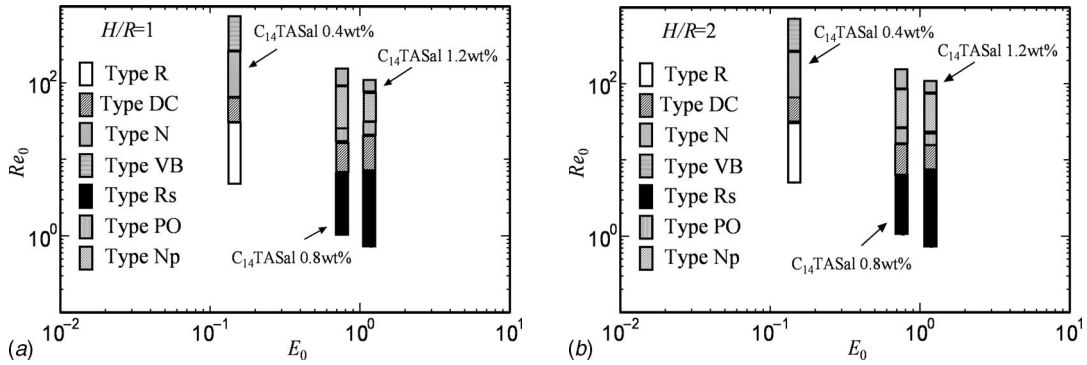


**Fig. 6 Dependence of secondary flow patterns on $E_0$ and $Re_0$: (*a*) H/R=1 and (*b*) H/R=2**

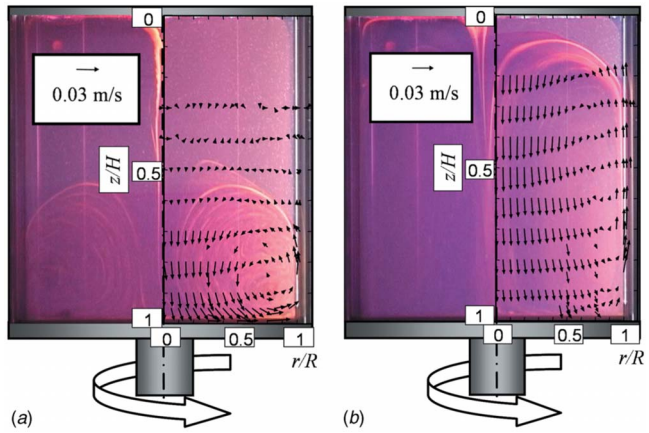


**Fig. 7 Velocity vectors on the *r-z* plane for $C_{14}$TASal 0.4 wt %: (*a*) $Re_0$ =87.0 and (*b*) $Re_0$=261**

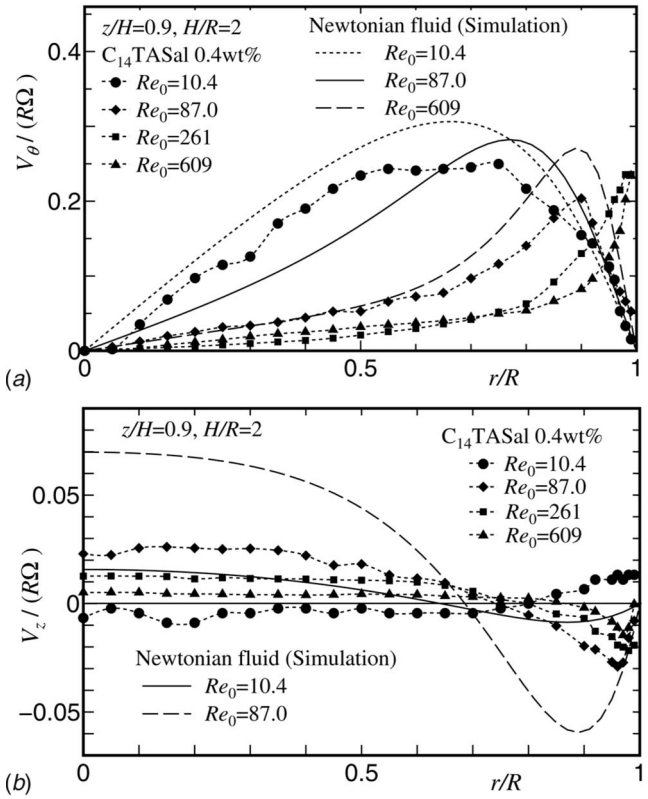


**Fig. 8 Radial distribution of velocity for $C_{14}$TASal 0.4 wt % at z/H=0.9 and H/R=2: (*a*) azimuthal velocity component and (*b*) axial velocity component**

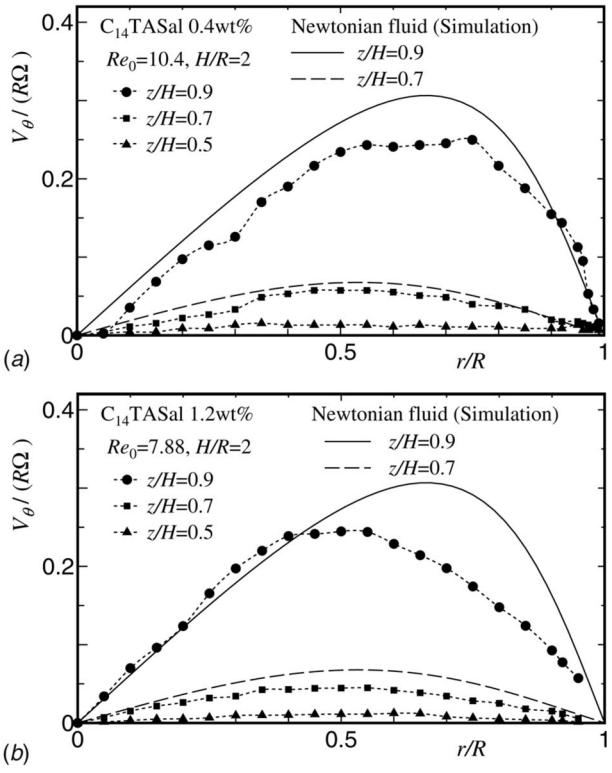


**Fig. 9 Radial distribution of the azimuthal velocity component at H/R=2: (*a*) $C_{14}$TASal 0.4 wt % and (*b*) $C_{14}$TASal 1.2 wt %**

distributions of the azimuthal velocity component $V_\theta/(R\Omega)$ at $z/H=0.5$, 0.7, and 0.9 and $H/R=2$ for $C_{14}$TASal 0.4 wt % ($E_0=0.145$) and $C_{14}$TASal 1.2 wt % ($E_0=1.20$) are shown in Figs. 9(*a*) and 9(*b*), respectively. The Reynolds numbers for $C_{14}$TASal 0.4 wt % and 1.2 wt % are $Re_0=10.4$ and 7.88, respectively, where the secondary flow direction is opposite to that of the Newtonian fluid (type R). Radial distributions of the axial velocity component $V_z/(R\Omega)$ at $z/H=0.5$, 0.7, and 0.9 and $H/R=2$ for $C_{14}$TASal 0.4 wt % and 1.2 wt % are also shown in Figs. 10(*a*) and 10(*b*), respectively.

Near the rotating disk ($z/H=0.9$), the radial location of the maximum of $V_\theta/(R\Omega)$ for $C_{14}$TASal 0.4 wt % ($r/R=0.7$) agrees well with that of the Newtonian fluid, while the maximum location for $C_{14}$TASal 1.2 wt % ($r/R=0.4$) moves toward the rotating axis compared to the Newtonian fluid (Fig. 9). At $z/H=0.9$, the strength of the secondary flow for $C_{14}$TASal 1.2 wt %, in which the flow direction is inward near the rotating disk in the radial direction, is larger than that for $C_{14}$TASal 0.4 wt %. Therefore, it can be deduced that the larger amount of high angular momentum near the edge of the rotating disk is transported inward in the radial direction for $C_{14}$TASal 1.2 wt %, where the elasticity number is larger than that of $C_{14}$TASal 0.4 wt %.

Figure 10 shows that the absolute value of $V_z/(R\Omega)$ for $C_{14}$TASal 1.2 wt % at $z/H=0.7$ and 0.9 is much larger than that for $C_{14}$TASal 0.4 wt %.

Figures 9 and 10 also indicate that the difference in the axial velocity component between $C_{14}$TASal 0.4 wt % and 1.2 wt % is larger than that in the azimuthal velocity component. This shows that the secondary flow is more affected by the effect of the elasticity number, while the main azimuthal flow is less affected.

**5.3 Effect of the Aspect Ratio.** In the case of a different aspect ratio, the axial location from the rotating disk $z'(=H-z)$ is also different even at the same nondimensional distance from the upper stationary disk $z/H$. Therefore, to investigate the effect of the aspect ratio ($H/R=1$ and 2) on the velocity profile, the axial distributions of the azimuthal velocity component for $C_{14}$TASal 0.4 wt % at $Re_0=87.0$ are shown in Fig. 11, where the abscissa is $z'/R$. Note that the profiles of the Newtonian fluid at $H/R=1$ and 2 overlap each other. The profile of $V_\theta/(R\Omega)$ for $C_{14}$TASal 0.4 wt % at $H/R=1$ agrees with that at $H/R=2$ at both radial locations $r/R=0.7$ and 0.9. Note that the profiles of $V_\theta/(R\Omega)$ at $H/R=1$ and 2 cannot collapse if $z/H$ is used as the abscissa. We also confirmed that the profiles of radial and axial velocity components, which correspond to the secondary flow velocity components, were well scaled using the abscissa of $z'/R$ (not shown here).

**5.4 Region of Rigid Rotation.** Figures 12(*a*)–12(*c*) show the radial distributions of the azimuthal velocity component $V_\theta/(R\Omega)$ at the axial locations $z/H=0.3$, 0.5, 0.7, and 0.9 and the aspect ratio $H/R=2$ for $C_{14}$TASal 0.4 wt % at the Reynolds number $Re_0=87.0$, 261, and 609, respectively. The profiles of $V_\theta/(R\Omega)$ at $Re_0=261$ and 609 are linear in the regions of $r/R<0.5$ and $r/R<0.8$, respectively, and are independent of the axial location $z/H$, which indicates that the fluid in these regions rotates with rigid body rotation. On the other hand, the region of rigid body rotation was not observed at $Re_0=87.0$. For the Newtonian fluid, it is known that the potential core region, in which the fluid rotates with rigid body rotation, is formed between the boundary layers on the upper and lower walls at much higher Reynolds numbers [23].

Next, radial distributions of the azimuthal velocity component at $z/H=0.3$ and $H/R=1$ and 2 for $C_{14}$TASal 0.4 wt % at $Re_0=261$ and 609 are shown in Fig. 13. $V_\theta/(R\Omega)$ at $H/R=1$ is larger than $V_\theta/(R\Omega)$ at $H/R=2$, which is independent of the Reynolds number. If the aspect ratio is the same, $V_\theta/(R\Omega)$ at $Re_0=261$ is smaller than $V_\theta/(R\Omega)$ at $Re_0=609$. The angular velocities of the

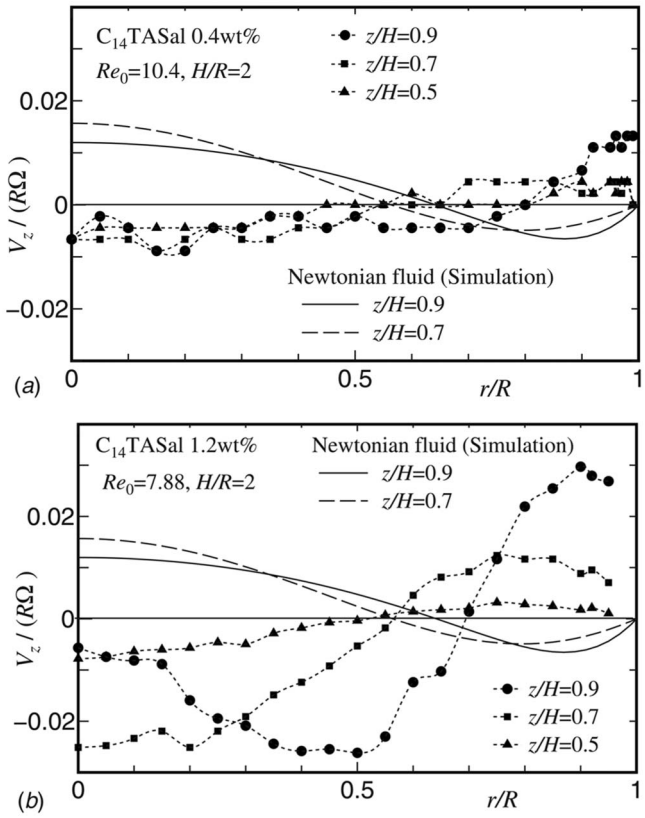


**Fig. 10 Radial distribution of the axial velocity component at H/R=2: (*a*) $C_{14}$TASal 0.4 wt % and (b) $C_{14}$TASal 1.2 wt %**

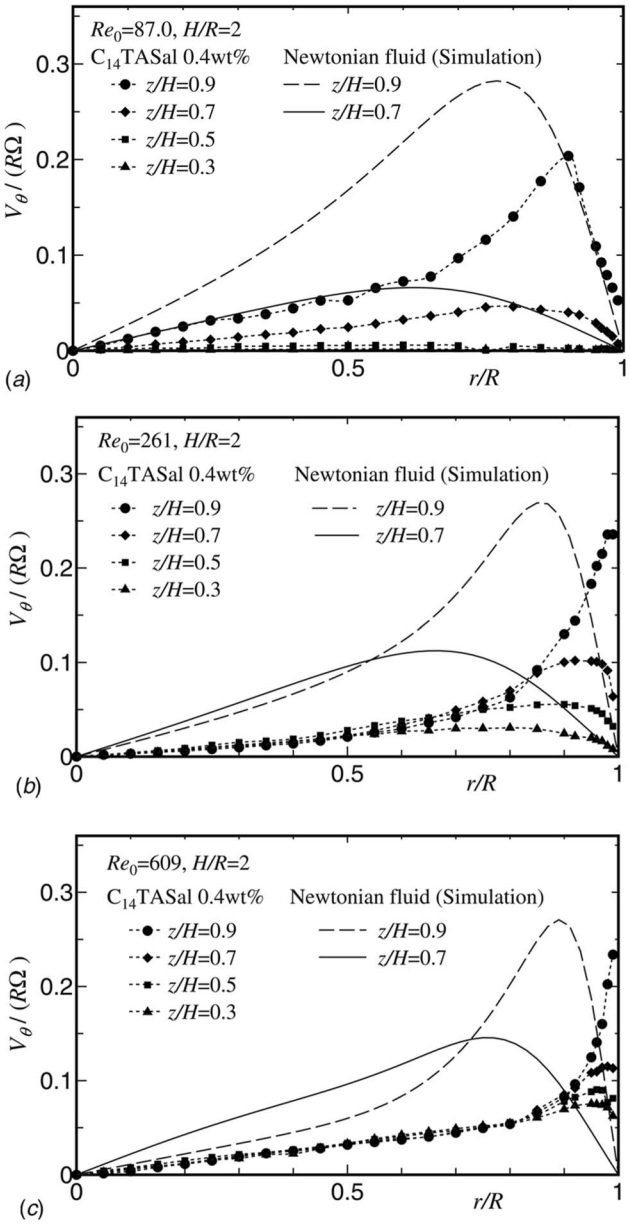


**Fig. 12 Radial distribution of the azimuthal velocity component for $C_{14}$TASal 0.4 wt % at H/R=2: (*a*) $Re_0$=87.0, (*b*) $Re_0$ =261, and (*c*) $Re_0$=609**

rigid body rotation at $(\mathrm{Re}_0, H/R)=(261,1)$, $(261,2)$, $(609,1)$, and $(609,2)$ are 0.18, 0.043, 0.22, and 0.071 times that of the rotating disk.

## 6 Oscillation Analysis

**6.1 Period of Projection Oscillation.** Figure 14 shows the time variations of azimuthal and axial velocity components $V_\theta$ and $V_z$ for $C_{14}$TASal 0.8 wt % at $r/R=0.3$, $z/H=0.9$, $\mathrm{Re}_0=22.7$, and $H/R=2$, where the projection oscillation (type PO) was clearly observed. It is found that $V_\theta$ and $V_z$ are periodically oscillating and the phase difference between $V_\theta$ and $V_z$ is about 90 deg. Taking account of the angular momentum conservation, the phase difference is explained as follows. When the fluid near the rotating disk, where $V_\theta$ is relatively large, moves away from the rotating disk ($V_z<0$), $V_\theta$ becomes larger. On the other hand, when the fluid away from the rotating disk, where $V_\theta$ is relatively small, moves toward the rotating disk ($V_z>0$), $V_\theta$ becomes smaller.

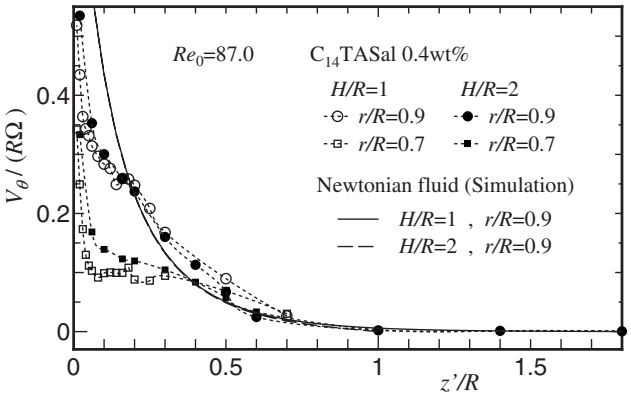


**Fig. 11 Axial distribution of the azimuthal velocity component for $C_{14}$TASal 0.4 wt % at $Re_0$=87.0**

Next, we investigate the frequency of periodic oscillations for the axial and azimuthal velocity fluctuations. Figures 15(*a*) and 15(*b*) show the power spectra of axial and azimuthal velocity fluctuations ($P_z$ and $P_\theta$) for $C_{14}$TASal 0.8 wt % at $z/H=0.9$, $\mathrm{Re}_0=22.7$, and $H/R=2$. The number of sampling data was 2048 for the power spectrum analysis. At $r/R=0.3$ and $z/H=0.9$, a distinct peak appears at the frequency $f\simeq 0.1$ Hz in the profile of $P_z$. On the other hand, such a distinct peak cannot be observed in the profile of $P_\theta$, which seems to protrude at $f\simeq 0.1$ Hz, which corresponds to the frequency of the peak of $P_z$.

To investigate the dependence of the period of projection oscillation on the Reynolds number, the nondimensional period

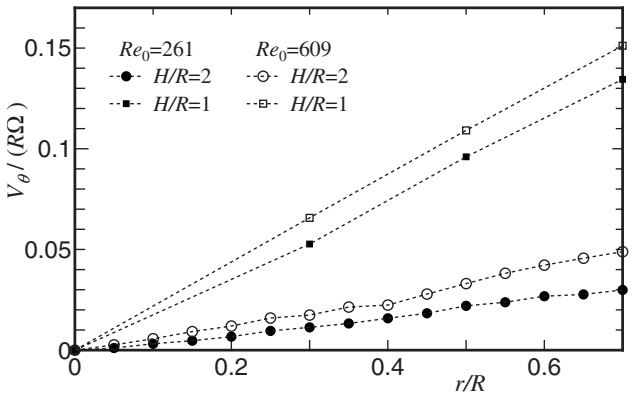


**Fig. 13 Radial distribution of the azimuthal velocity component for $C_{14}$TASal 0.4 wt % at z/H=0.3**

$T/(2\pi/\Omega)$ of the projection oscillation versus Reynolds number $Re_0$ for $C_{14}$TASal 0.8 wt % and 1.2 wt % at $H/R=2$ is shown in Fig. 16. The period $T/(2\pi/\Omega)$ represents the rotation number of the rotating disk during the once up and down oscillation. In the figure, the data obtained by both the sectional flow visualization and LDV measurement are presented. In terms of flow visualization, the period $T$ is obtained by measuring the time interval for one oscillation from the time sequence of flow images (movie). The period obtained by flow visualization is the average of ten measurements. In terms of LDV measurement, the period is obtained by averaging the periods evaluated by the profiles of power spectra at the different locations $(z/H, r/R)=(0.7, 0.1)$, (0.8, 0.1), and (0.9, 0.1). It is found that the period is independent of the Reynolds number $Re_0$ for both $C_{14}$TASal 0.8 wt % and 1.2 wt %, where the period for the flow visualization almost agrees with that for the LDV measurement. The period $T/(2\pi/\Omega)$ of projection oscillation for $C_{14}$TASal 1.2 wt % is smaller than that for $C_{14}$TASal 0.8 wt % with a smaller elasticity number. We confirmed that the period at $H/R=1$ was almost the same at $H/R=2$ (not shown here).

**6.2 Region of Projection Oscillation.** Figure 17(*a*) shows the contour of the root mean square of the axial velocity fluctuation $V_{zrms}/(R\Omega)$ on the *r-z* plane for $C_{14}$TASal 0.8 wt % at $Re_0=22.7$ and $H/R=2$. In the figure, the darker area represents the larger value of $V_{zrms}/(R\Omega)$. The contour is described using the measurements at 19 and 10 points in the radial and axial directions, respectively. Near the rotating axis, the value of $V_{zrms}/(R\Omega)$ becomes larger as the rotating disk is approached, which is supported by the flow visualization. However, $V_{zrms}/(R\Omega)$ is relatively large even near the side of the cylindrical casing, which does not correspond to the flow visualization. This is because the axial velocity fluctuation consists of various frequencies including $f=0.1$ Hz near the sidewall. Therefore, the contour of the integral value of the energy spectrum of filtered $V_z$ is shown in Fig. 17(*b*). The filter band is between 0.05 Hz and 0.13 Hz, which includes the frequency of the spectral peak of projection oscillation. It is found in Fig. 17(*b*) that the region (black area), in which the velocity fluctuation with the frequency of projection oscillation is dominant, exists only near the center of the rotating disk, which is consistent with the flow visualization.

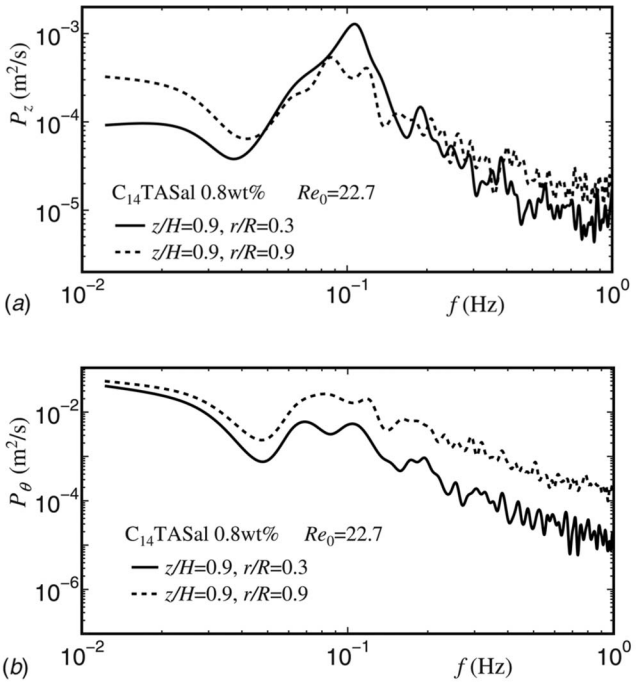


**Fig. 15 Power spectra for $C_{14}$TASal 0.8 wt % at z/H=0.9, $Re_0$ =22.7, and H/R=2: (*a*) axial velocity component and (*b*) azimuthal velocity component**

## 7 Conclusions

Confined swirling flows of an aqueous surfactant solution due to a rotating disk in a cylindrical casing were investigated using a sectional flow visualization technique and a two-component LDV system. The aspect ratios of the distance between the casing end wall and the rotating disk to the radius of the rotating disk were 1

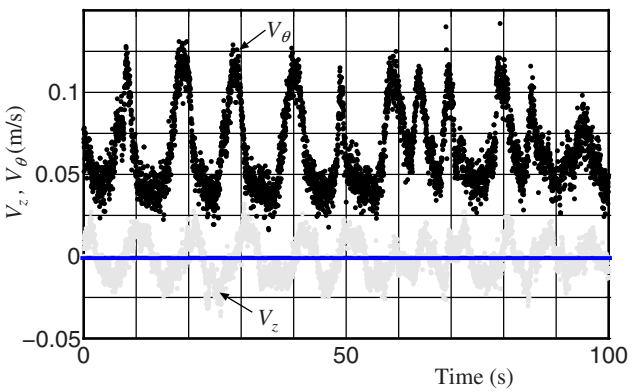


**Fig. 14 Time variations of $V_\theta$ and $V_z$ for $C_{14}$TASal 0.8 wt % at r/R=0.3, z/H=0.9, $Re_0$=22.7, and H/R=2**

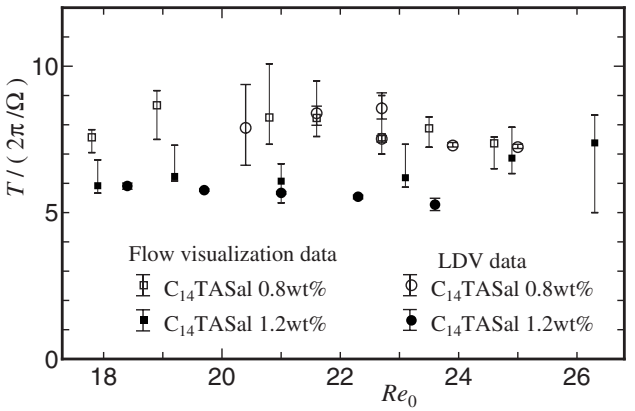


**Fig. 16 Period of oscillation versus Reynolds number for $C_{14}$TASal 0.8 wt % and 1.2 wt % at H/R=2**

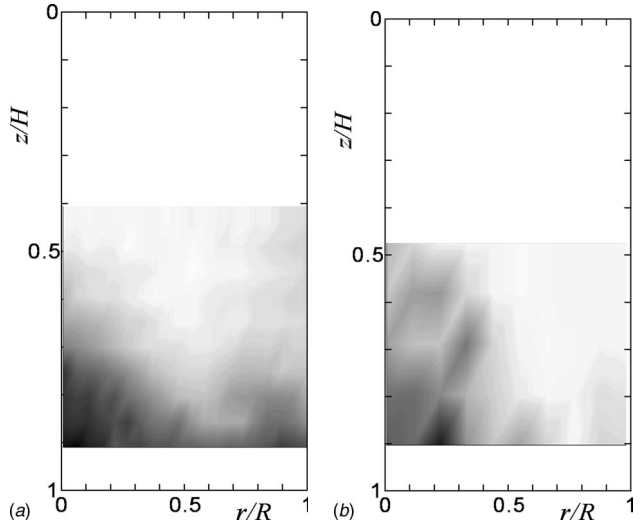


**Fig. 17 Contours on the *r-z* plane for $C_{14}$TASal 0.8 wt % at $Re_0$=22.7 and H/R=2: (*a*) $V_{zrms}/(R\Omega)$ and (*b*) integral value of the energy spectrum of filtered $V_z$. The filter band is between 0.05 Hz and 0.13 Hz.**

and 2, respectively. The aqueous surfactant solutions ($C_{14}$TASal), whose concentrations are 0.4 wt %, 0.8 wt % and 1.2 wt %, consisted of $C_{14}$TABr and NaSal. Rheological properties such as shear viscosity and first normal stress difference of the surfactant solution were measured with a rheometer. The patterns of the secondary flow were classified using the Reynolds and elasticity numbers. The effects of the Reynolds number, elasticity number, and aspect ratio on the velocity profiles were investigated. The main results of the present study may be summarized as follows.

(1) The secondary flow pattern of surfactant solutions is basically the same as those of polymer solutions and Boger fluids except for type PO.
(2) The pitch of the spiral vortex near the central axis for surfactant solutions, which was observed at the relatively low Reynolds number examined here, was much smaller than that for polymer solutions.
(3) For $C_{14}$TASal 0.8 wt % and 1.2 wt %, the projection was formed near the rotating disk and moved up and down at a constant frequency, while no such flow pattern was observed for $C_{14}$TASal 0.4 wt % with a smaller elasticity number. The period of the projection oscillation and the oscillating region were clarified by examining the energy spectrum of velocity fluctuations.
(4) With the increase on the Reynolds number, the radial location of the maximum of the azimuthal velocity becomes closer to the sidewall of the cylindrical casing due to the shear-thinning effect. On the other hand, the maximum of the azimuthal velocity shifts toward the rotating axis due to the effect of the first normal stress difference.
(5) The difference in the axial velocity component between $C_{14}$TASal 0.4 wt % and 1.2 wt % is larger than that in the azimuthal velocity component, which indicates that the secondary flow is more affected by the elasticity number, while the main flow is less affected.
(6) The region of rigid body rotation was revealed to exist at the high Reynolds number tested for $C_{14}$TASal 0.4 wt %.

In this study, we utilized the Giesekus model to determine the Giesekus model parameters and evaluate the Reynolds and elasticity numbers. Unfortunately, however, we could not predict the modification of the flow pattern and the projection oscillation observed in the present experiment using the corresponding numerical simulation of viscoelastic fluids with the Giesekus model at the moment. Further effort in improving our numerical code would be necessary in order to clarify whether the Giesekus model is appropriate to model the confined swirling flow of surfactant solutions.

## Acknowledgment

The gear motor with an inverter provided by Sumitomo Heavy Industries, Ltd. is gratefully acknowledged. The authors wish to thank Professor H. Suzuki for permission to use the rheometer (SR5). Special thanks are also due to M. Li and Y. Sugiyama for their unfailing assistance with the experimental measurements.

## References

[1] Hill, C. T., 1972, "Nearly Viscometric Flow of Viscoelastic Fluids in the Disc and Cylinder System, II: Experimental," Trans. Soc. Rheol., **16**, pp. 213–245.
[2] Day, C., Harris, J. A., Soria, J., Boger, D. V., and Welsh, M. C., 1996, "Behavior of an Elastic Fluid in Cylindrical Swirling Flow," Exp. Therm. Fluid Sci., **12**, pp. 250–255.
[3] Escudier, M. P., and Cullen, L. M., 1996, "Flow of a Shear-Thinning Liquid in a Cylindrical Container With a Rotating End Wall," Exp. Therm. Fluid Sci., **12**, pp. 381–387.
[4] Moroi, T., Itoh, M., Fujita, K., and Hamasaki, H., 2001, "Viscoelastic Flow Due to a Rotating Disc Enclosed in a Cylindrical Casing (Influence of Aspect Ratio)," JSME Int. J., Ser. B, **44**, pp. 465–473.
[5] Itoh, M., Suzuki, M., and Moroi, T., 2006, "Swirling Flow of a Viscoelastic Fluid in a Cylindrical Casing," ASME Trans. J. Fluids Eng., **128**, pp. 88–94.
[6] Stokes, J. R., Graham, L. J. W., Lawson, N. J., and Boger, D. V., 2001, "Swirling Flow of Viscoelastic Fluids. Part 1. Interaction Between Inertia and Elasticity," J. Fluid Mech., **429**, pp. 67–115.
[7] Stokes, J. R., Graham, L. J. W., Lawson, N. J., and Boger, D. V., 2001, "Swirling Flow of Viscoelastic Fluids. Part 2. Elastic Effects," J. Fluid Mech., **429**, pp. 117–153.
[8] Stokes, J. R., and Boger, D. V., 2000, "Mixing of Viscous Polymer Liquids," Phys. Fluids, **12**, pp. 1411–1416.
[9] Tamano, S., Itoh, M., Ide, Y., and Yokota, K., 2007, "Vortex Shedding in Confined Swirling Flow of Polymer Solutions," Phys. Fluids, **19**, No. 023103, pp.1–8.
[10] Kramer, J. M., and Johnson, M. W., 1972, "Nearly Viscoelastic Flow in the Disk and Cylinder System. I: Theoretical," Trans. Soc. Rheol., **16**, pp. 197–212.
[11] Xue, S.-C., Phan-Thien, N., and Tanner, R. I., 1999, "Fully Three-Dimensional, Time-Dependent Numerical Simulations of Newtonian and Viscoelastic Swirling Flows in a Confined Cylinder. Part I. Method and Steady Flows," J. Non-Newtonian Fluid Mech., **87**, pp. 337–367.
[12] Siginer, D. A., 2004, "On the Nearly Viscometric Torsional Motion of Viscoelastic Liquids Between Shrouded Rotating Discs," Trans. ASME, J. Appl. Mech., **71**, pp. 305–313.
[13] Chen, S., and Rothstein, J. P., 2004, "Flow of a Wormlike Micelle Solution Past a Falling Sphere," J. Non-Newtonian Fluid Mech., **116**, pp. 205–234.
[14] Arora, K., Sureshkumar, R., Scheiner, M. K., and Piper, J. L., 2002, "Surfactant-Induced Effects on Turbulent Swirling Flows," Rheol. Acta, **41**, pp. 25–34.
[15] Wei, J., Li, F.-C., Yu, B., and Kawaguchi, Y., 2006, "Swirling Flow of a Viscoelastic Fluid With Free Surface—Part 1: Experimental Analysis of Vortex Motion by PIV," ASME Trans. J. Fluids Eng., **128**, pp. 69–76.
[16] Li, F.-C., Oishi, M., Kawaguchi, Y., Oshima, N., and Oshima, M., 2007, "Experimental Study on Symmetry Breaking in a Swirling Free-surface Cylinder Flow Influenced By Viscoelasticity," Exp. Therm. Fluid Sci., **31**, pp. 237–248.
[17] Siginer, D. A., 1991, "Viscoelastic Swirling Flow With Free Surface in Cylindrical Chambers," Rheol. Acta, **30**, pp. 159–174.
[18] Siginer, D. A., and Knight, R., 1993, "Swirling Free Surface Flow in Cylindrical Containers," J. Eng. Math., **27**, pp. 245–264.
[19] Yu, B., Wei, J., and Kawaguchi, Y., 2006, "Swirling Flow of a Viscoelastic Fluid With Free Surface—Part II: Numerical Analysis With Extended Marker-and-Cell Method," ASME Trans. J. Fluids Eng., **128**, pp. 77–87.
[20] Munekata, M., Shibata, E., Matsuzaki, K., and Ohba, H., 2002, "Experimental Study of Swirling Flow With a Surfactant for Drag Reduction in a Pipe," JSME Int. J., Ser. B, **45**, pp. 35–40.
[21] Munekata, M., Matsuzaki, K., and Ohba, H., 2006, "Vortex Motion in a Swirling Flow of Surfactant Solution With Drag Reduction," ASME Trans. J. Fluids Eng., **128**, pp. 101–106.
[22] Bird, R. B., Armstrong, R. C., and Hassager, O., 1987, *Dynamics of Polymeric Liquids. Volume 1: Fluid Mechanics*, 2nd ed., Wiley Interscience, New York, pp. 353–369.
[23] Owen, J. M., and Rogers, R. H., 1989, *Flow and Heat Transfer in Rotating-Disc Systems*, Research Studies Press, pp. 137–142.

# Flow Induced Unstable Structure of Liquid Crystalline Polymer Solution in L-Shaped Slit Channels

**Takatsune Narumi**
Faculty of Engineering,
Niigata University,
2-8050 Ikarashi, Nishi Ward,
Niigata 950-2181, Japan
e-mail: narumi@eng.niigata-u.ac.jp

**Jun Fukada**

**Satoru Kiryu**

**Shinji Toga**

Graduate School of Science and Technology,
Niigata University,
2-8050 Ikarashi, Nishi Ward,
Niigata 950-2181, Japan

**Tomiichi Hasegawa**
Faculty of Engineering,
Niigata University,
2-8050 Ikarashi, Nishi Ward,
Niigata 950-2181, Japan

*An experimental study has been conducted on unstable structures induced in two-dimensional slit flows of liquid crystalline polymer solution. 50 wt % aqueous solution of hydroxyl-propylcellulose (HPC) was utilized as a test fluid and its flow behavior in L-shaped slit channels with a cross section of 1 mm height and 16 mm width was measured optically. The inner corner of the L-shaped channel was rounded off in order to clarify the influence of the radius of curvature on the unstable behavior. A conversing curved channel was also tested. The flow patterns of the HPC solution in the channels were visualized with two crossed polarizers and we observed that typical wavy textures generated in the upstream of the corner almost disappeared after the corner flow. However, an unstable texture was developed again only from the inner corner in downstream flow. The fluctuation of the orientation angle and dichroism were also measured with a laser opto-rheometric system and it was found that the unstable behaviors of the HPC solution have periodic oscillatory characteristics at a typical frequency. In the inner side flow after the corner, the periodic motion became larger toward the downstream and then higher harmonic oscillations were superimposed. Larger rounding off of the inner corner suppressed the redevelopment of unstable behavior, and it is considered that the rapid regrowth of unstable behavior was caused by rapid deceleration at the corner flow. Moreover, the unstable structure was stabilized with an accelerated (elongated) region in the corner flow and the converging channel was helpful to obtain a stable structure in the downstream region.* [DOI: 10.1115/1.2956604]

## Introduction

It is well known that the products made from liquid crystalline polymers (LCPs) have the advantages of higher modulus and higher heat resistance than those of conventional polymers. It is considered that the alignment structure of the LCP molecules causes these useful properties. However, it is difficult to control the LCP structures in a molding process, because the flow behaviors of LCPs strongly depend on its deformation history and there is a variety of complicated geometries used in the molding flows. We have investigated transient behaviors of a hydroxypropylcellulose (HPC) solution in Couette flow with sudden change in flow direction [1]. Periodic but complex behaviors were observed after the direction change and the behavior was strongly affected with the flow direction and shear rate of preshear flows. Moreover, it is known that unstable flow structures (textures) are generated under some conditions. For example, Guido et al. [2] investigated a slit flow of HPC solution in the low shear rate region and found that the morphology of the texture generated inside the flowing system was a function of the local shear rate. Baleo and Navard [3] observed flows of HPC solutions in slit channels with complex geometries and reported that a peculiar unstable behavior was observed after a diverging zone. Bedford and Burghardt [4,5] and Bedford et al. [6] showed the occurrence of wavy textures in the pressure-driven slit flow of LCPs of PBDG in *m*-cresol and HPC in *m*-cresol. They showed that in slit-contraction flows substantial enhancements in molecular orientation in the vicinity of the contraction and the frequency of the instability was directly proportional to the volumetric flow rate. Haw and Navard [7] studied the flow of the HPC solution in a divergent channel flow, and reported that a strong dependence of flow-induced texture on the position in the channel was observed and was related to the interplay of shear and elongational strains. Mori et al. [8] have found the wavy texture in a flow through a slit cell even with an abrupt contraction. In addition, these researchers [9,10] also examined the wavy texture in a pressure-driven startup flow of the 50 wt % solution of HPC for various flow cells such as abrupt contraction slit cells and abrupt expansion slit cells. They found that a comparatively long induction time after the startup of the flow was required for the emergence of the wavy texture.

In this study, we have investigated unstable behavior (wavy texture) in curved slit flows of HPC solution. We have employed the slit flows with a flow direction change in two-dimensional channels with a right-angled corner (L-shaped channel). The influence of the corner flow condition on the instability in downstream flow has been mainly clarified experimentally from polarized observations and measurements of the orientation angle of HPC polymer with a laser opto-rheometric system.

## Experiment

The solution of LCP tested in the present experiments is a 50 wt % aqueous solution of HPC (HPC-L, supplied by Nippon Soda), which was also tested in our previous study [1]. The experiments were conducted under room temperature (20–23 °C).

Figure 1 shows a schematic of a test channel. A vinyl chloride plate of 1 mm in thickness with a window-shaped flow cell is sandwiched between two glass plates mounted in brass frames. Four kinds of flow cells were tested and one of the concrete shapes of the flow cells is indicated in Fig. 2. Respective dimensions of the flow cells are listed in Table 1. The ST channel in Table 1 refers to a straight channel with no corner flow. The others

Contributed by the Fluids Engineering Division of ASME for publication in the JOURNAL OF FLUIDS ENGINEERING. Manuscript received May 15, 2007; final manuscript received August 28, 2007; published online July 24, 2008. Assoc. Editor: Dennis Siginer. Paper presented at the 2007 ASME Fluids Engineering Division Summer Meeting and Exhibition (FEDSM2007), San Diego, CA, July 30–Aug. 2, 2007.

  

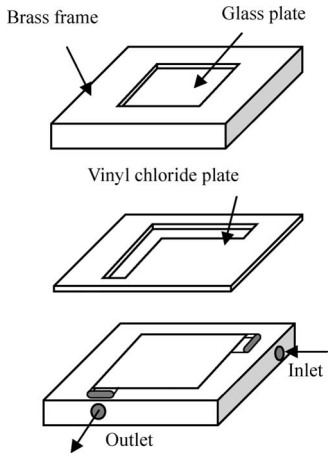


**Fig. 1 Schema of the test channel**

are all L-shaped channels, and R2 and R10 denote the radii of curvature of the inner corner. CONV channel has a contraction in width at the corner flow. The schema of the experimental setup is shown in Fig. 3. The test fluid in a reservoir was introduced into the channel by compressed air. After keeping the flow under a constant pressure for several minutes, a macroscopically steady state, but including unstable structure changes, was obtained in the HPC flow. The flow rate under the steady state was obtained with gravimetric method. We utilized crossed polarizers to visualize the flow patterns. The photographs of the flow patterns were taken with a charge coupled device video camera under Cross–Nicol condition (not shown in Fig. 3). A laser opto-rheometric system of the orientation angle and dichroism indicated in Fig. 3 was also utilized. A He–Ne laser beam through a rotary polarization modulator penetrates the test fluid. Then the orientation angle and the dichroism were evaluated with the beam intensity measured with a photodetector. We will mainly show the results of orientation angle ($\theta$) in this paper.

Figure 4 indicates the positions where the orientation angles were measured. The points are located on the inner, center, and outer lines indicated in the figure. The lines are separated by equal

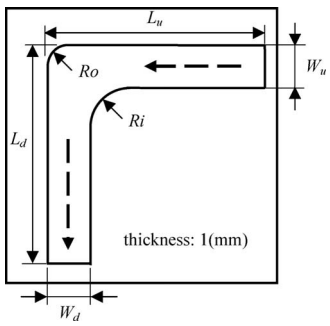


**Fig. 2 Shape of a flow cell**

**Table 1 Dimensions of flow cells (mm)**

| Channel | ST | R2 | R10 | CONV |
|---|---|---|---|---|
| $L_u$ | 120 | 98 | 98 | 94 |
| $W_u$ | 16 | 16 | 16 | 16 |
| $L_d$ | — | 98 | 98 | 98 |
| $W_d$ | — | 16 | 16 | 8 |
| $R_i$ | — | 2 | 10 | 10 |
| $R_0$ | — | 1 | 1 | Elliptic[a] |

[a]$R$=26 and 18 mm.

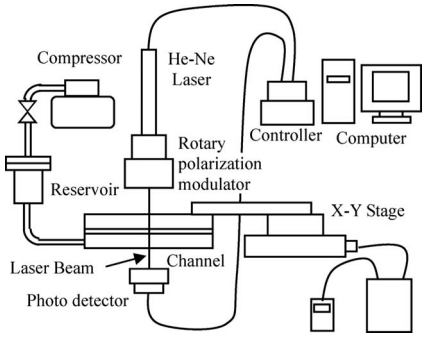


**Fig. 3 Experimental apparatus**

intervals and the points are spaced at 10 mm intervals in the flow direction (Fig. 4 indicates the case of R10 channel). The measurement points at the corner are the cross points of sets of lines defined in the up- and downstream regions. Since we have investigated the behavior of LCP mainly in the downstream region, the coordinate system is defined, as shown in Fig. 4. In this paper, the points are indicated with a respective combination of line symbols (I, C, O or i, c, o) and point numbers indicated in Fig. 4, e.g., I1, O6, i-2, etc. The points at the corner are denoted as o-I or i-C, using line symbols. As shown in Fig. 4, $\theta$=0 in the orientation angle means the flow direction of the downstream.

Since a similar velocity profile to the Newtonian one in the gap direction is expected [6], an apparent shear rate ($\dot{\gamma}_w$) at the wall (glass plates) defined with an assumption of Poiseuille flow is utilized in the present paper as a representative shear rate. The tests were conducted under the condition of $\dot{\gamma}_w \cong 7(1/\mathrm{s})$ in Region III, where the motion of the respective molecules is dominated with no polydomain [1].

## Results and Discussions

**Polarizing Observations of ST and R2 Channel Flows.** Figure 5 shows photographs of flow patterns taken with two polarizers whose orientations are (45 deg, −45 deg) to the flow direction. We see in Fig. 5(*a*) that wavy textures emerge in the downstream

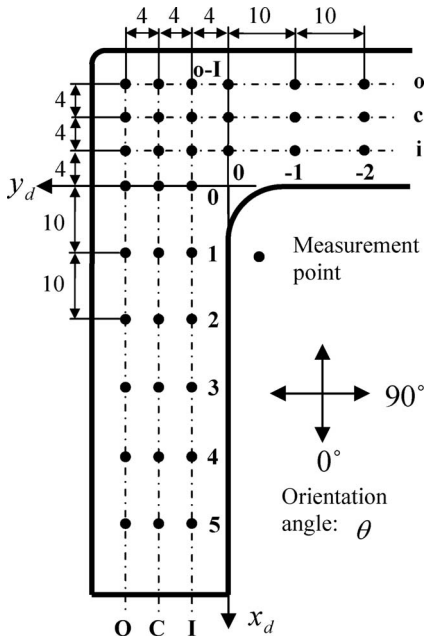


**Fig. 4 Measurement positions of the orientation angle and dichroism**

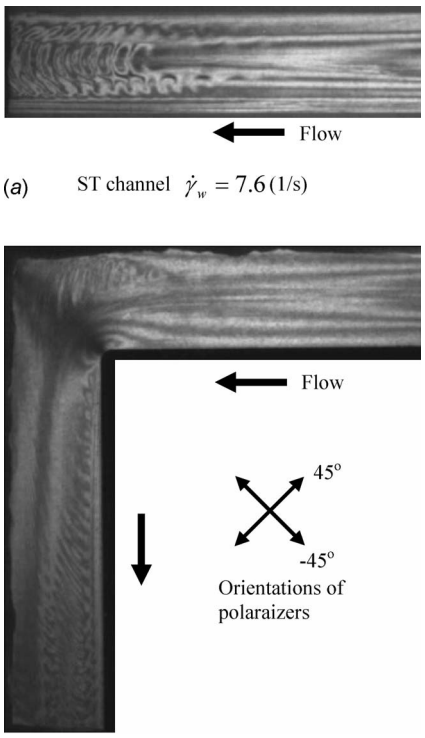


**Fig. 5 Photographs of flow patterns observed in the (*a*) ST channel and the (*b*) R2 channel between two crossed polaraizers with orientations of (45 deg, −45 deg) to the flow direction (*a*) ST channel $\dot{\gamma}_w$=7.6(1/s) (*b*) R2 channel $\dot{\gamma}_w$=7.7(1/s)**

region in a straight (ST) channel. In detail, flow patterns in the outer sides begin to sway in the middle of the channel and then two wavy textures develop and merge. We believe that the cause of these unstable behaviors is the complicated shape of the channel entrance and it is difficult to control the generation of the texture. Since these kinds of unstable textures easily emerge in many slit die flows [2–10], our experiments were conducted on the premise that the wavy texture is generated in the upstream region of the corner flow. Then we have tried to clarify how the textures change in the corner flow or how we can control the unstable behaviors. Figure 5(*b*) is a typical photograph taken with the R2 channel. A similar wavy texture is generated at the outer side in the upstream of the corner and it almost disappears through the corner flow. On the other hand, no texture is observed at the inner side of the upstream and corner flows, but another wavy texture emerges from the corner and develops toward the downstream region. This means that the unstable behaviors of the HPC solution generated in the upstream region disappear through the corner flow, but a new instability is generated at the inner corner.

**Unstable Behavior After the Corner Flow.** We have investigated characteristics of the unstable texture in the downstream region first. Figure 6 indicates orientation angles measured at the points on the I-line in Fig. 4. Since periodic property is observed in the fluctuation of the angle, we have evaluated the power spectrum of the angle fluctuation with digital Fourier transformation. Figure 7 shows the power spectrum change on the I-line of the R2 channel obtained from the same data in Fig. 6. The fluctuation has a basic frequency of about 0.3–0.4 Hz; in particular, a very regular periodic motion is observed at I2. Then, harmonic oscillations become larger toward the downstream region, that is, the fluctuation of the angle becomes more complicated. The same basic frequency and similar tendency of the harmonic component develop-

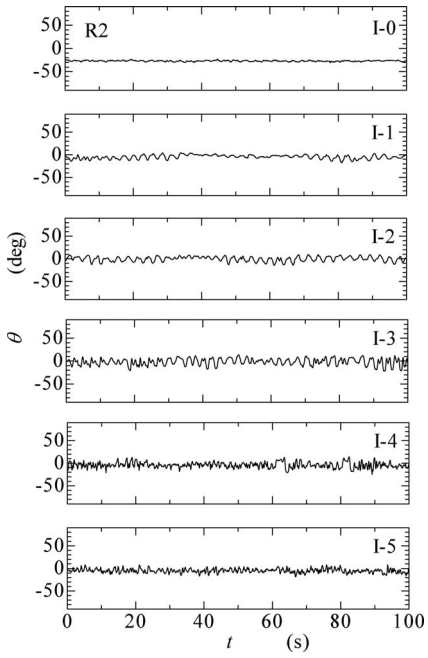


**Fig. 6 Orientation angle measured at the inner side of the downstream of the R2 channel at $\dot{\gamma}_w$=7.9(1/s)**

ment were obtained in the ST channel flow (not shown here). Hence, a similar kind of fluctuation was induced with the inner corner as that induced with the straight flow. One of the authors had investigated the shear rate (velocity) dependence of the basic frequency utilizing some similar slit channels with 1 mm gap [11]. Table 2 shows that the basic frequency is affected with the shear rate; however, strains defined with the shear rate and the frequency have similar values. This may mean the periodic behavior is controlled with the strain applied in the flow. Since these estimations are based on scattered data, it is necessary to conduct

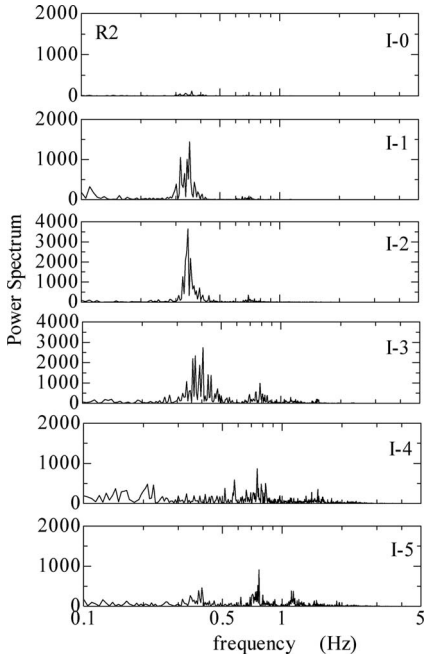


**Fig. 7 Power spectrum of the fluctuation in the orientation angle obtained with digital Fourier transformation from Fig. 6 (R2 channel)**

**Table 2 Dependence of basic frequency on the shear rate**

| Apparent wall shear rate $\dot{\gamma}_{w\_ave}$ (1/s) | Basic frequency $f_{ave}$ (1/s) | Apparent strain $\gamma_{ave}$ $(=\dot{\gamma}_w/f_{ave})$ |
|---|---|---|
| 10.0 | 0.52 | 19.2 |
| 7.3 | 0.35 | 20.9 |
| 3.8 | 0.16 | 23.8 |

more precise measurements for detailed discussions.

In order to clarify the stability change in the downstream region, we have defined the intensity of instability with the root mean square (rms) of the angle fluctuation. That is,

$$\tilde{\theta}_{\mathrm{rms}} = \sqrt{\frac{1}{N}\sum_{i=1}^{N}(\bar{\theta}-\theta_i)^2} \tag{1}$$

where $N$ is the number of data and $\bar{\theta}$ is average orientation angle. The $\tilde{\theta}_{\mathrm{rms}}$ obtained in radian for respective lines (I, C, O) in the downstream region were plotted in Fig. 8. We see that relatively stable flows were obtained just after the corner ($x_d$=0). Then, the instability develops rapidly in the inner side flow and expands toward the outer side.

From the viewpoint of the mold process, it is better to control the unstable behavior. In this problem of flow instability after the corner, it is clear that the inner corner is the main cause of the unstable behavior. Hence, the flow instability must be affected by the shape of the corner. We have tested a similar L-shaped slit channel with a different radius of curvature of the inner corner. Figure 9 indicates the power spectrum obtained in the test with the R10 channel. We can find the same basic frequency and its harmonic components, but oscillations are considerably smaller than those of the R2 channel (Fig. 7). Figure 10 shows the intensity of

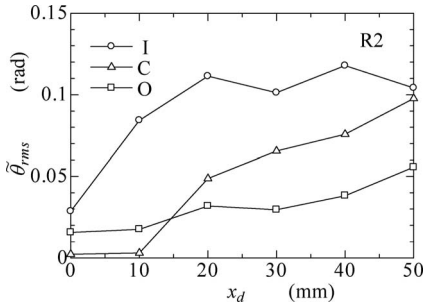


**Fig. 8 Instability of the downstream flow evaluated as the rms of the fluctuation in orientation angle measured with the R2 channel at $\dot{\gamma}_w$=7.9(1/s)**

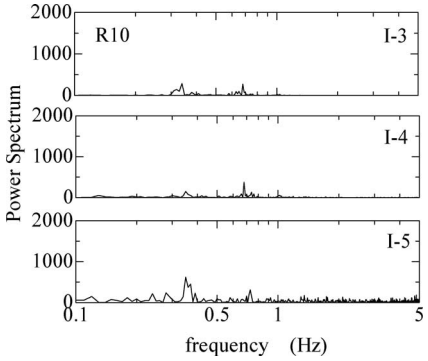


**Fig. 9 Power spectrum of the fluctuation in orientation angle obtained with digital Fourier transformation (R10 channel, $\dot{\gamma}_w$ =7.8(1/s))**

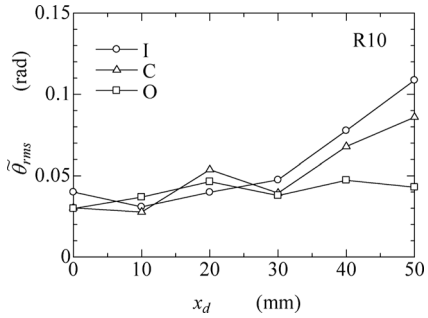


**Fig. 10 Instability of the downstream flow evaluated as the rms of the fluctuation in orientation angle (R10 channel, $\dot{\gamma}_w$ =7.8(1/s))**

the instability obtained from the R10 channel. No rapid increase in the instability was observed even along the I-line. Hence, it is considered that the rounded corner stabilizes the LCP behavior in the downstream region.

**Instability Change in the Corner Flow.** Figure 11 shows the instability ($\tilde{\theta}_{\mathrm{rms}}$) changes from the corner to the downstream flow three dimensionally. We easily see again the instability develop-

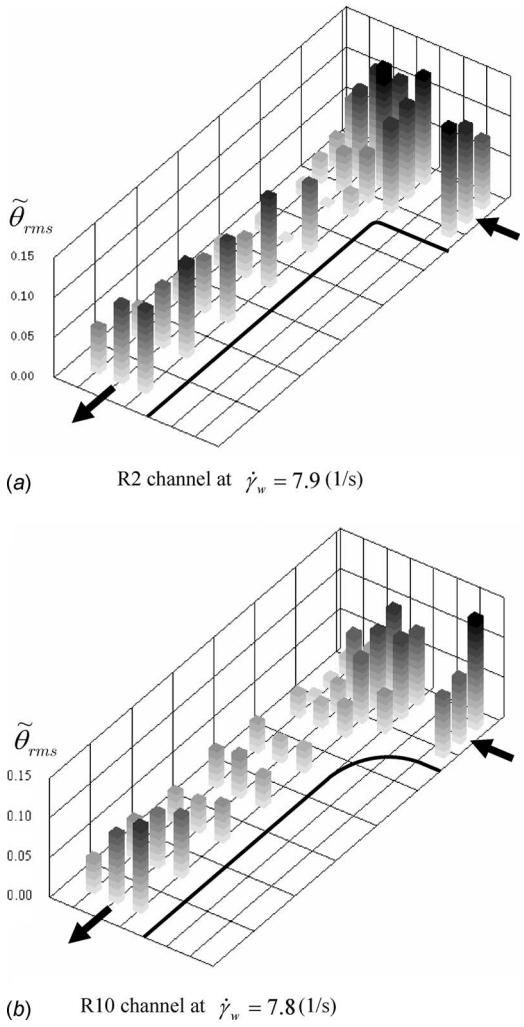


**Fig. 11 Instability change around the corner to the downstream region (*a*) R2 channel at $\dot{\gamma}_w$=7.9(1/s) (*b*) R10 channel at $\dot{\gamma}_w$=7.8(1/s)**

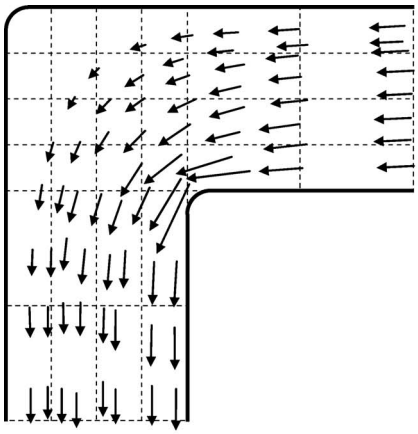

(*a*) R2 channel at $\dot{\gamma}_w = 7.5$ (1/s)

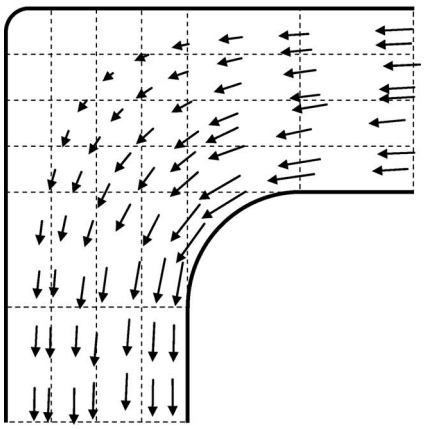

(*b*) R10 channel at $\dot{\gamma}_w = 7.3$ (1/s)

**Fig. 12 Velocity vectors in the corner flow obtained with bubbles' motion in the HPC solution (*a*) R2 channel at $\dot{\gamma}_w$ =7.5(1/s) (*b*) R10 channel at $\dot{\gamma}_w$=7.3(1/s)**

ments in the downstream region denoted in Figs. 8 and 10. Though the wavy texture was not observed in the inner upstream and the corner flow in Fig. 2, the instability in that region was not very low in Fig. 11. This means that there are unstable molecular motions that cannot be captured with the polarizing method. In both cases of the R2 and R10 channels, the instability at the entrance of the corner decreases along the corner flow.

Here, we will discuss the mechanism of the decrease in instability in the outer corner flow and the influence of the corner flow on the stability of the downstream flow. Since the corner flow includes not only a change in flow direction but also a change in flow area, we have measured the local velocity in the corner flow. Small bubbles about 0.5 mm in diameter included in the HPC solution were traced, and their velocities were estimated from the pictures. It was found that the velocities obtained in the ST channel were about 1.3–1.4 times larger than the average velocity estimated from flow rate. If we assume the Newtonian velocity profile of $v = 1.5V\{1-(z/h)^2\}$, where $V$ is average velocity, $h$ is half of the gap, and $z$ is the coordinate in gap direction from the center, an average velocity in the center region of $-0.5h \leq z \leq 0.5h$ is $1.38V$. This value is close to the measured ones. Hence, we believe the velocities measured were approximately equal to the average velocity in the center region in the gap. Velocity vectors obtained from the bubble motions are indicated in Fig. 12. We see that a similar velocity change of the outer corner flow is observed both in R2 and R10 channels and that the flow is decelerated first and then accelerated. On the other hand, though the velocity near the

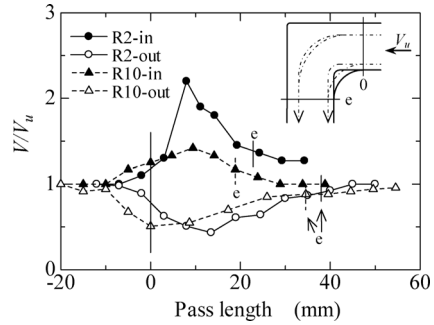


**Fig. 13 Local velocity changes on pass lines in the corner flows. Inner pass lines are about 2 mm away from the inside edge. The outer lines past through the o-1 point and the pass length was measured from the –1 position in Fig. 4. $\dot{\gamma}_w$ =7.5(1/s) in the R2 channel flow and $\dot{\gamma}_w$=7.3(1/s) in the R10 channel flow.**

inner corner is very different depending on the radius of curvature, both channel flows show the same tendency in velocity change, i.e., first accelerated then decelerated. In order to compare the detailed velocity change between R2 and R10 channels, the velocities on two typical lines are shown in Fig. 13. One is the inner pass line about 2 mm away from the inner corner and the other is the line through about the o-1 point in Fig. 4. We see that the inner flow of the R2 channel has very rapid acceleration and deceleration. It has been suggested that deceleration of the flow, i.e., negative elongational flow, causes wavy texture and acceleration, i.e., elongational effect, stabilize the unstable LCP motions [3,7]. It is clear that the acceleration in our curved flow is also caused with an elongational flow due to the flow area change. Comparing with Figs. 11, 12, or 13 in the outer corner flow, the instability is still high in the decelerated region and 10 w in the accelerated region. These results qualitatively agree with previous reports mentioned above. The acceleration in the inner corner flow would also stabilize the corner flow, but the deceleration does not generate immediate instability growth, especially in the case of the R10 channel. This result would correspond to that reported by Mori et al. [9]. It is clear that the very rapid deceleration, i.e., strong negative elongation, in the inner flow of the R2 channel causes the relatively rapid growth of the instability in the downstream region. Of course, we believe that the rapid direction change of the LCP molecules is also the cause of the instability.

**Stabilizing Effect of the Converging Curved Channel.** In order to clarify the validity of the explanation mentioned above experimentally, we have conducted another test utilizing a conversing curved channel. Figure 14 shows a polarized photograph taken with the same condition as Fig. 5. Because of the truncated design of the acceleration channel, weak textures are observed in this picture. In fact, the velocities estimated with the bubbles in the region with the weak textures were almost constant, i.e., no acceleration or deceleration. Hence, the weak texture was the same one generated in the ST channel; however, we can see the very stable structure in the downstream region. Figure 15 indicates the intensity of the instability in the downstream of the CONV channel. A very stable state is observed even in the inner flow. Since we had an unstable flow in the case of the ST channel at high shear rate as in the downstream region of the CONV channel (not shown here), it can be said that the stable state is induced with conversing flow. These results lend support to the notion that the generation or development of unstable behavior of the LCP is mainly affected with the acceleration and deceleration of the flow even in the curved flow.

## Conclusion

Unstable structures of the HPC solution induced in a curved slit flow were investigated with polarized observation and optical

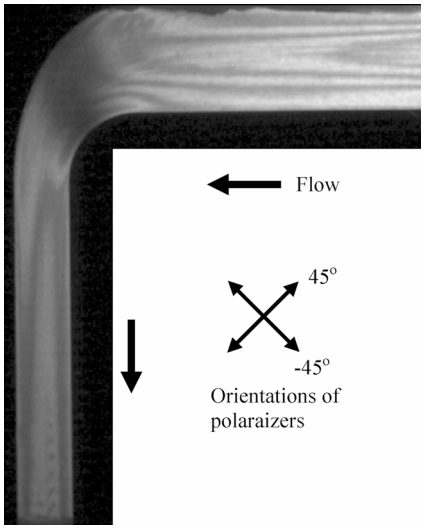


**Fig. 14 Photographs of flow patterns observed in the CONV channel between two crossed polarizers with orientations of (45 deg, –45 deg) to the flow direction. Shear rate ($\dot{\gamma}_w$) changes from 7.4 to 14.8 (1/s).**

measurements. Typical wavy textures generated in the upstream region at the outer side almost disappear through the corner flow. The development of the unstable texture was observed in the

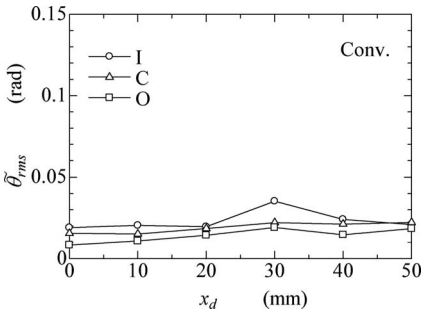


**Fig. 15 Instability of the downstream flow evaluated as the rms of the fluctuation in orientation angle (CONV channel, $\dot{\gamma}_w$ =14.8(1/s) in the downstream region)**

downstream region of the inner side flow from the corner. We have found that the unstable behaviors of the LCP solution have periodic oscillatory characteristics with a typical frequency. In the inner side flow after the corner, the periodic motion became larger toward the downstream and then higher harmonic oscillations were superimposed. Larger rounding off of the inner corner suppressed the development of unstable behavior, and the converging channel was helpful in stabilizing the unstable behavior. The acceleration (elongation) and deceleration (negative elongation) of the flow were, respectively, corresponding to the stabilization and growth of the unstable structures.

## Acknowledgment

The authors are indebted to Dr. Howard See for helpful suggestions and valuable discussions to this research. The authors also thank Mr. Ryuchi Kayaba, Mr. Kaitaro Oshima and Mr. Hiroya Ishizuki for technical assistance in the experiment.

## References

[1] Watanabe, H., Narumi, T., Mikuma, R., Kayaba, R., and Hasegawa, T., 2006, "Study of Structural Rearrangement of Liquid Crystalline Polymer Solution in a Transient Couette Flow With a Flow Direction Change (in Japanese)," Nihon Reoroji Gakkaishi, **34**(1), pp. 9–15.
[2] Guido, S., Frallicciardi, P., Grizzuti, N., and Marrucci, G., 1994, "Rheo-Optics of Hydroxypropylcellulose Solutions in Poiseuille Flow," Rheol. Acta, **33**, pp. 22–28.
[3] Baleo, J.-N., and Navard, P., 1994, "Rheo-Optics of Liquid-Crystalline Polymers in Complex Geometries," J. Rheol., **38**, pp. 1641–1655.
[4] Bedford, B. B., and Burghart, W. R., 1994, "Molecular Orientation and Instability in Plane Poiseuille Flow of a Liquid-Crystalline Polymer," J. Rheol., **38**, pp. 1657–1679.
[5] Bedford, B. B., and Burghardt, W. R., 1996, "Molecular Orientation of a Liquid-Crystalline Polymer Solution in Mixed Shear-Extensional Flows," J. Rheol., **40**, pp. 235–257.
[6] Bedford, B. B., Cinader, D. K., Jr., and Burghardt, W. R., 1997, "Unstable Slit Flow of a Liquid-Crystalline Polymer Solution," Rheol. Acta, **36**, pp. 384–396.
[7] Haw, M. D., and Navard, P., 2000, "Divergent Channel Flow of a Liquid Crystalline Polymer Solution," Rheol. Acta, **39**, pp. 280–293.
[8] Mori, N., Shindo, M., Takahashi, T., and Nakamura, K., 2001, "Unstable Slit Flows of Liquid Crystalline Solution of Hydroxypropylcellulose" Nihon Reoroji Gakkaishi, **29**, pp. 89–94.
[9] Mori, N., Shindo, M., Nakamura, K., and Yamamoto, T., 2003, "Pressure-Driven Startup Flows of Liquid Crystalline Polymers Through Slit Cells," Rheol. Acta, **42**(6), pp. 527–533.
[10] Mori, N., Origi, S., Numata, A., and Yamamoto, T., 2005, "Wavy Texture in Pressure-Driven Startup Flows of Liquid Crystalline Polymer Solutions Through a Slit Cell: Effects of Polymer Concentration and Solution Temperature," Rheol. Acta, **44**(5), pp. 478–484.
[11] Kiryu, S., 2006, "Study on Flow Induced Structure of Liquid Crystalline Polymer Solution in Two-Dimensional Channels With a Flow Direction Change (in Japanese)," MS thesis, Niigata University, Niigata, Japan.

# Drop Formation in Non-Newtonian Jets at Low Reynolds Numbers

**V. Dravid**[1]
**P. B. Loke**
**C. M. Corvalan**[2]
**P. E. Sojka**[2,3]
e-mail: Sojka@ecn.purdue.edu

Maurice J. Zucrow Laboratories,
School of Mechanical Engineering,
Purdue University,
500 Allison Road,
West Lafayette, IN 47907-2014

*The objective of this study was to develop an experimentally verified computational model that accurately predicts evolution of shear-thinning liquid jets. A secondary objective was to investigate the formation of satellite drops and to determine conditions under which their diameter can be controlled. The model employs the Galerkin finite/element approach to solve the complete two-dimensional set of axisymmetric governing equations and the corresponding kinematic and dynamic boundary conditions at the free surface. The effect of shear-thinning behavior on breakup was studied in detail for the case of an infinitely long non-Newtonian jet. It was found that shear-thinning behavior may be useful in controlling satellite drop sizes. (We observe that increasing the shear-thinning behavior at Re ~ 5 leads to an initial increase in the satellite drop size, followed by a subsequent decrease.) Comparison of model predictions with experimental data is presented for the case of a shear-thinning non-Newtonian jet. The experimental liquid was pumped through a capillary and drop shapes obtained using a high speed camera. The experimentally obtained shapes were compared to those predicted by the model and found to be in good agreement.* [DOI: 10.1115/1.2956612]

## 1 Introduction

Drop formation in jets of non-Newtonian fluids is a commonly observed phenomenon. Applications in industry are widespread, viz., encapsulation processes for controlled drug delivery, inkjet printing, spray drying of starches, spray painting, and emulsification.

Liquid jet dynamics were first considered by Rayleigh [1] who examined the linear instability of an infinitely long viscous thread in an inviscid fluid. Linear and nonlinear analyses of Newtonian liquid thread breakup have been reviewed by Eggers [2]. In contrast, the analysis of viscoelastic liquid threads [3,4] and the breakup of purely viscous, shear-thinning, non-Newtonian liquid threads are still in its infancy. Yildirim and Basaran [5] analyzed the one- and two-dimensional breakup of a shear-thinning stretching bridge and showed that the difference between Newtonian and non-Newtonian bridges is significant for a large zero-shear viscosity, but insignificant for low zero-shear viscosity. They also noted that the evolution of a shear-thinning liquid bridge can be modeled as a Newtonian liquid bridge of lower viscosity, and that modifying the shear-thinning behavior might be useful in controlling or eliminating the formation of satellite drops. Finally, they reported discrepancies between results obtained from one- and two-dimensional analyses.

Doshi et al. [6] and Renardy and Renardy [7] proved the existence of self-similar solutions near pinch-off for power-law shear-thinning liquid threads, using a one-dimensional nonlinear analysis and a one-dimensional linear analysis in both the viscous and high inertia limits, respectively. They concluded that viscous and inertial forces were equally important near pinch-off.

To summarize, current literature has merely begun analyzing jets of shear-thinning non-Newtonian fluids. While similarity solutions explain the singularity of the jet at breakup, they are unable to predict drop sizes or drop shapes in shear-thinning jets.

To address this limitation we report the effect of power-law shear-thinning behavior for the case of a two-dimensional axisymmetric filament, at Re=5, by solving the entire Navier–Stokes equations. The arbitrary Lagrangian-Eulerian (ALE) Galerkin/finite element method, as described by Campana et al. [8], was employed to solve the ensuing system of nonlinear governing equations. We compare model predictions against experimental data obtained using jets of power-law non-Newtonian fluids exiting from capillary tubes. Drop formation from these capillary jets was captured using a high speed digital camera. Agreement is excellent.

## 2 Method of Approach

**2.1 Governing Equations.** Consider the deformation of an incompressible, shear-thinning, axisymmetric liquid filament of constant density $\rho$ and zero-shear dynamic viscosity $\mu_0$ surrounded by an inertialess gas. The cylindrical filament with uniform radius $a$ is disturbed at time $t'=0$ by a sinusoidal wave with amplitude $\varepsilon_0'$ and wavelength $\lambda'$ (see Fig. 1). The position of the interface $h'$ during instability evolution is considered to be a function of time $t'$ and axial distance $z'$. Gravitational forces are neglected. The surface tension $\sigma_0$ on the filament interface is uniform.

Under these conditions, the mass and momentum balance in the filament are described by the dimensionless continuity and Navier–Stokes equations as follows:

$$\nabla \cdot \mathbf{v} = 0 \tag{1}$$

$$\mathrm{Re}\frac{D\mathbf{v}}{Dt} = \nabla \cdot \mathbf{T}, \quad \mathbf{T} = -p\mathbf{I} + \mu[\nabla\mathbf{v} + (\nabla\mathbf{v})^T] \tag{2}$$

where the following have been used: $(v_r, v_z) = (v_r', v_z')/(\sigma_0/\mu_0)$, $(r, z) = (r', z')/a$, and $p = ap'/\sigma_0$.

Since the length scale used is $a$ and the velocity scale is $\sigma_0/\mu_0$, the Reynolds number becomes $\mathrm{Re} = \rho a \sigma_0/\mu_0^2$.

The shear-thinning behavior is described by a three parameter Carreau model

[1]Present address: COMSOL, Inc., Waltham, MA 01803.
[2]Present address: Food Science Department, 745 Agriculture Mall Drive, West Lafayette, IN 47907.
[3]Corresponding author.

Contributed by the Fluids Engineering Division of ASME for publication in the JOURNAL OF FLUIDS ENGINEERING. Manuscript received May 31, 2007; final manuscript received April 16, 2008; published online July 29, 2008. Assoc. Editor: Dennis Siginer. Paper presented at the 2007 ASME International Mechanical Engineering Congress (IMECE2007), Seattle, WA, November 10–16, 2007.

  

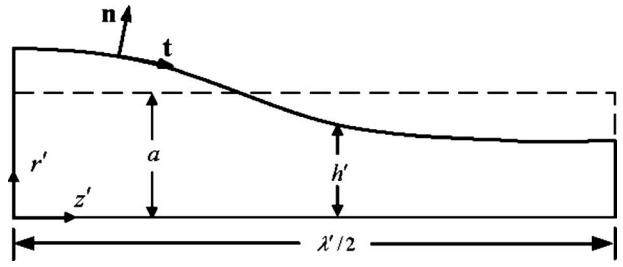


**Fig. 1 System geometry with basic dimensions**

$$\mu = (1-\beta)[1+(\alpha\dot{\gamma})^2]^{(n-1)/2} + \beta \tag{3}$$

where $\mu$ is the dimensionless apparent viscosity (also referred to as the effective viscosity) used in Eq. (2), $\alpha$ is a time constant, $0<\beta<1$ is the dimensionless infinite shear viscosity, $n$ is the power-law index, and $\dot{\gamma}$ is the second invariant of the rate-of-deformation tensor. Neither elastic effects nor strain hardening is accounted for in the Carreau model.

Equations (1) and (2) were solved by imposing the symmetry boundary conditions and $\nabla\mathbf{v}\cdot\mathbf{n}=0$ at the centerline of the filament, plus $\mathbf{v}\cdot\mathbf{n}=0$ and $\partial h/\partial z=0$ at $z=0$ and $z=\lambda/2$, where $\mathbf{n}$ is the outward directed unit normal at the liquid phase free surface. On the filament interface, $r=h'(t,z)/a=h(t,z)$, and the conditions to be satisfied are the kinematic and dynamic boundary conditions.

At $t=0$, a sinusoidal spatial perturbation is applied to the gas-liquid interface

$$h(z,0) = 1 + \varepsilon_o \cos(kz) \tag{4}$$

where $\varepsilon_0=\varepsilon_0{}'/a$ is the amplitude of perturbation and $k=2\pi/\lambda$ is the dimensionless perturbation wave number.

**2.2 Numerical Method.** The set of two-dimensional nonlinear equations governing deformation of the liquid filament were solved using the Galerkin/finite element method for discretization in space and the finite difference method for discretization in time in order to obtain pressure and velocity fields and the location of the interface. We have previously applied essentially the same numerical procedure to study two-dimensional Faraday waves in Ref. [9]; it was discussed in detail there.

The jet was partitioned into a set of quadrilateral elements using the method of spines proposed by Kistler and Scriven [10]. Each element consists of two straight sides with fixed axial coordinates determined by spines parallel to the radial direction and of two curved sides that are determined by the deformation of the free surface. Following the standard finite element procedure [11], the four-node bilinear basis functions $\psi^j$ used to weight the residual were also used to approximate the pressure field and the nine-node biquadratic finite element basis functions $\phi^j$ used to weight the residuals were also used to approximate the velocity field. On the interface, the nine-node biquadratic basis functions $\phi^j$-collapse into one-dimensional biquadratic functions $\tilde{\phi}^j$, which were used to expand the shape of the interface.

The procedure described above reduces the set of governing partial differential equations to a system of nonlinear ordinary differential equations in time. To solve this system we follow the method described by Gresho et al. [12]. After discretization in time, the resulting system of nonlinear algebraic equations was solved using the Newton method at each time step. The time steps were adaptively chosen using the method of Crisfield [13].

## 3 Results and Discussion

**3.1 Simulations.** To ensure model accuracy, predictions were first compared with the one-dimensional nonlinear similarity solution near pinch-off for a power-law generalized Newtonian liquid jet, as computed by Doshi et al. [6]. This similarity solution has the form $\tau \sim h_{\min}^n$, where $\tau$ is the time to breakup, $h_{\min}$ is the minimum radius of the filament, and $n$ is the power-law index. As Fig. 2 shows, agreement is within 0.1% for the region of $10^0 \geq \tau \geqslant 10^{-2}$.

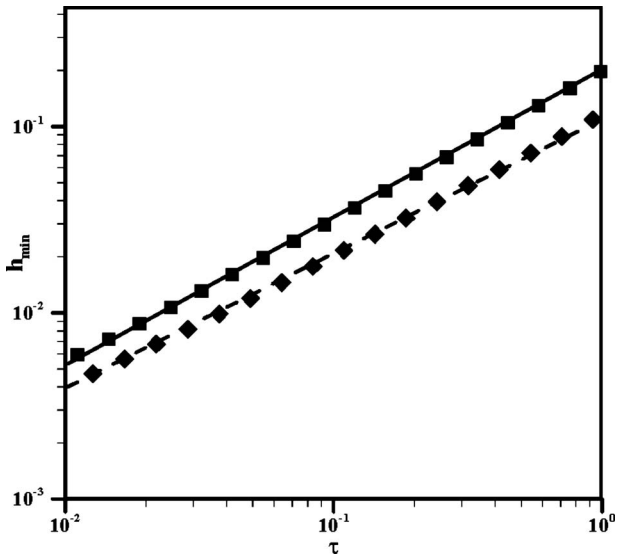


**Fig. 2 Comparison of model predictions (symbols) with the similarity solution results of Doshi et al. [6] (solid line). Re=0, $\varepsilon_0$=0.5, $\alpha$=1, $\beta$=0.02; $n$=0.8 (squares), $n$=0.9 (diamonds).**

All computational results used an initial perturbation amplitude, $\varepsilon_0$, of $10^{-3}$. When investigating the influence of non-Newtonian rheological behavior a dimensionless wave number, $k$, of 0.54 was chosen. This value was obtained from Timmermans and Lister [14] and corresponds to the maximum growth rate for a Newtonian fluid at Re=10.

All values for variables are reported in dimensionless form. The time to break up is defined as that at which the radius of the filament is reduced to, or falls below, 1/100 of the initial filament radius. This limit was chosen in order to avoid excessive distortion of the computational grid and to prevent numerical errors from entering the results.

We begin the discussion by examining the effect of the power-law index on drop formation at a moderate Reynolds numbers (Re=5), in particular, the formation of satellite drops. For the purposes of computation, we assume a single satellite drop is formed between two main drops and equate its diameter to that of a sphere whose volume lies between the two pinch-off points.

Figure 3 shows a steady increase in satellite drop radius as power-law index decreases from unity to 0.5. However, as $n$ decreases below 0.5, satellite drop radius decreases slightly. This phenomenon has not been reported in scientific literature. To understand it, we first examine the transition to pinch-off for a Newtonian jet and compare it with the transition for a non-Newtonian jet.

As seen in Fig. 1, the initial perturbation imposed on the uniform jet causes a spatial difference in curvature along the jet. This difference in curvature results in a surface-tension driven pressure gradient. Figure 4(*a*) shows the flow streamlines in a Newtonian jet at $t=86.05$. The forces that act on the fluid are the inertial force, driving the fluid towards the main drop; the pressure gradient, also driving the fluid towards the main drop; and the viscous force, which opposes the flow. Here the entire flow is in the direction of the main drop, due to the initial condition imposed on the jet.

Bulk flow into the main drop is also observed in Fig. 5, which presents surface pressure and tangential velocity for the case corresponding to Fig. 4(*a*). Figure 5(*a*) shows that the pressure gradient is from the right to the left. Consequently, as shown in Fig.

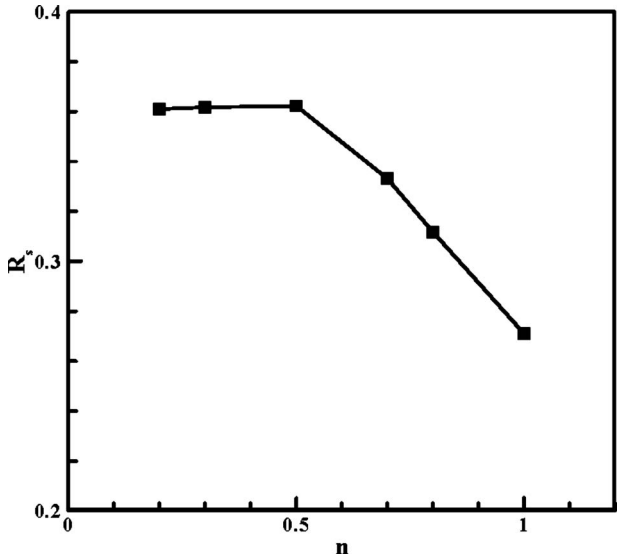


**Fig. 3 Satellite drop radius versus power-law index *n* for Re =5, $\alpha$=10, and $\beta$=0.002**

5(*b*), the entire surface moves toward the main drop. This pressure gradient, in conjunction with the viscous force, finally reverses the flow from the main to the satellite drop, as seen in Fig. 4(*c*), which shows streamlines at $t$=92.0. This behavior is further illustrated in Fig. 6, which shows the surface pressure and surface tangential

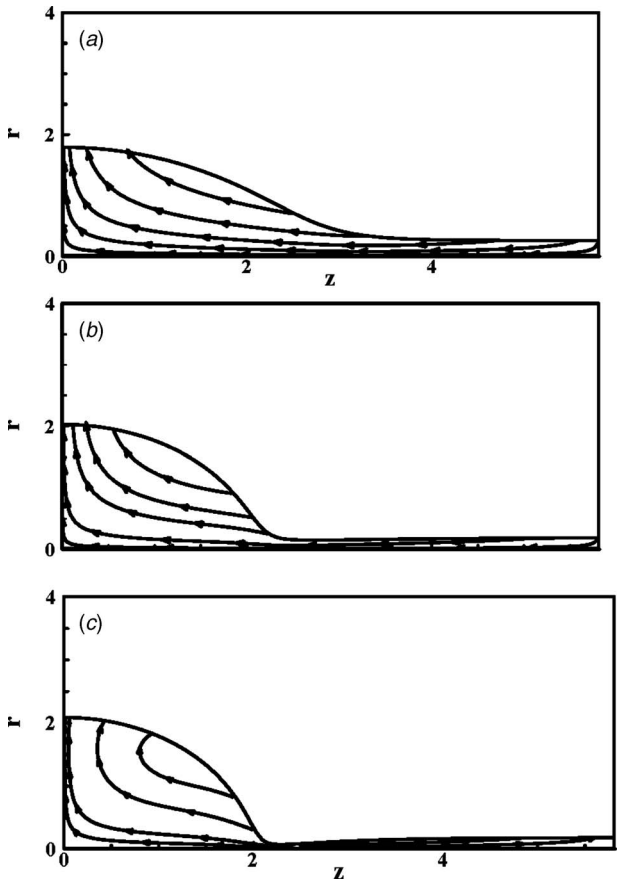


**Fig. 4 Streamlines for a Newtonian jet with Re=5 at three dimensionless times before pinch-off: (*a*) $t$=86.05, (*b*) $t$=90.05, and (*c*) $t$=92.00.**

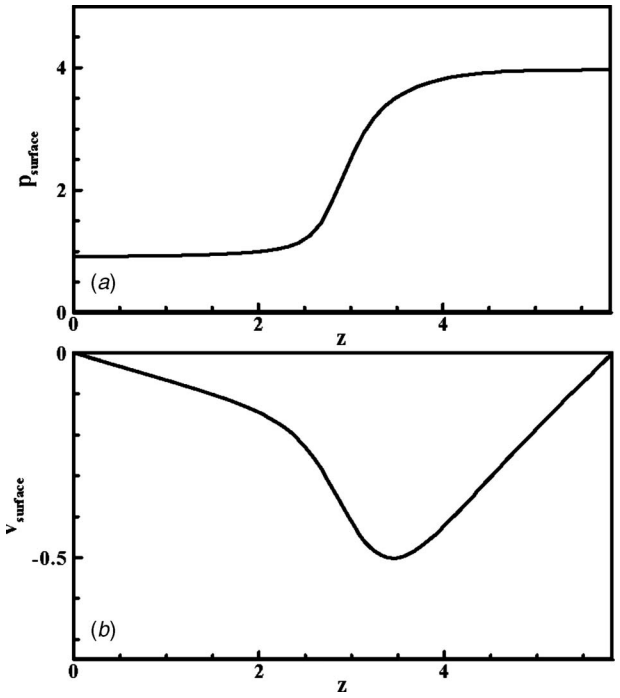


**Fig. 5 Axial variation in the surface pressure (*a*) and surface tangential velocity (*b*) for a Newtonian jet of Re=5 at $t$=86.05**

velocity at $t$=92.0. Figure 6(*a*) shows that there is a pressure gradient from the neck to the satellite drop. The change in direction of the velocity implies flow reversal.

Having understood the process of drop formation in a Newtonian jet, we now explain the effect of shear-thinning behavior on satellite drop formation at Re=5. Figure 7 demonstrates how the pinch-off and stagnation times ($t_{stag}$ is defined as the time when the flow reverses into the satellite drop) change with variations in

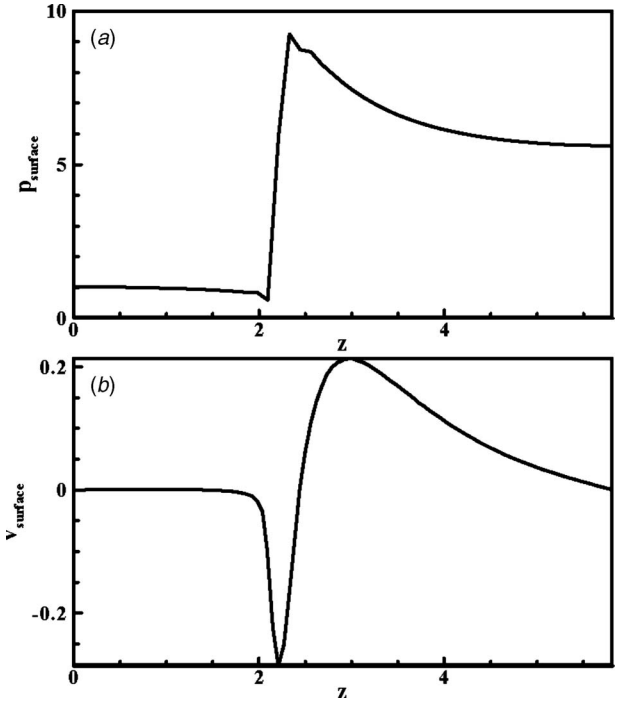


**Fig. 6 Axial variation in the surface pressure (*a*) and tangential velocity (*b*) for a Newtonian jet of Re=5 at $t$=92.0**

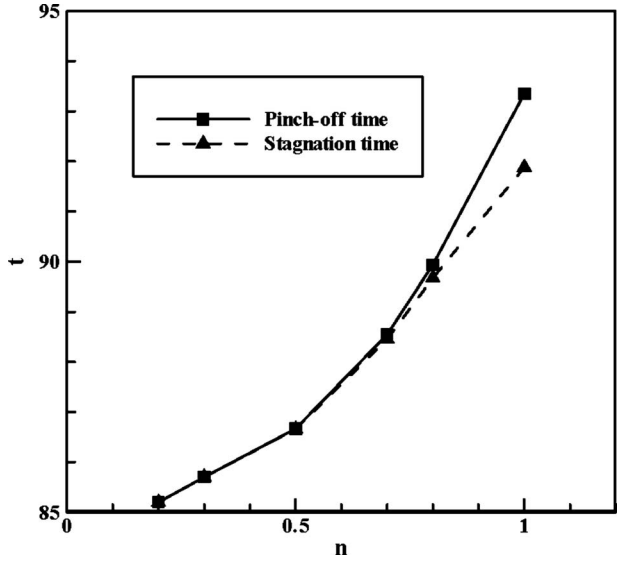


**Fig. 7 Pinch-off time (solid line) and stagnation time (dashed line) versus power-law index for Re=5**

the power-law index. Note that both the time to pinch-off and the stagnation time decrease as the power-law index decreases. However, the difference between the pinch-off and stagnation times decreases as the power-law index decreases, until eventually there is no reversal into the satellite drop. This is clearly illustrated by the streamlines in Fig. 8 ($n=0.3$). Figure 8($a$) shows streamlines at $t=74.3$, which is before neck formation. At this time the entire flow moves toward the main drop, due to the imposed initial condition as explained previously. Figure 8($b$) shows streamlines within the same jet at $t=85.5$, after the formation of a neck. At this instant, the entire flow moves towards the main drop despite neck formation.

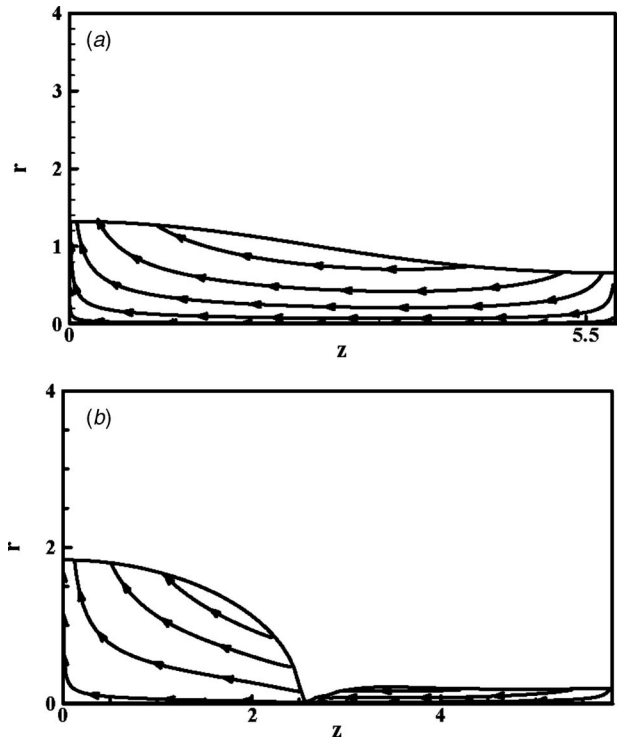


**Fig. 8 Streamlines for a shear-thinning jet ($n=0.3$) at Re=5: ($a$) $t=74.3$ and ($b$) $t=85.5$**

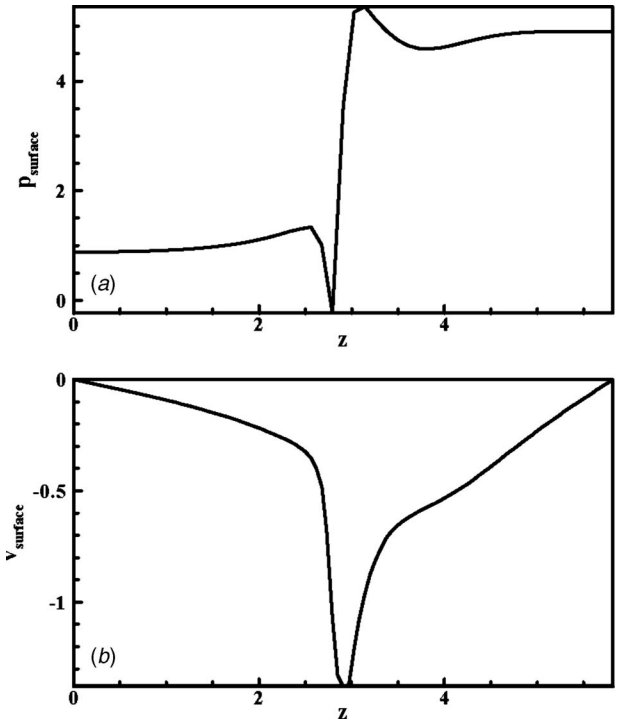


**Fig. 9 Axial variation in the surface pressure ($a$) and surface tangential velocity ($b$) for $n=0.3$ and Re=5 at $t=85.5$**

Figure 9 contains the surface pressure and tangential velocity for the non-Newtonian jet of Fig. 8($b$), where there is a pressure gradient from the neck to the satellite drop. However, despite this gradient, the entire fluid moves toward the main drop, as can be seen from Fig. 8($b$), which shows no change in direction of the surface tangential velocity. This behavior can be explained by two phenomena changes, which occur as a jet transitions from Newtonian to non-Newtonian. First, the normal pressure increases due to a decrease in the normal viscous forces. Second, the shear stresses opposing inertial flow towards the drop decrease due to a reduction in the effective viscosity.

Figure 10 shows the surface normal pressure at two different

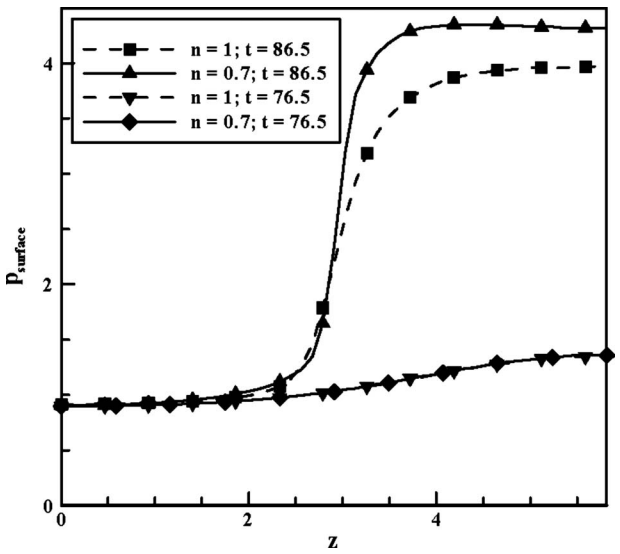


**Fig. 10 Capillary pressure at the liquid interface for two times. The dashed line denotes a Newtonian jet and the solid lines denote a shear-thinning jet ($n=0.7$)**

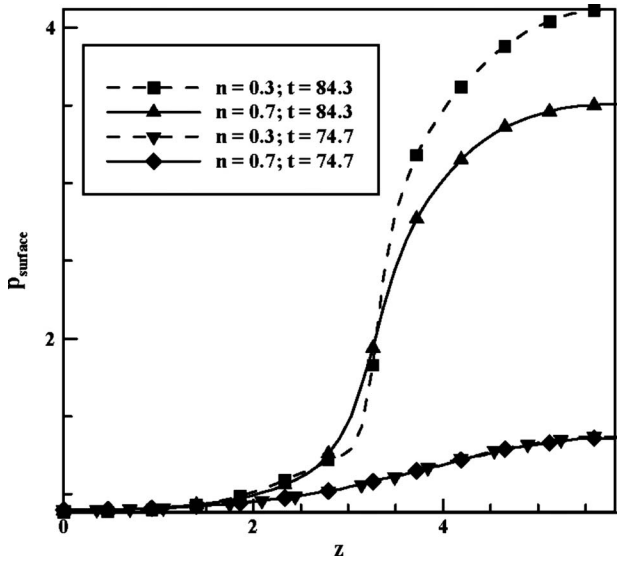


**Fig. 11 Capillary pressure at the liquid interface for two times. Here the dashed line denotes a shear-thinning jet with $n=0.7$ while the solid line indicates a shear-thinning jet with $n=0.3$.**

times for Newtonian and non-Newtonian jets. Initially, due to low shear rates, the surface normal pressure is similar for both cases. However, the shear rates in the non-Newtonian jet increase more rapidly as time progresses so at a later instant in time the normal surface pressure in a non-Newtonian jet is much higher than that in a Newtonian one.

It is also noted that the surface pressure is slightly lower at the right end of the domain than at the center for the shear-thinning jet. This is due to the onset of neck formation, whose curvature leads to a pressure gradient from the neck to the satellite. The increased normal pressure seen in Fig. 10 explains the earlier pinch-off times and earlier flow reversal times as the jet transitions from $n=1$ to $n=0.7$. The normal forces that lead to early reversal result in less fluid drainage into the main drop, which results in an increase in the satellite drop size as the power-law index is reduced.

Figure 11 shows the surface normal pressure at two different times for two different shear-thinning jets ($n=0.3$ and $n=0.7$). Here the surface pressure for a shear-thinning jet at $n=0.3$ is slightly higher than that for $n=0.7$, even at low shear rates. As the shear rates increase with time, the surface pressure in the jet with $n=0.3$ increases much more rapidly than for a jet with $n=0.7$. In addition, while the normal pressure increases, the reduction in effective viscosity fails to resist the initial flow towards the main drop before the normal forces cause pinch-off. This explains the lack of flow reversal at low power-law indices as seen in Fig. 7. This prevention of flow reversal, combined with earlier pinch-off times as the power-law index falls, leads to the absence of an increase in satellite drop size as the power-law index is reduced.

**3.2 Comparison of Simulations and Experiments.** Experiments to provide data for evaluating model accuracy were carried out with jets of power-law non-Newtonian fluids exiting from capillary tubes. Drop formation from these capillary jets was captured using a high speed digital camera. Digitized drop shapes were then compared to simulation results generated using the model described above.

The experimental apparatus included the following.

- A KD Scientific syringe pump with controllable flow rate that was used to force fluid through a Teflon® capillary tube (Upchurch Scientific®) with an inner diameter of $200\pm20$ $\mu$m. The axis of symmetry of the tube was aligned vertically.

**Table 1 Physical properties for XG-water solutions**

| XG concentration (%) | $n$ | $\mu_0$ (mPa s) | $\sigma$ (mN/m) | $\rho$ (kg/m$^3$) |
|---|---|---|---|---|
| 0.1 | 0.55 | $359\pm9$ | $72\pm1$ | $999\pm1$ |
| 0.2 | 0.40 | $732\pm2$ | $73\pm1$ | $999\pm1$ |
| 0.2 | 0.30 | $884\pm1$ | $73\pm1$ | $1000\pm1$ |

- A Phantom v7.1 high speed digital camera for visualization of the drop formation process. It can record images at 14,000 frames/s and has a pixel size of 14 $\mu$m. The camera was mated to a Nikon Nikkor™ lens with a focal length of 70 mm.
- A 200 W incandescent lamp for illumination of the experimental domain. The source was placed to provide backward lighting through a diffusive screen. Output from the camera was processed using NIH freeware.

The non-Newtonian liquids were Xanthan gum (XG) water solutions having concentrations of 0.1, 0.2, and 0.3% by weight. Their viscosities were measured using a Rhelogica Viscotech® rheometer. Power-law indices were determined by a fit to the shear stress and strain rate data (see Table 1). The confidence interval for the best-fit curves used to determine the power-law index was 95%.

When comparing experimental data and model simulations, Table 1 power-law index values were used along with a dimensionless infinite shear viscosity, $\beta$, of 0.002 and a time constant, $\alpha$, of 10, as prescribed by Doshi et al. [6]. The values chosen ($n$ ranging from 0.55 to 0.3) serve to validate the model predictions as all the analyses that have been performed were for $n\geqslant0.3$. Perturbation wave numbers were determined for each jet Re value from Timmermans and Lister's results [14].

Surface tensions were measured using a DuNuoy tensiometer, which had an accuracy of 0.001 N/m (CSC Scientific). Liquid densities were determined by weighing a known volume of the fluid on a Sartorius analytical balance (resolution 0.01 g). Liquid physical properties are summarized in Table 1. All experiments and physical property measurements were performed at $24.3\pm0.1\,^{\circ}$C.

Experimental operating conditions are listed in Table 2. Reynolds numbers were computed using initial liquid velocities determined from measured volumetric flow rates. The choice of Reynolds number range (0.19–0.65) is appropriate for assessing model accuracy since we have shown that shear-thinning behavior has the strongest effect on drop formation at low Re [15].

In passing, we note that that the Froude number ($gd_c/u_0^2$, where $d_c$ is the dimensional diameter of the capillary and $u_0$ is the dimensional jet mean velocity) is $\sim10^{-5}$, while the Bond number ($\rho gr'^2/\gamma$) is $\sim10^{-4}$. These values provide support for our assumption that gravitational forces are negligible in comparison to surface-tension and inertial forces.

Based on the work of Gaster [16], who found that spatially

**Table 2 Experimental operating conditions**

| XG concentration (%) | Reynolds number |
|---|---|
| 0.1 | $0.46\pm0.01$ |
| | $0.55\pm0.02$ |
| | $0.67\pm0.02$ |
| 0.2 | $0.22\pm0.01$ |
| | $0.28\pm0.02$ |
| | $0.33\pm0.02$ |
| 0.3 | $0.19\pm0.01$ |
| | $0.23\pm0.02$ |
| | $0.28\pm0.02$ |

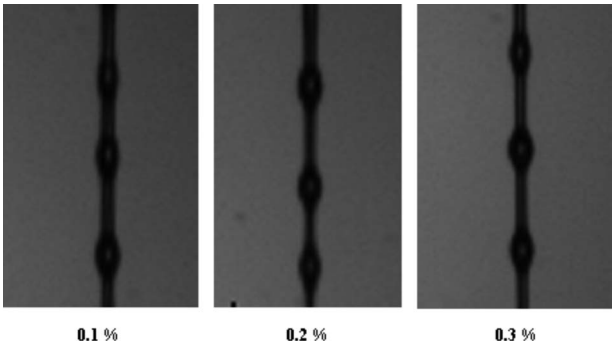


**Fig. 12 Typical experimental droplet streams**

increasing instability is negligible compared to temporally increasing instability for an infinitely long Newtonian liquid jet surrounded by an inviscid environment, we have assumed that the same holds true for shear-thinning jets. Therefore, drop shapes were captured at various times, with the time defined as $t' = d_n/v_0$, where $d_n$ is the distance from the nozzle to the drop and $v_0$ is the initial liquid velocity. The experimental data collection times were arbitrarily chosen. Their magnitudes and uncertainties are included in the figure legends. Since each of the result figures is for jet breakup at a different time value, results were acquired throughout the breakup process thereby helping us to assess the accuracy of the model at all times up to pinch-off.

A typical screenshot is provided in Fig. 12. Individual droplet images were clipped from their corresponding total image, jet boundaries defined using a MATLAB routine, and then processed into black and white images (see Fig. 13). The image analysis routine then divided the droplet into two halves by imposing a centerline. The locations of the pixels at the left and right drop boundaries were determined for each image row, averaged and plotted for comparison with model predictions at the same time.

Uncertainty in the experimental results arises from (i) uncertainty in digitally processing the images and (ii) uncertainty in rheological data. For (i), the uncertainty $u_d/d = 1/N_p$ is defined by the smallest measurable unit (a pixel) where $u_d$ is the uncertainty in the distance measured, $d$ is the distance measured during image processing, and $N_p$ is the number of pixels counted in an image. Uncertainties in the rheological data enter through the Reynolds number since it is an input to the model. This includes uncertainties in the liquid density and viscosity, in the jet diameter, and in the jet velocity. Density uncertainty includes contributions from the measured volume and mass. Viscosity uncertainty includes contributions from the measured torque and the sensor diameter. Velocity uncertainty includes contributions from the measured flow rate (volume and time) and the jet diameter. All were calculated using the approach of Kline and McClintock [17].

Comparisons of model predictions and experimental data are presented in Figs. 14 through 19 uncertainties. Model predictions are represented by solid lines, with their associated uncertainties indicated by dashed lines.

Figures 14 and 15 contain results for the highest and lowest Re cases when using the 0.1% XG-water solution. Model predictions

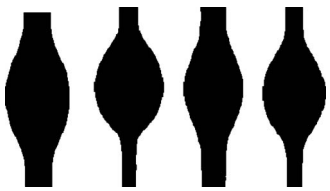

**Fig. 13 Typical extracted images of postprocessed droplets**

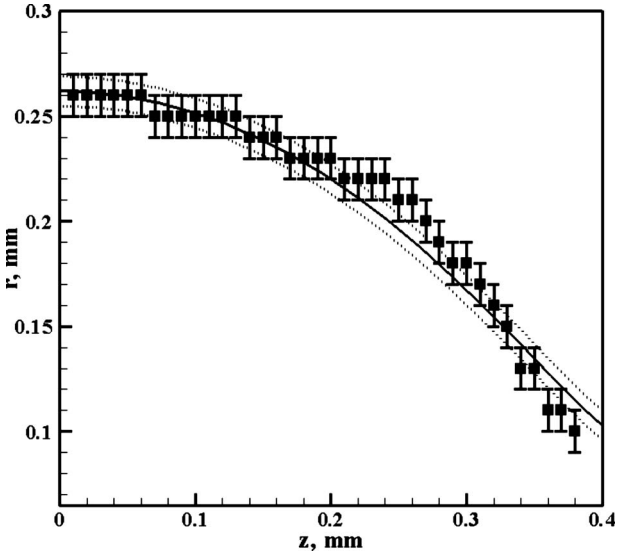


**Fig. 14 Comparison of model predictions (solid line) with experimental data (square symbols) for 0.1% water-XG solution at Re=0.46, $n$=0.55, and $t$=9.61±0.09 ms. The dashed lines indicate the uncertainty in model predictions.**

are equal to experimental data to within the sum of their uncertainties. Agreement is better for the higher Re case, especially nearest the pinch-off point.

Figures 16 and 17 contain results for highest and lowest Re cases when using the 0.2% XG-water solution. Model predictions are again equal to experimental data to within the sum of their uncertainties, and agreement is again better for the higher Re case, especially near pinch-off.

Figures 18 and 19 contain results for highest and lowest Re cases when using the 0.3% XG-water solution. As in the two previous cases, model predictions are equal to experimental data to within the sum of their uncertainties. Also, agreement is better for the higher Re case, especially nearest the pinch-off point.

In summary the data in Figs. 14–19 demonstrate that model predictions accurately match experimental data.

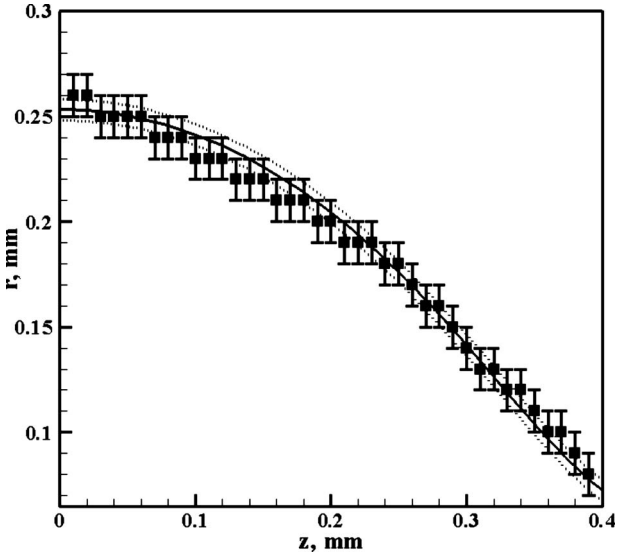


**Fig. 15 Comparison of model predictions (solid line) with experimental data (square symbols) for 0.1% water-XG solution at Re=0.67, $n$=0.55, and $t$=9.09±0.08 ms. The dashed lines indicate the uncertainty in model predictions.**

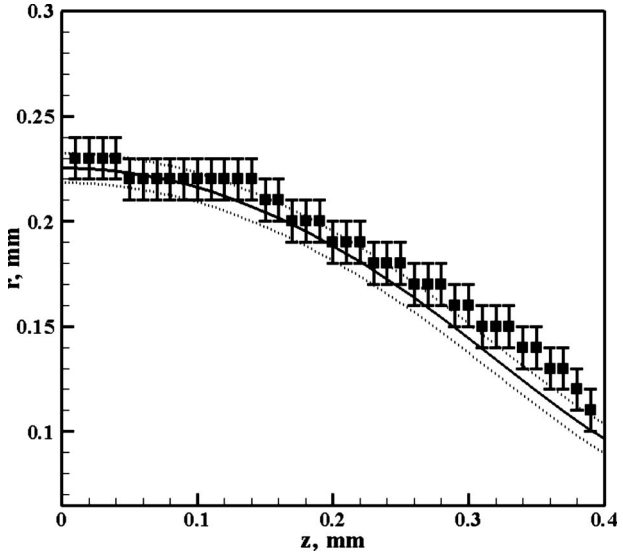


**Fig. 16 Comparison of model predictions (solid line) with experimental data (squares) for 0.2% water-XG solution at Re =0.22, $n$=0.40, and $t$=12.48±0.05 ms. The dashed lines depict the uncertainty in model predictions.**

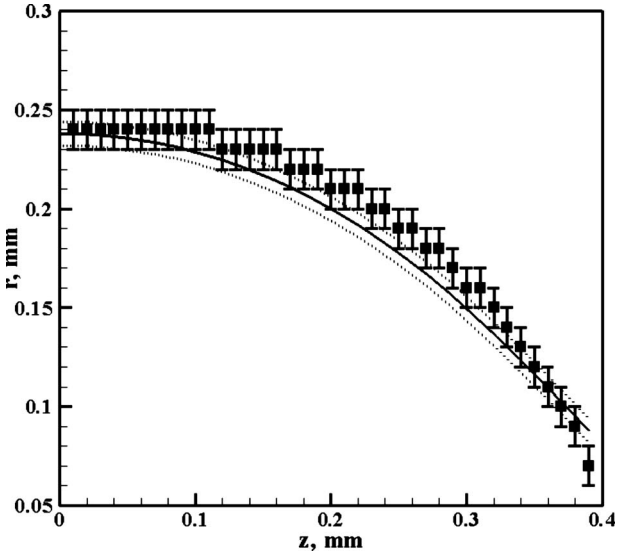


**Fig. 18 Comparison of model predictions (solid line) with experimental data (square symbols) for 0.3% XG-water solution at Re=0.19, $n$=0.30, and $t$=12.80±0.09 ms. The dashed lines indicate the uncertainty in model predictions.**

## 4 Summary and Conclusions

This study examined the effect of shear thinning on the behavior of a cylindrical jet. At Re=5, a decrease in the power-law index leads to an increase in satellite drop size. However, beyond a limiting power-law index, any further decrease leads to a slight decrease in the satellite drop size. This behavior is due to the twin effects of the increase in normal pressure and a reduction in viscosity as the power-law index falls. The increase in pressure leads to a reduction in pinch-off time, and also to earlier flow reversal as the power-law index is reduced. This lessens drainage into the main drop, which leads to an increase in the satellite drop diameter. Beyond a limiting power-law index there is no flow reversal into the satellite before pinch-off. This leads to the subsequent decrease in satellite drop size as the power-law index reduces further.

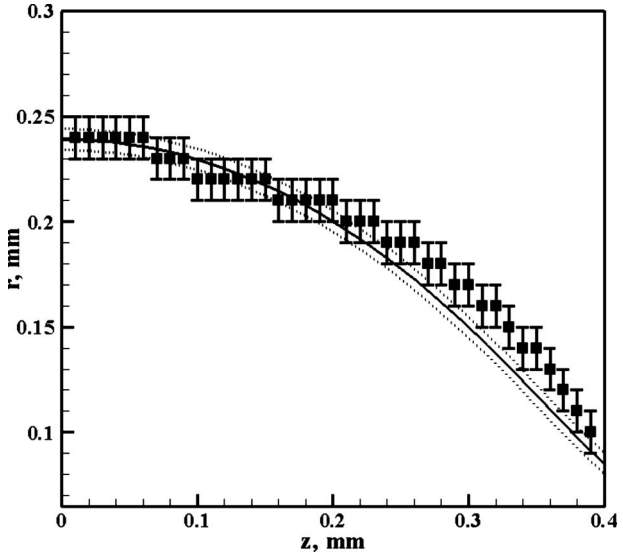


**Fig. 17 Comparison of model predictions (solid line) with experimental data (square symbols) for 0.2% water-XG solution at Re=0.33, $n$=0.40, and $t$=10.88±0.07 ms. The dashed lines depict the uncertainty in model predictions.**

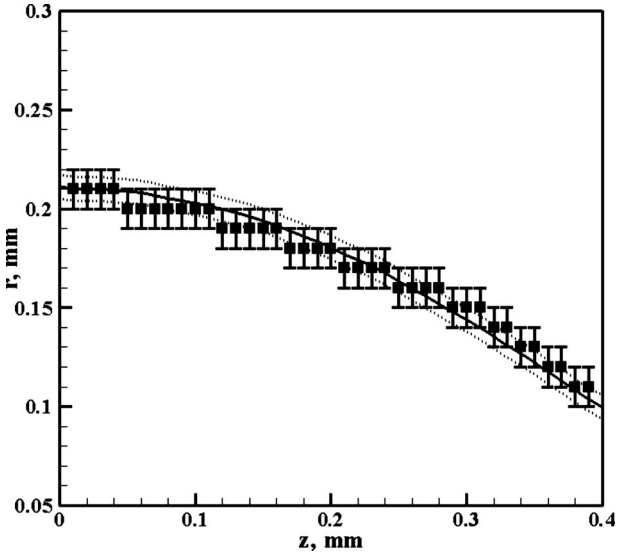


**Fig. 19 Comparison of model predictions (solid line) with experimental data (square symbols) for 0.3% XG-water solution at Re=0.28, $n$=0.30, and $t$=10.63±0.08 ms. The dashed lines indicate the uncertainty in model predictions.**

Model predictions were compared with experimental data. Agreement is within the sum of their uncertainties.

## Acknowledgment

The authors gratefully acknowledge support from the National Science Foundation through Grant No. 323622-DMI.

## References

[1] Rayleigh, L., 1879, "On the Instability of Jets," Proc. London Math. Soc., **10**, pp. 4–13.
[2] Eggers, J., 1997, "Nonlinear Dynamics and Breakup of Free-Surface Flows," Rev. Mod. Phys., **69**(3), pp. 865–930.
[3] Renardy, M., 2002, "Self-Similar Jet Breakup for a Generalized PTT Model," J. Non-Newtonian Fluid Mech., **103**(2–3), pp. 261–269.
[4] Bousfield, D. W., Keunings, R., and Marucci, G., 1986, "Nonlinear Analysis of

the Surface-Tension Driven Breakup of Viscoelastic Liquid Filaments," J. Non-Newtonian Fluid Mech., **21**(1), pp. 79–97.
[5] Yildirim, O. E., and Basaran, O. A., 1999, "Deformation and Breakup of Stretching Bridges of Newtonian and Sheer-Thinning Liquids: Comparison of One- and Two-Dimensional Models," Chem. Eng. Sci., **56**(1), pp. 211–233.
[6] Doshi, P., Suryo, R., Yildirim, O. E., McKinley, G. H., and Basaran, O. A., 2004, "Scaling in Pinch-Off of Generalized Newtonian Fluids," J. Non-Newtonian Fluid Mech., **113**(1), pp. 1–27.
[7] Renardy, M., and Renardy, Y., 2004, "Similarity Solutions for Breakup of Jets of Power Law Fluids," J. Non-Newtonian Fluid Mech., **122**(1–3), pp. 303–312.
[8] Campana, D., Paolo, J. D., and Saita, F. A., 2004, "A 2-D Model of Rayleigh Instability in Capillary Tubes Surfactant Effects," Int. J. Multiphase Flow, **30**, pp. 431–454.
[9] Ubal, S., Corvalan, C., Giavedoni, M. D., Saita, F. A., 2001, "A Numerical Study on Two-Dimensional Faraday Waves," *Computational Fluid and Solid Mechanics*, K. J. Bathe, ed., Springer New York, pp. 1000–1005.
[10] Kistler, S. F., and Scriven, L. E., 1983, *Coating Flows Computational Analysis of Polymer Processing*, J. R. A. Pearson and S. M. Richardson, ed., Applied Science, New York.
[11] Strang, G., and Fix, G. L., 1973, *An Analysis of the Finite Element Method*, Prentice-Hall, Englewood Cliffs, NJ.
[12] Gresho, P. M., Lee, R. L., and Sani, R. L., 1980, *Recent Advances in Numerical Methods in Fluids*, Pineridge, Swansea, UK, Vol. 1, Chap. 3.
[13] Crisfield, M. A., 1981, "A Fast Incremental-Iterative Solution Procedure That Handles Snap-Through," Comput. Struct., **13**(1–3), pp. 55–62.
[14] Timmermans, M.-L. E., and Lister, J. R., 2002, "The Effect of Surfactant on the Stability of a Liquid Thread," J. Fluid Mech., **459**, pp. 289–306.
[15] Dravid, V., Loke, P. B., Corvalan, C. M., and Sojka, P. E., 2006, "Drop Formation in Non-Newtonian Jets at Low Reynolds Numbers," *Proceedings of 2006 IMECE*, Chicago, IL, Nov.
[16] Gaster, M., 1962, "A Note on the Relation Between Temporally-Increasing and Spatially Increasing Disturbances in Hydrodynamic Stability," J. Fluid Mech., **14**, pp. 222–224.
[17] Kline, S. J., and McClintock, F. A., 1953, "Describing Uncertainties in Single Sample Experiments," Mech. Eng. (Am. Soc. Mech. Eng.), **75**, pp. 3–8.

# Modeling and Measurement of the Dynamic Surface Tension of Surfactant Solutions

**Tomiichi Hasegawa**
Faculty of Engineering,
Niigata University,
8050, Ikarashi-2, Nishi-ku,
Niigata-shi 950-2181, Japan
e-mail: hasegawa@eng.niigata-u.ac.jp

**Masahiro Karasawa**
Graduate School of Science and Technology,
Niigata University,
8050 Ikarashi-2, Nishi-ku,
Niigata-shi 950-2181, Japan

**Takatsune Narumi**
Faculty of Engineering,
Niigata University,
8050, Ikarashi-2, Nishi-ku,
Niigata-shi 950-2181, Japan

*Surfactant solutions are usually used under conditions accompanied by transient dynamic surfaces, and therefore the dynamic surface tension (DST) is important in many industrial processes. Theories regarding DST have been developed exclusively on the adsorption theory that molecules are transported from bulk solution to the interface. However, the adsorption theory is not closed and requires another relationship between the interfacial concentration of the adsorbing molecules and the bulk concentration of molecules near and at the surface, which at present is based on assumptions. In addition, DST obtained by the adsorption theory contains several parameters that must be determined beforehand, and it is not simple to use for practical purposes. Here, we propose a new model based on the concept that surfactant molecules rotate during the process reaching the equilibrium surface state, which is different from the conventional adsorption theory, and we obtained a simple expression of DST as a function of the surface age. In addition, an experiment was carried out to determine DST by measuring the period and weight of droplets falling from a capillary. The expression by the proposed model was compared with the results of this experiment and with those reported previously by several other authors, and good agreement was obtained. Furthermore, the characteristic time in the model was shown to be correlated with the concentrations of solutions regardless of the type of solutions examined.* [DOI: 10.1115/1.2956597]

*Keywords: surfactants, dynamic surface tension, model, droplet, momentum equation*

## Introduction

Surfactant solutions play an essential role in many industrial processes, such as foaming, jet printing, emulsification, coating, and detergency. The practical importance of surfactants is based on the ability of these molecules to quickly reach an equilibrium state at freshly created solution/air interfaces, thus decreasing the surface tension from the value of bulk solution to the equilibrium value at the surface. This decreased surface tension is called the dynamic surface tension (DST). The first physical model of DST for interfaces with time invariant area was derived by Ward and Tordai [1]. This model was based on the assumption that the time dependence of interfacial tension is caused by transport of molecules in bulk solution to the interface, i.e., by adsorption. There have since been many theoretical analyses of DST in surfactant solutions exclusively based on the idea of adsorption, with considerable success. However, the adsorption theory is not closed and requires another relationship between the interfacial concentration of the adsorbing molecules and the bulk concentration of molecules near and at the surface, which will be determined by a molecular theory in future but at present is based on some assumptions. In addition, the DST obtained by the adsorption theory contains several parameters that must be determined beforehand and is not simple to use for engineering purposes. There have been a number of reviews of this topic [2–4].

In general, the equilibrium surface tension of commonly used surfactant solutions is usually reached during the first several seconds after formation of a fresh surface. Thus, rapid experimental methods are required to measure the DST. Various such methods have been proposed and used, such as the oscillating jet [5], maximum bubble pressure [6], pendant drop [7], and fast formed drop FFD methods [8]. Overviews of the experimental methods were reported previously [2,9]. However, these methods require sophisticated equipment and techniques, and therefore do not always match engineering aims to obtain the DST in a simple manner.

In the present paper, we propose a model on DST, which is not based on the adsorption but based on the rotation of molecules during the process toward the equilibrium surface state. In addition, we report the result of a simple experiment performed to obtain DST by measuring the period and weight of droplets falling from a capillary. The predictions of the model are compared with the results of this experiment and of those reported previously by several other authors.

## Model of Dynamic Behavior of Surfactant Molecules

Existing theoretical analyses of the DST of surfactant solution have been based exclusively on the concept of adsorption of molecules to the surface. The adsorption theory is outlined schematically in Fig. 1 [2–4]. When the surface of a still liquid is suddenly expanded to a wider surface, the state of molecular array changes from the equilibrium state to a nonequilibrium state. In this case, the surface concentration of surfactant molecules at equilibrium $\Gamma_0$ also changes to that in the nonequilibrium state $\Gamma$, which is smaller than $\Gamma_0$. In turn, this change induces the transfer of molecules from bulk solution to the surface so that $\Gamma$ may return to $\Gamma_0$. During this transient process, the surface tension changes and is expressed as a function of time $t$, which is called DST. This is a general explanation of DST based on the adsorption theory, and raises the question of why the transient behavior of surfactant molecules at the surface is not taken into consideration during the nonequilibrium state. That is, molecules move toward a freshly created surface and change their orientations, but the hydraulic drag force caused by the motion has not been considered in the adsorption theory. This is thought to be a deficiency of the existing theory. Rather, we think that the transient behavior of surfac-

Contributed by the Fluids Engineering Division of ASME for publication in the JOURNAL OF FLUIDS ENGINEERING. Manuscript received May 4, 2007; final manuscript received February 17, 2008; published online July 29, 2008. Assoc. Editor: Theodore Heindel. Paper presented at the Fifth Joint ASME-JSME Fluids Engineering Conference.

  

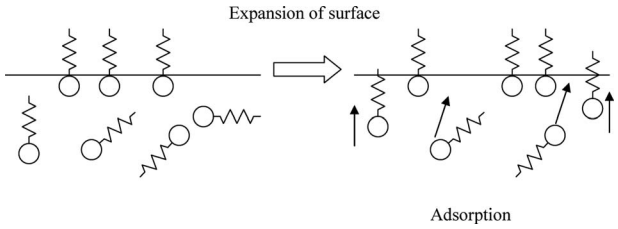


**Fig. 1 Schematic representation of the adsorption theory for surfactant solutions**

tant molecules, especially the rotation of molecule at the surface, is a major cause of DST, as shown schematically in Fig. 2: Since some time is required for a molecule lying on the freshly created surface to reach the final state where surfactant molecules stand at the surface with the lyophilic group (LG) projecting upward and the hydrophilic group (HG) immersed in the solvent, we think that it is this standing process of the molecule that causes the DST. In Fig. 2(*a*), it is assumed that the surface is suddenly expanded at time $t_0$, and at this time point the surface possesses the same properties as the bulk solution with the surfactant molecule lying on the surface with an incline angle $\theta$ of zero (of cause, this is an average story over all surfactant molecules, as they will be oriented randomly and there may be interactions among them). At time $t(>t_0)$, the molecule rises on the surface with LG inclined with angle $\theta$. Finally, at time $t_\infty(=\infty)$, the molecule stands with LG normal to the surface and HG immersed in water. This idea can be applied to general cases of surface expansion, but may be most proper for the outflow from an aperture to the air, like the flow in the present experiment discussed below: A molecule is set parallel to the surface near the exit and gradually stands as it flows downstream (Fig. 2(*b*)).

Figure 3 shows a schematic representation of a surfactant molecule rising on the surface. Here, it is assumed that $\theta=\pi/2$ when the surfactant molecule is parallel to the surface, and $\theta=\pi$ when the surfactant molecule is perpendicular to the surface at the end of the rising movement. If the molecule rotates about the center of HG, it shows rotary torque like a sphere $T$, which will be expressed as follows [10]:

$$T = 8\pi\mu R^3 \frac{d\theta}{dt} \tag{1}$$

Here, $R$ is the radius of HG mimicking a sphere, $\mu$ is the viscosity, $d\theta/dt$ is the angular velocity of the sphere, and the moment of

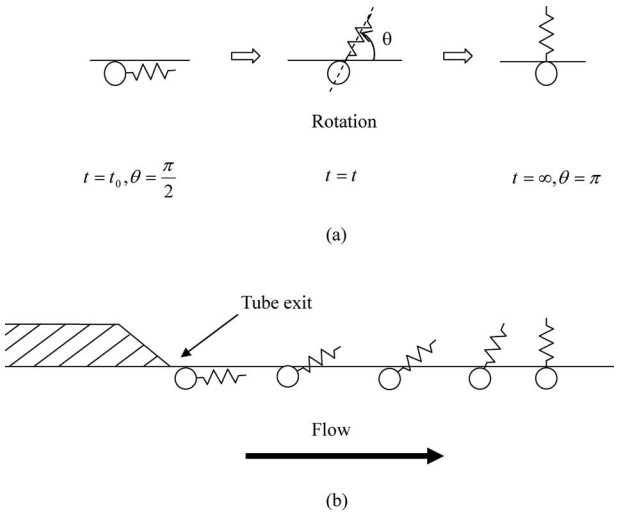


**Fig. 2 Schematic representation of the present modeling**

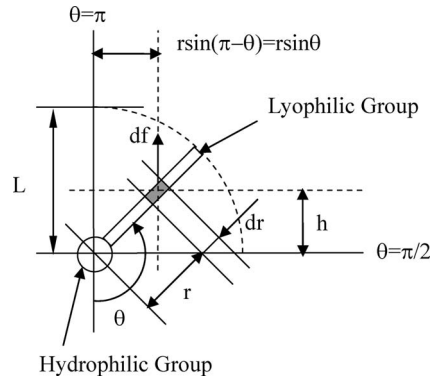


**Fig. 3 Image of a rotating surfactant molecule**

inertia is neglected. On the other hand, it is necessary to determine the upward force working on LG by the water on which the surfactant molecule stands (in reality, another force may be exerted by the surrounding surfactant molecules, but it is neglected because interaction among surfactant molecules is not considered here). However, it is very difficult to estimate the force accurately because repulsion between like charges may be related to this force, and it is too complicated to express by a simple relationship. Therefore, as a first approximation, we assume that the force $df$ working on a radial element $dr$ decreases linearly with height from the surface, i.e., it lessens by a force $df_0 \times h/r$, where $df_0$ is the initial force before rising, $r$ is the arbitrary radius, and $h$ is the height of $dr$ in the rising molecule. Then, the following equation is obtained:

$$df = df_0 - \frac{h}{r} df_0 \tag{2}$$

When $h=0$ and $h=r$, this becomes, respectively,

$$df = df_0 = \alpha dr \quad (h = 0) \tag{3}$$

$$df = 0 \quad (h = r) \tag{4}$$

where $\alpha$ is the force per unit length at the position of zero height. Then, LG takes the following reaction force from water:

$$df = \left(1 - \frac{h}{r}\right)\alpha dr \tag{5}$$

Torque $dT$ acting on $dr$ around the center of the sphere is then obtained by the relation

$$dT = r\sin(\pi - \theta)df = r\sin\theta df \tag{6}$$

That is,

$$dT = r\sin\theta\left(1 - \frac{h}{r}\right)\alpha dr \tag{7}$$

As $h$ is given by the following equation:

$$h = r\cos(\pi - \theta) = -r\cos\theta \tag{8}$$

the torque $dT$ becomes

$$dT = r\sin\theta(1 + \cos\theta)\alpha dr \tag{9}$$

Equation (9) is integrated with $r$ from $R$ to $L$ and then the total torque $T$ reads

$$T = \alpha\sin\theta(1 + \cos\theta)\frac{L^2 - R^2}{2} \tag{10}$$

where $L$ is the length of LG. Equating both torques given by Eqs. (1) and (10) provides

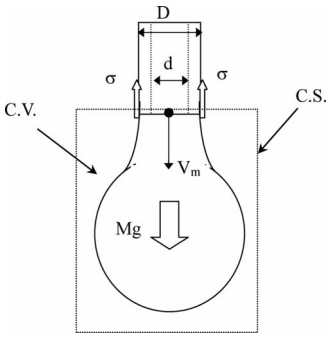


**Fig. 4 Schematic representation of a droplet**

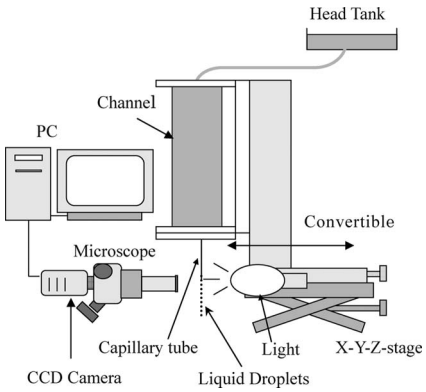


**Fig. 5 Experimental apparatus**

$$\frac{d\theta}{dt} = \frac{\alpha(L^2 - R^2)}{16\pi\mu R^3} \sin\theta(1 + \cos\theta) \tag{11}$$

Here, we introduce a coefficient, $K$, composed of $\alpha$, $\mu$, $L$, and $R$ as

$$K = \frac{16\pi\mu R^3}{\alpha(L^2 - R^2)} \tag{12}$$

and we obtain

$$\frac{d\theta}{dt} = \frac{1}{K} \sin\theta(1 + \cos\theta) \tag{13}$$

Integration from the initial state ($t=0$; $\theta=\pi/2$) to an arbitrary state ($t=t$; $\theta=\theta$) gives the elapsed time or the surface age, $t$, as a function of the rotation angle, $\theta$.

$$t = \int_{\pi/2}^{\theta} \frac{K}{\sin\theta(1 + \cos\theta)} d\theta = \frac{K}{2}\left(\frac{1}{1 + \cos\theta} + \log\left|\tan\frac{\theta}{2}\right| - 1\right) \tag{14}$$

Here, it is thought that the initial state ($\theta=\pi/2$) corresponds to the surface tension of the solvent (water) and the final state ($\theta=\pi$) is equivalent to the equilibrium surface tension.

Now, we introduce the normalized DST $\sigma_\theta$ as follows:

$$\sigma_\theta = (\sigma - \sigma_s)/(\sigma_w - \sigma_s) \tag{15}$$

where $\sigma$ is the measured DST, $\sigma_s$ is the equilibrium surface tension of samples, and $\sigma_w$ is the surface tension of water. It is natural that $\sigma_\theta$ is estimated by the degree of nonequilibrium state, and therefore we assume that it is expressed as the quantity ($L - L\cos(\pi-\theta)$), and obtain the following form by assigning a value of unity to $L$ (see Fig. 3):

$$\sigma_\theta = 1 + \cos\theta \tag{16}$$

By Eqs. (14) and (16), we obtain the following final relationship between the normalized DST $\sigma_\theta$ and the surface age $t$.

$$t = \frac{K}{2}\left(\frac{1}{\sigma_\theta} + \frac{1}{2}\log\left(\frac{2 - \sigma_\theta}{\sigma_\theta}\right) - 1\right) \tag{17}$$

## Experiment

**Calculation of the Dynamic Surface Tension.** Figure 4 shows the situation just before falling of a typical liquid droplet, and the following momentum equation is obtained.

$$F_s + Mg = \frac{\partial}{\partial t}\int_{CV} V_z \rho dv + \int_{CS} V_z \rho V_z dA \tag{18}$$

where $F_s$ is the total surface force, $Mg$ is the force of gravity on the droplet, CV designates a control volume fixed in space, $dv$ is the infinitesimal volume element, $V_z$ is the velocity in the flow direction, $\rho$ is the liquid density, CS denotes the control surface, and $dA$ is the infinitesimal area.

The first term on the left-hand side (LHS) of the equation is the force added directly on CS by the pressure and surface tension, the second term on the LHS is the weight of the droplet, the first term on the right-hand side (RHS) is the time rate of fluid momentum in CV, and the second term on the RHS is the rate of momentum of the fluid through CS. On estimation of the magnitude of each term in Eq. (18), the force caused by pressure in the first term on the LHS and the time rate of fluid momentum were found to be sufficiently small that they could be neglected [11]. According to observation, a droplet developing at the tube tip possessed a spherical shape in the early stage but took an ellipsoidal shape in the late stage, and finally just before falling the droplet adhered to the outside wall of capillary with the surface parallel to the wall, resulting in the contact angle of about 180 deg (see Fig. 4). Therefore, the force due to surface tension can be written as $-\pi D\sigma$, where $D$ is the outer diameter of the capillary tube and $\sigma$ is the DST to be measured. In addition, assuming the laminar capillary flow at the interface between the capillary exit and CS, we obtain the following relationship:

$$\int_0^{d/2} \rho V_z^2 2\pi r dr = \tfrac{4}{3}\rho Q V_m \tag{19}$$

where the laminar flow velocity is assumed as $V_z$, $r$ is an arbitrary radius, $d$ is the inner diameter of the capillary, $Q$ is the flow rate, and $V_m$ is the mean flow velocity.

Consequently, the following relationship can be used for calculating $\sigma$.

$$\sigma = \left(\frac{4}{3}\rho V_m^2 + \frac{4Mg}{\pi d^2}\right)\frac{d^2}{4D} \tag{20}$$

In the flow region where Reynolds number is less than about 100, the momentum term is negligibly small in comparison with the surface tension term in parentheses, and the following simple relationship is thus obtained [11]:

$$\sigma = \frac{Mg}{\pi D} \tag{21}$$

**Apparatus, Procedure, and Substances.** The experimental apparatus was composed of a head tank, channel, capillary tube, and video camera, as shown in Fig. 5. The head tank was moved up and down to adjust the flow rate. The channel was a cylinder 40 mm in inner diameter, and capillary tubes 0.27 mm and 0.31 mm in inner diameters were set at the tip. Movies were taken with a video camera attached to a microscope and uploaded onto a personal computer for analysis. The mass of a droplet for a flow rate was calculated by measuring the total mass of sequent falling droplets in a time and counting the number of the droplets in the time. The time interval between the droplets was identified with

**Table 1 Data of surfactants**

| Surfactant | [ppm] | $10^{-8}$[mol/cm$^3$] | K[s] |
|---|---|---|---|
| AE12(10) (C12E10) | 31.34 | 5.00 | 6 |
| $C_{12}H_{25}(OC_2H_4)_{10}OH$ | 100 | 15.95 | 1.6 |
| (Present experiment) | 313.43 | 50.00 | 0.21 |
| AE12(23) (C12E23) | 10 | 0.83 | 11 |
| $C_{12}H_{25}(OC_2H_4)_{23}OH$ | 20 | 1.67 | 7 |
| (Present experiment) | 40 | 3.33 | 3.4 |
| | 50 | 4.17 | 2.2 |
| | 59.98 | 5.00 | 1.6 |
| | 80 | 6.67 | 1.6 |
| | 100 | 8.34 | 0.9 |
| | 200 | 16.67 | 0.46 |
| | 599.77 | 50.00 | 0.08 |
| | 1000 | 83.37 | 0.27 |
| | 10000 | 833.65 | 0.18 |
| AE18(20) (C18E20) | 11.52 | 1.00 | 6 |
| $C_{18}H_{37}(OC_2H_4)_{20}OH$ | 115.15 | 10.00 | 1.8 |
| (Present experiment) | | | |
| AE18(100) (C18E100) | 46.76 | 1.00 | 2 |
| $C_{18}H_{37}(OC_2H_4)_{100}OH$ | 100 | 2.14 | 0.85 |
| (Present experiment) | 467.57 | 10.00 | 0.54 |

| Surfactant | [ppm] | $10^{-8}$[mol/cm$^3$] | K[s] |
|---|---|---|---|
| X-100 | 6.47 | 1 | 30 |
| $C_{14}H_{21}O(C_2H_4O)_{10}H$ | 16.69 | 2.58 | 9 |
| (Horozov *et al.* [13]) | 32.34 | 5 | 3.2 |
| | 48.51 | 7.5 | 1.8 |
| | 150.39 | 23.25 | 0.34 |
| | 200.52 | 31 | 0.13 |
| | 401.05 | 62 | 0.07 |
| X-405 | 24.61 | 1.25 | 3.2 |
| $C_{14}H_{21}O(C_2H_4O)_{40}H$ | 49.21 | 2.5 | 1 |
| (Horozov *et al.* [13]) | 98.42 | 5 | 0.23 |
| C10E8 | 0.10 | 0.02 | 3000 |
| $C_{10}H_{21}(OC_2H_4)_8OH$ | 0.26 | 0.05 | 800 |
| (Chang *et al.* [14]) | 0.51 | 0.1 | 400 |
| | 1.02 | 0.2 | 200 |
| | 2.04 | 0.4 | 70 |
| | 3.06 | 0.6 | 34 |
| | 5.11 | 1 | 16 |
| | 15.32 | 3 | 3 |
| C10E5 | 22.71 | 6 | 4.8 |
| $C_{10}H_{21}(OC_2H_4)_5OH$ | 37.85 | 10 | 1.7 |
| (Ravera *et al.* [15]) | | | |

surface age. The liquids used were pure water (here, pure water means the water that was distilled and de-ionized beforehand), tap water, and a series of aqueous solutions of nonionic surfactants AE: polyoxyethylene (10) lauryl ether (AE(10)), polyoxyethylene (23) lauryl ether (AE(23)), polyoxyethylene (20) stearyl ether (AE(20)), and polyoxyethylene (100) stearyl ether (AE(100)). By convention, these surfactants are called *CiEj*, where *i* is the number of carbon atoms and *j* indicates the number of $OC_2H_4$ groups. Table 1 shows the sample data, where the samples were selected such that the molecular weight (mw) of the LG would be the same for AE(10) and AE(23) and also the same for AE(20) and AE(100). The numbers in parentheses indicate mw of the (HG).

## Experimental Results

Figure 6 shows equilibrium surface tensions of AE(10) (●), AE(20) (△), AE(23) (○), AE(100) (▲) aqueous solutions, pure water, and tap water (■). These were obtained by the DuNouy method, where the vertical axis is the equilibrium surface tension $\sigma_s$ (mN/m) and the horizontal axis is the concentration $C$ (ppm). For both pure and tap water, the same value of 71 mN/m was obtained. From this figure, we can find the critical micelle concentration (cmc) at which $\sigma_s$ becomes constant with increasing concentration. For example, AE(23) aqueous solution reaches cmc at about 100 ppm.

Figure 7 shows examples of DST measured for AE(23) in pure water and tap water. There was no difference between them within

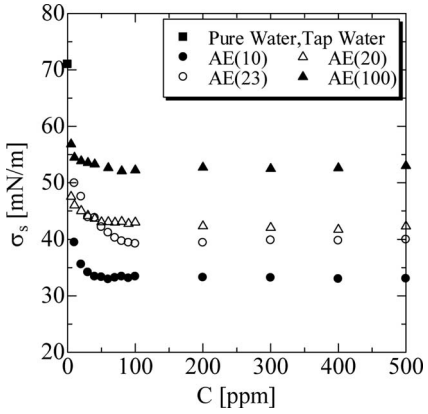


**Fig. 6 Equilibrium surface tension $\sigma_s$ plotted against concentrations of AE: Pure water (27°C), tap water (27°C), and AE(23) (22°C), AE(10) (24°C), AE(20) (16°C), and AE(100) (17°C) aqueous solutions**

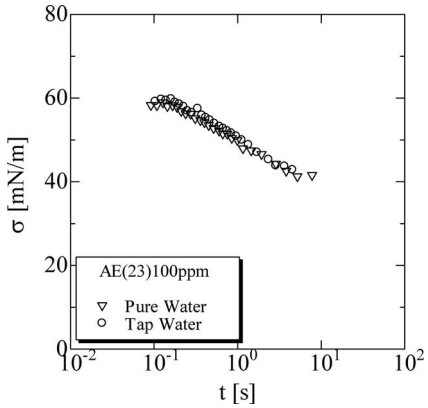


**Fig. 7 DST $\sigma$ of AE(23) in pure water (30°C) and tap water (27°C) plotted against surface age *t***

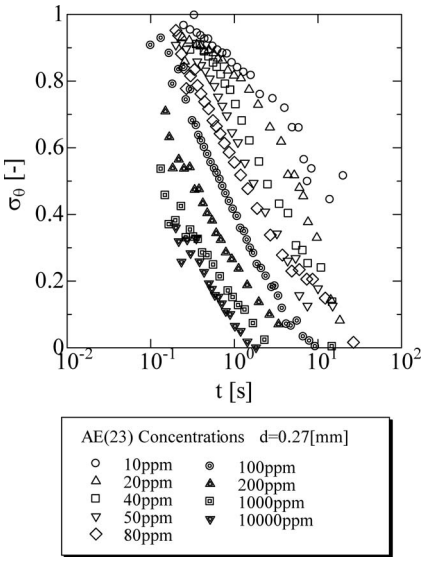


**Fig. 8 Normalized DST $\sigma_\theta$ plotted against the surface age $t$; 10 ppm (13°C), 20 ppm (15°C), 40 ppm (16°C), 50 ppm (14°C), 80 ppm (12°C), 100 ppm (14°C), 200 ppm (13°C), 1000 ppm (19°C), and 10,000 ppm (19°C) AE(23) solutions in water. Inner diameter is 0.27 mm**

the experimental errors as in the case of the equilibrium surface tension mentioned above, and therefore we used tap water as solvent in measurement for economy.

Figure 8 shows the normalized DST $\sigma_\theta$ of various concentrations of AE(23) aqueous solution obtained in the present experiment, where the vertical axis is $\sigma_\theta$ and the horizontal axis is the surface age $t$ (s), where $d$ is 0.27 mm. The experimental error of $\sigma_\theta$ was within $\pm 5\%$. We used 68 mN/m as the value of $\sigma_w$ because this value was measured both for pure water and tap water with the apparatus used in the present study for measuring DST. The reason why the measured value was lower than the surface tension of water, 72 mN/m, is not clear. Similar decrease in the surface tension for a pendant drop of water was also reported previously [12]. It can be seen from Fig. 8 that $\sigma_\theta$ decreases with increases in concentration, for example, it does not reach 0.6 even

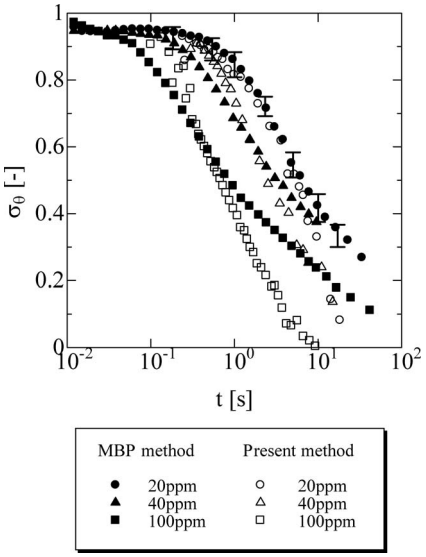


**Fig. 9 $\sigma_\theta$ measured by the maximum bubble method (MBP) (25°C) and the present drop weight method (14–16°C)**

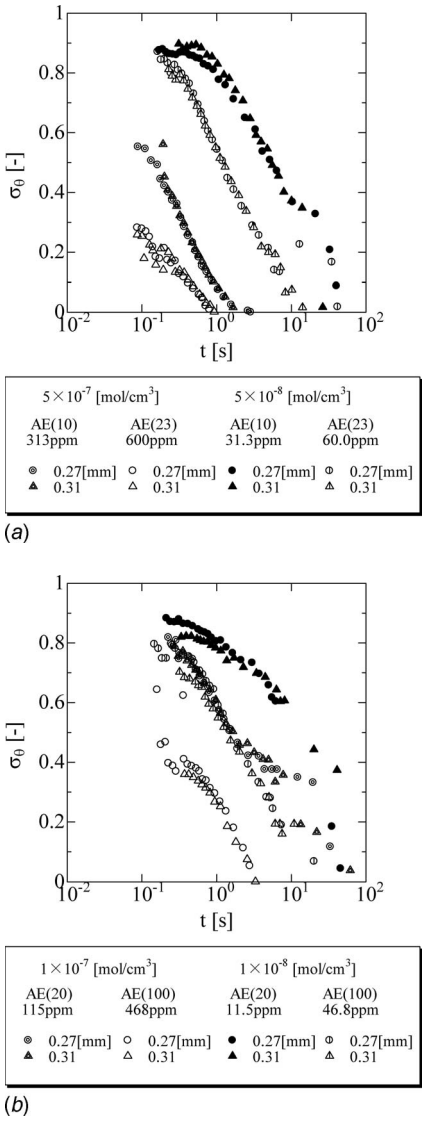


**Fig. 10 $\sigma_\theta$ against $t$ for different AEs at the same molar concentration. (*a*) AE(10) (27°C) and AE(23) (17°C) for 5 ×10⁻⁷ mol/cm³ and AE(10) (20°C) and AE(23) (20°C) for 5 ×10⁻⁸ mol/cm³. (*b*) AE(20) (25°C) and AE(100) (29°C) for 1 ×10⁻⁷ mol/cm³, and AE(20) (30°C) and AE(100) (31°C) for 1 ×10⁻⁸ mol/cm³.**

in short surface ages for concentrations higher than 1000 ppm, but the rate of decrease slows down at these high concentrations. Several identical solutions of AE(23) were also examined by the maximum bubble pressure method for comparison, and the results are shown in Fig. 9. As shown in the figure, $\sigma_\theta$ obtained by the present method generally agrees with that by the maximum bubble pressure method, but the data of long surface ages deviate.

Figures 10(*a*) and 10(*b*) show $\sigma_\theta$ for other AE solutions. The molar concentrations in each figure were selected such that one would be lower and the other would be higher than cmc (see Fig. 6). $\sigma_\theta$ was shown to decrease with increases in the mw of HG regardless of whether the concentration was beyond cmc.

## Comparison of the Model Equation With the Experimental Results and Discussion

Figures 11(*a*) and 11(*b*) show $\sigma_\theta$ of the present experimental results for AE(23) and the prediction by Eq. (17), where $K$ (s) was decided by best fit at each concentration. As shown in the figure,

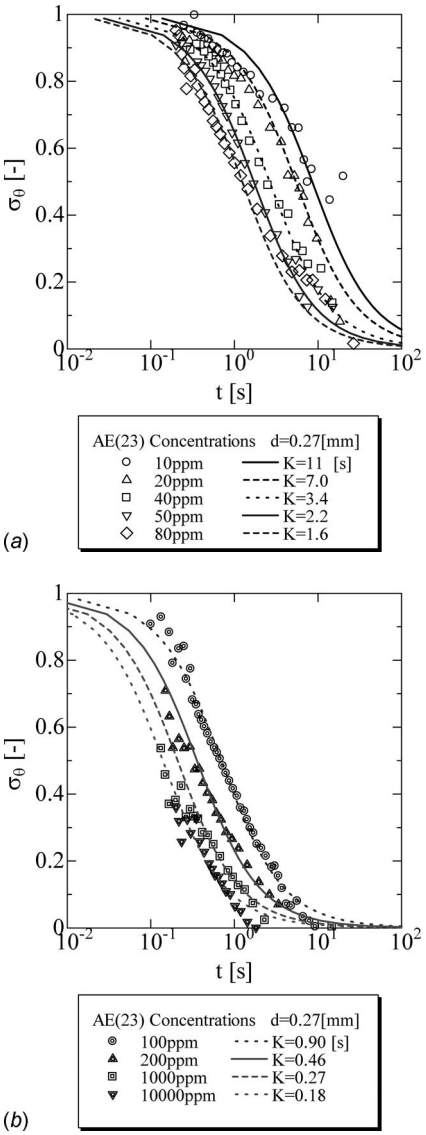


**Fig. 11 $\sigma_\theta$ against $t$; experimental data for AE(23) (symbols) and model predictions (lines). $K$ (s) was chosen for best fit of the model prediction to the experimental data at each concentration. (*a*) 10–80 ppm. (*b*) 100–10,000 ppm.**

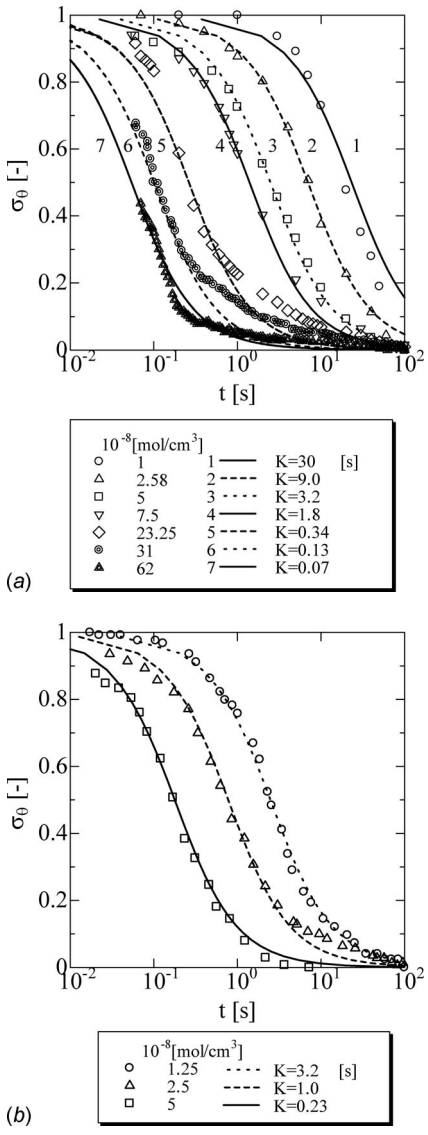


**Fig. 12 Comparison of the data (symbols) of (a) Triton X-100 and (b) Triton X-405 measured by the FFD method [13] and the model prediction (lines). $K$ (s) was chosen for the best fit.**

the model equation agrees with the experimental data except the cases for 10 ppm and 20 ppm concentrations at short surface ages $t$ around 1 s. However, agreement in high concentrations as shown in Fig. 11(*b*) is not to be accepted as it is because intermolecular forces are neglected in the present model. For the other kinds of solutions of AE(10), AE(20), and AE(100) used in the present experiment, the agreement similar to that of AE(23) was found, but the examples are omitted here. Figures 12–14 show comparisons of Eq. (17) with experimental results obtained using other methods. Figures 12(*a*) and 12(*b*) show the results of Triton X-100 and Triton X-405 by the FFD method [13]. As shown in the figure, there is good agreement between the present model and the experimental results. In addition, video-enhanced pendant bubble tensiometry was used for measurement of the DST of nonionic surfactant $C10E8$ aqueous solution [14]. The results in dimensionless form are shown in Fig. 13 along with the model prediction, and again there is fairly good agreement in this case. The dynamic maximum bubble and the drop shape techniques were also used for the aqueous solution of $C10E5$ [15], and the results are shown in Fig. 14 for comparison with the model results. The model predicts the experimental data well. Table 1 lists all the data of the solutions cited here for comparison. Figure 15 shows $K$ values for the examined solutions against both $C$ (mol/cm$^3$) and $C$ (ppm), and it can be seen that $K$ varies largely from 0.07 s to 3000 s according to the type and concentration of the surfactant. Comparison of Figs. 15(*a*) and 15(*b*) shows that $K$ is better correlated with $C$ (ppm) than with $C$ (mol/cm$^3$) irrespective of the type of molecule. The relationship between $K$ (s) and $C$ (ppm) can be approximated by the expression $K=185C^{-1.2}$, as shown by the line in Fig. 15(*b*), except at very high concentrations ($10^3$ ppm and $10^4$ ppm). Discrepancy in high concentrations is thought to be due to the effect of interaction between molecules. $K$ has the dimension of time, and it is useful here to consider what this means. If $K$ is substituted into $t$ on the LHS of Eq. (14), an equation with respect to $\theta$ is obtained and can be solved. The solution is $\theta=2.18$, and we obtain $\sigma_\theta=0.426$ from Eq. (16). That is, $K$ is a measure of the surface age at which the LG of the surfactant rotates from parallel to the liquid/air interface to an angle of 35 deg ($=2.18-\pi/2$) upward from the interface.

As mentioned above, the present model agrees generally with experimental data. However, diffusion and molecular interaction

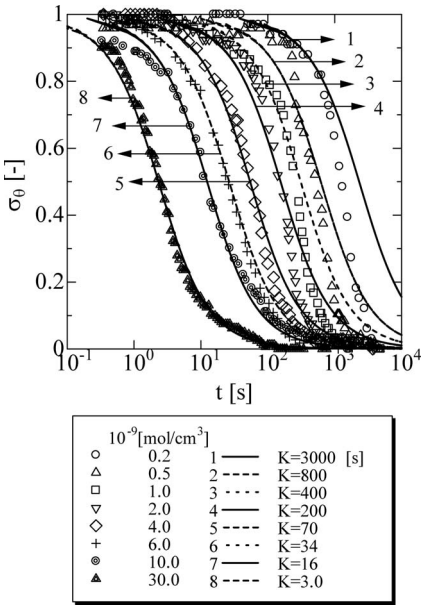


**Fig. 13 Comparison of the data (symbols) of *C*10*E*8 measured by video-enhanced pendant bubble tensiometry [14] with the model prediction (lines). *K* (s) was chosen for the best fit.**

are neglected in the present model. Diffusion and interaction are necessary hereafter to be quantitatively estimated from the behavior of molecules and compared with the effect of rotation.

## Conclusions

Surfactant solutions are usually used under conditions accompanied by transient dynamic surfaces, and the DST is important in many industrial processes. In the present paper, we proposed a new and simple model based on the concept that surfactant molecules rotate upward during the process of reaching the equilibrium surface state. That is, it was assumed that when a surface is expanded suddenly at time $t_0$, the surface possesses the same properties as that of bulk solution and a surfactant molecule lies on the surface with its LG parallel to the surface—i.e., the incline

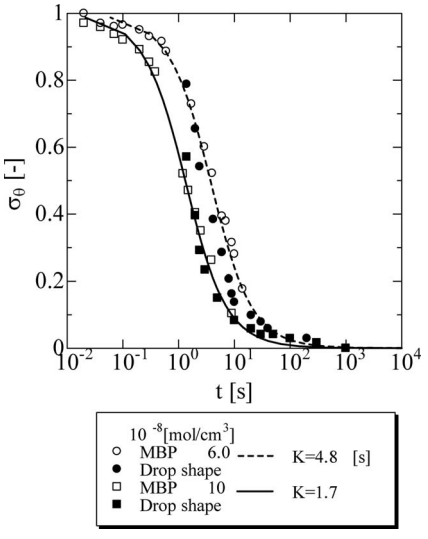


**Fig. 14 Comparison of the data of *C*10*E*5 measured by the maximum bubble pressure (MBP) method (open symbols) and the drop shape technique (solid symbols) [15] with the model prediction (lines). *K* (s) was chosen for the best fit.**

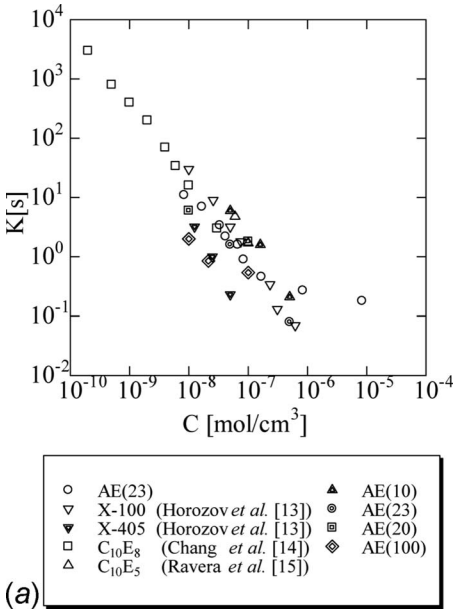


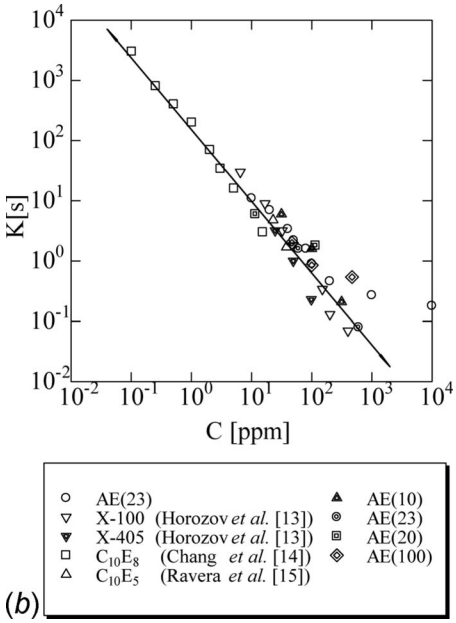


**Fig. 15 *K* (s) plotted against concentration *C* (mol/cm³ or ppm) for all solutions listed. (*a*) *K* (s) against molar concentration *C* (mol/cm³). (*b*) *K* (s) against weight concentration *C* (ppm). The line in shows the relationship $K=185C^{-1.2}$ between *K* (s) and *C* (ppm).**

angle is zero. Then, at a time $t(>t_0)$, the molecule rises up on the surface with LG inclined at some angle, and finally at time $t_\infty(=\infty)$ it stands with LG normal to the surface and the HG immersed in water. In this process, the torque acting on LG due to repulsion exerted by surface water is assumed to be balanced by the torque of flow resistance acting on HG in water. Consequently, the relationship between DST and the surface age $t$ was obtained. In addition, a simple experiment was performed to obtain DST by measuring the period and the weight of droplets falling from a capillary. The expression by the model was compared with both the present experimental results and the data reported previously by several other authors, and good agreement was obtained. Furthermore, it was found that the characteristic time appearing in the model is correlated with the concentration of the solution regard-

less of the type of solution examined. Thus, the simple model proposed here was found to be useful for expression of DST as a function of the surface age.


## Acknowledgment

We thank Mr. Masayuki Nagashima and Mr. Tomohiko Anazawa for measurement of dynamic surface tensions by the maximum bubble pressure method, and Mr. Ryuichi Kayaba, Mr. Takashi Irimichi, Mr. Katsuo Katou, and Mr. Takehiro Hoshina for many helps in experiment.


## Nomenclature

### Modeling

$\Gamma$ = surface concentration of surfactant molecules in the nonequilibrium state
$\Gamma_0$ = surface concentration of surfactant molecules at the equilibrium state
$R$ = radius of HG mimicking a sphere
$\mu$ = viscosity
$df$ = differential of force
$dr$ = length of small element
$df_0$ = initial differential force before rising
$\alpha$ = force per unit length
$L$ = length of LG
$r$ = radius
$h$ = height of $dr$ in the rising molecule
$dT$ = differential of torque
$T$ = total torque
$K$ = coefficient with the dimension of time, composed of $\mu$, $\alpha$, $L$, and $R$
$\theta$ = rotation angle
$t$ = arbitrary time or surface age
$\sigma$ = dynamic surface tension
$\sigma_w$ = surface tension of water
$\sigma_s$ = equilibrium surface tension of samples
$\sigma_\theta$ = normalized dynamic surface tension

### Experiment

$V_z$ = flow velocity
$D$ = outer diameter of the capillary tube
$d$ = inner diameter of the capillary tube
$M$ = mass of the liquid droplet
$g$ = acceleration due to gravity
$\rho$ = liquid density
$V_m$ = mean flow velocity
$C$ = concentration

## References


[1] Ward, A. F. H., and Tordai, L., 1946, "Time-Dependence of Boundary Tensions of Solutions, I. The Role of Diffusion in Time-Effects," J. Chem. Phys., **14**, pp. 453–461.
[2] Miller, R., Joos, P., and Fainerman, V. B., 1994, "Dynamic Surface and Interfacial Tensions of Surfactant and Polymer Solutions," Adv. Colloid Interface Sci., **49**, pp. 249–302.
[3] Dukhin, S. S., Kretzschmar, G., and Miller, R., 1995, *Dynamics of Adsorption at Liquid Interfaces*, Elsevier, Amsterdam, pp. 30–139.
[4] Miller, R., and Fainerman, V. B., 2004, "Characterization of Adsorption Layers at Liquid Interfaces—Studies With Drop and Bubble Methods," *Fluid Mechanics of Surfactant and Polymer Solutions* (CISM Courses and Lectures No. 463), V. Starov and I. Ivanov, eds., Springer, Wien, pp. 57–80.
[5] Thomas, W. D. E., and Potter, L., 1975, "Solution/Air Interfaces I. An Oscillating Jet Relative Method for Determining Dynamic Surface Tensions," J. Colloid Interface Sci., **50**, pp. 397–412.
[6] Miller, R., and Fainerman, V. B., 2004, "Characterisation of Adsorption Layers at Liquid Interfaces—Studies With Drop and Bubble Methods," *Fluid Mechanics of Surfactant and Polymer Solutions* (CISM Courses and Lectures No. 463), V. Starov and I. Ivanov, eds., Springer, Wien, pp. 81–94.
[7] Miller, R., and Fainerman, V. B., 2004, "Characterisation of Adsorption Layers at Liquid Interfaces—Studies With Drop and Bubble Methods," *Fluid Mechanics of Surfactant and Polymer Solutions* (CISM Courses and Lectures No. 463), V. Starov, and I. Ivanov, eds., Springer, Wien, pp. 94–105.
[8] Horozov, T., and Arnaudov, L., 1999, "A Novel Fast Technique for Measuring Dynamic Surface and Interfacial Tension of Surfactant Solutions at Constant Interfacial Area," J. Colloid Interface Sci. **219**, pp. 99–109.
[9] Dukhin, S. S., Kretzschmar, G., and Miller, R., 1995, *Dynamics of Adsorption at Liquid Interfaces*, Elsevier, Amsterdam, pp. 140–237.
[10] Bird, R. B., Armstrong, R. C., and Hassager, O., 1987, *Dynamics of Polymeric Liquids*, Wiley, New York, Vol. 1, p. 33.
[11] Karasawa, M., Hasegawa, T., and Narumi, T., 2007, "Measurement of Dynamic Surface Tension of Surfactant Solutions," J. Soc. Rheol., Jpn., **35**(5), pp. 265–271.
[12] Harkins, W. D., and Brown, F. E., 1919, "The Determination of Surface Tension (Free Surface Energy), and the Weight of Falling Drops: The Surface Tension of Water and Benzene by the Capillary Height Method," J. Am. Chem. Soc., **41**, pp. 499–524.
[13] Horozov, T., and Arnaudov, L., 2000, "Adsorption Kinetics of Some Polyethylene Glycol Octylphenyl Ethers Studied by Fast Formed Drop Technique," J. Colloid Interface Sci., **222**, 146–155.
[14] Chang, H.-C., Hsu, C.-T., and Lin, S.-Y., 1998, "Adsorption Kinetic of C10E8 at the Air-Water Interface," Langmuir, **14**, pp. 2476–2484.
[15] Ravera, F., Liggieri, L., and Miller, R., 2000, "Molecular Orientation as a Controlling Process in Adsorption Dynamics," Colloids Surf., A, **175**, pp. 51–60.

# Rheological and Hydraulic Properties of Welan Gum Fluids in Straight and Coiled Tubings

**Adedeji Asubiaro**
Graduate Research Assistant
e-mail: adedejiasu_biaro@ou.edu

**Subhash N. Shah**
Stephenson Chair Professor
e-mail: subhash@ou.edu

Mewbourne School of Petroleum and Geological Engineering,
Well Construction Technology Center,
The University of Oklahoma,
T-301 Sarkeys Energy Center,
100 Boyd Street,
Norman, OK 73019-1003

*This study involves experimental investigation of the hydraulic characteristics of aqueous based welan gum fluids of concentrations 1.4 kg/m$^3$, 2.9 kg/m$^3$, 5.7 kg/m$^3$, and 8.6 kg/m$^3$ in both straight and coiled tubings at 21°C, with particular emphasis on the effect of polymer concentration and coiled tubing curvature ratio. The flow loop available at the Well Construction Technology Center of the University of Oklahoma, consisting of 1.27 cm straight and coiled tubings (with curvature ratios of 0.01, 0.019, and 0.031), was utilized. It was observed that for all welan gum fluids investigated, friction losses in coiled tubing were significantly higher than those in straight tubing. In addition, increasing coiled tubing curvature ratio brings about higher friction loss for all fluids investigated. Rheological data for these fluids were obtained using a Model 35 Fann viscometer. Friction pressure data gathered from flow experiments are analyzed and correlations for friction pressure loss prediction of welan gum fluids have been developed for both straight and coiled tubings. These correlations, which represent the industry's first attempt in the fundamental investigation of friction loss prediction of welan gum fluids, are found to provide good accuracy when compared to the experimental data. Flow behavior of welan gum fluids is compared with 4.9 kg/m$^3$ guar fluid. It is found that in both straight and coiled tubings, the guar fluid exhibited higher drag reduction when compared to the welan gum fluids investigated in this study.* [DOI: 10.1115/1.2907414]

*Keywords: welan gum, coiled tubing, friction factor correlation, guar gum, drag reduction*

## Introduction

Welan gum is a commercially available biopolymer developed by Kelco, Division of Merck Co. Inc. USA in 1985 with a trade name Biozan. It is found to be suitable for drag reduction and viscosity enhancement purposes in many oil and gas production operations including hydraulic fracturing, acidizing, wellbore cleanup, cementing, and drilling. It possesses good thermal stability and is stable in the presence of calcium ions, high *p*H conditions, and in solutions containing high levels of glycols. The molecular structure of welan gum is shown in Fig. 1.

In recent years, coiled tubing has gained popularity in various petroleum engineering applications due to its numerous operational advantages. Polymeric fluids including welan gum have been pumped through both the straight and coiled sections of coiled tubing in production operations. Due to secondary flow effects caused by centrifugal forces in curved flow geometry, fluid flow behavior in coiled tubing differs significantly from that in straight tubing. It has been observed that friction pressure losses in coiled tubing are much higher when compared to straight tubing under the same flow conditions [1].

Several investigators [2–7] have conducted studies on welan gum fluids. Most of these investigations involved rheological characterization of welan gum fluids and their comparison with other polymeric fluids. To date, there has been no comprehensive investigation of the hydraulic properties of welan gum fluids of concentrations typically used in oilfield applications, especially in coiled tubing. This study, therefore, is the industry's first effort, focused toward experimentally determining the effect of polymer concentration and coiled tubing curvature ratio on welan gum fluids. The correlations developed in this study are applicable for flow in both straight and coiled tubings and would be of benefit for the prediction of friction factor of welan gum fluids.

## Experimental Setup

**Equipment.** The schematic diagram of the flow loop used is shown in Fig. 2. It consists of three coiled tubing reels, one 4.6 m straight tubing section, fluid mixing and pumping equipment, and data acquisition system. Three 1.27 cm o.d. and 1.1 cm i.d. coiled tubings made of stainless steel were used in this study. The dimensions of these tubings are presented in Table 1. These coils were made by spooling straight stainless tubings onto drums with various diameters. Since the tubing diameter is fixed, decreasing the coil diameter (from Coil 1 to Coil 3) increases the curvature ratio from 0.01 to 0.031. The typical range of curvature ratio encountered in the field applications is well within the range of these three coils. The wide curvature ratio range of the coils enables us to investigate the effect of curvature ratio on friction pressure losses in coiled tubing. The easy quick-connects allowed us to interchange coils during the flow tests.

Fluid mixing and preparation was accomplished by using a 3800 liter polyethylene tank. A Model 6P10 Moyno progressive cavity pump and a Model 5M Deming centrifugal pump were used to pump fluids in flow loops. The Moyno pump with its variable speed drive can deliver up to approximately 0.009 m$^3$/s at $4.1 \times 10^6$ Pa pressure. The centrifugal pump serves to boost the suction of the Moyno pump.

A Micromotion mass flowmeter (Model: CMF050M320NU) was used to measure the flow rate, fluid density, and temperature. It measures flow rate in the range of 0–0.0019 m$^3$/s, fluid density with accuracy of $\pm 0.0005$ g/cm$^3$, and temperature with accuracy of $\pm 1$°C or $\pm 0.5\%$ of reading in °C. Honeywell differential pressure transducers (Model: STD130) were used for the measurement of frictional pressure losses across straight tubing section and in

Contributed by the Fluids Engineering Division of ASME for publication in the JOURNAL OF FLUIDS ENGINEERING. Manuscript received June 26, 2007; final manuscript received February 5, 2008; published online July 29, 2008. Assoc. Editor: Dennis Siginer.

  

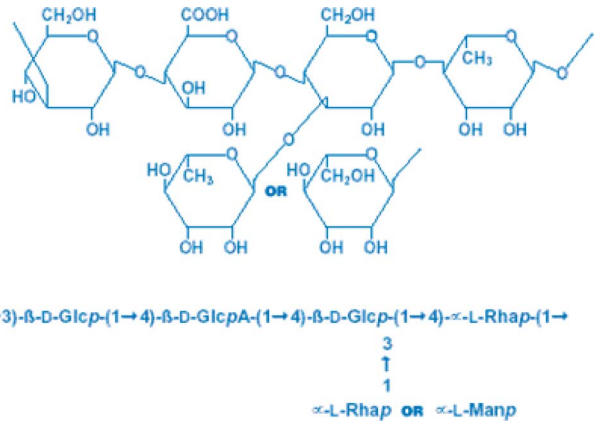


**Fig. 1 Molecular structure of welan gum**

coils. The measurement accuracy is ±0.075% of the calibration span. An absolute pressure transducer (Model: STG98LC) measures the entry pressure of the system. The flow loop has a working pressure limit of $6.9\times10^6$ Pa.

The data measured by the flowmeter and pressure transducers were transmitted to a computer where the data were displayed and saved for later analysis. This task was accomplished by the Fluke Hydra data acquisition system (Fluke Corporation, Everett, WA, Model 2625A). The Fluke Hydra system contains two hydras, each having 21 analog measurement channels. The sample rate is up to 10 samples/s. The Hydra data logger communicates with a host computer via a wireless modem radio link. The wireless tool can allow up to 366 m distance between the remote logger and the receiving computer. The data collected are transmitted to a personal computer in the control room.

**Fluids Investigated and Test Procedure.** Four concentrations of water based welan gum fluids typically used in oilfield operations were investigated. These concentrations are 1.4 kg/m$^3$, 2.9 kg/m$^3$, 5.7 kg/m$^3$, and 8.6 kg/m$^3$. The fluids were prepared and stored in the 3800 liter polyethylene tank. The mixing procedure recommended by polymer product supplier was followed. Adequate time was allowed for gel to hydrate in the mixing tank for proper gelation. Samples of fluid were collected and measured using a Model 35 Fann viscometer to check fluid viscosity. After the polymer solution was prepared, water was first circulated through the flow loop to conduct system check. This ensured that the pressure transducer settings and parameter settings of the data acquisition computer were set properly. Water was pumped through both straight and coiled tubings at various flow rates and corresponding pressure drop readings were recorded. The results of water tests were used as the base line for gel flow data analysis. Water in the flow loop was then displaced by pumping test fluid. The test fluid was pumped in a single-pass mode to avoid polymer degradation due to shear. Flow rate was set at a desired value and steady state pressure drop data across straight and coiled tubings were recorded. The flow rate was changed and corresponding pressure drops were recorded. At each flow rate, adequate time was allowed for the flow to achieve steady state condition. This was confirmed by monitoring the live display of measured flow rate and pressure drop signals.

**Table 1 Specification of tubing used in fluid flow loop**

| Tubing o.d. (cm) | o.d. (cm) | Core or reel diameter (m) | Ratio ($r/R$) | No. of turns | Total lenth (m) |
|---|---|---|---|---|---|
| 1.27 | 1.10 | 1.10 | 0.010 | 3 | 11.02 |
| | | 0.57 | 0.019 | 3 | 5.74 |
| | | 0.36 | 0.031 | 6 | 7.08 |

Fluid samples were collected from the mixing tank at the start and end of each test. The rheology of the samples was evaluated using a Model 35 Fann viscometer. By comparing rheology of the samples taken before and after the test, any change in rheology due to polymer degradation and viscous heating can be detected. In this experiment, no significant changes were observed in the rheology of the fluids before and after pumping. After testing with the first coil, the coil was replaced by another coil with a different curvature ratio. Similar test procedure was followed for all three coils to obtain pressure drop data at various flow rates.

**Data Reduction and Analysis.** For the analysis of the acquired flow rate versus differential pressure data, rheological property measurement of the fluids tested was necessary. These data were obtained by using a Model 35 Fann viscometer at ambient condition. From the data, logarithmic plots of wall shear stress versus wall shear rate were prepared and the power law model fluid parameters, $n$, flow behavior index, and $K_v$ consistency index for viscometer were determined. The $K_v$, subsequently, was converted to $K_p$, the pipe consistency index using the following:

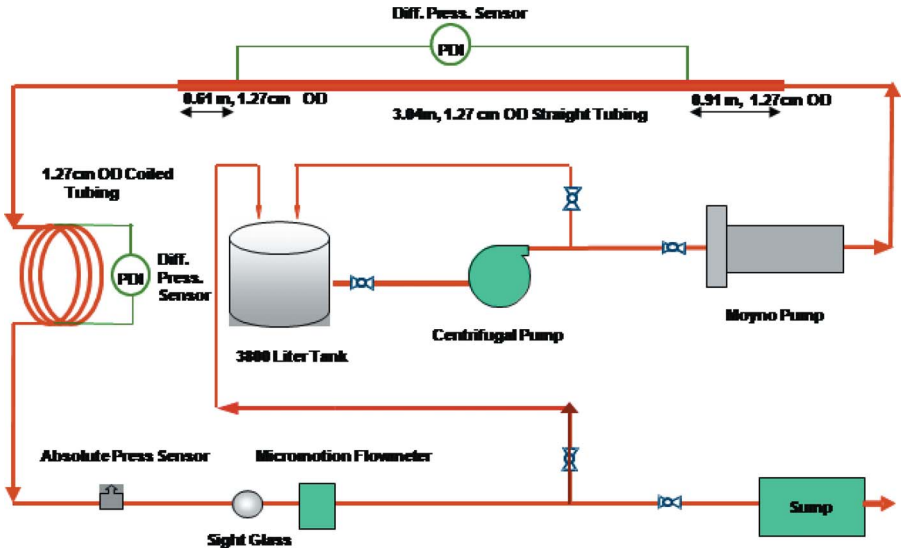


**Fig. 2 Schematic diagram of experimental setup**

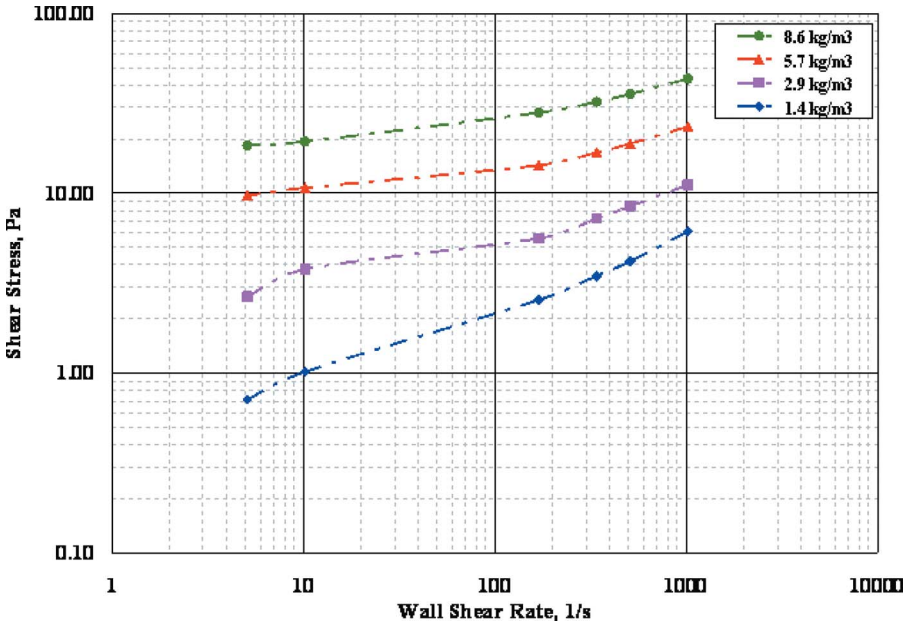


**Fig. 3 Rheograms of welan gum fluids investigated**

$$K_p = \frac{K_v}{\left[\frac{4n\sigma}{3n+1}\right]^n} \tag{1}$$

where $\sigma$ is a constant defined by

$$\sigma = \left[\frac{\beta^{2/n}}{n\beta^2}\right]\left[\frac{\beta^2 - 1}{\beta^{2/n} - 1}\right] \tag{2}$$

In Eq. (2), $\beta$ is the ratio of bob to cup radius of the Model 35 Fann viscometer used.

Flow rate and pressure drop values from the flow loop were converted to Fanning friction factor and generalized Reynolds number. These two dimensionless groups were used in characterizing fluid flow through straight and coiled tubings. Generalized Reynolds number, $N_{\mathrm{Re}\,g}$, is given by

$$N_{\mathrm{Re}\,g} = \left[\frac{d_i^n \rho v^{2-n}}{8^{n-1} K_p}\right] \tag{3}$$

Fanning friction factor $f$ is defined by the following expression:

$$f = \left[\frac{d_i \Delta p}{2lv^2\rho}\right] \tag{4}$$

where $v$ is the average velocity and is calculated from

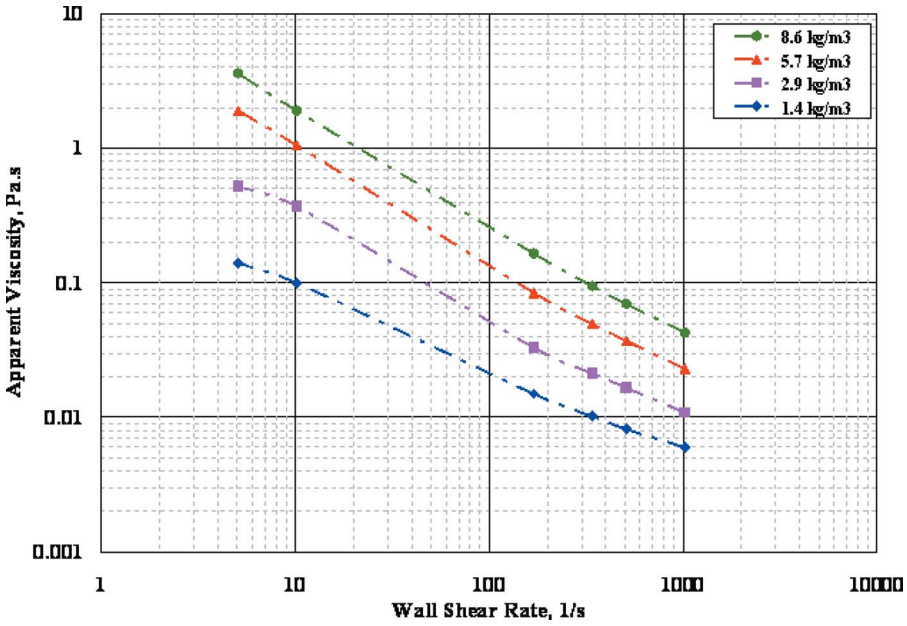


**Fig. 4 Apparent viscosity versus wall shear rate plots for welan gum fluids**

**Table 2 Maximum error in experimental measurements**

| Tubing type | Maximum error (%) Generalized Reynolds number | Fanning friction factor |
|---|---|---|
| Straight tubing | 0.1 | 3.0 |
| Coiled tubing, $r/R=0.01$ | 0.2 | 1.0 |
| Coiled tubing, $r/R=0.019$ | 0.2 | 1.0 |
| Coiled tubing, $r/R=0.031$ | 0.2 | 1.0 |

$$v = \left[ \frac{4q}{\pi d_i^2} \right] \tag{5}$$

Based on the accuracy of physical measurements including flow rate ($\pm 0.05\%$) and density ($\pm 0.0005$ g/cm$^3$) from the Micromotion flow meter and pressure drop ($\pm 0.075\%$) from differential pressure transducers, the maximum percentage error was computed for the dimensionless parameters: generalized Reynolds number and Fanning friction factor. Pipe length and diameter measurement accuracy used were $\pm 0.32$ cm and $\pm 0.00025$ cm, respectively. Table 3 presents the maximum experimental percentage error for the computed dimensionless parameters used in the analysis.

## Results and Discussion

**Rheological Characterization.** Figure 3 shows a logarithmic plot of wall shear stress and wall shear rate for all welan gum fluid concentrations investigated. The plot of apparent viscosity against wall shear rate for these fluids is depicted in Fig. 4. No significant difference was noticed between viscosity data taken before and after each test. These figures show that the behavior of all fluids can adequately be described by non-Newtonian pseudoplastic fluid over a large shear rate range. The following power law rheological model thus was used to characterize the behavior of these fluids:

$$\tau = k(\dot{\gamma})^n \tag{6}$$

The values of parameters $n$, $K_v$, and $K_p$ determined over a shear rate range of 10.2–1022 s$^{-1}$ are shown in Table 2. The correlation coefficient, $R^2$, for the $n$ and $K_v$ values is 0.99.

**System Calibration.** The accuracy of the measurement in straight and coiled tubings was examined by acquiring water data through 1.27 cm straight and coiled tubings at 21 °C. Water data from the straight pipe were compared with the following correlation of Drew et al. [8] for turbulent Newtonian flow in smooth straight pipes:

$$f = 0.0014 + 0.125(N_{\mathrm{Re}\,g})^{-0.32} \tag{7}$$

Data from the coiled tubing were compared with the following correlation of Srinivasan et al. [9], which is valid for turbulent Newtonian fluid flow in smooth coiled tubing:

$$f = \frac{0.084}{N_{\mathrm{Re}\,g}^{0.2}} \left( \frac{r}{R} \right)^{0.1} \tag{8}$$

$$(2100 < N_{\mathrm{Re}\,g} < 140{,}000; 0.0097 < r/R < 0.135)$$

Figures 5–7 show logarithmic plots of Fanning friction factor against Reynolds number for water through straight and the three coiled tubings. It is observed that the water data from the straight and coiled tubings are in good agreement with the corresponding correlations of Drew et al. and Srinivasan et al. This indicates that the straight tubing and three coils are hydraulically smooth. The system was calibrated every time a new test was performed to ensure that reliable data were gathered during the test.

**Table 3 Power law model parameters for welan gum fluids**

| Concentration (kg/m$^3$) | $n$ | $K_v$ (Pa s$^n$) | $K_p$ (Pa s$^n$) |
|---|---|---|---|
| 1.43 | 0.487 | 0.21 | 0.23 |
| 2.85 | 0.382 | 0.78 | 0.86 |
| 5.7 | 0.277 | 3.39 | 3.73 |
| 8.55 | 0.244 | 7.90 | 8.67 |

## Effect of Concentration

Flow data of 1.4 kg/m$^3$, 2.9 kg/m$^3$, 5.7 kg/m$^3$, and 8.6 kg/m$^3$ welan gum fluids investigated in straight pipe are presented in Fig. 8. This is a logarithmic plot of Fanning friction factor and generalized Reynolds number corresponding to the experimental pres-

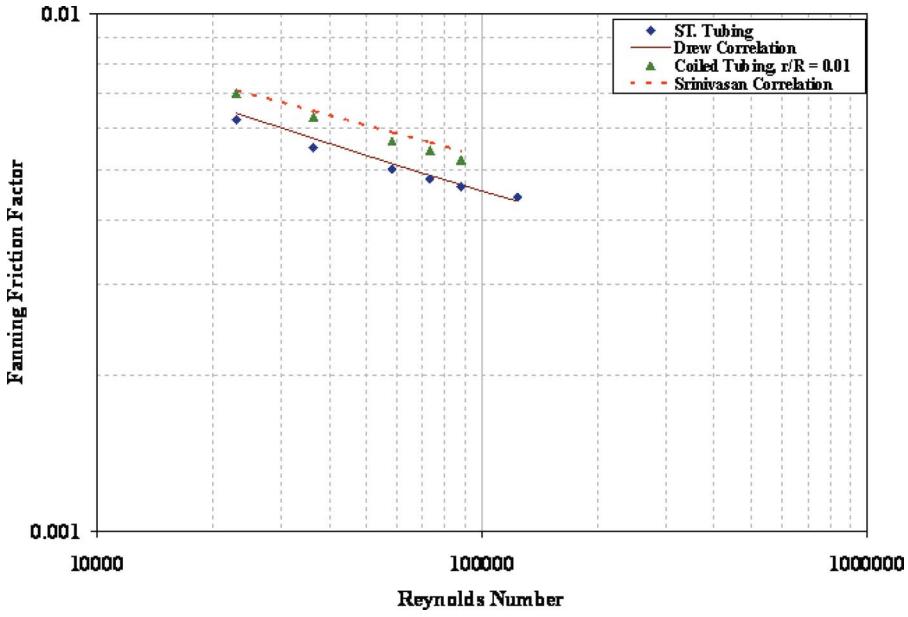


**Fig. 5 Water flow data through 1.27 cm o.d. straight and coiled tubings ($r/R=0.01$)**

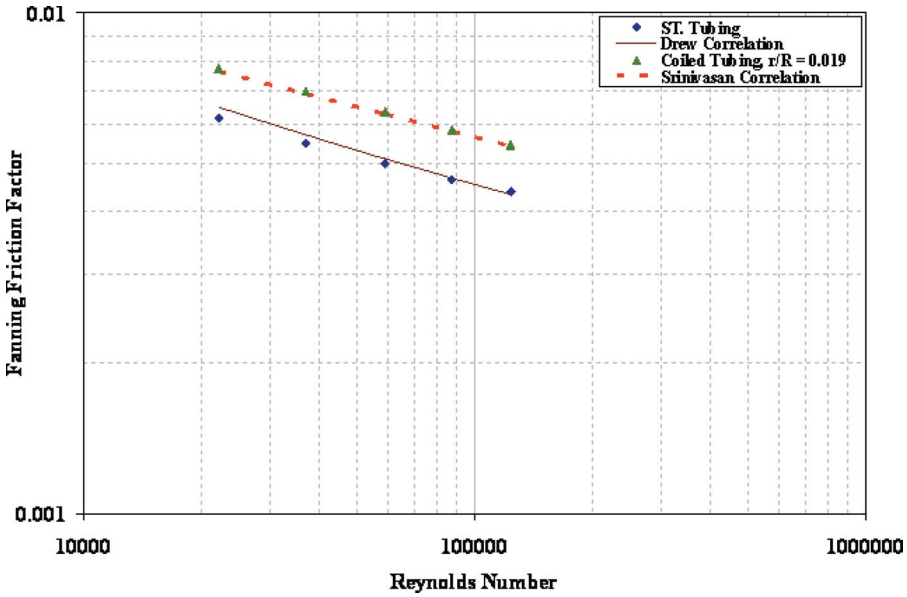


**Fig. 6 Water flow data through 1.27 cm o.d. straight and coiled tubings ($r/R$=0.019)**

sure drop versus flow rate data. The figure also shows plots of the modified Hagen–Poiseuille equation for laminar flow in straight pipe and is given by

$$f = 16/N_{\mathrm{Re}\,g} \tag{9}$$

Experimental laminar flow data are slightly below the modified Hagen–Poiseuille equation with a maximum deviation of about 7%, thus giving a reasonable fit. The data points in the turbulent region are noticed to be significantly lower than the correlation of Drew et al. for all concentrations, indicating that the welan gum fluids exhibit significant drag reduction characteristics.

The flow of welan gum polymer solutions in straight tubing exhibits extended laminar flow for much higher generalized Reynolds number up to about 10,000. The effect of increasing fluid concentration becomes visible as we approach the turbulent flow region. In this region, fluids with higher polymer concentration yield lower friction factor. Generally, in Fig. 8, as flow behavior index decreases (polymer concentration increases), friction factor decreases and more drag reduction is observed until a maximum concentration is reached above which viscous effects begin to set in thereby increasing the flow resistance.

As observed from Fig. 8, 1.4 $kg/m^3$ welan gum fluid exhibits the highest friction factor at any given generalized Reynolds number in the turbulent region and as concentration is increased the friction factor reduces. This reduction in friction factor progressively decreases with increasing concentration, indicating that friction factor becomes less sensitive to concentration as the latter increases. In fact, there seems to be no reduction in friction factor as concentration is increased from 5.7 $kg/m^3$ to 8.6 $kg/m^3$, indicating that a threshold of drag reduction may have been attained. This could, however, be due to the delay in the onset of drag reduction that may be experienced by the 8.6 $kg/m^3$ fluid due to increase in viscosity. This is rather difficult to conclude with cer-

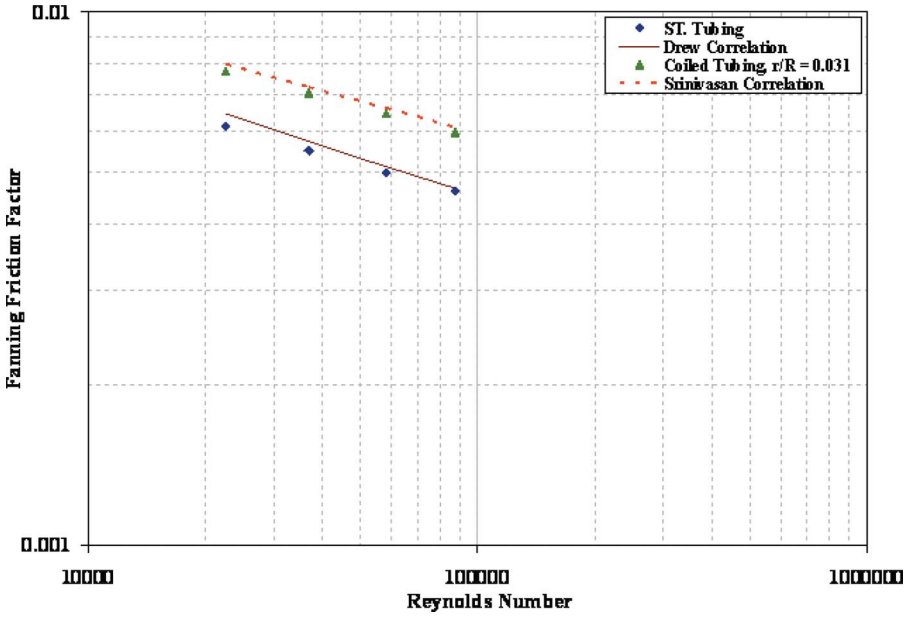


**Fig. 7 Water flow data through 1.27 cm o.d. straight and coiled tubing ($r/R$=0.031)**

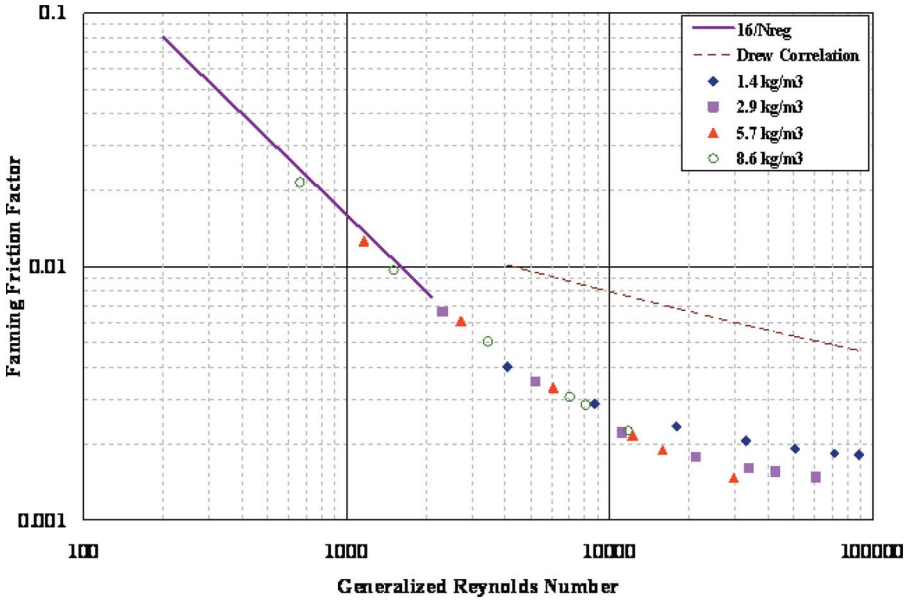


**Fig. 8 Friction factor of welan gum fluids in 1.27 cm o.d. straight pipe**

tainty since sufficient data at higher generalized Reynolds number for 8.6 kg/m$^3$ were not obtainable with the present flow loop.

Figures 9–11 present composite logarithmic plots of friction factor against generalized Reynolds number for various welan gum fluids in three coils along with corresponding correlation of Srinivasan et al. It can be seen from Figs. 9–11 that for the range of generalized Reynolds number considered the drag reduction characteristics of all fluids seem to be essentially the same for a given generalized Reynolds number and curvature ratio. The effect of increasing fluid concentration is barely discernible since all data points are scattered around a single curve. This might be due to more pronounced extended laminar flow region experienced in coiled tubing with this fluid, which brings about a delayed turbulent flow where drag reduction characteristics of the fluids begin to appear. These observations could also suggest that increasing polymer concentration has essentially no effect on drag reduction characteristics of welan gum fluids in coil tubing for the concentration and generalized Reynolds number range investigated.

## Effect of Coiled Tubing Curvature

Figures 12–15 present composite plots of Fanning friction factor against generalized Reynolds number of all welan gum fluids in straight pipe (base case of $r/R=0$) and coiled tubing. It is evident from Fig. 12 that for 1.4 kg/m$^3$ welan gum fluid at a given generalized Reynolds number, the friction factor increases as the curvature is increased from 0 to 0.031. Similar trends can be observed for the other three concentrations. This could be due to the fact that as the coiled tubing curvature ratio increases, the intensity of secondary flow effects becomes more pronounced, which increases the flow resistance. It should also be noted that as the coiled tubing curvature increases, the difference in increased

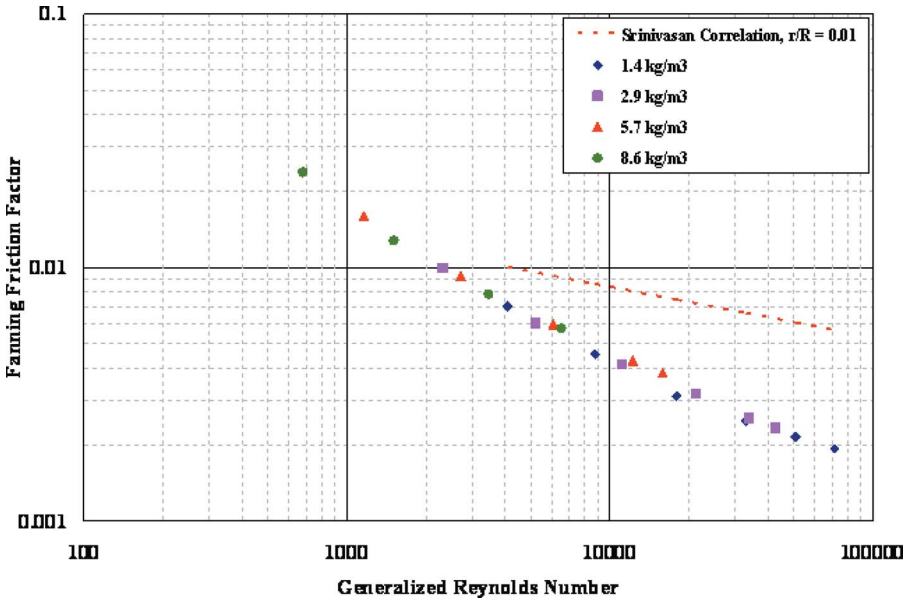


**Fig. 9 Friction factor of welan gum fluids in 1.27 cm o.d. coiled tubing ($r/R=0.01$)**

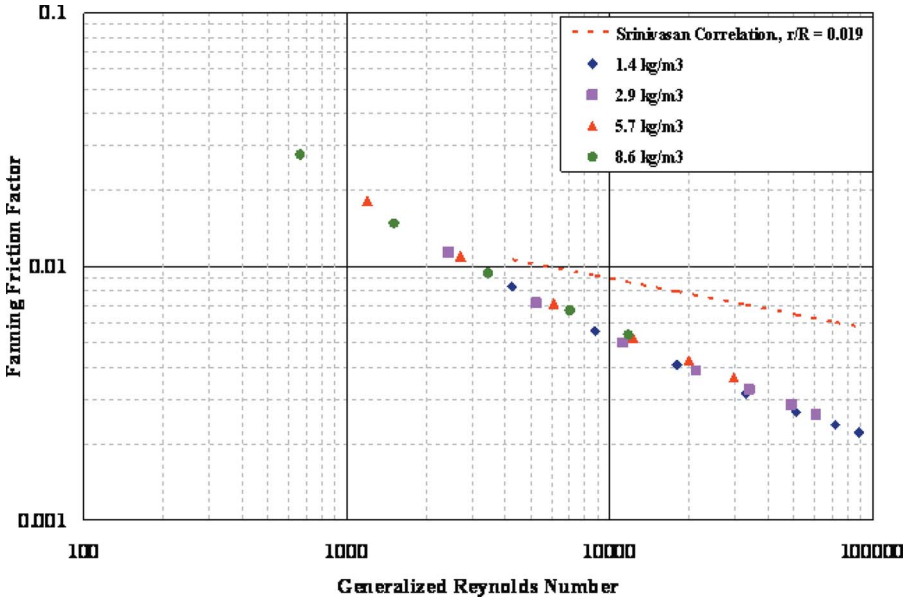


**Fig. 10 Friction factor of welan gum fluids in 1.27 cm o.d. coiled tubing ($r/R$=0.019)**

friction factor from one curvature to the next decreases progressively. Generally, the highest difference is observed between straight pipe data and coiled tubing with curvature ratio of 0.01.

## Development of Friction Factor Correlations

From a design standpoint, prediction of friction pressure losses of fluids is extremely important in pumping operations. Estimation of horse power requirement and real time treating pressure analysis require accurate prediction of pressure losses in the tubulars. With the increasing use of coiled tubing in various petroleum industry applications, especially in pumping services involving non-Newtonian fluids, correlations for such predictions have become extremely important.

**Straight Pipe Correlation.** The experimental friction pressure data of welan gum fluids flowing through straight tubing are correlated using dimensionless parameters; Fanning friction factor, $f$, generalized Reynolds number, $N_{\mathrm{Re}\,g}$, and fluid's flow behavior index, $n$. The straight pipe correlation for flow of welan gum is expressed as

$$f_{\mathrm{st}} = a + \frac{b}{n} + \frac{c}{n^2} + \frac{d}{N_{\mathrm{Re}\,g}} \tag{10}$$

where $a$, $b$, $c$, and $d$ are correlation constants.

The correlation has a coefficient of determination, $R^2$, of 0.98, which indicates a good fit. For this correlation, the average absolute percent deviation of the predicted friction factor from the measured values is 3.76%, with a maximum deviation of about 10%. This confirms the validity of the correlation for predicting friction factor of welan gum fluids in straight tubing. Figure 16 shows the comparison between the predicted and experimental friction factor values for flow in straight tubing. The correlation is valid for $3000 < N_{\mathrm{Re}\,g} < 90{,}000$ and $0.24 < n < 0.50$.

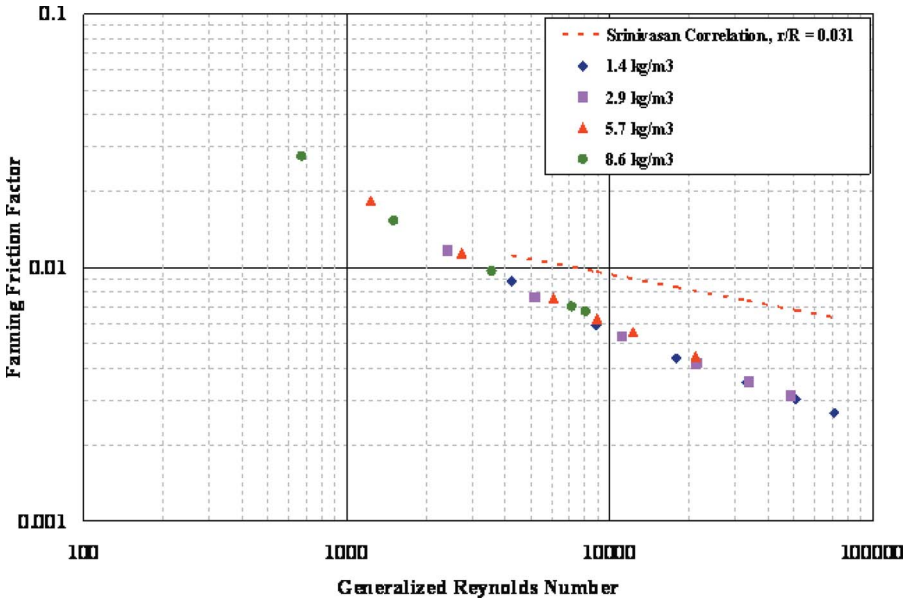


**Fig. 11 Friction factor of welan gum fluids in 1.27 cm o.d. coiled tubing ($r/R$=0.031)**

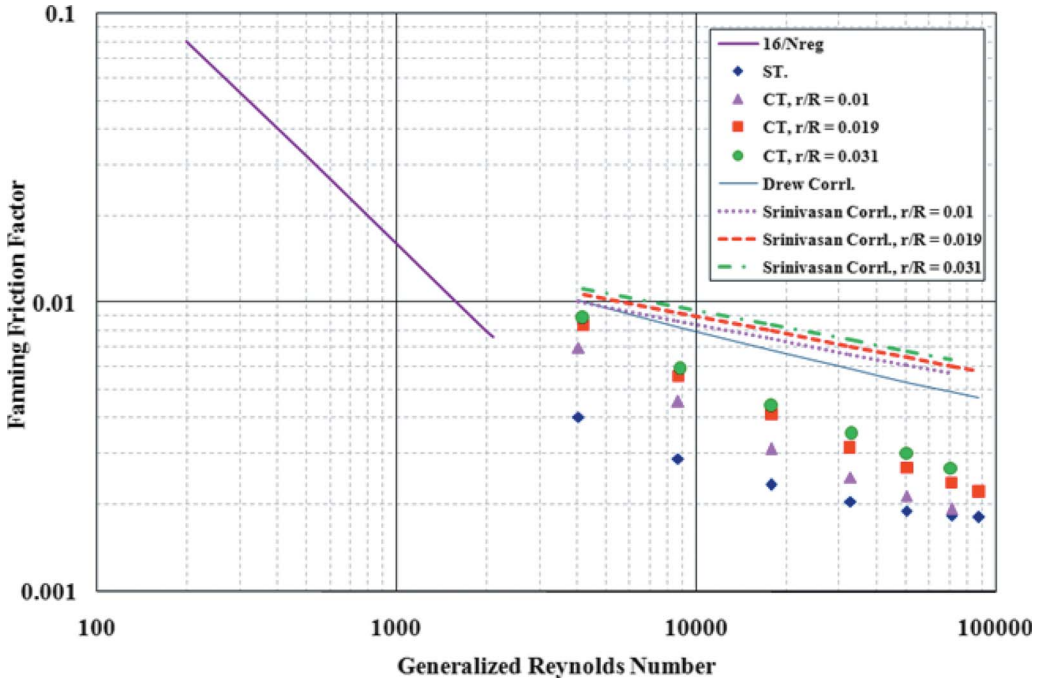


**Fig. 12 Effect of curvature ratio on friction factor of 1.43 kg/m$^3$ welan gum**

**Coiled Tubing Correlation.** Friction pressure data for flow of welan gum fluids in coiled tubing of various curvature ratios are correlated using dimensionless parameters: Fanning friction factor, $f$, generalized Reynolds number, $N_{\mathrm{Re}\,g}$, and curvature ratio, $r/R$. The developed correlation for welan gum fluid flow in coiled tubing is expressed as

$$\frac{1}{\sqrt{f_{\mathrm{ct}}}} = a[N_{\mathrm{Re}\,g}^{1-(r/R)}]^{b/2} \tag{11}$$

where $a$ and $b$ are constants given by the following equations:

$$a = c_1 + \frac{c_2 \ln(r/R)}{(r/R)^2} \tag{12}$$

$$b = c_3 + \left[\frac{c_4}{(r/R)^2}\right] \tag{13}$$

where $c_1$–$c_4$ are constants. This correlation is valid for $3000 < N_{\mathrm{Re}\,g} < 90{,}000$; $0.24 < n < 0.50$, and $0.01 < r/R < 0.031$.

Figures 17–19 show comparison of predicted friction factors from correlation with experimental values for three coiled tubing

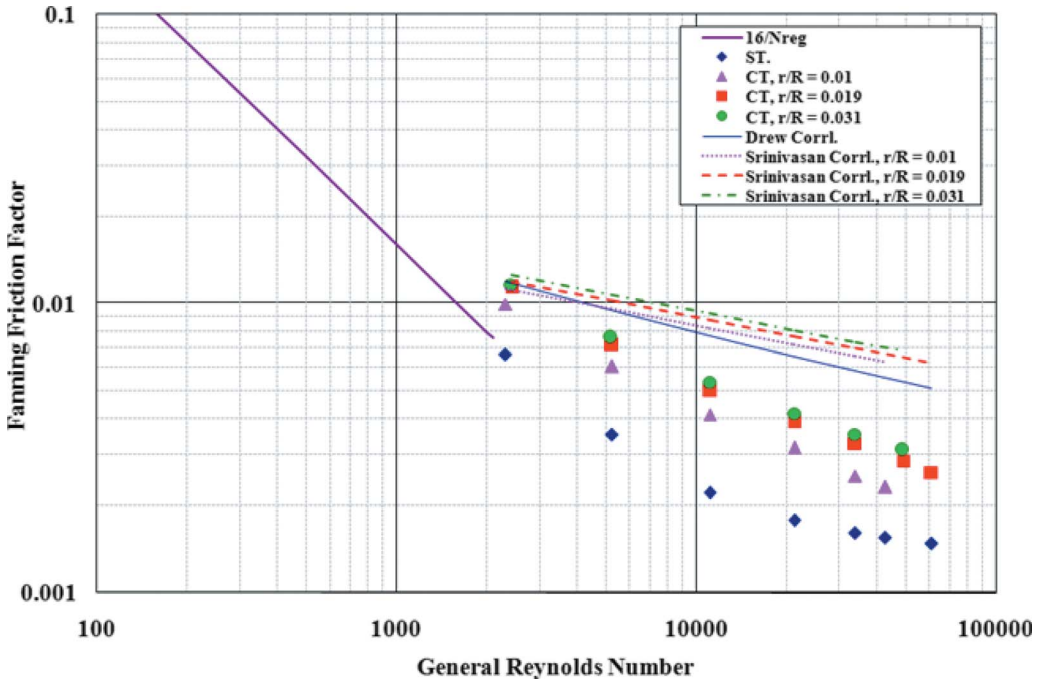


**Fig. 13 Effect of curvature ratio on friction factor of 2.85 kg/m$^3$ welan gum**

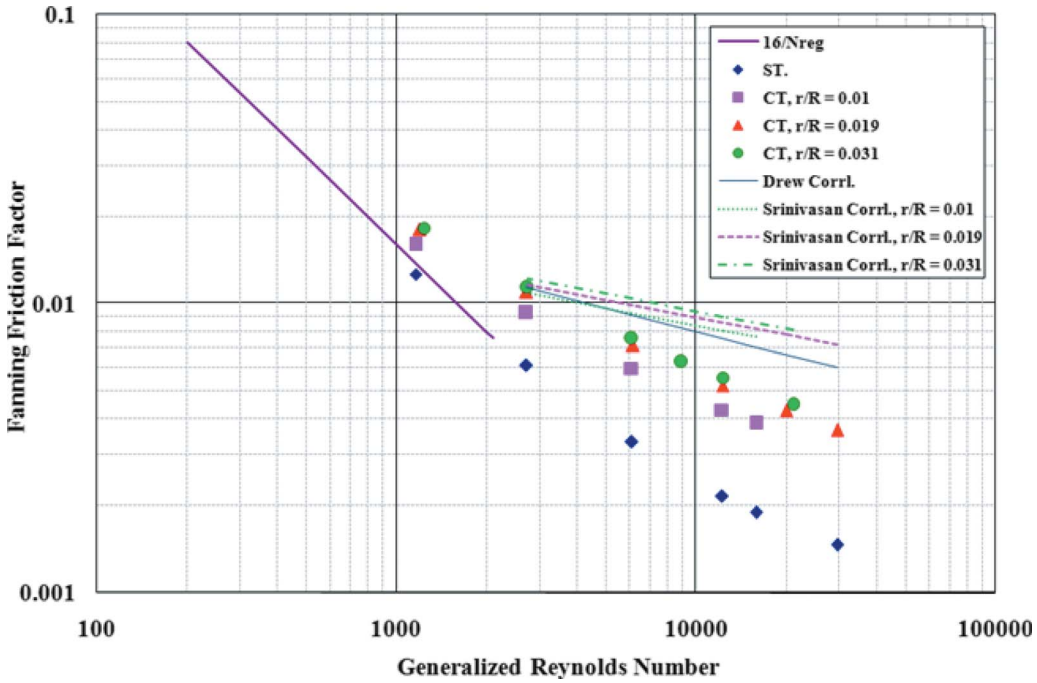


**Fig. 14 Effect of curvature ratio on friction factor of 5.7 kg/m$^3$ welan gum**

sizes. The correlation has a correlation coefficient of determination of 0.98, an average absolute percent deviation of 3.65%, and a maximum deviation of 7.14% for all curvature ratios. It provides a good fit with the experimental data. A cross plot of measured Fanning friction factors against predicted values from developed correlations for both straight and coiled tubings is presented in Fig. 20.

**Application of Developed Correlations.** The following example demonstrates the application of developed correlations for tubular friction pressure loss prediction of welan gum fluids in straight and coiled tubings. The objective is to determine the horse power requirement for pumping welan gum fluids through straight and coiled tubings.

**Example.** A formation at a depth of 1890 m is to be hydraulically fractured using coiled tubing. Given the following pad stage information, we compute the friction pressure loss across the tubular and the resulting horse power requirement for pumping of the fracturing fluid through the tubing.

Fluid Type=2.9 kg/m$^3$ welan gum

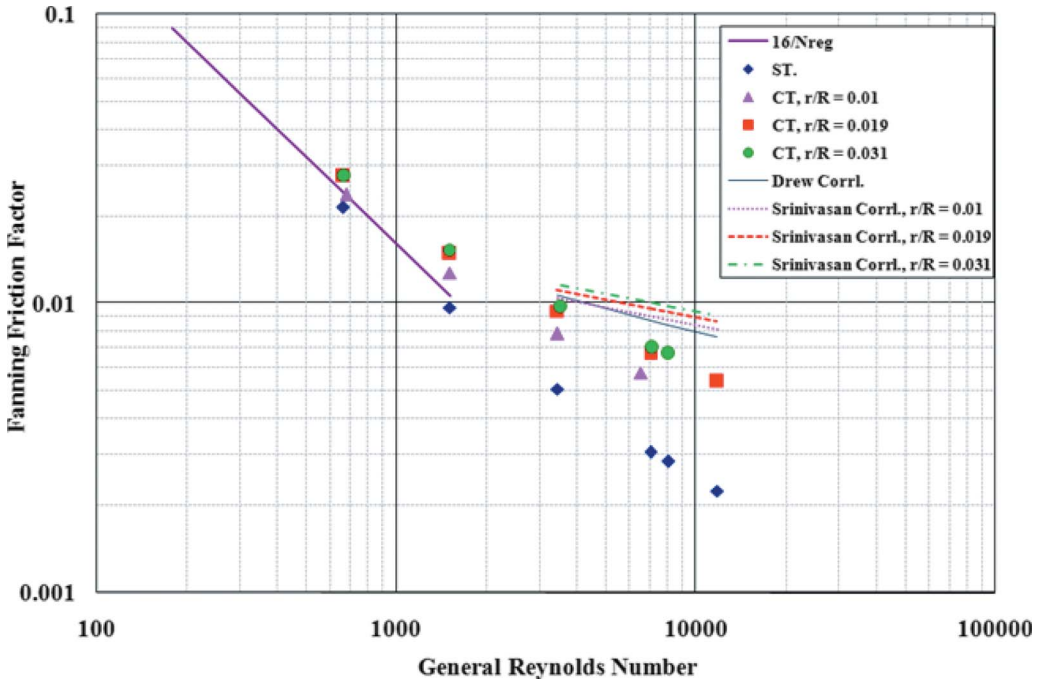


**Fig. 15 Effect of curvature ratio on friction factor of 8.6 kg/m$^3$ welan gum**

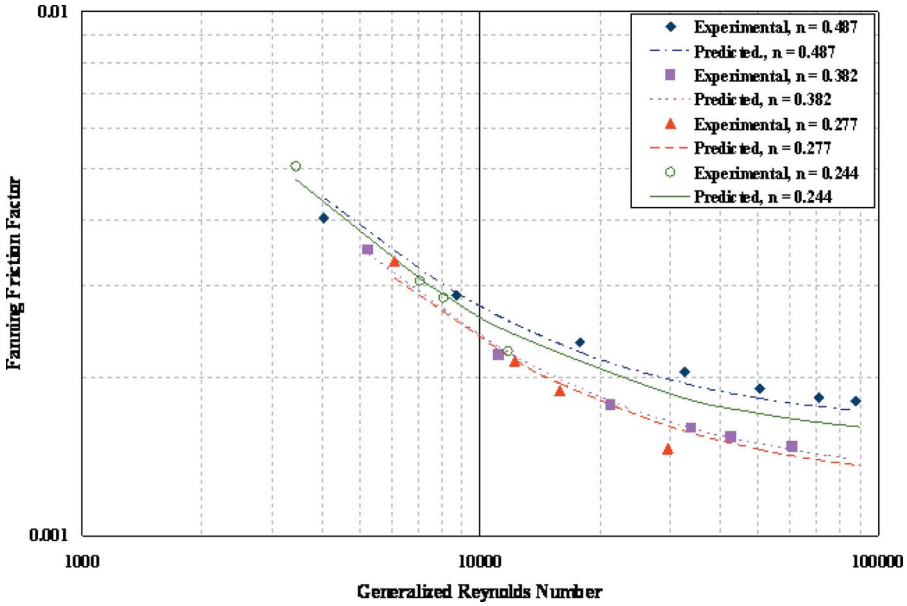


**Fig. 16 Comparison between predicted and experimental friction factors for welan gum fluids in straight pipe**

Fluid density, $\rho=1$ g/cm$^3$
Flow behavior index, $n=0.382$
Consistency index, $K_p=0.86$ Pa s$^n$
Injection rate, $q=0.026$ m$^3$/s
Liquid volume=228,000 liters
Tubing size=7.3 cm o.d., 6.2 cm i.d.
Reel diameter=3.3 m, $r/R=0.019$
Tubing length=3780 m

*Solution*. During the hydraulic fracturing operation, 1890 m of the coiled tubing length will be lowered into the wellbore as a straight section leaving 1890 m on the reel as coiled tubing. Hence, fluid is pumped through both straight and coiled sections.

*Straight Section*. From Eq. (3), the generalized Reynolds number is computed as $N_{\mathrm{Re}\,g}=48490$. Using the developed correlation for predicting Fanning friction factor in straight tubing, Eq. (10), the friction factor is computed to be $f_{\mathrm{st}}=0.00151$.

The pressure drop gradient is then calculated using Eq. (4), resulting in $\Delta p/l=3.6\times10^3$ Pa/m. The total pressure drop across the straight section of 1890 m is $6.8\times10^6$ Pa. The hydraulic horse power, $P_H$, requirement for this pumping operation is computed using the following expression:

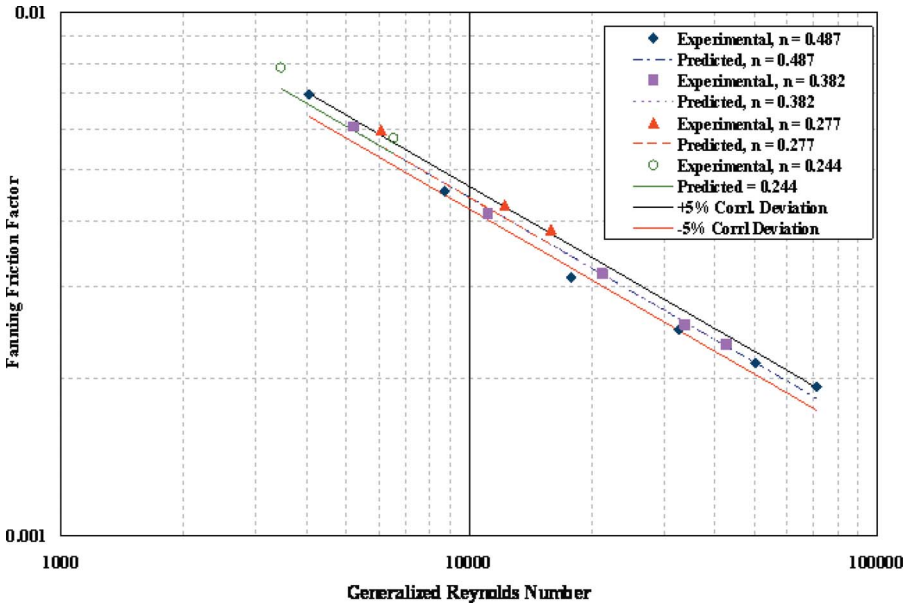


**Fig. 17 Comparison between predicted and experimental factors for welan 90 m fluids in CT ($r/R=0.01$)**

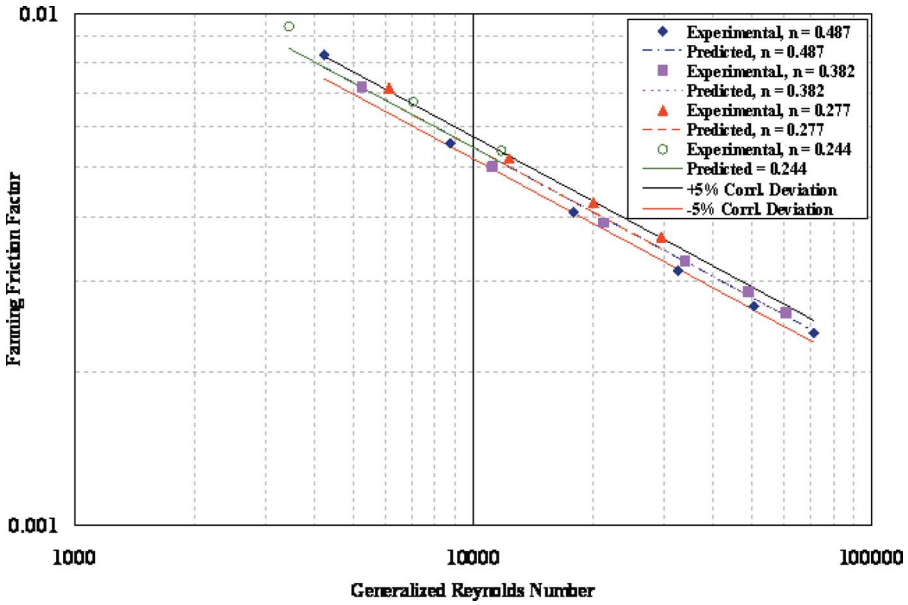


**Fig. 18 Comparison between predicted and experimental friction factors for welan gum fluids in CT ($r/R$=0.019)**

$$P_H = \frac{\Delta pq}{3940} \tag{14}$$

Hence, the pump power needed to overcome friction losses of welan gum fluid in the straight section is computed to be: $P_H$ =243 hp.

*Coiled Tubing*. Using the developed correlation for predicting Fanning friction factor in coiled tubing, Eqs. (11)–(13), the friction factor is computed to be $f_{ct}$=0.002823.

The pressure drop gradient is then calculated using Eq. (4), resulting in $\Delta p/l = 7.0 \times 10^3$ Pa/m. The total pressure drop across the entire tubing length is $1.3 \times 10^7$ Pa.

The hydraulic horse power, $P_H$, requirement for pumping through the coiled tubing is computed from Eq. (14). Pump power needed to overcome friction losses of welan gum fluid in the coiled tubing is computed to be $P_H$=471 hp.

The total pump power required to overcome friction losses in both straight and coiled sections is 714 hp. It is observed that the pump power required to overcome friction losses in the coiled section is much greater (about 94% higher) than what is needed for the straight section of the same length. This is in agreement with experimental observations.

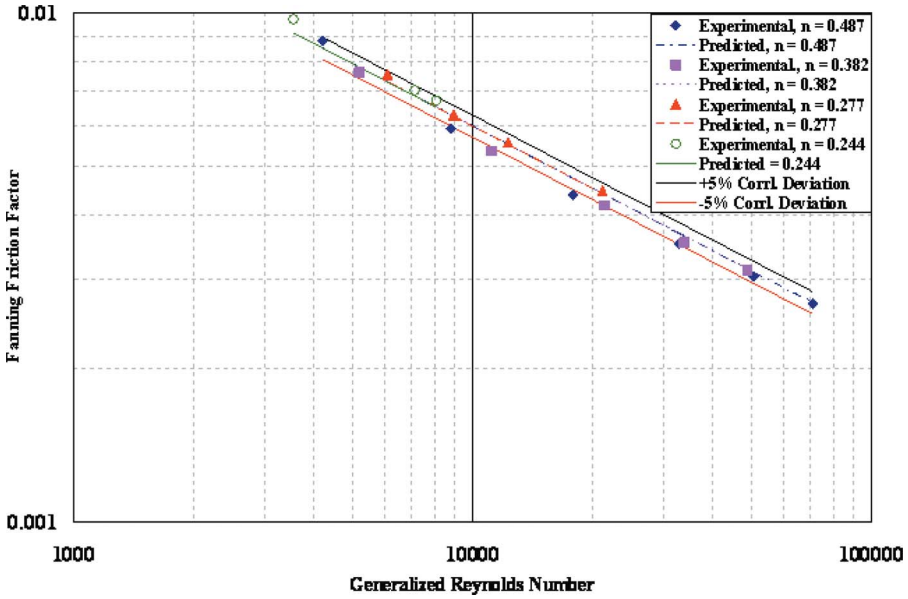


**Fig. 19 Comparison between predicted and experimental friction factors for welan gum fluids in CT ($r/R$=0.031)**

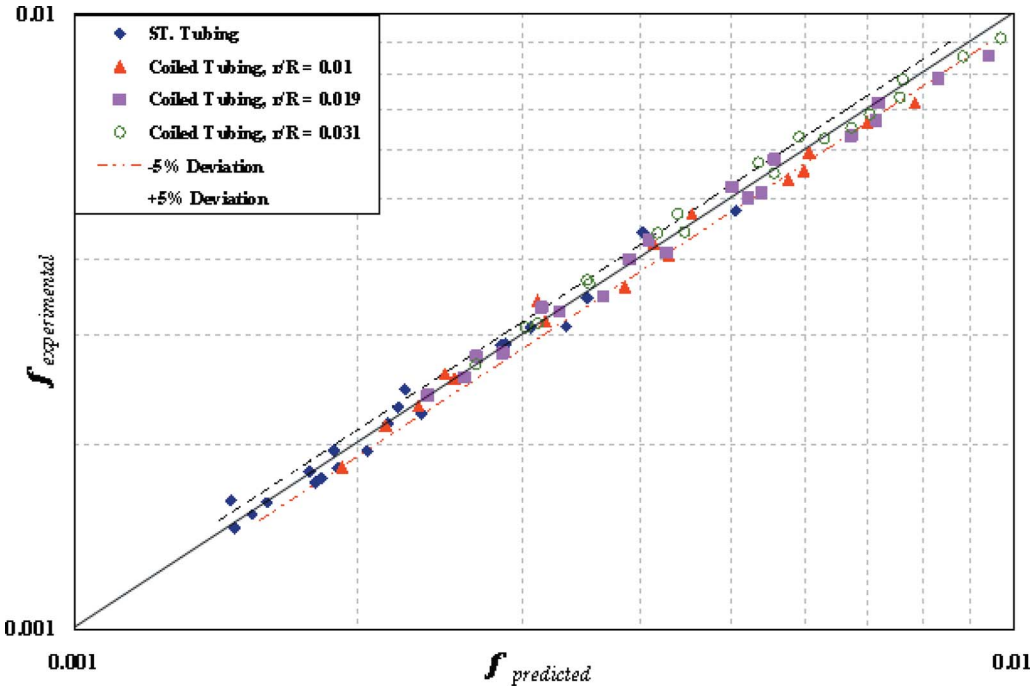


**Fig. 20 Comparison between predicted and experimental friction factors for welan gum fluids**

## Comparison of Welan Gum Fluids With 40 lbs/Mgal Guar Fluid

**Guar Gum.** Guar and its derivatives are the most widely used viscosifiers for water-based fracturing fluids. It is reported that over 70% of all fracturing treatments use aqueous-based guar or guar derivative (such as hydroxypropyl guar and carboxymethyl-hydroxypropyl guar) fluids [10]. Guar polymers are cost effective and readily available, possess good hydration properties, and can tolerate high concentration of monovalent salts. The structure of the guar molecule [10] is presented in Fig. 21. Over the years, based on field application, forty pound per thousand gallons 40 lbs/Mgal loading of guar has emerged as the preferred concentration for reservoir stimulation purposes. Hence, alternative polymer performance is usually evaluated against 4.9 $kg/m^3$ as a benchmark. Therefore, in the following, the performance of welan gum fluids is compared with 4.9 $kg/m^3$ guar fluid.

**Rheology Comparison.** Figure 22 presents a plot of apparent viscosity against wall shear rate for the welan gum fluids and 4.9 $kg/m^3$ guar fluid. It can be observed that the 2.9 $kg/m^3$ welan gum fluid exhibits greater low shear rate viscosity (LSRV) when compared to the guar fluid up to a shear rate of about 50 $s^{-1}$. At the lowest shear rate of 5 $s^{-1}$, 2.9 $kg/m^3$ welan gum fluid shows about 110% higher viscosity compared to 4.9 $kg/m^3$ guar fluid. However the difference progressively decreases as shear rate increases resulting in a crossover at 50 $s^{-1}$ from where the guar fluid begins to exhibit higher apparent viscosity compared to 2.9 $kg/m^3$ welan gum fluid. Among the various welan gum concentrations investigated, the 2.9 $kg/m^3$ fluid gives the closest equivalence to 4.9 $kg/m^3$ guar fluid based on rheological evaluation within the shear rate range investigated. Generally, it can be concluded that on a pound for pound basis welan gum exhibits higher LSRV compared to guar. Most of the oilfield operations where these polymers find application involve shear rate between 0.1 $s^{-1}$ and 100 $s^{-1}$, for which welan gum generally has better rheological characteristics.

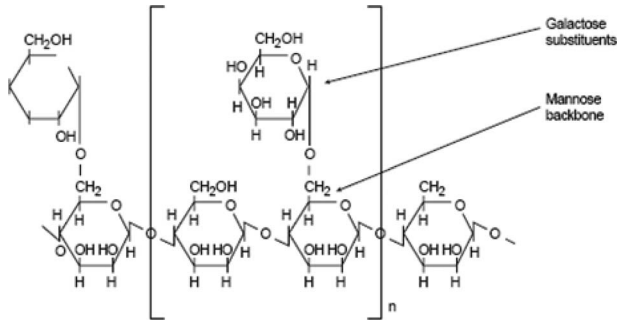


**Fig. 21 Molecular structure of guar gum**

**Comparison of Hydraulic Properties.** Established correlations [11,12] for non-Newtonian fluid flow in straight pipes and coiled tubing were used to generate flow data for guar gum fluid. The plot of Fanning friction factor versus generalized Reynolds number for welan gum fluids and 4.9 $kg/m^3$ guar fluid flowing in straight pipe is presented in Fig. 23. The straight tubing data for guar gum fluid were generated from Shah's correlation [11] for friction pressure of fracturing gels given as

$$f = f_{\infty}(n) + A(n)(N_{\mathrm{Re}\,g})^{-B(n)} \tag{15}$$

where $f_{\infty}(n)$ is the infinite friction factor, and $A(n)$ and $B(n)$ are empirical fluid parameters. It can be observed that in turbulent flow regime, 4.9 $kg/m^3$ guar fluid exhibits greater drag reduction when compared to all welan gum fluids studied. As Reynolds number increases, a progressively greater difference is noticed in friction factor between guar and welan gum fluids.

Plots of Fanning friction factor versus generalized Reynolds number for welan gum fluids and 4.9 $kg/m^3$ guar fluid in coiled tubing of curvature ratios 0.01, 0.019, and 0.031 are presented in Figs. 24–26. Zhou and Shah's [13] correlation, for predicting friction factor for laminar flow of non-Newtonian fluids in coiled tubing, is also plotted. Guar fluid data were generated from the correlation developed at the Well Construction Technology Center

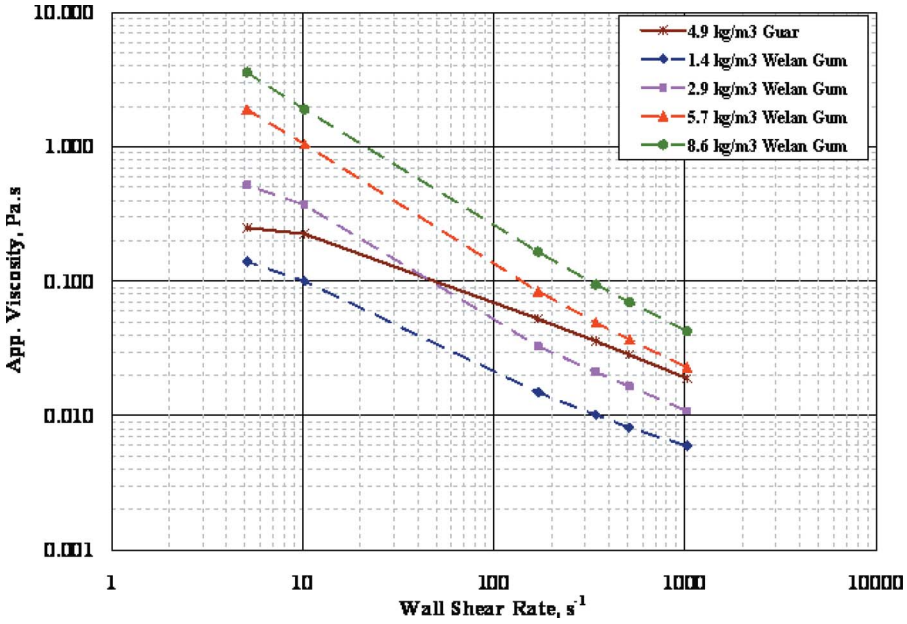


**Fig. 22 Apparent viscosity comparison between welan gum and guar fluids**

(WCTC) [12] based on experimental investigation of non-Newtonian fluids in coiled tubing. The WCTC correlation is given as

$$\sqrt{f} = a + \frac{b}{\sqrt{N_{\mathrm{Re}\,g}^{(1-r/R)}}} \tag{16}$$

where $a$ and $b$ are constants. The constant, $a$, is

$$\sqrt{a} = c_5 + c_6\sqrt{r/R} + \left(\frac{c_7 - c_8(r/R)^3}{\mu_a}\right)^2 \tag{17}$$

where $\mu_a$ is the apparent viscosity at shear rate of 511 $s^{-1}$.

The laminar guar data generated for all three curvature ratios give reasonable fit with Zhou and Shah's correlation. It can be observed from Figs. 24–26 that 4.9 $kg/m^3$ guar fluid exhibits greater drag reduction when compared to welan gum fluids studied. It should also be noticed that as curvature ratio increases from 0.01 to 0.031, drag reduction of all fluids decreases progressively.

It can be concluded from previous discussion that in both straight and coiled tubings, 4.9 $kg/m^3$ guar gum flluid exhibits better drag reduction than equivalent concentration of welan gum fluid. This behavior can be attributed to the differences in molecular weight and structure of the two polymers. Guar gum has been reported to have typical molecular weight of $3-5\times10^6$ [14], while welan gum is believed to be within the range of $2-3\times10^6$ [15]. It has been shown that for polymers with similar molecular structure, increasing molecular weight results in an increase in drag reduction [16]. This may be due to reduction of turbulent diffusivity and increased extensional viscosity.

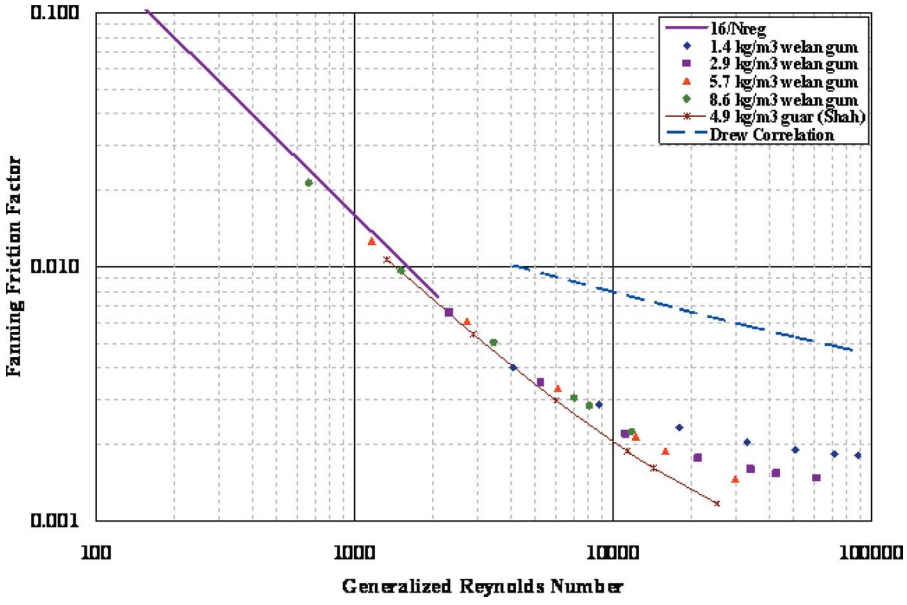


**Fig. 23 Comparison between welan gum and guar fluids for flow in straight tubing**

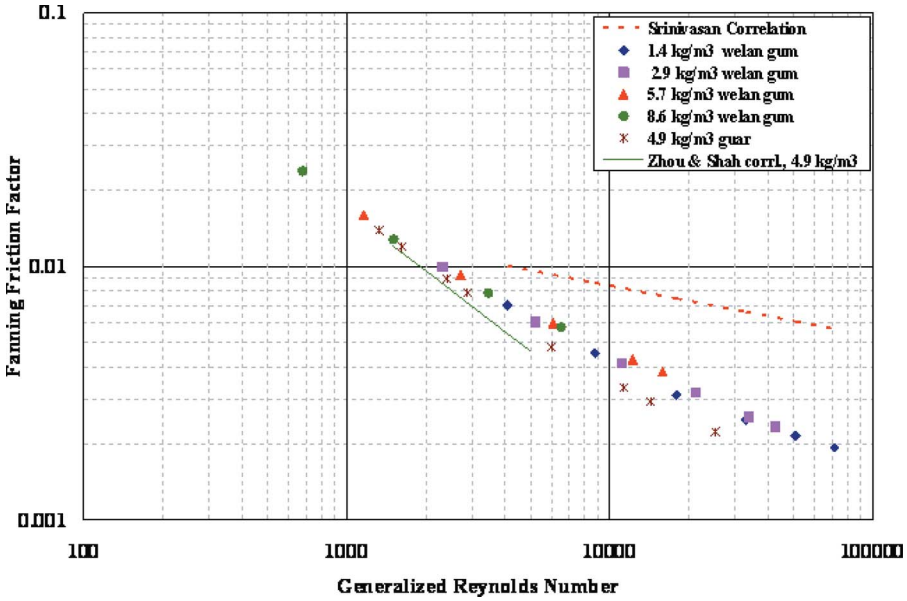


**Fig. 24 Comparison between welan gum and guar fluids for flow in coiled tubing ($r/R = 0.01$)**

In terms of molecular structure, guar gum has a linear structure, while welan gum is a branched microbial polysaccharide with relatively large mean chain extensions per backbone sugar residue. Virk [17] showed that polymers with longer-chain molecular structure exhibit greater drag reduction compared to polymers with branched structure given that both are of the same molecular weight. It can be inferred from the above analysis that the higher drag reduction experienced with guar fluid over welan gum fluids is because of the combined effect of higher molecular weight and long-chain linear structure.

## Conclusions

Correlations for predicting Fanning friction factor for flow of welan gum in both straight and coiled tubings have been developed.

The effect of increasing in polymer concentration of welan gum in straight tubing flow is seen as a reduction in friction factor until a maximum concentration is reached, above which viscous effects begin to set in.

In coiled tubing, at a given flow rate and curvature ratio, the friction factor exhibited by the welan gum fluids increases with increase in concentration. At any given generalized Reynolds number, the effect of increasing polymer concentration is, however, barely discernible.

For all welan gum concentrations, as coiled tubing curvature ratio is increased from 0 (for straight pipe) to 0.031, the friction factor increases at any given generalized Reynolds number.

On a pound for pound basis, welan gum fluid provides better viscosity and suspension properties compared to guar fluid. However, guar gum fluid exhibits better drag reduction characteristics.

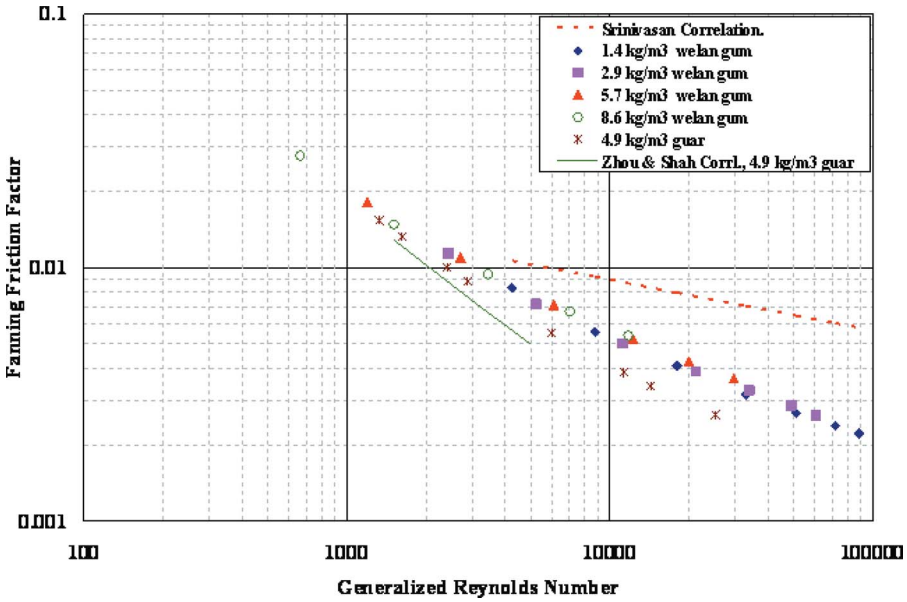


**Fig. 25 Comparison between welan gum and guar fluids for flow in coiled tubing ($r/R = 0.019$)**

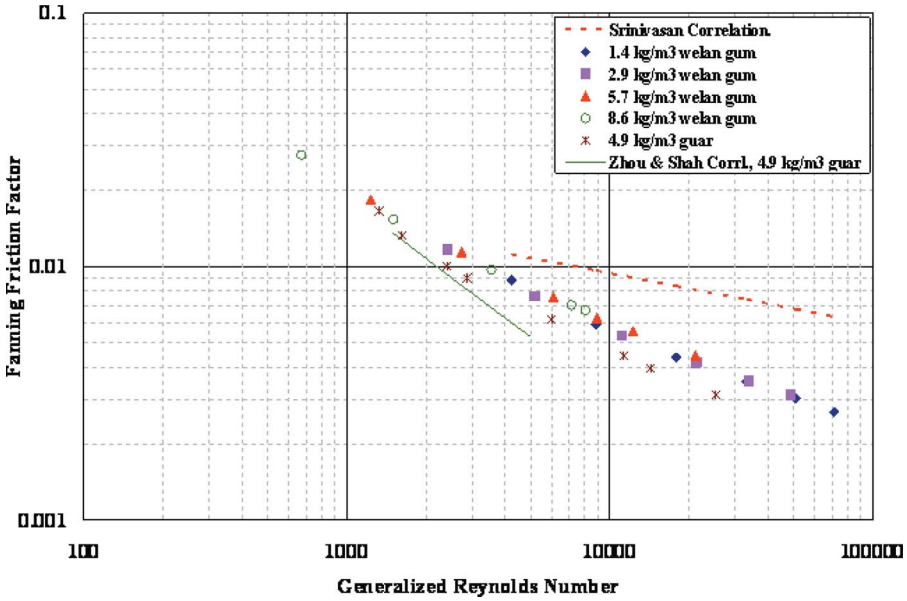


**Fig. 26 Comparison between welan gum and guar fluids for flow in coiled tubing ($r/R = 0.031$)**


## Acknowledgment

The authors wish to thank the members of the Coiled Tubing Consortium (CTC) for their continued support and the research team (especially Mr. Joe Flenniken) at the WCTC of the University of Oklahoma for their assistance in the experimental work.


## Nomenclature

$A$ = pipe cross sectional area ($cm^2$)
$a$, $b$, $c_1$–$c_8$, $d$ = correlation constants
DR = drag reduction
$f$ = Fanning friction factor, dimensionless
$f_{ct}$ = Fanning friction factor of coiled tubing, dimensionless
$f_{st}$ = Fanning friction factor of straight tubing, dimensionless
i.d. = internal diameter of tubing (cm)
$k$ = consistency index of power law fluid (Pa $s^n$)
$K_p$ = pipe Consistency index (Pa $s^n$)
$K_v$ = viscometer consistency index (Pa $s^n$)
$l$ = length between pressure ports (m)
$n$ = flow behavior index of power law fluid, dimensionless
$N_{Re}$ = Reynolds number, dimensionless
$N_{Re\ g}$ = generalized Reynolds number, dimensionless
o.d. = outside tubing diameter (cm)
$P_H$ = pump horse power
$q$ = flow rate ($m^3/s$)
$r$ = radius of coiled tubing (cm)
$R$ = radius of curvature of coiled tubing reel (cm)
$r/R$ = coiled tubing curvature ratio, dimensionless
$R^2$ = correlation coefficient, dimensionless
$v$ = average fluid velocity (m/s)
$\Delta p$ = pressure drop (Pa)

### Greek Symbols

$\dot{\gamma}$ = shear rate ($s^{-1}$)
$\dot{\gamma}_w$ = wall shear rate ($s^{-1}$)
$\beta$ = ratio of bob to cup radius for Model 35 Fann viscometer
$\sigma$ = constant defined in Eq. (2), dimensionless
$\tau$ = shear stress (Pa)
$\tau_w$ = wall shear stress (Pa)
$\mu$ = viscosity of fluid (Pa s)
$\mu_a$ = apparent viscosity of fluid (Pa s)
$\rho$ = fluid density ($g/cm^3$)

## References


[1] Azouz, A., Shah, S. N., Vinod, P. S., and Lord, D. L., 1998, "Experimental Investigation of Friction Pressure Losses in Coiled Tubing," SPE Prod. Facil., May, pp. 91–98.
[2] Urbani, R., and Brant, D. A., 1989, "Kelco Microbial Polysaccharides S-130 (Welan) and S-657 Display Similar Dilute Aqueous Solution Behavior," Carbohydr. Polym., **11**, pp. 16–191.
[3] Powell, J. W., Parks, C. F., and Seheult, J. M., 1991, "Xanthan and Welan: The Effects of Critical Polymer Concentration on Rheology and Fluid Performance," presented at the International Arctic Technology Conference, Anchorage, Alaska, SPE Paper No. 22066.
[4] Lopes, L., Andrade, C. T., Milas, M., and Rinuado, M., 1995, "Influence of Aggregates on the Sedimentation Properties of Welan Gum," Polym. Bull. (Berlin), **34**, pp. 655–662.
[5] Navarrete, R. C., Seheult, J.. M., and Coffey, M. D., 2000, "New Bio-Polymers for Drilling, Drill-in, Completions, Spacer Fluids and Coiled Tubing Applications," presented at the Asia Pacific Drilling Technology Conference, Kuala Lumpur, Malaysia, SPE Paper No. 62790.
[6] Hodder, M., Michel, C., and Kellingray, D., 2004, "Investigation of Polymeric and Mixed Metal Oxide Fluids for Use in Well Intervention Operations," presented at the SPE/ICoTA Coiled Tubing Conference and Exhibition Houston, TX, SPE Paper No. 89637.
[7] Sonebi, M., 2006, "Rheological Properties of Grouts With Viscosity Modifying Agents as Diutan and Welan Gum Incorporating Pulverized Fly Ash," Cem. Concr. Res., **36**, pp. 1609–1618.
[8] Drew, T. B., Koo, E. C., and McAdams W. H., 1932, "The Friction Factor for Clean Round Pipes," Trans. AICHE, **28**, 56–72.
[9] Srinivasan, P. S., Nandapurkar, S. S., and Holland, F. A., 1970, "Friction Factors for Coils," Trans. Inst. Chem. Eng., **48**, pp. T156–T161.
[10] Economides, M. J., and Nolte, K. G., 2000, *Reservoir Stimulation*, Wiley, New York.
[11] Shah, S. N., 1984, "Correlations Predict Friction Pressure of Fracturing Gels," Oil & Gas J., pp. 92–98.
[12] Shah, S. N., 1999, "Technical Report for the Coiled Tubing Consortium Semi-Annual Meeting," University of Oklahoma, Norman, OK.
[13] Zhou, Y., and Shah, S. N., 2002, "Non-Newtonian Fluid Flow in Coiled Tubing: Theoretical Analysis and Experimental Verification," presented at the SPE Annual Technical Conference and Exhibition, San Antonio, TX, SPE Paper No. 77708.
[14] Zhou, Y., and Shah, S. N., 2002, "New Friction Factor Correlation for Non-

Newtonian Fluid Flow in Coiled Tubing," presented at the SPE Asia Pacific Oil and Gas Conference, Melbourne, Australia, SPE Paper No. 77960.
[15] Peles, J., Wardlow, R. W., Cox, G., Haley, W., Dusterhoft, R., Walters, H. G., and Weaver, J., 2002, "Maximizing Well Production with Unique Low Molecular Weight Frac Fluid" presented at the SPE Annual Technical Conference and Exhibition, San Antonio, TX, SPE Paper No. 77746.
[16] Seheult, M., 2007, private communication.
[17] Grabowski, D. W., 1990, "Drag Reduction in Pipe Flows With Polymer Additives," MS thesis, Department of Mechanical Engineering, Rochester Institute of Technology, Rochester, New York.

# Galerkin Least-Squares Multifield Approximations for Flows of Inelastic Non-Newtonian Fluids

**Flávia Zinani**

**Sérgio Frey**[1]
e-mail: frey@mecanica.ufrgs.br

Laboratory of Applied and Computational Fluid Mechanics (LAMAC),
Mechanical Engineering Department,
Federal University of Rio Grande do Sul,
Rua Sarmento Leite 425,
90050-170 Porto Alegre (RS), Brazil

*The aim of this work is to investigate a Galerkin least-squares (GLS) multifield formulation for inelastic non-Newtonian fluid flows. We present the mechanical modeling of isochoric flows combining mass and momentum balance laws in continuum mechanics with an inelastic constitutive equation for the stress tensor. For the latter, we use the generalized Newtonian liquid model, which may predict either shear-thinning or shear-thickening. We employ a finite element formulation stabilized via a GLS scheme in three primal variables: extra stress, velocity, and pressure. This formulation keeps the inertial terms and has the capability of predicting viscosity dependency on the strain rate. The GLS method circumvents the compatibility conditions that arise in mixed formulations between the approximation functions of pressure and velocity and, in the multifield case, of extra stress and velocity. The GLS terms are added elementwise, as functions of the grid Reynolds number, so as to add artificial diffusivity selectively to diffusion and advection dominant flow regions—an important feature in the case of variable viscosity fluids. We present numerical results for the lid-driven cavity flow of shear-thinning and shear-thickening fluids, using the power-law viscosity function for Reynolds numbers between 50 and 500 and power-law exponents from 0.25 to 1.5. We also present results concerning flows of shear-thinning Carreau fluids through abrupt planar and axisymmetric contractions. We study ranges of Carreau numbers from 1 to 100, Reynolds numbers from 1 to 100, and power-law exponents equal to 0.1 and 0.5. Besides accounting for inertia effects in the flow, the GLS method captures some interesting features of shear-thinning flows, such as the reduction of the fluid stresses, the flattening of the velocity profile in the contraction plane, and the separation of the boundary layer downstream the contraction.* [DOI: 10.1115/1.2956514]

*Keywords: multifield formulations, finite elements in fluids, non-Newtonian, Galerkin least-squares, generalized Newtonian liquids*

## 1 Introduction

It is well known that many fluids in engineering applications, such as polymer melts and solutions, muds and drilling fluids in petroleum industry, food products, cosmetics, and paints, present a non-Newtonian behavior. They exhibit features such as shear-thinning or shear-thickening, normal stress differences in shearing flows, viscoplasticity, extension hardening, and elasticity (memory). Computational fluid dynamics has been a powerful tool for solving non-Newtonian flow problems, although it still faces considerable difficulties. From the mechanical modeling standpoint, the gap between the real behavior of materials and the constitutive theory for its representation prevents the generalization of rheological models and compromises the realism of the simulations. As for the numerical methods, some highly steep and nonsmooth viscosity models yield locally advection dominant regions and severe gradients, causing pathologies such as numerical instabilities and spurious oscillations. Moreover, constitutive models that are implicit for the extra-stress tensor, which are widespread in non-Newtonian fluid mechanics, introduce the difficulty of treating the extra stress as a primal variable, creating a so-called multifield formulation. In the finite element context, two compatibility conditions arise for such models: the classical Babuška–Brezzi condition for velocity and pressure approximation functions and the compatibility condition between the approximation functions of the extra stress and velocity fields [1]. For viscoelastic models, the hyperbolic character of the extra-stress based constitutive equations of differential types gives rise to a type of instability known as the high Weissenberg number problem (HWNP) [2].

Several researchers have introduced multifield formulations. They analyzed their stability and convergence properties and also established compatibility conditions for the finite element basis functions involved. Marchal and Crochet [3] proposed a finite element for the stress, which employed Hermite polynomials as shape functions, and proved that such element assures that the solution of the three-field problem is the same as the solution of the two-field one. Marchal and Crochet [4] proposed finite elements composed of several subelements, for which stable results were obtained for velocity and stress fields. Fortin and Pierre [5] proved that the element proposed by Marchal and Crochet [4] satisfied the compatibility condition between the stress and velocity basis functions. Ruas et al. [6] (references therein) proposed new mixed elements and performed a numerical analysis of a multifield formulation for the Stokes problem, also extending their methodology to the flow of viscoelastic fluids. Franca and Stenberg [1] proposed a three-field stabilized formulation based on the Galerkin formulation for the Stokes problem, establishing its convergence and stability properties. Behr et al. [7] improved the results of Franca and Stenberg [1], introducing a very similar stabilized formulation that also incorporated the inertia terms. Behr et al. [7] also used stability parameters depending on the local Reynolds number and the element size, as in Franca and Frey [8]. Baaijens [9] presented a summary of the advances in the approxi-

[1]Corresponding author.

Contributed by the Fluids Engineering Division of ASME for publication in the JOURNAL OF FLUIDS ENGINEERING. Manuscript received July 12, 2007; final manuscript received January 15, 2008. published online July 29, 2008. Assoc. Editor: Dimitris Drikakis.

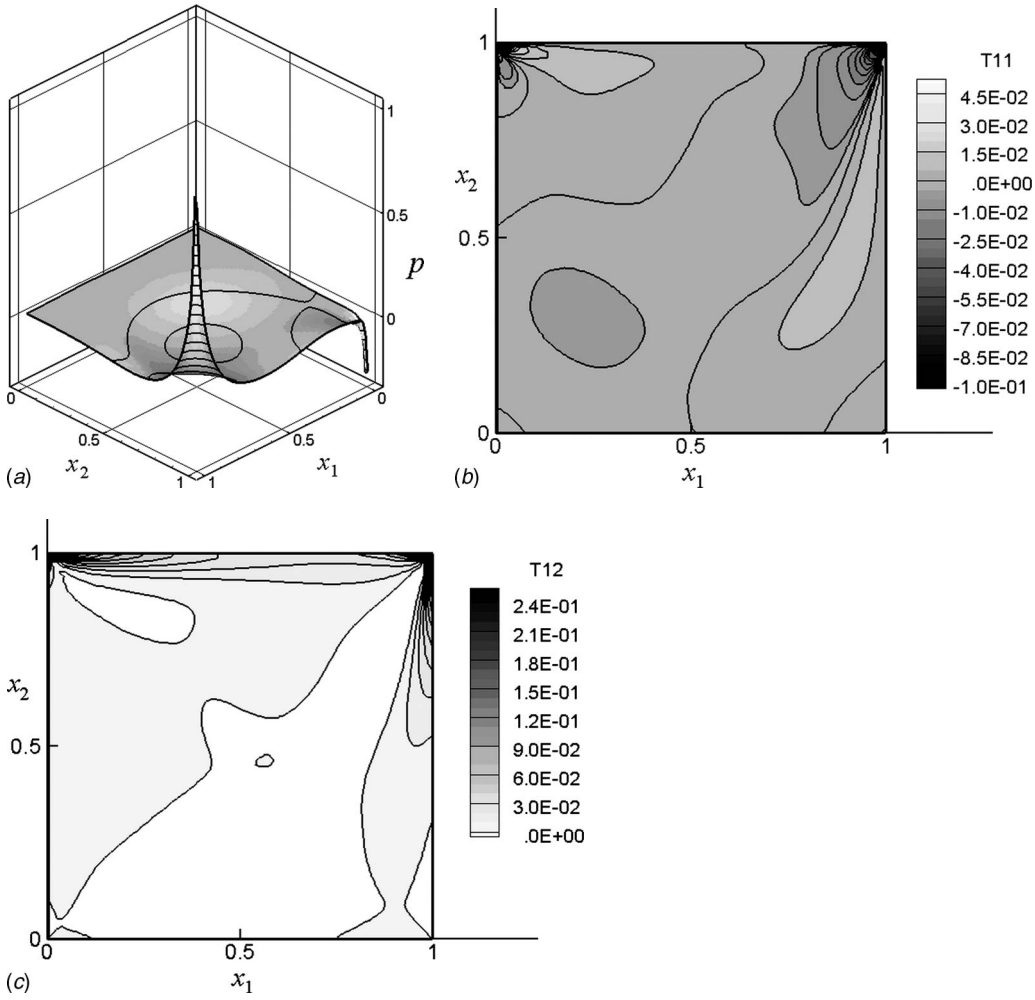


**Fig. 1 Lid-driven cavity flow, Re=400. (*a*) Pressure elevation, (*b*) $\tau_{11}$ contours, and (*c*) $\tau_{12}$ contours.**

mation of viscoelastic flows via finite element methods, reserving a topic for the strategies employed in overcoming the difficulties of approximating the extra-stress tensor as a primal variable. Bonvin et al. [10] introduced stabilized three-field formulations for the Stokes problem based on a linear version of the Oldroyd-B model, splitting the viscosity function into the polymeric and solvent (as first suggested by Crochet and Keunings [11]). They proved the uniqueness and existence of the Galerkin formulations and also established the compatibility conditions for the approximation functions of the extra stress, velocity, and pressure fields. Their stabilized formulations (one of them a Galerkin least-squares (GLS) formulation) are able to circumvent these conditions and are stable for any combination of triangular elements. Coronado et al. [12] employed a four-field GLS formulation in velocity, pressure, extra stress, and velocity gradient for the approximation of flows of viscoelastic Oldroyd-B fluids. They employed the GLS scheme both in the stabilization of motion and constitutive equations. Their numerical results were quite stable for equal-order quadrilateral elements. A four-field formulation known as *elastic viscous split stress* (EVSS) is an alternative, which employs the strain rate tensor as an additional variable in order to circumvent the compatibility condition between the extra stress and velocity [13–15].

Originally introduced in the context of the Stokes problem [16], the GLS method was developed to enhance the stability of the classical Galerkin method by adding mesh-dependent terms to that formulation. These terms are functions of the residuals of the Euler–Lagrange equations evaluated elementwise. Since the residuals of the Euler–Lagrange equations are satisfied by their exact solutions, consistency is preserved in these methods. This idea was also extended to incompressible Navier–Stokes equations by Franca and Frey [8] who introduced new stability parameters designed to optimize stability and convergence. When applied to multifield models, the GLS methodology inherits the capability to circumvent the compatibility conditions between pressure and velocity (Babuška–Brezzi condition) and between extra stress and velocity [1,7,10].

The aim of this article is to investigate the features of a multifield finite element formulation for extra stress, velocity, and pressure for the approximation of inelastic non-Newtonian fluid flows. Such formulation is a GLS scheme based on that of Behr et al. [7], but employing non-Newtonian viscosity functions. The GLS methodology was employed in order to enhance the stability of the classical Galerkin approximation for incompressible flows and also to circumvent the compatibility between the approximation functions of stress, velocity, and pressure. In addition, stabilization was necessary to preserve numerical stability in locally advection dominant flow regions, generated as a consequence of the material behavior of shear-thinning liquids.

We divide this article in the following sections: Sec. 2 presents the mechanical modeling of the problems we are concerned with based on the continuum theory, Sec. 3 discusses finite element formulation and solution methodology, and Sec. 4 gives the numerical results.

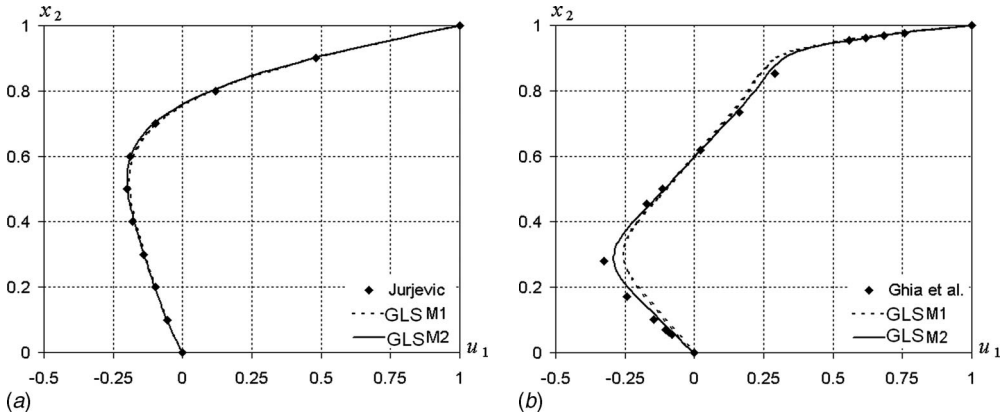


**Fig. 2 Horizontal velocity profiles in $x_1=0.5L$. (*a*) Re=1. (*b*) Re=400.**

## 2 Mechanical Model

The mechanical modeling presented herein concerns a material body $\mathcal{B}$, for which a flow is defined by the triple velocity, mass density, and stress tensor fields, $(\mathbf{v},\rho,\mathbf{T})$, and the associated system of contact and body forces, $(\mathbf{t}(\mathbf{n}),\mathbf{f})$ [17].

*Principle of mass conservation*. The mass of a mechanical body $\mathcal{B}$ does not change with time. Assuming an isochoric motion, the differential form of this principle is stated as

$$\operatorname{div}\mathbf{v}=0 \tag{1}$$

where $\mathbf{v}$ is the virtual fluid velocity.

*Momentum balance (Cauchy's theorem [17])*. The dynamic principle is equivalent to the laws of momentum balance for the system of forces acting on $\mathcal{B}$ during its motion. This theorem asserts that a necessary and sufficient condition for the laws of momentum balance to be satisfied is that the existence of a stress tensor field, $\mathbf{T}$, such that for each unit outward vector $\mathbf{n}$, $\mathbf{Tn}=\mathbf{t}(\mathbf{n})$, $\mathbf{T}$ is symmetric and $\mathbf{T}$ satisfies the motion equation

$$\rho D_t\mathbf{v}=\operatorname{div}\mathbf{T}+\mathbf{f} \tag{2}$$

**2.1 Material Behavior.** The particular relations between contact forces and body motion and deformation are modeled by constitutive laws, which are mathematical models for the stress tensor, $\mathbf{T}$. A functional dependence of $\mathbf{T}$ on the strain rate tensor, $\mathbf{D}$, is acceptable in view of the fact that this could represent a frame indifferent simple fluid [18,19]. The first-order fluid model [19,20] is the most general isotropic linear relation between $\mathbf{T}$ and $\mathbf{D}$, which is able to predict a viscous response.

The shear-thinning and shear-thickening phenomena in viscometric flows were the motivation for the derivation of the generalized Newtonian liquid (GNL) models [21]. These models were formulated employing the Newtonian law with a strain rate dependent viscosity function, $\eta(\dot\gamma)$, in which $\dot\gamma$ denotes a norm of tensor $\mathbf{D}$, $\dot\gamma=(2\operatorname{tr}\mathbf{D}^2)^{1/2}$—in simple shear flows, $\dot\gamma$ represents the shear rate. Mathematically, the GNL models may be written as

$$\mathbf{T}=-p\mathbf{I}+2\eta(\dot\gamma)\mathbf{D}=-p\mathbf{I}+\boldsymbol{\tau} \tag{3}$$

where $\eta(\dot\gamma)$ is the fluid viscosity, $p$ is the mean pressure, $\mathbf{I}$ is the unit tensor, and $\boldsymbol{\tau}$ is the extra-stress tensor.

Examples of well-known GNL viscosity functions are the Ostwald–de Waele power-law and Carreau models [21,22]. The latter may be mathematically expressed by

$$\frac{\eta(\dot\gamma)-\eta_\infty}{\eta_0-\eta_\infty}=[1+(\lambda\dot\gamma)^2]^{(n-1)/2} \tag{4}$$

where $\eta_0$ is the zero-shear-rate viscosity, $\eta_\infty$ the infinite-shear-rate viscosity, $n$ the power-law index, which controls the exponential viscosity decay, and $\lambda$ a time constant, which is the reciprocal of the minimum shear rate in which viscosity starts to decrease exponentially. As stated above, Eq. (4) represents the classical Carreau model. For $\eta_\infty$ equal to zero and large values of $\dot\gamma$, the Ostwald–de Waele power-law function is recovered, with the consistency index, $K$, corresponding to $\eta_0\lambda^{n-1}$ [21].

## 3 Multifield Finite Element Approximation

In this section, we present a stabilized multifield formulation for steady isochoric flows of Newtonian liquid and GNL. Based on the equation of continuity (Eq. (1)) and the motion equation (Eq. (2)), coupled to the constitutive equation for $\mathbf{T}$ (Eq. (3)), we may build the following multifield boundary value problem:

$$\begin{aligned}
&\rho[\operatorname{grad}\mathbf{u}]\mathbf{u}=-\operatorname{grad}p+\operatorname{div}\boldsymbol{\tau}+\mathbf{f} \quad \text{in } \Omega\\
&\boldsymbol{\tau}-2\eta(\dot\gamma)\mathbf{D}(\mathbf{u})=0 \quad \text{in } \Omega\\
&\operatorname{div}\mathbf{u}=0 \quad \text{in } \Omega\\
&\mathbf{u}=\mathbf{u}_g \quad \text{on } \Gamma_g\\
&(\boldsymbol{\tau}-p\mathbf{I})\mathbf{n}=\mathbf{t}_h \quad \text{on } \Gamma_h
\end{aligned} \tag{5}$$

where $\rho$, $p$, $\boldsymbol{\tau}$, $\mathbf{f}$, $\eta$, $\dot\gamma$, $\mathbf{I}$, and $\mathbf{D}$ are defined as before; $\mathbf{u}$ is the admissible velocity field; $\Omega\subset\mathcal{R}^{N=2,3}$ is a bounded domain with a regular boundary $\Gamma$; $\Gamma_g$ is the portion of $\Gamma$ where Dirichlet conditions are imposed and $\Gamma_h$ is the portion subjected to Neumann boundary conditions.

**3.1 A Galerkin Least-Squares Formulation.** Based on a finite element partition $\Omega^h$ of $\bar\Omega$ performed in the usual way (no overlapping is allowed between any two elements; the union of all element domains $\Omega_K$ reproduces $\bar\Omega$ [23]), we may introduce the following finite spaces of approximation functions for extra stress, velocity, and pressure fields:

$$\begin{aligned}
\mathbf{W}^h&=\{\mathbf{S}\in C^0(\Omega)^{N\times N}\cap L^2(\Omega)^{N\times N},\mathbf{S}_{ij}=\mathbf{S}_{ji},i,j=1,\ldots,N|\mathbf{S}_{\Omega_K}\\
&\quad\in R_k(\Omega_K)^{N\times N},K\in\Omega^h\}\\
\mathbf{V}^h&=\{\mathbf{v}\in H_0^1(\Omega)^N|\mathbf{v}_{|\Omega_K}\in R_l(\Omega_K)^N,K\in\Omega^h\}\\
\mathbf{V}_g^h&=\{\mathbf{v}\in H^1(\Omega)^N|\mathbf{v}_{|\Omega_K}\in R_l(\Omega_K)^N,K\in\Omega^h,\mathbf{v}=\mathbf{u}_g\text{ on }\Gamma_g\}\\
P^h&=\{q\in C^0(\Omega)\cap L_0^2(\Omega)|p_{|\Omega_K}\in R_m(\Omega_K),K\in\Omega^h\}
\end{aligned} \tag{6}$$

where $C^0(\Omega)$ represents the space of continuous functions, $L^2(\Omega)$ and $H^1(\Omega)$ Hilbert and Sobolev functional spaces in $\Omega$, and $R_k$, $R_l$, and $R_m$ the polynomials of degree in $k$, $l$, and $m$ in $\Omega_K$ [23]. The problem's degrees of freedom—extra stress, velocity, and

**Table 1 Vortex eye position for the lid-driven cavity**

| Reference | $x_1$ | $x_2$ |
|---|---|---|
| Re=100 | | |
| Schreiber and Keller [27] | 0.61667 | 0.74167 |
| Ku and Hatziavramidis [28] | 0.62109 | 0.73752 |
| Sivaloganathan and Shaw [29] | 0.61 | 0.73 |
| Present work (**u**-$p$ Galerkin) | 0.619 | 0.735 |
| Present work ($\boldsymbol{\tau}$-**u**-$p$ GLS M1) | 0.619 | 0.733 |
| Present work ($\boldsymbol{\tau}$-**u**-$p$ GLS M2) | 0.618 | 0.736 |
| Re=400 | | |
| Ku and Hatziavramidis [28] | 0.55463 | 0.60415 |
| Sivaloganathan and Shaw [29] | 0.56 | 0.61 |
| Present work (**u**-$p$ Galerkin) | 0.564 | 0.606 |
| Jurjevic [30] | 0.564 | 0.6055 |
| Present work ($\boldsymbol{\tau}$-**u**-$p$ GLS M1) | 0.570 | 0.605 |
| Present work ($\boldsymbol{\tau}$-**u**-$p$ GLS M2) | 0.561 | 0.605 |

pressure—are approximated by basis functions contained beneath the subspaces of Eq. (6). These approximations are denoted by $\boldsymbol{\tau}^h$, $\mathbf{u}^h$, and $p^h$, respectively. The weighting functions are approximated by $\mathbf{S}^h$, $\mathbf{v}^h$, and $q^h$.

A GLS formulation for Eq. (5) may be stated as follows: Find the triple $(\boldsymbol{\tau}^h, \mathbf{u}^h, p^h) \in \mathbf{W}^h \times \mathbf{V}_g^h \times P^h$ such that

$$B(\boldsymbol{\tau}^h, \mathbf{u}^h, p^h; \mathbf{S}^h, \mathbf{v}^h, q^h) = F(\mathbf{S}^h, \mathbf{v}^h, q^h)$$
$$\forall (\mathbf{S}^h, \mathbf{v}^h, q^h) \in \mathbf{W}^h \times \mathbf{V}^h \times P^h \tag{7}$$

where

$$B(\boldsymbol{\tau}, \mathbf{u}, p; \mathbf{S}, \mathbf{v}, q) = \rho([\text{grad } \mathbf{u}]\mathbf{u}, \mathbf{v}) - (p, \text{div } \mathbf{v}) - (\boldsymbol{\tau}, \mathbf{D}(\mathbf{v}))$$
$$+ (2\eta(\dot{\gamma}))^{-1}(\boldsymbol{\tau}, \mathbf{S}) - (\mathbf{D}(\mathbf{u}), \mathbf{S}) + (\text{div } \mathbf{u}, q)$$
$$+ \varepsilon(p, q) + \sum_{K \in \Omega^h} \alpha(\text{Re}_K)([\text{grad } \mathbf{u}]\mathbf{u} + \text{grad } p$$
$$- \text{div } \boldsymbol{\tau}, [\text{grad } \mathbf{v}]\mathbf{u} + \text{grad } q - \text{div } \mathbf{S})_{\Omega_K}$$
$$+ \delta(\text{div } \mathbf{u}, \text{div } \mathbf{v}) + 2\eta(\dot{\gamma})\beta((2\eta(\dot{\gamma}))^{-1}\boldsymbol{\tau}$$
$$- \mathbf{D}(\mathbf{u}), (2\eta(\dot{\gamma}))^{-1}\mathbf{S} - \mathbf{D}(\mathbf{v})) \tag{8}$$

and

$$F(\mathbf{S}, \mathbf{v}, q) = (\mathbf{f}, \mathbf{v}) + (\mathbf{t}, \mathbf{v})_{\mathbf{r}} \sum_{K \in \Omega^h} \alpha(\text{Re}_K)(\mathbf{f}, [\text{grad } \mathbf{v}]\mathbf{u}$$
$$+ \text{grad } q - \text{div } \mathbf{S})_{\Omega_K} \tag{9}$$

with $\varepsilon \ll 1$ and $0 \leq \beta \leq 1$ as suggested by Behr et al. [7]. The stability parameters $\alpha(\text{Re}_K)$ and $\delta$ are given as in Franca and Frey [8],

$$\alpha(\text{Re}_K) = \frac{h_K}{2|\mathbf{u}|_p}\xi(\text{Re}_K)$$

$$\xi(\text{Re}_K) = \begin{cases} \text{Re}_K, & 0 \leq \text{Re}_K < 1 \\ 1, & \text{Re}_K \geq 1 \end{cases}$$

$$\text{Re}_K = \frac{m_k|\mathbf{u}|_p h_K}{4\eta(\dot{\gamma})/\rho}$$

$$m_k = \min\{1/3, 2C_k\}$$

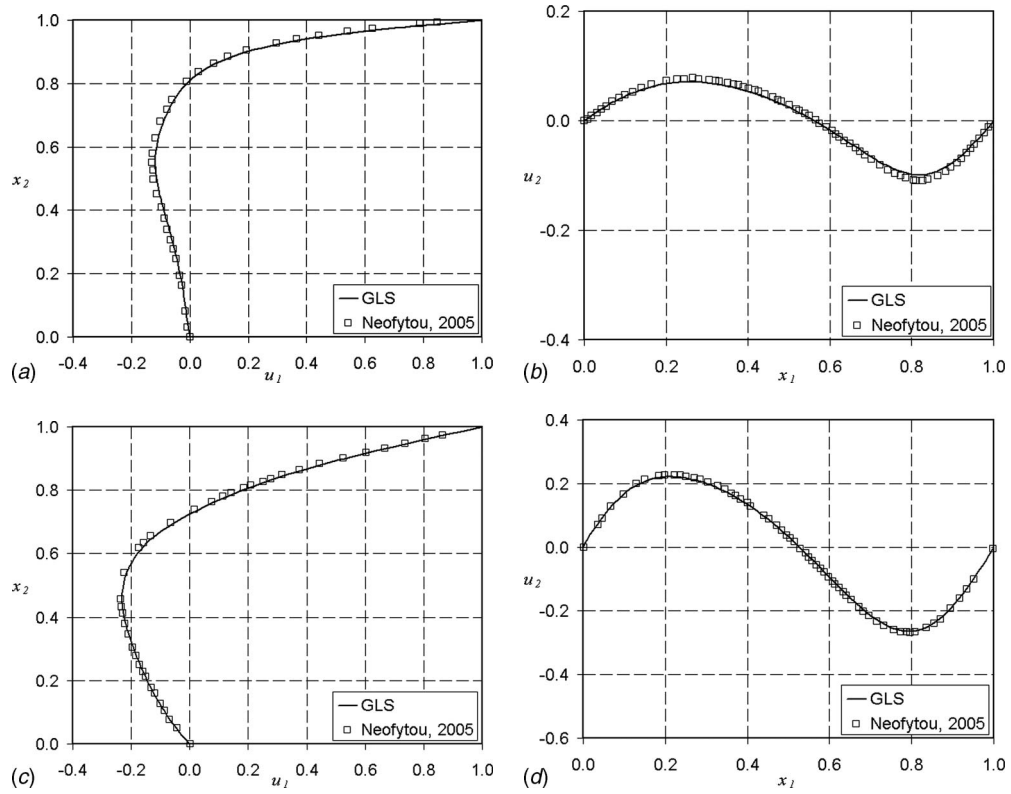


**Fig. 3 (*a*) Horizontal velocity versus $x_2$, Re=50, $n$=0.5. (*b*) Vertical velocity versus $x_1$, Re=50, $n$=0.5. (*c*) Horizontal velocity versus $x_2$, Re=100, $n$=1.5. (*d*) Vertical velocity versus $x_1$, Re=100, $n$=1.5.**

$$C_k \sum_{K \in \Omega^h} h_K^2 \|\mathrm{div}\, \mathbf{D}(\mathbf{v})\|_{0,K} \leq \|\mathbf{D}(\mathbf{v})\|_0^2, \quad \mathbf{v} \in \mathbf{V}^h$$

$$\delta = \chi |\mathbf{u}|_p h_K \xi(\mathrm{Re}_K) \tag{10}$$

where $\chi$ is a positive constant scalar, $h_K$ is the mesh size, the operators $(\cdot,\cdot)$ and $(\cdot,\cdot)_{\Omega_K}$ represent the $L^2$-inner products in the domains $\Omega$ and $\Omega_K$, respectively, and the $p$-norm on $\mathcal{R}^N$ is represented by $|\cdot|_p$.

*Remarks.*

1. Taking the stability parameters $\alpha$, $\beta$, and $\delta$ equal to zero, the GLS formulation defined by Eqs. (7)–(10) reduces to the three-field Galerkin approximation for Eq. (5), which suffers from the lack of coercivity, when the viscosity tends to zero and the need to satisfy both the Babuška–Brezzi condition and the compatibility condition between the extra-stress and velocity approximation functions.
2. The GLS formulation defined by Eqs. (7)–(10) is identical to a GLS formulation proposed by Behr et al. [7] for the context of constant viscosity fluids. Furthermore, if we drop the inertia terms, i.e., $\rho=0$, the formulation of Franca and Stenberg [1] is recovered.
3. As the GLS terms for the motion equation are added elementwise, as functions of the local Reynolds number, they add artificial diffusivity in a selective manner. Even for mild Reynolds number flows, advection dominant regions may be generated due to the employment of shear-thinning viscosity functions, which promote very low viscosities in high strain rates, causing the flow to be locally more advective.

**3.2 Solution Method.** The approximation functions for $\boldsymbol{\tau}^h$, $\mathbf{u}^h$, $p^h$, $\mathbf{S}^h$, $\mathbf{v}^h$, and $q^h$ are given by the polynomial expansions

$$S_{ij}^h(\mathbf{x}) = \sum_{\hat{A} \in \Omega^h} N_{\hat{A}}(\mathbf{x}) S_{ij}^{\hat{A}}$$

$$v_i^h(\mathbf{x}) = \sum_{A \in \Omega^h} N_A(\mathbf{x}) v_i^A$$

**Table 2 Minimum and maximum values of velocity components for Re=100 and *n*=1.5**

| | $u_1$ min | $u_2$ max | $u_2$ min |
|---|---|---|---|
| Neofytou [31] | −0.2393 | 0.2278 | −0.2683 |
| Present work ($\boldsymbol{\tau}$-$p$-$\mathbf{u}$ GLS) | −0.2308 | 0.2213 | −0.2632 |
| Error (% of $u_0$) | 0.85 | 0.66 | 0.51 |

$$q^h(\mathbf{x}) = \sum_{\tilde{A} \in \Omega^h} N_{\tilde{A}}(\mathbf{x}) q_{\tilde{A}} \tag{11}$$

and are substituted in the GLS formulation of Eqs. (7)–(10). In Eq. (11), $N_A(\mathbf{x})$, $N_{\hat{A}}(\mathbf{x})$, and $N_{\tilde{A}}(\mathbf{x})$ are polynomials of $A$, $\hat{A}$, and $\tilde{A}$, the nodal points for velocity, extra stress, and pressure, respectively. The integrals in the $L^2$ norms of the formulation of Eqs. (7)–(10) are approximated via a Gaussian quadrature [24]. The resulting algebraic system may be summarized as

$$\mathbf{R}(\boldsymbol{\mathcal{U}}) = \mathbf{0} \tag{12}$$

where $\boldsymbol{\mathcal{U}}$ is the vector of nodal degrees of freedom for the primal variables $\boldsymbol{\tau}^h$, $\mathbf{u}^h$, and $p^h$, so that $\mathbf{R}(\boldsymbol{\mathcal{U}})$ corresponds to the matrix expression

$$\begin{aligned}\mathbf{R}(\boldsymbol{\mathcal{U}}) = &[(1+\beta)\mathbf{E}(\eta) + (1-\beta)\mathbf{H} + \mathbf{E}_\alpha(\mathbf{u},\eta)]\boldsymbol{\tau} \\ &+ [\mathbf{M} + \mathbf{N}(\mathbf{u}) + \mathbf{N}_\alpha(\mathbf{u},\eta) + \beta\mathbf{K} - (1+\beta)\mathbf{H}^T - \mathbf{G}^T]\mathbf{u} \\ &+ [\mathbf{G} + \mathbf{G}_\alpha(\mathbf{u},\eta) + \mathbf{P}]\mathbf{p} - [\mathbf{F} + \mathbf{F}_\alpha(\mathbf{u},\eta)]\end{aligned} \tag{13}$$

where $[\mathbf{H}]$ and $[\mathbf{H}^T]$ are the matrices of coupling between $\boldsymbol{\tau}$ and $\mathbf{u}$, $[\mathbf{E}]$ is the matrix of the $\boldsymbol{\tau}$ terms, $[\mathbf{N}]$ is the matrix of advective terms, $[\mathbf{K}]$ is the matrices of diffusive terms, $[\mathbf{G}]$ and $[\mathbf{G}^T]$ are the pressure and continuity term matrices, and $[\mathbf{F}]$ are the matrices of body force terms in the motion equation. The matrices with subscript $\alpha$ denote the matrices of the GLS terms for the motion equation, $[\mathbf{M}]$ is the matrix of the $\delta$ term, and $[\mathbf{P}]$ is the matrix of

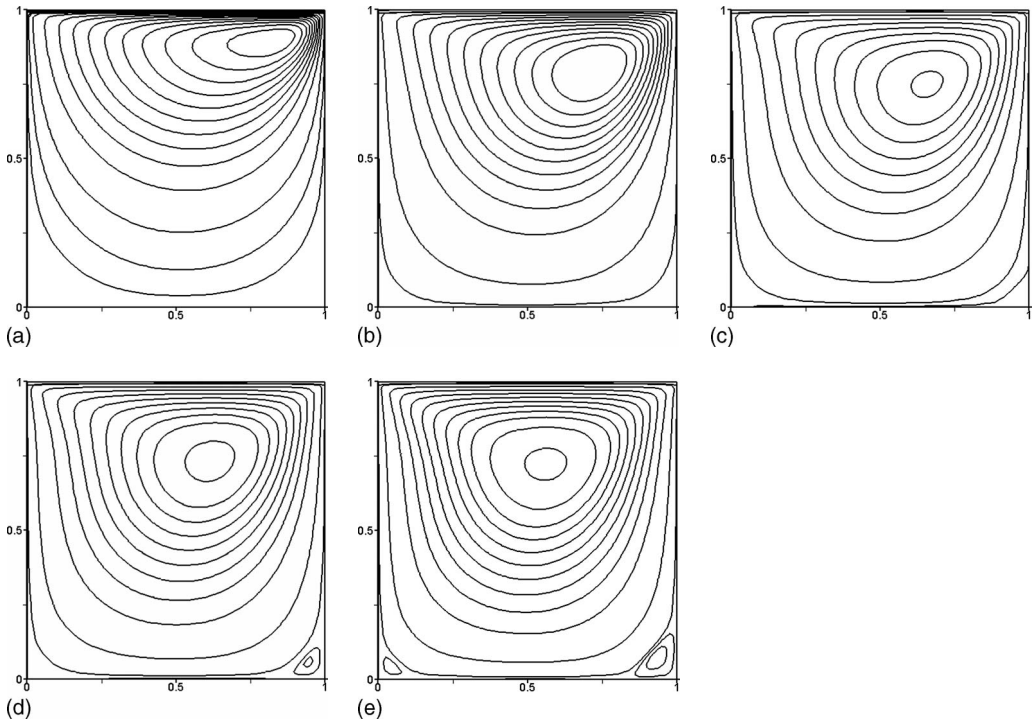


**Fig. 4 Streamlines for Re=100. (*a*) *n*=0.25. (*b*) *n*=0.5. (*c*) *n*=0.75. (*d*) *n*=1. (*e*) *n*=1.5.**

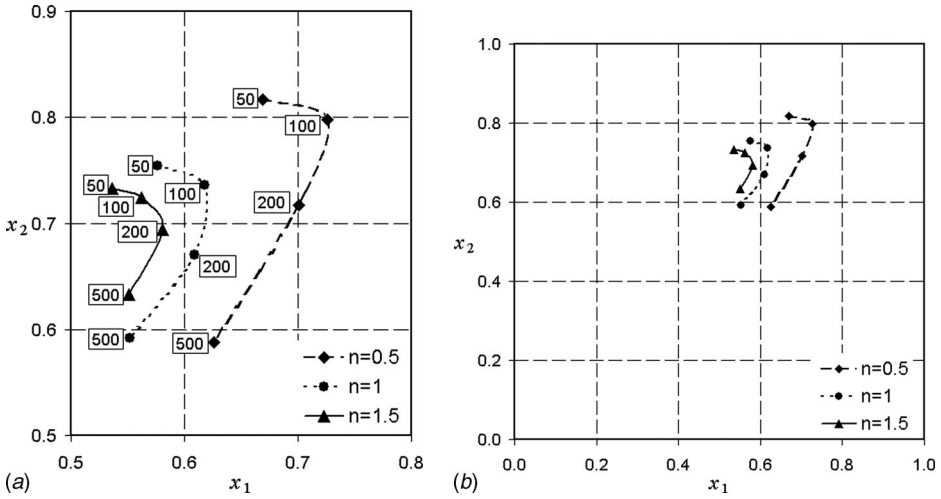


**Fig. 5 Vortex eye position. (*a*) Detail for various Re. (*b*) A general view in the cavity geometry.**

the $\varepsilon$ term in Eq. (8).

In order to obtain the solution of the algebraic system represented by Eq. (12), we employ a Newton-based method [25]. This method requires an initial guess $\boldsymbol{\mathcal{U}}^k$, $k=0$, and at each iteration, we solve the linear system

$$\mathbf{J}(\boldsymbol{\mathcal{U}}^k)\Delta\boldsymbol{\mathcal{U}}^{k+1} = -\mathbf{R}(\boldsymbol{\mathcal{U}}^k) \tag{14}$$

with the Jacobian matrix calculated analytically,

$$\mathbf{J}(\boldsymbol{\mathcal{U}}^k) = \left.\frac{\partial \mathbf{R}}{\partial \boldsymbol{\mathcal{U}}}\right|_{\boldsymbol{\mathcal{U}}^k} \tag{15}$$

in order to find the incremental vector $\Delta\boldsymbol{\mathcal{U}}^{k+1}$ and to compute

$$\boldsymbol{\mathcal{U}}^{k+1} = \boldsymbol{\mathcal{U}}^k + \Delta\boldsymbol{\mathcal{U}}^{k+1} \tag{16}$$

We assume that convergence is achieved when the norm of $\mathbf{R}(\boldsymbol{\mathcal{U}}^k)$ is less than a tolerance value—in this work, $10^{-7}$.

## 4 Numerical Results

We implemented the multifield GLS formulation of Eqs. (7)–(10) within a finite element code developed by the LAMAC Research Group. In Secs. 4.1 and 4.2 we study flows of Newtonian and non-Newtonian fluids using the lid-driven cavity problem. In Sec. 4.3 we investigate the results of flows of shear-thinning liquids through abrupt planar and axisymmetric contractions.

**4.1 Newtonian Flow in a Lid-Driven Cavity.** The lid-driven cavity problem was built as usual [26], with characteristic length $L$ and velocity $u_0$. The boundary conditions of non-slip and impermeability were imposed at side and lower walls. A constant horizontal velocity $u_0$ was prescribed at the upper boundary. The Reynolds number was varied from Re=1 to Re=400. We investigated approximations employing two meshes consisting of $40\times40$ (M1) and $80\times80$ (M2) equal-order bilinear finite elements ($Q_1/Q_1/Q_1$) for the variables $\boldsymbol{\tau}$-$\mathbf{u}$-$p$. We also performed computations using the classical Galerkin method for the problem in the variables $\mathbf{u}$ and $p$, employing $40\times40$ $Q_2/Q_1$ elements. We compared our results with several authors [26–30]—see Figs. 1 and 2 and Table 1.

In Fig. 1 we depict a pressure elevation plot and two graphics of the contours of the extra-stress components $\tau_{11}$ and $\tau_{12}$. These results correspond to the $80\times80$ mesh for Re=400. Such results were in good agreement with those that we obtained from the $\mathbf{u}$-$p$ standard Galerkin formulation and also agreed qualitatively with those of Behr et al. [7].

In Fig. 2, we compare our results for the horizontal velocity profile in $x_1=0.5L$ with those available in the literature [26,30]. A satisfactory agreement was observed for the whole range tested, from Re=1 (Fig. 2(*a*)) to Re=400 (Fig. 2(*b*)).

The vortex eye position was another feature compared with other authors in order to establish code verification. In Table 1 we list this comparison for Re=100 and Re=400, showing that the discrepancy is less than 1% in both cases for the two employed meshes.

**4.2 Lid-Driven Cavity Flows of Non-Newtonian Fluids.** In this subsection, the lid-driven cavity problem was employed to investigate non-Newtonian flows for problems involving material nonlinearity. The boundary conditions are the same as those described in Sec. 4.1. The GNL model was employed with a power-law function for the viscosity [21]. The Reynolds number for the cavity flow of power-law fluids was defined as

$$\mathrm{Re} = \frac{\rho L^n}{K u_0^{n-2}} \tag{17}$$

with $K$ being the consistency index and $n$ the exponent that controls the viscosity decay for $n<1$ (shear-thinning behavior) or its increase for $n>1$ (shear-thickening behavior).

We employed a mesh consisting of $80\times80$ equal-order bilinear finite elements $Q_1/Q_1/Q_1$ for the variables $\boldsymbol{\tau}$-$\mathbf{u}$-$p$. We investigated ranges of Reynolds numbers from Re=50 to Re=500 and power-law exponents from $n=0.25$ to $n=1.5$, and we compared the results with those by Neofytou [31], who employed a high-order finite volume method to solve the lid-driven cavity problem for various GNLs. All the results beneath these ranges were in fine agreement with that author's results. In Fig. 3, we depict some of the comparisons for the horizontal velocity profile at $x_1=0.5L$ and the vertical velocity profile in $x_2=0.5L$, for Re=50 and $n=0.5$ (Figs. 3(*a*) and 3(*b*)) and for Re=100 and $n=1.5$ (Figs. 3(*c*) and 3(*d*)). In Table 2, the maximum and minimum numerical values for the velocity are presented in comparison with those of Neofytou [31]. Such values are the smallest $u_1$ in the line $x_1=0.5L$ and the greatest and smallest $u_2$ at $x_1=0.5L$ for Re=100 and $n=1.5$. Again, we find a good agreement between our results and those of Neofytou [31].

Figure 4 depicts the flow streamlines for Re=100 and some distinct values of $n$. For a fixed Re, the effect of shear-thinning (Figs. 4(*a*)–4(*c*)) is to shift the vortex eye to an upper position inside the cavity, in comparison to the Newtonian case, $n=1$, Fig. 4(*d*). In the shear-thickening flow, Fig. 4(*e*), the vortex has its eye in a more central position. It is also easy to observe that shear-thinning fluids (Figs. 4(*a*)–4(*c*)) prevent the secondary vortex

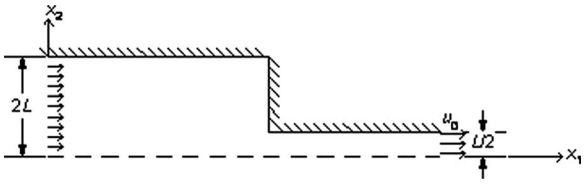


**Fig. 6 Problem statements for the abrupt contraction flows**

structure giving rise to a stagnant region in the lower region of the cavity. Meanwhile, shear-thickening fluids (Fig. 4(*e*)) tend to allow the formation of stronger secondary vortex than in the Newtonian case.

The effects of inertia, shear thinning, and shear thickening on lid-driven cavity flows are better understood with the aid of Fig. 5. In Fig. 5(*a*), the vortex eye positions for some distinct Reynolds numbers, Re, and power-law indices, $n$, are depicted in detail for the coordinates $x_1$ and $x_2$. Figure 5(*b*) gives a more general view of these positions in the problem domain. Compared to the Newtonian fluid case ($n=1$), the effects of shear thinning and shear thickening are to carry the vortex to a position more to the right and to the left, respectively. That happens because of the high strain rates in the cavity lid, which have the effect of, in the case of the shear-thinning fluid, decreasing the viscosity and allowing the vortex to be carried to the right by the flow. As for the shear-thickening fluid, the high strain rates cause the opposite: the viscosity grows near the cavity lid and hardens the vortex shift to the right as the flow becomes more advection dominant. We also observe that for any values of $n$, the vortex eye appears farther from the cavity lid as the Reynolds number increases. For the lowest values of Re, the vortex eye position is also shifted to the right, while for the lowest ones, it is shifted to the left. This inversion of behavior occurs because for low Re, diffusion is dominant in most regions, except for a region next to the cavity lid; but as Re increases, the whole domain becomes advection dominant and allows the advection of momentum from the right to the left. For the shear-thickening fluid, the Re in which inversion occurs Re $\approx 200$ is higher than the ones of the Newtonian and shear-thinning flows Re $\approx 100$. That difference is due to Re being a global flow parameter: where the viscosity increases due to shear thickening, the flow is locally more diffusive; the local Reynolds number is in fact lower, and the flow does not possess enough advection to cause the inversion.

**4.3 Flows of Shear-Thinning Liquids Through Abrupt Contractions.** In this subsection we present numerical results of the GLS approximation of Eqs. (7)–(10) for flows of shear-thinning liquids through 4:1 planar and axisymmetric contractions. The boundary conditions imposed were impermeability and non-slip at the walls, a uniform velocity profile of average velocity at the inflow boundary, symmetry at the centerline, and free traction at the outflow boundary, as is usual in finite element applications. This problem has been studied by Kim et al. [32] employing Carreau fluids in an axisymmetric domain for low Reynolds numbers, from 0 to 2. The viscosity function employed herein to model shear thinning is the Carreau equation (Eq. (4)). We built meshes of $Q_1/Q_1/Q_1$ elements for the geometry and problem statements summarized in Fig. 6, where the dashed line represents the symmetry plane and axis and $L$ represents the diameter and width of the narrow tube, for the planar and axisymmetric cases, respectively. The inflow and outflow lengths were long enough to ensure the flow's development ($18L$ and $12L$, respectively). The dimensionless Reynolds and Carreau numbers were calculated as follows:

$$\mathrm{Re} = \frac{\rho u_0 D_h}{\eta_0}, \quad \mathrm{Cu} = \lambda \dot{\gamma}_c \tag{18}$$

where $D_h$ is the hydraulic diameter of the narrow channel ($2L$ in the planar case and $L$ equal to the tube diameter, $D$, in the axisymmetric case) and $\dot{\gamma}_c$ is the characteristic flow shear rate given by $\dot{\gamma}_c = u_0/L$ for the planar case and $\dot{\gamma}_c = 2u_0/L$ for the axisymmetric one.

We varied Reynolds from Re=1 to Re=100 and Carreau numbers from Cu=1 to Cu=100 and employed power-law indices $n=0.1$ and $n=0.5$. As it can be inferred from Eq. (18), the Carreau number, Cu, accounts for the effects of varying λ in the viscosity function, Eq. (4). The consequences of a decrease or an increase in both λ and $n$ in the Carreau viscosity function is illustrated in

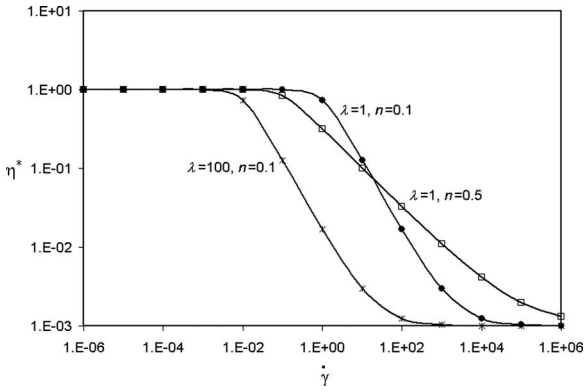


**Fig. 7 Carreau viscosity function**

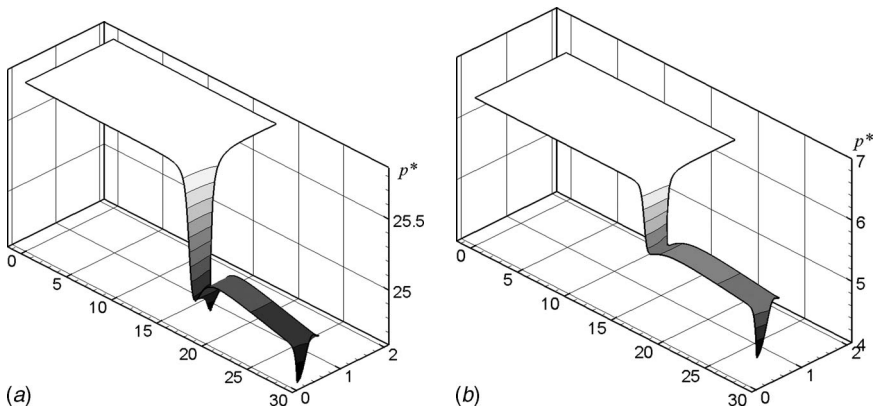


**Fig. 8 Pressure elevation plots for Re=100, Cu=100, and $n=0.5$. (*a*) Planar and (*b*) axisymmetric.**

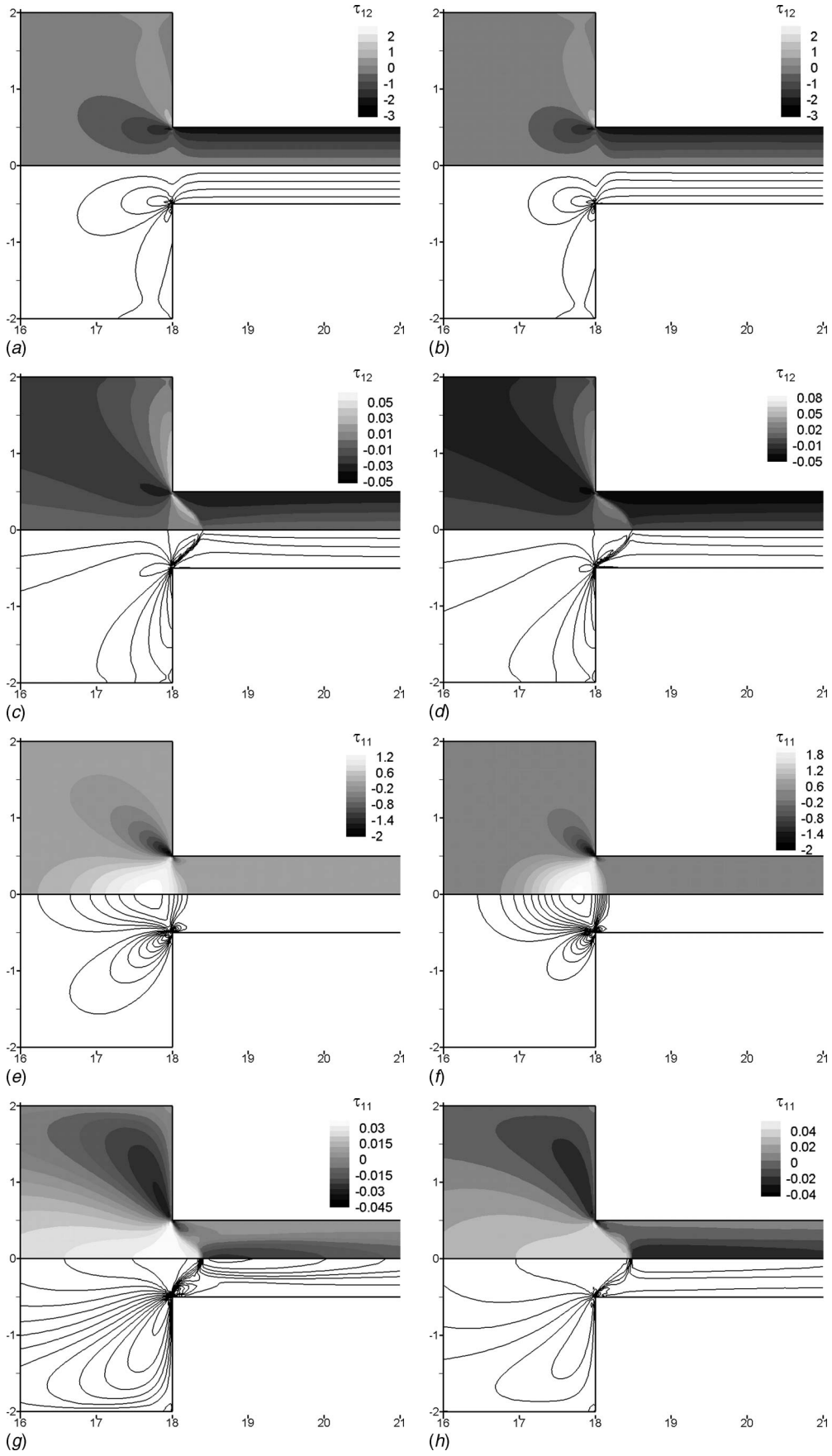


**Fig. 9** $\tau_{12}$ **fields: Cu=1 and** $n$**=0.1 for (***a***) planar and (***b***) axisymmetric. Cu=100 and** $n$**=0.1 for (***c***) planar and (***d***) axisymmetric.** $\tau_{11}$ **fields: Cu=1 and** $n$**=0.1 for (***e***) planar and (***f***) axisymmetric. Cu =100 and** $n$**=0.1 for (***g***) planar and (***h***) axisymmetric.**

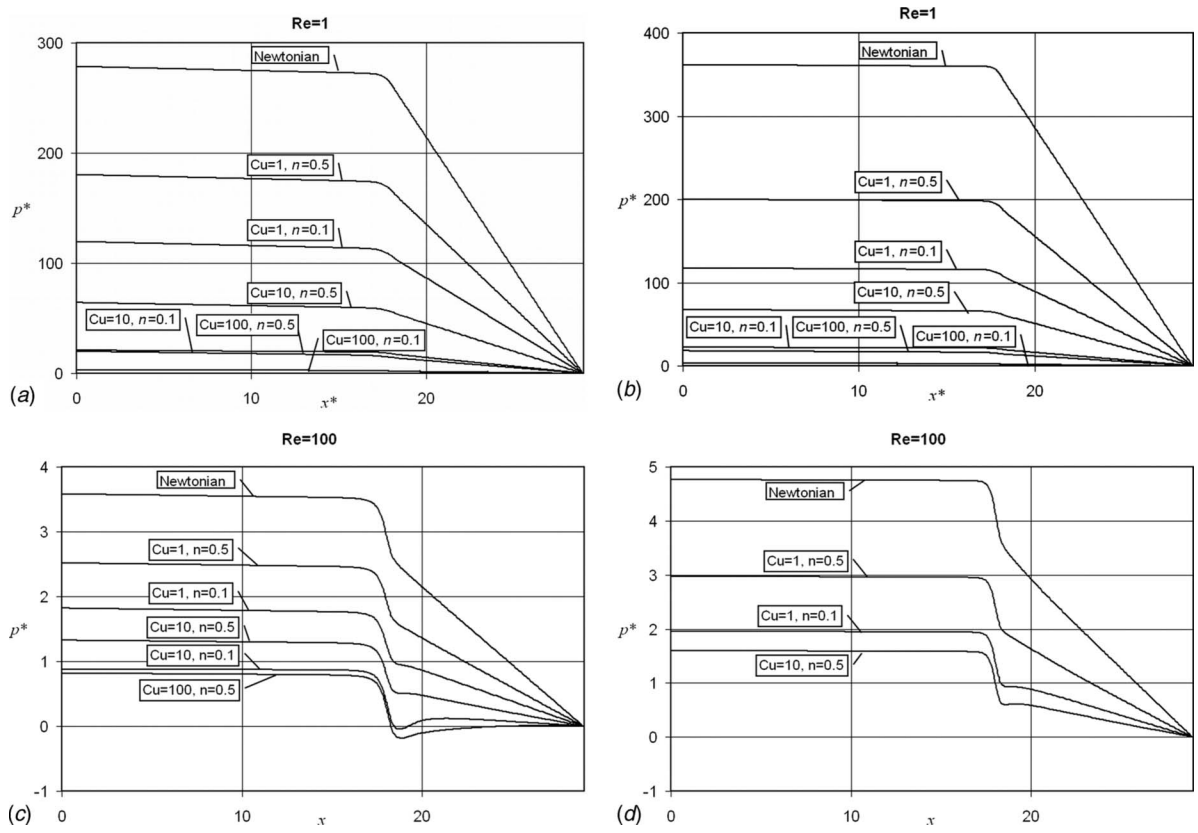


**Fig. 10 Pressure drop along the symmetry line. Re=1 for (*a*) planar and (*b*) axisymmetric. Re=100 for (*c*) planar and (*d*) axisymmetric.**

Fig. 7, which is a plot of the dimensionless viscosity function, $\eta^* = \eta/\eta_0$, versus the shear rate $\dot{\gamma}$. If two fluids have the same $\lambda$, they start to shear thin at the same shear rate, but the one with the smallest $n$ presents the steeper viscosity exponential decrease. On the other hand, for two fluids with the same $n$, the one with the highest $\lambda$ starts to shear thin at lower shear rates, but with the same exponential decrease.

We performed mesh independency studies controlling the pressure drop profile along the symmetry plane and axis and also the horizontal velocity profiles in the contraction plane. We assumed that the results were mesh independent for a 13,770 element mesh, employed both for planar and axisymmetric cases. Figure 8 displays pressure elevation plots for the situation Re=100, Cu=100, and $n=0.5$ when highly advective regions occur near the walls, showing that the GLS method was able to stabilize any spurious oscillations that could occur in the pressure field. The sudden pressure drop at the channel exit is due to the free traction boundary condition; it is not a physical feature but a numerical one that does not affect the solution in regions sufficiently far from the channel exit. The results discussed in the sequel correspond to those obtained using this mesh.

Figure 9 depicts the components $\tau_{11}$ and $\tau_{12}$ of the extra-stress tensor for Re=1 and $n=0.1$ and two values of Carreau numbers, Cu=1 and Cu=100. We observe the effects of the viscosity decrease caused by the high strain rates in the contraction. Shear thinning reduces the stress levels at the contraction. For the lowest Carreau number flow (Figs. 9(*a*), 9(*b*), 9(*e*), and 9(*f*)), the extra stresses are similar to the Newtonian ones at the same Reynolds number. For higher Carreau number flows (Figs. 9(*c*), 9(*d*), 9(*g*), and 9(*h*)), the decrease in stresses is well pronounced, consequently decreasing the head loss.

The head loss due to the viscosity decrease is compared in Fig. 10 for different shear-thinning fluids (Cu=1, 10, and 100 and $n$ =0.1, 0.5, and 1). This figure shows the pressure drop along the symmetry line for the all flows investigated, in (*a*) and (*b*) for Re=1 and in (*c*) and (*d*) for Re=100. (The contraction is located at $x=18L$ from the inlet flow boundary.) In all cases, the more shear thinning the fluid is (corresponding to lower $n$ and higher Cu), the more the pressure drop is reduced due to viscosity decrease. Indeed, the pressure drop in the wide channel is very similar for all fluids with the same Re since the pressure drop curves have similar slopes. At the contraction and in the narrow channel, where the greatest viscosity decreases happen, the slopes are clearly distinct for all fluids studied.

In Fig. 11 we show the plots of $u^*=u_1/u_0$ versus $x=x_1/L$ at the symmetry line, $y=0$, with $y=x_2/L$, for the planar case (Figs. 11(*a*), 11(*c*), 11(*e*), and 11(*g*)) and $u^*=u_1/u_0$ versus $x=x_1/D$ at the symmetry line, $r=0$, with $r=2x_2/D$, for the axisymmetric case (Figs. 11(*b*), 11(*d*), 11(*f*), and 11(*h*)), which corresponds to the maximum velocity value for each $x$-position. In Figs. 11(*a*) and 11(*b*), the Newtonian profile is depicted for two Reynolds numbers, Re=1 and Re=100. In the regions of fully developed flow, the maximum velocity is the same for both Re, as expected. Near the contraction the main differences between the advective (Re =100) and the diffusive (Re=1) cases occur. As expected, an increase in the entrance length is observed for the highest Re. In Figs. 11(*c*) and 11(*d*), we analyze the $u^*$ profile for Re=1 and Re=100 for a shear-thinning fluid—Cu=100 and $n=0.5$. The effect of increasing Reynolds is the same as for the Newtonian fluid, but two main differences arise. First, in the case of the shear-thinning fluid, the entrance length is longer than for the Newtonian fluid. Second, a peak in $u^*$ is formed immediately after the contraction plane, which is caused by the highly advective regime that occurs there. Figure 12 elucidates what happens: the flow acceleration is so great close to the contraction corner that the

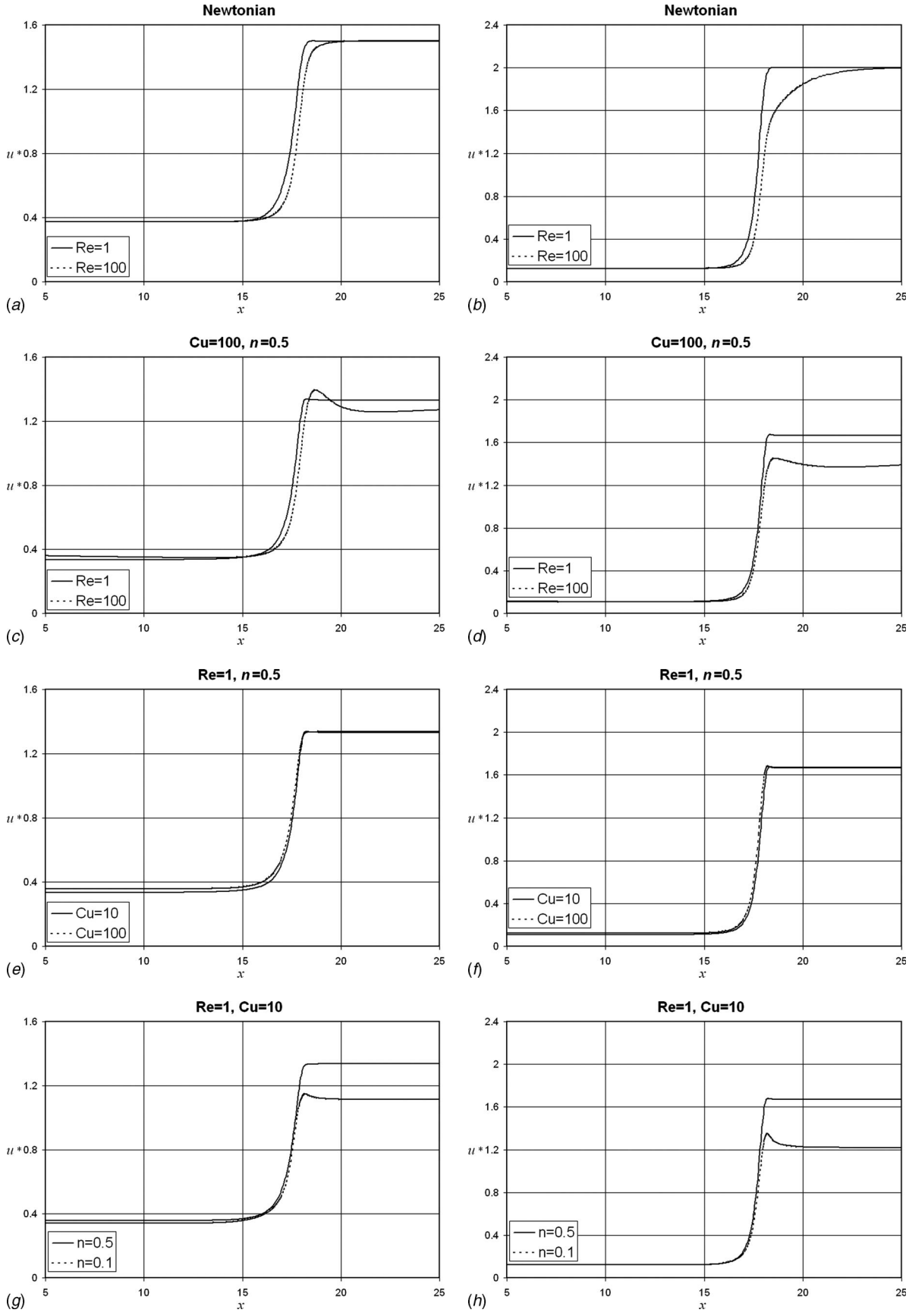


**Fig. 11 Profile of $u^*$ along the symmetry line: for Newtonian, (*a*) planar and (*b*) axisymmetric; for Cu=100 and $n$=0.5, (*c*) planar and (*d*) axisymmetric; for Re=1 and $n$=0.5, (*e*) planar and (*f*) axisymmetric; for Re=1 and Cu=10, (*g*) planar and (*h*) axisymmetric**

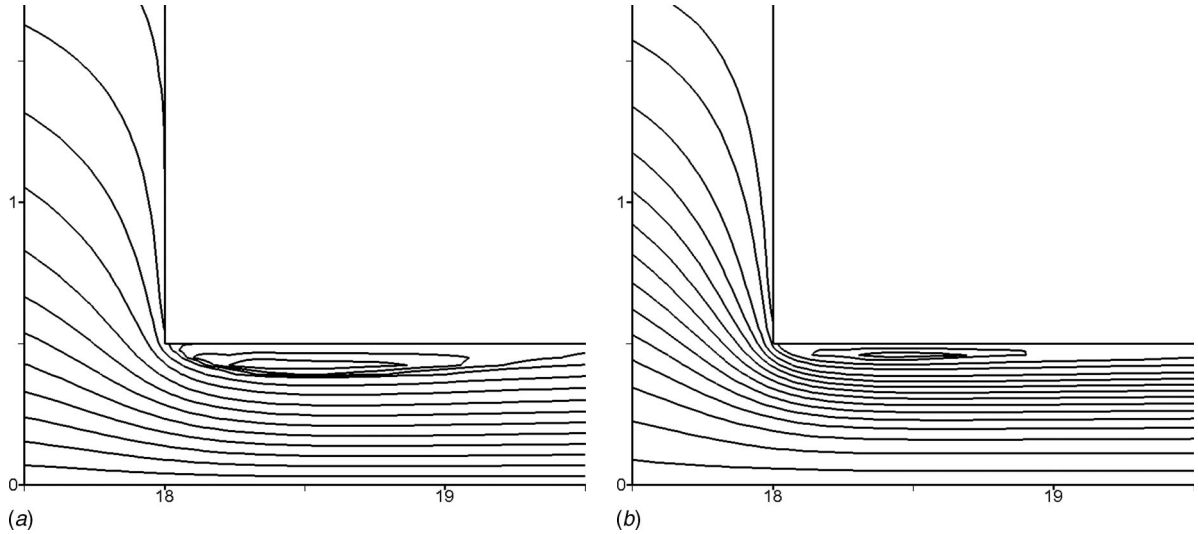


**Fig. 12 Streamlines. Re=100, Cu=100, and $n$=0.5: (*a*) planar and (*b*) axisymmetric.**

flow is detached from the wall, and a recirculation is formed, strangling the flow section and causing a peak in the velocity profile for both planar (Fig. 12(*a*)) and axisymmetric (Fig. 12(*b*)) cases. In Figs. 11(*e*) and 11(*f*) the effects of different Carreau numbers are investigated (Cu=10 and 100) for an inertialess flow, Re=1. It is possible to observe that an increase in Cu only causes a light decrease in the centerline velocity values upstream and close to the contraction, where this parameter controls the fluid thinning, since these regions are subjected to high strain rates. In Figs. 11(*g*) and 11(*h*) it is evident that for the same Re and Cu, a change in the $n$ index strongly affects the flow dynamics, especially downstream the contraction. Due to the high strain rates that are present in this region, as $n$ decreases, a more flattened velocity profile is formed. The distinction between the planar and the axisymmetric flows is mainly in the values of the centerline velocity, which is lower in the planar case. The planar flows are only subjected to shear in the upper and lower walls, while the axisymmetric flows are surrounded by the duct wall, which causes high deformation rates in a greater portion of the fluid, elongating the velocity profile in comparison with the planar flows.

In Fig. 13 we study how shear thinning affects the vortex upstream the contraction plane. For low Carreau and Reynolds numbers (Re=1 and Cu=1, Figs. 13(*a*) and 13(*b*)), a vortex is formed similar to Newtonian flows [32]. As Cu increases, keeping Re fixed, the viscosity decrease near the contraction renders the flow advection dominant, pushing the vortex against the wall until it disappears, as in Figs. 13(*c*) and 13(*d*), where the flow streamlines for Re=1 and Cu=100 look similar to those of a high Re Newtonian flow [32].

In Fig. 14 we show the axial velocity profiles, $u^*=u_1/u_0$ versus $y=x_2/L$ and $u^*=u_1/u_0$ versus $r=2x_2/D_0$, at the contraction plane.

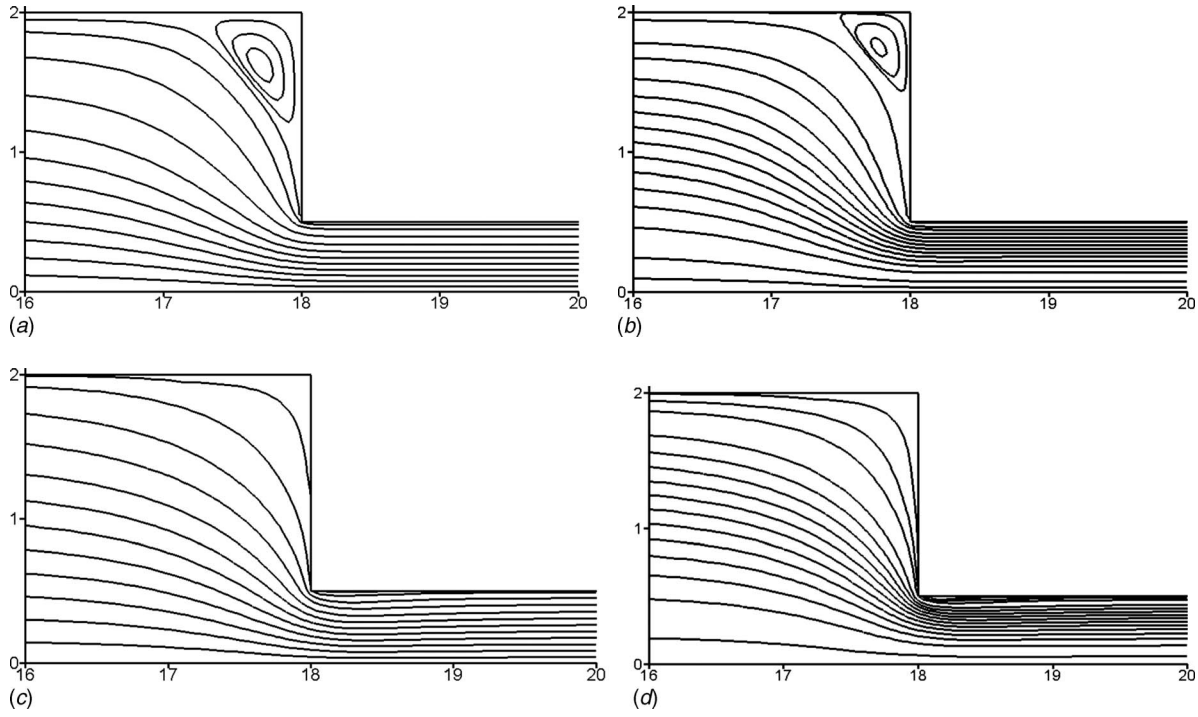


**Fig. 13 Streamlines. Re=1, Cu=1, and $n$=0.1; (*a*) planar and (*b*) axisymmetric. Re=1, Cu=100, and $n$=0.1; (*c*) planar and (*d*) axisymmetric.**

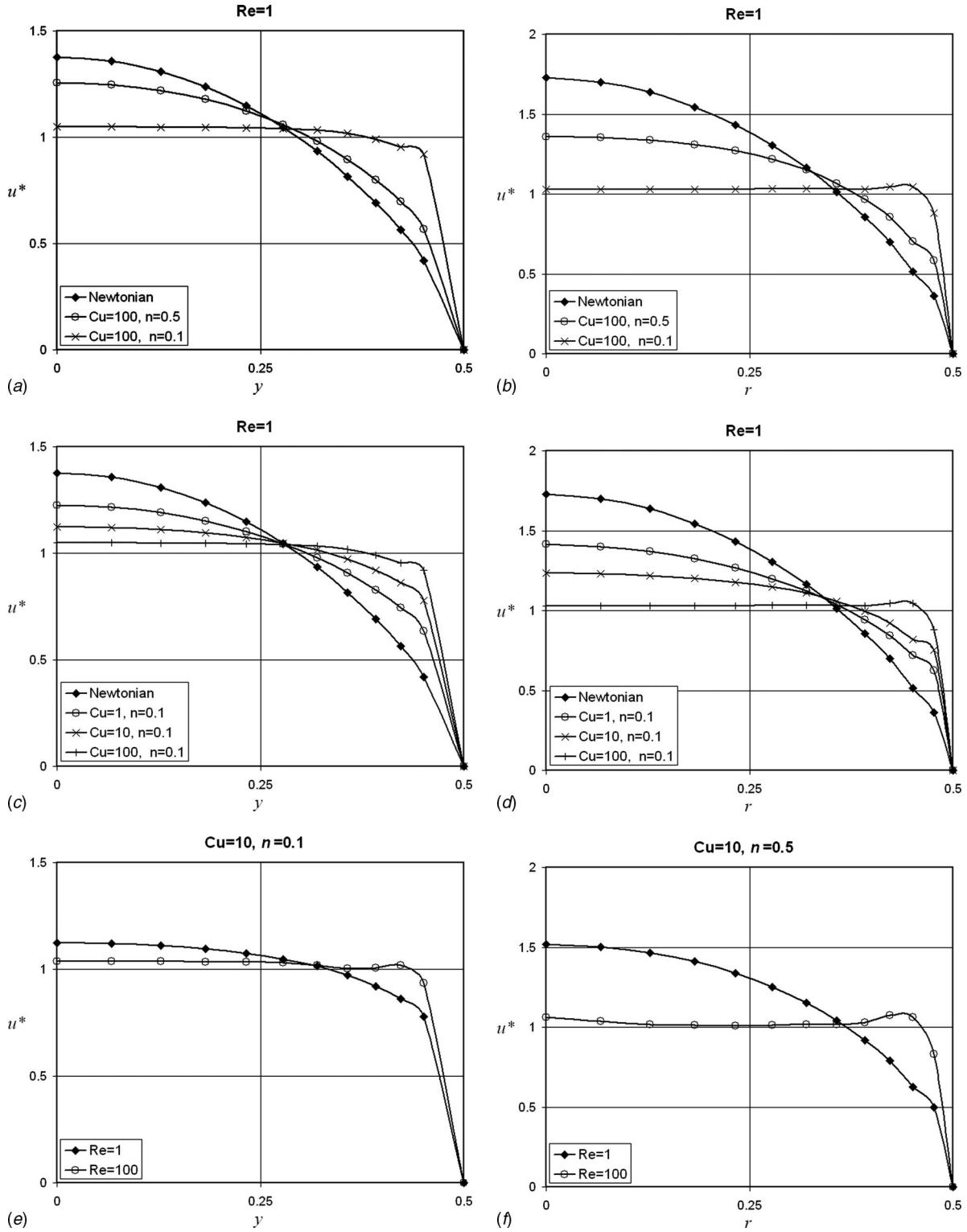


**Fig. 14 Profile of $u^*$ versus $y$ and $r$ in the contraction plane: (*a*) Re=1, Cu=100, planar; (*b*) Re=1, Cu=100, axisymmetric; (*c*) Re=1, $n$=0.1, planar; (*d*) Re=1, $n$=0.1, axisymmetric; (*e*) Cu=10, $n$=0.1, planar; (*f*) Cu=10, $n$=0.1, axisymmetric**

In items (*a*) and (*b*), the effect of the power-law index, $n$, is investigated while Cu and Re are kept fixed (Cu=100 and Re=1). We notice that the lower the $n$ parameter is the flatter the velocity profile becomes at the contraction plane. In items (*c*) and (*d*) the effect of the Carreau number is investigated while $n$ and Re are kept fixed ($n$=0.1 and Re=1). We notice that the higher the Cu is, the flatter the velocity profile becomes again due to shear thinning. Also, for low Cu (for Cu=1 in Figs. 14(*c*) and 14(*d*)), the velocity profiles are very similar to the Newtonian ones, indicating that the strain rates experimented by the fluid near the contraction plane were unable to achieve the power-law region of Carreau model (Eq. (4)). In items (*e*) and (*f*) the effects of varying

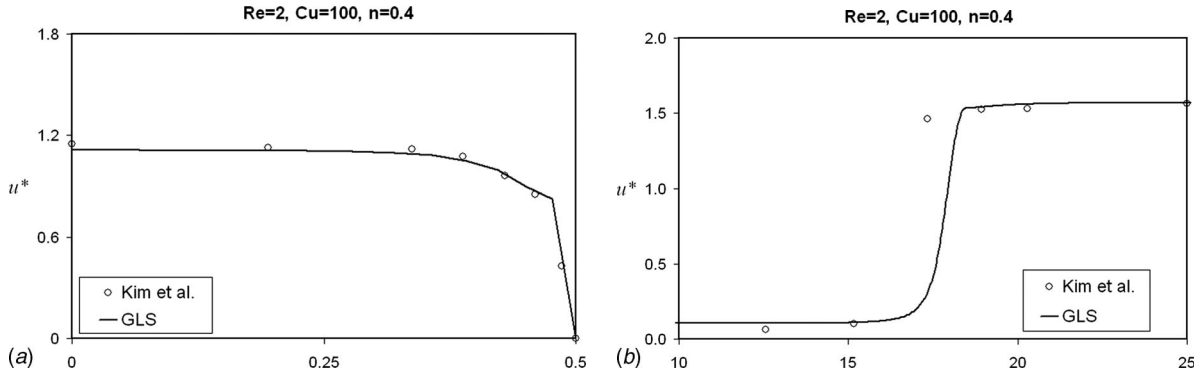


**Fig. 15 Comparison between the multifield GLS results and results of Kim et al. [32])**

the Reynolds number, i.e., adding inertia to the flows, for fixed $n$ and Cu ($n=0.5$ and Cu=10) are investigated. As inertia increases the advection dominant regions, the expected effects of increasing Re are the same effects of shear thinning, i.e., the flattening of the velocity profiles. In all cases investigated in Fig. 14, when the boundary layer is too steep, some numerical oscillations are present near the wall. These oscillations are due to the inability of methods based on the addition of artificial diffusivity, such as streamline upwind/Petrov-Galerkin (SUPG) method and GLS, to capture regions of shocks and steep gradients smoothly [33]. Such kind of pathology has been overcome by shock capture techniques such as those developed by Almeida and Galeão [34].

Finally, in Fig. 15 we depict a comparison between our multifield GLS results and the results of Kim et al. [32] for the axial velocity in the contraction plane (Fig. 15($a$)) and in the symmetry axis (Fig. 15($b$)), both in the axisymmetric geometry. These results were obtained employing Re=2, Cu=100, and $n=0.4$. We may detect a discrepancy in the centerline velocity profile, which is more abrupt for Kim et al. [32], probably due to the fact that the mesh employed by those authors is much coarser in the $x_1$ direction near the contraction than ours. Despite that, the results may be assumed to be in good agreement.

## 5 Final Remarks

We have investigated a three-field GLS formulation for generalized Newtonian fluid flows. Such formulation allows the use of simple combinations of finite elements, circumventing the compatibility conditions between extra-stress, velocity, and pressure approximations. Numerical results employing Lagrangian quadrilateral equal-order interpolations were presented, performing code verification and investigating some features of shear-thinning and shear-thickening flow dynamics. The GLS method was efficient in the stabilization of advection dominant flow regions, which occur mainly due to viscosity decrease in regions of high strain rates. Such regions are characterized by steep gradients in velocity, extra stress, and viscosity fields, which were satisfactorily dealt by the GLS method. For flows of Carreau fluids through planar and axisymmetric contractions, the multifield GLS method was able to capture stably the shear-thinning features, as the flattening of the axial velocity profiles in the contraction plane and the reduction in pressure drop due to viscosity decay. Besides, the GLS formulation employed in this article may be used as a first step in the development of a GLS formulation for the approximation of differential viscoelastic fluid models.


## Acknowledgment

F.Z. thanks CAPES (2002-2006) and MCT/CNPq (Proc. 154619/2006-0) for the grants provided. S.F. thanks MCT/CNPq Grant No. 50747/1993-8. They also acknowledge MCT/CNPq for the financial support provided by Projects No. 477063/2004-7 and 472094/2006-8


## Nomenclature

$A$ = global node
$B$ = GLS functional
$C^0$ = space of continuous functions
Cu = Carreau number
$\mathbf{D}$ = strain rate tensor
$D_h$ = hydraulic dyameter
div = divergence operator
$D_t$ = material derivative
$\mathbf{E}$ = matrix of stress terms
$\mathbf{f}$ = body force
$F$ = GLS functional
$\mathbf{F}$ = momentum load vector
$\mathbf{G}$ = incompressibility matrix
grad = gradient operator
$\mathbf{H}$ = matrix of coupling between velocity and stress
$H^1$ = Sobolev functional space
$h_K$ = element size
$\mathbf{I}$ = unit tensor
$\mathbf{J}$ = Jacobian matrix
$K$ = consistency index in the power-law model
$\mathbf{K}$ = momentum diffusive matrix
$L$ = characteristic length
$L^2$ = Hilbert functional space
$\mathbf{M}$ = matrix of stabilization terms
$\mathbf{N}$ = momentum advective matrix
$\mathbf{n}$ = outward unit vector
$n$ = power-law index
$N_A$ = shape function for global node $A$
$\mathbf{P}$ = matrix of stabilization terms
$p$ = pressure field
$P$ = pressure functional space
$Q$ = Lagrangian quadrilateral element
$q$ = pressure weighting function
$r$ = dimensionless position
$\mathbf{R}$ = residual vector
Re = Reynolds number
$R_k$ = polynomial functional space of degree $k$
$\mathbf{S}$ = stress weighting function
$\mathbf{T}$ = stress tensor
$\mathbf{t}$ = stress vector
tr = trace operator
$\mathbf{u}$ = admissible velocity field
$u$ = velocity vector components
$u_0$ = characteristic velocity
$\mathbf{V}$ = velocity functional space
$\mathbf{v}$ = virtual velocity field
$\mathbf{W}$ = extra-stress functional space
$x$ = dimensionless position
$y$ = dimensionless position

$\mathcal{B}$ = mechanical body
$\mathcal{R}$ = set of real numbers
$\boldsymbol{\mathcal{U}}$ = vector of degrees of freedom
$|\cdot|_p$ = $p$-norm on $\mathcal{R}^N$

**Greek Symbols**

$\alpha$ = GLS stability parameter
$\beta$ = GLS stability parameter
$\chi$ = positive constant scalar
$\delta$ = GLS stability parameter
$\varepsilon$ = GLS stability parameter
$\dot{\gamma}_c$ = characteristic shear rate
$\dot{\gamma}$ = magnitude of tensor $\mathbf{D}$
$\Gamma$ = domain boundary
$\eta$ = viscosity function
$\eta_0$ = zero shear rate viscosity
$\eta_\infty$ = infinite shear rate viscosity
$\lambda$ = time constant
$\rho$ = mass density
$\tau$ = extra-stress components
$\boldsymbol{\tau}$ = extra-stress tensor
$\Omega$ = problem domain
$\Omega^h$ = finite element partition
$\Omega_K$ = element domain
$\xi$ = upwind function

**Subscripts**

$\alpha$ = GLS stabilized matix
$g$ = Dirichlet boundary condition
$h$ = Neumann boundary condition
$K$ = finite element

**Superscripts**

$h$ = finite element approximation
$N$ = number of space dimensions
$*$ = dimensionless

## References


[1] Franca, L. P., and Stenberg, R., 1991, "Error Analysis of Some Galerkin Least Squares Methods for the Elasticity Equations," SIAM (Soc. Ind. Appl. Math.) J. Numer. Anal., **28**(6), pp. 1680–1697.
[2] Owens, R. G., and Phillips, T. N., 2002, *Computational Rheology*, Imperial College, London, UK.
[3] Marchal, J. M., and Crochet, M. J., 1986, "Hermitian Finite Elements for Calculating Viscoelastic Flow," J. Non-Newtonian Fluid Mech., **20**, pp. 187–207.
[4] Marchal, J. M., and Crochet, M. J., 1987, "A New Mixed Finite Element for Calculating Viscoelastic Flow," J. Non-Newtonian Fluid Mech., **26**, pp. 77–114.
[5] Fortin, M., and Pierre, R., 1989, "On the Convergence of the Mixed Method of Crochet and Marchal for Viscoelastic Flows," Comput. Methods Appl. Mech. Eng., **73**, pp. 341–350.
[6] Ruas, V., Carneiro de Araujo, J. H., and Silva Ramos, M. A. M., 2004, "Multi-Field Finite Element Methods With Discontinuous Pressures for Axisymmetric Incompressible Flow," J. Comput. Appl. Math., **168**, pp. 393–402.
[7] Behr, M., Franca, L. P., and Tezduyar, T. E., 1993, "Stabilized Finite Element Methods for the Velocity-Pressure-Stress Formulation of Incompressible Flows," Comput. Methods Appl. Mech. Eng., **104**, pp. 31–48.
[8] Franca, L. P., and Frey, S., 1992, "Stabilized Finite Element Methods: II. The Incompressible Navier-Stokes Equations," Comput. Methods Appl. Mech. Eng., **99**, pp. 209–233.
[9] Baaijens, F. P. T., 1998, "Mixed Finite Element Analysis for Viscoelastic Flow Analysis: A Review," J. Non-Newtonian Fluid Mech., **79**, pp. 361–385.
[10] Bonvin, J., Picasso, M., and Stenberg, R., 2001, "GLS and EVSS Methods for a Three-Field Stokes Problem Arising From Viscoelastic Flows," Comput. Methods Appl. Mech. Eng., **190**, pp. 3893–3914.
[11] Crochet, M. J., and Keunings, R., 1982, "Finite Element Analysis of Die Swell of a Highly Elastic Fluid." J. Non-Newtonian Fluid Mech., **10**, pp. 339–356.
[12] Coronado, O. M., Arora, D., Behr, M., and Pasquali, M., 2006, "Four-Field Galerkin/Least-Squares Formulation for Viscoelastic Fluids," J. Non-Newtonian Fluid Mech., **140**, pp. 132–144.
[13] Guénette, R., and Fortin, M., 1995, "A New Mixed Finite Element Method for Computing Viscoelastic Flows," J. Non-Newtonian Fluid Mech., **60**, pp. 27–52.
[14] Sun, J., Smith, M. D., Armstrong, R. C., and Brown, R. A., 1999, "Finite Element Method for Viscoelastic Flows Based on the Discrete Adaptative Viscoelastic Stress Splitting and the Discontinuous Galerkin Method: DAVSS-G/DG," J. Non-Newtonian Fluid Mech., **86**, pp. 281–307.
[15] Gatica, G. N., González, M., and Meddahi, S., 2004, "A Low-Order Mixed Finite Element Method for a Class of Quasi-Newtonian Stokes Flows. Part I: A Priori Error Analysis," Comput. Methods Appl. Mech. Eng., **193**, pp. 881–892.
[16] Hughes, T. J. R., Franca, L. P., and Balestra, M., 1986, "A New Finite Element Formulation for Computational Fluid Dynamics: V. Circumventing the Babuska-Brezzi Condition: A Stable Petrov-Galerkin Formulation of the Stokes Problem Accomodating Equal-Order Interpolations." Comput. Methods Appl. Mech. Eng., **59**, pp. 85–99.
[17] Gurtin, M. E., 1981, *An Introduction to Continuum Mechanics*, Academic, New York.
[18] Ferguson, J., and Kemblowski, Z., 1991, *Applied Fluid Rheology*, Cambridge University Press, Cambridge.
[19] Tanner, R. I., 1988, *Engineering Rheology*, Clarendon, Oxford, UK.
[20] Astarita, G., and Marrucci, G., 1974, *Principles of Non-Newtonian Fluid Mechanics*, McGraw-Hill, UK.
[21] Bird, R. B., Armstrong, R. C., and Hassager, O., 1987, *Dynamics of Polymeric Liquids*, Wiley, New York.
[22] Carreau, P. J., 1968, Ph.D. thesis, University of Wisconsin, Madison.
[23] Ciarlet, P. G., 1978, *The Finite Element Method for Elliptic Problems*, North-Holland, Amsterdam.
[24] Hughes, T. J. R., 1987, *The Finite Element Method: Linear Static and Dynamic Finite Element Analysis*, Prentice-Hall, Englewood Cliffs, NJ.
[25] Dahlquist, G., and Bjorck, A., 1969, *Numerical Methods*, Prentice-Hall, Englewood Cliffs, NJ.
[26] Ghia, U., Ghia, K. N., and Shin, C. T., 1982, "Hi-Re Solution for Incompressible Flow Using the Navier-Stokes Equations and the Multigrid Method." J. Comput. Phys., **48**, pp. 387–411.
[27] Schreiber, R., and Keller, H. B., 1983, "Driven Cavity Flows by Efficient Numerical Techniques," J. Comput. Phys., **49**, pp. 310–333.
[28] Ku, H. C., and Hatziavramidis, D., 1985, "Solutions of the Two Dimensional Navier-Stokes Equations by Chebyshev Expansion Methods," Comput. Fluids, **13**, pp. 99–113.
[29] Sivaloganathan, S., and Shaw, G. J., 1988, "A Multigrid Method for Recirculating Flows," Int. J. Numer. Methods Fluids, **8**, pp. 417–440.
[30] Jurjevic, R., 1999, "Modelling of Two-Dimensional Laminar Flow Using Finite Element Method," Int. J. Numer. Methods Fluids, **31**, pp. 601–626.
[31] Neofytou, P., 2005, "A 3rd Order Upwind Finite Volume Method for Generalized Newtonian Fluid Flows," Adv. Eng. Software, **36**, pp. 664–680.
[32] Kim, M. E., Brown, R. A., and Armstrong, R. C., 1983, "The Roles of Inertia and Shear-Thinning in Flow of an Inelastic Liquid Through an Axisymmetric Sudden Contraction," J. Non-Newtonian Fluid Mech., **13**, pp. 341–363.
[33] Brooks, A. N., and Hughes, T. J. R., 1982, "Streamline Upwind/Petrov-Galerkin Formulations for Convective Dominated Flows With Particular Emphasis on the Incompressible Navier-Stokes Equations," Comput. Methods Appl. Mech. Eng., **32**, pp. 199–259.
[34] Almeida, R. C., and Galeão, A. C., 1999, "An Adaptive Petrov-Galerkin Formulation for the Compressible Euler and Navier-Stokes Equations," Comput. Methods Appl. Mech. Eng., **129**, pp. 157–176.

# Numerical and Experimental Study on Metal Organic Vapor-Phase Epitaxy of InGaN/GaN Multi-Quantum-Wells

**Changsung Sean Kim**
**Jongpa Hong**
**Jihye Shim**
**Bum Joon Kim**
**Hak-Hwan Kim**
**Sang Duk Yoo**
**Won Shin Lee**

Corporate R&D Institute CAE Group,
SAMSUNG Electro-Mechanics Co. Ltd.,
Suwon, Gyunggi-Do 443-743, Korea

*A numerical and experimental study has been performed to characterize the metal organic vapor-phase epitaxy (MOVPE) growth of InGaN/GaN multi-quantum-wells. One of the major objectives of the present study is to predict the optimal operating conditions that would be suitable for the fabrication of GaN-based light-emitting diodes using three different reactors, vertical, horizontal, and planetary. Computational fluid dynamics (CFD) simulations considering gas-phase chemical reactions and surface chemistry were carried out and compared with experimental measurements. Through a lot of CFD simulations, the database for the multiparametric dependency of indium incorporation and growth rate in InGaN/GaN layers has been established in a wide range of growth conditions. Also, a heating system using radio frequency power was verified to obtain the uniform temperature distribution by simulating the electromagnetic field as well as gas flow fields. The present multidisciplinary approach has been applied to the development of a novel-concept MOVPE system as well as performance enhancement of existing commercial reactors.* [DOI: 10.1115/1.2956513]

*Keywords: metal organic vapor-phase epitaxy, InGaN, multi-quantum-well, light-emitting diode, surface chemistry, radio frequency power, electromagnetic field*

## Introduction

Light-emitting diodes (LEDs) have recently attracted more attention as a potential alternative of incandescent bulbs and fluorescent lamps, expecting an emerging market of general lighting. LEDs have promising advantages over existing electric light bulbs. It has been noted that the typical life span of LEDs is about 10 years, twice as long as fluorescent lamps and approximately 20 times longer than the incandescent bulbs. LEDs generate much less thermal energy than incandescent bulbs with the same light output. LEDs are also free of environmental pollutants such as neon, helium, and argon discharged from fluorescent lamps. Lighting modules with combination of red, green, and blue LEDs can emit light of an intended color without additional color filters that traditional lighting methods adopt.

One of most popular white LED technologies is the use of a GaN-based blue LED and an yttrium aluminum garnet (YAG) phosphor because of its noticeable characteristics of small size, light weight, and easy operation [1]. As an alternative approach, we have investigated the combination of discrete red, green, and blue LEDs in order to realize a high efficacy white LED. Compared to red and blue LEDs, green LED still leaves much more room for improvement in luminescent efficacy. The production of green LEDs by metal organic vapor-phase epitaxy (MOVPE) is closely related to the ability to grow InGaN/GaN multi-quantum-wells (MQWs) with high indium compositions. A conventional MOVPE process of Group-III-nitride compounds in a simple reactor is illustrated in Fig. 1. At inlet, Group-III precursors and ammonia as Group-V precursor are introduced into the reactor to build up the epitaxial layers including the InGaN/GaN MQWs, as depicted in Fig. 2. Typically, the thickness of GaN layer is 10–20 nm and that of InGaN layer is 3 nm, respectively. Each layer grows on the wafer at an elevated temperature due to the heater coil under the susceptor. Atomic incorporation occurs from the adsorption layer into the crystal. The growth rate of the crystal can be assumed as the net difference between the adsorption and desorption rates.

A high quality of the growing material is normally promoted by the use of elevated temperatures and pressures in the growth reactor. Under the growth condition of high temperature and high pressure, a high efficiency of indium incorporation becomes a challenging task. Elevated temperatures enhance strongly indium desorption, whereas high pressures may intensify the formation of indium particles in the gas phase due to higher partial pressure of gaseous indium.

Indium surface segregation and compositional fluctuation in InGaN/GaN MQW heterostructures have been studied to identify the mechanism of light emission from nitride-based blue or green LEDs [2–7]. In order to suppress the indium segregation near the InGaN/GaN interfaces during the growth of In-rich InGaN layer, a growth interruption method [2–4] has been introduced before GaN capping, and then the quality of In-rich InGaN layer was greatly improved. During the measurement of phase segregation in InGaN quantum wells, the fluctuations were found to be between 10 nm and 20 nm in size and up to 20% on either side of the average composition [5]. Numerical predictions proposed to find possible ways for improvement of the quantum well composition uniformity were discussed [6–8]. This numerical model was validated by comparing the theoretical predictions with the data on composition profiles in GaN/InGaN/AlGaN quantum well

Contributed by the Fluids Engineering Division of ASME for publication in the JOURNAL OF FLUIDS ENGINEERING. Manuscript received April 3, 2007; final manuscript received July 12, 2007; published online July 30, 2008. Assoc. Editor: Dennis Siginer. Paper presented at the 5th Joint ASME/JSME Fluids Engineering Conference, San Diego, CA, July 30–August 2, 2007.

  

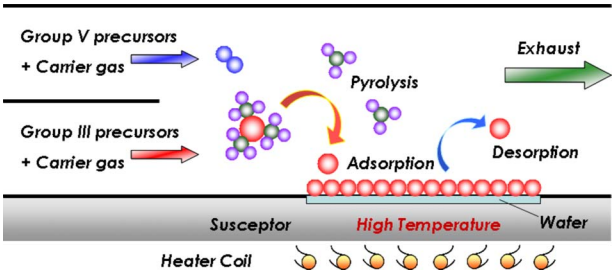


**Fig. 1 Schematic of a classical MOVPE process for Group-III-nitride semiconductors**

heterostructure. The comparison showed that the theoretical model reproduces quite well the lower interface of a quantum well.

In the present study, we have studied the characterization of three different commercial MOVPE reactors through both numerical and experimental approaches. Numerical simulations considering thermofluid dynamics, gas-phase chemical reactions, and chemical deposition on the surface have been validated by comparing with experimental data. Also, optimal speed of susceptor rotation was predicted for the temperature uniformity on the wafer due to the radio frequency (rf) induction heating.

## Numerical Approach

**Governing Equations.** Computational fluid dynamics (CFD) simulations considering gas-phase chemical reactions and surface chemistry were carried out to establish the database on multiparametric dependency of indium incorporation and well thickness in a wide range of growth conditions. Governing equations are three-dimensional Navier–Stokes equations with vapor-phase chemical reactions:

$$\frac{D\rho}{Dt} + \rho\frac{\partial U_i}{\partial x_i} = 0 \tag{1}$$

$$\rho\frac{\partial U_j}{\partial t} + \rho U_i\frac{\partial U_j}{\partial x_i} = -\frac{\partial P}{\partial x_j} - \frac{\partial \tau_{ij}}{\partial x_i} + \rho g_j$$

$$\rho c_\mu\frac{\partial T}{\partial t} + \rho c_\mu U_i\frac{\partial T}{\partial x_i} = -P\frac{\partial U_i}{\partial x_i} + \lambda\frac{\partial^2 T}{\partial x_i^2} - \tau_{ij}\frac{\partial U_j}{\partial x_i} \tag{2}$$

where

$$\tau_{ij} = -\mu\left(\frac{\partial U_j}{\partial x_i} + \frac{\partial U_i}{\partial x_j}\right) + \frac{2}{3}\delta_{ij}\mu\frac{\partial U_k}{\partial x_k} \tag{3}$$

For an example of InGaN growth, trimethylindium (TMIn), triethylgallium (TEGa), and ammonia are used as the indium, gallium, and nitrogen precursors, respectively. The following vapor-phase chemical reactions are coupled with the above equations:

$$\mathrm{TMIn} \rightarrow \mathrm{MMIn} + 2\mathrm{CH_3} \tag{4}$$

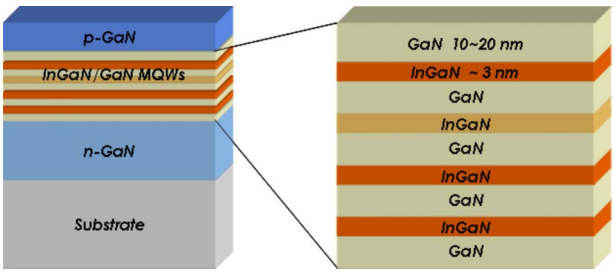


**Fig. 2 Epitaxial structure of LED with InGaN/GaN MQWs**

$$\mathrm{MMIn} \rightarrow \mathrm{In} + \mathrm{CH_3} \tag{5}$$

$$\mathrm{TEGa} + \mathrm{NH_3} \rightarrow \mathrm{TEGaNH_3} \tag{6}$$

$$\mathrm{TEGaNH_3} \rightarrow \mathrm{TEGa} + \mathrm{NH_3} \tag{7}$$

$$\mathrm{TMIn} + \mathrm{NH_3} \leftrightarrow \mathrm{TMInNH_3} \tag{8}$$

$$\mathrm{TEGa} \rightarrow \mathrm{Ga} + 3\mathrm{C_2H_5} \tag{9}$$

where the reaction constants of Eqs. (4)–(9) were determined by experimental measurements [7] and quantum mechanics calculations based on variational transition state theory [9,10]. The governing equations coupled with vapor-phase chemical reactions were solved with a finite volume method using a commercial flow solver well known as CFD-ACE+ [11]. For spatial discretization, a second-order upwind-difference scheme was adopted with limiters. For time integration for velocity solutions, the linear equation solver was the conjugate gradient squared (CGS) algorithm with preconditioning with 50 sweeps and a convergence criterion of 0.0001. The algebraic multigrid solver with 50 sweeps and a convergence criterion of 0.1 were also used for the other properties. This numerical approach can predict growth rates of GaN and InGaN layers as well as gallium and indium compositions in each layer by implementing the chemical vapor deposition (CVD) module [12] into the flow solver.

**Modeling of Surface Chemistry.** In the CVD module [12] released by STR Inc., the surface chemistry based on the quasithermodynamics approach was modified to consider the surface kinetics of Group-III nitrides [6]. A temperature dependent sticking/evaporation coefficient of molecular nitrogen on Group-III-nitride surfaces was implemented into the quasiequilibrium model of the molecular beam epitaxy (MBE) growth process. The values of the sticking coefficients were extracted from independent experimental data on Langmuir evaporation of binary nitrides in vacuum. The adsorption/desorption process can be described by using the Hertz–Knudsen equations that the net adsorption rate of the $i$th species at the surface can be expressed as

$$J_i = \alpha_i\beta_i(p_i - p_i^0) \tag{10}$$

where $\alpha_i$ is the sticking/evaporation coefficient accounting for kinetic limitations in the adsorption/desorption process, $\beta_i = (2\pi m_i kT)^{-1/2}$ is the Hertz–Knudsen factor for the $i$th species, $p_i$ is the partial pressure of the $i$th species, near the growing surface, and $p_i^0$ is the equilibrium partial pressure of the $i$th species, which corresponds to the saturated vapor pressure of the species over its solid phase. The adsorption/desorption kinetics of ammonia and nitrogen on/from the surface of growing crystal can be considered by introducing the sticking coefficients of these species into the model. Regarding the interaction of nitrogen with the surfaces of Group-III nitrides, the nitrogen sticking coefficients were extracted from the independent experiments and evaluated as a function of temperature [13]. The approximate value of the ammonia sticking coefficient of 0.04 was measured in Ref. [14]. The sticking coefficients of all the other species are given by unity in the present study.

For modeling of InGaN growth at the surface, the experimental data were taken from Ref. [7] and the following independent heterogeneous reactions are considered as follows:

$$\mathrm{TEGa}(g) + \mathrm{NH_3}(g) = \mathrm{GaN}(s) + 3\mathrm{C_2H_5}(g) + 1.5\mathrm{H_2}(g) \tag{11}$$

$$\mathrm{TMIn}(g) + \mathrm{NH_3}(g) = \mathrm{InN}(s) + 3\mathrm{CH_4}(g) \tag{12}$$

$$2\mathrm{GaN}(s) = 2\mathrm{Ga}(g) + \mathrm{N_2}(g) \tag{13}$$

$$2\mathrm{InN}(s) = 2\mathrm{In}(g) + \mathrm{N_2}(g) \tag{14}$$

$$2\mathrm{Ga}(g) + \mathrm{H_2}(g) = 2\mathrm{GaH}(g) \tag{15}$$

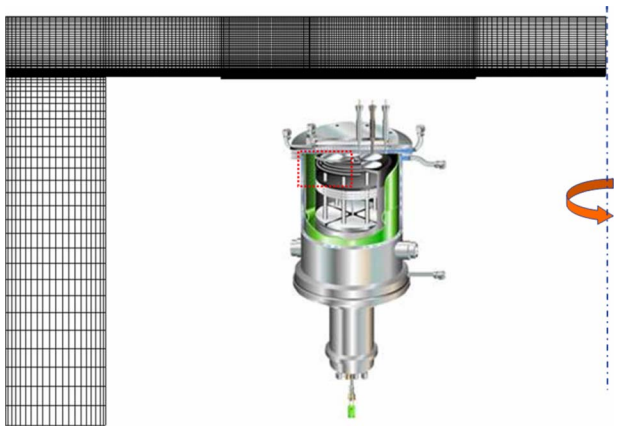

**Fig. 3 Two-dimensional axisymmetric modeling of a vertical MOVPE reactor (Thomas Swan CCS reactor, 6×2 in. wafers)**

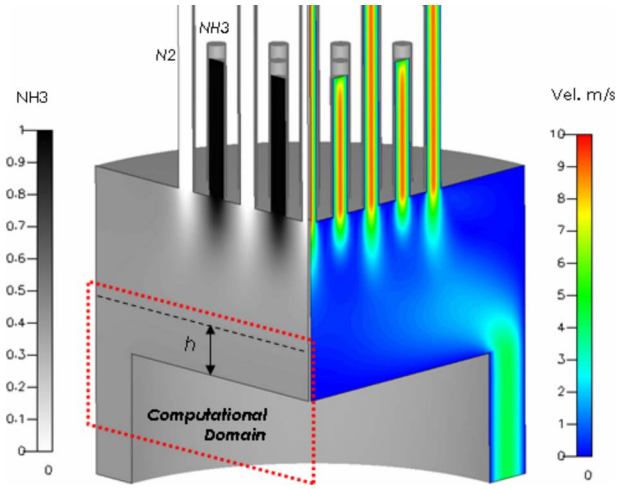


**Fig. 4 Three-dimensional simulation for prediction of mixing layer thickness of ammonia (black) and nitrogen (white)**

$$2\mathrm{In}(g) + \mathrm{H}_2(g) = 2\mathrm{InH}(g) \tag{16}$$

$$2\mathrm{NH}_3(g) = \mathrm{N}_2(g) + 3\mathrm{H}_2(g) \tag{17}$$

More detailed information on the basic principle and assumptions of the surface chemistry modeling for Group-III nitrides can be found in previous studies [6,12].

## Experimental Approach

Various growth experiments have been performed in commercial MOVPE reactors to understand the growth mechanism of Group-III nitrides. After heating the rf coil up to the desired growth temperature, TMIn, trimethylgallium (TMGa), and TEGa as group-III precursors, along with 100% ammonia as Group-V sources, were introduced into the reactor to grow the InGaN/GaN MQWs following *n*-GaN layer on 0.2 deg tilted sapphire (0001) substrates. The temperature of substrate holder, so-called susceptor, was monitored and controlled using a near-infrared pyrometer.

For determination of growth rate and strain, the high resolution x-ray diffractometry (HXRD) was used. Also, indium compositions of InGaN layers were determined by photoluminescence (PL) spectroscopy using an excitation beam of a 266 nm frequency tripled Nd:YAG laser.

## Results and Discussion

**Vertical-Type Reactor.** A commercial MOVPE (i.e., Thomas Swan's close coupled showerhead, six wafers by 2 in. diameter) reactor was modeled and then simulated under a typical growth condition for In-rich InGaN/GaN MQW heterostructures. Trimethyl compounds of indium and gallium (i.e., TMIn and TMGa) are used as metal organic precursors and chemically react with 100% ammonia at a reactor pressure of 300 Torr and a growth temperature of 1003 K.

For computational efficiency, the reactor was modeled as two dimensional axisymmetric and the total grid size was 10,773 nodes, as shown in Fig. 3. The maximum normalized residual for convergence criterion was less than $10^{-4}$ in about 1000 iterations

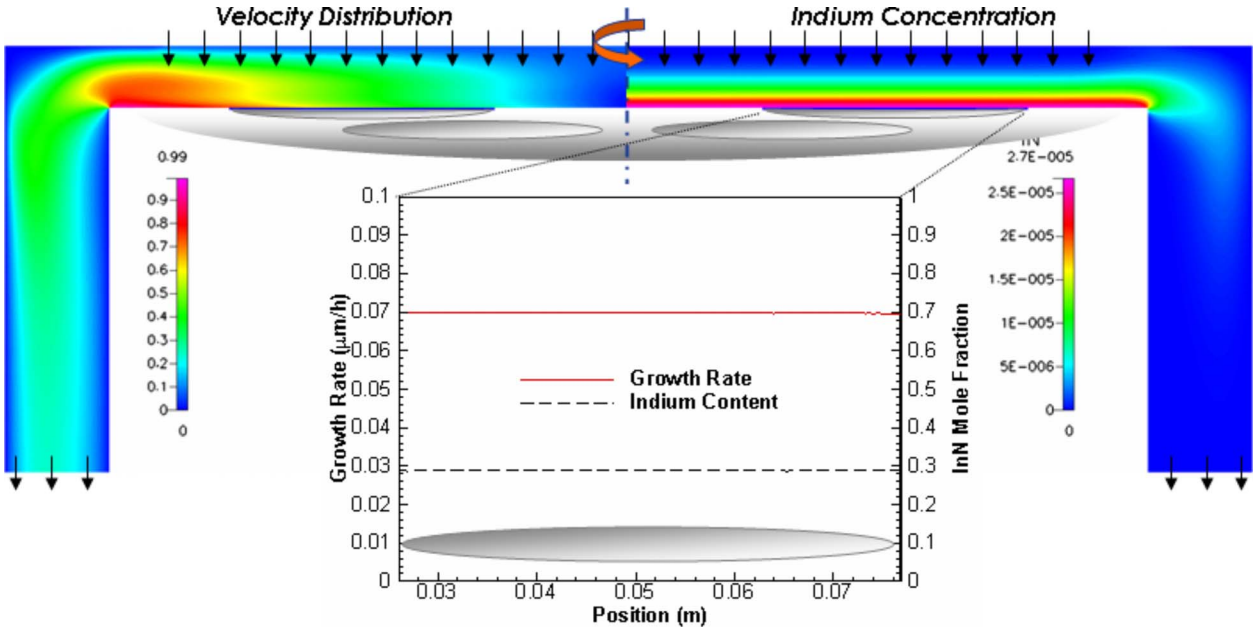


**Fig. 5 Contours of velocity magnitude and gas-phase indium distribution (top) and growth rate and indium content on a wafer surface (bottom)**

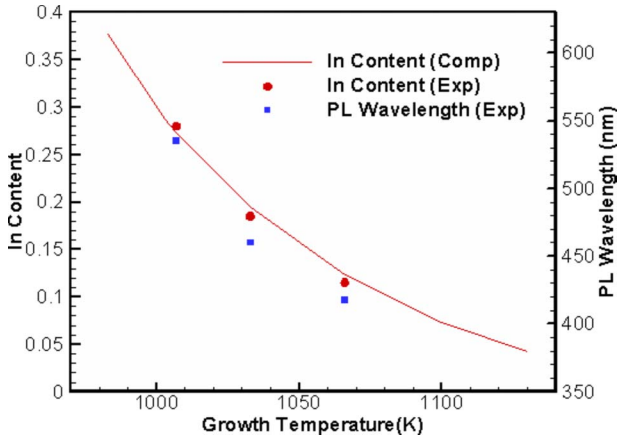


**Fig. 6 Comparison of computed and experimental data in indium content and PL wavelength in a wide range of growth temperature**

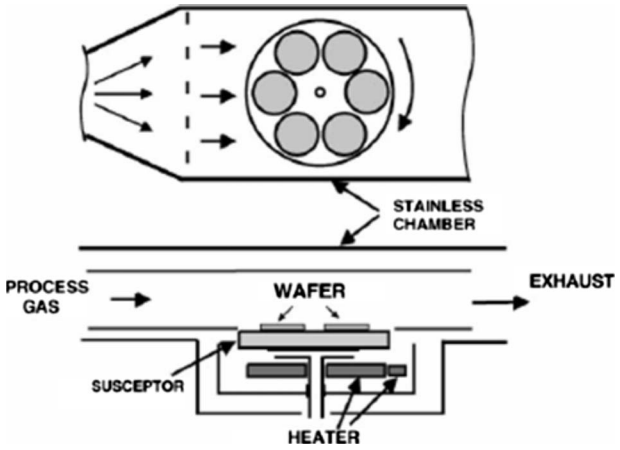


**Fig. 7 Schematic drawing of horizontal multiwafer MOVPE reactor (Nippon Sanso SR6000, Tokunaga et al. [15])**

and the elapsed time was 5500 s on an HP Workstation xw8200 with 3.6 GH CPU. Ammonia and carrier gases (nitrogen and/or hydrogen) are introduced into the reactor through numerous separate inlet holes in order to avoid prereactions outside the reactor chamber. It costs a lot of time and effort to numerically model the whole system including those inlet holes. Thus, a local computational domain was considered as defined in the diamond-shaped box since we noticed that the mixing layers of ammonia and nitrogen are fully developed not far from their inlets, as simulated in Fig. 4. For a simple test to predict the approximate thickness of mixing layers, only two dozens of inlet holes were modeled without considering susceptor rotation. Actually the mixing layer thickness was quite smaller than the height of the reactor chamber.

However, instead of full modeling of inlet pipes, we have included the surface chemistry and susceptor rotation for final results, as shown in Fig. 5. A uniform layer of high-concentration vapor-phase indium is observed on the high-temperature susceptor. Because of the susceptor rotation, the magnitude of velocity increases along with the susceptor radius. It was found that the susceptor rotation of 100 rpm results in a higher uniformity of growth rate and indium composition on wafer. Predicted values of growth rate and indium composition are 1.17 nm/min and 28.8%, respectively. Compared to experimental measurements, simulation results give over 90% accuracy for the growth rate as well as the indium composition. For a wide range of growth temperature, computed results of indium composition show quite a good agreement with experimental data, as shown in Fig. 6. It was also noticed that (PL) wavelength shows a similar tendency with the indium content, which has been well proved in many experimental measurements.

**Horizontal-Type Reactor.** Another commercial MOVPE system (SR6000, $6\times2$ in. wafers) has been developed by Nippon Sanso Co. and it has a horizontal-type reactor, as depicted in Fig. 7. This reactor was modeled with approximately 82,200 grid cells, as shown in Fig. 8. Since this reactor was not available in our affiliate, we simulated this reactor and then compared the computed results with the experimental measurements taken for Ref. [15]. They showed that uniformity and reproducibility of doping and film thickness were typically better than $\pm2\%$ across a full 2 in. wafer. PL peak wavelength uniformity was better than $450\pm7$ nm across a full 2 in. wafer. As already observed in Fig. 6, indium content shows quite a similarity with PL peak wavelength. The PL peak wavelength can be expressed as a function of

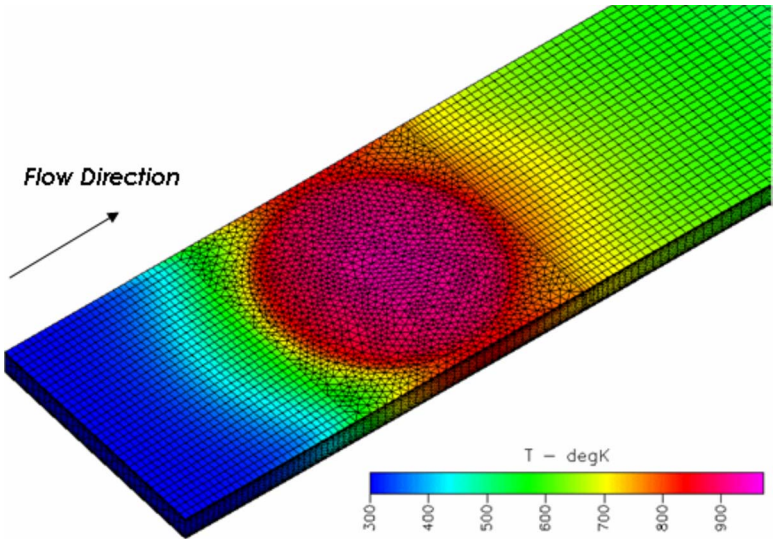


**Fig. 8 Three-dimensional modeling of horizontal MOVPE reactor (Nippon Sanso SR6000) and its temperature distribution during InGaN growth**

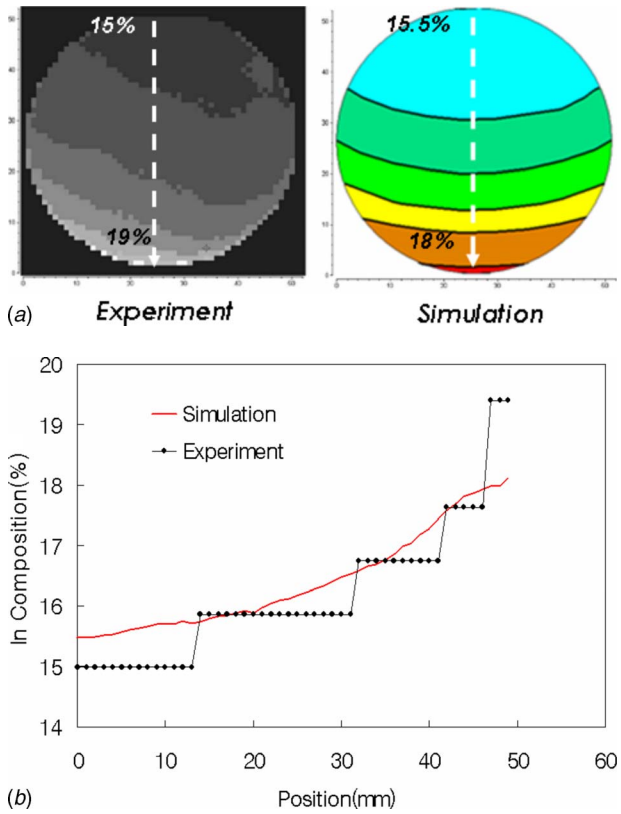


**Fig. 9 Comparison of experimental and computed indium distributions on a 2 in. full wafer; (*a*) contour lines of indium composition with the maximum and minimum values (left: experiment; right: simulation); (*b*) indium composition along a centerline**

thickness and indium composition of InGaN layer. Gain peak wavelength simulation showed the relationship as

$$\lambda_{PL}(\text{nm}) = 261.7 + 680.0X_{In} + 23.0t_{layer}(\text{nm}) \quad (18)$$

where $\lambda_{PL}$ is the peak wavelength, $X_{In}$ is the indium composition, and $t_{layer}$ is the thickness of the InGaN layer.

The PL mapping result was converted into indium composition contour lines, and then compared, as shown in Fig. 9. Computed indium distribution on a 2 in. full wafer shows a good agreement with converted experimental data. Simulation shows the minimum maximum range of 15.5–18% indium composition, whereas experimental measurement shows approximately 15–19% in Fig. 9(*a*). For the indium composition along the centerline, the simulation shows a good agreement with experimental data, as shown in Fig. 9(*b*).

**Planetary Reactor.** In addition, a large-scaled commercial MOVPE (AIXTRON's planetary multiwafer, 2 in.×11 wafers)

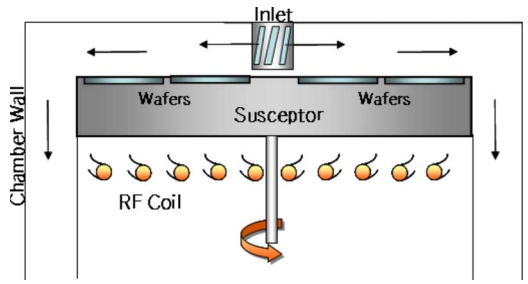


**Fig. 10 Schematic drawing of a planetary MOCVD reactor**

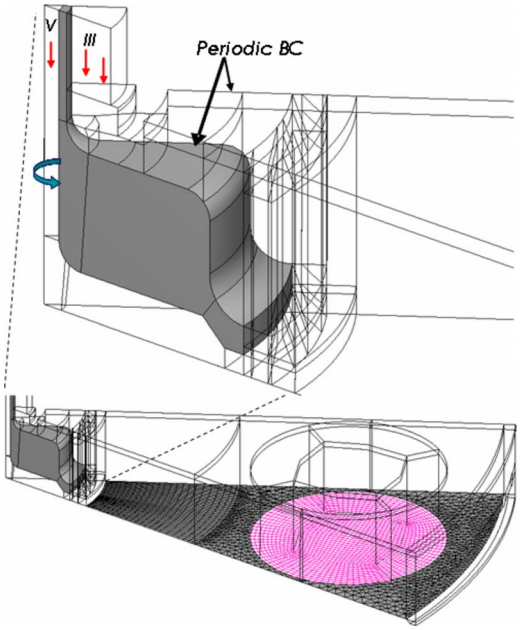


**Fig. 11 Three-dimensional modeling for one-eleventh of the whole reactor with centrifugal inlet nozzles (AIXTRON planetary reactor, 11×2 in.)**

system was also simulated to investigate the high-temperature flow field in the planetary reactor, as depicted in Fig. 10. The growth temperature for the InGaN layer was given by 750°C and the reactor pressure was maintained as 300 Torr. Independent of the main susceptor rotation, each wafer holder was designed to self-rotate by 50 rpm in order to improve the uniformity of growth rate and composition distribution at high-temperature conditions. Group-V precursors such as 100% ammonia and the trimethyl compounds of gallium and indium are introduced into the reactor chamber through the two dozens of centrifugal inlet nozzles. For

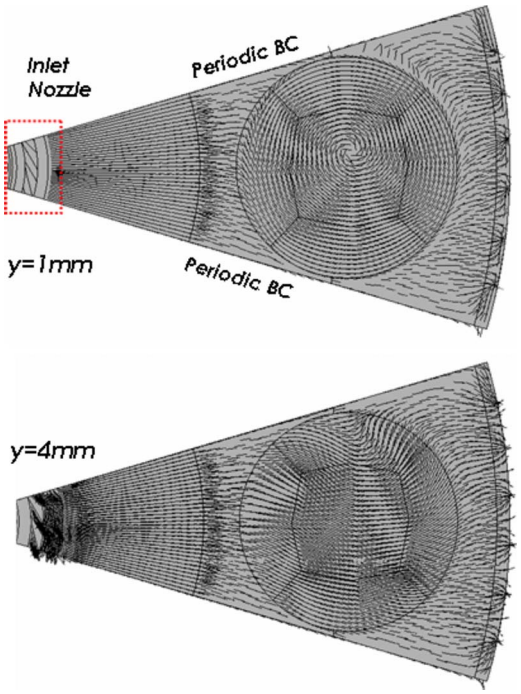


**Fig. 12 Velocity vectors on two planes at 1 mm and 4 mm above the susceptor with a wafer rotation of 50 rpm**

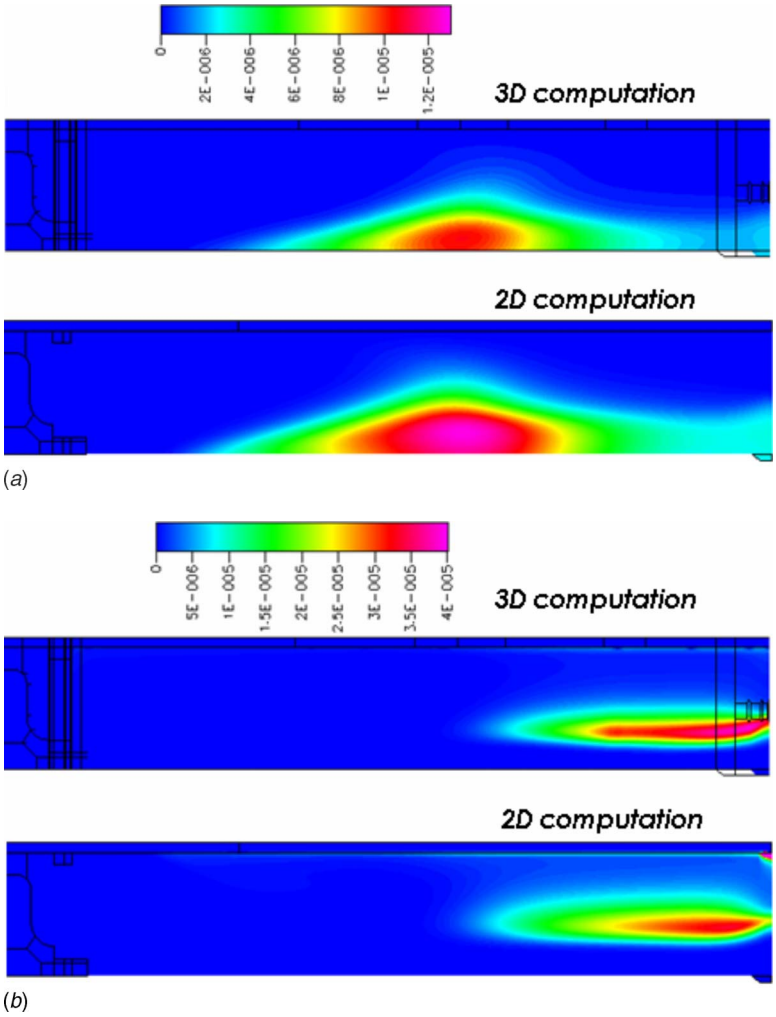


**Fig. 13 Comparison of two- and three-dimensional flow fields with and without wafer orientation; (*a*) contours of indium molar fraction; (*b*) contours of particle density of indium clusters**

computational efficiency, only one-eleventh of the entire domain with total 22,000 grid cells was modeled, as shown in Fig. 11. Rotating wall boundary conditions were imposed onto the wafer surfaces and periodic boundary conditions were given to both sides of the computational domain.

Figure 12 shows velocity vectors on both planes above the susceptor at 1 mm and 4 mm, respectively. Swirling vectors are also observed on the self-rotating wafer. The distributions of the indium molar fraction and particle density were obtained from both two- and three-dimensional approximations and then compared for the central cross section of the reactor. Three-dimensional modeling predicts somewhat lower indium concentration and higher particle density of indium clusters, as shown in Fig. 13. These differences attribute to self-rotation of each wafer in three-dimensional simulations. Because of the self-rotational motion, the flow residence time becomes longer, which promotes particle formation.

**RF Induction Heating.** Uniform temperature distribution around the susceptor is crucial in obtaining homogeneous MQWs with high indium composition. For a precise thermal control, heating methods using rf power have been widely adopted in MOVPE system. Thus, we have modeled and simulated inductance heating problems in a rf heater unit for 2 in. $\times$ six-wafer MOVPE reactor, as shown in Fig. 14.

Three-dimensional thermal flows in the same magnetic field were simulated for two cases with susceptor rotational speeds of 0 rpm and 5 rpm, as shown in Figs. 14(*a*) and 14(*b*), respectively. Operation gas was assumed nitrogen of 75 slm, magnetic field source was generated by 30 kHz ac in the copper coil, and current density is $1.75\times10^7$ A/m$^2$. For the stationary susceptor (i.e., no susceptor rotation), the front region has the lower-temperature distribution than the rear since the inlet flow of precursor gases cools down the front, as observed in Fig. 14(*a*). Along with the susceptor rotation, the difference between the maximum and minimum temperatures on the susceptor decreases, as shown in Fig. 15. It is found that the temperature uniformity within 3 °C standard deviation on all the wafers can be guaranteed with the minimal rotational speed of 5 rpm or more.

## Conclusion

Both numerical and experimental approaches have been carried out to characterize the MOVPE growth of InGaN/GaN MQW. Typical features of three different MOVPE reactors were simulated using CFD with vapor-phase chemical reactions and surface deposition. Those CFD simulations have been verified by comparing with experimental data for growth rate and indium composition of the InGaN layer in a wide range of growth temperature. Some rf induction heating simulations were also conducted to predict a minimal susceptor rotating speed of 5 rpm for uniform temperature distribution. The present approach combining numeri-

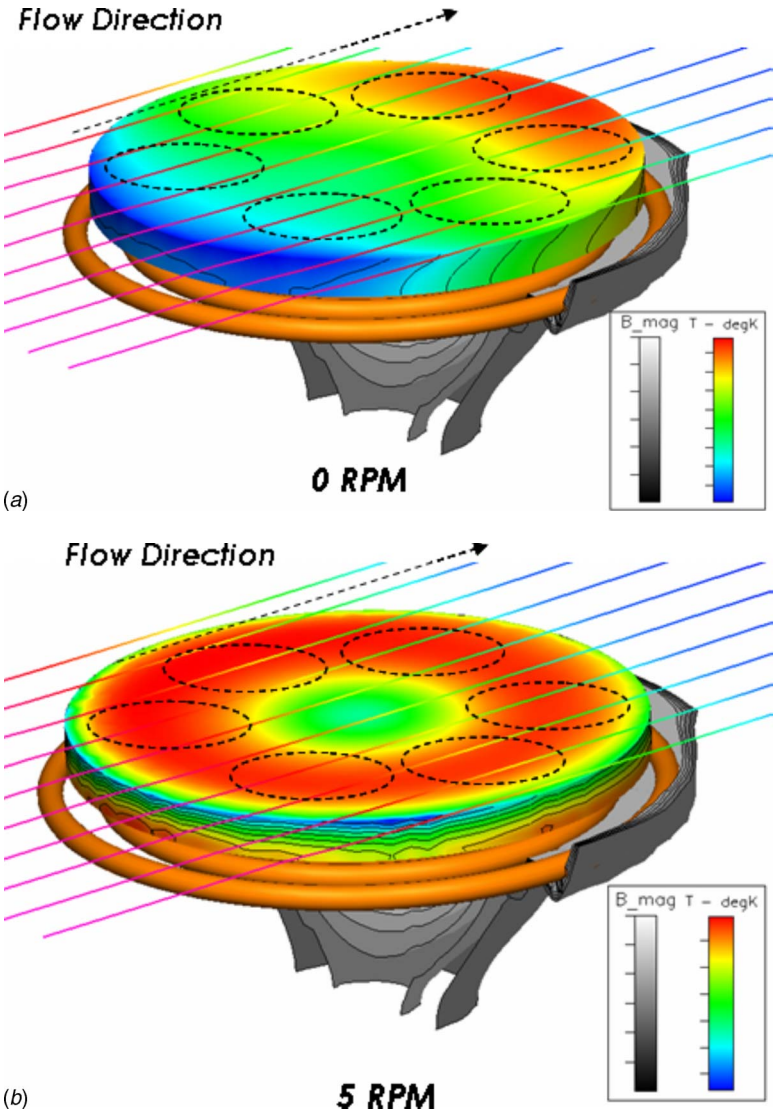


**Fig. 14 Temperature (color-scale) and magnetic (gray-scale) fields of a rf heater with two different susceptor rotating speeds**

cal simulation based on CFD and experimental measurement has been successfully applied to the development of in-house metal organic chemical vapor deposition (MOCVD) system as well as the performance enhancement of existing commercial MOCVD reactors.

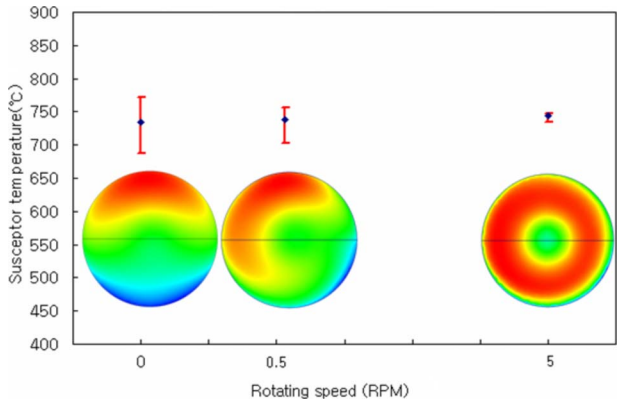


**Fig. 15 Temperature distribution on the susceptor with respect to rotating speed**


## Acknowledgment

The authors would like to thank Dr. Roman A. Talalaev and Eugene V. Yakovlev at Soft-Impact Ltd., Dr. Yuri Makarov at STR Inc., and Dr. Lada V. Yashina at Moscow State University for their technical support and discussion.


## Nomenclature

$c_\mu$ = specific heat
DMIn = dimethylindium
$k$ = Boltzmann constant
$m$ = mass of molecule, kg
MMIn = monomethylindium
$p$ = pressure, $N/m^2$
$t$ = time,
$T$ = temperature, K
$U, V, W$ = velocity vectors, m/s
$x, y, z$ = spatial coordinates, m

$\mu$ = fluid viscosity, kg/m s
$\rho$ = density, kg/m$^3$
$\tau$ = stress tensors

## References


[1] Nakamura, S., and Fasol, G., 1997, *The Blue Laser Diode*, Springer, Berlin.
[2] Moon, Y.-T., Kim, D.-J., Song, K.-M., Choi, C.-J., Han, S.-H., Seong, T.-Y., and Park, S.-J., 2001, "Effects of Thermal and Hydrogen Treatment on Indium Segregation in InGaN/GaN Multiple Quantum Wells," J. Appl. Phys., **89**(11), pp. 6514–6518.
[3] Cho, H. K., Lee, J. Y., Sharma, N., Humphreys, J., Yang, G. M., and Kim, C. S., 2001, "Structural and Optical Characteristics of InGaN/GaN Multiple Quantum Wells With Different Growth Interruption," Phys. Status Solidi B, **228**(1), pp. 165–168.
[4] Kwon, S.-Y., Kim, H. J., Na, H., Kim, Y.-W., Seo, H.-C., Kim, H. J., Shin, Y., Yoon, E., and Park, Y., 2006, "In-Rich InGaN/GaN Quantum Wells Grown by Metal-Organic Chemical Vapor Deposition," J. Appl. Phys., **99**, p. 044906.
[5] Duxbury, N., Bangert, U., Dawson, P., Thrush, E. J., Van der Stricht, W., Jacobs, K., and Moerman, I., 2000, "Indium Segregation in InGaN Quantum-Well Structures," Appl. Phys. Lett., **76**(12), pp. 1600–1602.
[6] Karpov, S. Yu., Prokofyev, V. G., Yakovlev, E. V., Talalaev, R. A., and Makarov, Yu. N., 1999, "Novel Approach to Simulation of Group-III Nitirdes Growth by MOVPE," MRS Internet J. Nitride Semicond. Res., **4**(4), pp. 1–7.
[7] Talalaev, R. A., Yakovlev, E. V., Karpov, S. Yu., Makarov, Yu. N., Schoen, O., Heuken, M., Strauch, G., and Juergensen, H., 1999, "Modeling of InGaN MOVPE in AIX 200 Reactor and AIX 2000 HT Planetary Reactor," MRS Internet J. Nitride Semicond. Res., **4**(5), pp. 1–5.
[8] Karpov, S. Yu., Talalaev, R. A., Evstratov, I. Y., and Makarov, Yu. N., 2002, "Indium Segregation Kinetics in MOVPE of InGaN-Based Heterostructures," Phys. Status Solidi A, **192**(2), pp. 417–423.
[9] Schmid, R., and Basting, D., 2005, "Gas Phase Chemistry in Gallium Nitride CVD: Theoretical Determination of the Arrhenius Parameters for the First Ga-C Bond Homolysis of Trimethylgallium," J. Phys. Chem. A, **109**(11), pp. 2623–2630.
[10] Kim, C. S., Shim, J., Hong, J., Moon, W. H., Ji, S.-Y., Yoon, Y. J., Kim, B. J., Park, S.-E., Han, J. W., and Lee, W. S., 2007, "Precise Composition Control of InGaN/GaN Multi Quantum Wells in Metal Organic Vapor Phase Epitaxy," SAMSUNG Journal of Innovative Technology, **3**(1), pp. 23–32.
[11] 2004, CFD-ACE+ V2004 Module Manual, Vol. 2, pp. 112–140.
[12] Karpov, S. Yu., 2003, "Advances in the Modeling of MOVPE Processes," J. Cryst. Growth, **248**, pp. 1–7.
[13] Averyanova, M. V., Przhevalsky, I. N., Karpov, S. Yu., Makarov, Yu. N., Ramm, M. S., and Talalaev, R. A., 1997, "Analysis of Vaporization Kinetics of Group-III Nitrides," Mater. Sci. Eng., B, **43**, pp. 167–171.
[14] Mesrine, M., Grandjean, N., and Massies, J., 1998, "Efficiency of NH3 as Nitrogen Source for GaN Molecular Beam Epitaxy," Appl. Phys. Lett., **72**(3), pp. 350–352.
[15] Tokunaga, H., Tan, H., Inaishi, Y., Arai, T., Yamaguchi, A., and Hidaka, J., 2000, "Performance of Multiwafer Reactor GaN MOCVD System," J. Cryst. Growth, **221**, pp. 616–621.

# Multiphysics Simulation of Electrochemical Machining Process for Three-Dimensional Compressor Blade

**Toshiaki Fujisawa**
Graduate School of Mechanical Engineering,
Tokyo University of Science,
1-14-6 Kudankita, Chiyoda-ku,
Tokyo 102-0073, Japan

**Kazuaki Inaba**

**Makoto Yamamoto**

Department of Mechanical Engineering,
Tokyo University of Science,
1-14-6 Kudankita, Chiyoda-ku,
Tokyo 102-0073, Japan

**Dai Kato**
Aero-Engine and Space Operations,
Ishikawajima-Harima Heavy Industries Co., Ltd.,
229 Tonogaya, Mizuho-machi, Nishitama-gun,
Tokyo 190-1297, Japan

*Electrochemical machining (ECM) is an advanced machining technology. It has been applied in highly specialized fields such as aerospace, aeronautics, and medical industries. However, it still has some problems to be overcome. The efficient tool design, electrolyte processing, and disposal of metal hydroxide sludge are the typical issues. To solve such problems, computational fluid dynamics is expected to be a powerful tool in the near future. However, a numerical method that can satisfactorily predict the electrolyte flow has not been established because of the complex nature of flows. In the present study, we developed a multiphysics model and the numerical procedure to predict the ECM process. Our model and numerical procedure satisfactorily simulated a typical ECM process for a two-dimensional flat plate. Next, the ECM process for a three-dimensional compressor blade was simulated. Through visualization of the computational results, including the multiphase flow, and thermal and electric fields between the tool and the blade, it is verified that the present model and numerical procedure could satisfactorily predict the final shape of the blade.* [DOI: 10.1115/1.2956596]

## Introduction

Electrochemical machining (below ECM) is one of advanced machining technologies. Gussef originally proposed and designed the ECM procedure in 1929. Since then, ECM has been developed and employed in highly specialized fields such as aerospace, aeronautics, defense, and medicine. In recent years, ECM has been used in the automobile and turbomachinery industries because it has no tool wear and can machine difficult-to-cut metals and complex geometries with relatively high accuracy and extremely smooth surfaces manufactured. However, ECM still has some problems with the efficient tool design, electrolyte processing, and disposal of metal hydroxide sludge. In order to solve these problems, a numerical simulation so-called computational fluid dynamics (CFD) is expected to be a powerful and helpful tool in the near future. In fact, authors such as Hourng and Chang [1], Chang and Hourng [2], Chang et al. [3], Filatov [4], Purcar et al. [5], Nied and Lamphere [6], Rajurkar et al. [7], Kozak [8], and Van Damme et al. [9] already developed numerical models and procedures and reported their findings in literature. However, a numerical code has not been established that can satisfactorily predict the machining process, including the thermal fields, electric fields, complex flow natures such as the generation of hydrogen bubbles and metal hydroxide sludge (i.e., three-phase effect), temperature increase by Joule heating, three dimensionality of the flow, and flow separation.

In the present study, we develop a multiphysics model and a numerical procedure to predict the three-phase and three-dimensional ECM process. First, multiphysics models and a numerical procedure for the ECM process were proposed. These were verified for a typical ECM process for a two-dimensional flat plate (i.e., two-dimensional channel). The numerical results indicate that the effects by Joule heating and hydrogen bubbles are dominant, whereas the effects of metal hydroxide sludge are negligible. Next, the model and numerical procedure were applied to the ECM process for fabricating a three-dimensional compressor blade. The present model and numerical procedure satisfactorily predicted the final shape of the blade. In addition, by using the computed results, the multiphase flow, thermal and electric fields between the tool and the blade were numerically visualized and investigated. The results indicate that multiphysics simulation is useful and essential for the prediction and analysis of an ECM process.

Contributed by the Fluids Engineering Division of ASME for publication in the JOURNAL OF FLUIDS ENGINEERING. Manuscript received April 20, 2007; final manuscript received December 10, 2007; published online July 30, 2008. Assoc. Editor: Paul Durbin. Paper presented at the 2007 ASME Fluids Engineering Division Summer Meeting and Exhibition (FEDSM2007), San Diego, CA, July–August 2, 2007.

## Numerical Procedures

**Governing Equations.** In the present study, the flow field was assumed to be incompressible, laminar, and three phase. That is, the electrolyte flow, hydrogen bubbles, and metal hydroxide sludge were considered. Moreover, Joule heating due to the electric field between the tool and the blade surface was considered. A one-way coupling method was adopted, because the void fractions are low on average and the two-way coupling method is time consuming and unavailable for the ECM process. Therefore, the flow field is governed by the equations of continuity, Navier–Stokes, energy, and transport of volume fractions of the hydrogen bubbles and metal hydroxide sludge. Neglecting buoyancy force and viscous dissipation, the governing equations can be expressed as follows:

$$\frac{\partial u_j}{\partial x_j} = 0 \tag{1}$$

$$\frac{\partial u_i}{\partial t} + u_j \frac{\partial u_i}{\partial x_j} = -\frac{1}{\rho}\frac{\partial p}{\partial x_i} + \nu \frac{\partial^2 u_i}{\partial x_j^2} \tag{2}$$

$$\frac{\partial T}{\partial t} + u_j \frac{\partial T}{\partial x_j} = \frac{\lambda}{\rho C_p}\frac{\partial^2 T}{\partial x_j^2} + \frac{I^2}{\rho C_p \kappa} \tag{3}$$

$$\frac{\partial \kappa}{\partial x_j}\frac{\partial E}{\partial x_j} + \kappa \frac{\partial^2 E}{\partial x_j^2} = 0 \tag{4}$$

  

$$\frac{\partial \alpha_i}{\partial t} + u_j \frac{\partial \alpha_i}{\partial x_j} = C_{\alpha i} \frac{\partial^2 \alpha_i}{\partial x_j^2} + \alpha_{gi} \tag{5}$$

The flow properties such as $\nu$, $\lambda$, and $C_p$ depend on the void fraction of hydrogen bubbles and the volumetric fraction of metal hydroxide sludge. We assumed a linear combination as

$$\phi = (1 - \alpha_{\text{hydrogen}} - \alpha_{\text{metal sludge}})\phi + \alpha_{\text{hydrogen}}\phi_{\text{hydrogen}} + \alpha_{\text{metal sludge}}\phi_{\text{metal sludge}} \tag{6}$$

where $\phi$ denotes the flow property.

These equations were discretized by the finite difference technique, using the explicit MAC method. The third-order upwind scheme was used for the convection terms, the second-order central difference scheme for other spatial terms, and the first-order Euler scheme for the temporal terms.

The time discretization is an important issue. There are two approaches in a multiphysics simulation. (1) One is a strongly coupling method. Considering an ECM process, in this method, the flow, thermal, electric, $H_2$, and metal sludge fields are simultaneously computed at every time step. To use this method, a high-order discretization scheme is necessary for the temporal terms. Since this method is too time consuming, it is not suitable for practical applications. (2) The other is a weakly coupling method. In this method, the flow, thermal, and electric fields are firstly computed, and then $H_2$ and metal sludge fields are estimated, based on the frozen flow, thermal, and electric fields. In other words, the ECM process is replicated by a series of quasisteady states. This assumption is justified by the fact that the timescales of flow and dissolution are quite different. Hence, we do not need a high-order discretization scheme for the temporal terms. However, in this method, much attention has to be paid to the number of quasisteady states (i.e., step number).

In the present study, we adopted a weakly coupling method. In order to find a step-number independent solution, we performed preliminary computations by changing the step number from about 40 to 90. Investigating the computational results, it was confirmed that we have to compute the flow, thermal, and electric fields every 10 s. Therefore, in the computations for a two-dimensional flat plate and a three-dimensional compressor blade described later, we adopted typically 70 steps.

**Metal Dissolution Model.** Faraday's law for electrolysis was employed to theoretically analyze the ECM process. The analysis is based on the following assumptions. (1) The processed material does not include impurities and is homogeneous. (2) The material valence is known before processing. (3) The dissolution of metal is the only reaction on the anode, that is, there are no subreactions on the anode. (4) The metal is removed by only the dissolution and not by the collapse, that is, the processed material is dissolved at the atomic level, and the atoms do not exfoliate and cluster in a group.

**Electric Current Efficiency.** Electric current efficiency indicates the rate of the electrons used for dissolution between electrodes in the target reaction. The efficiency is expressed as follows:

$$\eta = \frac{\text{real dissolution}}{\text{theoretical dissolution}} \tag{7}$$

In the case of $\eta > 100\%$, the metal dissolves with a valence lower than that used in the computation. That is, the metal collapses on the anode (i.e., Chank effect), and then the cluster of atoms drops out. Conversely, in the case of $\eta < 100\%$, the metal dissolves with a valence higher than that used in the computation: This means that some of the supplied electrons are consumed by some subreactions.

**Processing Speed.** The amount of electricity to dissolve the metal of $1(g)$ equivalence is $F$ (Faraday constant, coulombs) according to Faraday's law. Since the equivalence ratio for $1(g)$ metal with valence $n$ and an atomic weight $M$ is $n/M(g)$ equivalence, the amount of electricity needed to dissolve $1(g)$ metal is $nF/M$ (coulombs). Therefore, when $I$ (A) electric current for $t$ (seconds) dissolves $\omega(g)$ metal, the following equation can be obtained.

$$It = \frac{\omega n F}{M} \tag{8}$$

When the volume removed is $V_0$ and the atomic density is $\gamma$, we have the following:

$$\omega = \gamma V_0 \tag{9}$$

Substituting this relation into Eq. (8), we obtain the next equation.

$$V_0 = \frac{IM}{\gamma n F} t \tag{10}$$

If the distance between two points is $\Delta y$, the processing area is $S$, and the electric conductivity of the distance is $\kappa$, then the resistance $R$ between the two points is expressed by

$$R = \frac{1}{\kappa} \frac{\Delta y}{S} \tag{11}$$

Assuming that the voltage difference is $\Delta E$, the electric current $I$ through resistance $R$ is given by the following:

$$I = \kappa S \frac{\Delta E}{\Delta y} \tag{12}$$

Substituting this equation into Eq. (10), we obtain

$$V_0 = \frac{\kappa S M}{\gamma n F} \frac{\Delta E}{\Delta y} t \tag{13}$$

It should be noted that this equation is also used to estimate the source term in Eq. (5) (i.e., $\alpha_{gi}$).

Therefore, the theoretical processing speed $v_l$ is

$$v_{l_{\text{theoretical}}} = \frac{V_0}{St} = \frac{\kappa M}{\gamma n F} \frac{\Delta E}{\Delta y} \tag{14}$$

Multiplying this speed with the electric current efficiency $\eta$, the actual processing speed can be obtained as follows:

$$v_{l_{\text{real}}} = \eta v_{l_{\text{theoretical}}} = \frac{\eta \kappa M}{\gamma n F} \frac{\Delta E}{\Delta y} \tag{15}$$

Finally, the above equation can be rewritten into a derivative form.

$$v_{l_{\text{real}}} = \frac{\eta \kappa M}{\gamma n F} \frac{dE}{dy} \tag{16}$$

It should be noted that the direction of processing speed $v_{l_{\text{real}}}$ and the gradient $dE/dy$ is normal to the dissolved wall.

Dissolution depth during a step can be estimated at every grid point by using the processing speed $v_{l_{\text{real}}}$ and the time increment of a step $\Delta t$. That is, $v_{l_{\text{real}}} \Delta t$. Using this depth, a new workpiece configuration is calculated. Similarly, a new tool position can be calculated by using the tool feed speed.

Electric conductivity $\kappa$ is influenced by $H_2$ void fraction $\alpha$. Following Thorpe and Zerkle [10], we adopted the next relation,

$$\kappa = \kappa_0 (1 - \alpha)^{1.75} \{1 + 0.016(T - T_0)\} \tag{17}$$

where subscript 0 denotes the value at the flow inlet.

## Two-Dimensional Flat Plate Simulation

**Computational Conditions.** In order to clarify the effects of Joule heating, hydrogen bubbles, and metal hydroxide sludge, the ECM process for a two-dimensional flat plate was simulated. Fig-

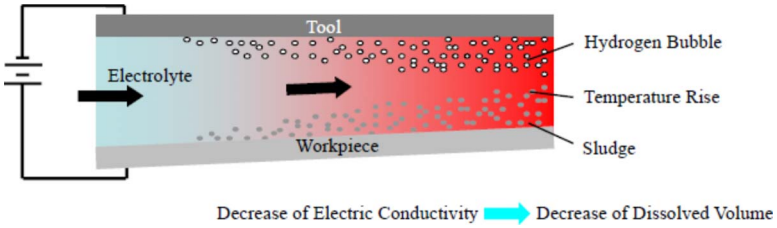


**Fig. 1 Schematic of physics in the ECM process**

ure 1 shows a schematic of the ECM process for a flat plate. The tool (cathode) is moved toward the workpiece (anode) and the workpiece surface is electrically dissolved. The electrolyte flows between the tool and the workpiece (Fig. 2). It was assumed that the metal is aluminum, the electrolyte is NaCl, the tool feed speed is $9.27\times10^{-6}$ m/s, the plate length is 4 mm, and the initial gap is 0.7 mm. These assumptions are based on the experiment by Hopenfeld and Cole [11]. The computational conditions and the physical properties of the electrolyte are listed in Tables 1 and 2.

A H-type grid was used, and the grid number was set at $161\times21$ in the streamwise and transverse directions, respectively. We should note the grid independent study. We performed preliminary computations with $61\times31$, $101\times21$, $101\times31$, $101\times41$, $161\times21$, $161\times31$, and $161\times41$ grid systems in order to check the grid independent solution. Through these computations, we found that the final gap in the $161\times21$ case has a deviation by less than 1% from the result in the finest grid case. Considering the computational time, we finally decided to use the $161\times21$ grid configuration.

The following boundary conditions were imposed: At the inlet a parabolic velocity profile, constant temperature, zero $H_2$ void fraction, and zero metal hydroxide sludge were fixed, and pressure is linearly extrapolated from the inner domain. On the wall, no-slip and adiabatic conditions were applied, and zero normal gradients of $H_2$ void fraction and metal hydroxide sludge were used. At the exit boundary, all variables except for pressure were linearly extrapolated, and atmospheric pressure of $1.0\times10^5$ Pa was fixed.

We computed five cases with different conditions. In Case 1, all flow effects were neglected, that is, only the electric field was considered. This corresponds to a conventional ECM simulation. The following were considered in the remaining four cases: Case 2, the electric field and Joule heating; Case 3, the electric field and hydrogen bubbles; Case 4, the electric field, Joule heating, and hydrogen bubbles; and Case 5, the electric field, Joule heating, hydrogen bubbles, and metal hydroxide sludge. Table 3 lists the conditions considered in each case.

The diffusion coefficients of hydrogen bubbles and hydroxide sludge are unknowns. In the present study, simply setting the diffusion coefficient to be $1.0\times10^{-6}$ m$^2$/s, $2.0\times10^{-6}$ m$^2$/s, $3.0\times10^{-6}$ m$^2$/s, $4.0\times10^{-6}$ m$^2$/s, and $5.0\times10^{-6}$ m$^2$/s, we performed the preliminary computations. The preliminary computations with these different values of coefficients indicated that these coefficients do not have much influence on the numerical results, and we found that the best match could be obtained with $3.0\times10^{-6}$ m$^2$/s. So, we decided to adopt $3.0\times10^{-6}$ m$^2$/s for the diffusion coefficient for the hydrogen bubbles and the hydroxide sludge.

**Numerical Results and Discussion.** Figure 3 compares the predicted gaps for Cases 1–5 with the experimental data measured by Hopenfeld and Cole [10]. From this figure, we can confirm the followings. (1) When no flow effect is taken into account (Case 1), the predicted gap is constant. (2) In Case 2, the thermal effect of Joule heating causes both the temperature in the downstream region and the electric conductivity to increase. Thus, the promotion of metal dissolution produces a larger predicted gap height downstream. This trend is the inverse of the experimental result. (3) When only hydrogen bubbles are included in the simulation (Case 3), the dissolved volume is greatly underestimated. This produces low electric conductivity, and the predicted gap becomes much narrower than the experiment downstream of the channel. (4) When Joule heating and hydrogen bubbles are considered (Case 4), the predicted curve satisfactorily follows the experimental data. This agreement implies that Joule heating and hydrogen bubbles are the key parameters in the ECM process, and thus the physics of ECM is primarily determined by the interaction be-

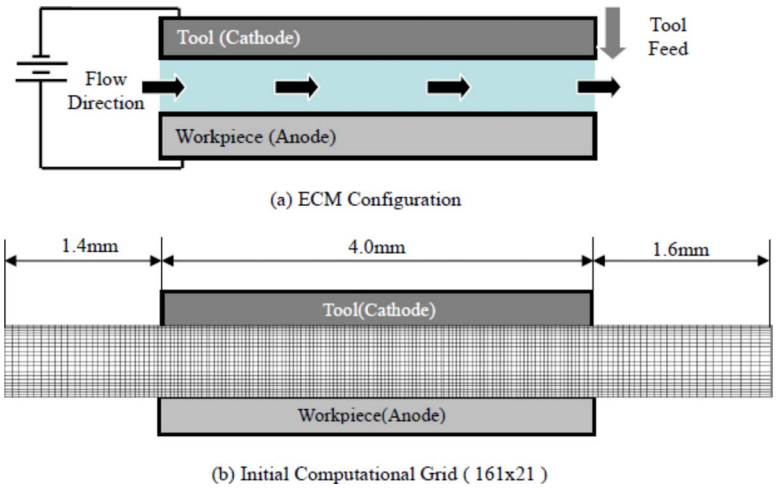


**Fig. 2 Schematic of ECM configuration and computational grid for 2D flat plate**

**Table 1 Computational conditions for 2D flat plate**

| | |
|---|---|
| Applied voltage (V) | 19.5 |
| Machining time (s) | 250 |
| Tool feed rate (m/s) | $9.27 \times 10^{-6}$ |
| Electrolyte flow flux ($m^2/s$) | $1.75 \times 10^{-3}$ |
| Reynolds number | 2000 |
| Metal type | Aluminum |
| Electrolyte type | NaCl |
| Electric current efficiency (%) | 100 |
| Conductivity ($1/\Omega$ m) | 7.0 |
| Inflow temperature (K) | 297.5 |

tween these two parameters. (5) In Case 5, metal hydroxide sludge is also taken into account. However, the predicted gap follows that in Case 4. This means that the effect of metal hydroxide sludge is negligible due to the extremely small volume fraction.

Figure 4 shows the streamwise change of the section-averaged flow characteristics (e.g., electric conductivity, $H_2$ void fraction, and temperature). In this figure, it is clearly exhibited that the electric conductivity decreases as the $H_2$ void fraction and flow temperature increase. It should be noted that the electric conductivity and void fraction curves are nonlinear, whereas the temperature curve is linear. If $H_2$ bubbles are not considered, temperature increases nonlinearly because the temperature increase causes electric conductivity to be larger. However, in this case $H_2$ bubbles are taken into account, and $H_2$ bubbles accumulate in the downstream. Since $H_2$ bubbles make electric current decrease,

**Table 2 Physical properties of electrolyte**

| | |
|---|---|
| Electrolyte conductivity ($1/\Omega$ m) | 7 |
| Electrolyte liquid density ($kg/m^3$) | 1027 |
| Specific heat capacity (J/kg K) | 4180 |
| Electrolyte liquid viscosity coefficient (kg/ms) | $0.781 \times 10^{-3}$ |
| Thermal conductivity (W/m K) | 0.63 |

**Table 3 Conditions for each simulation case**

| | Electric field | Joule's heat | Hydrogen bubble | Hydroxide sludge |
|---|---|---|---|---|
| Case 1 | Yes | No | No | No |
| Case 2 | Yes | Yes | No | No |
| Case 3 | Yes | No | Yes | No |
| Case 4 | Yes | Yes | Yes | No |
| Case 5 | Yes | Yes | Yes | Yes |

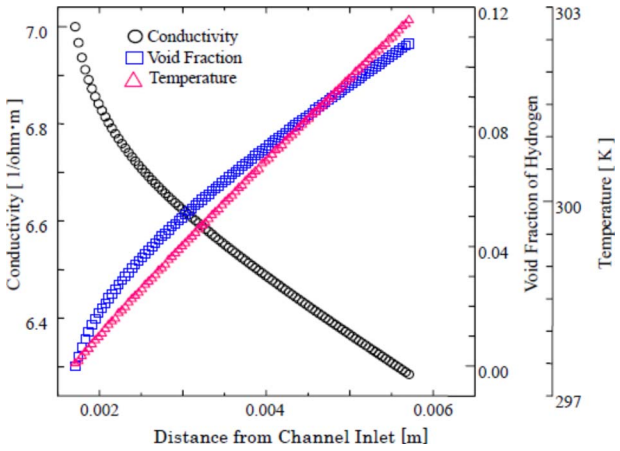


**Fig. 4 Streamwise change of section-averaged flow characteristics**

Joule heating is remarkably suppressed in the downstream, that is, nonlinear temperature increase is canceled out by the decrease in electric current. However, we think this trend does not always occur, and probably it depends on the electrolyte velocity and/or its flow rate. Therefore, we will need further investigations to clarify this phenomenon.

From the study of this typical configuration, it was confirmed that Joule heating and hydrogen bubbles are very important, but the effect of metal hydroxide sludge is negligible.

## Three-Dimensional Compressor Blade Simulation

**Computational Conditions.** Next, as a practical application of ECM, we simulated a three-dimensional compressor blade. Figure 5 shows a schematic view of ECM for a three-dimensional compressor blade. A metal block is initially held by the tools, then the tools are moved toward the center, and the compressor blade is produced. The computational domain for this simulation was separated into two parts: the inlet channel and the gap passage around the blade. We employed a H-type structure grid for each region. To calculate these two regions with an exchange of flow information, we adopted the over-set grid method. Furthermore, by dividing the machining process into 65 steps, the temporal changes of the flow and the blade geometry were simulated. The step number of 65 was determined by finding a solution that was step number independent.

In order to check the grid independence of the solution, we

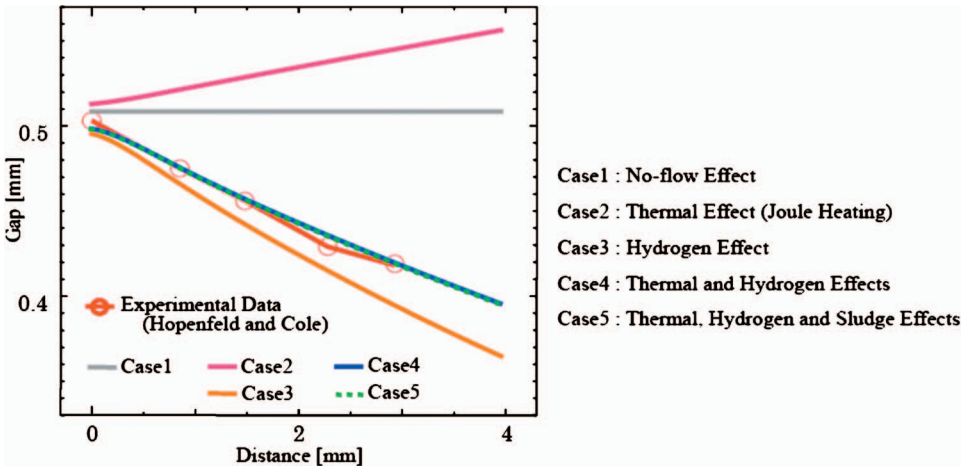


**Fig. 3 Comparison of predicted gaps for different conditions in 2D flat plate ECM**

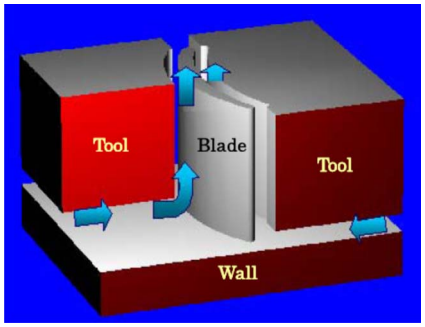


**Fig. 5 Schematic of ECM for 3D compressor blade**

performed preliminary computations with $146\times26\times81$, $201\times21\times61$, $201\times41\times61$, and $261\times41\times61$ grid systems. Through these preliminary computations, we found that, when the $201\times41\times61$ (about $5\times10^5$) grid system was used, the final shape around the midchord region has a deviation by less than 1% from that in the finest grid case. Therefore, in the present computation, we employed approximately $7\times10^5$ grid points in the initial step and $5\times10^5$ in the last step. Figure 6 shows a typical grid system. It should be noted that the interelectrode gap is highly three dimensional (an order of 1 mm in the first step and an order of 0.1 mm in the last step), and the minimum grid size was approximately 1 $\mu$m in the final step.

We used the same boundary conditions as in the two-dimensional channel. However, it should be noted that we neglected the dissolution of the inlet channel walls.

Four cases were computed. In Case 1, no flow effect is considered. In Case 2, the electric field, Joule heat, hydrogen bubbles, and hydroxide sludge were considered for a Reynolds number of 500. The Reynolds number was defined based on the chord length and the maximum velocity at the inlet. Case 3 was the same as Case 2, but the Reynolds number was 1000. This condition is nearly the same as that in the experiment. Case 4 was also the same as Case 2, but the Reynolds number was 2000. The Reynolds number was changed to clarify the effect of the Reynolds number on the ECM process. It should be noted that the workpiece material was nickel alloy, the machining time was 500 s, and other conditions are similar to those in the two-dimensional flat plate simulation.

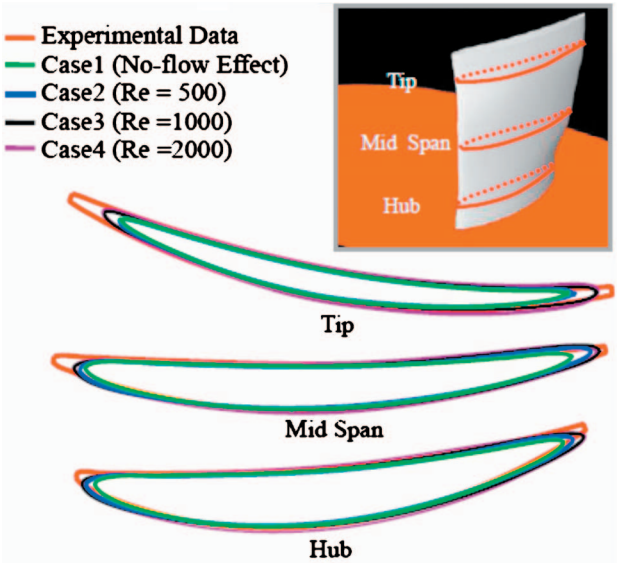


**Fig. 7 Comparison of predicted blade shapes**

**Numerical Results and Discussion.** First, the predicted blade shape and the error of each case are compared with the experimental data in Figs. 7 and 8. As shown in these figures, the pressure and suction sides are reasonably predicted, but the leading and the trailing edges are overdissolved. However, when all the physics are included and the Reynolds number matches that of the experiment (Case 3), this prediction is obviously the best. Therefore, Joule heating and hydrogen bubbles are again important effects in the compressor blade simulation. Overdissolution occurs around the leading and trailing edges due to simplification of the

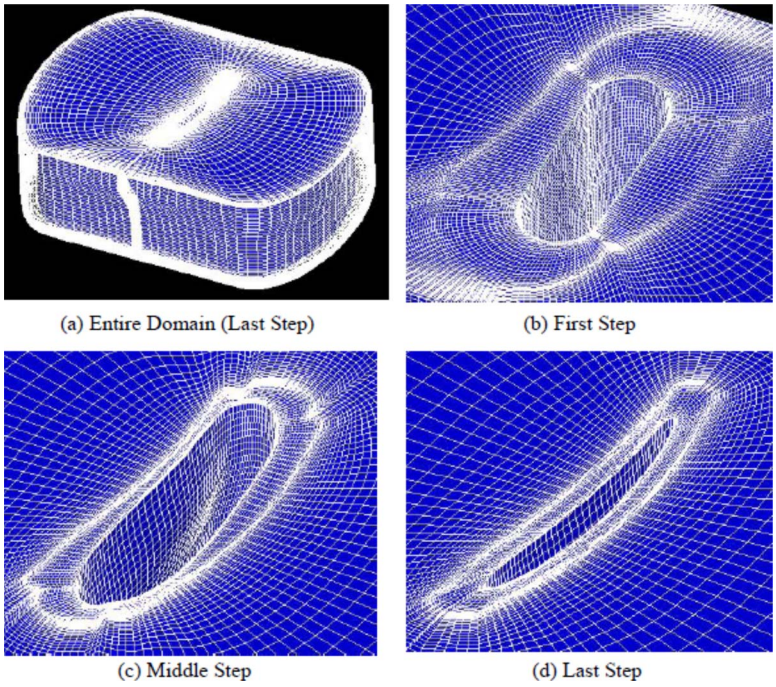


**Fig. 6 Computational grid**

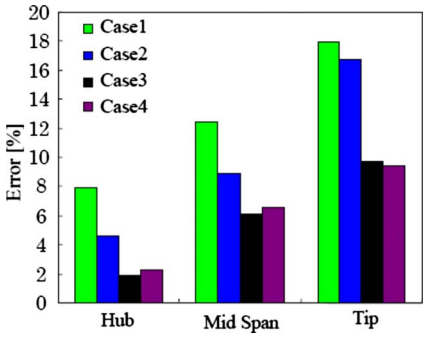


Fig. 8 Comparison of errors in each case

tool configuration there. (The actual tool consists of several pieces near the leading ad trailing edges. Each tool piece is independently controlled during the machining process. So it is too difficult to simulate the exact tool configuration and the movement.) Comparing the results in Cases 2–4, we can confirm that, if the Reynolds number is sufficiently high, the solution does not strongly depend on the Reynolds number because hydrogen bubbles are not accumulated by the high-speed flow. In Fig. 8, it is observed that the error is relatively large in the tip region. Since the tip region is the most downstream in this configuration, the three-phase effects accumulated there. Therefore, the relatively large error suggests that the one-way coupling method used in this

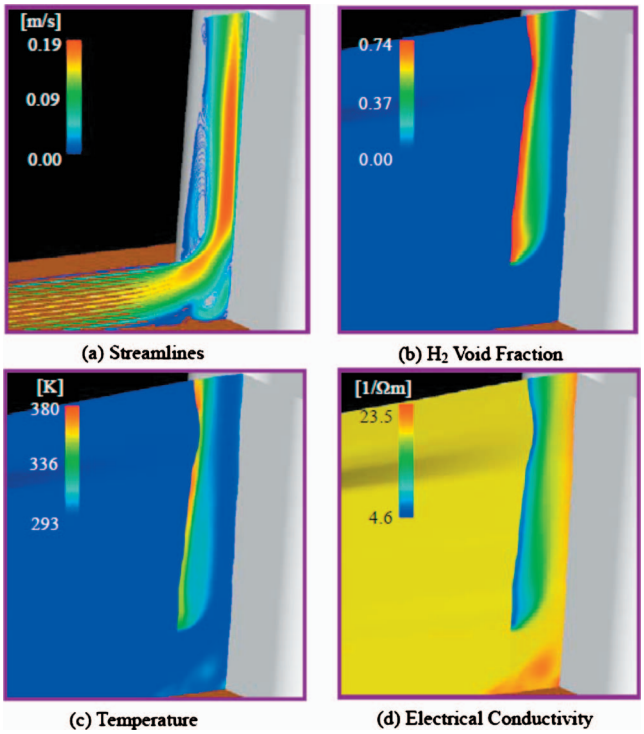


Fig. 9 Flow nature around the separation region near the hub

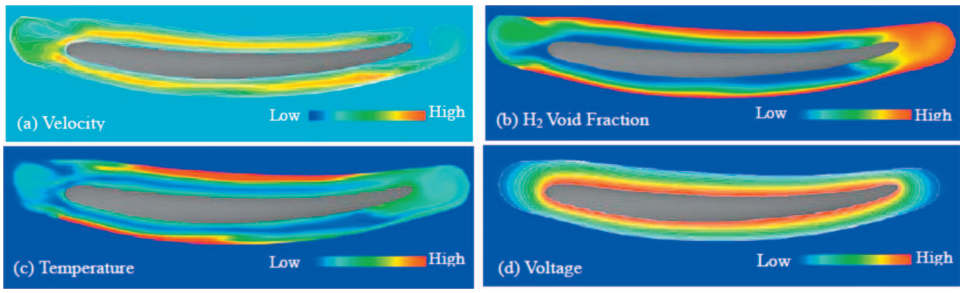


Fig. 10 Flow nature around the tip

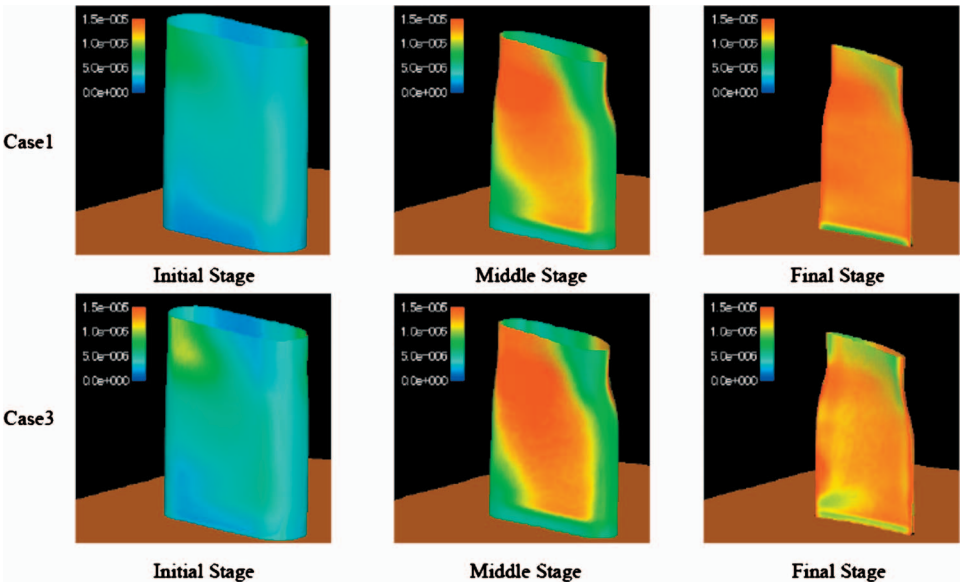


Fig. 11 Dissolved volume distributions on the pressure surface

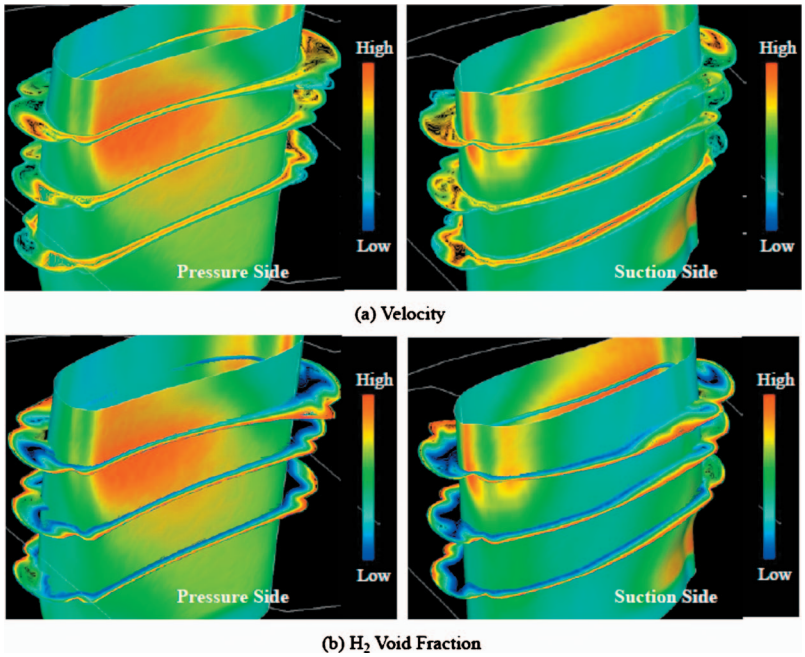


**Fig. 12 Contours of velocity and $H_2$ void fraction at different spanwise sections and dissolved volume distribution on blade surface (top: 81% span, middle: 61% span, and bottom: 40% span, at 25th stage)**

configuration is insufficient.

Figure 9 exhibits the flow nature (e.g., streamline, $H_2$ void fraction, temperature, and electrical conductivity) around the separation region near the hub. We can easily see that hydrogen bubbles are trapped in the separation region and the electrical conductivity decreases there. Figure 10 shows the flow nature around the tip. Clearly, the distributions are not uniform; the void fraction of hydrogen is high especially around the trailing edge, and this strongly affects the temperature distribution. These flow results indicate interaction among the flow, thermal, and electric fields; thus, a multiphysics simulation such as our computation is necessary.

The nonuniformity of the flow nature described above affects the dissolution on the metal surface. Figure 11 exhibits the dissolved volume on the pressure surface in Cases 1 and 3. This figure demonstrates the following. (1) The metal dissolution is nonuniform. (2) In the final stage, the dissolution is relatively uniform and enhanced by the narrow gap. By comparing the results in both cases, the Joule heating and hydrogen bubbles cause the distribution to be more nonuniform.

Figure 12 shows the velocity and $H_2$ void fraction contours at different spanwise sections and the dissolution volume distribution on the metal surface. The left and right figures show the pressure and suction sides, respectively. It is apparent that the flow is highly three dimensional, and the high dissolution region corresponds to the narrow gap in each section. This figure indicates that the gap size between the workpiece and the tool is the primary parameter in the ECM process for a compressor blade. Moreover, as can be expected, the low-speed region corresponds to the region with a high void fraction of hydrogen and a high temperature (not shown here). In other words, hydrogen bubbles reside and accumulate in the low-speed region.

## Summary

In the present study, the ECM process for a two-dimensional flat plate and a three-dimensional compressor blade was simulated, and the characteristics of the flow between the tool and the workpiece surface were investigated by observing the computed flow fields. The numerical results lead to the following conclusions.

(1) Joule heating and hydrogen bubbles are very important in the ECM process.
(2) The interaction of Joule heating and hydrogen bubbles is the primary determinant of workpiece dissolution.
(3) The effect of metal hydroxide sludge is negligible.
(4) In the three-dimensional simulation of the compressor blade, Joule heating and hydrogen bubbles strongly influence the flow nature, and thus essential.
(5) Joule heating and hydrogen bubbles cause the flow nature to be highly nonuniform.
(6) The nonuniform flow nature leads to the nonuniform dissolution of the workpiece surface.
(7) Hydrogen bubbles reside and accumulate in the low-speed region.

In the present study, we confirmed that the multiphysics simulation is useful and essential for prediction of the ECM process. However, we need to further investigate the accuracy of the predictions computed by our models and numerical procedure.

## Nomenclature

$C_p$ = specific heat at constant pressure
$C_{\alpha i}$ = diffusion coefficient of $\alpha_i$
$E$ = electric potential
$I$ = electric current
$p$ = pressure
$t$ = time
$T$ = temperature
$u_i$ = velocity vector
$x_i$ = Cartesian coordinate
$\alpha_i$ = void fraction of hydrogen or volume fraction of hydroxide sludge
$\alpha_{gi}$ = source of $\alpha_i$
$\eta$ = electric current efficiency

$\kappa$ = electric conductivity
$\lambda$ = heat conductivity
$\nu$ = kinetic viscosity
$\rho$ = fluid density

## References


[1] Hourng, L. W., and Chang, C. S., 1993, "Numerical Simulation of Electrochemical Drilling," J. Appl. Electrochem., **23**, pp. 316–321.

[2] Chang, C. S., and Hourng, L. W., 2001, "Two-Dimensional Two-Phase Numerical Model for Tool Design in Electrochemical Machining," J. Appl. Electrochem., **31**, pp. 145–154.

[3] Chang, C. S., Hourng, L. W., and Chung, C. T., 1999, "Tool Design in Electrochemical Machining Considering the Effect of Thermal-Fluid Properties," J. Appl. Electrochem., **29**, pp. 321–330.

[4] Filatov, E. I., 2001, "The Numerical Simulation of the Unsteady ECM Process," J. Mater. Process. Technol., **109**, pp. 327–332.

[5] Purcar, M., Bortels, L., Van den Bossche, B., and Deconinck, J., 2004, "3D Electrochemical Machining Computer Simulations," J. Mater. Process. Technol., **149**, pp. 472–478.

[6] Nied, H. A., and Lamphere, M. S., 1995, "2D Electrochemical Airfoil Machining Process Model," *ASME Paper No*. 95-GT-272.

[7] Rajurkar, K. P., Zhu, D., Geough, J. A., Kozak, J., and Silva, A., 1999, "New Development of Electro-Chemical Machining," CIRP Ann., **48**(2), pp. 567–579.

[8] Kozak, J., 1998, "Mathematical Models for Computer Simulation of Electrochemical Machining Processes," J. Mater. Process. Technol., **76**, pp. 170–175.

[9] Van Damme, S., Nelissen, G., Van den Bossche, B., and Deconinck, J., 2006, "Numerical Model for Predicting the Efficiency Behavior During Pulsed Electrochemical Machining of Steel in $NaNO_3$," J. Appl. Electrochem., **36**, pp. 1–10

[10] Thhorpe, J. F., and Zerkle, R. D., 1969, "Analytic Determination of the Equilibrium Electrode Gap in Electrochemical Machining," Int. J. Mach. Tool Des. Res., **9**, pp. 131–144.

[11] Hopenfeld, J., and Cole, R. R., 1969, "Prediction of the One-Dimensional Equilibrium Cutting Gap in Electrochemical Machining," ASME J. Eng. Ind., **8**, pp. 755–765.

# Calculation of DEP and EWOD Forces for Application in Digital Microfluidics

**Patrick M. Young**

**Kamran Mohseni**
e-mail: mohseni@colorado.edu

Department of Aerospace Engineering Sciences,
University of Colorado at Boulder,
Boulder, CO 80309

*Two primary methods for electrostatically actuating microdroplets in channels currently exist: dielectrophoresis (DEP) for electrically insulating fluids and electrowetting on dielectric (EWOD) for conducting fluids. In each case, a transverse electric field is used to create an electrostatic pressure, giving rise to the transport of individual liquid slugs. This paper examines the nature of the force distribution for both EWOD and DEP actuated droplets. The effects of system parameters such as contact angle and electrode length on the shape of the force density and its net integral are considered. A comparison of the scaling properties of DEP and EWOD for applications in digital microfluidics is presented. The net DEP force is shown to be strongly peaked when a droplet interface is located near the edge of a charged electrode and reduces to the well-known lumped parameter model in the appropriate limits. The effect of electrode spacing is seen to have an inversely proportional effect on the force experienced by the droplet, and the effect of increasing droplet contact angle is observed to increase the net force on the droplet.*
[DOI: 10.1115/1.2956606]

## 1 Introduction

The field of digital microfluidics, in which discrete droplets are manipulated in place of continuous flows, has seen rapid development over the past few years for a variety of applications, from engineering to the life sciences [1–7], including variable focus lenses, display technology, fiber optics, and lab-on-a-chip devices. In particular, efficient and cost-effective lab-on-a-chip devices are in great demand, as they allow for highly repetitive laboratory tasks to become automated with the introduction of miniaturized and integrated systems [8]. This technique typically makes use of forces possessing favorable scaling relationships; prevalent examples include thermal or chemical surface tension modulation, electrowetting, and dielectrophoresis (DEP). In our group, digital microfluidics has been employed for active thermal management of compact electronic devices [9–11], design of a zero leakage microvalve [12], investigation of droplet morphology under electrowetting actuation [13], and design of an electrowetting microlense [14].

Accurate descriptions of actuation forces and resultant droplet velocities must be available when designing an integrated device making use of discretized flows. Currently, the most promising methods of droplet actuation in microfluidic devices are electrowetting on dielectric (EWOD) for conductive droplets [15–17] and DEP for electrically insulating droplets [18–22], where in both cases droplets are transported by sweeping an applied voltage along a microchannel ahead of the droplet. Numerical modeling of the droplet dynamics for EWOD and DEP configurations has been done using approximations of the electrostatic effect [13,23], but incorporation of the electrostatic force density into a direct simulation of the fluid mechanics is desired. For an example of such a simulation, see Ref. [24]. This paper presents numerical results describing the forces in DEP and EWOD for a droplet of fixed geometry. The lumped parameter result for the net droplet force is stated for DEP, and then compared with the results from direct numerical simulation of electrostatic forces. An analysis of the lumped force acting on an EWOD droplet has previously been presented by our group and others [2,25,26]. Here we extend these results to DEP, investigate the net forces and force distributions in DEP actuation, and provide comparison with EWOD.

The primary difference between an EWOD and a DEP actuated droplet is the nature of the fluid and its effect on the electric field's penetration into the media, see Fig. 1 for the basic setup of EWOD and DEP. For EWOD, an electrically conducting droplet is placed in a dielectric-coated channel lined with electrodes. A given electrode is then activated, creating an electric field that induces a charge accumulation on the surface of the fluid. This charge accumulation allows for the creation of a net force on the droplet, drawing the droplet toward the actuated electrode. Investigation of the interface profile and electrostatic distribution in EWOD has been explored in several papers [27–29]. The charge distribution near the contact line was found analytically, giving rise to a force distribution that is clustered in a region near the contact line on the order of $h$, the thickness of the dielectric layer. The interface profile used in this paper is assumed circular and fixed for all time, so any dynamic response to the electric field is not included and is a topic of future research.

DEP differs from EWOD in that the liquid is insulating, charge does not accumulate on the surface, and the electric field penetrates into the liquid. It is well known that a dielectric material is drawn into the gap between the parallel plate of a charged capacitor [30]. This is a result of the nonuniform fringing field located at the edge of the capacitor, providing a force pointing toward its center [30,31]. As opposed to EWOD, the dielectrophoretic force can act over the droplet's front face or within the bulk of the fluid itself. Jones [20,21] has explored the close relationship between DEP and EWOD on a theoretical basis, but for direct simulation of EWOD and DEP flows including electrostatic effects, a clear description of the force distribution is required. The cases considered here are for a perfect conductor (EWOD) and a perfect insulator (DEP), but there exist many fluids that exhibit properties of both a conductor and a dielectric, namely, leaky dielectrics [32]. This will be the topic of a future publication.

## 2 Governing Equations

In the problems considered in this investigation, the focus is on droplet flow resulting from electrical forces. In many microfluidic

Contributed by the Fluids Engineering Division of ASME for publication in the JOURNAL OF FLUIDS ENGINEERING. Manuscript received June 19, 2007; final manuscript received December 21, 2007; published online July 30, 2008. Assoc. Editor: Dennis Siginer. Paper presented at the ASME Fluids Engineering Division Summer Meeting and Exhibition (FEDSM2007), San Diego, CA, July 30–August 2, 2007.

  

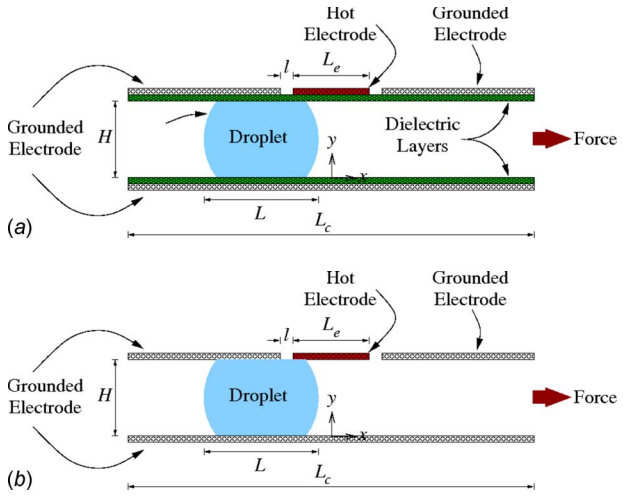


**Fig. 1 The (*a*) EWOD and (*b*) DEP configurations. *H* is the droplet and the channel height and *L*, $L_e$, and $L_c$, are the droplet, the electrode, and the channel widths. *l* is the spacing between the hot and grounded electrodes.**

applications, the dynamic currents are so small that the magnetic field can be ignored. In this situation, the governing equations for the electrical field are the electrostatic laws [33].

The governing equations of motion for incompressible fluids under electric effects are the mass, momentum, and electrostatic equations. Aside from the mechanical forces (pressure and shear stress), there exists Columbic forces due to any existing free charge as well as forces due to polarization. The corresponding boundary conditions at a fluid interface are obtained by integrating the mass and momentum equations through the interface.

The net effect of an applied electrical field on a given fluid is represented by an extra body force on the right hand side of the Navier–Stokes equations. The body force density $\mathbf{f_b}$ in a fluid resulting from the influence of an electric field can be written as

$$\mathbf{f_b} = \rho_f \mathbf{E} - \frac{1}{2}E^2\nabla\epsilon + \nabla\left(\frac{1}{2}\mathbf{E}\cdot\mathbf{E}\frac{\partial\epsilon}{\partial\rho}\right) \tag{1}$$

where $\epsilon$ is the fluid permittivity, $\rho$ is the density of the fluid, $\rho_f$ is the free electric charge density, and $\mathbf{E}$ is the electric field. This is the Korteweg–Helmholtz electric force density formulation [34–36]. The last term in this equation, the electrostriction force density term, can be ignored for incompressible flows. Hence, the body force density considered here is given by

$$\mathbf{f_b} = \rho_f \mathbf{E} - \tfrac{1}{2}E^2\nabla\epsilon \tag{2}$$

This force density provides a coupling between the droplet hydrodynamics and electric field. The first term of Eq. (2) is attributed to free charge in the system, while the second term is the contribution from the polarization of the medium.

The body force density (2) can be identically written as the divergence of a stress tensor, namely, the Maxwell stress tensor

$$\mathbf{f_b} = \nabla\cdot\mathbf{T}^M \tag{3}$$

or in tensorial notation

$$T_{ij}^M = \epsilon E_i E_j - \frac{\epsilon}{2}\delta_{ij}E_k E_k \tag{4}$$

This stress term accounts for both the forces due to the free electric charges and the forces due to the polarization of the material.

For a system consisting of perfectly insulating fluids (such as in DEP) with no free charge present, the first term in Eq. (2) can be disregarded. The second term in Eq. (2) is only nonzero at the interface between the two fluids, where there exists a gradient in $\epsilon$. This indicates that the force density is located at the fluid interface, not distributed throughout the bulk of the fluid as the physical interpretation of the polarization effect indicates. The debate as to what point of view is correct is longstanding, but these seemingly contradictory interpretations of the body force density can be shown to be equivalent if care is taken [37]. The body force density due to the polarization forces is traditionally given by the Kelvin polarization body force density [38],

$$\mathbf{f_b} = (\mathbf{P}\cdot\nabla)\mathbf{E} = ((\epsilon-\epsilon_0)\mathbf{E}\cdot\nabla)\mathbf{E} = \epsilon\nabla\left(\frac{1}{2}E^2\right) - \nabla\left(\frac{\epsilon_0}{2}E^2\right) \tag{5}$$

where $\mathbf{P}=(\epsilon-\epsilon_0)\mathbf{E}$ is the polarization field. For an incompressible fluid, the scalar pressure only appears in the Navier–Stokes equations in terms of a gradient. The role of pressure is to ensure that continuity of the vector field is satisfied, and it takes on whatever value is needed to guarantee that this condition is always fulfilled. Hence, any other term that appears in the Navier–Stokes equations as the gradient of a scalar can be absorbed into the pressure [38]. This is true of the last term in Eq. (5), and so the effective body force density in view of the Kelvin representation is

$$\mathbf{f_b} = \epsilon\nabla\left(\tfrac{1}{2}E^2\right) \tag{6}$$

Now consider the Korteweg–Helmholtz formulation. Using the vector identity $\nabla(\phi\psi)=\phi\nabla\psi+\psi\nabla\phi$ and recalling that there is no free charge present in this system, Eq. (2) becomes

$$\mathbf{f_b} = \epsilon\nabla\left(\frac{1}{2}E^2\right) - \nabla\left(\frac{\epsilon}{2}E^2\right) \tag{7}$$

Since the last term in Eq. (7) is the gradient of a scalar, it can be absorbed into the pressure. Therefore, the difference in the Kelvin and Korteweg–Helmholtz body force densities is the gradient of a scalar, a term that has no dynamic significance for incompressible flows.

For a system where one fluid is significantly more conductive than the other (such as EWOD), the electric relaxation time for the conductive liquid can be assumed to be significantly shorter than the relevant hydrodynamic time scales. As a result, the interface can be regarded as a perfect conductor. For such a conductor under the influence of an electric field, all free charge in the system accumulates on the surface of the droplet. For such a setup, the force density is given by the first term in Eq. (2), except that for an ideal conductor we have $\rho_f \to \sigma_f$, where $\sigma_f$ is the surface charge density. Note that this is no longer a body force density; it is confined to the surface of the droplet. The surface charge density can be rewritten using Gauss' law and the field itself is expressed as the average electric field intensity at the surface. Applying these two conditions and recalling that the electric field is always normal to the surface of a conductor gives the surface force density $\mathbf{f_s}$ at the interface,

$$\mathbf{f_s} = \sigma_f\mathbf{E} = \frac{\epsilon_{\text{ext}}}{2}E^2 \tag{8}$$

where $\epsilon_{\text{ext}}$ refers to the dielectric constant of the fluid external to the conductive droplet [39].

Thus, the difference in the force distribution for dielectric and conductive fluids is that of a body force density as opposed to a surface force density. This is an essential difference in regard to a numerical implementation of these forces coupled with the fluid equations.

The investigation of the electric force acting on droplets that are perfectly conductive and perfectly insulating is now considered in detail. The following introduces the nondimensionalization of the system considered in this paper.

**2.1 Nondimensionalization.** Figure 1 shows the setup for both the EWOD and DEP systems considered in this paper. Let the primes denote the nondimensionalized variables and set

$$x' = \frac{x}{H}, \quad y' = \frac{y}{H}, \quad V' = \frac{V}{V_0}, \quad \epsilon' = \frac{\epsilon}{\epsilon_0} \tag{9}$$

where $H$ is the channel height, $V_0$ is the charged electrode voltage, and $\epsilon_0$ is the electric permittivity of free space. This nomenclature is used to nondimensionalize the governing equations.

*2.1.1 DEP.* In electrostatics, $\mathbf{E}=-\nabla\mathbf{V}$ defines the relationship between the electric field $\mathbf{E}$ and the electric potential $V$. Using the potential formulation, Gauss' law reads

$$\nabla \cdot (\epsilon \nabla V) = \epsilon\left(\frac{\partial^2 V}{\partial x^2} + \frac{\partial^2 V}{\partial y^2}\right) + \frac{\partial \epsilon}{\partial x}\frac{\partial V}{\partial x} + \frac{\partial \epsilon}{\partial y}\frac{\partial V}{\partial y} = 0 \tag{10}$$

For the system considered in this paper, $\epsilon$ is a continuous function that takes on the value $\epsilon_{\text{ext}}$ outside the droplet, $\epsilon_{\text{int}}$ inside the droplet, and continuously transitions between $\epsilon_{\text{ext}}$ and $\epsilon_{\text{int}}$ linearly on the scale of the grid. Nondimensionalization of Eq. (10) gives

$$\epsilon'\left(\frac{\partial^2 V'}{\partial x'^2} + \frac{\partial^2 V'}{\partial y'^2}\right) + \frac{\partial \epsilon'}{\partial x'}\frac{\partial V'}{\partial x'} + \frac{\partial \epsilon'}{\partial y'}\frac{\partial V'}{\partial y'} = 0 \tag{11}$$

In the presence of the electric field, the atoms in a dielectric material polarize. The resulting dipoles experience a force from the electric field, and this electrostatic force density $\mathbf{f_b}$ of the electrically insulating droplet is given by Eq. (5). Equation (5) can then be integrated over the entire domain to give the net force acting on the insulating droplet. The relationship between the nondimensional body force density $\mathbf{f_b'}$ and the dimensional body force density $\mathbf{f_b}$ is

$$\mathbf{f_b} = \frac{\epsilon_0 V_0^2}{H^3}\mathbf{f_b'}$$

*2.1.2 EWOD.* In EWOD, the droplet is a conductor and hence there is no electric field present internally. Therefore, Eq. (10) reduces to Laplace's equation,

$$\frac{\partial^2 V'}{\partial x'^2} + \frac{\partial^2 V'}{\partial y'^2} = 0$$

with the appropriate boundary conditions.

The charge distribution resulting from the electric field present on the conducting droplet feels a force from the external electric field, giving rise to an electrostatic force always felt normal to the surface, given by Eq. (8). The integration of this force density gives the net force on the conductive droplet. The relationship between the nondimensional surface force density $\mathbf{f_s'}$ and the dimensional surface force density $\mathbf{f_s}$ for the EWOD configuration considered here is

$$\mathbf{f_s} = \frac{\epsilon_0 V_0^2}{H^2}\mathbf{f_s'}$$

The use of the primes has been dropped in the remainder of this paper for notational clarity.

**2.2 Lumped Forced Calculations.** The next two sections pertain to the forces at work in DEP and EWOD. The *total* force per unit area experienced by a droplet can be directly derived from capacitive energy considerations [30,31]. Differentiation of the system energy $U$ gives the net force $F$ in the horizontal direction, per unit area,

$$F = \frac{dU}{dx}$$

This method is demonstrated for both EWOD and DEP droplets in the section below. To calculate force *distributions*, numerical methods must be utilized, and this is presented in Sec. 3.

**2.3 Lumped EWOD Force.** Under EWOD actuation, the droplet is a conductor, and so all the charge is located at the fluid interface. Hence, the droplet experiences a surface force near its front and rear contact lines. We consider here only the case of a continuously grounded electrode, with the opposing side of the droplet in contact with a hot electrode with potential $V$ on its advancing face and a grounded electrode on its receding face, as seen in Fig. 1(*a*). Ignoring the contributions of edge effects at the contact lines and the hot/cold electrode interface, the total capacitive energy in the system is

$$W = \frac{1}{2}c_l L V_{\text{drop}}^2 + \frac{1}{2}c_u\left(x + \frac{L}{2}\right)(V - V_{\text{drop}})^2 + \frac{1}{2}c_u\left(\frac{L}{2} - x\right)(-V_{\text{drop}})^2 \tag{12}$$

where $c_u$ and $c_l$ are the capacitances per unit area of the top and bottom dielectric coatings, $V_{\text{drop}}$ is the voltage of the droplet, $d$ is the thickness of the dielectric layers insulating the droplet from the electrode, and $x=0$ when the center of the droplet is directly under the left edge of the electrode. Assume $c_u=c_l=c=\epsilon_{\text{lay}}/d$, where $\epsilon_{\text{lay}}$ is the dielectric constant of the insulating layers. Then the droplet voltage is found by minimizing the total energy with respect to $V_{\text{drop}}$, giving a result of [36,39,40]

$$V_{\text{drop}} = \frac{V}{2}\left(\frac{x}{L} + \frac{1}{2}\right) \tag{13}$$

Adding Eq. (13) to Eq. (12) gives the system energy, which can be differentiated by $x$ to give the net force in the horizontal direction,

$$F = \frac{dU}{dx} = \frac{\epsilon_{\text{lay}}}{4d}V^2\left(1 - \frac{2x}{L}\right) \tag{14}$$

Note that the total force on the droplet is a function of the droplet position with respect to the electrode. As a result, a droplet under EWOD actuation experiences a cyclic total force as it moves over a periodic array of electrodes. However, one should note that this lumped model breaks down when the droplet interfaces approach the electrode edges, as edge effects play an important role [26]. In such cases, one requires direct numerical simulation of the governing equations to obtain the net force, as described in Sec. 3.

**2.4 Lumped DEP Force.** Let $\epsilon_{\text{int}}$ and $\epsilon_{\text{ext}}$ be the dielectric constant of the droplet and the external fluid, respectively. Consider the system in Fig. 1(*b*) and recall that $x=0$ when the center of the droplet is directly under the left edge of the electrode in this section. The energy stored in the region where the droplet is under the charged electrode is given by $\frac{1}{2}c_{\text{int}}V^2$, where $c_{\text{int}}=\epsilon_{\text{int}}/H(x-L)V^2$ is the capacitance per unit area of this region. The energy stored in the region under the charged electrode where the droplet is *not* present is given by $\frac{1}{2}c_{\text{ext}}V^2$, where $c_{\text{ext}}=\epsilon_{\text{ext}}/H(L_e-x)V^2$ is the capacitance per unit area of this second region. Then the net force per unit area is given by

$$F = \frac{dU}{dx} = \frac{d}{dx}\left(\frac{1}{2}c_{\text{int}}V^2 + \frac{1}{2}c_{\text{ext}}V^2\right) = \frac{1}{2}\frac{\epsilon_{\text{int}} - \epsilon_{\text{ext}}}{H}V^2 \tag{15}$$

where $\epsilon_{\text{int}}$ is the dielectric constant of the fluid itself and $\epsilon_{\text{ext}}$ is the dielectric constant of the external fluid. This force is seen to be the difference in capacitive energy between a dielectric-filled channel and an empty channel. Again, this model is only valid when the droplet interfaces are well away from any fringing fields. Note that the droplet height, $H$, appears directly in this expression for $F$; this factor gives DEP a different scaling than EWOD [26,41]. The velocity of an EWOD droplet depends on $H/L$, where $L$ is the length of the droplet. In contrast, the velocity of a dielectric droplet depends only on $1/L$, making DEP increasingly effective for very small channel sizes.

*2.4.1 Maxwell Stress Tensor.* The above lumped parameter analysis can equivalently be derived using the Maxwell stress tensor with a judicious choice of integration path [20]. However, the stress tensor calculation fails when the droplet interface is near the edge of the electrode.

First, consider the integration paths in Fig. 2(*a*). Here the drop-

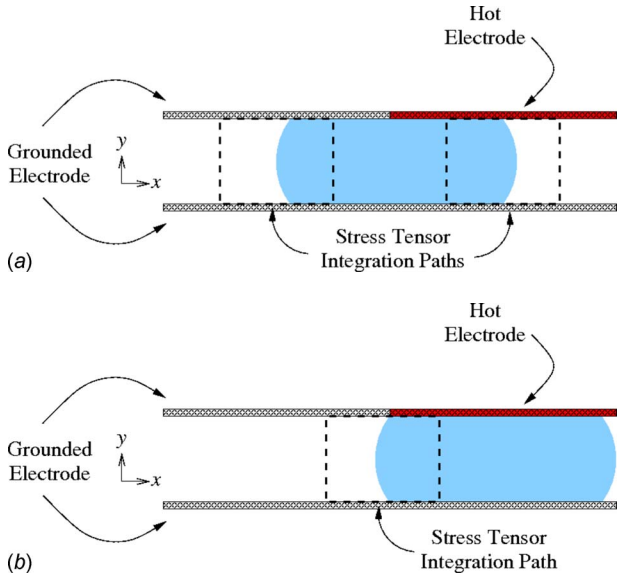


**Fig. 2 Integration paths used when calculating the force with the Maxwell stress tensor when (*a*) the droplet interface is far away from the electrode interface and (*b*) when the droplet interface is near the electrode interface.**

let interface is well away from the electrode interface. The vertical components of the integration path are assumed to be far enough away from regions of nonuniformity that **E** is known analytically. The contributions along the horizontal components of the integration path take the form (when only concerned with force in the horizontal direction)

$$\int T_{12} da = \int \epsilon E_1 E_2 da$$

where the subscripts 1 and 2 refer to the $x$ and $y$ directions, respectively. Since the horizontal components lie along the electrodes, $E_1=0$ and so these parts of the integration path contribute nothing to the stress tensor integration.

Now consider the integration path in Fig. 2(*b*). The droplet interface is now near the electrode interface, and the integration path must lie across the hot/cold electrode interface to ensure that the vertical components of the path are in regions where **E** is known analytically. Unfortunately, it can no longer be assumed that $E_1=0$ all along the upper horizontal path because of the discontinuity, and so the stress tensor method fails when droplet interfaces are near electrode interfaces. In order to calculate the net force in these regions, numerical methods need to be utilized.

Note that the same problem persists even when a gap is added between the hot and cold electrodes, as one would need to integrate around the corners of the electrode, where the normal direction is ambiguous.

## 3 Force Distribution

In this section, we present a detailed analysis of the electric force distribution of a droplet for both EWOD and DEP. The lumped analysis is only valid when the interface is far from the fringing fields. While the total force experienced by a droplet under EWOD and DEP was given in the previous section, a complete solution of the Navier–Stokes equations including electrohydrodynamic effects requires a detailed knowledge of the force distribution, as given below.

**3.1 EWOD Force Distribution.** Consider a droplet with no net charge while it is electrically isolated from the electrodes. Since no volumetric free charge exists in the solution region, the potential is found by solving Laplace's equation outside of the droplet with the appropriate boundary conditions[42]. The boundary condition on the surface of the conductor is

$$\sigma_f = -\epsilon_{\text{ext}} \frac{\partial V}{\partial n} \tag{16}$$

with the entire droplet itself held at a constant potential $V_{\text{drop}}$. The charge distribution and droplet potential are not in general known a priori and must be found as part of the numerical solution[43]. This is accomplished via a shooting method in which two initial guesses for the droplet voltage are assumed; the net charge on the surface is calculated by integrating $\sigma_f=-\epsilon_{\text{ext}}(\partial V/\partial n)$ over the boundary, and a subsequent guess for $V_{\text{drop}}$ is calculated via the secant method. Convergence is reached when the integration of the surface charge is near enough to zero, specified by the user (a value of $10^{-6}$ was used in these calculations), see Ref. [26] for details.

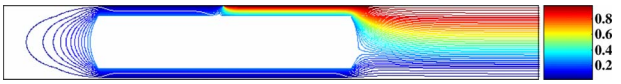


**Fig. 3 Example calculation of the electric equipotentials surrounding a droplet in EWOD configuration; the contact angle is 10 deg. In nondimensional units, $h=1$, $L=2$, and the length of the computational domain=10. See Ref. [26] for more details.**

The Laplace equation is discretized using second-order centered differences and the resulting system is solved iteratively. An example calculation of the electric potential around a conducting droplet is shown in Fig. 3. The droplet is centered over the voltage step, and the channel is lined with dielectric layers equal thicknesses given by $d=0.1H$. The contour lines are densely concentrated around the four corners of the droplet, indicating the outward pressure along both faces.

The charge distribution and force densities on the surfaces of a straight-sided centered droplet are shown in Fig. 4. On the rear interface, the distributions are symmetric about the centerline and always of the same sign. On the front of the droplet, the charge changes sign at a location given roughly by

$$y = \frac{V_{\text{drop}}}{V} H \tag{17}$$

and the force density is most strongly peaked near the hot electrode. Note that the force distributions are localized within a distance of order $d$ near the droplet edges. In many EWOD applications, $d$ is less than 1% of $H$, and the force is often treated as if it were a point force acting exactly at the contact line [27]. For more details on the numerical force calculation in EWOD including verification, see Ref. [26].

**3.2 DEP Force Distribution.** The simple bulk parameter analysis presented earlier for a dielectric medium is only valid for certain locations of the dielectric fluid slug relative to the actuating electrode. When the fluid interface is near a voltage jump, the form of the system energy will be strongly dependent on the exact location of the fluid. Equation (15) is therefore expected to be accurate only when the droplet is straddling the hot/cold electrode interface with its own faces reasonably far away. In addition, Eq. (15) does not address the force on a droplet approaching, but not yet in contact with, a voltage jump. To address these situations, numerical methods must be utilized.

To calculate the desired force density, we must first solve Eq. (10) numerically to obtain the electric field of the system. The net force on the droplet is an artifact of the increase in the gradient of the square of the electric field. If the interface is located in a region where the divergence of $E^2$, the contribution to the net body force of this region is greatly increased. Because of this, it is critically important that the electric field is accurately resolved

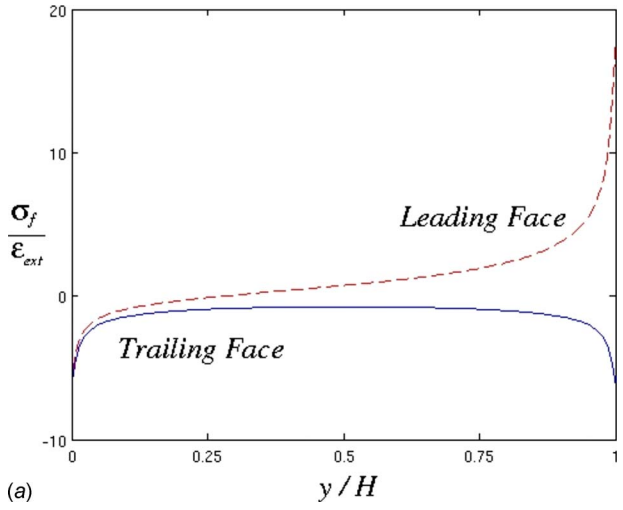


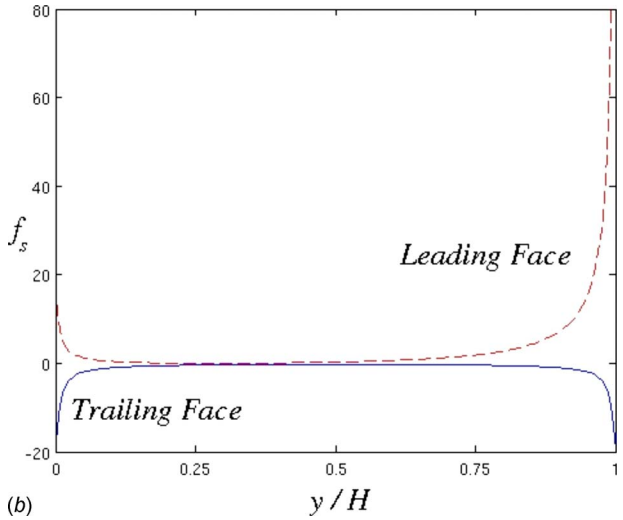


**Fig. 4 Charge distributions (*a*) and force densities (*b*) on the leading and trailing interfaces of an EWOD-activated droplet. Contact angle is 0 deg. See Ref. [26] for more details.**

near the fringing fields located at the edges of the electrodes. To achieve this resolution, a nonuniform grid is applied in the $x$-direction. Let $x$ and $x'$ denote the horizontal coordinate in the physical and computational planes, respectively. We define the relationship between the two planes as

$$x' = x_{\max}\left(A + \frac{1}{\beta_x}\sinh^{-1}\left(\left(\frac{x}{x_0} - 1\right)B\right)\right)$$

where

$$A = \frac{1}{2\beta_x}\log\left(\frac{1 + (e^{\beta_x} - 1)x_0/x_{\max}}{1 + (e^{-\beta_x} - 1)x_0/x_{\max}}\right)$$

$$B = \sinh(\beta_x A)$$

where $x_{\max}$ is the maximum value in the physical domain, $x_0$ is where we desire to cluster nodes, and $\beta_x$ controls the amount of clustering about $x_0$, where greater values of $\beta_x$ lead to a higher concentration of points about $x_0$ [44]. See Fig. 6 for schematics of the grid distribution in the computational domain.

Transforming Eq. (10) to the computational plane, we arrive at

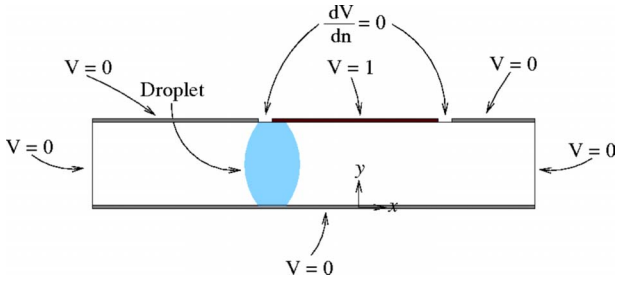


**Fig. 5 Boundary conditions used in numerically solving for the electric potential surrounding a dielectric fluid in DEP configuration**

$$\epsilon\left(\frac{\partial^2 V}{\partial x'^2}\left(\frac{\partial x'}{\partial x}\right)^2 + \frac{\partial V}{\partial x'}\frac{\partial^2 x'}{\partial x^2} + \frac{\partial^2 V}{\partial y^2}\right) + \frac{\partial \epsilon}{\partial x'}\frac{\partial V}{\partial x'}\left(\frac{\partial x'}{\partial x}\right)^2 + \frac{\partial \epsilon}{\partial y}\frac{\partial V}{\partial y} = 0 \tag{18}$$

where

$$\frac{\partial x'}{\partial x} = \frac{x_{\max}B}{\beta_x x_0((x/x_0 - 1)^2B^2 + 1)^{1/2}}$$

$$\frac{\partial^2 x'}{\partial x^2} = -\frac{x_{\max}B^3(x/x_0 - 1)}{\beta_x x_0^2((x/x_0 - 1)^2B^2 + 1)^{3/2}}$$

Each term in Eq. (18) is discretized using the standard second-order centered finite difference approximation. For a given node $(i,j)$, the discretization of Eq. (18) yields the following relationship:

$$\frac{1}{(\Delta y)^2}\left(\epsilon_{i,j} - \frac{\epsilon_{i,j+1} - \epsilon_{i,j-1}}{4}\right)V_{i,j-1} + \left(\frac{\epsilon_{i,j}}{(\Delta x)^2}\left(\frac{\partial x'}{\partial x}\right)^2 - \frac{\epsilon_{i,j}}{2\Delta x}\frac{\partial^2 x'}{\partial x^2} - \frac{\epsilon_{i+1,j} - \epsilon_{i-1,j}}{4(\Delta x)^2}\left(\frac{\partial x'}{\partial x}\right)^2\right)V_{i-1,j} - 2\epsilon_{i,j}\left(\frac{1}{(\Delta x)^2}\left(\frac{\partial x'}{\partial x}\right)^2 + \frac{1}{(\Delta y)^2}\right)V_{i,j} + \left(\frac{\epsilon_{i,j}}{(\Delta x)^2}\left(\frac{\partial x'}{\partial x}\right)^2 + \frac{\epsilon_{i,j}}{2\Delta x}\frac{\partial^2 x'}{\partial x^2} + \frac{\epsilon_{i+1,j} - \epsilon_{i-1,j}}{4(\Delta x)^2}\left(\frac{\partial x'}{\partial x}\right)^2\right)V_{i+1,j} + \frac{1}{(\Delta y)^2}\left(\epsilon_{i,j} + \frac{\epsilon_{i,j+1} - \epsilon_{i,j-1}}{4}\right)V_{i,j+1} = 0$$

The domain in Fig. 5 is discretized using this formula, and the resulting matrix equation is then solved using iterative methods. For the gap between the hot and cold electrodes, the boundary condition $\partial V/\partial n = 0$, where $n$ designates the normal direction, is applied.

Recall that the electrostatic force density is given by Eq. (6). To find the net force on a fluid slug, it is necessary to integrate Eq. (6) all along the channel, not just over the volume of droplet itself. This is because the fringing fields at the edge of the charged capacitor exert an inward force on whatever material is present, including the external fluid surrounding the droplet; this force is felt as a pressure on the droplet interfaces, and the flow proceeds

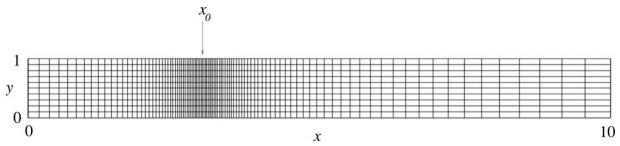


**Fig. 6 Representative grid used in computation; not all computational nodes are shown. $x_0$ is the point of maximum clustering.**

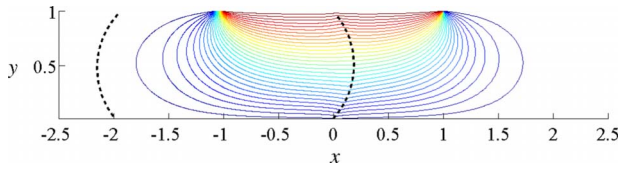


**Fig. 7 Example calculation of the electric potential *V* for a droplet centered under the left edge of an electrode**

such that the material with greatest electric permittivity is drawn into the "hot" capacitive region. The force on a droplet thus changes sign as it moves over a charged electrode. In addition, the DEP force becomes repulsive for droplets immersed in a fluid of higher dielectric permittivity. Note that, for completeness, in this paper we consider the full, symmetric case of a droplet moving into and out of a capacitor, resulting in antisymmetric force peaks on the fluid. Therefore, it is recommended that the electrodes in a DEP device be narrower than the droplet's length, and that they be actuated so that a fluid slug is pulled forward with a force always of the same sign.

The nondimensionalized values used in the following computations are $H=1$, $L=2$, $L_c=10$, $L_e=2$, $\epsilon_{ext}=1$, and $\epsilon_{int}=3$, unless otherwise stated. Generally 2001 nodes were used in the horizontal direction with $B_x=2$ and $x_0$ located at the leading edge of the droplet, and 51 nodes were used in the vertical direction unless otherwise specified. Figure 7 shows an example calculation of the electric potential for a droplet centered underneath the left edge of the electrode. The electric field is found by taking the gradient of this potential and the electrostatic force density is then found by squaring the electric field and again taking the gradient. As a consequence, the force density is very strongly localized in regions where the potential gradient is largest, i.e., near the hot/cold electrode interface.

To ensure that the resolution is high enough to capture the behavior of the net force, the force was calculated as the droplet moved over the edge of the electrode. The convergence of the method for a varied number of points in the horizontal direction is seen in Fig. 8. Note that capturing the height of the peak requires more resolution than nearby values of the total force.

Figure 9(*a*) shows the net force experienced by the droplet as a function of position. The gap width between the hot and cold electrodes is set to 2.5% of $H$. A sharp spike in force as the droplet approaches the electrode can be seen. Once the leading droplet edge has passed underneath the electrode, the force experienced by the droplet approaches a net nondimensionalized force of 1, which agrees with the theoretical result (15) from the lumped force calculation. As the droplet continues to move, it experiences a strong *increase* in force to the right as the leading edge of the droplet approaches the far edge of the electrode. It is at this point that one would want to activate the next electrode in the series to keep the droplet moving to the right. This force is counteracted as the leading edge exits the region covered by the hot electrode and the behavior described above is repeated but in the opposite direction.

Figures 9(*b*) and 9(*c*) show a similar force plot but with wider electrodes so that the active electrode is longer than the entire length of the droplet. In this case, we observe a *decrease* in net

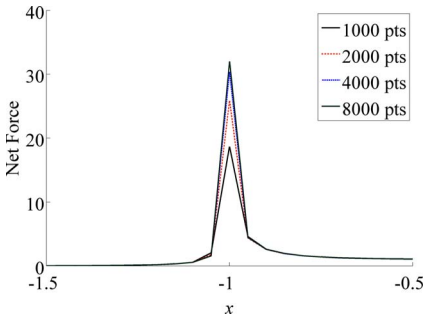


**Fig. 8 Convergence of force calculation as resolution increases. The number of points is in terms of the discretization in the *x*-direction.**

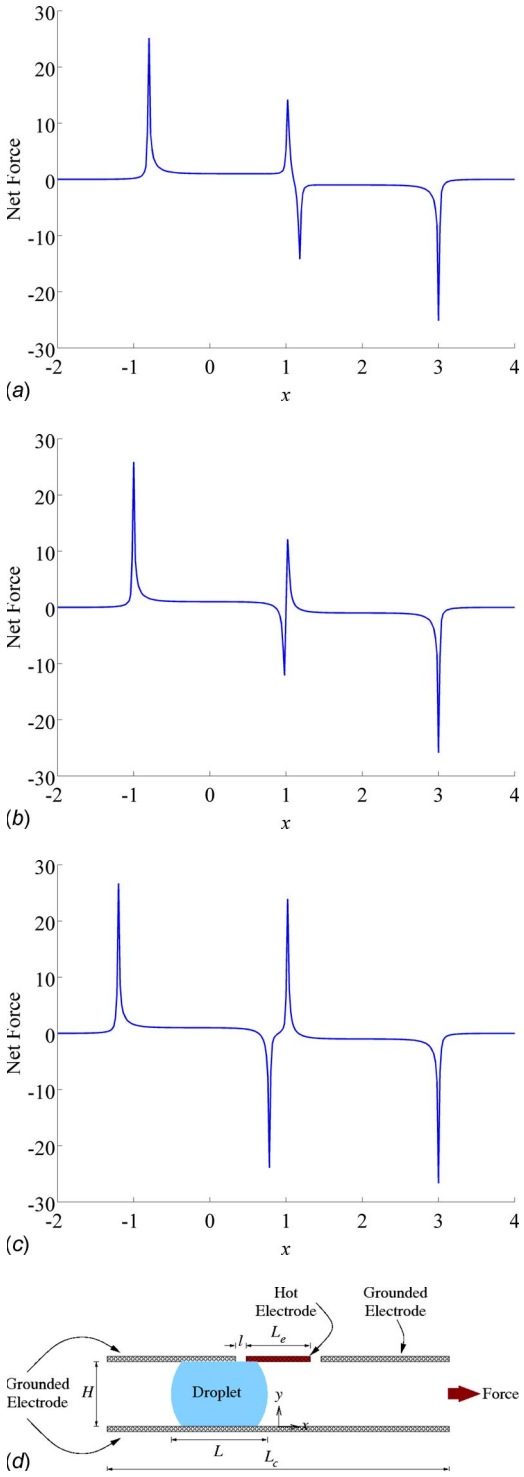


**Fig. 9 The net horizontal force experienced by the droplet as a function of position. Position is given by the location of the center of the droplet with respect to the center of the electrode. (*a*) $L_e=1.8$ and $L=2.0$; (*b*) $L_e=2.0$ and $L=2.0$; (*c*) $L_e=2.2$ and $L=2.0$; and (*d*) setup for force calculations in (*a*)–(*c*).**

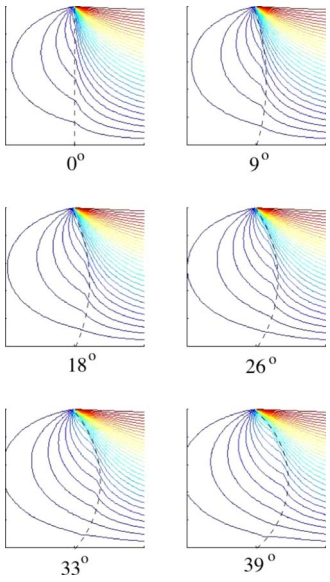


**Fig. 10 Electric potential for various contact angles. The increased gradient from the curvature results in greater net horizontal force.**

force as the leading droplet edge approaches the right edge of the active electrode. Because the electrode is longer than the droplet, the trailing edge of the droplet experiences a negative force as it nears the left edge of the electrode, causing the force to be directed to the left. This occurs before the leading edge of the droplet is near the right edge of the electrode, as in Fig. 9(*a*). This situation is not ideal if one hopes to use a sequence of electrodes to transport the droplet to the right. Clearly, a smaller electrode is desirable in applications. This phenomenon demonstrates how the use of narrow electrodes and the importance of accurate electrode actuation is critical in DEP to avoid "stalling" the droplet in the channel.

The spikes in force seen in Figures 9(*a*)–9(*c*) can be explained by the drastic change in the gradient of the electric field when the droplet edge (and hence the dielectric medium) passes through the fringing field induced by the electrodes. The effect of droplet contact angle can enhance this effect, see Figs. 10 and 11, increasing the net force on the droplet while it is in this region. This effect will only be seen when the droplet interface is located near the fringing field; otherwise the net force can be obtained by the previously mentioned analytical results. This is a result of the interface physically extending farther into the domain when the contact angle is increased; the nonuniformity of the fringing field gives rise to the increase in force as the interface extends further into the region.

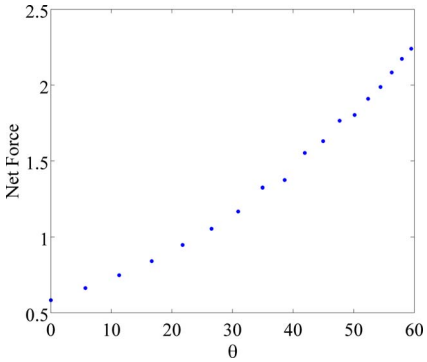


**Fig. 11 Increase in net horizontal force as the contact angle $\theta$ increases for a droplet with the leading edge placed near the left edge of the electrode near the fringing field**

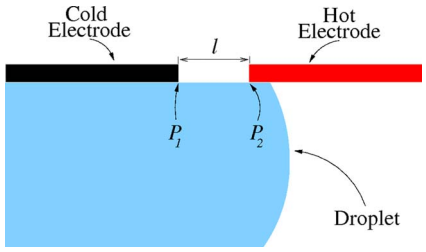


**Fig. 12 DEP configuration. The gap between the adjacent electrodes is *l*.**

The scaling in DEP varies with $L$, when the droplet interfaces are well removed from the electrode edges. However, when the interfaces are near the edges of the electrode, the force scaling is dependent on $l$, the distance between the hot and cold electrodes, as seen in Fig. 12. In EWOD, a surface force density is distributed over the droplet's front and rear interfaces and is localized within a length scale equal to the thickness of the dielectric layers lining the channel. DEP differs from EWOD in that a volumetric force density is localized within a radius on the order of the gap between the hot and cold electrodes. While varying the electrode gap width does not affect the net force when the droplet interfaces are sufficiently far from the voltage jump, it does spread the force distribution over a larger area.

Figure 13(*a*) shows the decrease in total force on the droplet as $l$ increases. As the leading edge of the droplet approaches the electrode, the net force felt by the droplet begins to grow. The rise in force occurs over the same distance as $l$, resulting in a broadening of the peak as $l$ increases and a reduction in maximum force obtained. Reducing the magnitude of the force by increasing the gap width of the electrodes may be beneficial in applications, as strong electric fields can cause local dielectric breakdown of the fluid.

Scaling these peaks with respect to the gap width demonstrates the linearity of the relationship. We see the same characteristic features of the peaks align when scaled in this manner, as seen in

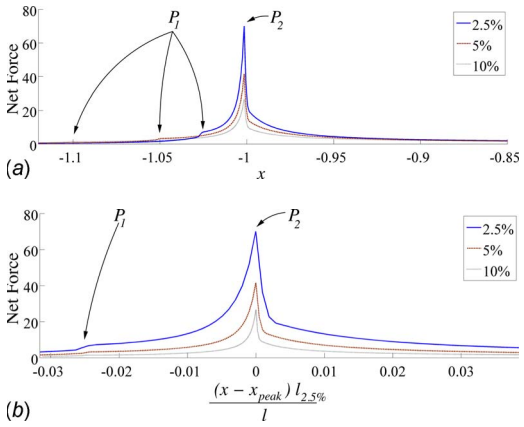


**Fig. 13 Net horizontal force versus *x*, for various values of *l*. The percentage shown indicates the width of the gap with respect to *H*. $P_1$ and $P_2$ are the same, as shown in Fig. 12. (*a*) Force versus position. $x=-1$ when the leading edge of the droplet is flush with the edge of the electrode. (*b*) Net horizontal force versus nondimensional position (relative to the length of the gap between the electrodes). $l_{2.5\%}$ is the length of the gap for $l=0.025H$ and $x_{peak}$ is the location of the maximum net force.**

Fig. 13(*b*). This is a beneficial relationship for the fabrication of microfluidic devices, as the behavior of droplets with different gap scalings can be extrapolated from known data.

Note that the net forces calculated in this paper pertain to a solid as well as a liquid; the dynamics of the medium do not play a role in these calculations. To fully integrate the electrostatics into a fluid solver, the force density (2) resulting from the electric field can be added as a body force acting upon the fluid. Investigation into fluid solvers coupled with the electrostatic effect is beginning to occur, for example, see Ref. [24]. Besides the bulk transport of the droplet, it is expected that some interesting dynamics would arise from adding the force distribution into a fluid solver. For instance, consider a droplet centered over the edge of a hot electrode, as seen in Fig 7. The droplet experiences a net force pulling it into the region of the hot electrode resulting from nonuniformity of the field. The field is particularly nonuniform in the region of the droplet located near the gap separating the hot and cold electrodes (i.e., the points $P_1$ and $P_2$ seen in Fig. 12). This region contains two peaks of extremely large magnitude but opposite signs. The net effect from this region is canceled out in the integration of the force density, but one would expect the fluid to respond to these peaks locally, creating some local fluid circulation. Furthermore, the net force is only in the horizontal direction, but forces are present in the vertical direction as well, which certainly will change the shape of the droplet.

## 4 Conclusion

The two primary methods for droplet transport in digital microfluidics, namely, DEP and EWOD have been investigated. EWOD works with conductive fluids while DEP pertains to insulating fluids. In both cases, droplet transport is achieved by sweeping a voltage along a microchannel ahead of the droplet. A review of the Korteweg–Helmholtz and Kelvin force density formulations has been given as well as how these force densities apply to DEP and EWOD.

An energy minimization approach was used to calculate the total force acting on a droplet under EWOD and DEP actuation. It is seen that the total force for EWOD scales as $1/d$, where $d$ is the dielectric layer thickness, while for DEP the total force scales as $1/H$, where $H$ is the channel height, which leads to different velocity scalings of $H/L$ and $1/L$ for EWOD and DEP, respectively. This indicates that DEP will be increasingly effective for small channel heights.

Investigation of the force distributions for EWOD shows how the force density is confined to the surface of the droplet while in DEP it is spread throughout the bulk. This is a critical difference to note when implementing any computational simulation of EWOD and DEP. Two methods were demonstrated for numerically calculating the force distribution for EWOD and DEP. To fully resolve the force when interfaces are located near regions of nonuniformity in the electric field, greater resolution is required. In DEP, it is noted that interface curvature can enhance the net force experienced by the droplet as a result of the fluid interface extending further into the electric field. When a droplet is under DEP actuation, small electrode sizes in comparison to droplet length are preferable, as they keep the net force pointing in the same direction as the droplet moves under the electrode and avoiding any possible stalling of the droplet in the channel. Investigation of the gap width $l$ between electrodes demonstrates how DEP scales with respect to $l$. As the interface travels through the region represented by $l$, the net force acting on the droplet increases. A decrease in the maximum force obtained also occurs as $l$ grows. In engineering applications, this parameter could be used to lessen the magnitude of the force if dielectric breakdown of the fluid was a concern.


## Acknowledgment

The authors would like to acknowledge partial funding from the Defense Advanced Research Projects Agency (DARPA) and the National Science Foundation (NSF). The authors benefited from discussions with Mr. E. Baird.


## References


[1] Cho, S. K., Moon, H., and Kim, C. J., 2003, "Creating, Transporting, Cutting, and Merging Liquid Droplets by Electrowetting-Based Actuation for Digital Microfluidic Circuits," J. Microelectromech. Syst., **12**(1), pp. 70–80.

[2] Cooney, C. G., Chen, C.-Y., Nadim, A., and Sterling, J. D., 2006, "Electrowetting Droplet Microfluidics on a Single Planar Surface," Microfluid. Nanofluid., **2**(5), pp. 435–446.

[3] Lee, J., Moon, H., Fowler, J., Kim, C. J., and Schoellhammer, T., 2001, "Addressable Micro Liquid Handling by Electric Control Of Surface Tension," *Proceedings of the IEEE International Conference MEMS*, Interlaken, Switzerland, Jan., pp. 499–502.

[4] Pollack, M. G., Fair, R. B., and Shenderov, A. D., 2000, "Electrowetting-Based Actuation of Liquid Droplets for Microfluidic Applications," Appl. Phys. Lett., **77**(11), pp. 1725–1726.

[5] Pollack, M. G., Shenderov, A. D., and Fair, R. B., 2002, "Electrowetting-Based Actuation of Droplets for Integrated Microfluidics," Lab Chip, **2**(2), pp. 96–101.

[6] Shapiro, B., Moon, H., Garrell, R. L., and Kim, C. J., 2003, "Equilibrium Behavior of Sessile Drops Under Surface Tension, Applied External Fields, and Material Variations," J. Appl. Phys., **93**(9), pp. 5794–5811.

[7] Wang, K. L., and Jones, T. B., 2005, "Electrowetting Dynamics of Microfluidic Actuation," Langmuir, **21**, pp. 4211–4217.

[8] Charkrabarty, K., and Zeng, J., 2006, *Design Automation Methods and Tools for Microfluidics-Based Biochips*, Springer, New York.

[9] Baird, E., and Mohseni, K., 2008, "Digitized Heat Transfer: A New Paradigm for Thermal Management of Compact Micro-Systems," IEEE Trans. Compon. Packag. Technol., **31**(1), pp. 143–151.

[10] Mohseni, K., 2005, "Effective Cooling of Integrated Circuits Using Liquid Alloy Electrowetting," *Proceedings of the Semiconductor Thermal Measurement, Modeling, and Management Symposium (SEMI-Therm)*, San Jose, CA, Mar. 15–17. IEEE.

[11] Mohseni, K., and Baird, E., 2007, "Digitized Heat Transfer Using Electrowetting on Dielectric," Nanoscale Microscale Thermophys. Eng., **11**(1&2), pp. 99–108.

[12] Mohseni, K., and Dolatabadi, A., 2006, "An Electrowetting Microvalve: Numerical Simulation," Ann. N.Y. Acad. Sci., **1077**(1), pp. 415–425.

[13] Dolatabadi, A., Mohseni, K., and Arzpeyma, A., 2006, "Behaviour of a Moving Droplet Under Electrowetting Actuation, Numerical Simulation," Can. J. Chem. Eng., **84**(1), pp. 17–21.

[14] Chang, Y.-J., Mohseni, K., and Bright, V., 2007, "Fabrication of Tapered SU-8 Structure and Effect of Sidewall Angle for a Variable Focus Microlens Using EWOD," Sens. Actuators, A, **136**(2), pp. 546–553.

[15] Cho, S. K., Fan, S. K., Moon, H., and Kim, C. J., 2002, "Towards Digital Microfluidic Circuits: Creating, Transporting, Cutting, and Merging Liquid Droplets by Electrowetting-Based Actuation," in *Technical Digest. MEMS, Proceedings 15th IEEE International Conference MEMS*, pp. 32–35.

[16] Fair, R. B., Srinivasan, V., Ren, H., Paik, P., and Pollack, M. G., 2003, "Electrowetting-Based On-Chip Sample Processing for Integrated Microfluidics," Tech. Dig. - Int. Electron Devices Meet., **2003**, pp. 32.5.1–32.5.4.

[17] Moon, H., Cho, S. K., Garrell, R., and Kim, C. J., 2002, "Low Voltage Electrowetting-On-Dielectric," J. Appl. Phys., **92**(7), pp. 4080–4087.

[18] Deval, J., Tabeling, P., and Ho, C. M., 2002, "A Dielectrophoretic Chaotic Mixer," *15th IEEE International Conference on MEMS (MEMS 2002)*, Las Vegas, NV, pp. 36–39.

[19] Gascoyne, P. R. C., Vykoukal, J. V., Schwartz, J. A., Anderson, T. J., Vykoukal, D. M., Current, K. W., McConaghy, C., Becker, F. F., and Andrews, C., 2004, "Dielectrophoresis-Based Programmable Fluidic Processors," Lab Chip, **4**(4), pp. 299–309.

[20] Jones, T. B., 2002, "On the Relationship of Dielectrophoresis and Electrowetting," Langmuir, **18**, pp. 4437–4443.

[21] Jones, T. B., Fowler, J. D., Chang, Y. S., and Kim, C. J., 2003, "Frequency-Based Relationship of Electrowetting and Dielectrophoretic Liquid Microactuation," Langmuir, **19**, pp. 7646–7651.

[22] Jones, T. B., and Wang, K. L., 2004, "Frequency-Dependent Electromechanics of Aqueous Liquids, Electrowetting and Dielectrophoresis," Langmuir, **20**, pp. 2813–2818.

[23] Walker, S. W., and Shapiro, B., 2006, "Modeling the Fluid Dynamics of Electrowetting on Dielectric (EWOD)," J. Microelectromech. Syst., **15**(4), pp. 986–1000.

[24] Singh, P., and Aubry, N., 2007, "Transport and Deformation of Droplets in a Microdevice Using Dielectrophoresis," Electrophoresis, **28**, pp. 644–657.

[25] Bahadur, V., and Garimella, S. V., 2006, "An Energy-Based Model for Electrowetting-Induced Droplet Actuation," J. Micromech. Microeng., **11**(8), pp. 1994–1503.

[26] Baird, E., Young, P., and Mohseni, K., 2007, "Electrostatic Force Calculation for an Ewod-Actuated Droplet," Microfluid. Nanofluid., **3**(6), pp. 635–644.

[27] Buehrle, J., Herminghaus, S., and Mugele, F., 2003, "Interface Profiles Near Three-Phase Contract Lines in Electric Fields," Phys. Rev. Lett., **91**(4), p.

208301.
[28] Kang, K. H., 2002, "How Electrostatic Fields Change Contact Angle in Electrowetting," Langmuir, **18**(26), pp. 10318–10322.
[29] Vallet, M., Vallade, M., and Berge, B., 1999, "Limiting Phenomena for the Spreading of Water on Polymer Films by Electrowetting," Eur. Phys. J. B, **11**(4), pp. 583–591.
[30] Jackson, J. D., 1998, *Classical Electrodynamics*, Wiley, New York.
[31] Landau, L. D., Lifshitz, E. M., and Pitaevskii, L. P., 1984, *Electrodynamics of Continuous Media*, 2nd ed., Pergamon, New York, Vol. 8.
[32] Saville, D. A., 1984, "Electrohydrodynamics: The Taylor–Melcher Leaky-Dielectric Model," Annu. Rev. Fluid Mech., **29**, pp. 27–64.
[33] For the electrostatic approximation to apply, the characteristic time scale for electric phenomena, $\tau=\epsilon=\sigma$ must be small. Note that $\tau$ is the ratio of dielectric permeability to conductivity of the medium. For the microfluidic applications considered here, this condition will usually be valid. For example, pure water has a electrical relaxation time of $\approx 10^{-4}$ and a hydrodynamic time scale of $\approx 0.045$. See [45] for more details.
[34] Penfield, P. A., and Haus, H. A., 1967, *Electrodynamics of Moving Media*, MIT, Cambridge.
[35] Stratton, J. A., 1941, *Electromagnetic Theory*, McGraw-Hill, New York.
[36] Woodson, H. H., and Melcher, J. R., 1968, *Electromechanical Dynamics, Part I: Discrete Systems*, Wiley, New York.
[37] Bobbio, S., 2000, *Electrodynamics of Materials: Forces, Stresses, and Energies in Solids and Fluids*, Academic, New York.
[38] Melcher, J. R., 1981, *Continuum Mechanics*, MIT, Cambridge.
[39] Woodson, H. H., and Melcher, J. R., 1968, *Electromechanical Dynamics, Part II: Fields, Forces, and Motion*, Wiley, New York.
[40] Woodson, H. H., and Melcher, J. R., 1968, *Electromechanical Dynamics, Part III: Elastic and Fluid Media*, John, New York.
[41] Mohseni, K., and Baird, E., 2007, "A Unified Velocity Model for Digital Microfluidics," Nanoscale Microscale Thermophys. Eng., **11**(1&2), pp. 109–120.
[42] If the droplet is initially charged or if it is short cut to the electrodes on one side of the channel while isolated from the electrodes on the other side, there will be another source of force on the droplet represented locally by $\rho_f \mathbf{E}$. Our approach here can be easily extended to this case as well.
[43] Unless the droplet is isolated only from the electrodes on one side of the channel. In this case the droplet stays at the voltage of the electrodes on the other side of the channel.
[44] Holst, T. L., 1977, "Numerical Solution of Axisymmetric Boattail Flow Fields With Plume Simulators," *15th Aerospace Sciences Meeting and Exhibit*, Los Angeles, CA, Jan. 24–26, Paper No. AIAA 77-224.
[45] Melcher, J. R., and Taylor, G. I., 1969, "Electrohydrodynamics: A Review of the Role of Interfacial Shear Stresses," Annu. Rev. Fluid Mech., **1**, pp. 111–146.

**Y. Berrouche**

**Y. Avenas**

**C. Schaeffer**

Grenoble Institute of Technology,
38402 Saint-Martin-d'Hères Cedex,
Grenoble, Isère 38402,
France

**P. Wang**

**H.-C. Chang**

University of Notre Dame,
Notre Dame, IN 46556

# Optimization of High Flow Rate Nanoporous Electroosmotic Pump

*We present a theory for optimizing the thermodynamic efficiency of an electroosmotic (EO) pump with a large surface area highly charged nanoporous silica disk substrate. It was found that the optimum thermodynamic efficiency depends on the temperature, the silica zeta potential, the viscosity, the permittivity, the ion valency, the tortuosity of the nanoporous silica but mainly the effective normalized pore radius of the substrate scaled with respect to the Debye length. Using de-ionized water as the pumping liquid, the optimized EO pump generates a maximum flow rate of 13.6 ml/min at a pressure of 2 kPa under an applied voltage of 150 V. The power consumed by the pump is less than 0. 4 W. The EO pump was designed to eliminate any bubble in the hydraulic circuit such that the pump can be operated continuously without significant degradation in the performance.* [DOI: 10.1115/1.2956609]

## Introduction

Micropumps have potential applications in medical devices, portable fuel cells, and electronic cooling. There are generally two types of micropumps: mechanical pumps (using moving parts such as check valves and oscillating membranes) and nonmechanical pumps (converting electrical energy into kinetic energy in the fluid). The disadvantage of using mechanical pumps is that they are unreliable because of the high friction wear of microelectromechanical system (MEMS) devices, they generate noise, and they are expensive, particularly for applications with high-pressure requirement (e.g., chromatography and microcooling of power electronics). Electrokinetic (EK) pumps do not suffer from these disadvantages of mechanical pumps. One of the most popular EK pumps is the electroosmotic (EO) pump, which is very cheap to fabricate in comparison to other EK pumps [1] and can generate high pressure with a small volume substrate. Nevertheless, because the shear stress is confined to a thin Debye layer, EO pumps suffer from high viscous dissipation and exhibit a very low thermodynamic efficiency like all other EK pumps. In addition, Faradic reactions at the electrodes generate bubbles by electrolysis and change the pH of the working fluid—both do not allow EO pumps to operate continuously for more than a few hours [2].

In this paper the theory of EO pumping in a capillary and a porous medium is recalled to increase the thermodynamic efficiency. In particular, the volume flow rate is increased by several orders by extending the previous silica capillary design to one using a large silica disk. New housing designs are introduced in this prototype to solve the major problems of EO pumps (bubble generation and instability due to pH change).

## Theory of the EO Pump

The basis of EO pumps is the presence of a Maxwell body force on the liquid within the charged electric double layers (EDLs) (Fig. 1). Due to the charged dielectric wall, counterions of the bulk electrolyte are attracted to the surface such that the net charge is zero. This charged Debye layer is divided into two layers, the inner one (Stern layer), which is immobile due to strong electrical forces, and the outer one (the diffusive layer), which contains free charges [3]. The counterion distribution within the diffused layer is at Boltzmann equilibrium with the electromigration flux canceled exactly by the diffusion flux. This balance stipulates that thickness of the diffused layer to be the Debye length $\lambda$ [4]:

$$\lambda = \sqrt{\frac{\varepsilon k_B T}{2e^2 z^2 n}} \tag{1}$$

where $\varepsilon$, $n$, $k_B$, $T$, $e$, and $z$ are the dielectric permittivity of the liquid, the concentrations of counterions in the bulk solution, the Boltzmann number, the temperature of the liquid, the electron charge, and the valance number of the counter ions, respectively.

For an aqueous solution with an asymmetric electrolyte at 25°C, the Debye length becomes [5]

$$\lambda = \frac{9.61 \times 10^{-9}}{\sqrt{z^2 n}} \tag{2}$$

with $\lambda$ in meters and $n$ in mol m$^{-3}$. Here we see that the Debye length is dependent on the concentration of counterions, which can be controlled by changing the conductivity of the liquid.

The electrical potential between these layers is called the zeta potential $\zeta$, which highly depends on the pH of the working fluid, as the surface charge density can vary due to the oxidation and reduction reactions at different pH. In the presence of a tangential electric field, ions in the diffused layer suffer a Coulombic force and move toward the electrode of the opposite polarity. Viscous drag by the migrating ions creates fluid motion within the diffused layer and transfers momentum via viscosity into the bulk (Fig. 2).

The Navier–Stokes equation for an incompressible liquid can be given as

$$\rho\left(\frac{\partial U}{\partial t} + (U\nabla)U\right) = -\nabla P + \mu\nabla^2 U + \rho_V g + \rho_E E \tag{3}$$

where $\rho$, $U$, $P$, $\mu$, $g$, $\rho_E$, and $E$ are the density of the liquid, the velocity vector, the pressure, the fluid viscosity, the gravity, the electrical charge density in the Debye layer, and the electric field intensity, respectively.

In a capillary of radius $a$, Rice et al. [6] derived the velocity profile $u(r)$ under a tangential electrical field $E$, assuming that the pressure gradient is constant, the gravity force is neglected, and the fluid is incompressible.

$$u(r) = \frac{-a^2}{4\mu}\frac{\Delta P}{l_c}\left(1 - \frac{r^2}{a^2}\right) - \frac{\varepsilon\xi E}{\mu}\left(1 - \frac{\psi(r)}{\xi}\right) \tag{4}$$

In Eq. (4), $\mu$, $\zeta$, $\Delta P$, and $l_c$ are the viscosity of the working fluid, the zeta potential, the pressure drop, and the capillary

Contributed by the Fluids Engineering Division of ASME for publication in the JOURNAL OF FLUIDS ENGINEERING. Manuscript received July 16, 2007; final manuscript received December 17, 2007; published online July 31, 2008. Assoc. Editor: Dennis Siginer.

  

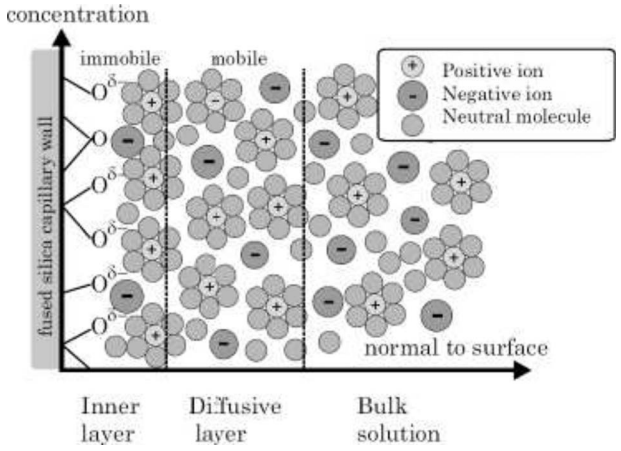


**Fig. 1 Structure of EDL**

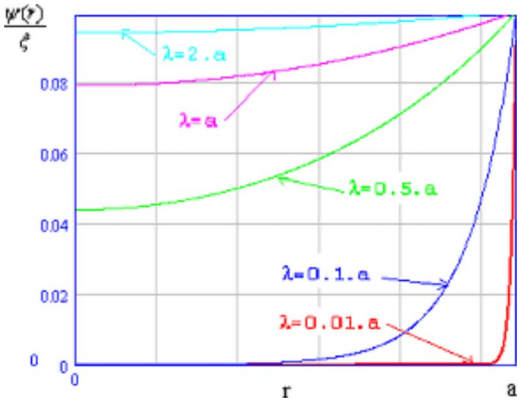


**Fig. 4 The variation of the normalized inner potential profile for different values of the Debye length.**

length, respectively. $\psi(r)$ is the potential in the capillary due to the EDL called the inner potential. The velocity profile in a capillary of a radius $a$ for different pressure drops has been drawn in Fig. 3, where the pressure drop influences the velocity profile. It is seen that by decreasing the pressure, the deformation in the velocity profile will decrease. This profile corresponds to the EO pump presented in Fig. 2.

In order to get a closed-form analytical solution of the profile of the inner potential across the capillary, the Debye–Huckle approximation can be used [5]. This assumption gives

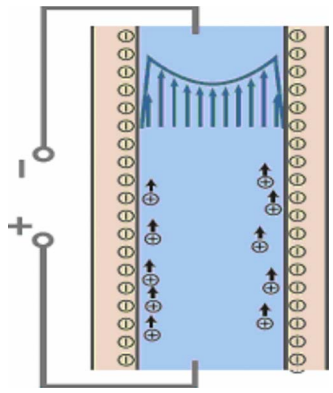


**Fig. 2 The EO pumping in a capillary**

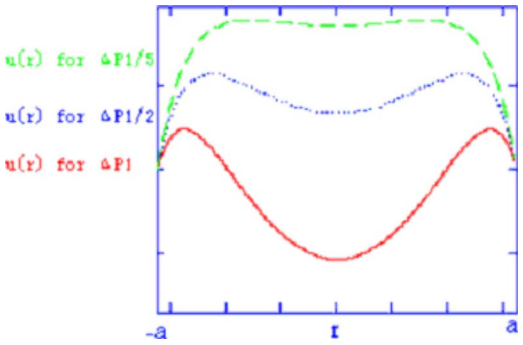


**Fig. 3 The velocity profile $u(r)$ in a capillary of radius $a$ for different values of the pressure drop ($\Delta P=\Delta P1$, $\Delta P=\Delta P1/2$, and $\Delta P=\Delta P1/5$, $\Delta P1$ are the given pressure drops less than $\Delta P_m$).**

$$\psi(r) = \xi \frac{I_0\left(\frac{r}{\lambda}\right)}{I_0\left(\frac{a}{\lambda}\right)} \tag{5}$$

where $I_0$ is the zero-order modified Bessel function of the first kind.

The variation of the normalized inner potential profile $\psi(r)/\xi$ in a capillary of radius $a$ for various values of the Debye length is shown in Fig. 4. It can be seen that the inner potential profile depends on the Debye length and hence on the conductivity of the liquid. The integration of Eq. (4) in a capillary over a section $\pi a^2$, gives the flow rate as

$$Q_c = \frac{-\pi a 4}{8\mu l_c}\Delta P - \frac{\pi a^2 \xi \varepsilon E}{\mu}\int_0^a \left(1 - \frac{I_0\left(\frac{r}{\lambda}\right)}{I_0\left(\frac{a}{\lambda}\right)}\right)\frac{2r}{a^2}dr \tag{6}$$

**Extension to a Nanoporous Pump Substrate.** The very small value of the Debye length (nanometers) gives a very low range for the flow rate ($\mu$l/min) [1,7,8]. This low flow rate can be increased with a large cross section of the pump section. However, as the pumping electric Maxwell stress is confined to the diffused layer, this large cross section should consist of a bundle of small capillaries whose radii approach the Debye length. A monolithic silica matrix, which can be made from sol-gel synthesis, is a nanoporous structure resembling this massive capillary bundle. However, the mechanical resistance of the monolithic silica matrix is low and it can hence be used only for a capillary EO pump [1], unless the porosity of the sintered silica can be reduced [4]. The monolithic silica matrix can be easily prepared by the procedures of Refs. [9–11]. Other authors such as Zeng et al. [12] and Brask [4] have used sintered borosilicate disks that contain 80.60% silica ($SiO_2$), 12.60% boric oxide ($B_2O_3$), and 4.20% sodium oxide ($Na_2O$). These samples are fabricated by ROBU (Germany). A third method used to create a porous structure is to pack silica particles [13], which is rather tedious and difficult to carry out.

The theoretical study of electroosmosis in a porous structure is very complicated due to the complex geometry of the sintered silica. To simplify the study of a porous disk, Zeng et al. [14] extended the maximum pressure $\Delta P_m$ and the maximum flow rate $Q_m$ for a porous EO pump as follows:

$$Q_m = \frac{\Psi A \xi \varepsilon V}{\mu l \tau}\left(1 - \frac{2}{a_{\text{eff}}/\lambda}\frac{I_1(a_{\text{eff}}/\lambda)}{I_0(a_{\text{eff}}/\lambda)}\right) \tag{7}$$

$$\Delta P_m = \frac{8\xi\varepsilon V}{a_{\text{eff}}^2}\left(1 - \frac{2}{a_{\text{eff}}/\lambda}\frac{I_1(a_{\text{eff}}/\lambda)}{I_0(a_{\text{eff}}/\lambda)}\right) \tag{8}$$

In Eqs. (7) and (8), $\Psi$, $\tau$, $a_{\text{eff}}$, and $V$ are the porosity, the tortuosity ($(l_c/l)^2$), the effective pore radius of porous silica disk, and the applied voltage, respectively. $I_0$ and $I_1$ are the zero and the first order modified Bessel functions of the first kind. It is seen that the maximum pressure and the maximum flow rate are functions of the geometry ($A$,$L$), the porous structure ($\psi$, $\tau$, $a_{\text{eff}}$), the nature of the wall and the liquid ($\zeta$, $\varepsilon$, $\mu$, $\lambda$), and the applied voltage ($V$).

## Optimization of a Nanoporous EO Pump

In order to increase the thermodynamic efficiency of the EO pump, a study of an analytical formula of the optimum thermodynamic efficiency will be calculated. The thermodynamic efficiency of an EK pump represents the hydraulic power generated over the total electrical power consumed by the pump, which can then be given as

$$\eta(\Delta P) = \left|\frac{Q(\Delta P)\Delta P}{VI_T(\Delta P)}\right| \tag{9}$$

In Eq. (9), $Q$, $\Delta P$, $V$ and $I_T$ are the operating flow rate, the operating pressure drop, the applied voltage, and the total consumed current in EO pump, respectively, assuming that the losses due to electrochemical reactions are negligible.

Because of the linearity of the flow rate with respect to the back pressure, the flow rate and the back pressure are related by a convenient universal relationship when normalized by their maximum values [15].

$$Q(\Delta P) = Q_m\left(1 - \frac{\Delta P}{\Delta P_m}\right) \tag{10}$$

Let us consider a porous silica disk, which has a section $A$, a length $l$, a porosity $\Psi$, a tortuosity $\tau$, and an effective pore radius $a_{\text{eff}}$. This disk therefore can be considered as a collection of parallel capillary pumps of radius $a_{\text{eff}}$. In Eq. (9), the total current is divided into three parts: the electroconvection current $I_{\text{con}}$, the electromigration current $I_{\text{meg}}$, and the diffusion current. The last is neglected compared to the other two [2]. The currents $I_{\text{con}}$ and $I_{\text{meg}}$ can hence be given as

$$I_{\text{con}} = \iint_S \rho_E(r)u(r)ds \tag{11}$$

$$I_{\text{meg}} = \iint_S \sigma(r)Eds \tag{12}$$

where $S$, $\sigma(r)$, and $\rho_E(r)$ are the cross section, the electrical conductivity, and the free density charge in the Debye layer, respectively, and they can be written as [5]

$$\rho_E(r) = -\frac{\varepsilon}{\lambda^2}\psi(r) \tag{13}$$

$$\sigma(r) = Kn\cosh\left(\frac{ze\psi(r)}{k_BT}\right) \tag{14}$$

where $K$ is the ion mobility.

In a capillary of a radius $a_{\text{eff}}$, using Eq. (13), Eqs. (11) and (12) become

$$I_{\text{con}} = 2\pi\left(\frac{\lambda^2\varepsilon {a_{\text{eff}}}^{*2}}{4\mu}\frac{\Delta P}{l_c}\int_0^{{a_{\text{eff}}}^*}\left(1 - \frac{r^{*2}}{{a_{\text{eff}}}^{*2}}\right)\psi(r^*)r^*dr^* - \frac{\varepsilon^2\xi V}{\mu l}\int_0^{{a_{\text{eff}}}^*}\left(1 - \frac{\psi(r^*)}{\xi}\right)\psi(r^*)r^*dr^*\right) \tag{15}$$

$$I_{\text{meg}} = -\int_0^{{a_{\text{eff}}}^*}\lambda^2\frac{V}{l}\sigma(r^*)r^*dr^* \tag{16}$$

where ${a_{\text{eff}}}^* = a_{\text{eff}}/\lambda$, $r* = r/\lambda$, and $V = -El$ are the normalized pore radius, the normalized radial coordinate in the capillary, and the applied voltage, respectively.

Hence the current can be written as

$$I = \Delta P\Gamma_1 - V\Gamma_2 \tag{17}$$

with

$$\Gamma_1 = \frac{2\pi\lambda^2\varepsilon {a_{\text{eff}}}^{*2}}{4\mu l_c}\int_0^{{a_{\text{eff}}}^*}\left(1 - \frac{r^{*2}}{{a_{\text{eff}}}^{*2}}\right)\psi(r^*)r^*dr^* \tag{18}$$

$$\Gamma_2 = \frac{2\pi\varepsilon^2\xi}{l_c\mu}\int_0^{{a_{\text{eff}}}^*}\left(1 - \frac{\psi(r^*)}{\xi}\right)\psi(r^*)r^*dr^* + \int_0^{{a_{\text{eff}}}^*}\frac{2\pi\lambda^2}{l_c}\sigma(r^*)r^*dr^* \tag{19}$$

Therefore, the total current in a porous structure is the resultant current of the currents in a collection of parallel capillary pumps.

The current $I_T$ in Eq. (18) then becomes

$$I_T = \Delta P\Xi_1 - V\Xi_2 \tag{20}$$

with

$$\Xi_{1,2} = \frac{\Psi A}{\sqrt{\tau}\pi {a_{\text{eff}}}^2}\Gamma_{1,2} \tag{21}$$

Defining $\Delta P^* = \Delta P/\Delta P_m$, Eq. (9) becomes

$$\eta(\Delta P^*) = \left|\frac{\alpha\Delta P^*(1 - \Delta P^*)}{\Delta P^* - \beta}\right| \tag{22}$$

with

$$\beta = \frac{V\Xi_2}{\Delta P_m\Xi_1}$$

and

$$\alpha = \frac{Q_m}{V\Xi_1} \tag{23}$$

When $\eta$ is a maximum, the value of $\Delta P^*$ becomes

$$\Delta {P_{\text{op}}}^* = \beta\left(1 - \sqrt{1 - \frac{1}{\beta}}\right) \tag{24}$$

As $\beta$ is small, a Taylor expansion in the parameter yields

$$\Delta {P_{\text{op}}}^* \approx \frac{1}{2} + \frac{1}{8\beta} \tag{25}$$

Therefore,

$$\eta_{\text{op}} = \alpha\frac{\frac{1}{4} - \frac{1}{(8\beta)^2}}{\beta - \frac{1}{2} - \frac{1}{8\beta}} \tag{26}$$

When $\beta$ is higher than 1, this gives

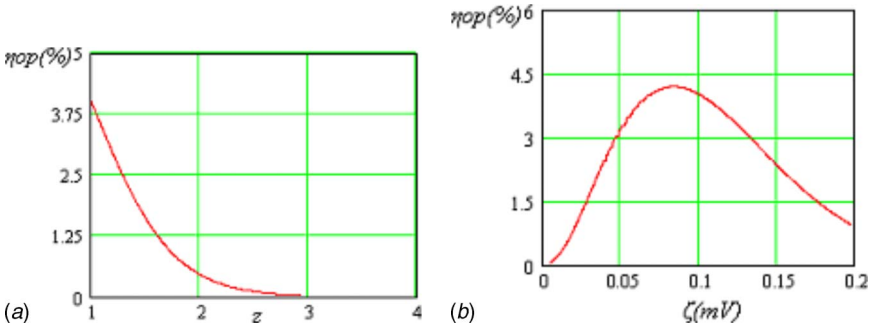


**Fig. 5 Influence of the valance number (*a*), and the Zeta potential (*b*) on the optimum thermodynamic efficiency for an effective normalized pore radius of 4.**

$$\eta_{\text{op}} \approx \frac{\alpha}{4\beta} \tag{27}$$

Finally, the optimum thermodynamic efficiency can be approximated as

$$\eta_{\text{op}}(a_{\text{eff}}^{*}) \approx \frac{\left[\int_0^{a_{\text{eff}}^{*}} \left(1 - \frac{I_0(r^*)}{I_0(a_{\text{eff}}^{*})}\right) \frac{2r^*}{a_{\text{eff}}^{*2}} dr^*\right]^2}{\sqrt{\tau}\left[\left(\int_0^{a_{\text{eff}}^{*}} \left(1 - \frac{I_0(r^*)}{I_0(a_{\text{eff}}^{*})}\right) \frac{I_0(r^*)}{I_0(a_{\text{eff}}^{*})} r^* dr^* + \int_0^{a_{\text{eff}}^{*}} \frac{k_B K T \mu}{ze\varepsilon\xi^2} \cosh\left(\frac{ze\xi}{k_B T} \frac{I_0(r^*)}{I_0(a_{\text{eff}}^{*})}\right) r^* dr^*\right)\right]} \tag{28}$$

**Discussion.** We see that the optimum thermodynamic efficiency depends only on the temperature, the zeta potential (pH), the viscosity, the permittivity, the valance number, and the tortuosity but mainly the effective normalized pore radius. The thermodynamic efficiency is not a function to the cross section ($A$) and the length ($l$); hence, this formula is given for any porous disk cross section and length.

Because the working fluid is, in general, a liquid (DI water, methanol, and electrolyte), the range in variation of either the temperature, the viscosity ($0.2\times10^{-3}$ to $2\times10^{-3}$ PI), or the permittivity of the liquid is very small; hence, there is no big effect on the flow parameters on the thermodynamic efficiency.

In Fig. 5($a$), it is seen that the optimum thermodynamic efficiency is higher for the univalent liquids, and it will be very small for a valance number more than 3. The optimum thermodynamic efficiency is at a maximum for zeta potentials equal to 95 mV for $a_{\text{eff}}^{*}=4$. (Fig. 5($b$)). The tortuosity does not have a large effect on the optimum thermodynamic efficiency because of its small interval of variety (1–1.5). In practice for the given liquid and solid (silica), the only way to control the optimum thermodynamic efficiency is by adjusting the effective normalized pore radius $a_{\text{eff}}^{*}$ or more clearly the Debye length. From Fig. 6, it is seen that the optimum thermodynamic efficiency is at a maximum when the normalized effective pore radius is 4.

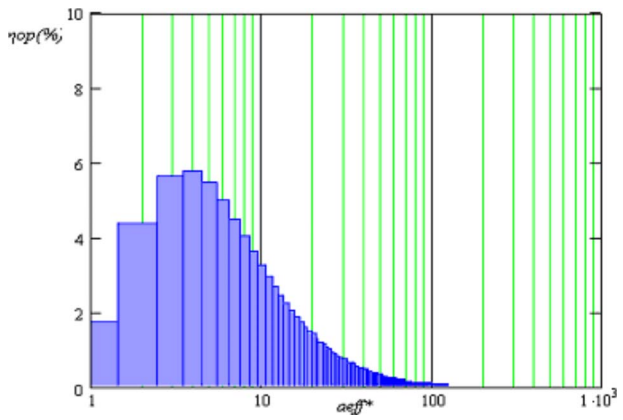


**Fig. 6 The variation of the optimum efficiency in function of the normalized pore radius $a_{\text{eff}}^{*}$**

**Conclusion on the Optimum Thermodynamic Efficiency.** Hence for any EO porous pump with a cross section ($A$) and a length ($l$), the optimum thermodynamic efficiency is given for an effective pore radius of the porous structure about four times the Debye length, which can be controlled by adjusting the conductivity of pumping liquid or by changing the effective pore radius.

The effective capillary radius of the porous medium in our theory can be estimated from the radius of the silica particles that have been sintered to form the disk from the model in our earlier paper [17]. This model gives the effective pore radius to be about 0.16 times the particle radius. This model has been applied for different designs found in literature (Table 1). In order to verify the optimum thermodynamic calculation, an experimental setup is presented in the next section.

## Fabrication and Characterization

**The Design.** The design and characterization of the porous EO pump have been presented in Ref. [17]. In Fig. 7 the EO pump design can be divided into three big parts; the electrode chamber

**Table 1 Test of the model for tow pumps given in the literature**

| | D.S. Reichmuth pump | Santiago pump |
|---|---|---|
| Effective pore radius[a] ($\mu$m) | 0.53 | 0.55 |
| Real radius of the particles[a] ($\mu$m) | 3.5 | [1–5] |
| Real radius of the particles[m] ($\mu$m) | 3.43 | 3.5 |

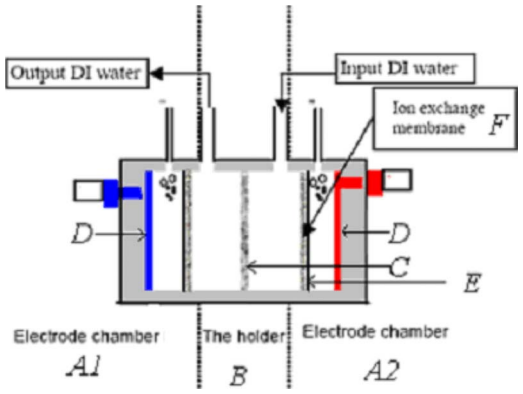


**Fig. 7 The Schematic of the porous EO pump**

anode ($A_1$), the electrode chamber cathode ($A_2$), and the disk holder ($B$). All of these parts are made of Plexiglas, which has the advantage of being transparent and easily machined. Each electrode chamber contains electrodes made of carbon ($D$) and good contact between the carbon and the external wire is assured by a gilded copper connector. The use of carbon avoids the corrosion of the electrode when the pump is operating. Next to the carbon electrode there is a mesh ($E$) made of Plexiglas, which holds ion exchange membranes (IEMs) ($F$). The aim of the IEM is to keep a stable pH of the working fluid [4] and to avoid the existence of gas bubbles (in the hydraulic circuit) generated by electrolysis in the electrode chambers. These IEMs have been bought from Fumatech (Germany). The disk holder is used to hold a sintered pure silica disk ($C$). This disk has been bought from ROBU. It has a cross section $A=\pi(2.5\ \text{cm})^2$ and a length $l=3.5$ mm, with a porosity $\Psi=35\%$, a tortuosity $1<\tau<1.5$, and an effective pore radius of 0.75 $\mu$m.

The volume of the first prototype is $80\times80\times60\ \text{mm}^3$ (Fig. 8).

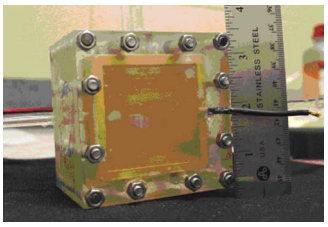

**Fig. 8 The design of the porous EO pump**

This volume can be reduced for the same performance. Indeed in Eq. (16), $A/l$ is constant; therefore, if the cross section and the length of the porous disk are reduced by the same factor, the maximum flow rate is kept the same.

**Measurement Setup.** The characterization of the pump consists of determining the maximum pressure drop, the maximum flow rate, and the power consumption. The measurement setup is presented in Fig. 9. In the maximum pressure drop measurement setup, the outlet of the EO pump is closed by a pressure sensor, which forbids the fluid motion, hence the measured pressure is the maximum pressure drop generated by the pump. In the maximum flow rate measurement setup, the input and output of the pump are put at the same height, hence the pressure at the inlet and outlet of an EK pump may still be quite different. In our application, this pressure difference is negligible when compared to the pressure generated by the EO pump because we did not consider the viscous effect due to the very short distances between the reservoirs and the inlet and the outlet of the EO pump. For example, in a cylindrical conduct of a length $L_{cc}=10$ cm and a diameter $2R_{cc}=1$ cm, when the flow rate $Q_{cc}$ is 18 ml/min, the pressure losses due to the viscous effect are given as

$$\Delta P_{\text{loss}}=\frac{8L_{cc}\mu Q_{cc}}{\pi R_{cc}^{\ 4}} \tag{29}$$

As a numerical application, $\Delta P_{\text{loss}}=0.12$ Pa, which is still negligible when compared to the pressure generated by the EO pump. The maximum flow rate of the pump can be measured by weighing the pumped liquid on a balance, which is connected to a computer. The software used to control the balance is WINCT Data Communication from the A&D company. In both setups, the power consumption is given by measuring the applied voltage and current consumed by the pump. The EO has been tested with DI water and with a conductive liquid (electrolyte).

**Operation of the Pump With DI Water.** The $Q_m$-$\Delta P_m$ diagram of the EO pump with DI water is presented in the Fig. 10. The EO pump can generate flow rates of 13.6 ml/min and pressures of 1.9 kPa at 150 V and 18 ml/min at 200 V. The electric power used by the pump at 150 V is only 217.5 mW and it gives a hydraulic power of 0.47 mW; hence the thermodynamic efficiency is 0.2%. The pump works without any noise compared to mechanical pumps and without any bubbles in the hydraulic circuit due to the IEM.

**Operation of the Pump With an Electrolyte.** This test targets the verification of the model of the optimum thermodynamic efficiency. The optimum thermodynamic efficiency can be approximated by the maximum thermodynamic efficiency, which is given

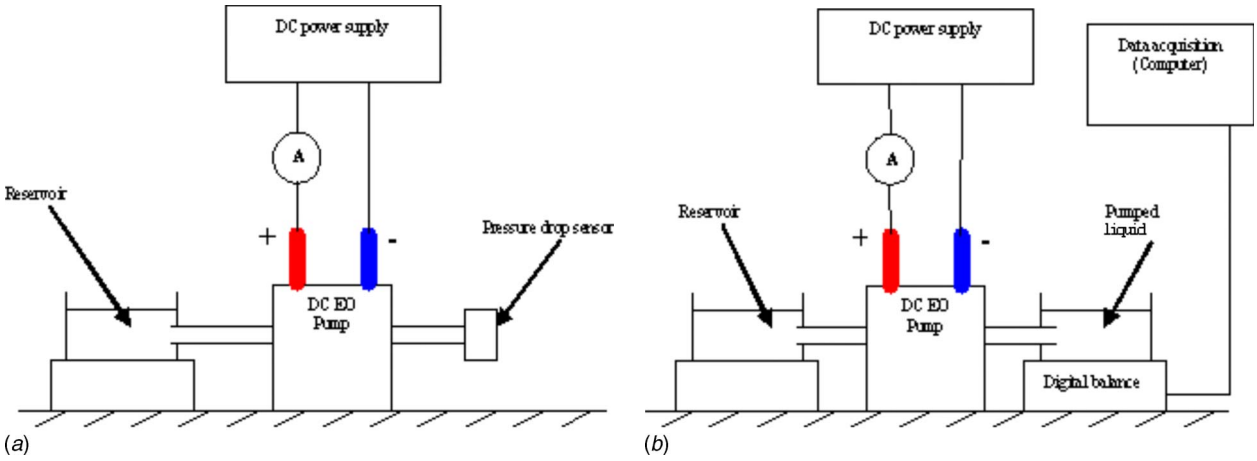


**Fig. 9 Measurement setup**

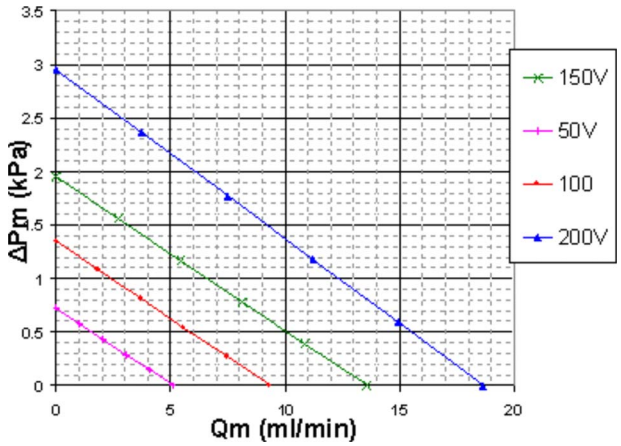


**Fig. 10 Performance curves for the EO pump showing max flow rate versus max pumping pressure for different operating voltages. The pumping liquid is DI water.**

for the maximum hydraulic power. From Fig. 11 the maximum hydraulic power of an EK pump is given for a flow rate $Q_m/2$ and a pressure $\Delta P_m/2$. The experimental maximum thermodynamic efficiency is then calculated by Eq. (30)

$$\eta_{\exp,m} = \frac{\frac{Q_m}{2}\frac{\Delta P_m}{2}}{V\frac{I_{Q_m} + I_{\Delta P_m}}{2}} \tag{30}$$

with $I_{Q_m}$ and $I_{\Delta P_m}$ being the maximum currents consumed by the EO pump, in the maximum flow rate measurement setup and the maximum pressure measurement setup, respectively.

In order to change the normalized effective pore radius, the Debye length has been changed by using various values of conductivity of NaCl electrolyte. The tested silica disk has an effective pore radius of about 0.75 $\mu$m (from the datasheet), Table 2 represents the normalized pore radius and the Debye length for different values of conductivity of this disk.

The variation of the thermodynamic efficiency for various normalized pore radii is given in Fig. 12. It can be clearly seen that the optimum thermodynamic efficiency is given for a normalized pore radius of 4.5, which corresponds to a Debye length 0.17 $\mu$m and to a conductivity of 25 $\mu$S/m. This result hence verifies the optimization of the thermodynamic efficiency model given above.

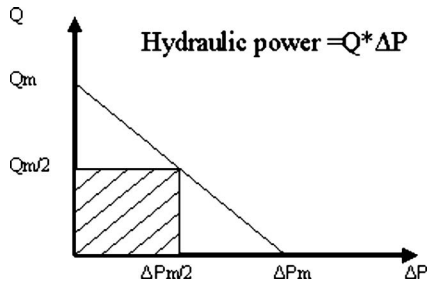


**Fig. 11 *Q-P* diagram for EK pumps**

**Table 2 The normalized pore radius for various conductivities, the effective pore radius is 0.75 $\mu$m**

| Conductivity $\mu$S/m | 5 | 25 | 110 | 300 | 734 | 1000 |
|---|---|---|---|---|---|---|
| $\lambda(\mu m)$ | 0.373 | 0.167 | 0.079 | 0.048 | 0.031 | 0.026 |
| $a_{\text{eff}}^*$ | 2.0 | 4.5 | 9.4 | 15.6 | 24.4 | 28.5 |

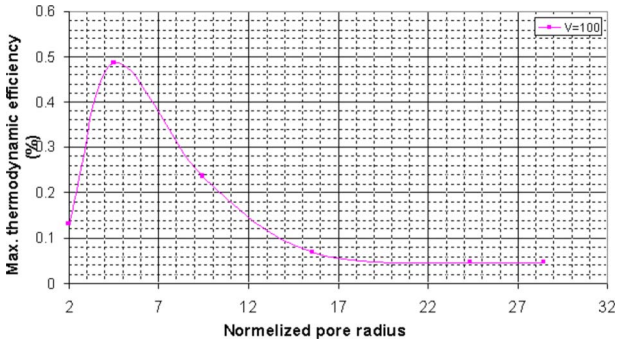


**Fig. 12 The variation of the thermodynamic efficiency for various normalized pore radius**

## Conclusion

In this paper, we have presented an analytical expression for the flow rate, pressure, and thermodynamic efficiency of a nanoporous EO pump. After describing a model of a porous EO pump, the pump is optimized. It is illustrated that for any volume of the EO pump and for any applied voltage, the optimum thermodynamic efficiency is achieved for pore radius four times higher than the Debye length. This estimate has been verified by the experiment. The optimum thermodynamic efficiency decreases with increasing temperature, viscosity, high ion valency, and permitivity of the working liquid. Using DI water as a pumping liquid the pump generates a maximum flow rate of 13.6 ml/min at pressures of 1.9 kPa at 150 V and 18.7 ml/min and 2.95 kPa at 200 V; the electrical power consumption of the pump is less than 0.4 W. The thermodynamic efficiency is low (0.2%) but the power consumption of the EO pump remains low. The EO pump works without any noise and no bubbles that are observed in the hydraulic circuit.

## Nomenclature

- $A$ = cross-sectional area of the porous silica disk ($m^2$)
- $E$ = Electric field intensity (V/m)
- $I$ = current (A)
- $I_n$ = $n$ order modified Bessel function of the first kind
- $K$ = ion mobility ($4\times10^{-8}$ $m^2/V/s$)
- $\Delta P$ = pressure drop (Pa)
- $Q$ = flow rate (ml/min)
- $T$ = temperature of the liquid (K)
- $U$ = velocity vector (m/s)
- $V$ = applied voltage (V)
- $a$ = capillary radius (m)
- $a_{\text{eff}}^*$ = normalized pore radius ($a/\lambda$)
- $e$ = electron charge ($1.6\times10^{-19}$°C)
- $e_e$ = the width of the microcanal of the microheat exchanger (m)
- $g$ = gravitational constant (9.8 $m/s^2$)
- $k_B$ = Boltzmann constant ($1.38\times10^{-23}$ $m^2\,kg/s^2/K$)
- $l$ = length of the porous silica disk (m)
- $l_c$ = capillary length
- $n$ = counterions concentration of bulk solution (M)
- $r$ = radial coordinate (m)
- $r^*$ = normalized radial coordinate ($r/\lambda$)
- $z$ = valance number of the counter ions
- $\varepsilon$ = permittivity of liquid (C/V/m)
- $\eta$ = thermodynamic efficiency
- $\lambda$ = debye length (m)
- $\psi$ = inner potential at a point distance $r/\lambda$ from the wall (V)

$\mu$ = viscosity (Pa s)
$\sigma(r^*)$ = conductivity at a point distance r/λ from the wall (S/m)
$\sigma$ = conductivity of the bulk (S/m)
$\rho$ = density of the working fluid ($kg/m^3$)
$\rho_E$ = electrical charge density ($C/m^3$)
$\zeta$ = zeta potential (V)
$\tau$ = tortuosity
$\Psi$ = porosity

**Subscripts**

$c$ = capillary
cc = cylindrical conduct
eff = effective
loss = losses
$m$ = maximum
op = optimum
$T$ = total

## References


[1] Wang, P., Chen, Z., and Chang, H. C., 2005, "A New Electro-Osmotic Pump Based on Silica Monoliths," Sens. Actuators B, **133**, pp. 500–509.
[2] Bruus, H., 2005, "Theoretical Microfluidics," *Lecture Notes*, 2nd ed., Department of Micro and Nanotechnology Technical University of Denmark, Copenhagen, pp. 115–149.
[3] Laser, J. D., and Santiago, J. G., 2004, "A Review of Micropumps," J. Magn. Soc. Jpn., **14**, pp. 35–64.
[4] Brask, A., 2005, "Electroosmotic Micropumps," Ph.d. thesis, Department of Micro and Nanotechnology Technical University of Denmark, Copenhagen, pp. 3–58.
[5] Probstein, R. F., 1994, *Physicochemical Hydrodynamics*, 2nd ed., Wiley, New York, pp. 165–208.
[6] Rice, C. L., and Whitehead, R., 1965, "Electrokinetic Flow in a Narrow Cylindrical Capillary," J. Phys. Chem., **69**, pp. 4017–4023.
[7] Goodson, K., Santiago, J., Kenny, T., Jiang, L., Zeng, S., Koo, J. M., Zhang, L., Yao, S., and Wang, E., 2002, "Electroosmotic Microchannel Cooling System for Microprocessors. Electronics-Cooling," Electron. Cooling, **8**, pp. 46–47.
[8] Takamura, Y., and Oki, A., 2003, "Low Voltage Electroosmosis Pump for Stand-Alone Microfluidics Devices," Electrophoresis, **24**, pp. 185–192.
[9] Chen, Z., and Hobo, T., 2001, "Chemically l-prolinamide-modified Monolithic Silica Column for Enantiomeric Separation of Dansyl Amino Acids and Hydroxy Acids by Capillary Electrochromatography and High Performance Liquid Chromatography," Electrophoresis, **22**, pp. 3339–3346.
[10] Chen, Z., and Hobo, T., 2001, "Chemically l-Phenylalaninamide-Modified Monolithic Silica Column Prepared by a Sol-Gel Process for Enantioseparation of Dansyl Amino Acids by Ligand Exchange Capillary Electrochromatography," Anal. Chem., **73**, pp. 3348–3357.
[11] Leinweber, F. C., Lubda, D., Cabrera, K., and Tallarek, U., 2002, "Characterization of Silica-Based Monoliths With Bimodal Pore Size Distribution," Anal. Chem., **74**, pp. 247022477.
[12] Zeng, S., Chen, C., Mikkelsen, J. C., and Santiago, J. G., 2001, "Fabrication and Characterization of Electrokinetic Micro Pumps," Sens. Actuators B, **79**, pp. 107–114.
[13] Gong, Q. L., Zhou, Z. Y., Yang, Y. H., and Wang, X. H., 2000, "Design, Optimization and Simulation on Microelectromagnetic Pump," Sens. Actuators, A **83**, pp. 200–207.
[14] Zenga, S., Chena, C. H., Santiago, J. G., Chen, J. R., Zareb, R. N., Trippc, J. A., Svec, F., and Fréchet, J. M. J., 2002, "Electroosmotic Flow Pumps With Polymer Frits," Sens. Actuators B, **82**, pp. 209–212.
[15] Jiang, L., Mikkelsen, J., Koo, J. M., Huber, D., Yao, S., Zhang, L., Zhou, P., Maveety, J. G., Prasher, R., Santiago, J. C., Kenny, T. W., and Goodson, K. E., 2002, "Closed-Loop Electroosmotic Microchannel Cooling System for VLSI Circuits," IEEE Trans. Compon. Packag. Technol., **25**(3), pp. 347–355.
[16] Grieser, F., 1985, "Thermal and Radiation Controle of the Electrical Double Layer Properties of Silica and Glass," Radiat. Phys. Chem., **22**(1–2), pp. 43–48.
[17] Berrouche, Y., Avenas, Y., Schaeffer, C., Wang, P., and Chang, H. C., 2007, "Design of a Porous Electroosmotic Pump, Used in Power Electronics Cooling," *IEEE, Industry Applications Society*, New Orleans, LA, Sept. 23–27.

# An Analytical Method for Dielectrophoresis and Traveling Wave Dielectrophoresis Generated by an *n*-Phase Interdigitated Parallel Electrode Array

**Hongjun Song**
e-mail: hongjs1@umbc.edu

**Dawn J. Bennett**
e-mail: dawnb@umbc.edu

Department of Mechanical Engineering,
University of Maryland,
Baltimore County, MD 21250

*In this paper, we present an analytical method for solving the electric potential equation with the exact boundary condition. We analyze the dielectrophoresis (DEP) force with an n-phase ac electric field periodically applied on an interdigitated parallel electrode array. We compare our analytical solution with the numerical results obtained using the commercial software CFD-ACE. This software verifies that our analytical method is correct for solving the problem. In addition, we compare the analytical solutions obtained using the exact boundary conditions and the approximate boundary conditions. The comparison shows that the analytical solution with the exact boundary condition gives a more accurate analysis for DEP and traveling wave DEP forces. The DEP forces of latex beads are also investigated with different phase arrays for* $(n=2,3,4,5,6)$.
[DOI: 10.1115/1.2956610]

## Introduction

Alternating current (ac) electrokinetic techniques have been used widely in basic colloid and separation science applications for many years. Currently, these techniques are considered as the main technology for a wide variety of lab-on-a-chip devices since they do not require moving parts and, therefore, can be incorporated more favorably into microanalytical systems. Dielectrophoresis (DEP) and traveling wave dielectrophoresis (twDEP), as typical ac electrokinetic techniques, have been proven to be very suited for manipulating and separating biological particles such as DNA, cells, and bacteria [1–3]. Compared to other available methods, DEP is a good and effective method for the manipulation of particles in micro- and nanofluidics. This is due to the fact that an ac field suppresses undesirable electrolytic effects such as Faradic reactions and electroconvection in the liquid, and employs polarization forces that are insensitive to the particle charge [4,5].

As a typical design, a long array of interdigitated parallel electrodes has been used for analyzing both DEP and twDEP. In particular, this design is especially useful for positive DEP applications such as the concentration of microsamples suspended in relatively low ionic concentration media. When the potential with different phases is alternatively applied on the electrodes, a nonuniform electric field is established, which induces a DEP force with polarizable particles [6]. Since the movement of the particle is directly dependent on the DEP and twDEP forces, which come from the interaction between the electric field and the induced dipole of particle, it is very important to accurately calculate the electric field for theoretical analysis. In order to derive the equations for the DEP force and the twDEP force, the electric potential equation needs to be solved. Unfortunately, the mixed type of boundary condition (Dirichlet and Neumann) for the electric potential equation brings a big challenge to getting an analytical solution. An analytical approximation for the electric potential and force using Green's theorem [7,8] and Fourier series [9] has been presented by adopting a linear approximation for the surface potential in the gaps between the electrodes instead of the exact boundary condition. These models bring some inaccuracy especially in the zone close to the electrodes. An improved third-order polynomial fit boundary condition for the surface potential in the gaps [10] has been developed, and the accuracy is greatly improved. However, there is still some inaccuracy near the electrodes. Feng et al. [11] gave an approach to obtain the series solution using the exact boundary condition. A closed form solution was derived [12] based on the work in Ref. [11], but it only works for a two-phase electrode array. Recently Sun et al. [13] used the Schwarz–Christoffel mapping (SCM) method to obtain analytical solutions with the exact boundary condition. Their method works very well, but requires complex mapping and transformation processes. In addition, this method cannot give a general expression for the solutions having any phases in the electrode array when different potentials are applied. In contrast, numerical methods can solve the exact boundary condition without difficulty. Several numerical methods such as point charge, charge density, finite element methods, and least-square finite difference (LSFD) have been used for the analysis of DEP and twDEP forces [14–17]. However, each geometric design requires a separate mesh, which brings some inconvenience to getting the general analysis of parameters such as the geometric effects.

In this paper, we present an analytical method for solving the electric potential equation with the exact boundary condition to analyze the DEP force with *n*-phase ac electric field applied on an interdigitated parallel electrode array. Based on the Fourier series solution in Ref. [9], we describe a method to find the unknown coefficients of the solution with the exact boundary condition. Compared to the previous solution using the exact boundary condition [11–13], our method can give a general expression of the

Contributed by the Fluids Engineering Division of ASME for publication in the JOURNAL OF FLUIDS ENGINEERING. Manuscript received July 19, 2007; final manuscript received February 28, 2008; published online August 1, 2008. Assoc. Editor: Ali Beskok.

  

solution for $n$-phase electrode array using the exact boundary condition. Also our method is simple and does not need the complex map and transformation technique.

In our paper, we will first describe a detailed solving process of our method. To verify our method, we compare our analytical solution with the numerical results obtained using commercial software CFD-ACE+. In addition, comparisons are made between the analytical solutions having the exact boundary condition and the approximate boundary condition. These comparisons show that the analytical solution with the exact boundary condition gives a more accurate analysis for DEP and twDEP forces. Finally the DEP forces are investigated with the different phase ($n=2,3,4,5,6$) ac electric fields.

## Dielectrophoretic Force Model

In this paper, we introduce the phasor notation for an arbitrary potential oscillating at frequency $\omega$ as

$$\phi(\vec{x},t) = \mathrm{Re}[\tilde{\phi}(\vec{x})e^{iwt}] \tag{1}$$

Here Re[$\cdots$] indicates the real part of the complex function and $\tilde{\phi}(\vec{x})$ is the complex potential, which is independent of time $t$. So the electric field is given by $E(\vec{x},t)=\mathrm{Re}[\tilde{E}(\vec{x})e^{iwt}]$. We define $\phi_R=\mathrm{Re}[\tilde{\phi}(\vec{x})]$ and $\phi_I=\mathrm{Im}[\tilde{\phi}(\vec{x})]$, which are the real part and imaginary part of $\tilde{\phi}(\vec{x})$, respectively. So the complex electric field can be written down as $\tilde{E}=-\nabla\tilde{\phi}=-(\nabla\phi_R+i\nabla\phi_I)$. For a homogenous fluid medium, the electric potential satisfies the Laplace equation, which is derived by the quasielectrostatic form of Maxwell's equations [6,9].

$$\nabla^2\tilde{\phi}=0 \tag{2}$$

Thus we can get $\nabla^2\phi_R+i\nabla^2\phi_I=0$, which indicates that both $\phi_R$ and $\phi_I$ satisfy the Laplace equation.

When a particle is put into the electric field $\tilde{E}$, the dipole moment $\tilde{p}$ is induced in the particle. The time-averaged DEP force is given by [4]

$$\langle\vec{F}\rangle = \tfrac{1}{2}\,\mathrm{Re}(\tilde{p}\cdot\nabla)\tilde{E} \tag{3}$$

For a spherical particle the dipole moment $\tilde{p}$ is defined as a linear function with the electric field $\tilde{E}$ as follows:

$$\tilde{p} = \tfrac{4}{3}\pi a^3\varepsilon_0\varepsilon_f\beta(\omega)\tilde{E} \tag{4}$$

Here $a$ is the particle radius, $\varepsilon_0$ is the vacuum permittivity, $\varepsilon_f$ is the relative dielectric permittivity of the fluid, and $\omega$ is the angular frequency of applied electric field. $\beta(\omega)$ is the dipolar Clausius–Mossotti factor. Using the Maxwell–Wagner expression for the complex dielectric permittivity [6,18–20], $\varepsilon^*=\varepsilon'-i\varepsilon''$, where $\varepsilon''=\sigma/\omega$. $\varepsilon'$ is the permittivity and $\sigma$ is the conductivity. $\beta(\omega)$ is expressed as follows [6]:

$$\beta(\omega) = \frac{\varepsilon_p^* - \varepsilon_f^*}{\varepsilon_p^* + 2\varepsilon_f^*} \tag{5}$$

Substituting Eq. (4) into Eq. (3) and replacing $\tilde{E}$ with $\phi_R$ and $\phi_I$, the final expression of the time-averaged: DEP force is given by

$$\langle\vec{F}\rangle = 2\pi\varepsilon_0\varepsilon_f a^3\,\mathrm{Re}(\beta)\,\nabla\,(|\nabla\phi_R|^2+|\nabla\phi_I|^2) - 4\pi\varepsilon_0\varepsilon_f a^3\,\mathrm{Im}(\beta)\,\nabla \times(\nabla\phi_R\times\nabla\phi_I) \tag{6}$$

The first term on the right side depends on the spatially varying field magnitude, which corresponds to the conventional dielectrophoretic (cDEP) force; the second term depends on the spatially varying phase, which corresponds to the twDEP force. To obtain the final expression of the time-averaged DEP force, we need to solve $\phi_R$ and $\phi_I$, respectively.

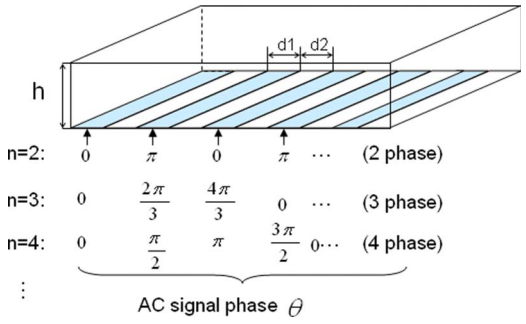


**Fig. 1 The schematic physical model of the interdigitated parallel electrode array**

## Physical Model and Analytical Method

A schematic physical model of the interdigitated parallel electrode array is shown in Fig. 1. A chamber with interdigitated parallel electrodes on the bottom is used in our investigation. The width of each electrode is $d1$ and the space between adjacent electrodes is $d2$. The height from the bottom to the top is $h$. The thickness of the electrodes is neglected because it is very small compared with the chamber geometry. Generally an $n$-phase ac electric field with the single frequency $\omega$ is periodically applied on the interdigitated parallel electrode array. The phase difference between two adjacent electrodes is $2\pi/n$. For example, the phase periodically changed as 0 and $\pi$ for the two-phase ac electric field ($n=2$); the phase periodically changed as $0, 2\pi/3$, and $4\pi/3$ for the three-phase ac electric field ($n=3$); the phase periodically changed as $0, \pi/2$, $\pi$, and $3\pi/2$ for the four-phase ac electric field ($n=4$); and so on. Because the length of the electrodes is much longer than their width, the model can be simplified as two dimensional. Meanwhile, due to the fact that the phase is periodically changed on the interdigitated parallel electrode array, we only need to solve the model at one periodic zone. A simplified 2D periodic model is shown in Fig. 2

There are two types of boundary conditions mixed in this model. One is the Dirichlet boundary condition and the other is the Neumann boundary condition. All of the boundary conditions are shown in Fig. 2. On the top of the chamber and in the gap between the electrodes, the boundary conditions are satisfied by $\partial\phi_R/\partial n=0$ and $\partial\phi_I/\partial n=0$. On the periodic plane, the boundary condition satisfies $\partial\phi_R/\partial n=0$ and $\phi_I=0$. Because the phase difference between two adjacent electrodes is $2\pi/n$, the complex potential applied on the $k$th electrode is given by $\tilde{\phi}=V_0e^{i(2k\pi/n)}$ ($k=0,1,\ldots,n$). Here $V_0$ is the amplitude of ac electric potential. So the corresponding boundary conditions on the $k$th electrode are $\phi_R=V_0\cos(2k\pi/n)$ and $\phi_I=V_0\sin(2k\pi/n)$. Applying all the boundary conditions, we can solve $\phi_R$ and $\phi_I$, respectively. Here, we only give a detailed process to solve the real part $\phi_R$. A similar process obtains the imaginary part $\phi_I$.

As we know $\phi_R$ satisfies the Laplace equation. The following are all the boundary conditions for $\phi_R$:

$$\frac{\partial\phi_R(x,y=h)}{\partial n}=0,\quad \frac{\partial\phi_R(x=0,y)}{\partial n}=0,\quad \frac{\partial\phi_R(x=L,y)}{\partial n}=0 \tag{7}$$

$$\frac{\partial\phi_R(x,y=0)}{\partial n}=0$$

$$k(d1+d2)+\frac{d1}{2}<x<(k+1)(d1+d2)-\frac{d1}{2}\quad(k=0,1,\ldots,n)$$

$$\phi_R(x,y=0)=V_0,\quad 0<x<\frac{d1}{2}\quad\text{and}\quad L-\frac{d1}{2}<x<L \tag{8}$$

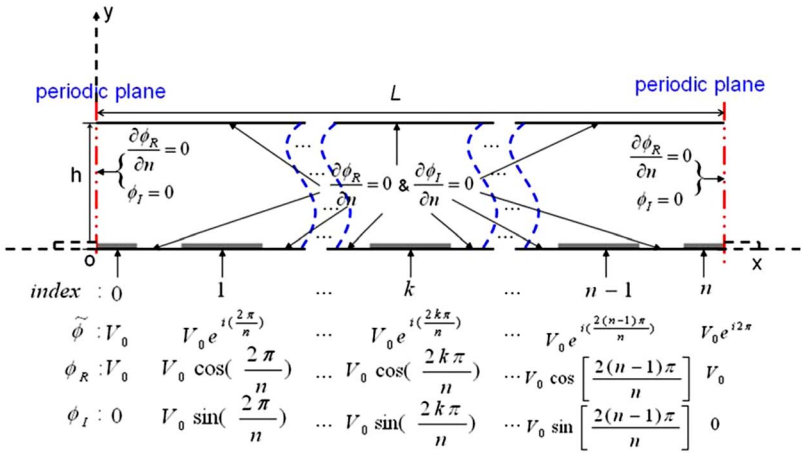


**Fig. 2 The simplified 2D periodic model and boundary condition**

$$\phi_R(x,y=0)=V_0\cos(2k\pi/n)$$

$$k(d1+d2)-\frac{d1}{2}<x<(k+1)(d1+d2)+\frac{d1}{2} \quad (k=1,\ldots,n-1)$$

Here $L=(n+1)(d1+d2)$ is the total length of one periodic zone at the $x$ direction. We can easily write down the solution of $\phi_R$ by using the separation of variables method for the Laplace equation with the boundary condition in Eq. (7) as follows:

$$\phi_R(x,y)=\sum_{j=1}^{\infty} C_j\cos(\lambda_j x)\cosh(\lambda_j(y-h)) \tag{9}$$

where $\lambda_j=j\pi/L$, $(j=1,2,3,\ldots)$ is the $j$th eigenvalue. The coefficient $C_j$ needs to be determined by applying the mixed boundary condition in Eq. (8). Normally a dual orthogonal series is obtained from the Dirichlet boundary condition and Neumann boundary condition using the boundary integration, respectively. Since the uniqueness is complicated and difficult to prove for the solution of dual orthogonal series [21], we only need to find a particular solution of $C_j$. It is difficult, however, to get the particular solution of $C_j$ by solving the dual orthogonal series directly. Our idea was to assume that there is another particular solution with coefficient $D_m$. To distinguish the solution $\phi_R(x,y)$ with coefficient $C_j$, we wrote the solution with coefficient $D_m$ as follows:

$$\phi_R^*(x,y)=\sum_{m=1}^{\infty} D_m\cos(\lambda_m x)\cosh(\lambda_m(y-h)) \tag{10}$$

At first, we applied the Dirichlet boundary condition for $\phi_R$. However, the boundary condition of the gaps between the electrodes for $\phi_R$ does not satisfy the Dirichlet boundary condition. Our method is using $\phi_R^*$ instead of $\phi_R$ at these gaps. So we have

$$\phi_R(x,y=0)=\begin{cases}\phi_R^*(x,y=0), & k(d1+d2)+\frac{d1}{2}<x<(k+1)(d1+d2)-\frac{d1}{2} \quad (k=0,1,\ldots,n)\\ \phi_R=V_0, & 0<x<\frac{d1}{2} \text{ and } L-\frac{d1}{2}<x<L\\ \phi_R=V_0\cos(2k\pi/n), & k(d1+d2)-\frac{d1}{2}<x<(k+1)(d1+d2)+\frac{d1}{2} \quad (k=1,\ldots,n-1)\end{cases} \tag{11}$$

Second, we applied the Neumann boundary condition for $\phi_R^*$. To avoid the Dirichlet boundary condition on the electrodes, we used $\phi_R$ instead of $\phi_R^*$ on the electrodes. We similarly have

$$\frac{\partial\phi_R^*(x,y=0)}{\partial y}=\begin{cases}0, & k(d1+d2)+\frac{d1}{2}<x<(k+1)(d1+d2)-\frac{d1}{2} \quad (k=0,1,\ldots,n)\\ \frac{\partial\phi_R(x,y=0)}{\partial y}, & 0<x<\frac{d1}{2} \text{ and } L-\frac{d1}{2}<x<L\\ \frac{\partial\phi_R(x,y=0)}{\partial y}, & k(d1+d2)-\frac{d1}{2}<x<(k+1)(d1+d2)+\frac{d1}{2} \quad (k=1,\ldots,n-1)\end{cases} \tag{12}$$

By using the orthogonality integrals along the whole bottom boundary $(y=0)$, an infinite system can be obtained as follows:

$$C_j=F_j/P_j+\sum_{m=1}^{\infty} D_m R_{mj}/P_j \tag{13}$$

$$D_m=\sum_{j=1}^{\infty} C_j S_{jm}/Q_m \tag{14}$$

Here

**Table 1 The calculated $C_j$ (only the first 18 terms were shown) for the two-phase array**

| $j$ | $C_j$ | $j$ | $C_j$ | $j$ | $C_j$ |
|---|---|---|---|---|---|
| 1 | −0.00000000000000 | 7 | 0.00000000000000 | 13 | −0.00000000000000 |
| 2 | 0.09285941458537 | 8 | −0.00000000000000 | 14 | −0.00000000000121 |
| 3 | 0.00000000000000 | 9 | −0.00000000000000 | 15 | −0.00000000000000 |
| 4 | −0.00000000000000 | 10 | −0.00000003255223 | 16 | −0.00000000000000 |
| 5 | 0.00000000000000 | 11 | −0.00000000000000 | 17 | 0.00000000000000 |
| 6 | 0.00000058089101 | 12 | −0.00000000000000 | 18 | 0.00000000000005 |

$$P_j = \cosh(-\lambda_j h)\int_0^L \cos^2(\lambda_j x)dx$$

$$Q_m = \lambda_m \sinh(-\lambda_m h)\int_0^L \cos^2(\lambda_m x)dx$$

$$F_j = \int_0^{d1/2} V_0 \cos(\lambda_j x)dx + \sum_{k=1}^{n-1}\int_{k(d1+d2)-d1/2}^{(k+1)(d1+d2)+d1/2} V_0 \cos(2k\pi/n)\cos(\lambda_j x)dx + \int_{L-d1/2}^{L} V_0 \cos(\lambda_j x)dx$$

$$R_{mj} = \cosh(-\lambda_m h)\sum_{k=0}^{n}\int_{k(d1+d2)+d1/2}^{(k+1)(d1+d2)-d1/2} \cos(\lambda_j x)\cos(\lambda_m x)dx$$

and

$$S_{jm} = \lambda_j \sinh(-\lambda_j h)\left\{\int_0^{d1/2} \cos(\lambda_j x)\cos(\lambda_m x)dx + \sum_{k=1}^{n-1}\int_{k(d1+d2)-d1/2}^{(k+1)(d1+d2)+d1/2} \cos(\lambda_j x)\cos(\lambda_m x)dx + \int_{L-d1/2}^{L} \cos(\lambda_j x)\cos(\lambda_m x)dx\right\}$$

In practice, the infinite system can be approximately solved by truncating the finite number $J$ for $C_j$ $(j=1,2,\ldots,J)$ and $M$ for $D_m$ $(m=1,2,\ldots,M)$ instead of using an infinite number. Although this process will cause some error, enough numbers $J$ and $M$ can be chosen, and the error can be neglected. We introduce matrices $C$, $D$, $F$, $R$, and $S$ to represent $C_j$, $D_m$, $F_j/P_j$, $R_{mj}/P_j$, and $S_{jm}/Q_m$, respectively. Equations (13) and (14) can be rewritten as follows:

$$C = F + DP \tag{15}$$

$$D = CS \tag{16}$$

Substituting Eq. (16) into Eq. (15) we can finally obtain

$$C(I - SP) = F \tag{17}$$

Here $I$ is the identity matrix, and $F$, $S$, and $P$ are known. We can easily get a particular solution for $C_j$ by using MATLAB™. Finally, we obtain the solution for $\phi_R(x,y)$ by substituting $C_j$ into Eq. (10). In Table 1, we show an example of the calculated coefficients $C_j$ for the two-phase array with the truncated number $J=M=400$ (only the first 18 terms were shown).

## Error Analysis and Comparison Study

In this paper, we chose the special case $d1=d2=d$ and $h=2d$ for all analyses. The amplitude of the ac electric potential was $V_0=1$ V, and $d=10$ $\mu$m for all the cases. Here, we only give the error analysis and comparison study for the simplest case, the two-phase electrode array $(n=2)$. The analysis is similar for the $n$-phase array. Figure 3 shows the contour plot of the electric field $\phi_R(x,y)$, which is calculated by the sum of the infinite Fourier series with the truncated number $J=M=600$.

To determine the effect of the truncated numbers $J$ and $M$, the comparison of the distributed electric potential at the bottom boundary $(y=0)$ with different $J=M=10,50,100,200,400,600$ was shown in Fig. 4. A selected zone of the electric potential was enlarged to compare the tiny difference. It is clear that the difference of electric potential becomes much smaller when the truncated numbers $J$ and $M$ increased from 10 to 600, and the error can be neglected when $J$ and $M$ increased to 600 or above.

Also, we compared the truncated solution $\phi_R(x,y)$ with coefficient $C_j$ and the truncated solution $\phi_R^*(x,y)$ with coefficient $D_m$.

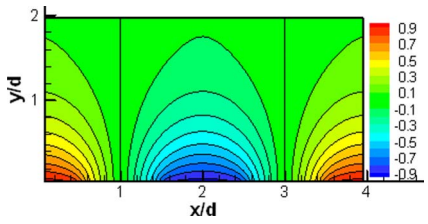


**Fig. 3 The contour plot of the electric field $\phi_R(x,y)$ for the two-phase array**

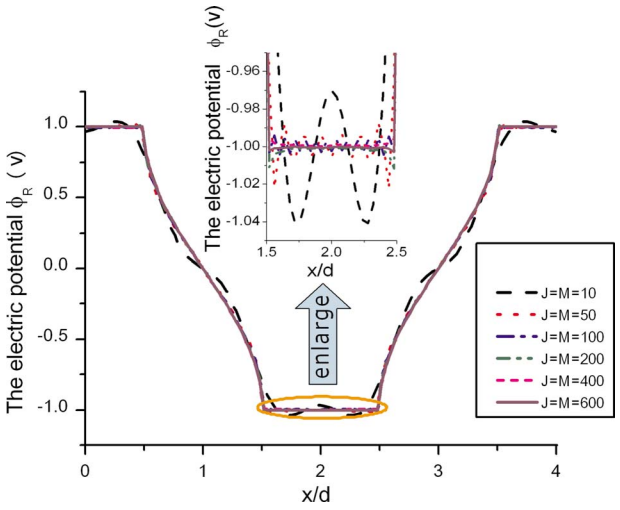


**Fig. 4 The comparison of the distributed electric potential at the bottom boundary $(y=0)$**

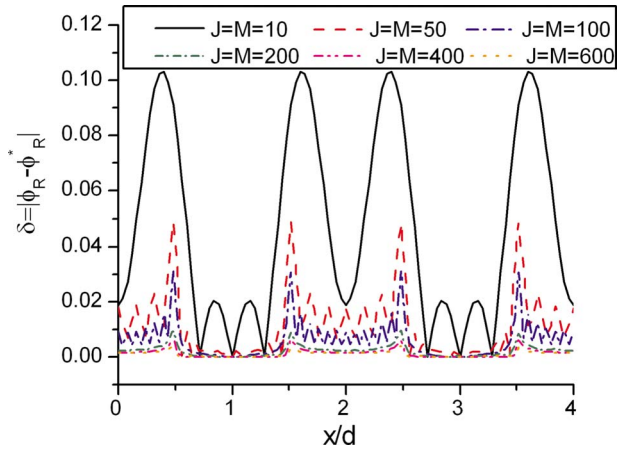


**Fig. 5 The difference value $\delta=|\phi_R-\phi_R^*|$ at the bottom boundary ($y=0$)**

We plotted the difference $\delta=|\phi_R-\phi_R^*|$ at the bottom boundary ($y=0$) in Fig. 5. It shows that the difference $\delta$ decreased from $10^{-1}$ to $10^{-3}$ when the truncated numbers $J$ and $M$ increased from 10 to 600, which means the relative error is only approximately 0.1% when $J=M=600$. It can be seen that taking the truncated values of $J$ and $M$ as 600 is sufficiently safe for our solution.

To verify our analytical method, we compared our analytical results with the numerical results using the commercial software CFD-ACE+. To show that our analytical solution gives a more accurate analysis, we also compared our results using the approximate linear boundary condition. Figure 6 shows the comparison of the electric field $\phi_R(x,y)$ at the bottom boundary ($y=0$). We can see that the exact boundary in our results exactly matches that in the numerical solution, but is much different from the approximate linear boundary.

As we know, the DEP force is the most important factor in the analysis of DEP. Thus, it is necessary to compare the DEP force in our results with the numerical results using CFD-ACE+, and the analytical solution using the approximate boundary condition. For a two-phase electrode array, we only need to calculate the real part $\phi_R(x,y)$ because the imaginary part $\phi_I(x,y)$ is 0. So the imaginary part of electric field Im($E$) equals 0, which shows the twDEP

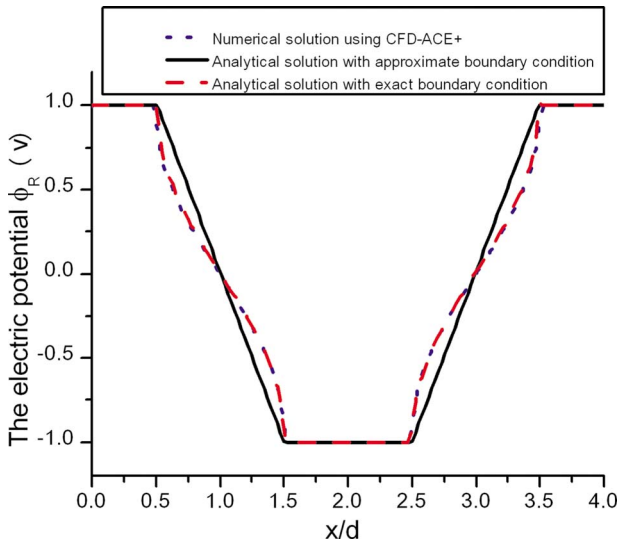


**Fig. 6 The comparison of the electric field $\phi_R(x,y)$ at the bottom boundary ($y=0$)**

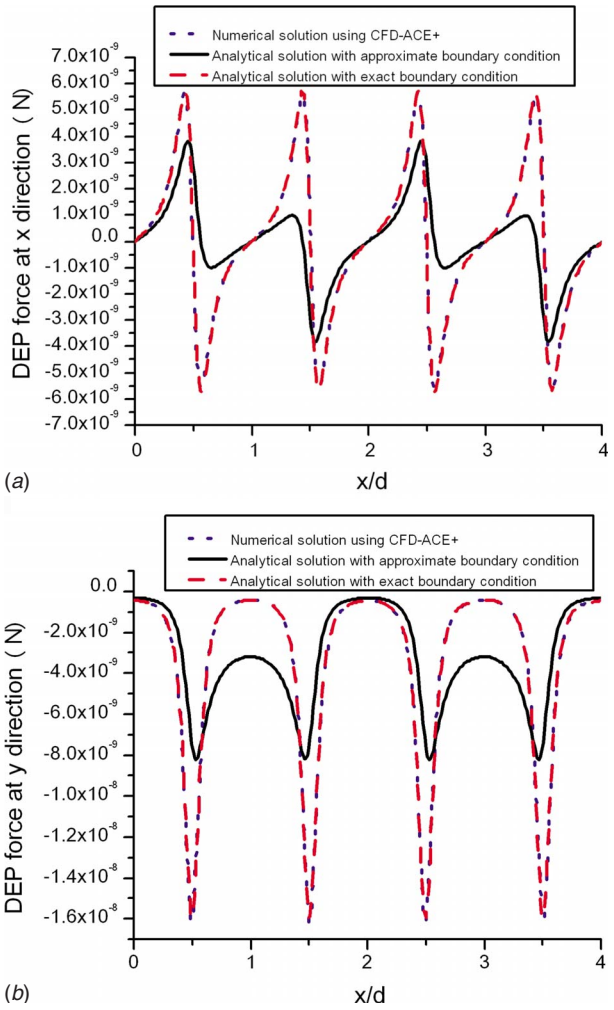


**Fig. 7 The comparison of the DEP force near the electrode plane ($y/d=0.1$): (*a*) the *x*-component of the DEP force and (*b*) the *y*-component of the DEP force**

force equals 0 and only the cDEP force is generated on the particles. A simplified expression of time-averaged DEP force is obtained by replacing $\phi_I(x,y)=0$ in Eq. (6) as follows:

$$\langle \vec{F}_{2\ \text{phaseDEP}} \rangle = 2\pi\varepsilon_0\varepsilon_f a^3\ \text{Re}(\beta)\ \nabla\ (\ |\nabla\phi_R|^2|) \qquad (18)$$

As the term Re($\beta$) depends on the choice of particles and medium, we do not take it into account in the calculations. By assuming the particles radius is 1 $\mu$m, we compared the component in the $x$ direction and the $y$ direction, respectively near the electrode plane ($y/d=0.1$), which is shown in Fig. 7.

It is obvious that both the DEP forces in the $x$ direction and in the $y$ direction in our results are extremely close to the numerical results using CFD-ACE+, showing an excellent agreement between our results and the numerical results. The comparison verified that our method is correct for this problem. The comparison of the DEP force in the $x$ direction shows that the $x$-component of the DEP force obtained from the approximate linear boundary condition is less than that obtained from the exact boundary condition, especially near the edge of electrodes. Also, the comparison of the DEP force in the $y$ direction shows that the $y$-component of the DEP force obtained from the approximate linear boundary condition is less than that obtained from the exact boundary condition at the electrode zone, but is larger at the zone without the electrodes. All the differences show that the approximate linear boundary condition brings inaccuracies, especially near the elec-

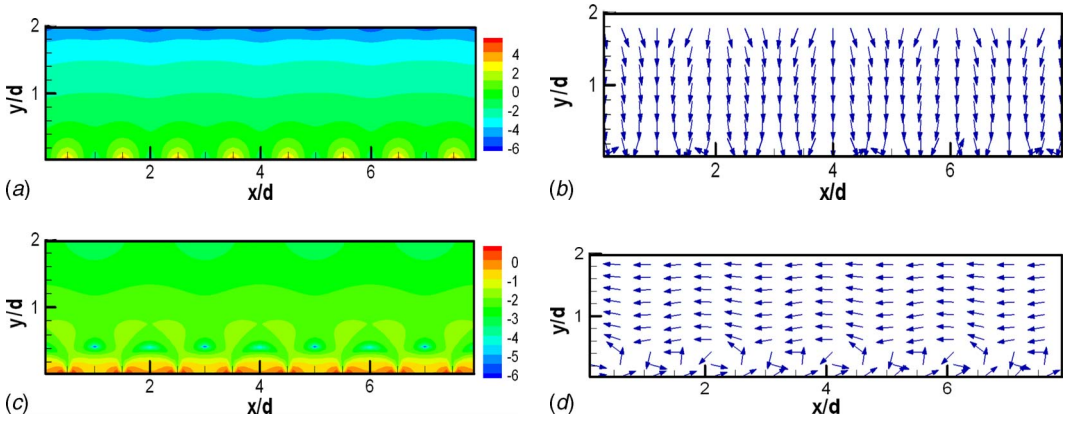


**Fig. 8 The magnitude and vector of the cDEP force and the twDEP force for the four-phase array. The scale on the magnitude plots for both fields are $\log_{10}$. (*a*) Magnitude of $\nabla(|\nabla\phi_R|^2+|\nabla\phi_I|^2)$ (*b*) the vector of $\nabla(|\nabla\phi_R|^2+|\nabla\phi_I|^2)$, (*c*) magnitude of $\nabla\times(\nabla\phi_R\times\nabla\phi_I)$, and the vector of (*d*) $\nabla\times(\nabla\phi_R\times\nabla\phi_I)$.**

trode plane. Based on the comparison, our analytical solution gives a more accurate analysis than the analytical solution with the approximate linear boundary condition.

## Investigation of DEP Force With *n*-Phase Array

From Eq. (6), we found that the total time-averaged force on the particle generated by the *n*-phase array includes two types of forces: the first type of force is the cDEP force (denoted as $\langle\vec{F}_{\mathrm{cDEP}}\rangle$) and the second type force is the twDEP force (denoted as $\langle\vec{F}_{\mathrm{twDEP}}\rangle$).

$$\langle\vec{F}_{\mathrm{cDEP}}\rangle = 2\pi\varepsilon_0\varepsilon_f a^3\,\mathrm{Re}(\beta)\,\nabla\,(|\nabla\phi_R|^2+|\nabla\phi_I|^2) \qquad (19a)$$

$$\langle\vec{F}_{\mathrm{twDEP}}\rangle = -4\pi\varepsilon_0\varepsilon_f a^3\,\mathrm{Im}(\beta)\,\nabla\times(\nabla\phi_R\times\nabla\phi_I) \qquad (19b)$$

The DEP motion of the particle is determined by the two forces, which act independently. Each type of force can be considered as a multiplication with two parts: the first part is determined by the property of particles and the second part is determined by the spatial distribution of electric field. Here, we only focus on the spatial distribution of electric field. We investigate the term $\nabla(|\nabla\phi_R|^2+|\nabla\phi_I|^2)$ in the cDEP force $\langle\vec{F}_{\mathrm{cDEP}}\rangle$ and the term $\nabla\times(\nabla\phi_R\times\nabla\phi_I)$ in the twDEP force $\langle\vec{F}_{\mathrm{twDEP}}\rangle$. We compare $\nabla(|\nabla\phi_R|^2+|\nabla\phi_I|^2)$ and $\nabla\times(\nabla\phi_R\times\nabla\phi_I)$ of the two-phase array, three-phase array, four-phase array, five-phase array, and six-phase array. We should mention here that this is a special case for the two-phase array because the imaginary part of the applied electric field is 0. Consequently, we only have the cDEP force for the two-phase array. Both the cDEP force and the twDEP forces occur for the other phase arrays.

By plotting the magnitude and vector of $\nabla(|\nabla\phi_R|^2+|\nabla\phi_I|^2)$ and $\nabla\times(\nabla\phi_R\times\nabla\phi_I)$, we found that each type of force has a similar pattern for different phase arrays. Here, we only plot the magnitude and vector of $\nabla(|\nabla\phi_R|^2+|\nabla\phi_I|^2)$ and $\nabla\times(\nabla\phi_R\times\nabla\phi_I)$ for the four-phase array to describe how the pattern looks. From Fig. 8(*a*) we can see that the maximum value of $\nabla(|\nabla\phi_R|^2+|\nabla\phi_I|^2)$ exists near the edge of the electrodes, which corresponds to the maximum DEP force. As the distance increases from the electrodes, the value of the DEP force decreases very fast. The corresponding vector of $\nabla(|\nabla\phi_R|^2+|\nabla\phi_I|^2)$ is shown in Fig. 8(*b*), which shows the vector almost straight toward the electrodes from the top zone. This means that the particle will be attracted toward the electrodes if $\mathrm{Re}(\beta)>0$ (positive DEP) and the particle will be repelled away from the electrodes if $\mathrm{Re}(\beta)<0$ (negative DEP). We also plot the magnitude and the vector of $\nabla(|\nabla\phi_R|^2+|\nabla\phi_I|^2)$ in Figs. 8(*c*) and 8(*d*), respectively. At the zone near the electrodes, a series of vortex rotation is generated. When the zone is farther from the electrodes, a parallel force along the *x* direction is

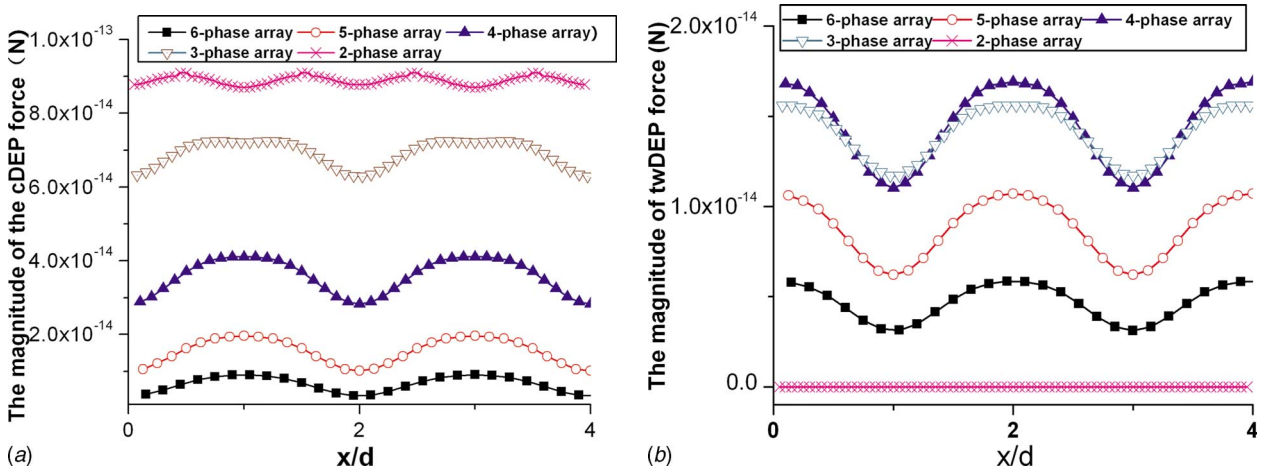


**Fig. 9 The comparison of the DEP force at the center plane ($y$=10 $\mu$m) with *n*-phase array ($n$=2,3,4,5,6). (*a*) The magnitude of $\langle\vec{F}_{\mathrm{cDEP}}\rangle$ and (*b*) the magnitude of $\langle\vec{F}_{\mathrm{cDEP}}\rangle$.**

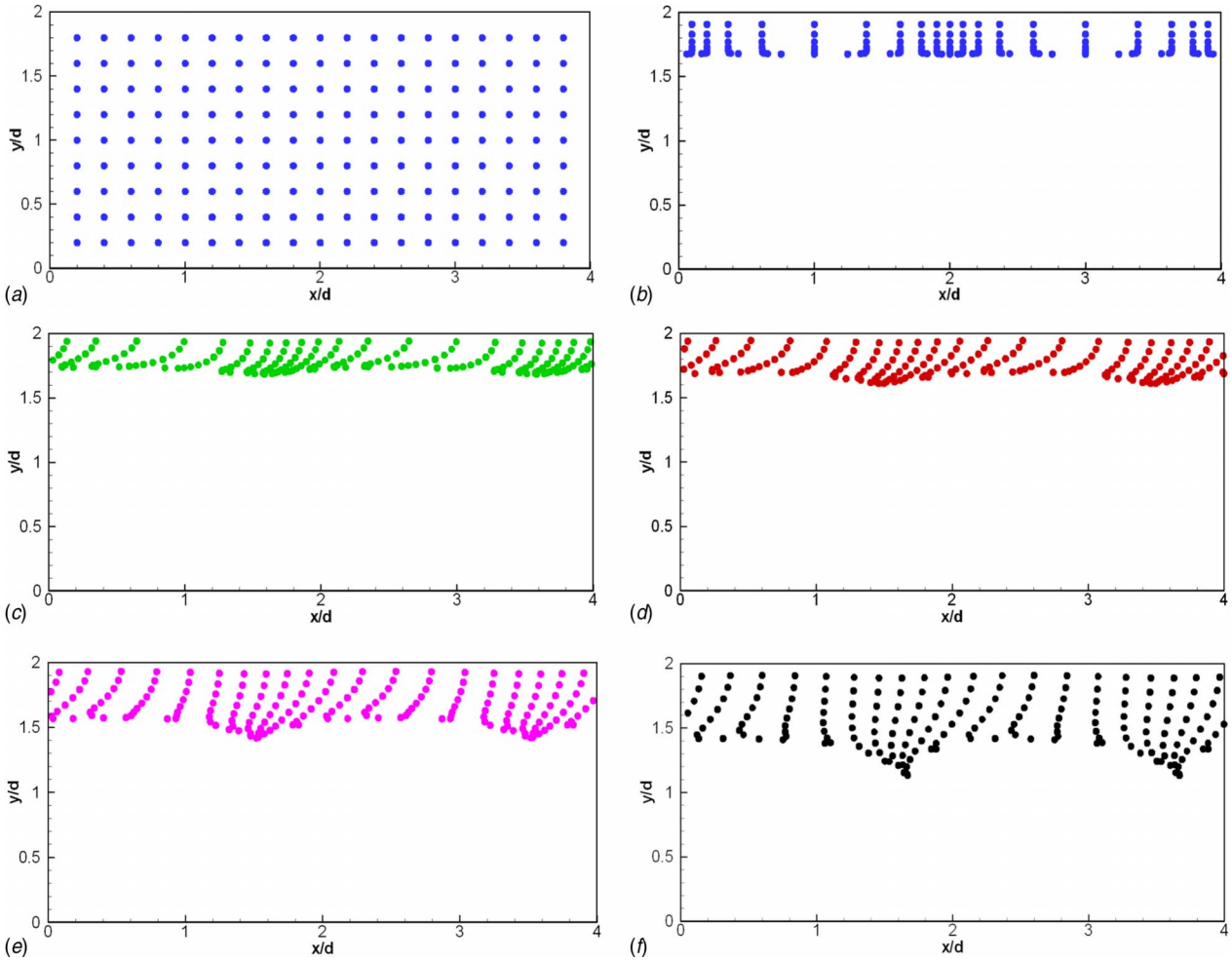


**Fig. 10 The distribution pattern of the latex beads: (*a*) the Initial position of the particles and (*b*)–(*f*) the position of the particles with two-phase, three-phase, four-phase, five-phase, and six-phase arrays respectively, at the dimensionless time $t^{\#}=16$. (*a*) The initial position of the particles, (*b*) two-phase array, (*c*) three-phase array, (*d*) four-phase array, (*e*) five-phase array, and (*f*) six-phase array.**

generated. The direction of the force is from the right to the left if the imaginary part is less than zero, $\mathrm{Im}(\beta)<0$, and is from the left to the right if the imaginary part is greater than zero, $\mathrm{Im}(\beta)>0$.

To investigate the DEP force, the same model consisting of latex beads of radius 1 $\mu$m with the Clausius–Mossotti factor $\beta=-0.45+0.27i$ was used. The width of the electrodes and the gap between electrodes are the same value $d=10$ $\mu$m, and the height of the chamber $h=20$ $\mu$m. Since latex beads $\mathrm{Re}(\beta)=-0.45<0$, a negative DEP force acts on them. The beads will be repelled by the electrodes. In this paper, we are interested in the effect of the negative DEP of latex beads with different phases being applied over a long period of time. Up to this point, the beads have been far away from the electrodes. We assume that the DEP force in the center line is approximately the average DEP force ($y=10$ $\mu$m or $y/d=1$). A comparison of the magnitude of the DEP force at the center plane ($y=10$ $\mu$m) with two-phase array, three-phase array, four-phase array, five-phase array, and six-phase array is shown in Fig. 9. For all cases, both the patterns of the cDEP force $\langle \vec{F}_{\mathrm{cDEP}} \rangle$ and the twDEP force $\langle \vec{F}_{\mathrm{twDEP}} \rangle$ change like a periodic force between the adjacent electrodes. However, the magnitude is varied. From Fig. 9(*a*), we can see the cDEP force decreases when the phase number $n$ increases from 2 to 6. Meanwhile, Fig. 9(*b*) shows the traveling wave force increased when the phase number increases from 2 to 4. However, the traveling wave force decreased when the phase number continued to increase to 6, which means the four-phase array will act as the maximum twDEP force on the particles.

Furthermore, we track the distribution pattern of latex beads under the action of the DEP force using an $n$-phase array. We assume the latex beads are neutrally buoyant, and we also neglect the gravitational effect, Brownian motion, and electric-thermal effect. By balancing the Stokes drag force and the DEP force, we obtain the velocity of the beads $\vec{u}$.

$$6\pi\eta a\vec{u} = 2\pi\varepsilon_0\varepsilon_f a^3\,\mathrm{Re}(\beta)\,\nabla\left(|\nabla\phi_R|^2+|\nabla\phi_I|^2\right) - 4\pi\varepsilon_0\varepsilon_f a^3\,\mathrm{Im}(\beta)\,\nabla\times(\nabla\phi_R\times\nabla\phi_I) \tag{20}$$

Here $\eta$ is the viscosity of the suspending media. We introduce the characteristic time of DEP, $\tau$, as follows:

$$\tau=\frac{3d^4\eta}{a^2\varepsilon_0\varepsilon_f V^2} \tag{21}$$

Meanwhile, we introduce the characteristic length $d$ and the characteristic velocity $U$, which is defined as $d/\tau$. We rewrite Eqs. (19*a*) and (19*b*) in dimensionless form.

$$\vec{u}^{\#} = \mathrm{Re}(\beta)\,\nabla\,(|\nabla\phi_R^{\#}|^2 + |\nabla\phi_I^{\#}|^2) - 2\,\mathrm{Im}(\beta)\,\nabla\,\times(\nabla\phi_R^{\#}\times\nabla\phi_I^{\#}) \tag{22}$$

Here $\vec{u}^{\#}=\vec{u}/U$ is the dimensionless velocity and $\phi_R^{\#}=\phi_R/V$ and $\phi_I^{\#}=\phi_I/V$ are the imaginary and real components of the dimensionless potential. The particle trajectory was determined by

$$\frac{d\vec{X}}{dt} = \vec{u}^{\#}(\vec{X}, t^{\#}) \tag{23}$$

Here $\vec{X}$ is the dimensionless displacement and $t^{\#}$ is the dimensionless time. The track of the particles can be obtained by integrating the velocity vector for each particle with the fourth order Runge–Kutta scheme and the time step length $\Delta t^{\#}=0.001$. At the initial time, particles have a uniform distribution, which is shown in Fig. 10(*a*). Due to the cDEP force, particles will move away from the electrodes and move to the left due to the twDEP force. Figures 10(*b*)–10(*f*) show the distribution pattern of latex beads with two-phase, three-phase, four-phase, five-phase, and six-phase arrays, respectively, when the dimensionless time $t^{\#}=16$. If we track the position of the particles at each rank, we can see that the latex beads move vertically away from the electrodes. The shape of each rank remains vertical for the two-phase array because it only has the cDEP force as the twDEP force is always 0. However, the shape of each vertical rank at the initial time becomes a horizontal leaning curve for the three-phase, four-phase, five-phase, and six-phase arrays, which mean the particles also have a motion in the horizontal direction due to the twDEP force. By comparing the distance of particles far from the electrode plane, we can qualitatively obtain that the cDEP force decreases when the ac electric field increases from two-phase to six-phase. Meanwhile, by comparing the particle movement to the left, we can qualitatively obtain that the twDEP force increased when the ac electric field increased from two-phase to four-phase. The twDEP force decreased if the ac electric field continued to increase from four-phase to six-phase. These conclusions match the above analytical result of the DEP force at the center plane ($y=10$ $\mu$m or $y/d=1$).

## Conclusion

In this paper, we presented an analytical method for DEP and twDEP generated by an interdigitated parallel electrode array. The electric potential equation with the mixed type of boundary condition was solved by this analytical method. We compared our analytical solution with the numerical results obtained using commercial software CFD-ACE+, which verified that our analytical method is correct for solving this problem. In addition, comparisons are made to the analytical solutions with approximate linear boundary conditions. The comparisons show that our analytical solution gives a more accurate analysis for the cDEP and twDEP forces. By investigating the DEP force of latex beads with different phase ac electric field ($n=2,3,4,5,6$), we draw the conclusion that the cDEP force decreases when the ac electric field increases from two-phase to six-phase, and the twDEP force increases when the ac electric field increases from two-phase to four-phase, but decreases if the ac electric field continues to increase from four-phase to six-phase.

## References


[1] Asbury, C. L., Diercks, A. H., and van den Engh, G., 2002, "Trapping of DNA by Dielectrophoresis," Biotechnol. Lett., **23**, pp. 2658–2666.

[2] Prasad, B., Du, S., Badawy, W., and Kaler, K. V. I. S., 2005, "Real-Time Multiple-Cell Tracking Platform for Dielectrophoresis (DEP)-Based Cellular Analysis," Meas. Sci. Technol., **16**, pp. 909–924.

[3] Suehiro, J., Hamada, R., Noutomi, D., Shutou, M., and Hara, M., 2003, "Selective Detection of Viable Bacteria Using Dielectrophoretic Impedance Measurement Method," J. Electrost., **57**, pp. 157–168.

[4] Cui, L., Holmes, D., and Morgan, H., 2001, "The Dielectrophoretic Levitation and Separation of Latex Beads in Microchips," Electrophoresis, **22**, pp. 3893–3901.

[5] Gascoyne, P. R. C., and Vykoukal, J., 2002, "Particle Separation by Dielectrophoresis," Electrophoresis, **23**, pp. 1973–1983.

[6] Jones, T., 1995, *Electromechanics of Particles*, Cambridge University Press, Cambridge, Chaps. 2 and 3.

[7] Wang, X. J., Wang, X. B., Becker, F., and Gascoyne, P. R. C., 1996, "A Theoretical Method of Electrical Field Analysis for Dielectrophoretic Electrode Arrays Using Green'S Theorem," J. Phys. D: Appl. Phys., **29**, pp. 1649–1660.

[8] Clague, D., and Wheeler, E., 2001, "Dielectrophoretic Manipulation of Macromolecules: The Electric Field," Phys. Rev. E, **64**, p. 026605.

[9] Morgan, H., Izquierdo, A. G., Bakewell, D., Green, N. G., and Ramos, A., 2001, "The Dielectrophoretic and Traveling Wave Forces Generated by Interdigitated Electrode Arrays: Analytical Solution Using Fourier Series," J. Phys. D: Appl. Phys., **34**, pp. 1553–156.

[10] Albrecht, D. R., Sah, R. L., and Bhatia, S. N., 2004, "Geometric and Material Determinants of Patterning Efficiency by Dielectrophoresis," Biophys. J., **87**, pp. 2131–214

[11] Feng, J. J., Krishnamoorthy, S., Chen, Z. J., and Makhijani, V. B., 2002, "Numerical and Analytical Studies of AC Electric Field in Dielectrophoretic Electrode Arrays," *Proceedings International Conference on Computational Nanoscience and Nanotechnology*, Vol. 2, pp 85–88.

[12] Chang, D. H., Loire, S., and Mezic, I., , 2002, "Closed-Form Solutions in the Electrical Field Analysis for Dielectrophoretic and Travelling Wave Inter-Digitated Electrode Arrays" J. Phys. D: Appl. Phys., **36**, pp. 3073–3078.

[13] Sun, T., Morgan, H., and Green, N. G., 2007, "Analytical Solutions of Acelectrokinetics in Interdigitated Electrode Arrays: Electric Field, Dielectrophoretic and Traveling-Wave Dielectrophoretic Forces," Phys. Rev. E, **76**, p. 046610.

[14] Green, N. G., Ramos, A., and Morgan, H., 2002, "Numerical Solution of the Dielectrophoretic and Travelling Wave Forces for Interdigitated Electrode Arrays Using the Finite Element Method," J. Electrost., **56**, pp. 235–254.

[15] Schnelle, T., Hagedorn, R., Fuhr, G., Fiedler, S., and Muller, T., 1993, "Three-Dimensional Electric Field Traps for Manipulation of Cells—Calculation and Experimental Verification." Biochim. Biophys. Acta, **1157**, pp. 127–14.

[16] Wang, X., Huang, Y., Burt, J. P. H., Markx, G. H., and Pethig, R., 1993, "Selective Dielectrophoretic Confinement of Bioparticles in Potential Energy Wells," J. Phys. D: Appl. Phys., **26**, pp. 1278–1285.

[17] Chen, D. F., Du, H., Li, W. H., and Shu, C., 2005, "Numerical Modeling of Dielectrophoresis Using a Meshless Approach," J. Micromech. Microeng., **15**, pp. 1040–104.

[18] Landau, L. D., Lifshiz, L. P., and Pitaevski, L. P., 1984, *Electrodynamics of Continuous Media*, Pergamon, New York, Chaps. 1–4.

[19] Green, N. G., Ramos, A., and Morgan, H., 2000, "AC Electrokinetics: A Survey of Submicrometre Particle Dynamics." J. Phys. D: Appl. Phys., **33**, pp. 632–641.

[20] Cui, L., Holmes, D., and Morgan, H., 2001, "The Dielectrophoretic Levitation and Separation of Latex Beads In Microchips," Electrophoresis, **22**, pp. 3893–3901.

[21] Feinerman, R. P., and Kelman, R. B., , 1975, "Dual Orthogonal Series: An Abstract Approach," Bull. Am. Math. Soc., **81**(4), pp. 733–73.

**Hidemasa Takana**[1]
Institute of Fluid Science,
Tohoku University,
2-1-1 Katahira, Aoba-ku, Sendai,
Miyagi, 980-8577, Japan
e-mail: takana@paris.ifs.tohoku.ac.jp

**Kazuhiro Ogawa**
e-mail: kogawa@rift.mech.tohoku.ac.jp

**Tetsuo Shoji**
e-mail: tshoji@rift.mech.ac.jp

Fracture and Reliability Research Institute,
Tohoku University,
6-6-1, Aoba, Aramaki, Aoba-ku,
Sendai 980-8579, Japan

**Hideya Nishiyama**
Mem. ASME
Institute of Fluid Science,
Tohoku University,
2-1-1 Katahira, Aoba-ku, Sendai,
Miyagi, 980-8577, Japan
e-mail: nishiyama@ifs.tohoku.ac.jp

# Computational Simulation on Performance Enhancement of Cold Gas Dynamic Spray Processes With Electrostatic Assist

*A real-time computational simulation on the entire cold spray process is carried out by the integrated model of compressible flow field, splat formation model, and coating formation model, in order to provide the fundamental data for the advanced high performance cold gas dynamic spray process with electrostatic acceleration. In this computation, viscous drag force, flow acceleration added mass, gravity, Basset history force, Saffman lift force, Brownian motion, thermophoresis, and electrostatic force are all considered in the particle equation of motion for the more realistic prediction of in-flight nano/microparticle characteristics with electrostatic force and also for the detailed analysis of particle-shock-wave-substrate interaction. Computational results show that electrostatic acceleration can broaden the smallest size of applicable particle diameter for successful adhesion; as a result, wider coating can be realized. The utilization of electrostatic acceleration enhances the performance of cold dynamic spray process even under the presence of unavoidable shock wave.* [DOI: 10.1115/1.2907417]

*Keywords: cold gas dynamic spray, nano/microparticle, supersonic jet, shock wave, particle-shock-wave-substrate interactions, computational simulation*

## Introduction

A cold gas dynamic spray process (cold spray process) is a novel and promising coating technology and was originally developed in the 1980s at the Institute of Theoretical and Applied Mechanics of the Russian Academy of Sciences in Novosibirsk [1–3]. In the conventional cold spray process, powder particles are accelerated through the momentum transfer from the supersonic gas jet. The temperature of supersonic gas jet is always lower than the melting point of the powder material; thus, the coating is formed from the particles in solid state. With utilizing low temperature gas flow, the common problems for traditional thermal spray methods, such as high-temperature oxidation, evaporation, melting, crystallization, residual stresses, debonding, gas release, etc., are eliminated [4]. Furthermore, in a cold spray process, a wide variety of pure metals, metal alloys, and composites can be deposited onto a variety of substrate material through the optimization of particle conditions such as impact velocity, temperature, and size. Because of these attractive advantages, the cold spray process is a promising coating technology and is now paid a special attention for many industrial applications.

The adhesion of the particles in a cold spray process occurs only when the particles have large enough kinetic energy to cause their extensive plastic deformation at the contact surface. The previous both experimental and numerical studies showed that the critical particle impact velocity exists for successful particle adhesion. If the particle impact velocity is lower than the critical velocity, particles rebound and as a consequence, surface erosions are observed. Therefore, the particle impact velocity is one of the most important parameters in a cold spray process for the improvement of the deposition efficiency. Recently, a new method of particle acceleration in cold spray process has been proposed [5]. In this method, an electrostatic force is used to assist the acceleration of the particles besides the conventional particle acceleration by supersonic flow. In addition to that, repulsive Coulomb force, which acts between each charged particle, can suppress in-flight particle aggregation. The simulation results show that this method is effective especially for the acceleration of nanoparticles in a supersonic flow.

A number of experimental and numerical investigations on the cold spray process are intensively conducted. However, most numerical studies focus either on particle behavior in the supersonic flow [5–7] or the splat formation [8,9] separately. There are only a few studies that cover the entire cold gas dynamic spray process. Therefore, in this study, a real-time computational simulation on the entire cold gas dynamic spray process is carried out by the integrated model [10–12] of flow considering shock wave, splat formation, and coating formation. The behavior of in-flight nano/microparticle and the particle-shock-wave-substrate interaction are clarified in detail by considering viscous drag force, flow acceleration, added mass, gravity, Basset history force, Saffman lift force, Brownian motion, thermophoresis, and electrostatic force. The effect of the acceleration by electrostatic forces acting on a nano/microparticle is also examined in detail for the wide range of particle diameters from several hundreds of nanometers to over 10 $\mu$m. The main objective of this study is to provide the fundamental data of the advanced high performance cold gas dynamic spray process by clarifying the effect of electrostatic force on the coating formation in the cold gas dynamic spray process.

## Numerical Modeling

In order to derive the governing equations, the following assumptions have been introduced.

[1]Corresponding author.

Contributed by the Fluids Engineering Division of ASME for publication in the JOURNAL OF FLUIDS ENGINEERING. Manuscript received March 5, 2007; final manuscript received December 25, 2007; published online July 30, 2008. Assoc. Editor: Theodore Heindel. Paper presented at the 2007, Fifth Joint ASME/JSME Fluids Engineering Conference.

(1) The flow is compressible and turbulent.
(2) The flow field is axisymmetric.
(3) In-flight particles have the same temperature and particle temperature does not change in time and space.
(4) In-flight particles are without aggregation.
(5) There is a one-way coupling between the dispersed phase and the carrier phase under the dilute particle-loading condition. Collision between particles is also neglected.
(6) The uniform electrical field is applied between the nozzle exit and the substrate for the electrostatic-assisted acceleration of particles.
(7) The effect of the presence of particles does not affect the space charge for simplicity.

Under the above assumptions, the governing equations for flow field are described as follows.

Continuity equation:

$$\frac{\partial \rho}{\partial t} + \nabla \cdot (\rho \boldsymbol{u}) = 0 \tag{1}$$

Momentum equation:

$$\frac{\partial}{\partial t}(\rho \boldsymbol{u}) + \nabla \cdot (\rho \boldsymbol{u}\boldsymbol{u}) = -\nabla p + \nabla \cdot \bar{\bar{\tau}} \tag{2}$$

Energy equation:

$$\frac{\partial e}{\partial t} + \nabla \cdot [(e+p)\boldsymbol{u}] = \Phi_D + \nabla \cdot (\kappa \nabla T) \tag{3}$$

Equation of state:

$$p = \rho R T \tag{4}$$

In this study, large eddy simulation of compressible flow [13] is carried out in order to capture the unsteady turbulent behavior during the cold gas dynamic spray process.

Based on the Lagrangian approach, the particle trajectories are calculated by solving the equation of motion for the particles. To predict the in-flight behavior of nano- or microscale particle in an unsteady flow precisely, the present study applies the following particle equation of motion [14] including terms of viscous drag force, flow acceleration, added mass, gravity, Basset history force, Saffman lift force [15,16], Brownian motion [17], thermophoresis [18], and electrostatic force [5,19].

$$m_p \frac{d\boldsymbol{u}_p}{dt} = \boldsymbol{F}_{\text{drag}} + \boldsymbol{F}_{\text{acc}} + \boldsymbol{F}_{\text{mass}} + \boldsymbol{F}_g + \boldsymbol{F}_{\text{Basset}} + \boldsymbol{F}_{\text{lift}} + \boldsymbol{F}_{\text{Brown}} + \boldsymbol{F}_{\text{therm}} + \boldsymbol{F}_{\text{elec}} \tag{5}$$

$$\frac{d\boldsymbol{x}_p}{dt} = \boldsymbol{u}_p \tag{6}$$

The viscous drag force is described as follows:

$$\boldsymbol{F}_{\text{drag}} = \frac{\pi}{8} d_p^2 \rho C_D (\boldsymbol{u} - \boldsymbol{u}_p)|\boldsymbol{u} - \boldsymbol{u}_p| \tag{7}$$

where $C_D$ is the drag coefficient. In this study, the drag coefficient of sphere particle considering compressible effect and Knudsen effect is adapted [20]. This representation of drag coefficient is accurate over the wide range and flow regime including continuum, slip, transition, and molecular flow at particle Mach number up to 6. The correlating equations for $C_D$ consist of three equations: the equation representing all of the subsonic flow regimes, the equation representing the supersonic flow regime at particle Mach numbers greater than 1.75, and the linear interpolation equation for the intervening region between particle Mach numbers of 1 and 1.75. The detailed descriptions of correlating equations for $C_D$ are given as follows:

For subsonic flow ($M_p < 1$):

$$C_{D(\text{sub})} = 24\left[\text{Re}_p + S\left\{4.33 + \left(\frac{3.65 - 1.53\frac{T_p}{T}}{1 + 0.353\frac{T_p}{T}}\right) \times \exp\left(-0.247\frac{\text{Re}_p}{S}\right)\right\}\right]^{-1} + \exp\left(-\frac{0.5M_p}{\sqrt{\text{Re}_p}}\right) \times \left[\frac{4.5 + 0.38(0.33\,\text{Re}_p + 0.48\sqrt{\text{Re}_p})}{1 + 0.03\,\text{Re}_p + 0.48\sqrt{\text{Re}_p}} + 0.1M_p^2 + 0.2M_p^8\right] + \left[1 - \exp\left(-\frac{M_p}{\text{Re}_p}\right)\right]0.6S \tag{8}$$

where $\text{Re}_p$ and $M_p$ are particle Reynolds number and Mach number based on the relative velocity between particle and gas flow, respectively. $\text{Re}_p$ and $M_p$ are defined as

$$\text{Re}_p = \frac{\rho d_p}{\mu}|\boldsymbol{u} - \boldsymbol{u}_p| \tag{9}$$

$$M_p = \frac{|\boldsymbol{u} - \boldsymbol{u}_p|}{\sqrt{\gamma R T}} \tag{10}$$

$S$ is the molecular speed ratio given by $S = M_p\sqrt{\gamma/2}$.

For supersonic flow ($M_p \geqslant 1.75$):

$$C_{D(\text{super})} = \frac{0.9 + \frac{0.34}{M_p^2} + 1.86\left(\frac{M_p}{\text{Re}_p}\right)^{1/2}\left[2 + \frac{2}{S^2} + \frac{1.058}{S}\left(\frac{T_p}{T}\right)^{1/2} - \frac{1}{S^4}\right]}{1 + 1.86\left(\frac{M_p}{\text{Re}_p}\right)^{1/2}} \tag{11}$$

For supersonic flow ($1 < M_p < 1.75$):

$$C_D(M_p, \text{Re}_p) = C_{D(\text{sub})}(1.0, \text{Re}_p) + \tfrac{4}{3}(M_p - 1.0)[C_{D(\text{super})}(1.75, \text{Re}_p) - C_{D(\text{sub})}(1.0, \text{Re}_p)] \tag{12}$$

where $C_{D(\text{sub})}(1.0, \text{Re})$ represents the coefficient calculated using Eq. (8) with $M_p = 1.0$, and $C_{D(\text{super})}(1.75, \text{Re}_p)$ represents the coefficient obtained using Eq. (11) with $M_p = 1.75$. The effect of temperature difference between particle and gas is considered in Eqs. (8) and (11); however, in this simulation the temperatures of particle and flow are assumed to be the same throughout the calculation.

The electrostatic force $\boldsymbol{F}_{\text{elec}}$ on the charged particle is given by the following relation [5,12,19]:

$$\boldsymbol{F}_{\text{elec}} = q_p \boldsymbol{E} + \frac{q_p^2}{16\pi\varepsilon_0 a^2}\boldsymbol{n} \tag{13}$$

where $q_p$ is the particle charge [21] and $a$ is the distance between the particle and the biased substrate.

The detailed description of other forces can be given as follows. Here, the convective total derivatives are denoted by $D/Dt$ for the flow and $d/dt$ for the particle.

Flow acceleration

$$m_f \frac{D\mathbf{u}_f}{Dt} \tag{14}$$

Added mass:

$$-\frac{m_f}{2}\frac{d}{dt}(\mathbf{u}_p - \mathbf{u}_f) \tag{15}$$

Buoyancy force:

$$(m_p - m_f)\mathbf{g} \tag{16}$$

Basset history force:

$$-\frac{3}{2}\pi\mu d_p^2 \int_0^t \frac{1}{\sqrt{\pi\nu(t-s)}}\frac{d}{ds}(\mathbf{u}_p - \mathbf{u}_f)ds - 3\pi\mu d_p(\mathbf{u}_p - \mathbf{u}_f)\frac{1}{\sqrt{\pi\mu t}} \tag{17}$$

Saffman lift force ($z$-component):

$$6.46\rho_f \nu^{0.5}\left(\frac{d_p}{2}\right)^2 (u_{z_p} - u_{z_f})\left|\frac{\partial u_{z_f}}{\partial r}\right|^{0.5} \mathrm{sgn}\left(\frac{\partial u_{z_f}}{\partial r}\right) \tag{18}$$

Brownian motion:

$$m_p G_i \sqrt{\frac{2\nu}{S_c \tau_p^2 \Delta t}}, \tag{19}$$

where $S_c$ is Schmidt number of the particle in flow and $G_i$ is zero-mean, unit variance independent Gaussian random number.

Thermophoresis:

$$-\frac{1}{\rho_f} 6\pi\mu^2 d_p \frac{1.17\left(\frac{\lambda_f}{\lambda_p} + 2.18Kn\right)}{(1+3.42Kn)\left(1+2\frac{\lambda_f}{\lambda_p}+4.36Kn\right)}\frac{\nabla T}{T} \tag{20}$$

As discussed later in detail, only viscous drag force, flow acceleration, added mass, and Saffman lift force are taken into account in Eq. (5) for coating simulations.

**Modeling of Splat Formation.** The splat formation in a cold gas dynamic spray process is modeled by utilizing the flattening ratio of the particle with plastic deformation [8] and also by the empirical projectile penetration law [22]. The flattening ratio is defined as the ratio of the diameter of splat to that of a spherical particle of the same volume. The flattening ratio is given as a linear function of particle impact velocity [8]. The volume of created crater upon particle impact on the substrate can be expressed as follows [22].

$$\mathrm{Vol} = \frac{4\times 10^{-8}}{B}\frac{1}{2}\left(\rho_p \frac{1}{6}\pi d_p^3\right)u_p^2 \tag{21}$$

where $B$ is the Brinell hardness number of the substrate material. Using the assumption of cylindrical crater formation with the diameter of $d_s$, the depth of the crater $L$ can be derived from Eq. (21) and written as

$$L = \frac{4\times 10^{-8}}{B}\frac{1}{3}\rho_p u_p^2 \frac{d_p^3}{d_s^2} = \frac{4\times 10^{-8}}{B}\frac{1}{3}\frac{\rho_p u_p^2}{f^2}d_p \tag{22}$$

where $f$ is a flattening ratio. When the particle transforms into a disk shape with the diameter of $d_s$ upon the impact on the substrate, the height of the disk $h_d$ under the constant particle volume during the splat formation is given as

**Table 1 Computational conditions for a cold gas dynamics spray process**

| | |
|---|---|
| Working gas | Air |
| Mass flow rate | $6.72\times 10^{-3}$ kg/s |
| Inlet cross sectional area | $5.67\times 10^{-5}$ m$^2$ |
| Inlet gas temperature | 700 K |
| Inlet gas pressure | 0.810 MPa |
| Ambient gas pressure | 0.101 MPa |
| Ambient gas temperature | 300 K |
| Particle material | Copper |
| Substrate material | Steel |

$$h_d = \frac{2}{3}\frac{d_p^3}{d_s^2} = \frac{2}{3}\frac{d_p}{f^2} \tag{23}$$

Therefore, the height of each created splat $h_s$ is given by the following equation:

$$h_s = h_d - L = \frac{1}{3}\left(2 - \frac{4\times 10^{-8}}{B}\rho_p u_p^2\right)\frac{d_p}{f^2} \tag{24}$$

The coating is formed by superposing each splat [10,11], in other words, by adding up the height of each splat obtained from Eq. (24).

The computational conditions are given in Table 1. These operating conditions are decided by referring to actual experimental conditions. The detailed descriptions on the numerical procedures and boundary conditions are found in the literature [12].

## Results and Discussion

**Flow Structure.** Figure 1 shows axial flow velocity distribution in $r$-$z$ plane 690 $\mu$s after air spraying. Airflow chokes at the throat and pseudo-shock-wave appear at the location of flow deflection around $z=20$ mm, as shown in Fig. 1. Flow velocity fluctuates by the passage through pseudo-shock-wave. Airflow is accelerated up to ~980 m/s at the nozzle exit due to the underexpansion of gas flow. As can be observed in Fig. 1, a bow shock wave is formed in the vicinity of the substrate and the flow is decelerated drastically by the bow shock wave and substrate. Due to a short nozzle-substrate separation distance, the bow shock appears in the expansive region of the first cell, but a series of shock diamonds does not appear in front of the substrate. The in-flight particles experience the interaction with the bow shock wave prior to impact on substrate.

**In-Flight Particle Characteristics.** Figure 2 shows the trajectories of flight particles with different diameters at the injection velocity of 30 m/s without electrostatic acceleration. Particles in the range of 500 nm to 1.5 $\mu$m impact the substrate with penetrating the bow shock. With the decrease in diameter, particles fly closer to the nozzle wall and impact the substrate radially more

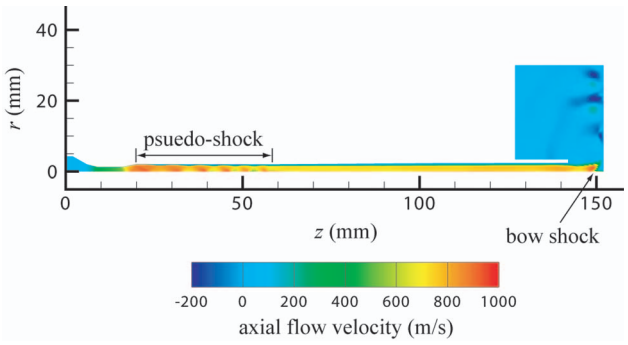


**Fig. 1 Axial flow velocity distributions in $r$-$z$ plane**

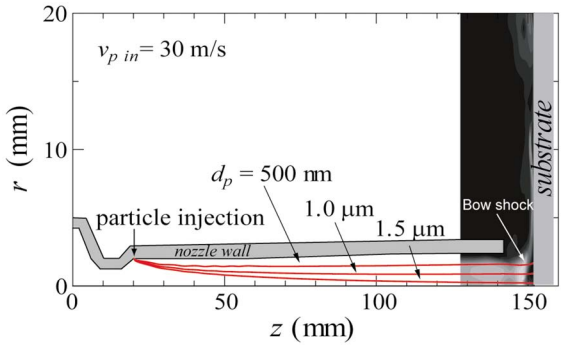


**Fig. 2 Effect of particle size on flight trajectory without electrostatic acceleration**

outward. Particles less than 500 nm attaches to the nozzle wall during the flight and cannot impinge on the substrate. It requires higher injection velocity to utilize the particle smaller than 500 nm.

Figure 3 shows particle impact velocities as a function of diameter with or without electrostatic force at the particle injection velocities of 5 m/s and 30 m/s. Because of smaller particle inertia, higher injection velocity of 30 m/s is required to carry particles smaller than 1.5 $\mu$m toward the center of the nozzle. Under constant injection velocity, particle impact velocity decreases with the decrease in particle diameter. This is because the smaller particles are decelerated more through the interaction between particle and shock wave, as described later. Without the application of electrical field, the maximum impact velocity of 668 m/s can be obtained for the particle diameter of 1.5 $\mu$m at the injection velocity of 30 m/s. By applying the electrical field of $3.0 \times 10^4$ kV/m between the nozzle exit and substrate, electrostatic force acts directly on the charged particles. The highest impact velocity is obtained for the particle diameter of 1.5 $\mu$m at the injection velocity of 30 m/s. In this case, the particle impact velocity increases by 16% up to 777 m/s by electrostatic acceleration. The effect of electrostatic acceleration can be observed for all particle diameters and injection velocities. The more significant increase in particle impact velocity is observed as particle diameter decreases. The critical velocity for copper particle is reported to be 570 m/s for 5–22 $\mu$m particles. Under the assumption that this critical velocity is also applicable to smaller particle than 5 $\mu$m, the particles having the diameter in the range of 900 nm–6 $\mu$m can be possibly deposited on a substrate. With the assist of electrostatic acceleration, the lower and upper limits of operating particle diameter for the possible bonding can be broadened to 500 nm and 8 $\mu$m, respectively. Therefore, the utilization of electrostatic force can broaden especially the smallest applicable particle diameter for the possible bonding in a cold gas dynamic spray process even in the presence of unavoidable shock wave.

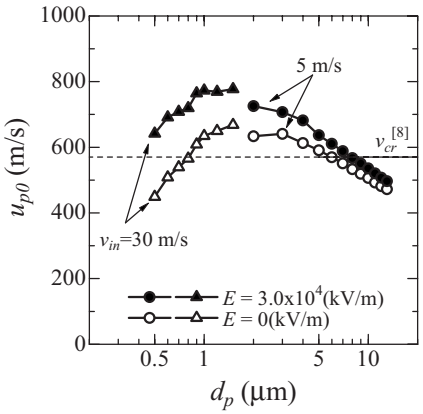


**Fig. 3 Effect of electrostatic acceleration on the particle impact velocities for various particle diameters**

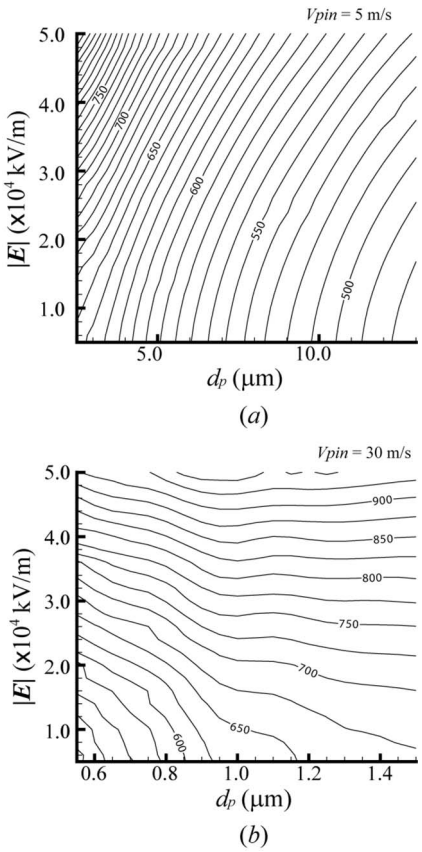


**Fig. 4 Dependence of electrostatic field intensity and particle diameter on particle acceleration: (*a*) $v_{pin}$=5 m/s and (*b*) 30 m/s**

Figure 4 shows the dependence of electrostatic field intensity and particle diameter on particle impact velocity at particle injection velocities of 5 m/s and 30 m/s, respectively. In the range of particle diameter of 2.5–13 $\mu$m at the injection velocity of 5 m/s, higher acceleration can be obtained with decreasing particle diameter and increasing electrostatic field intensity. On the other hand, for the particle with the diameter ranging from 550 nm to 1.5 $\mu$m at the injection velocity of 30 m/s, particle velocity decreases as particle diameter decreases due to the strong interaction with shock wave near the substrate. The dependence of particle diameter on electrostatic acceleration becomes smaller with increasing electrostatic field intensity. For the particle larger than 1 $\mu$m, the particle impact velocity becomes almost the same at electrostatic field intensity higher than $3.0 \times 10^4$ kV/m.

Figure 5 shows the axial evolutions of particle velocities for different particle diameters of 900 nm, 4 $\mu$m, and 12 $\mu$m, respectively. For comparison, the flight trajectories of these particles are almost the same by the adjustment of particle radial injection velocities and then all these particles impact on the substrate near $r$=0. As can be seen from this figure, airflow is decelerated rapidly from 980 m/s to 0 m/s by the bow shock wave, which appears in the vicinity of a substrate. All particles penetrate shock wave prior to the impact on substrate. The deceleration of impact velocity through particle-shock wave interaction is significant especially for the case of 900 nm. For the particle with the diameter of 900 nm, although the particle has been accelerated almost up to the velocity of the gas in the nozzle, particle velocity decreases by

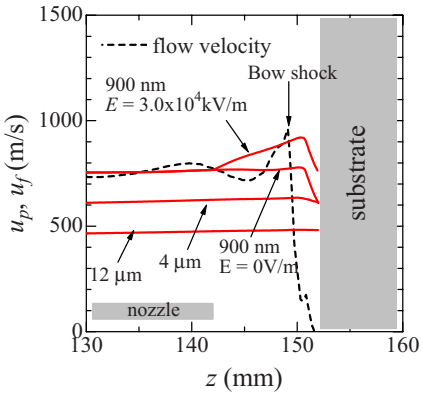


**Fig. 5 Axial evolutions of particle velocities for different particle diameters of 900 nm, 4 $\mu$m, and 12 $\mu$m**

70 m/s though the passage of bow shock wave. With the electrostatic acceleration of 900 nm particle, the particle velocity increases up to 921 m/s in front of the shock wave and then decreases to 764 m/s through the passage of shock wave resulting from the large difference between particle and gas velocities and large increase in gas density.

Figure 6 shows the contribution ratios of the absolute value of each force acting on a particle without electrostatic acceleration. Viscous force, flow acceleration, added mass, and Saffman lift force are the dominant forces among other ones considered in this computation. Contribution ratios of other forces are too small that they do not appear in the figure. The ratios of flow acceleration, added mass, and Saffman lift force become larger especially for 12 $\mu$m particle behind the shock wave attributed to a drastic change in gas velocity and gas density. In the case of 900 nm particle, flow acceleration and added mass are negligibly small compared to the viscous drag force.

Figure 7 shows the contribution ratios of the absolute value of each force with electrostatic acceleration. The contribution of electrostatic force is considerably larger than that of drag force for all particles in front of the shock wave. On the other hand, behind the shock wave, the ratio of electrostatic force becomes relatively smaller than the drag force for 4 $\mu$m and 900 nm particles. Therefore, the acceleration by electrostatic force works more effectively for smaller particles in front of the shock wave. However, behind the shock wave, viscous drag force becomes dominant for lighter particle.

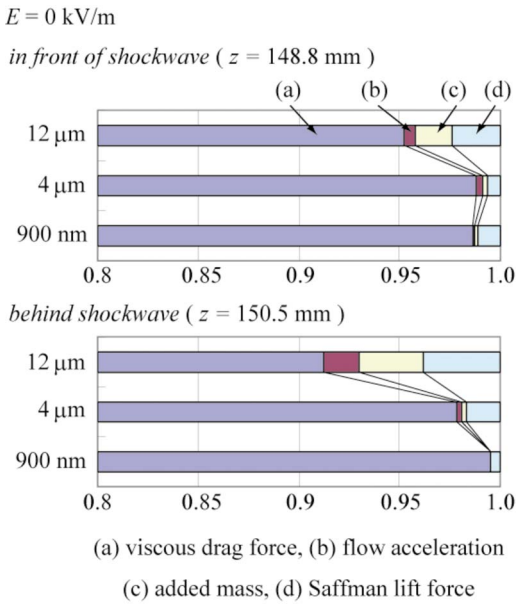


**Fig. 6 Contribution ratios of each force acting on a particle without electrostatic acceleration**

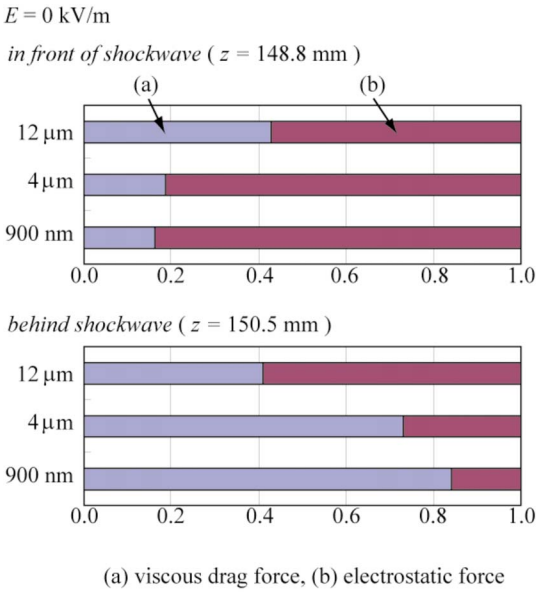


**Fig. 7 Contribution ratios of each force acting on a particle with electrostatic acceleration**

**Coating Characteristics.** Figure 8 shows the radial distributions of particle impact velocities on the substrate with or without electrostatic force. As for the coating simulation, only viscous drag, flow acceleration, added mass, and Saffman lift force are considered in equation of particle motion, since other forces are found to be negligibly small by a single particle computation, as shown in Figs. 6 and 7. The number of sample particles is 2000 and particles are injected continuously with time step of 0.01 $\mu$s at the injection velocity of 5 m/s. Particles have the size distribution ranging from 5.5 $\mu$m to 10.7 $\mu$m. The size distribution of the particles follows the Gaussian distribution with the average of 8 $\mu$m at standard deviation of 0.9 so that the effect of electrostatic

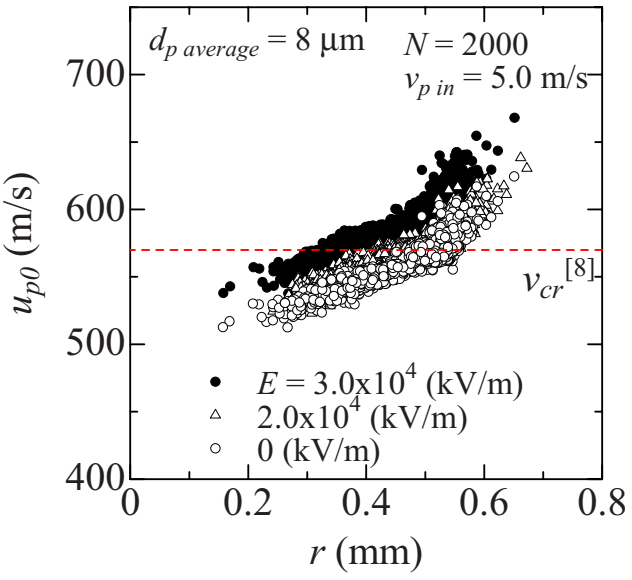


**Fig. 8 Particle impact velocities and particle impact positions on the substrate with or without electrostatic acceleration**

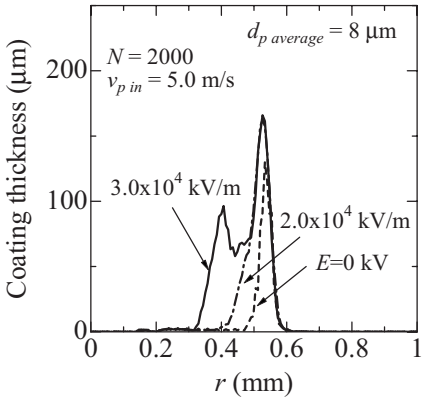


**Fig. 9 Effect of electrostatic acceleration on coating characteristics**

force is clearly observed as found in Fig. 3. Without electrostatic acceleration, only the particles impacting at the radial position greater than 0.5 mm are accelerated more than the critical velocity through momentum transfer from airflow. With increasing electrostatic field intensity, the number of particles above the critical velocity clearly increases. As a result of that, the position of particles having over critical velocities extends radially inward.

Figure 9 shows the effect of electrostatic assist on coating thickness distribution. The coating region increases radially inward with the increase in electrostatic field intensity corresponding to Fig. 8. This shows the increase in the considerable deposition efficiency. It was revealed from the previous studies that the critical velocity of copper has a dependence on particle conditions, i.e., particle size, oxygen content, and particle temperature [9,23]. Low oxygen content and high particle temperature cause a decrease in critical velocity [23]. On the other hand, the critical velocity increases with the decrease in particle size [9]. Since the effective electrostatic acceleration can be performed for smaller particle, as shown in Fig. 3, particles can be effectively accelerated over high critical velocity by the electrostatic force without any particle optimization. Therefore, the utilization of electrostatic acceleration enhances the performance of cold gas dynamic spray coating and contributes the extension of applicable particle diameters for successful adhesion.

Figure 10 shows the comparison with available experimental result [24] for the relative velocity of particles at the exit of a supersonic nozzle without electrostatic acceleration in order to verify this computational model for a general case. The dimensionless quantity Ω shown in the figure is related to a particle diameter and is defined as

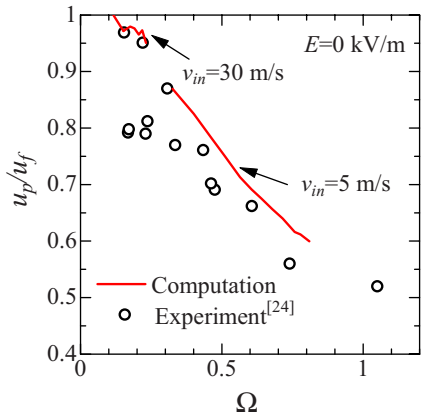


**Fig. 10 Comparison with experimental result for the relative velocity of particles at the exit of a supersonic nozzle**

$$\Omega = \sqrt{\frac{d_p}{L}\frac{\rho_p u_{fe}^2}{p_0}} \tag{25}$$

where $L$ is the length of a supersonic part of the nozzle, $u_{fe}$ is gas velocity at the nozzle exit, and $p_0$ is an inlet stagnation pressure, respectively. Although the computational result for Ω larger than 0.3 is slightly higher, there is a good agreement with experimental result. Therefore, the validity of this computational simulation is evaluated for the prediction of particle in-flight behavior.

## Conclusions

The effect of electrostatic force on the nano/microparticle acceleration, the particle-shock-wave-substrate interaction, and also coating formation in a cold gas dynamic spray process are numerically clarified in detail to provide the fundamental data for the advanced high performance cold gas dynamic spray process. In this computation, viscous drag force, flow acceleration added mass, gravity, Basset history force, Saffman lift force, Brownian motion, thermophoresis, and electrostatic force are all considered in the particle equation of motion for the realistic analyses. The obtained results can be summarized as follows.

(1) Besides viscous drag force, the influence of flow acceleration and added mass attributed to a drastic change in flow velocity and flow density and also Saffman lift force becomes more important behind the shock wave with increase in particle diameter.
(2) The electrostatic acceleration effectively works for smaller particles in front of the shock wave. On the contrary, viscous drag becomes dominant behind the shock wave with the decrease in particle diameter.
(3) As a result of electrostatic acceleration broadening the smallest size of applicable particle diameter for successful adhesion, coating region increases even though there is a lack of particle acceleration only through momentum transfer from high speed airflow. Therefore, the utilization of electrostatic acceleration enhances the performance of cold dynamic spray process even under the presence of unavoidable shock wave.

## Acknowledgment

The authors would like to give their sincere thanks to Professor Goro Masuya of the Department of Aerospace and Astronautics Engineering of Tohoku University for his valuable comments. The present study was partly supported by a Grant-in-Aid for Scientific Research (A) and for Young Scientists (B) from the Japan Society for Promotion of Science and also by a 21st Century COE program Grant of the International COE of Flow Dynamics from the Ministry of Education, Culture, Sports, Science and Technology.

## Nomenclature

$A_{\text{in}}$ = inlet cross sectional area (m$^2$)
$d_p$ = particle diameter (m)
$d_s$ = splat diameter (m)
$C_D$ = drag coefficient
$e$ = stagnation internal energy per unit volume (J/m$^3$)
$\boldsymbol{E}$ = electric field vector (V/m)
$\boldsymbol{F}$ = force vector (N)
$m_f$ = fluid mass (kg)
$m_p$ = particle mass (kg)
$\boldsymbol{n}$ = normal direction
$p$ = static gas pressure (Pa)
$q_p$ = particle charge (C)
$r$ = radius (m)
$r_p$ = particle radius (m)
$\text{Re}_p$ = particle Reynolds number

$t$ = time (s)
$T$ = static gas temperature (K)
$\boldsymbol{u}$ = gas velocity vector (m/s)
$u_f$ = axial gas velocity (m/s)
$u_{fe}$ = axial gas velocity at nozzle exit (m/s)
$\boldsymbol{u}_p$ = particle velocity vector (m/s)
$u_p$ = axial particle velocity (m/s)
$u_{pe}$ = axial particle velocity at nozzle exit (m/s)
$v_{\text{pin}}$ = particle injection velocity (m/s)
$x_p$ = position of particle (m)
$z$ = axis (m)

**Greek Symbols**

$\gamma$ = specific heat ratio
$\kappa$ = gas thermal conductivity (W/(m K))
$\lambda$ = mean free path (m)
$\lambda_f$ = thermal conductivity of gas (W/(m K))
$\lambda_p$ = thermal conductivity of particle (W/(m K))
$\mu$ = viscosity coefficient (Pa s)
$\rho$ = flow density ($\text{kg}/\text{m}^3$)
$\rho_p$ = particle density ($\text{kg}/\text{m}^3$)
$\bar{\bar{\tau}}$ = viscosity stress tensor (Pa)
$\tau_p$ = particle relaxation time (s)
$\Phi_D$ = viscous dissipation ($\text{W}/\text{m}^3$)

## References


[1] Alkhimov, A. P., Papyrin, A. N., Kosarev, V. F., and Nesterovich, N. I., 1994, U.S. Patent No. 5,302,414.
[2] Alkhimov, A. P., Papyrin, A. N., Kosarev, V. F., and Nesterovich, N. I., 1995, European Patent No. EP 0,484,533,B1.
[3] Tokarev, A. O., 1996, "Structure of Aluminum Powder Coatings Prepared by Cold Gasdynamic Spraying," Met. Sci. Heat Treat., **38**, pp. 136–139.
[4] Papyrin, A., Kosarev, V., Klinkov, S., Alkhimov, A., and Fomin, V., 2007, *Cold Spay Technology*, Elsevier, New York.
[5] Jen, T.-C., Pan, L., Li, L., Chen, Q., and Cui, W., 2006, "The Acceleration of Charged Nano-Particles in Gas Stream of Supersonic de-Laval-Type Nozzle Coupled With Static Electric Field," Appl. Therm. Eng., **26**, pp. 613–621.
[6] Jodoin, B., 2002, "Cold Spray Nozzle Mach Number Limitation," J. Therm. Spray Technol., **11**(4), pp. 496–507.
[7] Jodoin, B., Raletz, F., and Vardelle, M., 2006, "Cold Spray Modeling and Validation Using an Optical Diagnostic Method," Surf. Coat. Technol., **200**, pp. 4424–4432.
[8] Assadi, H., Gärtner, F., Stoltenhoff, T., and Hreye, H., 2003, "Bonding Mechanism in Cold Gas Spraying," Acta Mater., **51**, pp. 4379–4394.
[9] Schmidt, T., Gärtner, F., Assadi, H., and Kreye, H., 2006, "Development of a Generalized Parameter Window for Cold Spary Deposition," Acta Mater., **54**, pp. 729–742.
[10] Sato, T., Solonenko, O. P., and Nishiyama, H., 2002, "Optimization for Plasma Spraying Processes by Numerical Simulation," Thin Solid Films, **407**, pp. 54–59.
[11] Sato, T., Solonenko, O. P., and Nishiyama, H., 2004, "Evaluations of Ceramic Spraying Processes by Numerical Simulation," Mater. Trans., **45**, pp. 1874–1879.
[12] Takana, H., Ogawa, K., Shoji, T., and Nishiyama, H., 2008, "Computational Simulation of Cold Spray Process Assisted by Electrostatic Force," Powder Technol., in press.
[13] Erlebacher, G., Hussainu, M., Speziale, C., and Zang, T., 1992, "Toward the Large-Eddy Simulation of Compressible Turbulent Flows," J. Fluid Mech., **238**, pp. 155–185.
[14] Karniadakis, G., Beskok, A., and Aluru, N., 2005, *Microflows and Nano Flows*, Springer, New York, 2005.
[15] Saffman, P. G., 1965, "The Lift on a Small Sphere in a Slow Shear Flow," J. Fluid Mech., **22**, pp. 385–400.
[16] Saffman, P. G., 1968, "Corrigendum to 'The Lift on a Small Sphere in a Slow Shear Flow,'" J. Fluid Mech., **31**, p. 624.
[17] Li, A., and Ahmadi, G., 1993, "Deposition of Aerosols on Surfaces in a Turbulent Channel Flow," Int. J. Eng. Sci., **31**(3), pp. 435–451.
[18] Pfender, E., and Lee, Y. C., 1985, "Particle Dynamics and Particle Heat and Mass Transfer in Thermal Plasmas. Part I. The Motion of a Single Particle Without Thermal Effects," Plasma Chem. Plasma Process., **5**(3), pp. 211–237.
[19] Ye, Q., Steigleder, T., Scheibe, A., and Domnik, J., 2002, "Numerical Simulation of the Electrostatic Powder Coating Process With a Corona Spray Gun," J. Electrost., **54**, pp. 189–205.
[20] Henderson, C. B., 1976, "Drag Coefficient of Spheres in Continuum and Rarefied Flows," AIAA J., **14**, pp. 707–708.
[21] Pauthenier, M. M., and Moreau-Hanot, M., 1932, "The Charge on a Spherical Particle in an Ionized Field," J. Phys. Radium, **7**, pp. 590–613.
[22] Eichelberger, R. J., and Gehring, J. W., 1962, "Effects of Meteoroid Impacts on Space Vehicles," J. Am. Rocket Soc., **32**, pp. 1583–1591.
[23] Li, C.-J., Li, W.-Y., and Liao, H. L., 2006, "Examination of the Critical Velocity for Deposition of Particles in Cold Spraying," J. Therm. Spray Technol., **15**, pp. 212–222.
[24] Alkhimov, A. P., Kosarev, V. F., and Klinkov, S. V., 2000, "The Features of Cold Spray Nozzle Design," J. Therm. Spray Technol., **10**, pp. 375–381.

# Dense Particulate Flow in a Cold Gas Dynamic Spray System

**B. Samareh**

**A. Dolatabadi**
e-mail: dolat@encs.concordia.ca

Department of Mechanical and Industrial Engineering,
Concordia University,
Montreal, QC, H3G 1M8 Canada

*The effect of particle-gas and particle-particle interactions in a cold spray process is studied when the particle loading is high. To examine the effect of the presence of a dense particulate flow on the supersonic gas, an Eulerian-Eulerian approach is used. It is found that when the volume fraction of the injected particles is increased, the turbulence of the gas phase will be augmented by the motion of particles and consequently, the shape, the strength, and the location of the compression and expansion waves will be altered. Shock-particle interactions are demonstrated for various volume fractions. Another important parameter, which will affect the spraying deposition efficiency, is the substrate stand-off distance. It is found that the stagnation pressure alternates for different stand-off distances because of the formation of compression and expansion waves outside the nozzle exit. The particle normal velocity on impact is a strong function of the stagnation pressure on the substrate as particles must pierce through the bow shock formed on that region. The effect of the particle size and number density are also studied for different loading conditions. It is found that small and large particles behave differently as they pass through shock diamonds and the bow shock, i.e., in the case of very small particles, as the loading increases, the impact velocity increases, while, for the large particles, the trend is reversed.* [DOI: 10.1115/1.2957914]

*Keywords: cold spray, fluid dynamics, numerical modeling, particle dynamics, shock-particle interaction*

## Introduction

Particle-laden flows are widely encountered in many engineering applications such as pneumatic conveying of granular materials, dispersion of pollutants in the atmosphere, solid particle separation from flue gas, and particle deposition in thermal spray coating. The cold gas dynamic spray (CGDS) is a process used to deposit high speed (higher than 500 m/s) particles on a substrate. This method is a direct deposition technique, which utilizes the kinetic energy of particles. When compared to other commonly used methods such as plasma spraying and high velocity oxy-fuel (HVOF) processes, cold spray is a relatively new thermal spray process, which can be used for deposition of fine particles typically between 1 $\mu$m and 60 $\mu$m at temperatures below melting point. Higher coating qualities can be achieved with dense layers of coating with a higher bonding force and a lower oxidation rate of particles exposed to ambient air. The method was originally developed at the Institute of Theoretical and Applied Mechanics of the Russian Academy of Science in Novosibirsk [1].

A cold spray system is composed of a converging-diverging De Laval nozzle, a powder feeder, a high pressure gas tank, and a gas heater, as shown in Fig. 1. The compressed gas expands and accelerates in the nozzle, developing a supersonic flow in the diverging section of the nozzle. At the nozzle exit, the gas Mach number can be between 2 and 4 for different pressure differences.

Particles are also injected into the nozzle at the same time, where they are propelled and accelerated by the high speed gas flow. Two methods are available and commonly in use to introduce the particles into the nozzle. In the first method, referred to as the Papyrin's process [2,3], the particles are injected into the converging section along the axis of the nozzle. In the second approach, the particle feeder is placed downstream of the nozzle throat where the gas pressure is lower than the ambient pressure [4]. The nozzle used in this simulation utilizes the second method as the powder feeder is placed after the nozzle throat and at the beginning of the nozzle's diverging section. At the nozzle exit, the particles may attain velocities as high as 800 m/s when nitrogen is used as the carrier gas and particles are injected downstream of the nozzle throat. However, as very small (typically smaller than 10 $\mu$m) or low density particles pass through a series of diamond shocks and a strong bow shock formed on the substrate, their velocities decrease drastically. One of the most important characteristics of such a flow field is the deposition efficiency (DE) defined as follows:

$$\mathrm{DE} = \frac{\text{mass of particles deposited on the substrate}}{\text{mass of particles fed into the nozzle}} \tag{1}$$

In practice, improving the coating deposition efficiency is one of the main technological challenges for the CGDS nozzles as some of the particles are washed away because of the presence of high velocity and high pressure regions near the substrate; as well, some of them can bounce off the substrate and escape into the surrounding environment. This relatively low deposition efficiency can be the result of having many particles among the particulate flow with velocities lower than the critical velocity, which is the minimum required velocity for a particle to stick to the substrate [5]. The deposition efficiency is a strong function of particle material and size distributions as well as the flow field parameters. One of the parameters that can highly improve the efficiency is the particle normal velocity upon impact on the substrate. This, in turn, is a function of nozzle geometry, stagnation temperature, and pressure of the gas phase, particle and gas materials, particle size, and substrate location as well as geometry.

Many studies on two-phase supersonic gas and solid particles have been conducted recently. Power et al. [6] and Smith et al. [7] modeled the flow field of a sonic nozzle. Due to the choked flow at the nozzle exit, the internal and external flows were solved separately. Particles were modeled using a Lagrangian scheme with one way coupling between the gas and solid phases. Similar studies were done by Oberkampf et al. [8,9], Yang and Eidelman

Contributed by the Fluids Engineering Division of ASME for publication in the JOURNAL OF FLUIDS ENGINEERING. Manuscript received May 29, 2007; final manuscript received February 25, 2008; published online July 30, 2008. Assoc. Editor: Dennis Siginer.

  

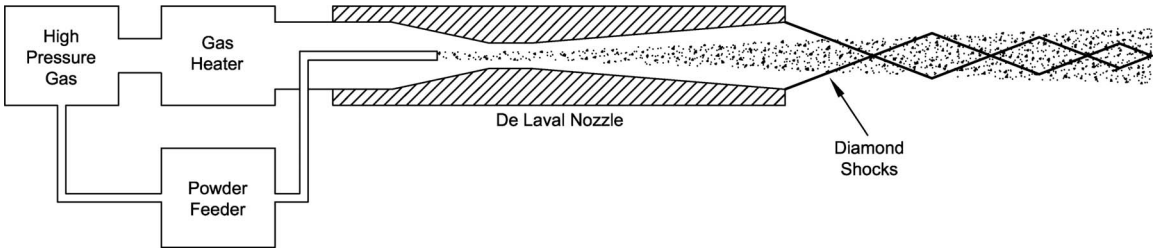


**Fig. 1 Schematic of the cold spray process**

[10], Hassan et al. [11], and Dolatabadi et al. [12] in which Eulerian and Lagrangian formulations for the gas and particle phases were considered, respectively. Dolatabadi et al. [13] used an Eulerian model for the cloud of particles in high speed flows. Samareh and Dolatabadi [14] also conducted a Lagrangian three dimensional CGDS system simulation and analyzed the effect of the substrate location and geometry on the gas phase and particles.

According to Elghobashy [15], a two-phase flow with a local particle volume fraction greater than $10^{-3}$ and a Stokes number ranging from $10^{-4}$ to $10^{3}$ can be considered as a dense flow regime. In most of the processes mentioned, the two-phase flow of gas and solid particles is dense, and the volume fraction occupied by the particles is so high that it may play an important role in the gas flow configuration and particle motion [16]. As a result, a two-way coupled analysis is required to resolve the important features of particle and gas interactions. In this study, a dense supersonic flow of gas and solid particles is modeled based on an Eulerian approach to investigate the effect of solid particles on the gas phase. In many cases, the local particle loading near the nozzle axis is moderate to high and a dense suspension of solid particles exists in the medium. Under this condition, characteristics of the continuous phase are highly dependent on and affected by the solid phase. This dependency is more magnified when the problem deals with a supersonic flow, since the solid phase can even change the flow regime (i.e., from supersonic to subsonic). The objective of this study is to address and resolve the effect of solid particles on the gas phase and its interaction with shocks, as well as the effect of the substrate on various flow field parameters.

## Methodology

As the Eulerian approach is based on the treatment of the dispersed phase as a continuum, therefore, two continua are present in the flow field. As a result, it is necessary to introduce a volume fraction, $\theta_m$, for each phase.

**Governing Equations.** The governing equations are the conservation of mass, momentum, and energy equations for a two-phase compressible flow at the continuum level [17].

$$\frac{\partial \rho_m}{\partial t} + \nabla \cdot \rho_m \mathbf{U}_m = 0 \tag{2}$$

$$\frac{\partial \rho_m \mathbf{U}_m}{\partial t} + \nabla \cdot \rho_m \mathbf{U}_m \mathbf{U}_m = -\theta_m \nabla p - \nabla \cdot (\alpha_m \rho_o \mathbf{U}'_m \mathbf{U}'_m) + \nabla \cdot (\alpha_m \tau_o) + \rho_m \mathbf{g} + \sum_l \theta_m \theta_l K_{ml} (\mathbf{U}_l - \mathbf{U}_m) \tag{3}$$

$$\frac{\partial \rho_m e_m}{\partial t} + \nabla \cdot \rho_m e_m \mathbf{U}_m = -p \nabla \cdot \mathbf{U}' + \nabla \cdot (\alpha_m \rho_o e_o \mathbf{U}'_m) + \frac{\alpha_m \tau_o : \varepsilon_o}{2} - \nabla \cdot \alpha_m q_o + \sum_l \theta_m \theta_l R_{ml} (T_l - T_m) \tag{4}$$

where the subscripts $m$, $l=1$ or 2 correspond to Phases 1 and 2, $\mathbf{U}$ and $\mathbf{U}'$ represent the velocity and the instantaneous velocity vectors, respectively. Since the flow is nonreactive, the mass exchange coefficient, which results from the conversion of material $m$ into or from the other material, is zero. The two phases also share the same pressure field. This is a valid assumption for two-phase flows of gas and solid particles. In order to distinguish between the phases, the phase indicator function, $\alpha$, is used.

$$\alpha_m(x,t) = \begin{cases} 1 & \text{if } x \text{ is in phase } m \text{ at time } t \\ 0 & \text{otherwise} \end{cases} \tag{5}$$

The expected volume fraction of phase $m$ is defined as [17,18] follows:

$$\theta_m = \langle \alpha_m \rangle \tag{6}$$

The nonequilibrium condition results in an equation for $\theta_m$ expressed as follows:

$$\frac{\partial \theta_m}{\partial t} + \nabla \cdot \theta_m \mathbf{U}_m + \nabla \cdot (\alpha_m \mathbf{U}'_m) = 0 \tag{7}$$

Equation (7) is constrained by the fact that for the equilibrium or nonequilibrium state, the following expression always holds:

$$1 - \sum_m \theta_m = 0 \tag{8}$$

For compressible flows, continuity, momentum, and energy equations are solved. These equations contain six unknowns, i.e., $\rho$, $p$, $e$, $T$, $u$, and $v$. It is obvious that two additional equations are required. In order to close the system of equations, relationships between the thermodynamic variables and the transport properties will be used. A perfect gas obeys the gas law $p=\rho R_g T$, where $R_g$ is the gas constant. For constant specific heats, the equations of state are:

$$p = (\gamma - 1)\rho e \tag{9}$$

and

$$T = \frac{(\gamma - 1)}{R_g} e \tag{10}$$

where $\gamma$ is the specific heat ratio for an ideal gas. Turbulence is modeled using the multiphase turbulence theory proposed by Kashiwa and VanderHeyden [19]. This model is applicable to a wide range of common multiphase flows including gas-solid, liquid-solid, and gas-liquid flows. In this method, using the exact averaged equations, a portion of the total energy decay rate is assigned to each phase, which results in a transport equation for energy decay rate associated with each phase. The model reduces to a standard $k$-$\varepsilon$ form in the limit of a single phase pure material.

The interphase momentum exchange between the two phases of gas and solid particles is due to the particles moving with a relative velocity to the gas flow. The drag force acting on each single spherical particle moving relative to the gas with a velocity $U_{\text{rel}}$ is

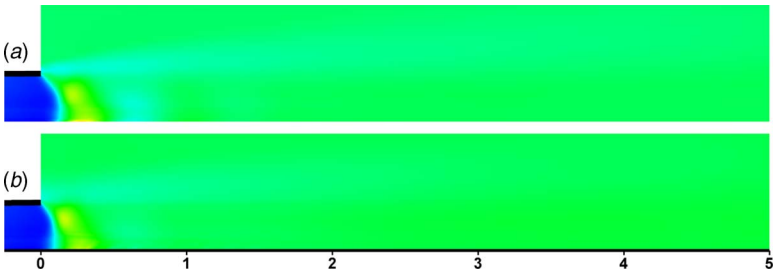


**Fig. 2 Pressure contours for two different grid resolutions of (*a*) 80×375 and (*b*) 120×800 at a loading of 0.1% (distances shown are from nozzle exit, cm)**

$$F = \frac{1}{2}\rho_c U_{\text{rel}}^2 C_D A \tag{11}$$

where $\rho_c$ is the density of the continuous phase, $C_D$ is the drag coefficient of each spherical particle, and $A$ is the cross sectional area of each particle. The volume fraction of the dispersed phase can be computed when there are $N$ particles of the same size (with a radius $r$) per unit volume.

$$\theta_d = (4/3)\pi r^3 N \tag{12}$$

As a result, the force acting on the dispersed phase per unit volume is:

$$\mathbf{f} = \rho_c |\mathbf{U}_{\text{rel}}| \mathbf{U}_{\text{rel}} C_D \theta_d (3/4r) \tag{13}$$

Equation (13) can be generalized for multifluids in the following form:

$$\mathbf{f}_{ml} = \sum_l \theta_m \theta_l K_{ml} (\mathbf{U}_l - \mathbf{U}_m) \tag{14}$$

where $K$ is the momentum exchange coefficient. For two-phase flows of gas and solid particles, the coefficient can be expressed as [17]:

$$K_{12} = K_{21} = (3/8)\frac{\rho_c}{\theta_c} C_D \frac{|\mathbf{U}_{\text{rel}}|}{r} \tag{15}$$

To accommodate the interactions between shocks and particles, a drag law proposed by Crowe [20] is used. This correlation covers a large range of particle Mach and Reynolds numbers ($0.1 < \text{Ma}_p < 2$ and $0.2 < \text{Re}_p < 10^4$). This range is sufficient for a typical CGDS process and will accommodate all the conditions encountered inside the flow field. The equation proposed by Crowe is:

$$C_D = (C_{D(\text{inc})} - 2) e^{-3.07\sqrt{\gamma}(\text{Ma}_p/\text{Re}_p) g(\text{Re}_p)} + \frac{h(\text{Ma}_p)}{\sqrt{\gamma}\text{Ma}_p} e^{-\text{Re}_p/2\text{Ma}_p} + 2 \tag{16}$$

where $C_{D(\text{inc})}$ is the drag coefficient for a sphere in incompressible flow, and $g(\text{Re}_p)$ and $h(\text{Ma}_p)$ are the devised functional relations.

$$\log_{10} g(\text{Re}_p) = 1.25[1 + \tanh(0.77 \log_{10} \text{Re}_p - 1.92)] \tag{17}$$

$$h(\text{Ma}_p) = \{2.3 + 1.7[T_p/T_g]^{1/2}\} - 2.3 \tanh(1.17 \log_{10} \text{Ma}_p) \tag{18}$$

The drag coefficient for the sphere in an incompressible gas is taken from a correlation by Clift et al. [21].

**Numerical Scheme and Discretization.** The two-phase flow of gas and particles is solved using a finite volume scheme with an implicit continuous-fluid Eulerian (ICE) method proposed by Kashiwa et al. [22]. Quadrilateral control volumes with fully cell-centered state vectors are employed and all the dependent variables and fluid properties are stored at the control volume center. A multiblock structured grid is used. One of the main issues in multiphase Eulerian methods is to satisfy the continuity of the dispersed phase. To overcome this problem, the selected control volumes should be in such a way that there are enough particles in each cell [22]. The computational grid inside of the nozzle consists of 30 radial and 1075 axial cells. Outside the nozzle, there are 80 radial and 375 axial cells. A grid dependency study is also performed to ensure the independence of the solution to the mesh size. Pressure contours and line plots for two different mesh resolutions of 80×375 and 120×800, with 2 $\mu$m particles injected at a loading of 15% (which is the highest loading studied in the present work), are shown in Figs. 2 and 3, respectively. The location and strength of the shocks agree to an acceptable extent in both cases.

**Geometry.** A schematic of the CGDS system modeled in this study is shown in Fig. 4. The nozzle has a circular cross section with an inlet of 10 mm. The converging section has a length of 50 mm and is attached to the throat section with a diameter of 4 mm and a length of 30 mm. It then expands to a diameter of 6 mm located at a distance of 97 mm from the throat end. The particle feeder is placed at the beginning of the diverging section and has an inner diameter of 0.6 mm. The substrate stand-off distance is 50 mm from the nozzle exit. In all the cases, the boundaries are extended in such a way that the independency of the solution to the computational domain is guaranteed. The orientation of the nozzle and substrate will allow having an axis of symmetry, which will result in a considerable reduction in the computational time.

**Boundary Conditions.** A schematic of the computational domain is shown in Fig. 5. There are two velocity inlets. Nitrogen is injected at a mass flow rate of 660 g/min with a density and a temperature of 2.8 kg/m$^3$ and 773 K, respectively. At this condition, the pressure at the inlet will be 0.62 MPa, which is the normal operating pressure of the nozzle. The particle feeder is located at the beginning of the diverging section of the nozzle and injects a mixture of gas and solid particles. At this point, gas is injected with an axial velocity of 530 m/s and a density and a temperature equal to 1.4 kg/m$^3$ and 600 K, respectively. This will ensure a smooth attachment of the gas injected at this point to the main flow and promotes the convergence. The coating powder used is aluminum, which has a density of 2719 kg/m$^3$, and is injected with an axial velocity of 60 m/s. Particle sizes of 2 $\mu$m, 5 $\mu$m, 10 $\mu$m, 20 $\mu$m, 40 $\mu$m, and 60 $\mu$m are used to study the effect of the particle size and number density. Particle mass flow rates for different cases are tabulated in Table 1.

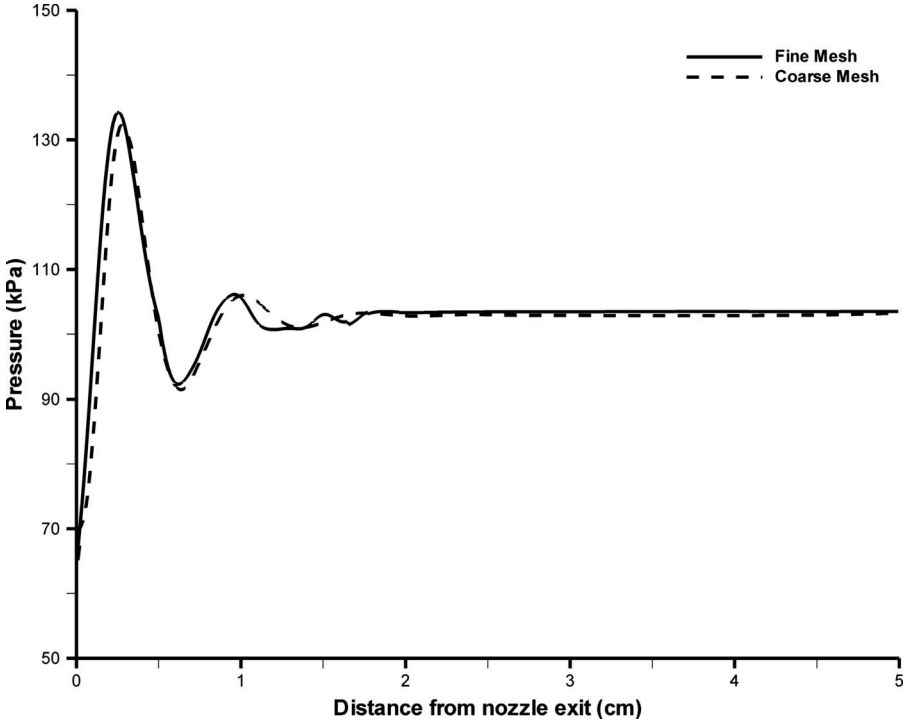


**Fig. 3 Grid dependency test for the two-phase analysis at a loading of 15% and mesh sizes of 80×375 and 120×800**

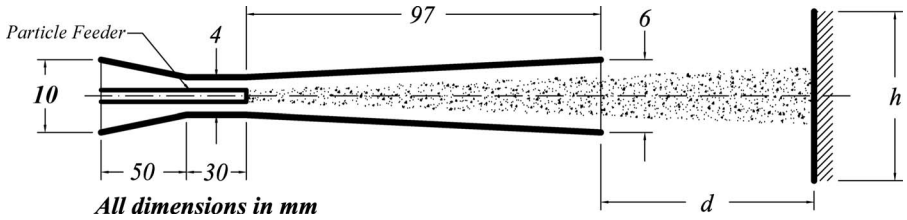


**Fig. 4 Schematic of the nozzle and substrate (Not to scale)**

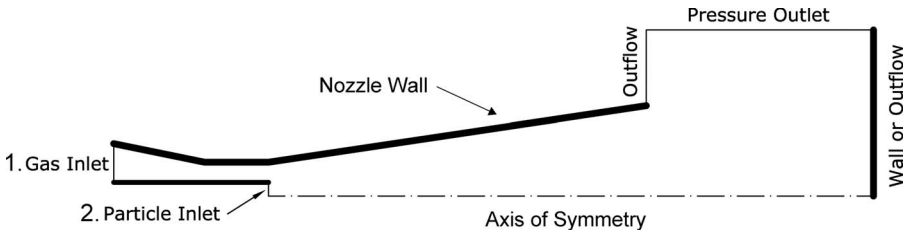


**Fig. 5 Nozzle geometry and boundary conditions (not to scale)**

**Table 1 Inlet mass flow rates**

| Inlet | Species | Mass flow rate (g/min) | Particles volume fraction | Loading by mass |
|---|---|---|---|---|
| 1 | Carrier gas | 650 | — | — |
| 2 | Carrier gas | 12.8 | — | — |
| | Particles (Case 1) | 0.66 | 0.00024 | 0.1% |
| | Particles (Case 2) | 6.69 | 0.0024 | 1.0% |
| | Particles (Case 3) | 116.96 | 0.042 | 15.0% |

## Results and Discussions

Results for the single phase analysis are shown in Fig. 6. Mach number, pressure, and temperature contours are presented in this figure without introducing the particles. The flow regime variations can be extracted from Mach number contours. The flow accelerates in the converging section of the nozzle. The Mach number reaches unity at the throat, and it further accelerates in the diverging section of the nozzle. At the exit of the nozzle, the Mach number is around 2.3 for the free-jet case without particle injection. At this point, the pressure is below the ambient pressure, and an overexpanded flow produces shock diamonds, which are a series of oblique shocks and expansion fans (i.e., Prandtl–Meyer fans).

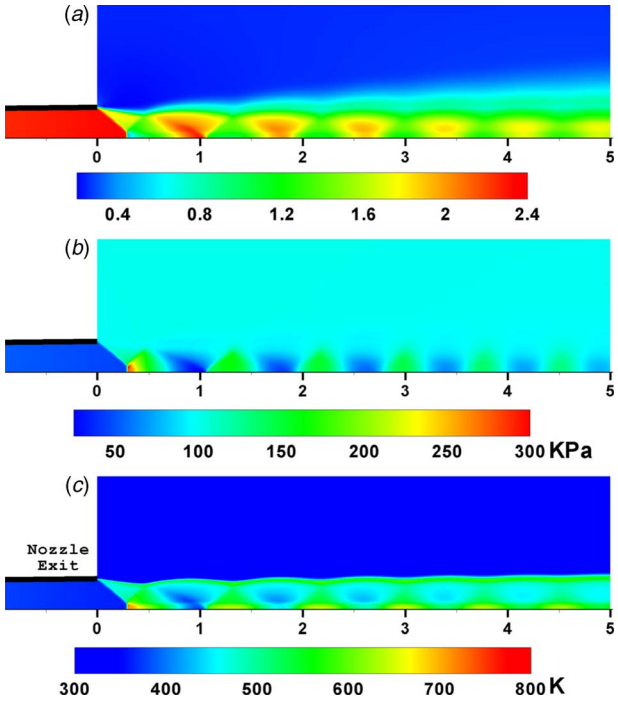


**Fig. 6 Contours of the flow field variables for the free-jet case without particle injection. (*a*) Mach number contours, (*b*) pressure contours (kPa), and (*c*) Temperature contours (K) (distances shown are from nozzle exit, cm).**

It can be observed that as the gas passes through the diamond shocks, its kinetic energy dissipates gradually until the pressure reaches the surrounding pressure. Pressure adjustment starts with an oblique shock. This shock reflects from the plane of symmetry as a Mach reflection. As the gas goes through this reflected shock, it is compressed to a pressure higher than that of the ambient. This compression will result in a sudden temperature rise in the gas flow, which is quite visible in Fig. 6(*c*). Plots of pressure, temperature, and Mach number at the nozzle centerline are shown in Fig. 7. The gas phase parameter variations mentioned above can be observed in this plot.

Results for the free-jet case with 2 $\mu$m particles injected are presented in Fig. 8. For a better comparison, Mach number contours for the free-jet case without injection are shown as well. The characteristics of the gas phase in the two-phase flow are completely different from those of the single phase due to the dense particulate flow injected from the particle feeder. Shock diamonds tend to move to the dilute area away from the centerline. As can be seen in this figure, unlike the single phase flow, the gas phase has the potential to become subsonic in the regions near the centerline when the loading is high. As most of the particles travel in this region, having a good knowledge of the gas phase near the centerline is vital for the dispersed phase behavior prediction. The location and strength of the shock diamonds also change because of the presence of the particles. The variation in the strength strongly depends on the loading of the dispersed phase. If the loading is high enough, shock diamonds can even die away, as can be seen in Fig. 8(*d*). The loading in this case is too high and the value is not practical. It is just presented to show the effect of high loading on the shocks.

Variations in the volume fraction of the dispersed phase be-

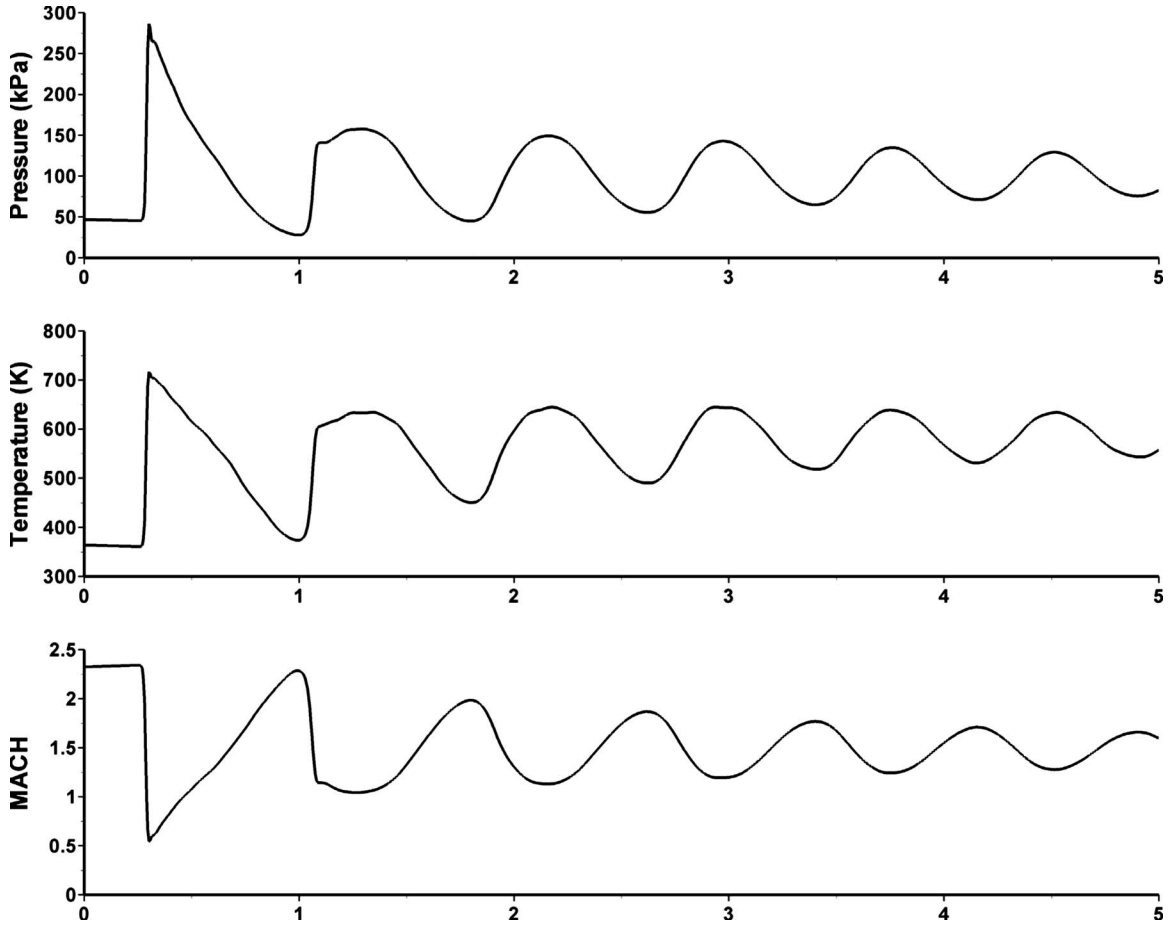


**Fig. 7 Pressure, temperature, and Mach number plots (distances shown are from nozzle exit, cm)**

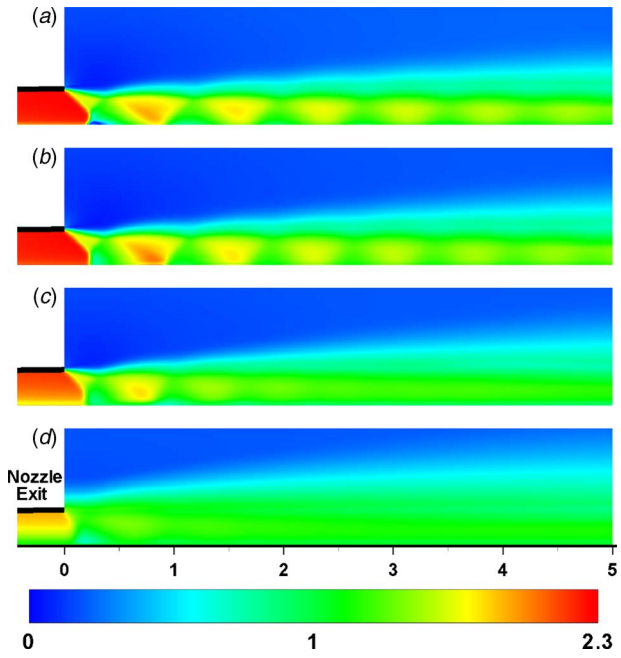


**Fig. 8 Mach number contours for the free-jet case with 2 $\mu$m particles injected at loadings of (*a*)=0, (*b*)=0.1%, (*c*)=1.0%, and (*d*)=15% (distances shown are from nozzle exit, cm)**

tween the nozzle exit and the domain exit is shown in Fig. 9. It can be seen that the second phase is affected by the gas phase. In the regions where the gas is accelerating, lower volume fractions can be expected and vice versa. On the other hand, as the particle loading increases, the effect of shocks on the second phase will be reduced. This is the result of a large reduction in shock strength by increasing the volume fraction. This trend is demonstrated in Fig. 9. For higher volume fractions, particle acceleration is smoother, while for lower values, more changes in the volume fraction are observed.

The prediction of the flow regime in a highly compressible flow such as the flow field in a cold spray system plays an important role in calculating the drag force on particles. In highly compressible flows, the relative velocity between the particles and the gas phase can reach values higher than the local sound speed. In this case, the compression shocks forming in front of the particles can accelerate the particles to a higher velocity, which is known as wave drag. In fact, for this flow regime the drag coefficient is a strong function of the particle Mach number, $M_r$ [23]:

$$M_r = \frac{|U_g - U_p|}{\sqrt{\gamma R_g T}} \tag{19}$$

Because of the subsonic flow regime near the centerline during a moderate or high particle loading, the particle Mach number is essentially smaller than 1. Therefore, the wave drag will be ineffective in this case and the dominant drag force acting on each individual particle is the form drag. This will result in a significant decrease in the particle velocity, and as a result, coating deposition efficiency reduces.

Placing a substrate in front of the free-jet flow coming out of the nozzle will result in a pressure rise on the substrate. Static pressure versus the distance from the nozzle exit for a flat substrate located at different stand-off distances is shown in Fig. 10. In the case of a subsonic flow, the peak pressure rise will decrease by increasing the substrate stand-off distance from the nozzle exit. However, for a supersonic flow with shocks, due to the compression and expansion waves formed outside the nozzle, the peak

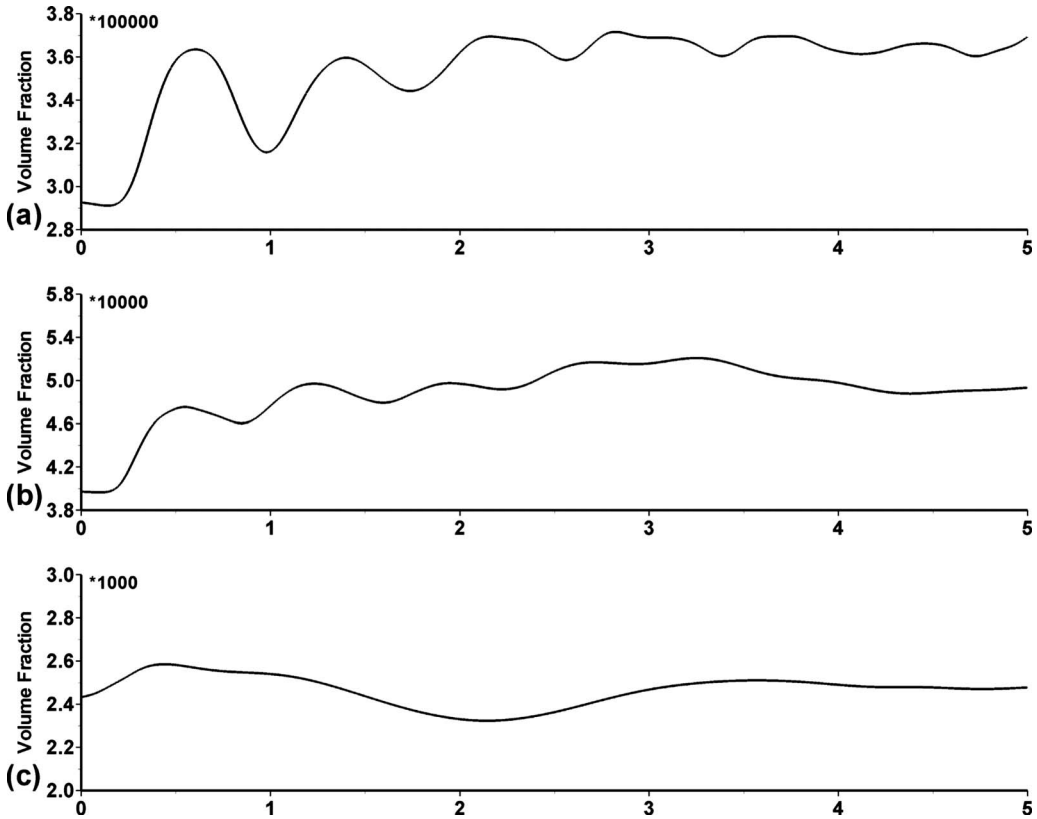


**Fig. 9 Axial volume fraction variations for 2 $\mu$m particles injected at loadings of (*a*)=0.1%, (*b*)=1.0%, and (*c*)=15% (distances are from nozzle exit, cm)**

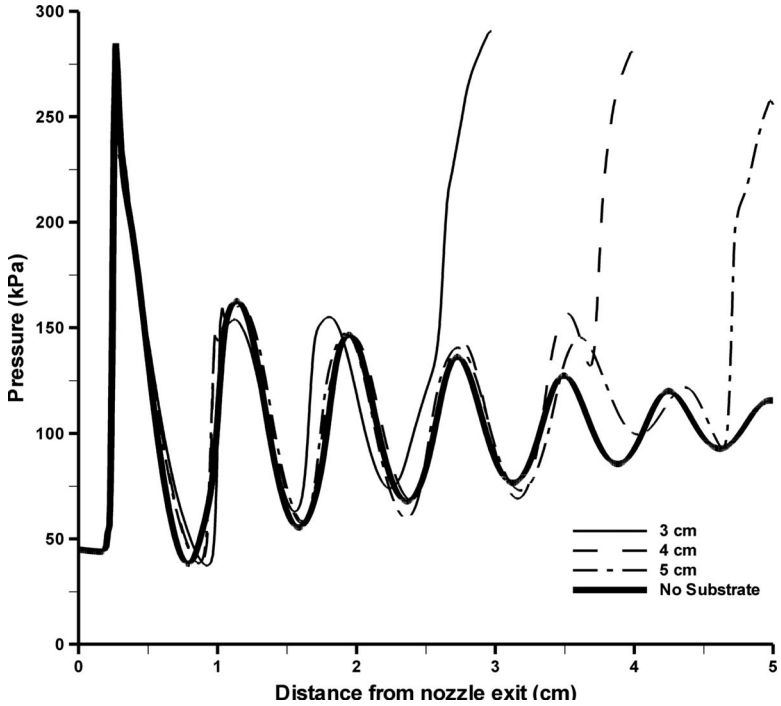


**Fig. 10 Pressure variations on a flat substrate for different stand-off distance from nozzle exit**

pressure alternates by changing the location of the substrate. Pressure rise starts at a small distance from the substrate where the flow starts to feel the presence of the plate. The value of the maximum pressure rise depends on the location where the pressure starts to increase, i.e., where the flow starts to feel the presence of the substrate. A high stagnation pressure region on the substrate decelerates particles before hitting the substrate and results in lower deposition efficiency; hence, having the minimum pressure buildup on the substrate is strongly desirable and will result in a weaker bow shock and consequently higher particle impact velocity, lower dispersion, and higher deposition efficiency. The minimum value can be reached by placing the substrate at a distance, which results in a pressure rise starting in a pressure valley [14].

Pressure contours for the case with a substrate located at a stand-off distance of 5 cm from the nozzle exit and different particle loadings are shown in Fig. 11. Gas phase pressure distribution along the centerline for different loadings for the case with the substrate located at 5 cm from the nozzle exit is shown in Fig. 12. It is clear that as the loading increases, the location and strength of the shocks change. For the case with a loading of 15%, the pressure at the nozzle exit is higher compared to the other cases, which indicates that high loading can also affect the flow regime inside the nozzle.

The particle axial velocity for the case with the substrate located at 5 cm and two different particle sizes of 2 $\mu$m and 60 $\mu$m and various loadings are shown in Fig. 13. For the case of 2 $\mu$m particles, the effect of diamond shocks and the bow shock are quite visible in the axial velocity plots. It is also noticeable that as the loading increases, the maximum velocity and the effect of the shocks decrease. 2 $\mu$m particles will experience an abrupt reduction in the velocity before hitting the substrate, which is due to the bow shock formed on the substrate. On the other hand, 60 $\mu$m particles are not affected by the shocks and accelerate smoothly as they exit the nozzle; however, the effect of the loading on the impact velocity is still obvious.

The impact velocity versus particle size for different loading conditions is presented in Fig. 14. As expected, the impact velocity reduces as the particle size and loading increase. However, this trend is reversed for 2 $\mu$m particles. This phenomenon can be analyzed as follows. For large particles (>10 $\mu$m), the effect of the bow shock on particle velocity is negligible and the impact velocity is mainly a function of loading. Referring to Fig. 14, it can be seen that as the loading increases, the impact velocity decreases. However, the impact velocity for small particles is

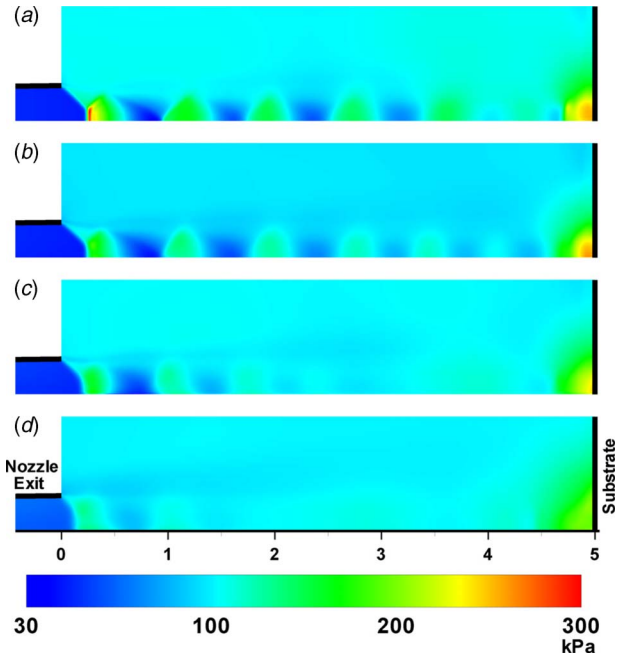


**Fig. 11 Pressure (kPa) contours for the case with a substrate located at 5 cm from nozzle exit with particle loadings of (*a*) =0, (*b*)=0.1%, (*c*)=1.0%, and (*d*)=15% (distances are from nozzle exit, cm)**

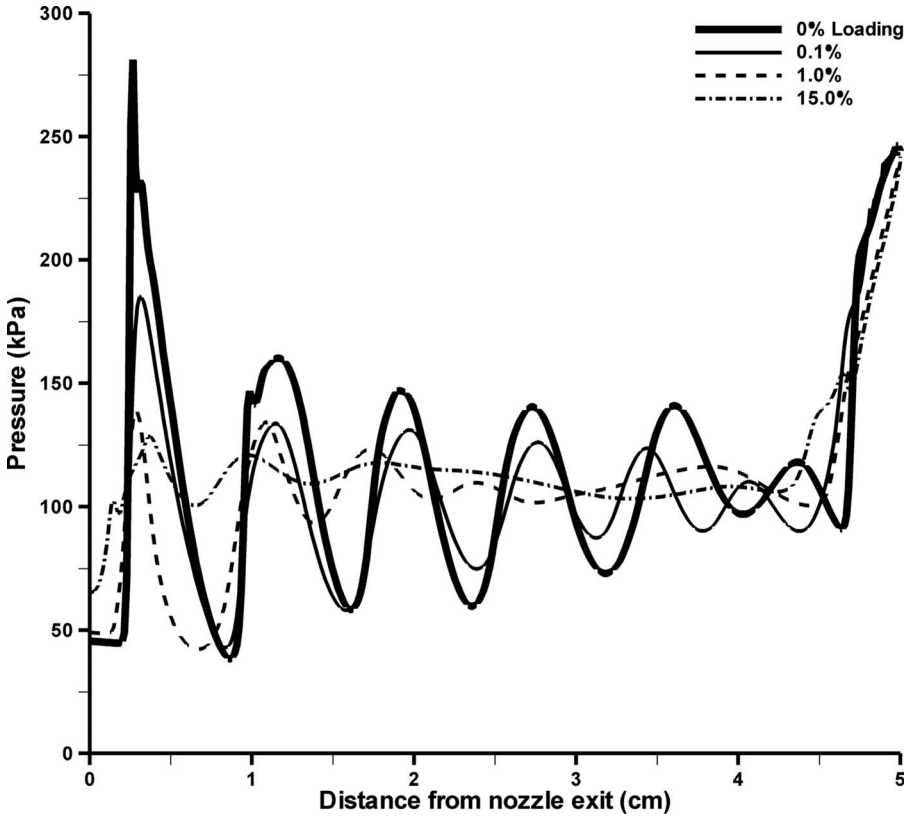


**Fig. 12 Pressure distribution on centerline for the case with a substrate located at 5 cm from nozzle exit and with different loadings**

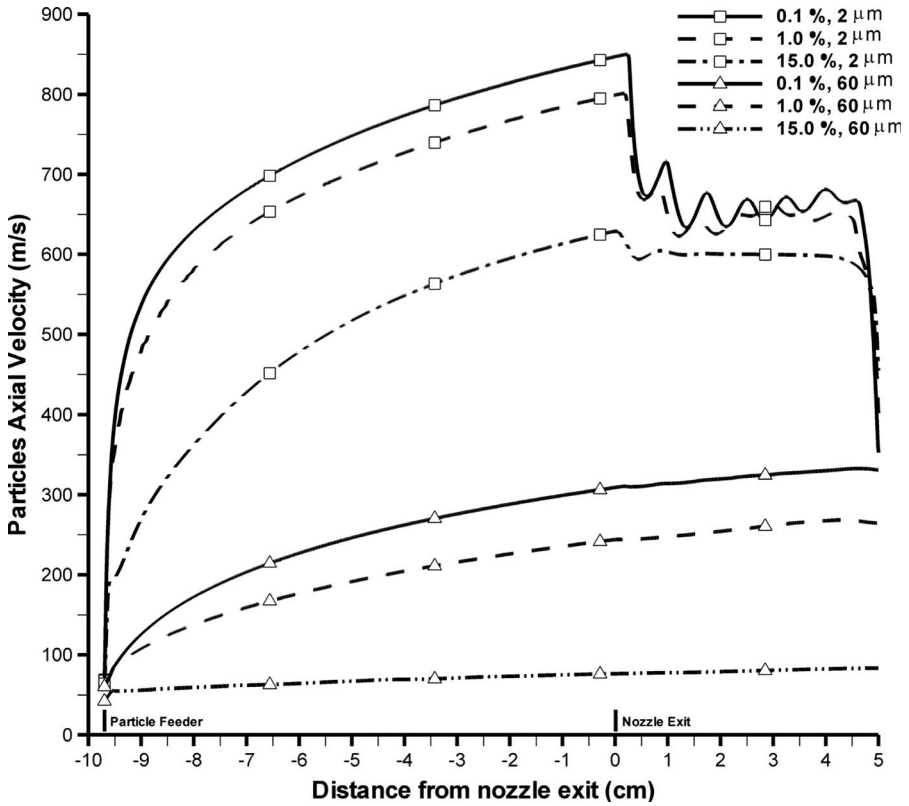


**Fig. 13 2 $\mu$m and 60 $\mu$m particle axial velocities for the case with a substrate located at 5 cm from the nozzle exit and with different loadings**

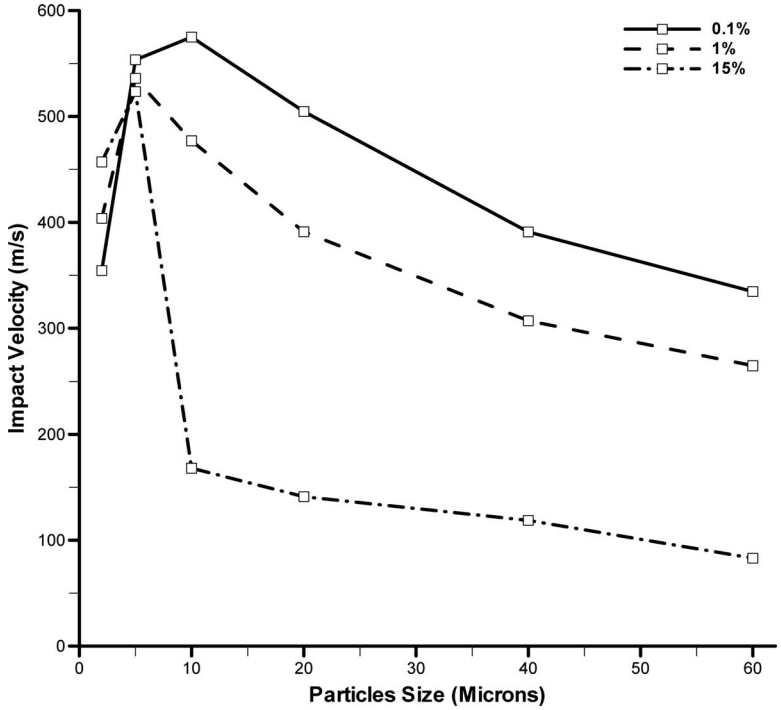


**Fig. 14 Particle impact velocity on a substrate at a stand-off distance of 5 cm for various loadings**

highly dependent on the strength of the bow shock. Higher loadings will result in a gas flow with less momentum striking on the substrate and subsequently a lower stagnation pressure will form on the substrate. As a result, when the coating particles are small (i.e., 2 $\mu$m and 5 $\mu$m), a higher loading will help the particles to pierce through a weaker bow shock and have a higher impact velocity.

The volume fraction of the particulate phase at the nozzle exit is also presented in Fig. 15. For low to moderate loadings, a bimodal distribution can be observed, while for higher loadings, the volume fraction distribution is trimodal. This trend can be the resultant of the imposed boundary conditions at the injection point. Since the particulate phase is fed into the nozzle with a lower velocity compared to the gas phase (60–530 m/s), a high

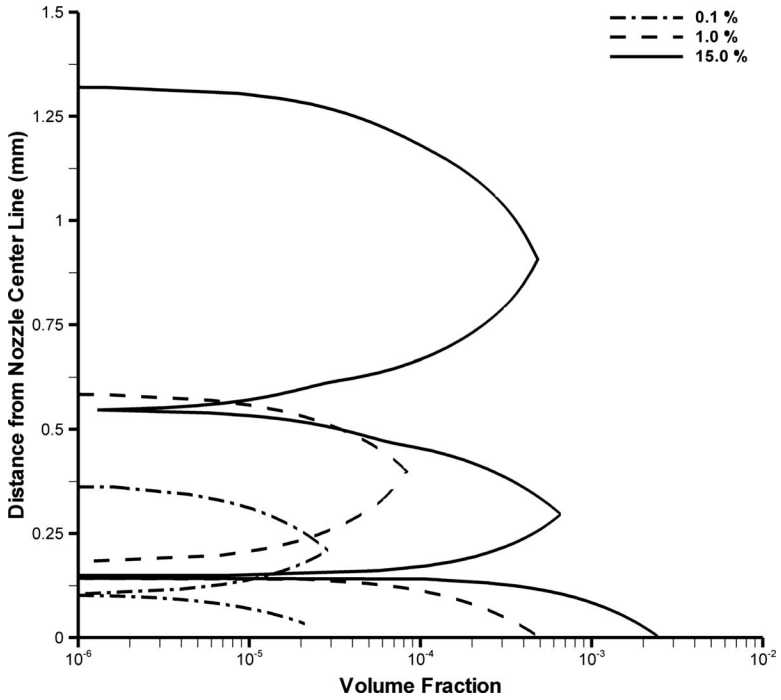


**Fig. 15 Volume fractions of 2 $\mu$m particles with different loadings at the nozzle exit**

pressure region is formed in front of the powder injector, which is due to the momentum transfer from the gas to the particles. This pressure difference tends to disperse and to deviate the particles from the centerline. In addition, this sudden change in the velocity will produce a circulating region, which further promotes the dispersion. Such a behavior has been observed experimentally in the HVOF process for a similar exit Mach number [24].

## Conclusions

In this study, a dense suspension of solid particles in a highly compressible gas flow was analyzed using a fully Eulerian approach as well as the effect of the particle size and the presence of a substrate. Simulations were performed for the cases with both dilute and high powder loadings near the centerline to examine the effect of the dispersed phase on the continuous phase and to inspect the interactions of the particles and diamond shocks. The simulation shows large variations in the flow regime where most of the particles exist. The location and strength of the diamond shocks are a strong function of the particle loading. For loadings higher than 20%, all of the shock diamonds die away.

It is found that the stand-off distance of the substrate has a significant effect on the gas phase near the particle deposition area. This is mainly due to the nature of the supersonic flow, which generates compression and expansion waves. The interactions between the shock diamonds and the bow shock formed on the substrate should be examined carefully in order to find the optimum stand-off distance for the highest deposition efficiency, i.e., substrate should be placed at a location, which results in a pressure rise that begins in a pressure valley. With this condition satisfied, the maximum stagnation pressure on the substrate will be minimized, which in turn results in higher impact velocity and less dispersion and consequently higher deposition efficiency.

The effect of the particle size and number density is also studied. It is shown that as the particle size and loading increase, the impact velocity decreases due to the reduction in the gas speed, which is the result of higher momentum transfer between the gas and solid phases. However, this trend is reversed for very small particles as higher loading helps them to penetrate into a weaker bow shock formed on the substrate.

A Lagrangian particle tracking approach is not capable of capturing the phenomenon discussed above. In a fully Eulerian scheme, similar to a two-way Lagrangian method, the two phases are coupled through momentum and energy exchanges, which are expressed in the form of source terms in the governing equations. However, there is an additional two-phase coupling effect in the fully Eulerian approach, the effect of volume fraction of each phase in the conservation laws. Volume fraction variations significantly change the average density of each phase over each computational cell. In this way, the interactions between the two phases are implicitly provided in the convective terms. Therefore, a fully Eulerian formulation can produce more realistic results compared to the Lagrangian methods when a dense particulate flow is under study [16].

## Acknowledgment

The authors would like to thank Los Alamos National Laboratory for providing the use of CFDLIB code for this study. This work was supported by the National Research Council Canada-Industrial Materials Institute (NRC-IMI), Boucherville, QC, Canada.

## Nomenclature

$A$ = cross sectional area of the particle, $m^2$
$C_D$ = drag coefficient
$e$ = internal energy, J
$f$ = force acting on dispersed phase per unit volume, $N/m^3$
$F$ = force acting on a single particle, N
$g$ = gravitational acceleration, $m/s^2$
$K$ = momentum exchange coefficient
$p$ = pressure, Pa
$R$ = energy exchange coefficient
$R_g$ = specific gas constant, J/kg K
$t$ = time, s
$T$ = temperature, K
$U$ = velocity vector, m/s

### Greek Symbols

$\alpha$ = phase indicator
$\gamma$ = specific heat ratio
$\varepsilon$ = rate of stress tensor
$\theta$ = expected volume fraction
$\rho$ = density, $kg/m^3$
$\tau$ = stress tensor

### Subscripts

$c$ = continuous phase
$d$ = dispersed phase
$o$ = pure material
$m, l = 1, 2$ = Phase 1 and Phase 2, respectively

## References

[1] Alkhimov, A. P., Kosareve, V. F., and Papyrin, A. N., 1990, "A Method of Cold Gas Dynamic Spray Deposition," Dokl. Akad. Nauk SSSR, **315**(5), pp 1062–1065.
[2] Alkhimov, A. P., Papyrin, A. N., Kosarev, V. F., Nesterovich, N. I., and Shushapanov, M. M., 1994, "Gas Dynamic Spray Method for Applying a Coating," U.S. Patent, 5,302,414.
[3] Alkhimov, A. P., Papyrin, A. N., Kosarev, V. F., Nesterovich, N. I., and Shushapanov, M. M., 1995, "Method and Device for Coating," European Patent 0 484 533 B1.
[4] Karimi, M., Fartaj, A., Rankin, G. W., Vanderzwet, D., Villafuerte, J., and Birtch, W., 2006, "Numerical Simulation of the Cold Gas Dynamic Spray Process," *Building on 100 Years of Success: Proceedings of the 2006 International Thermal Spray Conference*, B. R. Marple, M. M. Hyland, Y. C. Lau, R. S. Lima, and J. Voyer, eds., ASM International, Seattle, WA.
[5] Stoltenhoff, T., and Kreye, H., 2000, "Cold Spraying—From Thermal Spraying to High Kinetic Energy Spraying," *Fifth HVOF Colloquium Proceedings*, GTS E. V., Erding, Germany.
[6] Power, G. D., Smith, E. B., Barber, T. J., and Chiappetta, L. M., 1991, "Analysis of a Combustion (HVOF) Spray Deposition Gun," Report No. 91-8. United Technologies Research Center.
[7] Smith, E. B., Power, G. D., Barber, T. J., and Chiappetta, L. M., 1992, "Application of Computational Fluid Dynamics to the HVOF Thermal Spray Gun," *Thermal Spray: International Advances in Coating Technology*, C. C. Berndt, ed., ASM International, pp. 805–810.
[8] Oberkampf, W. L., and Talpallikar, M., 1996, "Analysis of a High Velocity Oxy-Fuel (HVOF) Thermal Spray Torch, Part 1: Numerical Formulation," J. Therm. Spray Technol., **5**(1), pp. 53–61.
[9] Oberkampf, W. L., and Talpallikar, M., 1996, "Analysis of a High Velocity Oxy-Fuel (HVOF) Thermal Spray Torch, Part 2: Numerical Formulation," J. Therm. Spray Technol., **5**(1), pp. 62–81.
[10] Yang, X., and Eidelman, S., 1996, "Numerical Analysis of a High Velocity Oxy-Fuel Thermal Spray System," J. Therm. Spray Technol., **5**(2), pp. 175–184.
[11] Hassan, B., Lopez, A. R., and Oberkampf, W. L., 1998, "Computational Analysis of a Three-Dimensional High Velocity Oxygen Fuel (HVOF) Thermal Spray Torch," J. Therm. Spray Technol., **7**(1), pp. 71–77.
[12] Dolatabadi, A., Mostaghimi, J., and Pershin, V., 2002, "Effect of a Cylindrical Shroud on Particle Conditions in High Velocity Oxy-Fuel Spray Process," Sci. Technol. Adv. Mater., **3**, pp. 245–255.
[13] Dolatabadi, A., Mostaghimi, J., and Ivanovic, M., 2001, "Modeling All Speed Particle Laden Flows Using a Fully Eulerian Approach," *Proceedings of the ninth Annual Conference of the CFD Society of Canada*, Waterloo, Canada, pp. 412–417.
[14] Samareh, B., and Dolatabadi, A., 2007, "A Three-Dimensional Analysis of the Cold Spray Process: Effect of Substrate Location and Shape," J. Therm. Spray Technol., **16**(5), pp. 634–642.
[15] Elghobashi, S., 1994, "On Predicting Particle-Laden Turbulent Flows," Appl. Sci. Res., **52**(4), pp. 309–329.
[16] Dolatabadi, A., Mostaghimi, J., and Pershin, V., 2004, "Modeling Dense Suspension of Solid Particles in Highly Compressible Flows," Int. J. Comput. Fluid Dyn., **18**(2), pp. 125–131.
[17] Kashiwa, B. A., and Rauenzahn, R. M., 1994, "A Multi-Material Formulism," Los Alamos National Laboratory, Technical Report No. LA-UR-94-771.
[18] Comer, J. K., 1998, "Computational Two-Phase Flow Analysis and Applications to Gas-Liquid and Gas-Solid Flows," Ph.D. thesis, North Carolina State University, Raleigh.

[19] Kashiwa, B. A., and VanderHeyden, W. B., 2000, "Toward a General Theory for Multiphase Turbulence, Part I: Development and Gauging of the Model Equations," Los Alamos National Laboratory Report No. LA-13773-MS.
[20] Crowe, C. T., 1967, "Drag Coefficient on Particles in a Rocket Nozzle," AIAA J., **5**(5), pp. 1021–1022.
[21] Clift, R., Grace, J. R., and Weber, M. E., 1978, *Bubbles, Drops and Particles*, Academic, New York.
[22] Kashiwa, B. A., Padial, N. T., Rauenzahn, R. M., and VanderHeyden, W. B., 1994, *A Cell-Centered ICE Method for Multiphase Flow Simulations*, ASME, *New York*, p. 185.
[23] Crowe, C. T., Sommerfeld, M., and Tsuji, Y., 1998, *Multiphase Flows With Droplets and Particles*, CRC, Boca Raton, FL.
[24] Dolatabadi, A., Pershin, V., and Mostaghimi, J., 2005, "New Attachment for Controlling Gas Flow in the HVOF Process," J. Therm. Spray Technol., **14**(1), pp. 91–99.

# Soret Effect for a Ternary Mixture in Porous Cavity: Modeling With Variable Diffusion Coefficients and Viscosity

**T. J. Jaber**

**Y. Yan**

**M. Z. Saghir**[1]
e-mail: zsaghir@ryerson.ca

Department of Mechanical and Industrial Engineering,
Ryerson University,
350 Victoria Street,
Toronto, ON, M5B 2K3, Canada

*A porous cavity filled with methane (C1), n-butane (nC4), and dodecane (C12) at a pressure of 35.0 MPa is used to investigate numerically the flow interaction due to the presence of thermodiffusion and buoyancy forces. A lateral heating condition is applied with the left wall maintained at 10°C and the right wall at 50°C. The molecular diffusion and thermal diffusion coefficients are functions of temperature, concentration, and viscosity of mixture components. It has been found that for permeability below 200 md the thermodiffusion is dominant; and above this level, buoyancy convection becomes the dominant mechanism. The variation of viscosity plays an important role on the molecular and thermal diffusion.* [DOI: 10.1115/1.2960492]

*Keywords: thermodiffusion, Soret effect, convection, separation ratio, permeability, Peng–Robinson EOS*

## 1 Introduction

Thermodiffusion, also known as thermal diffusion, or the Ludwig–Soret effect [1,2], refers to the phenomenon of component separation in a convection free mixture under a temperature gradient. The thermodiffusion process can occur in both liquid and gaseous mixtures. Studies based on the thermodynamics of irreversible processes have shown that thermodiffusion in liquids, along with the effect of natural convection, can, in fact, greatly influence the composition distribution in hydrocarbon reservoirs.

The Ludwig–Soret effect is commonly represented by the thermal diffusion coefficient ($D^T$), especially for multicomponent mixtures. Theoretical study of this effect is usually carried out based on nonequilibrium thermodynamics [3]. Recently, a large amount of research has been done on thermodiffusion in porous medium (Leahy-Dios et al. [4], Haugen and Firoozabadi [5], and Platten [6]). It is known that convection has a significant influence on the accuracy of Soret measurements. Utilization of porous media may help in reducing the convection-induced distortion. Costeseque et al. [7] conducted diffusion experiments in both free and porous medium Soret cells. They reported that the molecular diffusion and thermal diffusion coefficients in porous media were related to those ones in clear fluid via the tortuosity. However, the Soret coefficient (the ratio of molecular diffusion coefficient to thermal diffusion coefficient for binary mixtures) is identical for both configurations.

Riley and Firoozabadi [8] presented a model to investigate the effects of natural convection and diffusion (thermal, pressure, and Fickian) on a single-phase binary mixture of methane and *n*-butane in a horizontal cross-sectional reservoir in the presence of a prescribed linear temperature field. The compositional distribution in the reservoir under both horizontal and lateral heating conditions was carefully examined. It was found that increasing the permeability increased the horizontal compositional variation. A local maximum and/or minimum value exists in the compositional gradient as a function of the permeability.

Delware et al. [9] studied these phenomena for a binary system in a square cavity. The energy equation is solved simultaneously allowing observing temperature variation in the model. Various thermal boundary conditions are examined. Their results revealed that in the lateral heating case the Soret effect is found to be weak, whereas in the bottom heating case the Soret effect is more pronounced.

Firoozabadi et al. [10] developed a model for thermal diffusion factors in multicomponent nonideal mixtures. This model was based on the thermodynamics of irreversible processes where the effects of both equilibrium and nonequilibrium properties are incorporated. The equilibrium properties, such as partial internal energies and fugacities, were estimated using the volume-translated Peng–Robinson equation of state (EOS). On the other hand, the nonequilibrium properties, such as viscosity, were accounted for by incorporating the energy of viscous flow. This model has been used by Jiang et al. [11] to examine the thermodiffusion convection of a water-ethanol mixture in porous medium under high pressure. Pan et al. [12] further compared different multicomponent thermodiffusion models and concluded that the model of Firoozabadi et al. was the best in general.

In this paper, the thermodiffusion convection of a ternary mixture of methane, *n*-butane, and Dodecane (C1–*n*C4–C12) in a porous medium cavity will be studied. Section 2 presents the model description. The differential equations used to solve the problem are explained in Secs. 3 and 4. The solution technique is explained in Sec. 5 and the results and discussion are shown in Sec. 6.

## 2 Model Description

The porous cavity has a horizontal length of 32 mm, a width of 10 mm, and a vertical height of 10 mm, as shown in Fig. 1. The porous material is $Al_2O_3$ power, and the cavity is saturated with the ternary fluid mixture. Physical properties of the mixture are given in Table 1. The left wall of the cavity is kept at a temperature of $T_c=10°C$ and the right wall at $T_h=50°C$. Due to the Soret effect, component separation will happen in the porous cavity

[1]Corresponding author.

Contributed by the Fluids Engineering Division of ASME for publication in the JOURNAL OF FLUIDS ENGINEERING. Manuscript received May 31, 2007; final manuscript received June 20, 2008; published online August 1, 2008. Assoc. Editor: Dimitris Drikakis. Paper presented at the 2006 ASME International Mechanical Engineering Congress (IMECE2006), Chicago, IL, November 5–10, 2006.

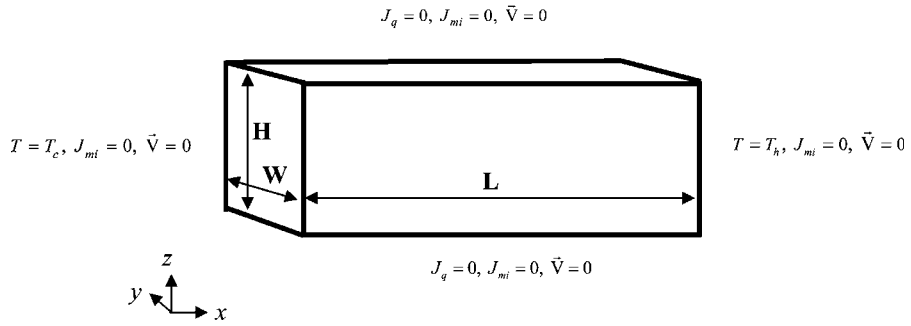


**Fig. 1 Schematic of the horizontal porous cavity and boundary conditions**

even under the gravity condition; and the system will gradually reach the steady state. The pressure in the cavity is maintained at 35.0 MPa.

## 3 Governing Equations and Boundary Conditions

The mass continuity equation is shown as

$$\frac{\partial \rho_m}{\partial t} + \nabla \cdot (\rho_m \mathbf{V}) = 0 \tag{1}$$

where $\rho_m$ is the molar density of the mixture and $\mathbf{V} = u\mathbf{i} + v\mathbf{j} + w\mathbf{k}$ is the average velocity vector of the mixture, $u$, $v$, and $w$ are the velocity components of $x$, $y$, and $z$ directions, respectively. For multicomponent mixture, the continuity equation of component $i$ is given as

$$\frac{\partial(\rho_m x_i)}{\partial t} + \nabla \cdot (\rho_m x_i \mathbf{V}) = -\nabla \cdot \mathbf{J}_{mi}, \quad i = 1,2, \ldots, n-1 \tag{2}$$

where $\mathbf{J}_{mi}$ is the molar diffusion flux of the $i$th component and $x_i$ is the mole fraction of the component $i$. The mole flux is subjected to linear relationship to driving forces of temperature and concentration gradient and it can be expressed by

$$\{\mathbf{J}_{mi}\} = -\rho_m \left( \sum_{j=1}^{n-1} [D^*_{Mij}] \nabla X + \{D^*_{Ti}\} \nabla T \right) \tag{3}$$

where $T$ is the temperature. For binary mixtures, $\nabla X = \nabla x_1$ and $\mathbf{J}_{mi} = \mathbf{J}_{m1}$, and for ternary mixtures, $\nabla X = \begin{pmatrix} \nabla x_1 \\ \nabla x_2 \end{pmatrix}$ and $\mathbf{J}_{mi} = \begin{pmatrix} \mathbf{J}_{m1} \\ \mathbf{J}_{m2} \end{pmatrix}$. $D^*_M$ and $D^*_T$ are the molecular diffusion and thermal diffusion coefficients of the fluid mixture in the $Al_2O_3$ porous medium, respectively, which are related to molecular diffusion coefficient and thermal diffusion coefficient in free liquid as

$$[D^*_{Mij}] = \frac{1}{\tau^2_M}[D^M_{ij}], \quad \{D^*_{Ti}\} = \frac{1}{\tau^2_T}\{D^T_i\} \tag{4}$$

where $D^M$ and $D^T$ are the molecular and thermal diffusion coefficients, which are functions of the temperature and composition of the fluid mixture. $\tau_M$ and $\tau_T$ are tortuosities for molecular diffusion and thermal diffusion coefficients in the cavity, respectively.

**Table 1 Physical properties of the mixture and porous material**

| Name | Value | Unit |
|---|---|---|
| $Al_2O_3$ density | 3983.6 | $kg/m^3$ |
| $Al_2O_3$ heat capacity | 786.2745 | J/kg K |
| $Al_2O_3$ thermal conductivity | 43 | W/mol K |
| $Al_2O_3$ porosity | 0.4 | |
| $Al_2O_3$ porous medium tortuosity | 1.3 | |
| Heat capacity of mixture | 2355.4 | J/kg K |
| Thermal conductivity of mixture | 0.1158 | W/m K |

Based on the findings of Costeseque et al. [7], the molecular diffusion and thermal diffusion tortuosities were set equal to the tortuosity of the porous media. The porous matrix is assumed homogeneous and isotropic. Therefore the Darcy equation is applied:

$$\mathbf{V} = -\frac{\kappa}{\phi \eta_m}(\nabla P - \rho \mathbf{g}) \tag{5}$$

where $\kappa$ and $\phi$ are the permeability and the porosity? of porous media, respectively, $\eta_m$ is the dynamic viscosity of the fluid mixture, $\rho$ is the mass density of the fluid mixture, and $\mathbf{g}$ is the gravitational acceleration vector. By substituting the Darcy relation, Eq. (5), into the mass conservation equation, Eq. (1), the pressure can be solved from the obtained differential equation, which leads to the following equation for pressure:

$$\frac{\partial(\rho_m)}{\partial t} - \frac{\kappa}{\phi \eta_m}\frac{\partial}{\partial x}\left(\rho_m\left(\frac{\partial P}{\partial x} + \rho g_x\right)\right) - \frac{\kappa}{\phi \eta_m}\frac{\partial}{\partial y}\left(\rho_m\left(\frac{\partial P}{\partial y} + \rho g_y\right)\right) - \frac{\kappa}{\phi \eta_m}\frac{\partial}{\partial z}\left(\rho_m\left(\frac{\partial P}{\partial z} + \rho g_z\right)\right) = 0 \tag{6}$$

The thermal energy conservation equation is expressed as follows:

$$\frac{\partial(\rho C_p)_e T}{\partial t} + \phi \mathbf{V} \cdot \nabla((\rho C_p)_f T) = k_e \nabla^2 T \tag{7}$$

where $(\rho C_p)_e$ is the effective volumetric heat capacity of the system and $k_e$ is the effective thermal conductivity of the system. These effective physical parameters are related to the fluid properties and the solid matrix properties as follows:

$$(\rho C_p)_e = \phi(\rho C_p)_f + (1-\phi)(\rho C_p)_p \tag{8}$$

$$k_e = \phi k_f + (1-\phi)k_p \tag{9}$$

where $(\rho C_p)_f$ is the fluid volumetric heat capacity, $(\rho C_p)_p$ is the matrix volumetric heat capacity, $k_f$ is the fluid thermal conductivity, and $k_p$ is the matrix or porous thermal conductivity. The boundary conditions in this model are (1) zero mass flux through all walls, (2) no-slip walls, and (3) lateral heating condition on two side walls and other walls are adiabatic. Figure 1 depicts the boundary conditions.

## 4 Molecular Diffusion and Thermal Diffusion Model

The thermal diffusion can be described through the theory of nonequilibrium thermodynamics [3]. In an $n$-component fluid, by neglecting the viscous phenomena and reaction, and assuming a mechanical equilibrium in the system, linear relations can be established between the mass and heat fluxes and their driving forces, respectively. These relations are called Onsager equations and can be expressed by

$$J'_q = -L_{qq}\frac{1}{T^2}\nabla T - \frac{1}{T}\sum_{k=1}^{n-1} L_{qk}\left\{\frac{\nabla_T \mu_k}{M_k} - \frac{\nabla_T \mu_n}{M_n}\right\} \tag{10}$$

$$J_i = -L_{iq}\frac{1}{T^2}\nabla T - \frac{1}{T}\sum_{k=1}^{n-1} L_{ik}\left\{\frac{\nabla_T \mu_k}{M_k} - \frac{\nabla_T \mu_n}{M_n}\right\} \tag{11}$$

where $J'_q$ is the heat flux, $L_{qq}$, $L_{qk}$, $L_{iq}$, and $L_{ik}$ are the phenomenological coefficients called Onsager coefficients, and $\mu_k$ is the chemical potential of component $k$. Through Eqs. (3) and (11), one can get the following formulation [10]:

$$D_{ij}^M = \frac{R}{\rho_m x_n M_n}\sum_{k=1}^{n-1} L_{ik}\sum_{l=1}^{n-1}\frac{x_l M_l + x_n M_n \delta_{lk}}{M_j}\left.\frac{\partial \ln f_l}{\partial x_j}\right|_{x_j,T}$$

$$D_i^T = \frac{L_{iq}}{\rho_m T^2} \tag{12}$$

where $x_j$ is the mole fraction of component $j$, $M_j$ is the molecular weight of component $j$, $M=\Sigma_{j=1}^n M_j x_j$ is the molecular weight of the mixture, $f_j$ is the fugacity of component $j$, $R$ is the gas constant, $L_{ik}$ and $L_{iq}$ are Onsager coefficients, and $\delta_{jk}$ is the Kronecker delta ($\delta_{jk}=1$, if $j=k$ and $\delta_{jk}=0$, if $j\neq k$).

All diffusion coefficients are defined as functions of thermodynamic properties of the mixture and Onsager coefficients. As shown from Eq. (12), both thermal diffusion and molecular diffusion coefficients can be given in terms of phenomenological coefficients.

According to the theory of nonequilibrium thermodynamics, we can have a relationship between $L_{iq}$ and $L_{ik}$ by introducing the net heat of transport $Q_k^*$. This relation is given below,

$$L_{iq} = \sum_{k=1}^{n-1} L_{ik}\left(\frac{Q_k^*}{M_k} - \frac{Q_n^*}{M_n}\right) \tag{13}$$

In the model of Firoozabadi et al. the net heat of transport is given by

$$Q_i^* = -\frac{\Delta\bar{U}_i}{\tau_i} + \left(\sum_{j=1}^{n}\frac{x_j\Delta\bar{U}_j}{\tau_j}\right)\frac{V_i}{\Sigma_{j=1}^n x_j V_j} \tag{14}$$

where $\Delta\bar{U}_i$ is the residual partial molar internal energy of component $i$, $V_i$ is the partial molar volume of component $i$, and $\tau_i$ is the ratio of energy of vaporization and the energy of viscous of the flow of component $i$. In this work, the value of $\tau_i$ is fixed to 4.0, as suggested by Firoozabadi et al. [10].

For an ideal gas, the molecular diffusion coefficient can be obtained by a theoretical approach. However, for nonideal mixtures, empirical expressions are usually used [13]. The expression given by Hayduk–Minhas [13] is used in this study to calculate the diffusion coefficient in dilute binary mixture.

$$D_{ij}^0 = 13.3\times 10^{-8} V_i^{-0.71}\eta_j^{(10.2/V_1-0.791)}T^{1.47} \tag{15}$$

where $D_{ij}^0$ is the binary infinite dilution diffusion coefficient of solute $i$ in solvent $j$, ($cm^2/s$), $V_i$ is the molar volume of component $i$ at its normal boiling point ($cm^3/mol$), $\eta_j$ is the viscosity of pure component $j$ (mPa s), and $T$ is the mixture temperature (K).

For a multicomponent mixture, the Maxwell–Stephan diffusion coefficient,$\tilde{D}_{ij}$, is calculated based on the binary coefficients, $D_{ij}^0$. Taylor and Krishna [13] suggested the following formula:

$$\tilde{D}_{ij} = (D_{ij}^o)^{x_j}(D_{ji}^o)^{x_i}\prod_{\substack{k=1\\k\neq i,j}}^{n}(D_{ik}^o D_{jk}^0)^{x_k/2} \tag{16}$$

From the multicomponent mass transfer theory, the mass flux is given by

$$\mathbf{J}_m = -\rho_m B^{-1}\Gamma\nabla X \tag{17}$$

Here the matrix $B$ is defined by

$$B_{ij} = -x_i\left(\frac{1}{\tilde{D}_{ij}} - \frac{1}{\tilde{D}_{in}}\right), \quad i\neq j$$

$$B_{ij} = \frac{x_i}{\tilde{D}_{in}} + \sum_{\substack{k=1\\k\neq i}}^{n}\frac{x_k}{\tilde{D}_{ik}}, \quad i=j \tag{18}$$

and the elements of matrix $\Gamma$ are

$$\Gamma_{ij} = x_i\frac{1}{f_i}\frac{\partial f_i}{\partial x_j} \tag{19}$$

From Fick's law, the mass flux can be written as

$$\mathbf{J}_m = -\rho_m D^M \nabla X \tag{20}$$

Comparing Eq. (20) with Eq. (17), we have

$$D^M = B^{-1}\Gamma \tag{21}$$

Therefore, the diffusion coefficient, $D_{ij}^M$, can be determined based on the elements in $B$ and $\Gamma$ matrices.

With the model of Firoozabadi et al. for multicomponent mixtures and an equation of state, molecular diffusion coefficient and the thermal diffusion coefficient can be calculated according to the following procedure: (1) calculate thermodynamic properties using the equation of state; (2) calculate the molecular diffusion coefficients, $B$ ($B_{ij}$) and $\Gamma$ $\Gamma_{ij}$ matrices; (3) calculate the Onsager coefficients, $L_{ik}$ from molecular diffusion coefficients following Eq. (12); (4) calculate the Onsager coefficients, $L_{iq}$ using Eq. (13); and (5) finally, calculate the thermal diffusion coefficient and all mass flux terms.

In this work, the viscosity of the fluid mixture ($\eta_m$) is obtained with a method proposed by Lohrenz et al. [14] and given by

$$\eta_m = \eta^* + (\xi^4 - 10^{-4})/\zeta \tag{22}$$

where $\eta^*$ is the gas-mixture viscosity [15], $\zeta$ is the mixture viscosity parameter, and $\xi$ is a variable related to the reduced density ($\rho_r$) with a fourth-order polynomials.

## 5 Numerical Solution Procedure

Equations (1)–(7) are solved numerically by using the control volume method, subject to the boundary conditions of zero flux at the rigid wall; all the walls are assumed to be solid walls, so three zero components of the velocity are maintained.

The second-order centered scheme is used in the space discretization, and a semi-implicit first-order scheme is used for the temporal integration. With respect to the nonlinear convection terms, power-law scheme is applied in order to achieve higher accuracy for the combined convection and diffusion cases. The obtained linear system of algebraic equations is solved at each time step using a biconjugated gradient iteration method with a given convergence criterion, which has been confirmed over many tests for the required accuracy. At the initial time step, the velocities were set to zero in the computational domain where initial pressure and concentration are specified. The convergence criterion is set for three parameters, the pressure, temperature, and composition, respectively. The relative errors between internal iteration and any two successive time steps are calculated as follows.

For internal iteration at each time step,

$$\gamma_\theta = \frac{1}{nx\times ny\times nz}\sum_{i=1}^{nx}\sum_{j=1}^{ny}\sum_{l=1}^{nz}\left|\frac{\theta_{ijl}^{k,s+1} - \theta_{ijl}^{k,s}}{\theta_{ijl}^{k,s+1}}\right| \tag{23}$$

For convergence checking between two successive time steps after the convergence of the internal iteration,

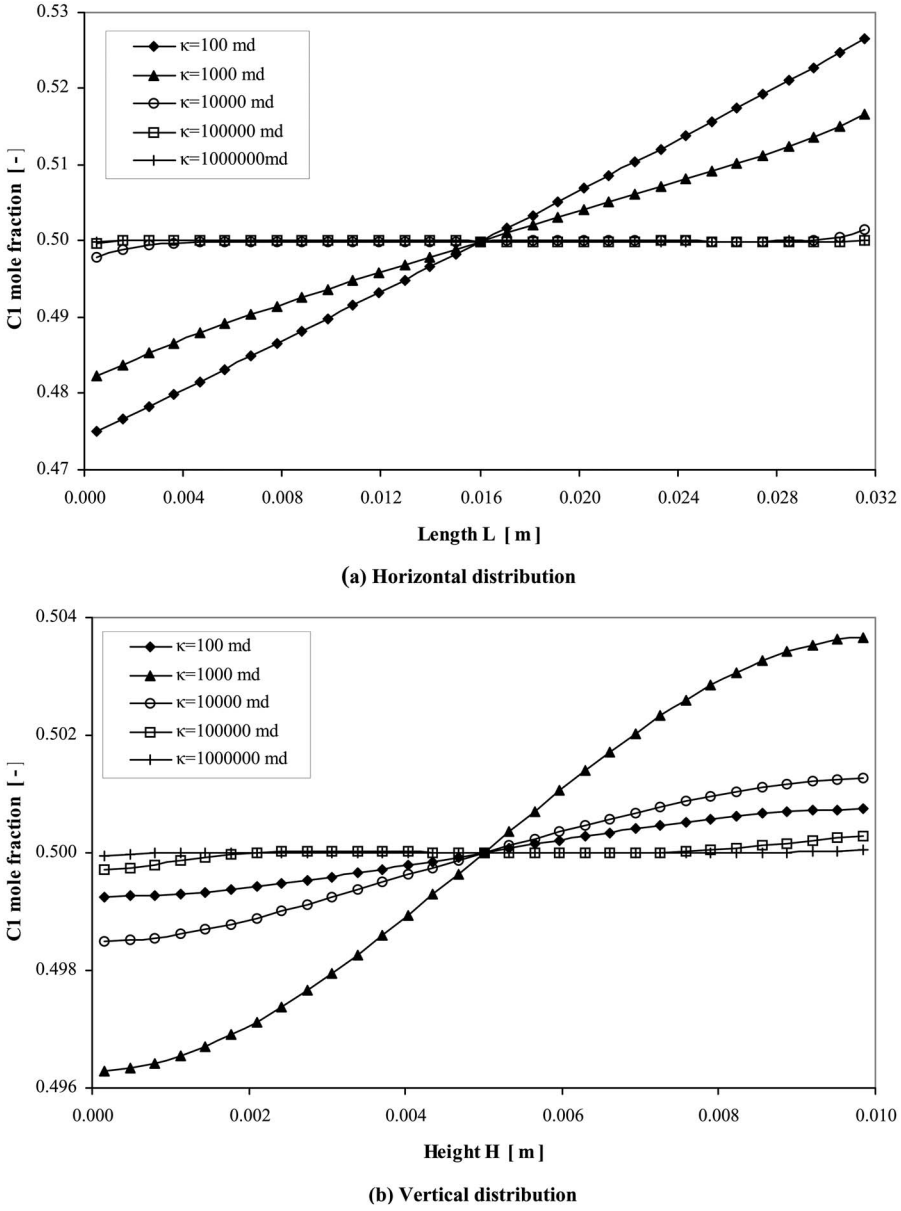


**Fig. 2 Methane (C1) mole fraction distributions along the center of the cavity**

$$\gamma_\theta = \frac{1}{nx \times ny \times nz} \sum_{i=1}^{nx} \sum_{j=1}^{ny} \sum_{l=1}^{nz} \left| \frac{\theta_{ijl}^{k,s+1} - \theta_{ijl}^{k-1,s0}}{\theta_{ijl}^{k-1,s0}} \right| \tag{24}$$

where $\theta$ represents the pressure, temperature, and composition, respectively; $i$, $j$, and $l$ represent mesh indices along $x$, $y$, and $z$ directions of the porous cavity; $k$ denotes the time step; $s$ is the indicator of inner iterations; $s0$ is the indicator of the converged inner iteration at last time step; and $nx$, $ny$, and $nz$ represent mesh numbers in $x$, $y$, and $z$ directions, respectively. The values of pressure, temperature, and composition are defined in the center of each control volume but the velocities are defined on the surface of each control volume or grid cell. Different mesh size is tested and a $31 \times 31 \times 31$ control volume has been adopted.

The solution procedure begins by assuming initial pressure, temperature, and concentration values in the mixture. The fluid is considered to be weakly compressible and the Peng–Robinson EOS is used to calculate the fluid thermodynamic properties. In fact, the density and molecular diffusion and thermal diffusion coefficients are functions of the temperature and species compositions. They are evaluated for each control volume. The thermal conductivity is assumed constant in the analysis.

## 6 Results and Discussion

**6.1 Permeability Effect on Composition Distribution.** As known, the ternary mixture in this simulation consists of 50% methane (C1, Component 1), 20% *n*-butane (*n*C4, Component 2), and 30% dodecane (C12, Component 3). The compositional separation in the mixture is investigated for permeability ranging from $10^2$ md to $10^6$ md. It is found that the effect of permeability on separation is very strong, see Figs. 2 and 3, where the distribution of methane (C1) and *n*-butane (*n*C4) is illustrated along the vertical ($z=0\sim H$, $x=L/2$, $y=W/2$) and horizontal ($x=0\sim L$, $z=H/2$, $y=W/2$) directions. It is clear to see that the separation of mixture components in the horizontal direction decreases continuously as the permeability increases from $10^2$ md to $10^6$ md. When

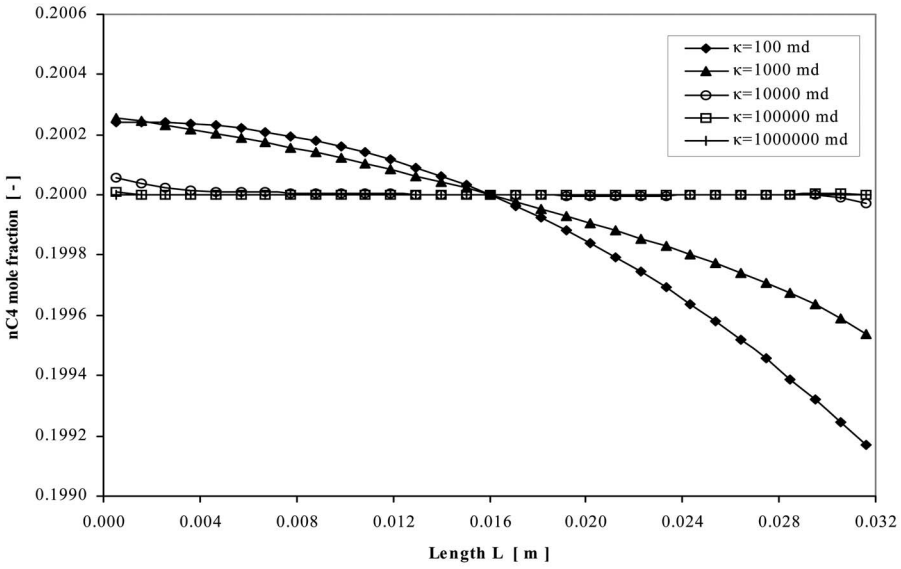


(a) Horizontal distribution

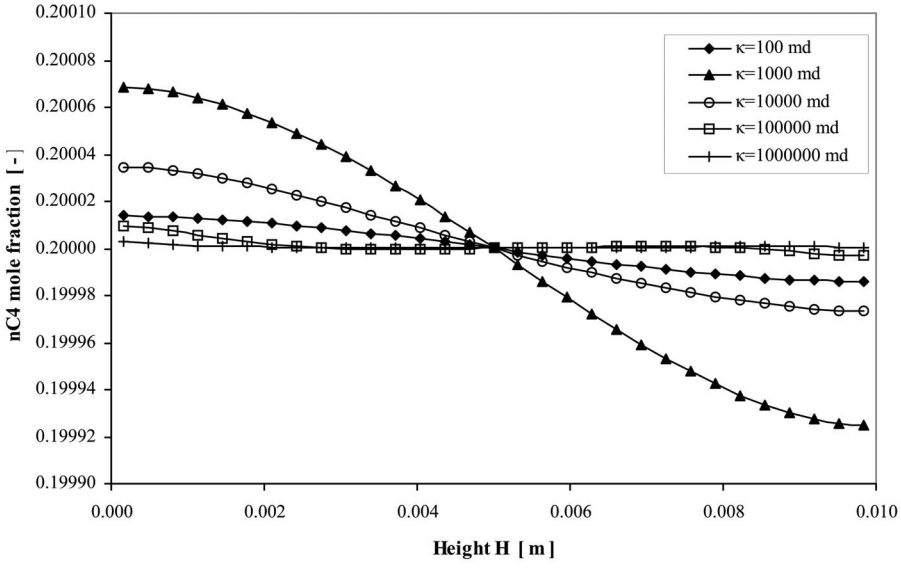


(b) Vertical distribution

**Fig. 3** ***n*-butane (*n*C4) mole fraction distributions along the center of the cavity**

the permeability is $10^2$ md, the separation happens mainly along the horizontal direction, see Figs. 2(*a*) and 3(*a*); while in the vertical direction it is very weak, see Figs. 2(*b*) and 3(*b*).

Figure 4 displays C1 and *n*C4 compositions distributions in the center *x*-*z* plane for different permeabilities ($\kappa$=10 md, $10^2$ md, $10^4$ md, and $10^6$ md). Clearly almost linear contour of methane and *n*-butane along the horizontal direction at 10 and $10^2$ md. At those low permeabilities, the convection effect is greatly suppressed and the thermodiffusion effect is dominant, see Figs. 4(*a*) and 4(*b*). As the permeability increases to $10^4$ md, the buoyancy convection begins to play a role causing a mixing in the cavity; therefore the separations of methane and *n*-butane weakened in the horizontal direction, and curved lines are found in the vertical direction, see Fig. 4(*c*). As the permeability continues to increase beyond $10^5$ md the Soret effect is greatly weakened and the dominant effect of convection makes the separation almost impossible (Fig. 4(*d*)). Figures 4(*a*) and 4(*b*) also illustrate the direction of the component separation due to thermodiffusion at low permeabilities. Methane, being the light component, moves toward the hot wall and *n*-butane, being heavier than methane, moves toward the cold wall.

As already noticed, the permeability has a significant effect on the separation of mixture components. At low permeability the Soret effect shows significant; while at high permeability convection becomes dominant. To further examine this phenomenon, a variable known as the separation ratio, $q$, is introduced:

$$q = \frac{\dfrac{C_{\max}}{(1 - C_{\max})}}{\dfrac{C_{\min}}{(1 - C_{\min})}} \tag{25}$$

where $C_{\max}$ and $C_{\min}$ are the maximum and minimum concentrations of a solute component in the porous cavity, respectively.

Figure 5 displays the variation of separation ratio as a function of permeability for methane and *n*-butane. Three distinct zones

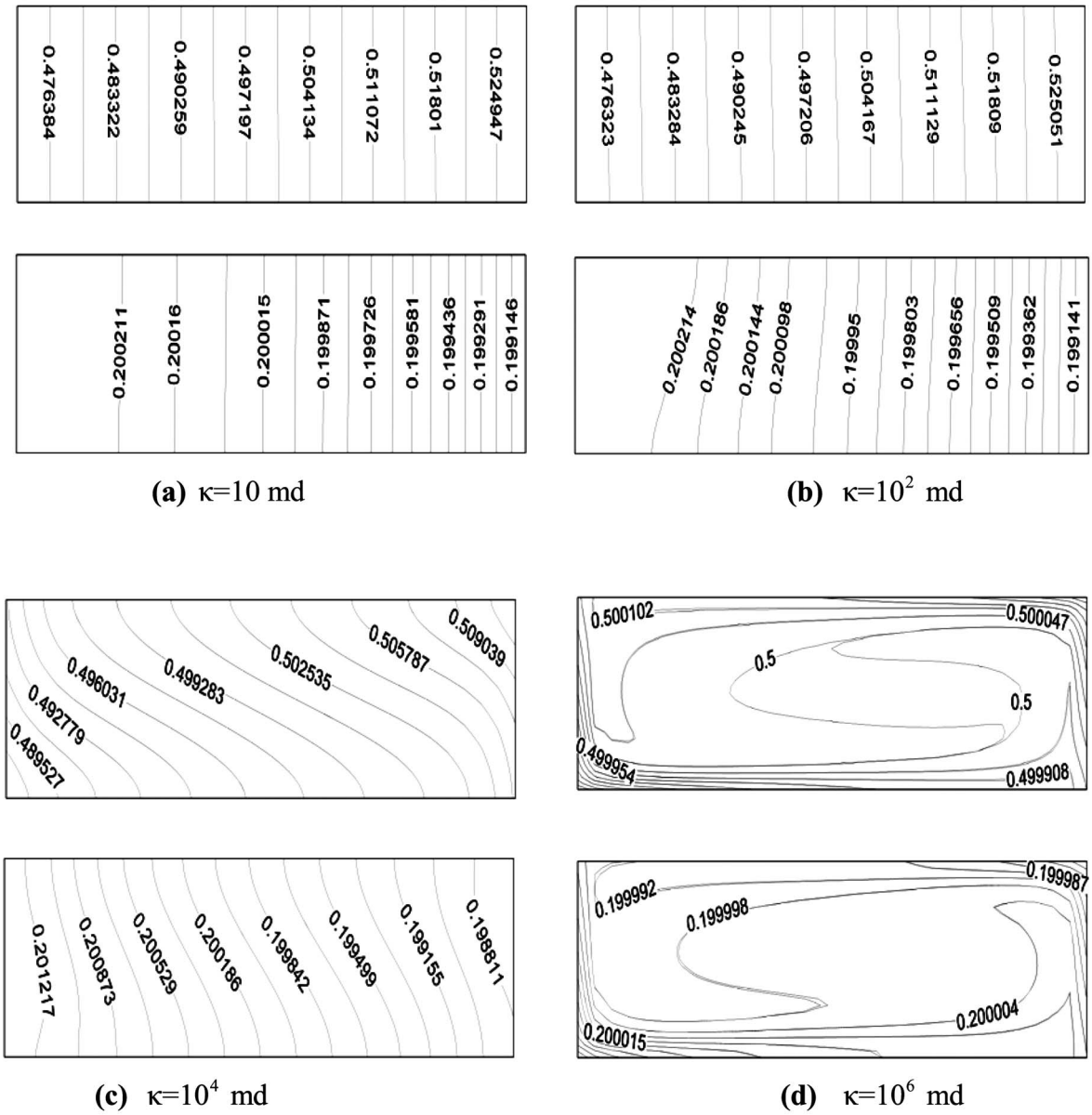


**Fig. 4 Methane and *n*-butane compositional distributions in the *x-z* plane**

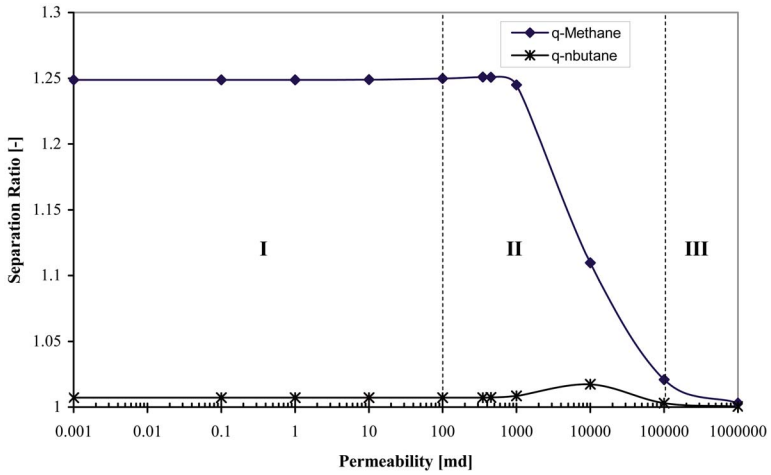


**Fig. 5 Variation of the separation ratio with the permeability for the methane and *n*-butane components**

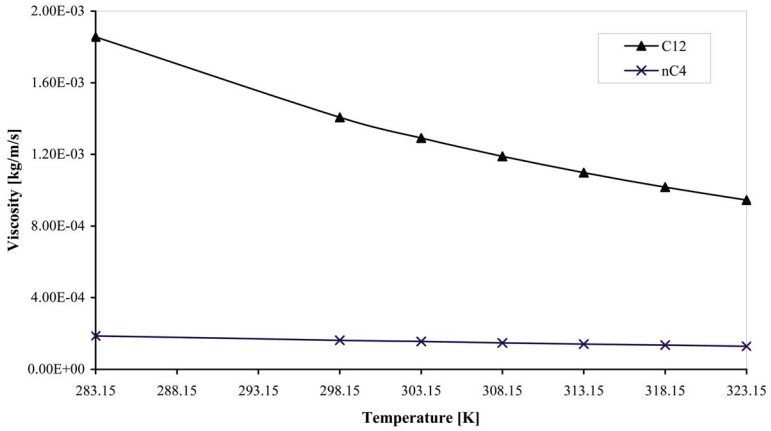


**Fig. 6 Viscosity variations with temperature of dodecane and *n*-butane**

can be identified. (I) the permeability is below $10^2$ md. In this zone, the Soret effect is completely dominant. The separation ratio remains constant, which is about 1.248 for methane and 1.007 for *n*-butane. (II) The permeability is between $10^2$ md and $10^5$ md. In this zone both Soret and convection play important roles and as a result of this combined effect the separation ratio gradually reduces as the permeability increases. (III) The permeability is higher than $10^5$ md. In this zone the convection is the dominant mechanism; therefore the separation ratio decreases rapidly toward 1, which indicates that the components are largely mixed in the cavity and no noticeable separation can be achieved.

This theoretical analysis can be very useful in many ways. For

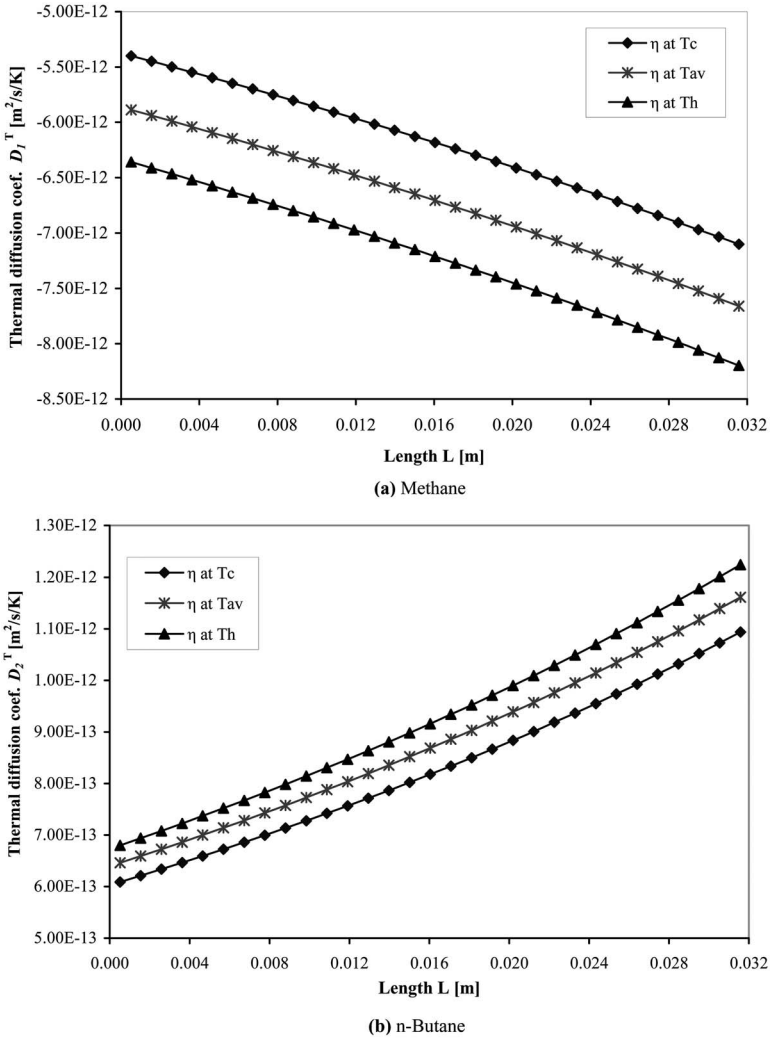


**Fig. 7 Thermal diffusion coefficient distributions for methane and *n*-butane along the horizontal direction ($\kappa=10^2$ md)**

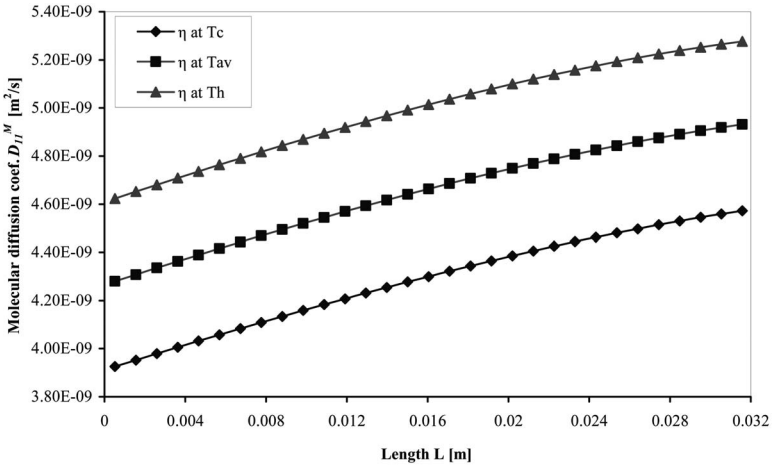


**Fig. 8 Variation of the molecular diffusion coefficient of methane along the horizontal cavity ($\kappa=10^2$ md)**

example, in the case of measuring diffusion coefficients in porous cavity, an optimal design of the porous cavity will be the key to determine if the experiments can be feasibly performed. A too low permeability cavity will cause a long time for experiments to establish the steady state; therefore it is ineffective or even infeasible. A too high permeability cavity, on the other hand, will fail to suppress the negative effect of convection. If the mixture of methane (50%), *n*-butane (20%), and dodecane (30%) is to be measured, the optimal permeability would be around $10^2$ md.

Benano-Melly et al. [16] found that the maximum value for the separation ratio, $q=q_{\max}$, existed for the permeability value, $\kappa=\kappa_m$, given by

$$\kappa_m = \frac{\eta_m D^M \phi \sqrt{120}}{g\beta_T \Delta T H \rho} \tag{26}$$

This analytical expression predicts that the maximum separation of methane will occur at $\kappa_m=320$ md whereas our numerical calculation showed the maximum separation ratio at $\kappa_m=350$ md ($q_{\max}=1.2509$). This discrepancy between the analytical and the numerical modeling is justified by the fact that in our case the solutal buoyancy is included and both the thermal and molecular diffusion coefficients are functions of temperature and fluid mixture.

**6.2 Viscosity Effect on Diffusion Coefficients..** All the calculations in previous sections assume that the viscosities of the mixture components are constants and they are evaluated at the average temperature ($T_{\text{av}}=303$ K). In this section the viscosity variation due to the temperature will be considered for each component in order to investigate the viscosity effect on $D^T$, $D^M$ and the compositional calculation. Figure 6 shows the variation of the dodecane and *n*-butane viscosity as a function of the temperature. It can be seen that the viscosity of dodecane (C12, carrier fluid) changes significantly with the temperature. When the temperature varies between $T_c=283$ K and $T_h=323$ K the viscosity of dodecane varies between $1.85\times10^{-3}$ Pa s and $9.45\times10^{-4}$ Pa s, while for *n*-butane no major variation is observed. As for the methane it was found that the viscosity does not vary with temperature, which is similar to the *n*-butane.

In this section we estimated the viscosity at three different temperatures, which are the cold temperature $T_c$, the hot temperature $T_h$, and the average temperature $T_{\text{av}}$. For each temperature condition, the calculation is repeated taking into consideration the new estimated viscosity. The variations of molecular diffusion and thermal diffusion coefficients are shown in Figs. 7 and 8 when the permeability is set equal to $10^2$ md. It is found that the thermal diffusion is affected by the change in viscosity. The deviation of methane thermal diffusion coefficient is about $\pm10\%$ (see Fig. 7(*a*)), while the deviation of *n*-butane thermal diffusion coefficient is about $\pm4.5\%$, (see Fig. 7(*b*)).

Figure 8 illustrates the variation of molecular diffusion coefficient along the horizontal center line direction for methane when the permeability is set equal to $10^2$ md. Results reveal that again the molecular diffusion coefficient based on the viscosity at $T_c$ and $T_h$ deviates about $\pm9\%$ from the one at $T_{\text{av}}$, see Fig. 8. Similar variation is observed for the *n*-butane.

## 7 Conclusion

The thermosolutal convection of a ternary mixture of C1–*n*C4–C12 in $Al_2O_3$ porous cavity maintained at 35.0 MPa, is investigated for different permeabilities. The model was based on the nonequilibrium thermodynamics theory and diffusion coefficients were calculated with time and space dependent fluid properties and compositions. The component concentration distribution and the separation ration were used to examine the behavior of the thermodiffusion and buoyancy-driven convection. The impact of permeability variation on the component separation results at steady state is numerically investigated. The viscosity is found to influence the evaluation of the molecular and thermal diffusion coefficients. The result showed that with variable viscosity the flow due to thermodiffusion is affected.

## Acknowledgment

The authors acknowledge the full support of the Canadian Space Agency (CSA) and the Natural Sciences and Engineering Research Council of Canada (NSERC).

## Nomenclature

$C_p$ = heat capacity at constant pressure (J kg$^{-1}$ K$^{-1}$)
$D^M$ = molecular diffusion coefficient in a free fluid (m$^2$ s$^{-1}$)
$D_T$ = thermal diffusion coefficient in a free fluid (m$^2$s$^{-1}$ K$^{-1}$)
$D_1^T$ = thermal diffusion coefficient in Component 1 (methane) (m$^2$ s$^{-1}$ K$^{-1}$)
$D_2^T$ = thermal diffusion coefficient in Component 2 (*n*-butane) (m$^2$ s$^{-1}$ K$^{-1}$)
$\tilde{D}_{ij}$ = the Maxwell–Stephan diffusion coefficient, (m$^2$ s$^{-1}$)
$g$ = gravitational acceleration=9.81 (m/s$^2$)
$\mathbf{J}_{mi}$ = molar diffusion flux (mol m$^{-2}$ s$^{-1}$)
$k$ = thermal conductivity (W m$^{-1}$ K$^{-1}$)

$L_{ij}$ = onsager coefficient
md = millidarcy (1 md=$9.87\times10^{-16}$ $m^2$) is a unit of permeability
$n$ = number of components in the mixture
$q$ = separation ratio
$T$ = temperature (K)
$t$ = time (s)
$u$ = velocity component in the $x$-direction ($m\ s^{-1}$)
$v$ = velocity component in the $y$-direction ($m\ s^{-1}$)
$\mathbf{V}$ = fluid velocity vector $(u,v,w)$ ($m\ s^{-1}$)
$w$ = velocity component in the $z$-direction ($m\ s^{-1}$)
$x_1$ = mole fraction of Component 1
$x$ = dimension (m)
$y$ = dimension (m)
$z$ = dimension (m)

### Greek Symbols

$\beta_T$ = coefficient of thermal expansion ($1/K$)
$\phi$ = porosity
$\kappa$ = permeability ($m^2$)
$\eta_m$ = dynamic viscosity of the fluid mixture ($kg\ m^{-1}\ s^{-1}$)
$\rho$ = fluid mixture density ($kg/m^3$)
$\rho_m$ = molar density of fluid mixture ($kmol/m^3$)
$\omega$ = mass fraction

### Subscripts

$e$ = effective
$f$ = fluid mixture
$m$ = molar quantities
$p$ = porous media

## References


[1] Ludwig, C., 1856, Sitzber. Akad. Wiss. Vien Math.-Naturw., **20**, p. 539.
[2] Soret, C., 1880, "Influence de la Temperature sur la Distribution des sels dans leurs Solutions," Acad. Sci., Paris, C. R., **91**, pp. 289–291.
[3] de Groot, S. R., and Mazur, P., 1984, *Non-Equilibrium Thermodynamics*, Dover, New York.
[4] Leahy-Dios, A., Bou-Ali, M., Platten, J. K., and Firoozabadi, A., 2005, "Measurements of Molecular and Thermal Diffusion Coefficients in Ternary Mixtures," J. Chem. Phys., **122**(23), p. 234502.
[5] Haugen, K. B., and Firoozabadi, A., 2005, "On Measurement of Thermal Diffusion Coefficients in Multicomponent Mixtures," J. Chem. Phys., **122**(1), p. 014516.
[6] Platten, J. K., 2006, "The Soret Effect: A Review of Recent Experimental Results," ASME J. Appl. Mech., **73**, pp. 5–15.
[7] Costeseque, P., Pollak, T., Platten, J. K., and Marcoux, M., 2004, "Simultaneous Evaluation of Soret and Fick Coefficients in a Free and a Packed Vertical Gradient Soret Cell," *Sixth International Meeting on Thermodiffusion*, IMT6, Varenna, Italy.
[8] Riley, M. F., and Firoozabadi, A., 1998, "Compositional Variation in Hydrocarbon Reservoirs With Natural Convection and Diffusion," AIChE J., **44**(2), pp. 452–464.
[9] Delware, F., Chacha, M., Ghoraye, K., and Saghir, M. Z., 2004, "Compositional Variation Considering Diffusion and Convection for Binary Mixture in Porous Media," J. Porous Media, **7**(2), pp. 1–19.
[10] Firoozabadi, A., Ghorayeb, K., and Shukla, K., 2000, "Theoretical model of Thermal Diffusion Factors in Multicomponent Mixtures," AIChE J., **46**(5), pp. 892–900.
[11] Jiang, C. G., Jaber, T. J., Batalle, H., and Saghir, M. Z., 2008, "Simulation of Ludwig-Soret Effect of a Water-Ethanol Mixture in a Cavity Filled With Aluminum Oxide Powder Under High Pressure," Int. J. Therm. Sci., **47**(2), pp. 126–135.
[12] Pan, S., Yan, Y., Jaber, T. J., Kawaji, M., and Saghir, M. Z., 2007, "The Evaluation of Thermal Diffusion Models for Ternary Hydrocarbon Mixture," J. Non-Equilib. Thermodyn., **32**(3), pp. 1–9.
[13] Taylor, R., and Krishna, R., 1993, *Multicomponent Mass Transfer*, Wiley, New York.
[14] Lohrenz, J., Bray, B. G., Aime, M., and Clark, C. R., 1964, "Calculation of Viscosities of Reservoir Fluids From Their Compositions," J. Pet. Technol., **16**, pp. 1171–1176.
[15] Jossi, J. A., Stiel, L. I., and Thodos, G., 1962, "The Viscosity of Pure Substances in the Dense Gaseous and Liquid Phases," AIChE J., **8**(1), pp. 59–63.
[16] Benano-Melly, L. B., Caltagirone, J. P., Faissat, B., Montel, F., and Costeseque, P., 2001, "Modeling Soret Coefficient Measurement Experiments in Porous Media Considering Thermal and Solutal Convection," Int. J. Heat Mass Transfer, **44**(7), pp. 1285–1297.